Dicle Üniversitesi
Mühendislik Fakültesi

mühendislikdergisi
journal of engineering

Dicle Üniversitesi Mühendislik Fakültesi
mühendislikdergisi
Cilt: 16, Sayı: 3, Eylül 2025 ISSN: 1309-8640

Dicle Üniversitesi Adına yayın Sahibi / Privilige Owner
Mehmet Siraç ÖZERDEM

Baş Editör / Editor-in-Chief
Mehmet Siraç ÖZERDEM

Alan Editörleri / Field Editors
Mehmet Siraç Özerdem
Atilla Gencer Devecioğlu
Mehmet Salih Keskin
İdris Bedirhanoğlu
Cafer Budak
Mehmet Emin Öncü
Hasan Polat
Ömer Türk
Önder Aydemir
Abdulkadir Albayrak
Murat Erdemoğlu
Bilal Gümüş
Dilek Eren Akyüz
Erkan Bahçe

Teknik Editör / Technical Editor
Mesut ŞEKER

Yazışma Adresi
Mühendislik Dergisi, Koordinatörlük ve Yayın Bürosu,
Dicle Üniversitesi, Mühendislik Fakültesi, 21280 Diyarbakır
Telefon : +90-412 241 10 00 (Dahili: 3637)
Elektronik posta : muhendislikdergisi@dicle.edu.tr
web : http://dergipark.gov.tr/dumf, https://duje.dicle.edu.tr/journal/

Dergide yayınlanan yazılar izinsiz başka bir yerde yayınlanamaz veya bildiri olarak sunulamaz.

ISSN Basılı Materyal: 1309-8640
Online ISSN: 2146-4391

Hakem Listesi / *Reviewers List*

Dergimize yayınlanmak üzere gönderilmiş olan makaleleri titiz bir şekilde değerlendiren kıymetli hakem hocalarımıza, değerli katkılarından dolayı teşekkür eder, katkılarının devamını dileriz.

We greatly appreciate the contributions made by the scientists, who worked as reviewers for Dicle University Journal of Engineering (DUJE) and we expect their contributions to the following journal issues.

Halil Şenol (Giresun Üniversitesi)

Mehtap Erşan (Sivas Cumhuriyet Üniversitesi)

Müge Balkaya (ITU)

Gökçe Çiçek İnce (Muğla Sıtkı Koçman Üniversitesi)

Selçuk Bildik (Nişantaşı Üniversitesi)

Arda Burak Ekmen (Harran Üniversitesi)

Kemal Beyen (Kocaeli Üniversitesi)

Fevzi Sarıtaş (ITU)

Mumin Tolga Emirler (YTU)

Senem Kurşun Bahadır (ITU)

Osman Taha Şen (ITU)

Bilal Alatas (Fırat Üniversitesi)

Ersin Çağlar (Lefke Avrupa Üniversitesi)

Mustafa Özen (Harran Üniversitesi)

Gurbet Örçen (DU)

Murat Karabatak (Fırat Üniversitesi)

Selma Bulut (Kırklareli Üniversitesi)

Mustafa Mikail Özçiloğlu (Kilis 7 Aralık Üniversitesi)

Burak Yön (Munzur Üniversitesi)

Mehmet Karataş (Munzur Üniversitesi)

Gürcan Samtaş (Düzce Üniversitesi)

Yunus Emre Gür (Fırat Üniversitesi)

Senem Yılmaz Çetin (DU)

Yunus Efe (Karacadağ Kalkınma Ajansı)

İnan Ünal (Munzur Üniversitesi)

Emrah Aslan (Mardin Artuklu Üniversitesi)

Mustafa Tosun (Kütahya Dumlupınar Üniversitesi)

Eda Akman Aydın (Gazi Üniversitesi)

Onur Onat (İnönü Üniversitesi)

Arif Gürel (Harran Üniversitesi)

Busra Akturk (İstanbul Bilgi Üniversitesi)

Senem Bilici (Akçansa Çimento Sanayi ve Ticaret A.Ş)

Muhammed Cihad Arslanoğlu (DU)

Ahmet Elbir (YTU)

Uğur Çavdar (İzmir Demokrasi Üniversitesi)

Kadir Turan (DU)

Mustafa Kumral (McGill Üniversitesi)

Didem Eren Sarıcı (İnönü Üniversitesi)

Sinan Maraş (Ondokuz Mayıs Üniversitesi)

Mesut Hüseyinoğlu (DU)

Hüseyin Fırat (DU)

Musab Coşkun (Bingöl Üniversitesi)

Bahadır Ok (Adana Alparslan Türkeş Bilim ve Teknoloji Üniversitesi)

Özgür Yıldız (YTU)

Sadık Özgür Değertekin (DU)

İbrahim Baran Karaşin (DU)

Ercan Işık (Bitlis Eren Üniversitesi)

Vedat Çelik (Fırat Üniversitesi)

Arif Gülten (Fırat Üniversitesi)

Fuat Peker (DU)

Berna Gürler Arı (Milli Savunma Üniversitesi)

Çağatay Murat Yılmaz (KTU)

Musa Demir (Giresun Üniversitesi)

Nesin İlgin Beyazit (DU)

Mesut Hüseyinoğlu (DU)

Osman Yiğid (Bitlis Eren Üniversitesi)

Zeki Omaç (Munzur Üniversitesi)

Mehmet Emin Asker (DU)

Erol Kılıçkap (DU)

Halil Kılıç (Kirklareli Universitesi)

Abdullah Erhan Akkaya (İnönü Üniversitesi)

Mehmet Zübeyir Ünlü (İYTE)

Abdullah Dilsiz (Ankara Yıldırım Beyazıt Üniversitesi)

Ebru Harmandar (Muğla Sıtkı Koçman Üniversitesi)

Murat Şen (Fırat Üniversitesi)

Ahmet Burak Tatar (Fırat Üniversitesi)

Kadir Kaya (Ondokuz Mayıs Üniversitesi)

Bahadır Akkurt (Abant İzzet Baysal Üniversitesi)

İçindekiler / *Table of Contents*

Elektrik Elektronik Mühendisliği / Electrical and Electronics Engineering

Hybrid Heuristic and Particle Swarm Optimization Approach to Cloud Task Scheduling (Research Article)
Cebrail Barut, Kazım Fırıldak **549**

Explainable Hybrid Deep Learning–Transformer Approach for Insulin Prediction (Research Article)
İhsan Uysal **559**

Investigation of Geometric Invariance Properties of Hu Moments for Image Processing Applications (Research Article)
Ethem Sefa Küçükyılmaz, Erhan Akın **571**

Improving Fish Weight Estimation with Quantile and Box-Cox Transforms: Comparative Machine Learning Models (Research Article)
Hatice Esen, Havvanur Taşdelen, Sefa Küçük, Işıl Karabey Aksakallı **581**

EEG-Based Comparative Study of Brain Activity during Imagined Natural and Induced Water and Saliva Swallowing (Research article)
Sevgi Gökçe Aslan **599**

Integrated Biometric Signature Verification: A Hybrid Framework for Digital and Physical Signature Authentication (Research Article)
Zeynep Akalın, Fatih Mehmet Gürbüz, Hasan Şenmemiş, Ahmet Bilge, Nursena Bayğın, Sefa Küçük **611**

Digital Twin Prototype in Unity 3D: Real-Time Greenhouse Monitoring and Control (Research Article)
Sezen Bal, Kübra Nur Akpınar, Ayşe Yayla, Yekta Muhammet Özcan, Oğuz Ayçiçek **625**

Chen Kaotik Sisteminin Adaptif Kontrolü (Research Article)
Mehmet Güzel, Muhittin Bayram **633**

NeuroHybridNet: A Hybrid EEG Classification Model with Autoencoder-Enhanced Fractal-Wavelet Features (Research Article)
Hazret Tekin **643**

Investigation of the Effect of Notches Opened on the Stator Shoe on the Cogging Torque by Parametric Analysis in Inner Rotor Single-Phase BLDC Motors (Research Article)
Sedat Yıldız, Ahmet Orhan **663**

Classification of Lumbar Spine Degenerative Diseases Using Deep Learning Techniques (Research Article)
Bora Bingöl, İbrahim Öztürk, Zeynep Çağla Dönmez, Ahmet Sagılı **669**

Makina Mühendisliği / Mechanical Engineering

Advancing Welding Quality through Intelligent TIG Welding: A Hybrid Deep Learning Approach for Defect Detection and Quality Monitoring (Research Article)
Emre Görgün **677**

An Investigation of Driver Brake Pedal Stroke Input on Regenerated Braking Energy in Electric Vehicles via Dynamic Programming (Research Artilce)
Nurettin Okan Çaycı, Erkin Dinçmen, İlyas İstif **687**

CTP kompozit plakaların çoklu cıvata bağlantı davranışlarının incelenmesi (Araştırma Makalesi)
Investigation of multi-bolted connection behaviors of GFRP composite plates (Research Article)
Çağdaş Şen, Fırat Aydın, Mehmet Emin Deniz **697**

Investigation of mechanical properties in variable oriented glass fiber reinforced insulators (Research Artilce)
Selçuk ilhan Bilgin, Hakan Çetinel, Enver Yalçın **707**

Modal Analysis of Sandwich Structure Using Finite Element Approach (Research Article)
Kübra Çağla Çıbıkçı **717**

Parametric Impacts of Metabolic Rate and Occupancy on Internal Thermal Gains in Buildings (Research Article)
Ahmet Yüksel **725**

Determination of the Effects of Structural Design Parameters on Dynamic Characteristics of Centrifugal Pump Systems (Research Artilce)
Murat Şen **739**

Worm Gear Reducer Design An Strength Analysis KissSoft-KissSys Program (Research Artilce)
Mustafa Timur **749**

Identification of Dynamic Properties of a Fixed-Supported T-Frame Using Experimental Modal Analysis (Research Artilce)
Ali Osman Yaşa, Mesut Hüseyinoğlu **755**

Tensile and Wear Behaviour of Hybrid SiC-C Reinforced Epoxy Composites (Research Artilce)
Mehmet Emin Demir, Raşit Koray Ergün **763**

Maden Mühendisliği / Mining Engineering

Değişken piyasalar için memetik algoritma ile sınır tenörleri eniyilemesi (Araştırma Makalesi)
Optimization of cut-off grades with memetic algorithms for volatile markets (Research Article)
Erhan Çetin **771**

İnşaat Mühendisliği / Civil Engineering

Yerel zemin koşullarının ve deprem ivmelerinin betonarme yüksek katlı binaların performansına etkisi (Araştırma Makalesi)
The Effect of Local Soil Conditions and Earthquake Zones on the Performance of High-Rise RC Buildings (Research Article)
Jülide Yüzbaşı, Fatih, Avcil, Aydın Büyüksaraç, Mehmet Salih Keskin, Ercan Işık, Enes Arkan **777**

Effects of Alternative Binder and Aggregate Use on the Compressive Strength of Concrete (Research Article)
Mustafa Pala, Nihan Gülmez **789**

Tarihi yapılarda tespit edilen sorunların yapı malzemeleri üzerinden iyileştirilmesi (Derleme Makalesi)
Improving the deteriorations of historic buildings through building materials (Review Article)
Ebru Kılıç Bakırhan **797**

Damage and Interventions to Historical Masonry Buildings: Good and Ill Practices (Research Article)
Elizabeth Vintzileou **805**

Nanofiber Selüloz Katkılı Kireç Esaslı Enjeksiyon Malzemelerinin Tasarımı ve İncelenmesi (Araştırma Makalesi)
Design and Investigation of the Lime Based Grouts Incorporated with Nanofiber Cellulose (Research Article)
Ali Sayar, Didem Oktay **813**

Zayıf bir zeminin ıslahı için oluşturulan geçirimli kazıklarda farklı agrega ve bağlayıcı kullanımının etkisinin araştırılması (Araştırma Makalesi)
Investigation the effect of using different aggregates and binders in pervious piles for the soil stabilization of a weak soil (Research Article)
Talha Sarıcı, Mustafa Özcan, Rüçhan Enes Korkmaz **825**

Endüstri Tipi Çelik Yapıların Farklı Rüzgâr Yönetmeliklerine Göre Yapısal Analizlerinin Karşılaştırılması (Araştırma Makalesi)
Comparative Analysis of Structural Performance of Industrial Steel Buildings According to Different Wind Codes (Research Article)
Hakan Küni, İbrahim Behram Uğur **833**

Seismic Risk Assessment of Existing RC Buildings in Muğla (Research Article)
Vesile Hatun Akansel, Mehmet Artun Baki **849**

Dicle Üniversitesi Mühendislik Fakültesi (DÜMF) Mühendislik Dergisi yayınlarında varılan sonuçlar veya fikirlerin sorumluluğunu taşımamaktadır. Üniversite'nin, bu yayında ileri sürülen bilgi, alet, ürün veya işlevin doğruluğu, bütünlüğü, uygunluğu ve kullanılırlığı konusunda bir yüklenimi ve iddiası bulunmamaktadır. Bu nedenle herhangi bir şekilde sorumlu tutulamaz.

Bu yayının herhangi bir kısmı, mühendislik dergisinin yazılı izni olmadıkça kaynak gösterilmeden yayınlanamaz, bilgi saklama sistemine alınamaz veya elektronik, mekanik, fotokopi, kayıt veya başka sistemlerle çoğaltılamaz.

Dicle University
Journal of Engineering
https://dergipark.org.tr/tr/pub/dumf
duje.dicle.edu.tr

Research Article

Hybrid Heuristic and Particle Swarm Optimization Approach to Cloud Task Scheduling

Cebrail BARUT[1]*, Kazım FIRILDAK[2]

[1] Firat University, Continuing Education Center, cbarut@firat.edu.tr, Orcid No: 000-0003-2756-5434

[2] Firat University, Department of Computer Technology, kfirildak@firat.edu.tr, Orcid No: 0000-0002-1958-3627

ARTICLE INFO

Article history:

Received 20 March 2025
Received in revised form 8 May 2025
Accepted 31 July 2025
Available online 30 September 2025

Keywords:

Cloud Computing, Task Scheduling, Heuristic Particle Swarm Optimization

Doi: 10.24012/dumf.1662221

* Corresponding author

ABSTRACT

Scheduling tasks on cloud systems is a critical optimization problem that aims to distribute tasks among available resources in the most effective way. This issue falls under the category of NP-hard problems and generating exact and deterministic solutions requires high computational costs. Metaheuristic approaches have proven to provide successful results in solving such problems. Particle Swarm Optimization (PSO), one of these algorithms, is a widely used method in the literature due to its advantages, such as fast convergence, simple applicability, and low computational cost. In this study, a hybrid heuristic-based Particle Swarm Optimization approach is proposed to improve task scheduling efficiency. The proposed approach improves the solution quality by integrating a heuristic mechanism into the random population generation process of PSO. In comparison to First Come First Serve, Ant Colony Optimization (ACO), and conventional PSO, the suggested approach delivers better makespan and reduced energy consumption, according to the simulation analysis carried out in the CloudSim simulation environment. According to simulations, Heuristic PSO outperforms traditional PSO and ACO methods in terms of makespan time, reducing it by an average of 61.42% and 62.84%, respectively. It also uses 26.18% less energy than PSO and 27.33% less than ACO, according to its energy consumption data. The results show that the suggested method offers a more effective substitute for scheduling tasks in cloud computing systems.

Introduction

The architecture of cloud services, which are becoming an essential part of the modern digital world, is extremely complicated. These systems can consist of a variety of components, ranging from network servers to personal computers, and are built by integrating numerous computers with advanced engineering techniques [1]. They can react quickly to different user task demands because of their large resource pool [2].

In terms of their vast hardware infrastructure and services, cloud systems are complicated, and managing them can be difficult [3]. Task scheduling is a crucial procedure in these systems that guarantees that tasks are assigned to the best available resources [4]. Task scheduling is made considerably more difficult by the cloud environment's abundance of large-scale resources. By guaranteeing effective resource utilization, an efficient task scheduling system maximizes workloads. By taking into account various user requests, it simultaneously enhances resource management, boosts performance, lowers expenses, and greatly improves Quality of Service (QoS). For this reason, the task scheduling procedure is crucial to the efficacy and durability of cloud systems. Because task scheduling in cloud systems is a complicated problem that needs to be optimized, numerous approaches have been put out in the literature to address this issue [5]. Metaheuristic approaches are widely employed in task scheduling problems because they can produce efficient solutions by conducting effective searches in a vast solution space. These techniques can, however, occasionally have drawbacks such becoming trapped in local minima, slow convergence, and high processing costs. The mixed usage of heuristic approaches and metaheuristics gives substantial advantages to overcome these issues and obtain more effective solutions. By employing strategies unique to the problem's structure, heuristic approaches can generate quick and effective first solutions; however, metaheuristic methods optimize these answers and arrive at the global optimum more quickly. This hybrid strategy can offer high efficiency in task scheduling processes and has the ability to lower computing costs while improving the quality of the solutions.

This work proposes a heuristic approach to a hybridized version of Particle Swarm Optimization (PSO) [6], a metaheuristic method commonly employed in cloud system task scheduling research. Below is a list of the suggested method's most inventive features:

• Heuristic approaches reduce the propensity of conventional PSO to become trapped in local minima, leading to quicker and more effective solutions.

• In certain applications, PSO's poor convergence speed is a drawback. The suggested approach strengthens with heuristic elements to achieve faster convergence.

• By improving both makespan (completion time) and total energy consumption, the suggested approach helps cloud systems become more sustainable.

• The addition of heuristic components to the PSO algorithm yields more reliable and superior results when compared to First Come First Server (FCFS), ACO, and PSO methods.

The remaining of the paper is organized as follows: Section 2 presents the literature review. Section 3 describes the problem definition and methodology. Section 4 presents and discusses the experimental results. Finally, Section 5 concludes the paper by highlighting the main findings.

Literature Research

Real-time computing capabilities can be unilaterally provided and managed by cloud computing without the need for human contact[7]. It uses task scheduling to perform these operations. Task scheduling is the procedure used in cloud systems [8]. Of allocating user tasks to the best virtual machines based on a predetermined plan. The cloud system's dynamic and multifaceted structure must be considered in the task scheduling method. The goal for which the task scheduling technique is employed is also crucial. Scheduling tasks on cloud systems can be designed to include one or more of these factors, including makespan, energy consumption, and financial cost. The task requested by the users can be completely allocated to the virtual machines or the tasks can be assigned to the servers in parts. In this case, it is necessary to consider the interdependencies of the parts within the task. In general, task scheduling methods used in cloud systems can be shown in Fig.1.



Figure 1. Task categories and the nature of the suggested.

Heuristic algorithms offer an effective solution for low-complexity and static systems [9]. The algorithms are easy to implement and have low computational cost. However, they give low performance to dynamic systems such as clouds and edges. Since heuristic methods are designed for a specific problem, they are difficult to apply directly to different problems. In the literature, Min-Min, Max-Min, Round Robin (RR), Shortest Job First (SJF), FCFS and Best Fit (BF) are the main heuristic methods. A modified round-robin (MRR) algorithm, an improved version of RR, is proposed [10]. The proposed method gave better results in terms of average waiting time and turnaround time. An improved Min-Min method that maximizes the total execution time and resource utilization of tasks is proposed [11]. Experimental results show that the proposed method achieves the best makespan values compared to the Sufferage and Min-Min algorithms.

Metaheuristic methods generally provide effective solutions for complex and dynamic task scheduling problems in cloud environments [12]. Numerous NP-hard problems can be effectively solved using metaheuristic techniques, which have also been successfully adapted for use in cloud systems. Metaheuristic algorithms used in the literature can be modified to address issues with task scheduling, with appropriate representation. PSO [13], Grey Wolf Algorithm (GWO) [14], Firefly Algorithm [15], ACO [16], Whale Optimization algorithm (WOA) [17], and Jellyfish Search Optimizer (JSO) [18] have been effectively modified to address issues with cloud work scheduling. PSO has been used for task scheduling in a cloud environment [19]. This research compares the work plans produced using techniques such as the Genetic Algorithm (GA), Brute Force (BF), First-In-First-Out (FIFO), and Delay Scheduling Policy (DSP). According to the experimental results, the PSO algorithm offers a more effective way to schedule tasks in a cloud environment than other approaches. It also gives notable benefits when it comes to optimizing the makespan value. An enhanced variant of Henry Gas Resolution Optimization, the Henry Gas-Harris Hawks-Comprehensive Contrast (HGHHC) approach, is suggested in [20]. The values of 34.30, 72.95 and 28.67 are for makespan and 16.92, 28.72 and 25.58 for resource utilization, respectively. Experimental results show that the HGHHC algorithm provides better simulated makespan and resource utilization compared to previous approaches. An adapted Chimpanzee Optimization Algorithm with improved exploration and exploitation stages is proposed to solve the task scheduling problem in cloud systems [21]. The success of the proposed method is tested for different simulation scenarios and the proposed method achieves a makespan improvement of approximately 30% compared to standard task scheduling algorithms. A method based on the Cloneable Jellyfish Algorithm is proposed for optimal task allocation in metaheuristic cloud environments [18]. The suggested algorithm's most innovative feature is its regulated dynamic population expansion, which helps to prevent local minima during the exploration stage. It also has a distinct cloning method to minimize the similarity between candidates in population growth. The experiments performed on the

Cloudsim simulator proved the success of the suggested approach in compared to traditional scheduling techniques.

Hybrid methods are used by combining different optimization techniques to provide more effective solutions addressing issues with cloud computing task scheduling [22]. These techniques, which are usually a combination of metaheuristic (e.g. GA, PSO, ACO, SA) and heuristic (e.g. RR, SJF) methods, provide higher efficiency and accuracy by utilizing the strengths of both methods. While some algorithms (e.g., SA and ACO) can get stuck in local minima, hybrid approaches minimize this problem by integrating multiple strategies [23]. Since cloud environments are dynamic, classical methods may not be able to adapt to changing workloads. However, hybrid algorithms can better adapt to this dynamism by combining metaheuristic and heuristic techniques [24]. A hybrid method is proposed using the Heterogeneous Earliest Finish Time(HEFT) algorithm [25]. According to simulation data, the suggested approach performs better in terms of makespan on random Direct Acyclic Graphs (DAG) than three heuristic and genetic algorithms. An approach to task scheduling that uses a hybrid optimization technique is presented [26]. The method considers other parameters such as minimum waiting time, overall production time, execution time, productivity and utilization in the scheduling of tasks. Results from simulations indicate that the suggested approach outperforms the traditional ACO and PSO-based scheduling algorithms in terms of performance. A hybrid algorithm is proposed by combining the ACO algorithm with the concept of gravitational search [27]. Simulation results performed with the CloudSim tool show that the proposed method outperforms ACO and the basic Gravitational Search Algorithm (GSA) [28].

The issue of task scheduling in cloud systems has garnered the interest of many researchers in the literature. A technique for building the PSO's initial population using heuristic methods is presented [29]. The authors use the Longest Job to Fastest Processor (LJFP) and Minimum Completion Time (MCT) to build the PSO population. The makespan, total execution time, degree of imbalance, and total energy consumption are used to assess the effectiveness of the suggested approaches. According on experimental findings, the suggested approaches outperform the conventional PSO. The drawbacks of PSO, including early convergence issues during the optimization process and becoming trapped in local minima, are addressed by using a Simulated Annealing approach [30]. According to experimental findings, the suggested approach can improve the ratio of average runtime to resource availability. A mathematical model known as the Load Balancing Mutation (LBMPSO), which considers availability and dependability, is proposed [31]. This model is a cloud computing particle swarm optimization (LBMPSO) scheduling technique that takes dependability, round-trip time, creation interval, execution time, transmission time, and load balancing between tasks and virtual machines into account. LBMPSO can improve the cloud computing environment's dependability by taking into account the resources that are available and delaying jobs that haven't been assigned yet. LBMPSO is contrasted with the randomized approach, standard PSO, and the Longest Cloud to Fastest Processor (LCFP) algorithm. Experimental results show that LBMPSO can lower execution times, round-trip times, and transmission costs.

Problem Definition and Methodology

Before being allocated to cloud virtual machines, user-submitted tasks are first put in the task queue. The task scheduler (TS) retrieves the specified number of tasks from the task queue and allocates them to the virtual machines according to the working principle. Tabular, matrix, graph, list, and coding techniques are commonly used in optimization methods. This study adopts the tabular method, illustrated in Fig.2, where tasks and virtual machines are represented. Here, the case of allocating 10 tasks to 3 virtual machines is represented. The tabular representation shown in Figure 2 represents a solution to be optimized. Fig. 3 shows a visualization of the execution of this representative solution on virtual machines. The makespan value is expressed as the highest of the amount of time needed for the tasks assigned to the servers to complete.

$VM/Tasks$	T_1	T_2	T_3	T_4	T_5	T_6	T_7	T_8	T_9	T_{10}
V_1	1	0	0	0	1	0	0	0	0	1
V_2	0	0	1	0	0	1	0	1	0	0
V_3	0	1	0	1	0	0	1	0	1	0

Figure 2. Solution Representation of A Task Scheduling.

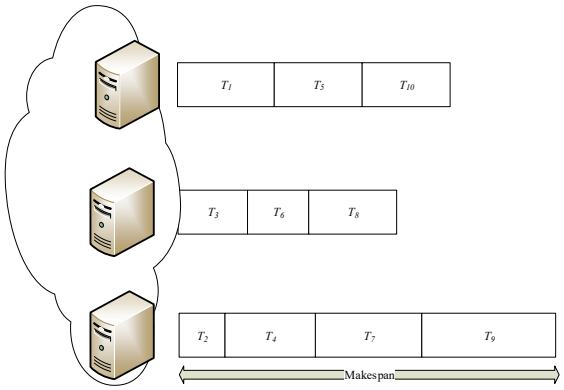


Figure 3. Makespan Representation.

Each task in the work queue is distinct and independent of the others. Each time a predetermined quantity of tasks are pulled from the queue of tasks and the tasks to be assigned are denoted by $T = \{T_1, T_2, .., T_i, .., T_n\}$. Here, t_k represents the quantity of instructions contained in the i'th task and n represents the number of tasks. The active virtual machines in the cloud to which the tasks will be assigned have different command processing capacities, and the total number of m active virtual machines in the system is denoted by $V = \{v_1, v_2, .., v_j, .., v_m\}$. v_l indicates how many million instructions per second (MIPS) that the l'th virtual machine processes. Consequently, the time of execution (ET_{lk}) of the k th task

on the l'st virtual machine is calculated by Equation (1). It is not necessary to allocate every task in the task queue to a separate machine. If whether the k'th task is allocated to the l'st virtual machine is expressed by a boolean parameter e_{lk}, then the entire amount of time needed to complete all tasks allocated to the j th virtual machine ($\mathcal{E}_l$) is found by Equation (2). When scheduling tasks in cloud systems, makespan is optimized by considering various objectives such as energy, cost, user service quality, task priority. In this study, optimization of the makespan value is performed. When using cloud systems, makespan (MS) expresses the greatest amount of time needed to complete a set of tasks across a collection of virtual machines and is represented by Equation (3).

$$ET_{lk} = \frac{t_k}{v_l} \quad (1)$$
$$\mathcal{E}_l = \sum_{k=0}^{N} e_{lk} * ET_{lk}$$

$$e_{lk} \begin{cases} 1, if\ k'th\ task\ \ was\ agined\ to\ l'th\ VM \\ 0,\ otherwise \end{cases} \quad (2)$$

$$MS = {}_{l=1}^{m}\, max(\mathcal{E}_l) \quad (3)$$

Particle Swarm Optimization

PSO is inspired by nature, in particular the collective movements of flocks of birds and groups of fish. The algorithm works by modelling the interactive movement of particles to scan a solution space. PSO uses a randomly initialized particle swarm to solve optimization problems. Each particle represents a point in the solution space and has two basic properties: position and velocity. Each particle moves by being influenced both by its own past experience (P_{best}) and by the best experience of other particles in the swarm (G_{best}) [1]. In this way, both exploration and exploitation processes are balanced. Equation (4-5) computes these particle movements. Here X_p and V_p are the particle's location and velocity values. $rand_1$ and $rand_2$ are the random coefficients. W is the particle's coefficient of inertia, which establishes the ratio of exploration to exploitation. c_1, c_2 are the particle motion's acceleration coefficients. In the representation form used for task scheduling, every vector index denotes a task, and the value contained within it corresponds to the VM's ID. The floating values' counterparts in integers were found by Equation (6) are considered since the VM ID is an integer. The scheduling vector is also these values (S_v). Algorithm 1 provides the PSO pseudo-code that was utilized in this investigation and modified for the task-scheduling issue. If any of the S_v's constituent parts value is greater than the upper and lower bound values, the appropriate component then selects an integer value between the lower and higher bounds that is created at random.

$$V_p = W * V_p + c_1 * rand_1 * \left(P_{best,i} - X_i\right) + c_2 * rand_2 * (P_{gbest} - X_i) \quad (4)$$
$$X_p{}^{new} = X_p + V_p \quad (5)$$
$$S_v = round\left(X_p{}^{new}\right) \quad (6)$$

Algorithm 1 The task-scheduling pseudo code of PSO

```
Initialize parameters
Initialize population
Itr_max ← maximum iteration number
N_pop ← Population size
For i=0 to N_pop
    F_i ←Calculate Fitness Value P_i
    If F_i > P_best
        P_best = F_i
G_best ← Particles with the highest fitness value overall
For itr=0 to Itr_max
  For i=0 to N_pop
    Determine the particle velocity using Equation 4.
    Particle position should be updated using Eq. 5.
    The position of particle is rounded to the closest value
    If (X_p < X_Lower ) or (X_p > X_Upper)
        X_p = Random(X_Lower, X_Upper)
```

Initialize population

Population generation in PSO is usually performed in a randomized manner. However, when the initially generated solutions are far from the optimum solution, this adversely affects the performance of the optimization process. The randomly generated solutions may be very similar to each other and may fall into undesired regions of the search space. This situation negatively affects the optimization process [22]. The heuristic method proposed in this study is realized by considering the population initially generated by PSO with various criteria. Firstly, the method calculates a load coefficient (LC) with Equation (7). This load factor is then multiplied by the capacities of the active virtual machines in the cloud and the amount of load that each server can take is calculated. This is as shown in Equation (8).

$$LC = \frac{\sum_k^n T_k}{\sum_l^m V_l} \quad 7$$

$$LD_k = V_k \times LC \quad \forall\ k\ \in \{1,2,3,\dots,m\} \quad 8$$

After determining the amount of load that can be assigned to all virtual machines, the tasks that will be subjected to scheduling are sorted from biggest to smallest based on how many instructions there are and allocated to virtual machines respectively. The reason for this is to reduce the makespan by prioritizing tasks with a high number of commands. When a task is assigned to a virtual machine, the current task load of the virtual machine must be greater than the time it takes to execute this task on this machine Equation (1). If the load of a virtual machine is greater than the time taken to execute a task, the task is allocated to this virtual machine and the new load of the virtual machine is

updated. If a task is not allocated to any virtual machine (if the current load of the virtual machines is less than the time it takes to execute the task), the task is allocated to the virtual machine with the minimum impact on the makespan time. Algorithm 2 displays the algorithm's pseudo code.

Algorithm 2 The pseudo-code of Heuristic approach for task-scheduling

```
Calculate Load Coefficient according to Eq7
LD← Calculate the workload that each virtual machine
can take according to Eq.8
T← Sort tasks from largest to smallest by command
V← CPU capacities of all VM's
For i to Size(T)
    IsAssign=False
    For j to Size(V)
        ET← Calculate according to Eq.1
        If (LD(i)>ET)
            Assign task i to VM j
            LDi= LDi -ET
            IsAssign=True
    If (!IsAssign)
        Assign task to Vm according to minimum
                    makespan
```

Results and Discussion

The success of the proposed method is tested in the CloudSim environment considering different scenarios [32]. In the simulations, the performance of Heuristic PSO is presented comparatively with FCFS, ACO, and PSO in terms of makespan and energy consumption. To evaluate the performance of proposed method used scenarios with varying quantities of tasks and virtual machines (VMs). The computational capacity of each VM is randomly assigned to reflect the heterogeneity of real cloud environments. Similarly, the quantity of task instructions was also randomized to simulate loads of different complexity.

Two main performance metrics were considered:

Makespan

The overall task completion times were measured to assess scheduling efficiency. The results indicate that Heuristic-PSO consistently achieved a shorter makespan compared to FCFS, ACO, and standard PSO. This demonstrates its ability to allocate tasks more effectively across available resources, leading to balanced load distribution and improved scheduling efficiency.

Energy Consumption

Energy usage was analyzed by calculating the power consumed by VMs during both idle and active states. The findings show that Heuristic-PSO reduced total energy consumption more effectively than the benchmark algorithms. This improvement highlights the capability of the proposed method to minimize energy expenditure while maintaining scheduling performance.

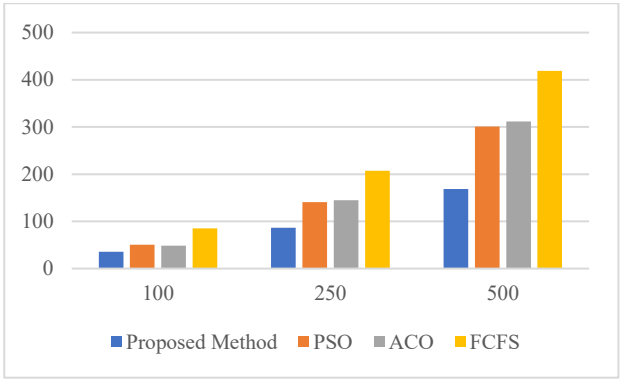
Overall, the experimental results confirm that integrating heuristic strategies into PSO not only enhances task scheduling efficiency but also improves energy awareness in cloud environments.The number of instructions and virtual machine processor capacities of the tasks used in each scenario were performed randomly. The amount of energy spent for instruction execution was assigned in proportion to the processor capacity of each virtual machine. In addition, the amount of energy consumed by the virtual machines when idle was taken as 30% of the amount of energy at load. Thus, the amount of energy consumed by the servers when they are idle is also taken into account in a task scheduling. In this study, the results obtained for each scenario are averaged over 100 independent simulations. The simulations were run on a machine with an Intel(R) Core(TM) i5-10400 CPU running at 2.90 GHz and 8.00 GB of RAM. Table 1 lists other simulation parameters.

Table 1 The simulations parameters

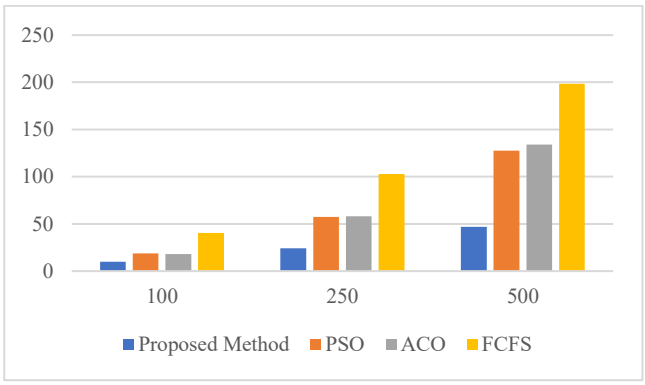
CloudSim	Number of tasks	100-250-500
	Number of task commands	4.000-6.000
	VM numbers	5-10-20
	MIPS	1 000-20 000
	Maximum Iteration	100
	Number of Particles and Ant	20
PSO	c_1	1
	c_2	2
	w	0.5
	Maximum Iteration	100
ACO	Ant Numbers	20
	α	1
	β	2
	σ	0.1

In the simulations, the first performance evaluation was carried out in terms of makespan. The average makespan findings from 100 separate simulations are displayed in Fig. 4, and the statistical summaries of these experimental data are displayed in Table 2. The results shown in Fig. 4 and Table 2 indicate that Heuristic PSO produces lower makespan values compared to FCFS, ACO and PSO algorithms. Especially in scenarios where the number of virtual machines and the amount of tasks increases, Heuristic PSO provides more stable and lower makespan times. In the five virtual machine scenarios, Heuristic PSO produced shorter makespan values than FCFS, ACO and PSO for all task numbers. The most significant difference was observed in the scenario with 500 tasks. In scenarios with 5 virtual machines, the average makespan value of Heuristic PSO was 168.63, while that of standard PSO was 301, ACO was 312.03 and FCFS was 419.07. In scenarios with 10 virtual machines, Heuristic PSO achieved very good results in terms of makespan. In scenarios with 20 virtual machines, the average makespan value of Heuristic

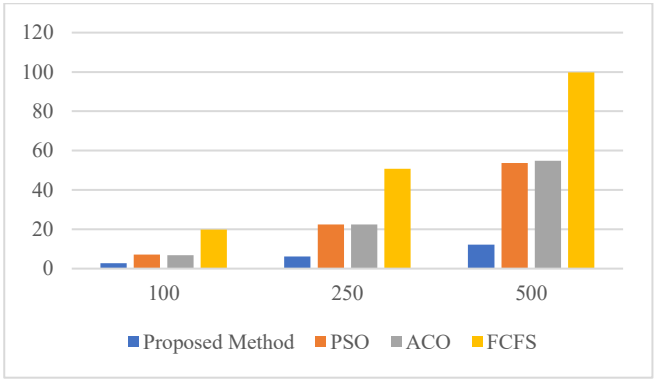
PSO was determined as 47.01, while it was calculated as 127.66 for standard PSO. In the 20 virtual machine scenarios, increasing the number of virtual machines generally decreased the makespan times, but Heuristic PSO again achieved better results compared to FCFS, ACO and PSO. In the 500 task scenario, the average makespan value of Heuristic PSO was 12.26, while standard PSO was 53.63. These results show that Heuristic PSO can significantly reduce the makespan time by distributing the tasks more evenly. Especially in large-scale systems, the proposed method minimizes the early convergence problem and achieves a better scheduling success.



A. Average makespan results for scenarios with 5 VMs



B. Average makespan results for scenarios with 10 VMs



C. Average makespan results for scenarios with 20 VMs

Figure 4. Average makespan outcomes across all techniques

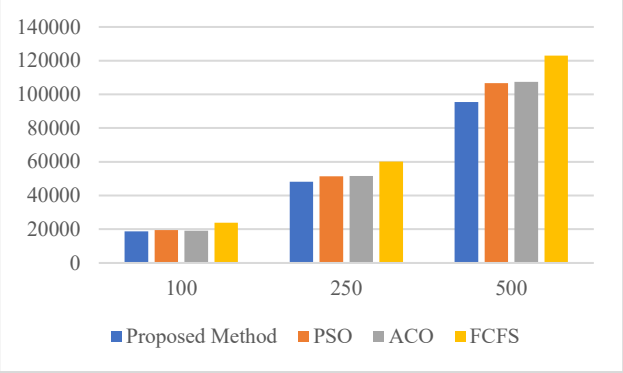
Table 2. Statistical results of makespan simulations

Scenarios		Heuristic PSO				PSO				ACO				FCFS			
VM	**Task**	**Mean**	**Min**	**Max**	**Median**	**Mean**	**Min**	**Max**	**Median**	**Mean**	**Min**	**Max**	**Median**	**Mean**	**Min**	**Max**	**Median**
5	**100**	35.80	23.77	84.25	33.56	50.71	25.41	93.40	49.93	48.79	24.01	88.52	46.25	85.06	32.11	105.89	99.97
	250	86.49	52.32	182.87	83.70	140.59	53.69	252.85	143.65	144.85	53.55	227.93	149.52	207.12	61.99	261.64	247.98
	500	168.63	108.91	250.32	165.90	301.00	122.40	496.25	301.59	312.03	116.57	473.23	350.04	419.07	128.04	513.84	497.82
10	**100**	9.80	7.30	17.53	9.38	18.62	8.62	38.70	17.10	18.09	8.59	36.40	16.64	40.48	15.35	54.28	49.71
	250	24.05	16.60	42.62	23.39	57.33	21.86	99.41	59.09	58.22	19.93	105.62	57.78	102.79	24.77	132.65	123.52
	500	47.01	34.51	97.53	44.10	127.66	48.77	227.60	128.73	134.09	48.59	226.55	140.29	198.49	64.97	259.04	248.42
20	**100**	2.74	2.03	4.07	2.67	7.13	2.96	16.58	6.59	6.89	3.23	15.70	6.41	19.85	5.44	28.30	24.02
	250	6.18	4.62	8.14	6.09	22.52	8.14	51.76	19.93	22.46	7.79	51.13	19.92	50.72	13.53	68.15	60.34
	500	12.26	8.77	16.52	12.32	53.63	14.1	108.76	49.45	54.83	14.21	105.22	49.34	99.73	24.98	133.61	124.00

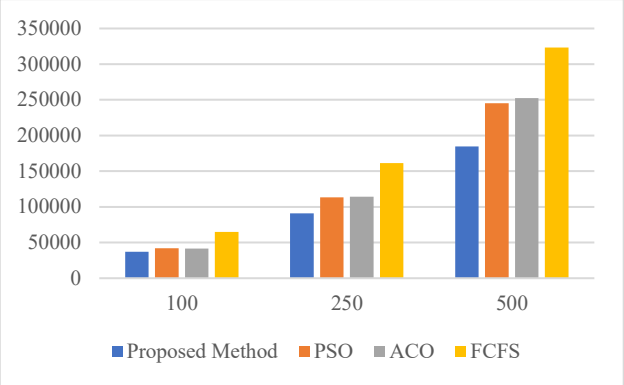
Table 3. Statistical results of energy consumption (joules) simulations

Scenarios		Heuristic PSO				PSO				ACO				FCFS			
VM	**Task**	**Mean**	**Min**	**Max**	**Median**	**Mean**	**Min**	**Max**	**Median**	**Mean**	**Min**	**Max**	**Median**	**Mean**	**Min**	**Max**	**Median**
5	**100**	18 690.3	6 919.7	2 4654.0	19 333.1	19 495.4	6 784.5	28 578.1	19 625.5	19 163.7	6 771.3	27 700.8	19 674.1	23 871.1	6 618.8	42 295.4	22 434.4
	250	48 115.7	21 081.3	63 845.6	49 025.6	51 481.5	20 850.6	76 778.8	52 200.0	51 678.7	21 001.8	78 312.0	51 636.8	60 201.6	21 018.8	104 409.7	59 685.3
	500	95 475.5	62 567.4	124 900.5	95 743.1	106 651.4	65 794.3	171 799.0	105 962.7	107 530.3	65 453.6	162 155.4	105 187.1	122 945.9	70 608.8	194 945.4	117 098.1
10	**100**	36 847.2	22 706.3	48 263.5	37 372.1	42 167.0	23 520.3	68 351.5	40 709.3	41 517.2	23 269.0	60 734.8	40 012.9	64 761.8	35 269.4	110 941.8	60 742.9
	250	90 759.4	56 760.2	117 986.3	90 927.7	113 509.2	58 428.5	187 464.5	106 698.0	114 175.9	57 483.5	182 402.6	107 246.9	161 196.2	74 495.4	318 193.7	152 883.4
	500	184 656.9	99 382.6	220 893.9	186 892.5	245 162.9	113 312.2	404 191.6	236 176.3	252 298.6	110 292.4	438 957.3	240 085.4	323 368.8	120 371.3	581 132.8	304 918.5
20	**100**	74 632.7	52 081.0	114 731.7	74 655.6	100 427.9	62 762.8	177 449.2	94 736.1	98 650.4	62 458.4	167 559.9	94 229.7	205 792.7	76 528.7	368 780.9	207 398.9
	250	182 657.2	147 394.1	219 206.7	184 468.2	291 055.9	155 899.2	52 6540.8	279 832.3	289 231.4	160 443.7	508 569.9	285 331.8	531 021.1	197 144.0	845 138.7	517 731.8
	500	363 855.1	286 992.2	430 766.6	363 908.9	643 860.2	351 918.9	126 7283.0	615 555.9	650 094.9	364 609.0	1 285 109.0	612 781.6	1 028 482	463 413.9	1 677 298.0	1 065 899.0

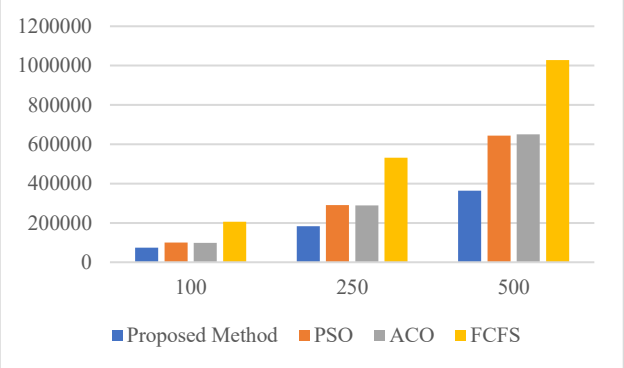
The second performance evaluation was conducted by looking at how much energy the cloud environment's virtual machines used. The average energy consumption findings from the separate tests are displayed in Fig. 5, and the statistical summaries of these experimental results are displayed in Table 3. Fig. 5 and Table 3 show that Heuristic PSO is more efficient in terms of energy consumption compared to FCFS, ACO and PSO. In the 5 virtual machine scenarios, Heuristic PSO achieved lower energy consumption at all task numbers. For example, in the scenario with 500 tasks, the average energy consumption of Heuristic PSO was calculated as 95475.49 units, while the consumption of standard PSO was 106651.44 units. In 10 virtual machine scenarios, energy consumption decreased with increasing the number of virtual machines. The energy consumption of Heuristic PSO in the scenario with 500 tasks was 184656.92 units, while the standard PSO, which is the closest algorithm, showed a consumption of 245162.91 units. In the 20 virtual machine scenarios, the presence of more virtual machines further increased the efficiency of Heuristic PSO. In the case with 500 tasks, the energy consumption of Heuristic PSO was calculated as 363855.14 units, while the consumption of standard PSO reached 643860.2 units. These results show that Heuristic PSO optimizes not only the makespan time but also the energy consumption by distributing the tasks more evenly. Especially in large-scale systems, the proposed method achieves a more efficient scheduling success by minimizing the problem of excessive energy consumption compared to other algorithms.



A. Average energy consumption results for scenarios with 5 VMs



B. Average energy consumption results for scenarios with 10 VMs



C. Average energy consumption results for scenarios with 20 VMs

Figure 5. Average energy consumption outcomes across all techniques

Conclusion

In this study, a heuristic PSO-based approach is proposed to solve the task scheduling problem in cloud environments. The proposed method provides a more balanced task distribution by improving the initial population of PSO with a heuristic mechanism. The extensive simulations show that the heuristic PSO reduces the makespan time by 61.42% and 62.84% on average compared to the standard PSO and ACO algorithms. It was also found to consume 26.18% less energy than PSO and 27.33% less energy than ACO. Especially in large systems, heuristic PSO provides a more balanced distribution of tasks by minimizing the early convergence problem. The results show that the proposed method offers a more efficient, scalable and energy-saving alternative for task scheduling in cloud computing. In the future, it is planned to further develop the method with multi-objective optimization approaches, to integrate it with dynamic load balancing strategies and to test it in large-scale applications such as big data processing.

Ethics committee approval and conflict of interest statement

There is no need to obtain permission from the ethics committee for the article prepared

There is no conflict of interest with any person / institution in the article prepared

Authors' Contributions

Barut Cebrail: Study conception and design, visualization, analysis, and interpretation of data, drafting of manuscript

Firildak Kazım: conceived the original idea, supervised the project, critical revision

References

[1] C. Barut, G. Yildirim, and Y. Tatar, "An intelligent and interpretable rule-based metaheuristic approach to task scheduling in cloud systems," *Knowledge-Based Syst.*, vol. 284, no. December 2023, p. 111241, 2024, doi: 10.1016/j.knosys.2023.111241.

[2] G. Boss, P. Malladini, D. Quan, L. Legregni, and H. Hall, "Cloud Computing Authors:," *Cloud Comput.*, vol. 17, no. 1, pp. 111–136, 2012.

[3] Y. Pachipala, K. S. Sureddy, A. B. S. Sriya Kaitepalli, N. Pagadala, S. S. Nalabothu, and M. Iniganti, "Optimizing Task Scheduling in Cloud Computing: An Enhanced Shortest Job First Algorithm," *Procedia Comput. Sci.*, vol. 233, no. 2023, pp. 604–613, 2024, doi: 10.1016/j.procs.2024.03.250.

[4] A. Keivani and J. R. Tapamo, "Task scheduling in cloud computing: A review," *icABCD 2019 - 2nd Int. Conf. Adv. Big Data, Comput. Data Commun. Syst.*, pp. 1–6, 2019, doi: 10.1109/ICABCD.2019.8851045.

[5] A. R. Arunarani, D. Manjula, and V. Sugumaran, "Task scheduling techniques in cloud computing: A literature survey," *Futur. Gener. Comput. Syst.*, vol. 91, pp. 407–415, 2019, doi: 10.1016/j.future.2018.09.014.

[6] J. Kennedy and R. Eberhart, "Particle Swarm Optimization," *Ind. Electron. Handb. - Five Vol. Set*, pp. 1942–1948, 2011, doi: 10.1007/978-3-319-46173-1_2.

[7] A. S. Abohamama, A. El-Ghamry, and E. Hamouda, *Real-Time Task Scheduling Algorithm for IoT-Based Applications in the Cloud–Fog Environment*, vol. 30, no. 4. Springer US, 2022. doi: 10.1007/s10922-022-09664-6.

[8] P. Y. Zhang and M. C. Zhou, "Dynamic Cloud Task Scheduling Based on a Two-Stage Strategy," *IEEE Trans. Autom. Sci. Eng.*, vol. 15, no. 2, pp. 772–783, 2018, doi: 10.1109/TASE.2017.2693688.

[9] C. Barut, G. Yildirim, and Y. Tatar, "An intelligent and interpretable rule-based metaheuristic approach to task scheduling in cloud systems," *KNOWLEDGE-BASED Syst.*, vol. 284, 2024, doi: 10.1016/j.knosys.2023.111241.

[10] H. Jin *et al.*, "A survey of energy efficient methods for UAV communication," *Veh. Commun.*, vol. 41, p. 100594, 2023, doi: 10.1016/j.vehcom.2023.100594.

[11] P. Banerjee, A. Tiwari, B. Kumar, K. Thakur, A. Singh, and M. Kumar Dehury, "Task Scheduling in cloud using Heuristic Technique," *7th Int. Conf. Trends Electron. Informatics, ICOEI 2023 - Proc.*, no. Icoei, pp. 709–716, 2023, doi: 10.1109/ICOEI56765.2023.10126030.

[12] K. Beghdad Bey, F. Benhammadi, and R. Benaissa, "Balancing heuristic for independent task scheduling in cloud computing," *12th Int. Symp. Program. Syst. ISPS 2015*, pp. 7–12, 2015, doi: 10.1109/ISPS.2015.7244959.

[13] S. Nabi, M. Ahmad, M. Ibrahim, and H. Hamam, "AdPSO: Adaptive PSO-Based Task Scheduling Approach for Cloud Computing," *Sensors*, vol. 22, no. 3, pp. 1–22, 2022, doi: 10.3390/s22030920.

[14] N. Bacanin, T. Bezdan, E. Tuba, I. Strumberger, M. Tuba, and M. Zivkovic, "Task Scheduling in Cloud Computing Environment by Grey Wolf Optimizer," *27th Telecommun. Forum, TELFOR 2019*, no. June 2020, 2019, doi: 10.1109/TELFOR48224.2019.8971223.

[15] S. Mangalampalli, G. R. Karri, and A. A. Elngar, "An Efficient Trust-Aware Task Scheduling Algorithm in Cloud Computing Using Firefly Optimization," *Sensors*, vol. 23, no. 3, 2023, doi: 10.3390/s23031384.

[16] S. Asghari and N. J. Navimipour, "Cloud service composition using an inverted ant colony optimisation algorithm," *Int. J. Bio-Inspired Comput.*, vol. 13, no. 4, p. 257, 2019, doi: 10.1504/IJBIC.2019.100139.

[17] X. Chen *et al.*, "A WOA-Based Optimization Approach for Task Scheduling in Cloud Computing Systems," *IEEE Syst. J.*, vol. 14, no. 3, pp. 3117–3128, 2020, doi: 10.1109/JSYST.2019.2960088.

[18] M. Bürkük and G. Yıldırım, "Cloneable Jellyfish Search Optimizer Based Task Scheduling in Cloud Environments," *Türk Doğa ve Fen Derg.*, vol. 11, no. 3, pp. 35–43, 2022, doi: 10.46810/tdfd.1123962.

[19] S. H. Adil, K. Raza, U. Ahmed, S. S. A. Ali, and

M. Hashmani, “Cloud task scheduling using nature inspired meta-heuristic algorithm,” *ICOSST 2015 - 2015 Int. Conf. Open Source Syst. Technol. Proc.*, pp. 158–164, 2016, doi: 10.1109/ICOSST.2015.7396420.

[20] N. O. Alkaam, A. B. M. Sultan, M. B. Hussin, and K. Y. Sharif, “Hybrid Henry Gas-Harris Hawks Comprehensive-Opposition Algorithm for Task Scheduling in Cloud Computing,” *IEEE Access*, vol. 13, no. January, pp. 12956–12965, 2025, doi: 10.1109/ACCESS.2025.3530860.

[21] E. GÜNDÜZALP, G. YILDIRIM, and Y. TATAR, “Efficient Task Scheduling in Cloud Systems with Adaptive Discrete Chimp Algorithm,” *Balk. J. Electr. Comput. Eng.*, vol. 10, no. 3, pp. 328–336, 2022, doi: 10.17694/bajece.989467.

[22] B. F. Azevedo, A. M. A. C. Rocha, and A. I. Pereira, *Hybrid approaches to optimization and machine learning methods: a systematic literature review*, vol. 113, no. 7. Springer US, 2024. doi: 10.1007/s10994-023-06467-x.

[23] N. Mansouri, B. Mohammad Hasani Zade, and M. M. Javidi, “Hybrid task scheduling strategy for cloud computing by modified particle swarm optimization and fuzzy theory,” *Comput. Ind. Eng.*, vol. 130, no. July 2018, pp. 597–633, 2019, doi: 10.1016/j.cie.2019.03.006.

[24] Sandeep Kumar Patel and Avtar Singh, “Task scheduling in cloud computing using hybrid optimization algorithm,” *Soft Comput.*, vol. 26, no. 23, pp. 13069–13079, 2022, doi: 10.1007/s00500-021-06488-5.

[25] A. Kamalinia and A. Ghaffari, “Hybrid Task Scheduling Method for Cloud Computing by Genetic and DE Algorithms,” *Wirel. Pers. Commun.*, vol. 97, no. 4, pp. 6301–6323, 2017, doi: 10.1007/s11277-017-4839-2.

[26] M. S. A. Khan and R. Santhosh, “Task scheduling in cloud computing using hybrid optimization algorithm,” *Soft Comput.*, vol. 26, no. 23, pp. 13069–13079, 2022, doi: 10.1007/s00500-021-06488-5.

[27] S. Rani and P. K. Suri, “An efficient and scalable hybrid task scheduling approach for cloud environment,” *Int. J. Inf. Technol.*, vol. 12, no. 4, pp. 1451–1457, 2020, doi: 10.1007/s41870-018-0175-3.

[28] E. Rashedi, H. Nezamabadi-pour, and S. Saryazdi, “GSA: A Gravitational Search Algorithm,” *Inf. Sci. (Ny).*, vol. 179, no. 13, pp. 2232–2248, 2009, doi: 10.1016/j.ins.2009.03.004.

[29] S. A. Alsaidy, A. D. Abbood, and M. A. Sahib, “Heuristic initialization of PSO task scheduling algorithm in cloud computing,” *J. King Saud Univ. - Comput. Inf. Sci.*, vol. 34, no. 6, pp. 2370–2382, 2022, doi: 10.1016/j.jksuci.2020.11.002.

[30] S. Zhan and H. Huo, “Improved PSO-based task scheduling algorithm in cloud computing,” *J. Inf. Comput. Sci.*, vol. 9, no. 13, pp. 3821–3829, 2012.

[31] A. I. Awad, N. A. El-Hefnawy, and H. M. Abdel-Kader, “Enhanced Particle Swarm Optimization for Task Scheduling in Cloud Computing Environments,” *Procedia Comput. Sci.*, vol. 65, no. Iccmit, pp. 920–929, 2015, doi: 10.1016/j.procs.2015.09.064.

[32] R. N. Calheiros, R. Ranjan, A. Beloglazov, C. A. F. De Rose, and Rajkumar Buyya, “CloudSim: a toolkit for modeling and simulation of cloud computing environments and evaluation of resource provisioning algorithms Rodrigo,” *Softw. - Pract. Exp.*, vol. 39, no. 7, pp. 701–736, 2009, doi: 10.1002/spe.

Dicle University
Journal of Engineering
https://dergipark.org.tr/tr/pub/dumf
duje.dicle.edu.tr

Research Article

Explainable Hybrid Deep Learning–Transformer Approach for Insulin Prediction

İlhan UYSAL[1*]

[1] Burdur Mehmet Akif Ersoy University, Bucak Zeliha Tolunay School of Applied Technology and Business Administration, Information Systems and Technologies Department, iuysal@mehmetakif.edu.tr, Orcid No: 0000-0002-6091-9110

ARTICLE INFO

Article history:

Received 23 March 2025
Received in revised form 21 July 2025
Accepted 4 September 2025
Available online 30 September 2025

Keywords:

Hybrid Modeling, Ensemble Learning, Deep Learning, Transformer Architectures, Explainable AI

Doi: 10.24012/dumf.1663768

* Corresponding author

ABSTRACT

Accurate predictive modeling is critical for enhancing patient outcomes and facilitating personalized care. This study introduces a hybrid modelling framework that combines deep learning, transformer-based architectures, and classical regression methods. The framework integrates multiple approaches, including Artificial Neural Networks, Long Short-Term Memory Networks, Convolutional Neural Networks, Random Forest, to model complex patterns in insulin biomarker data. By integrating these models into a unified framework, the approach enhances predictive accuracy while ensuring interpretability. Explainable AI techniques, including SHAP and LIME, are employed to identify key features influencing predictions, thereby promoting transparency and clinical trust. The proposed framework achieves superior performance on clinical datasets, with improved metrics such as MSE, MAE, and R^2, outperforming baseline models. Additionally, it identifies critical biomarkers associated with insulin regulation. Subgroup-level interpretations provide clinically relevant insights that inform personalized treatment strategies. This work demonstrates how advanced machine learning, coupled with explainability, establishes a robust foundation for clinical decision support systems to deliver effective and individualized patient care.

Introduction

Modern healthcare systems collect vast amounts of clinical data, which presents significant challenges for accurate analysis and interpretation of data. This challenge is more significant for chronic conditions such as diabetes and metabolic syndrome, where insulin levels significantly influence on the management of the disease. Precise estimation of insulin levels is fundamental for guiding clinical decisions and for developing tailored treatment plans. Recent evidence suggests that improvement in insulin prediction significantly enhances patient care, which highlights the need for more sophisticated insulin models and advanced modeling methods in clinical medicine [1].

Clinical data analysis has been based on traditional statistical frameworks, such as logistic regression. Although these models have a adequate performance in less complex cases, they often fail of capturing the complexity and high-dimensional clinical biomarker data. Recent comparative studies show that classical statistical methods often underperform than modern machine learning methods when dealing with advanced medical datasets. Capable of modeling non-linear relationships among numerous biomarkers, advanced deep learning frameworks, such as CNNs and LSTMs, provide effective methods for the accurate prediction of biologically complex phenomena. An illustrative example is precise prediction of insulin levels that depend on a large number of biological factors [2,3].

Insulin remains a central biomarker in metabolic studies due to its crucial role in managing diseases like diabetes. Our random forest-based feature importance analysis identified critical biomarkers associated with insulin regulation, including *AST, 25-Hydroxy Vitamin D, Glucose (Fasting), and TSH*. These findings illustrate complex interactions between liver function, thyroid health, glucose metabolism, and overall endocrine status. Addressing these diverse clinical variables together appears necessary for effectively managing complex metabolic disorders. Such observations are consistent with previous studies, which emphasize the multifaceted nature of metabolic dysfunction and support incorporating clinical and demographic data in predictive models [4, 5].

Explainable Artificial Intelligence (XAI) has emerged as a critical tool in clinical applications to enhance trust and transparency. Integrating interpretability techniques into predictive models helps clinicians better understand and accept model outputs. For example, SHapley Additive exPlanations (SHAP) is widely used to visualize how individual features contribute to insulin predictions. This

visualization aids clinicians in aligning computational results with clinical experience, fostering trust and supporting informed medical decision-making [6,7].

The subsequent stage of this research in our investigation will focus on an in-depth assessment and synthesis of predictive approaches. We focus on assessing conventional statistical methods alongside modern deep learning approaches to ascertain which one more accurately predicts insulin fluctuations. Conducting this comparative evaluation is crucial, given that previous works have documented significant variations in prediction accuracy between older and more advanced machine learning techniques [8]. Utilizing these methods of such methods to actual clinical datasets will provide empirical evidence of their value [9, 10] in guiding clinical decisions concerning the optimal analytical methods for tailored patient management.

In conducting our investigation, we have systematically applied systematic validation procedures to evaluate the reliability of the predictive frameworks. We relied on commonly accepted metrics, namely the Mean Absolute Error (MAE), Mean Squared Error (MSE), and the coefficient of determination (R-squared), to quantify the accuracy of predictions compared to actual values. Such comprehensive quantification supports the validity of the analytical process and helps in adopting predictive tools into routine clinical settings. Collectively, these contributions support the operationalization of precision medicine and provide clinicians with empirical evidence to deliver accurate, patient-centered interventions supported by computational analyses [11, 12].

In conclusion, as healthcare systems grapple with increasing data complexity, integrating deep learning and XAI provides a robust approach to enhancing patient care. By focusing on key biomarkers, such as insulin, and integrating classical and modern machine learning methods, the approach facilitates precise analysis of metabolic disorders. This integrated approach enables more accurate predictions and supports individualized therapeutic strategies. Moving forward, adopting these methods will be crucial for aligning computational advances with clinical reasoning, thereby enhancing clinical decision-making and improving patient outcomes [13,14].

The remainder of this paper is structured as follows: Section 2 describes data preprocessing and model development; Section 3 reports the results; Section 4 discusses the findings; and Section 5 concludes with clinical implications. Figure 1 illustrates the overall workflow, from raw data to interpretable predictions. The proposed hybrid ensemble model advances insulin level prediction by integrating transformer-based deep learning, classical regression, and explainable AI techniques, including SHAP [38] and LIME [41]. Unlike previous approaches, this strategy optimizes predictive performance through multi-model integration while ensuring interpretability via global and local explanation tools. It directly addresses clinical needs for actionable and trustworthy artificial intelligence (AI).

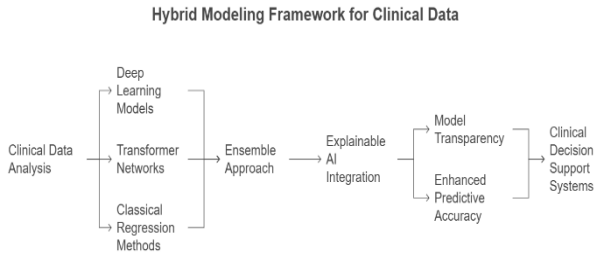


Figure 1. Model Framework

Related Works

The combined application of ensemble deep learning techniques, transformer architectures, classical regression approaches, and explainable artificial intelligence materially improves both the precision and cogency of clinical prediction models, with notable impact in diabetes management and the broader biomedical landscape [15,16]. Methods like Boosting and Random Forest steadily outperform baseline classifiers, exhibiting heightened resistance to heterogeneous and noisy clinical observations [17]. Simultaneously, convolutional neural networks and their hybrid configurations, when directed at medical imaging datasets, mitigate overfitting and foster broader generalization to external cohorts [18,19]. Transformers further expand these advantages by accommodating both structured clinical records and free-text notes, while the self-attention mechanism furnishes an intuitive basis for clinical stakeholders to interrogate model decisions [20,21]. Classical regression techniques remain important for analyzing clinical relationships and patient outcomes, especially when dealing with specific data distributions or hierarchical structures [22,23]. Additionally, explainable AI methods like SHAP and LIME play a critical role in understanding and trusting model predictions, thereby facilitating their integration into clinical practice [21]. Although transformer-based architectures have shown strong predictive performance including Badgeley et al. [21], their limited use of explainability mechanisms has restricted clinical uptake. Likewise, Afshar et al. [14] employed CNNs on clinical datasets but did not fully resolve interpretability challenges. Our approach closes these gaps by uniting hybrid deep-learning architectures with classical regression and advanced XAI frameworks, thereby improving both predictive accuracy and model transparency. In comparison to these studies, our proposed hybrid ensemble framework uniquely combines multiple deep learning architectures, classical regression models, and advanced XAI approaches. This integrated strategy aims to leverage complementary strengths of each method to improve both predictive accuracy and interpretability in insulin level prediction tasks. A concise comparative summary of important methods, domains, and key contributions—including our proposed approach—is presented in Table 1.

Table 1. Comparative Analysis of Important Studies

Reference	Method / Approach	Data / Domain	Key Contribution / Relevance
Dai et al. (2020)	Ensemble (e.g., Boosting, Random Forest)	Clinical data (various datasets)	Highlights the robustness and accuracy of ensemble methods across different healthcare datasets, addressing noise and variability through model aggregation.
Kamnitsas et al. (2018)	CNN ensemble frameworks	Medical imaging (tumor segmentation)	Demonstrates how combining multiple CNN architectures mitigates overfitting, improving generalization in medical image analysis.
Sukegawa et al. (2021)	CNN-based deep learning	Medical imaging (osteoporosis detection)	Shows CNN models' effectiveness in identifying conditions such as osteoporosis; suggests ensemble integration for improved diagnostic accuracy.
Yamamoto et al. (2020)	CNN-based approaches	Medical imaging	Explores advanced convolutional methods for enhanced diagnostic performance, reinforcing the benefits of deep learning in clinical imaging.
Badgeley et al. (2019)	Transformers + XAI	Structured and unstructured clinical data	Underscores the potential of transformer architectures for analyzing diverse clinical data, emphasizing interpretability via XAI for transparent decision-making.
Famoye & Singh (2021)	Zero-Inflated Generalized Poisson Regression	Count data in clinical outcomes	Illustrates the continued importance of classical regression methods for specialized data distributions, advocating hybrid approaches when dealing with complex clinical phenomena.
Obasohan et al. (2020)	Mixed Effects Model	Hierarchical clinical datasets	Demonstrates the use of classical statistical models to capture multi-level or hierarchical structures, providing complementary insights alongside advanced ML techniques.
Habibov et al. (2019)	Ensemble frameworks for heterogeneous data	Heterogeneous clinical data	Showcases how ensemble methods can adaptively learn from multiple data sources and handle confounding variables, offering flexibility in clinical analytics.
Proposed model	***Hybrid Ensemble (Deep Learning + Classical Regression + XAI)***	***Clinical biomarker data (single-center diabetes dataset)***	***Combines complementary modeling approaches and integrates XAI for enhanced predictive accuracy and interpretability, addressing limitations of prior single-method studies in clinical data.***

Material and Method

This study employed a clinical dataset to predict insulin levels using multiple modeling approaches. The focus is on deep learning methods, with comparisons made to classical machine learning algorithms. Hybrid ensemble models were also evaluated. This analysis is highly relevant given the growing reliance on automated techniques in medicine. Diabetes care depends heavily on accurate insulin requirement data [15,16].

Base Models with Deep Learning

ANN (MLP) Model

It is designed a model based on a Multi-Layer Perceptron (MLP) architecture, where all layers are fully connected and dropout layers are incorporated to mitigate overfitting. The model optimization step was done with the Adam algorithm, which is indicative of its popularity for regression tasks across multiple fields [25]. Recent works validate MLP's capacity to model even the most intricate datasets and thus, suitable for healthcare [15,26].

LSTM Model

The LSTM model was designed to consider the tabular data as sequential information so that the temporal insulin secretion and absorption relationships can be captured. Although the dataset contains single time-point clinical measurements without explicit temporal sequences, LSTM models were explored to capture possible latent sequential dependencies. It appears that capturing long-range dependencies and sequential patterns in glucose profiles is indeed helpful to improve prediction accuracy [27,28]. In LSTM implementations, optimization options including RMSprop are commonly chosen due to adaptive learning rates [29].

CNN Model

Sifting through the data using a one-dimensional convolutional neural network (1D CNN) enabled us to focus on the most relevant features pertaining to insulin levels. Efficient feature extraction was achieved through the stacking of Conv1D layers, flatten layers, and dense layers. SGD has also been the chosen optimizer in the recent literature [25] which supports the use of sequential data analysis [30].

Classical Machine Learning Models

Random Forest Regressor

A benchmark model and a model to evaluate feature importance was the Random Forest Regressor. Random forest models have been shown to perform particularly well when predicting outcomes related to health [15,31]. The model's robustness and efficiency in managing high-dimensional clinical data were corroborated by previous works. Random forests are usually built as an ensemble and are very useful in indicating the most important parameters that impact health metrics [30].

Hybrid Ensemble Framework

Meta-ANN (Stacking Meta-Model)

For the ensemble approach, a meta-ANN model is built using the outputs of individual deep learning models (ANN, LSTM and CNN). This stacking method utilizes various outputs from different models to improve the overall regression results. Previous research has proven the effectiveness of such hybridization to improve model accuracy and generalizability [16,32].

Hybrid (Out-of-Fold, OOF) Stacking Model

In the OOF framework, each base model is fitted on $k-1$ folds and generates predictions for the held-out fold. These out-of-fold predictions then serve as features for training the meta-model. By relying solely on unseen data for meta-level inputs, the procedure mitigates overfitting and improves generalization. This study utilizes k-fold cross-validation to obtain OOF estimates, which are subsequently used to train the meta-learner and further curb model over-learning.

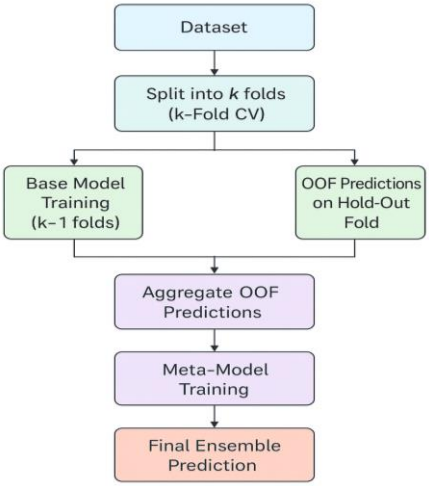


Figure 2. Diagram of Hybrid Stacking Model

Model Evaluation and Explainability

Model performance was evaluated using MSE, MAE, and R^2, each capturing distinct aspects of predictive accuracy [25]. To enhance clinical interpretability, we implemented a hybrid XAI framework combining SHAP and LIME. SHAP provides global feature importance by quantifying each variable's contribution across the dataset, while LIME offers local interpretability by approximating the model's behavior around individual predictions. Together, these methods link population-level insights with patient-specific explanations, addressing clinicians' demands for both transparency and actionable decision support [16, 24].

Application Process

The dataset from a private hospital in Antalya contains blood values of patients diagnosed with myalgia. The data set contains a total of 67 clinical variables and 2822 instances including demographic information including age, gender and biochemical parameters such as AST, ALT, glucose, TSH, ferritin. After data preprocessing steps, feature engineering was performed and the number of features was reduced to 21. The feature importance graph with random forest regressor is given in Figure 3.

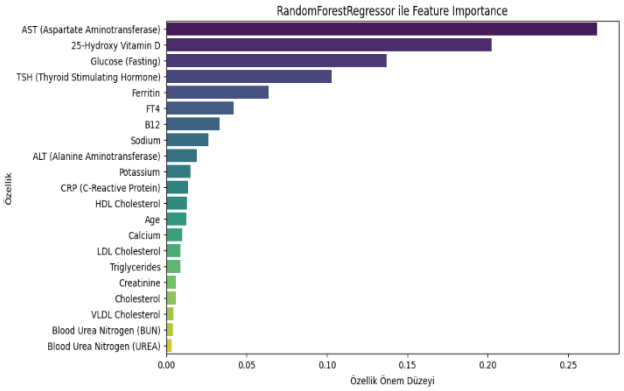


Figure 3. Feature Importance with Random Forest Regressor

During the implementation of the study, the dataset was first cleaned of missing values; columns with 90% or more missing values were removed. Remaining missing values were imputed using the Iterative Imputer method, which models missing data based on other features to provide accurate estimates. All data was scaled with Standard Scaler and then divided into a training-test set, with an 80-20 split. For deep learning models, the data was reshaped appropriately, while classical models were trained directly with scaled data. The predictions produced by the base models were used for meta-model training using stacking.

Model architectures, hyperparameters, and software libraries including their versions (Python 3.11, TensorFlow 2.12, scikit-learn 1.0.2, SHAP 0.40) are detailed in the appendix.

Results

We evaluated the predictive performance of multiple models for insulin level estimation using our clinical dataset. Table 2 compares model performances based on MSE, MAE, and R^2 score, which quantify prediction error magnitude and explained variance, respectively. The Hybrid Ensemble Model, combining MLP and Optimized Transformer architectures, demonstrated superior performance with the lowest MSE (11.43), MAE (1.43),

and highest R^2 (0.92), highlighting the advantages of integrating complementary modeling approaches.

Table 2. Comparison of Model Performances

Model	MSE	MAE	R^2 Score
Random Forest Regressor	25.3563	1.8267	0.9051
CNN+LSTM	33.3777	2.9058	0.6153
MLP	24.9893	2.6739	0.8219
Transformer	69.0674	4.5055	0.4377
Baseline Transformer	66.3250	4.4578	0.4674
Transformer + Positional Encoding	36.7644	2.5394	0.7867
Optimized Transformer	26.5052	2.3304	0.8219
Keras Tuner Optimized Model	28.6607	2.1431	0.8743

Classical machine learning methods proved remarkably effective, with the Random Forest Regressor achieving competitive results (MSE: 25.36, MAE: 1.83, R^2: 0.91) - outperforming several deep learning base models. Among individual deep learning architectures, the MLP showed stronger predictive capability (MSE: 24.99, MAE: 2.67, R^2: 0.82) compared to the CNN+LSTM model (MSE: 33.38, MAE: 2.91, R^2: 0.62), suggesting MLPs may be better suited for tabular clinical data without extensive feature engineering.

Transformer-based models exhibited varying performance levels. The baseline Transformer configurations initially underperformed ($R^2 < 0.47$), likely due to hyperparameter sensitivity and moderate dataset size. However, architectural enhancements yielded significant improvements: positional encoding increased R^2 to 0.79, while comprehensive hyperparameter optimization boosted performance further (Optimized Transformer R^2: 0.82; Keras Tuner-optimized model R^2: 0.87).

These results demonstrate that while classical algorithms like Random Forest remain robust for clinical prediction tasks, carefully designed hybrid ensembles combining optimized deep learning models achieve superior accuracy. The ensemble's performance advantage stems from its ability to capture complex, nonlinear relationships in clinical data through multiple complementary approaches.

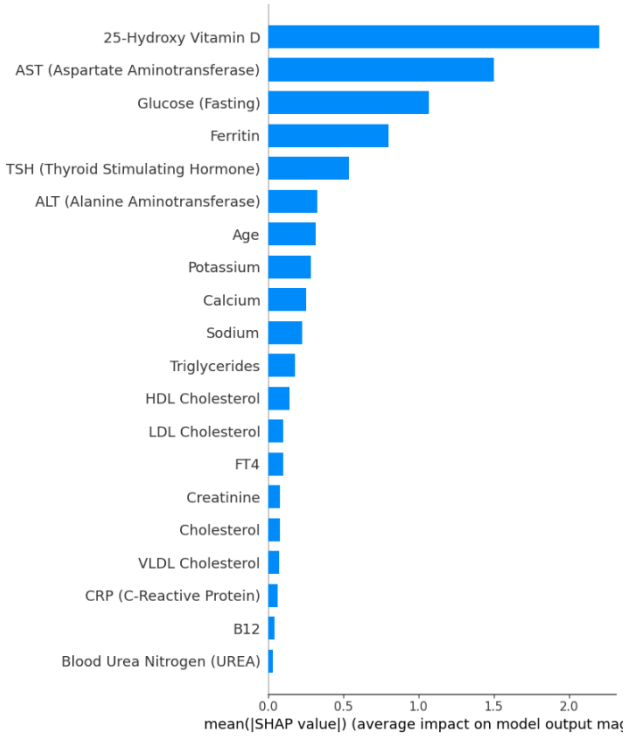


Figure 4. Average SHAP Feature Importance for Insulin Prediction Model

Using the SHAP method, the importance levels of features influencing the model's predictions are revealed. Figure 4 ranks the features based on their absolute average SHAP values, highlighting *25-Hydroxy Vitamin D* and *AST* as the most critical biomarkers for predicting insulin levels. This aligns with existing literature where vitamin D deficiency or excess significantly affects insulin regulation [35]. Other features like fasting glucose and ferritin also contribute notably, reflecting the close link between glycemic control, iron metabolism, and insulin dynamics, while *TSH* and *ALT* have smaller yet relevant impacts, with *ALT* emphasizing liver function's role in insulin metabolism.

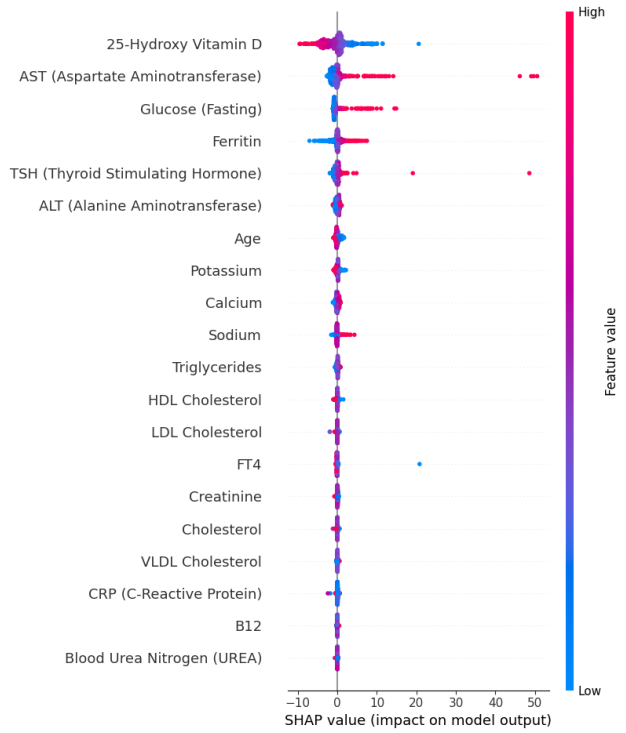


Figure 5. SHAP Bee Swarm Plot Showing Feature Value Impact on Insulin Prediction

Figure 5 complements this by illustrating how individual feature values influence insulin predictions across patients. Each point represents a patient's SHAP value for a feature, colored from blue (low feature value) to red (high feature value). For example, high fasting glucose levels (red points) correspond to positive SHAP values, increasing predicted insulin levels, whereas low glucose levels (blue points) reduce them. Similar patterns are observed for *25-Hydroxy Vitamin D* and *AST*, showing their variable contributions depending on measured values.

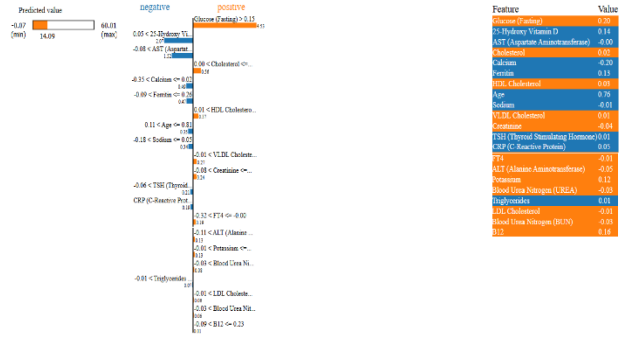


Figure 6. LIME Explanation of Feature Contributions for a Single Patient's Insulin Prediction

Figure 6, generated using the LIME method, details the positive or negative contribution of features to insulin prediction in a single example (one patient data point). This graph clearly shows that high glucose values are the strongest factor increasing insulin prediction. Some biomarkers, such as *B12* and *FT4* values, have a smaller effect on insulin levels on a sample basis and, although locally effective, have a lower effect in the general population.

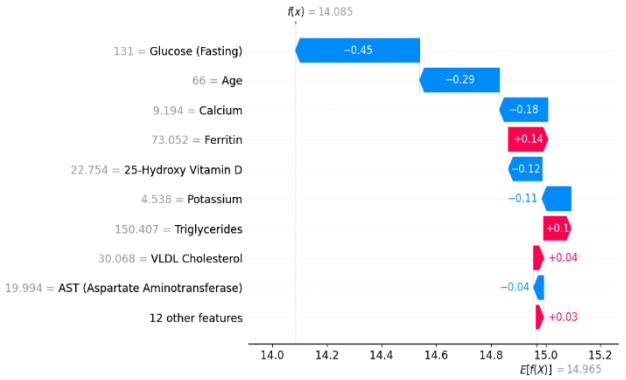


Figure 7. SHAP Waterfall Plot (Single Instance)

Figure 7 presents a SHAP waterfall plot illustrating how each feature incrementally adjusts the model's baseline prediction (14.085) to arrive at the final predicted value (14.965) for a single patient. In this instance, *Glucose (Fasting)* and *Age* exert the most pronounced negative contributions, collectively reducing the prediction by approximately 0.74 units. Conversely, *Calcium* and *Ferritin* provide moderate positive shifts, suggesting that elevated levels of these biomarkers are associated with an increased *Insulin* estimate. The contribution of *25-Hydroxy Vitamin D*—also positive—reinforces the broader observation that *25-Hydroxy Vitamin D* status plays a significant role in insulin regulation. Smaller effects, such as the negative impact of *Potassium* and the positive shifts from *Triglycerides, VLDL Cholesterol*, and *AST*, further refine the prediction. When these individual contributions are summed, the model's final prediction is slightly higher than the baseline. This granular view of how each biomarker influences the predicted *insulin* level underscores the interpretability benefits of SHAP, enabling clinicians and researchers to pinpoint the clinical factors that most strongly drive the model's decision for this particular patient.

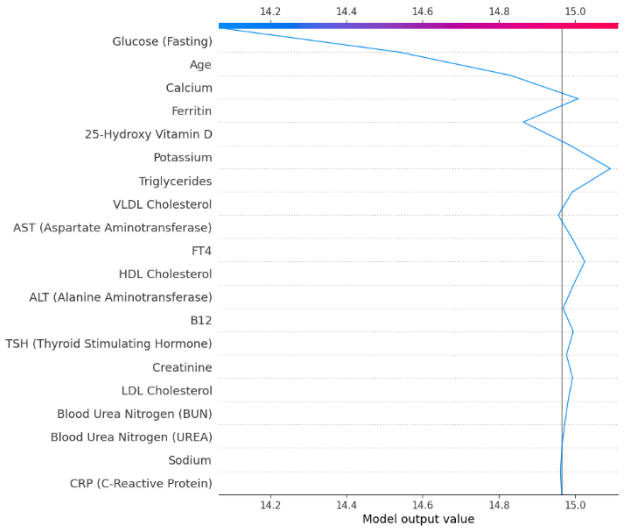


Figure 8. SHAP Decision Plot Illustrating Feature Contributions Across Individual Predictions

Figure 8 displays a SHAP decision plot that sequentially demonstrates how each clinical feature modifies the model's predicted insulin value from an initial baseline (approximately 14.2) to the final output (near 15.0) for a single instance. The horizontal axis represents the model's prediction scale, while each step in the plot shows the incremental contribution—positive or negative—of a specific biomarker:

- *Glucose (Fasting)* and *Age* appear as the top contributors, with their combined influence shaping the initial shift from the baseline.
- *Calcium, Ferritin, 25-Hydroxy Vitamin D, and Potassium* provide additional refinements, indicating that variations in these features can further raise or lower the predicted insulin level.
- The subsequent features, including *Triglycerides, VLDL Cholesterol, AST*, and others, exert smaller but still meaningful effects, cumulatively guiding the model to its final prediction.

By illustrating each feature's incremental impact, the decision plot offers a transparent view of the model's internal reasoning. Clinically, it underscores how multiple biomarkers—ranging from glucose metabolism to mineral balance—interact to influence insulin levels, thereby offering a nuanced perspective for personalized patient management.

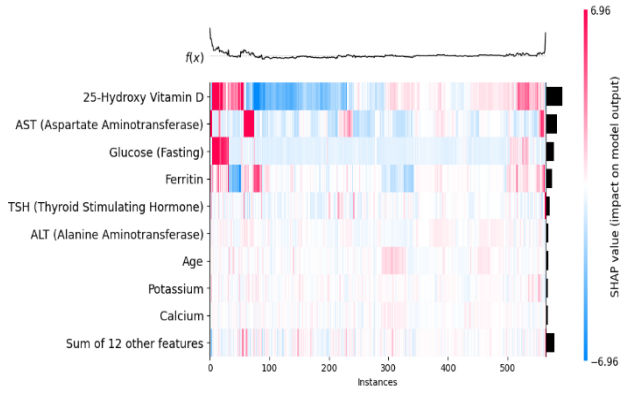


Figure 9. SHAP Heatmap Displaying Feature Impact on Model Output Across All Instances

In Figure 9, the visualization is organized into columns representing individual cases, while the rows correspond to clinical features ranked by their overall significance to the model's output. The color scale used conveys both the size and sign of each feature's influence on the resultant insulin value: saturated red denotes a feature positively influencing insulin predictions, and saturated blue denotes its negative impact. The leading feature, serum 25-Hydroxy Vitamin D, exhibits a noticeable spread of red and blue colors across the observation columns, suggesting that alterations in vitamin D status may critically impact insulin estimation according to the underlying risk profile of concurrent biomarkers. Similar spread is evident for aspartate aminotransferase, fasting glucose, and ferritin, each demonstrating distinct patterns that confirm their significant effect on the variation in predictions. Lower rows in the heatmap, containing thyroid-stimulating hormone, alanine aminotransferase, and other clinical covariates, reveal segments with less intense colors yet still instrumental in marginal adjustment of the insulin predictions. The horizontal bands of color further delineate clusters of patients whose combinatorial biomarker portraits converge to similar model predictions, suggesting the presence of latent clinical subgroups influenced by specific biomarker combinations. This heatmap illustrates both the global importance and the instance-specific role of selected biomarkers, providing clinicians and researchers with understanding of the interactions between features that collectively contribute to predictive results.

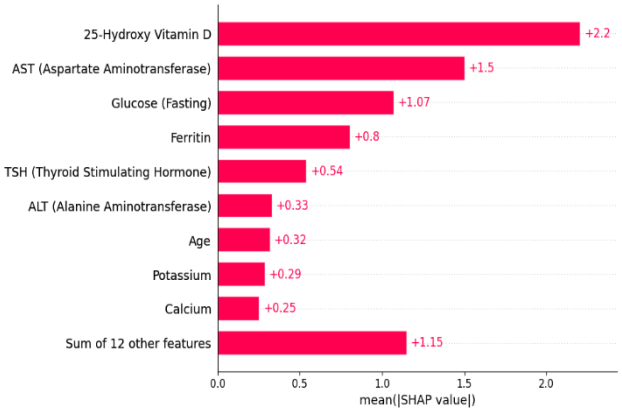


Figure 10. SHAP Bar Plot Showing Average Feature Importance in Insulin Prediction

In Figure 10, each horizontal bar indicates the mean absolute SHAP value for a given feature, illustrating its overall impact on the model's insulin predictions. The highest bar corresponds to *25-Hydroxy Vitamin D*, which stands out as the most influential predictor, with a mean SHAP value of +2.2. This suggests that variations in vitamin D levels produce larger shifts in the model's output than any other single biomarker. Following closely, *AST* and *Glucose (Fasting)* exhibit substantial mean SHAP values, highlighting their critical roles in shaping insulin estimates—an observation aligned with established clinical knowledge regarding liver enzymes and glycemic control. *Ferritin, TSH,* and *ALT* also show meaningful contributions, indicating that metabolic and endocrine factors collectively inform the model's decisions. Lower-ranked features, including *Potassium and Calcium,* have more modest mean SHAP values but nonetheless refine the prediction. The aggregated "*Sum of 12 other features*" category demonstrates that while individually less influential, a group of features still exerts a combined effect on insulin level estimation. Overall, this visualization underscores the multifactorial nature of insulin regulation, highlighting the diverse set of biomarkers—spanning vitamin levels, hepatic function, and mineral homeostasis—that the model deems most pertinent in forecasting insulin concentrations.

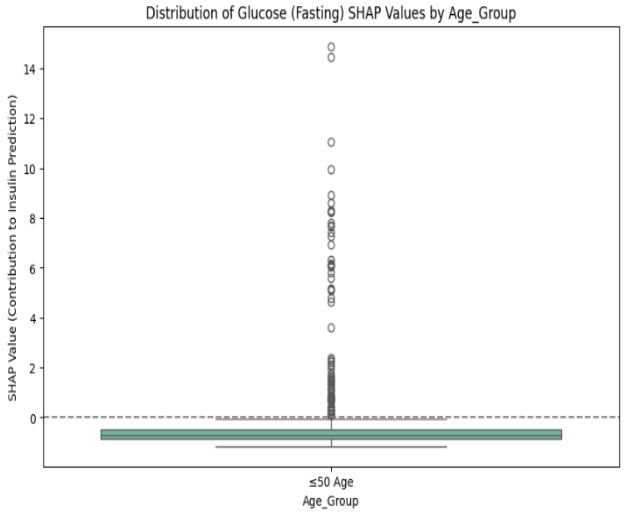


Figure 11. Distribution of Glucose (Fasting) SHAP Values by Age Group

In Figure 11, the distribution of SHAP values for fasting glucose across age groups reveals a wider spread of values in the younger subgroup (≤50 years), with several positive outliers strongly contributing to insulin prediction. This suggests that glucose levels may have a more variable influence on insulin prediction among younger individuals compared to older ones. The median SHAP value appears closer to zero, indicating that while some individuals show strong influence, the overall effect is moderate.

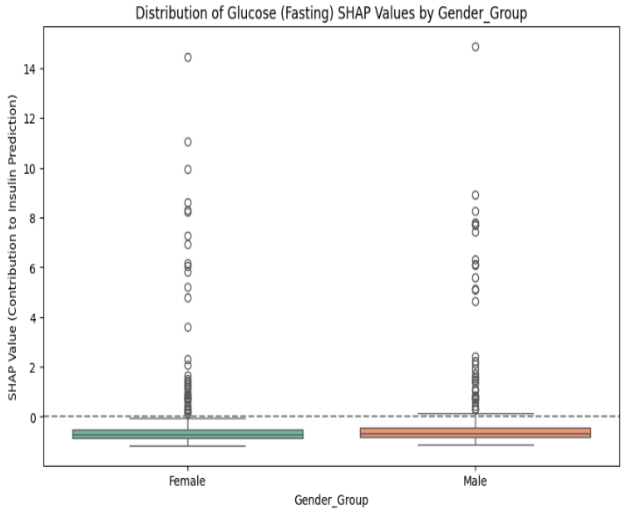


Figure 12. Distribution of Glucose (Fasting) SHAP Values by Gender Group

In Figure 12, the SHAP value distributions for fasting glucose are similar between females and males, with overlapping medians and ranges. Although outliers with high positive contributions exist in both genders, no substantial difference in the overall impact on insulin prediction is evident. This is consistent with the statistical test result ($p = 0.1842$), indicating no significant difference between genders in the predictive contribution of fasting glucose.

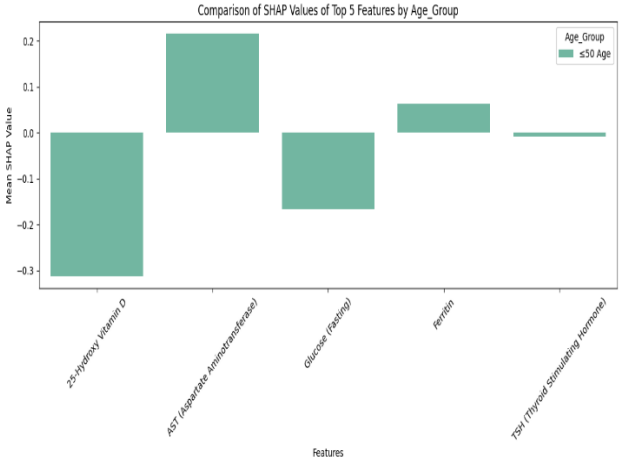


Figure 13. Comparison of SHAP Values of Top 5 Features by Age Group

In Figure 13, a comparison of the mean SHAP values of the top five features across age groups reveals notable differences. The younger group (≤50 years) exhibits higher mean SHAP values for *AST* and *25-Hydroxy Vitamin D*, suggesting these features contribute more strongly to insulin prediction in this subgroup. Conversely, the older group's influence is comparatively lower for these features. *Glucose (Fasting)* maintains a moderate effect across both groups, suggesting it is an important predictor regardless of age.

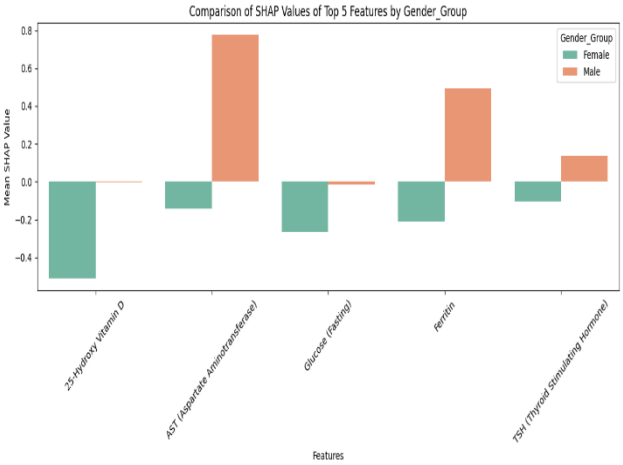


Figure 14. Comparison of SHAP Values of Top 5 Features by Gender Group

Figure 14 demonstrates distinct patterns in the comparison of mean SHAP values for the top features between genders. Males exhibit higher mean SHAP contributions for *AST* and *Ferritin*, while females show a stronger influence of *25-Hydroxy Vitamin D*. *Glucose (Fasting)* shows a relatively consistent effect in both groups. These differences imply that the model's explanation for insulin prediction varies subtly between males and females, highlighting potential biological or clinical differences in feature relevance.

Discussion

Despite the excellent performance achieved by the hybrid ensemble model, several issues remain that warrant further attention. Furthermore, it is essential to clarify whether the dataset inherently contains temporal or sequential structures that justify the use of recurrent architectures such as LSTM. If the data exhibits temporal dependencies, leveraging LSTM could provide meaningful advantages; otherwise, Transformer-based or other non-sequential models might require alternative design considerations [37].

Moreover, the success of the stacking methodology is highly contingent on the quality of out-of-fold predictions and the design of the meta-model. Transformer-based architectures initially exhibited suboptimal results, underscoring their sensitivity to hyperparameters such as learning rate, dropout, and attention mechanisms. These findings point to the necessity of advanced optimization techniques, such as Bayesian search, to unlock their full potential. Moreover, although combining MLP and optimized Transformer outputs yielded strong results (R^2 = 0.9157), further gains might be achieved by incorporating additional learners—like Random Forests or other deep models—offering diverse perspectives and improving robustness. Additionally, employing regularization strategies—such as L2 regularization or dropout at the meta-model level—could mitigate overfitting risks, leading to more robust and reliable predictions.

XAI analyses confirmed the importance of biomarkers including *25-Hydroxy Vitamin D, AST*, and *Glucose (Fasting)* in predicting insulin levels. Notably, subgroup analyses demonstrated statistically meaningful variations in feature importance across demographic strata, highlighting the need for personalized approaches tailored to demographic differences. For example, fasting glucose exhibited greater variability in predictive influence among younger patients (≤50 years), indicating heterogeneous metabolic profiles or disease manifestations in this subgroup. Gender-based comparisons, while showing no statistically significant difference in fasting glucose contribution, identified subtle but potentially clinically relevant distinctions in features including AST and Ferritin. These findings underscore the importance of integrating subgroup-specific interpretability within predictive modeling frameworks to enhance clinical transparency and support personalized medicine [38, 39]. Future work should strive to incorporate these interpretability tools more seamlessly to provide clinicians with actionable insights alongside high model performance, ultimately fostering trust in automated decision support systems [40].

The study's single-center dataset poses limitations in terms of generalizability. Broader validation across multicenter cohorts with diverse clinical profiles is essential to ensure robustness and external applicability. Future studies are needed to validate these models on larger, multicenter datasets with diverse demographic and clinical characteristics. In addition to technical improvements, ethical and practical considerations are crucial for clinical deployment. Ensuring patient data privacy, addressing potential algorithmic bias, and evaluating the clinical consequences of false predictions are essential steps for safe integration into decision support systems. These safeguards will enhance clinician trust and ensure responsible application of the model in diverse healthcare settings. Additionally, expanding the scope to include other relevant clinical outcomes, such as hypoglycemic events and long-term complications, could provide a more comprehensive understanding of disease progression and model utility in real-world settings [40].

In conclusion, our study demonstrates that hybrid ensemble methodologies, which integrate advanced deep learning architectures with classical regression techniques and robust XAI approaches, offer a promising avenue for predicting insulin levels in clinical data. Nonetheless, further optimization of model parameters, incorporation of additional base learners, explicit consideration of temporal data structure, and expansion of datasets are essential next steps to improve model generalizability and clinical utility. Additionally, embedding subgroup-specific explainability analyses will be critical for translating predictive models into trustworthy, personalized clinical decision support tools, ultimately contributing to more effective patient care [37, 38].

Conclusion

This study introduces a hybrid ensemble framework that outperforms individual models in predicting insulin levels from clinical data by combining deep learning and classical methods. However, several limitations remain. The dataset was sourced from a single center, which restricts the generalizability of the findings. Further refinement of model hyperparameters is needed, and incorporating additional biomarkers, including genetic and epigenetic factors, could enhance predictive power. Validation on larger, multicenter cohorts and the integration of real-time data streams, including continuous glucose monitoring, will be crucial to capture more complex physiological patterns. Moreover, ensuring that model explanations adapt to patient subgroups will be key to clinical acceptance, allowing for personalized and transparent decision-making. The future success of machine learning in healthcare depends on balancing high accuracy with explainable models, while addressing ethical considerations centered on patient care, including data privacy, model transparency, and potential algorithmic bias. These considerations are essential for safe and responsible use of AI in real-world clinical environments. Collectively, this study not only achieves high predictive accuracy but also provides clinically meaningful interpretations tailored to patient subgroups, representing a significant advancement in personalized AI-driven clinical decision support. Such progress holds promise for enhancing patient outcomes.

Ethics committee approval

There is no need to obtain permission from the ethics committee for the article prepared.

Conflict of Interest

There is no conflict of interest with any person / institution in the article prepared.

References

[1] Abhari, S., Kalhori, S., Ebrahimi, M., Hasannejadasl, H., and Garavand, A. (2019). *Artificial intelligence applications in type 2 diabetes mellitus care: focus on machine learning methods*. Healthcare Informatics Research, 25(4), 248. https://doi.org/10.4258/hir.2019.25.4.248.

[2] Christodoulou, E., Ma, J., Collins, G., Steyerberg, E., Verbakel, J., and Calster, B. (2019). *A systematic review shows no performance benefit of machine learning over logistic regression for clinical prediction models*. Journal of Clinical Epidemiology, 110, 12-22. https://doi.org/10.1016/j.jclinepi.2019.02.004.

[3] Juárez-Orozco, L., Niemi, M., Yeung, M., Benjamins, J., Maaniitty, T., Teuho, J., and Klén, R. (2023). *Hybridizing machine learning in survival analysis of cardiac pet/ct imaging*. Journal of Nuclear Cardiology, 30(6), 2750-2759. https://doi.org/10.1007/s12350-023-03359-4

[4] Yang, Z., Dehmer, M., Yli-Harja, O., and Emmert-Streib, F. (2020). *Combining deep learning with token selection for patient phenotyping from electronic health records*. Scientific Reports, 10(1). https://doi.org/10.1038/s41598-020-58178-1

[5] Cheng, X., Li, S., Deng, L., Luo, W., Wang, D., Cheng, J., and Zhang, G. (2022). *Predicting elevated tsh levels in the physical examination population with a machine learning model.* Frontiers in Endocrinology, 13. https://doi.org/10.3389/fendo.2022.839829

[6] Zhang, H., Yang, Y., Yang, C., Yang, Y., He, X., Chen, C.,and Li, W. (2023). *A novel interpretable radiomics model to distinguish nodular goiter from malignant thyroid nodules*. Journal of Computer Assisted Tomography, 48(2), 334-342. https://doi.org/10.1097/rct.0000000000001544

[7] Alam, M., Islam, R., Sizan, M., and Akash, A. (2024). *The integration of machine learning in information technologies: future trends and predictions*. Journal of Computer Science and Technology Studies, 6(5), 75-84. https://doi.org/10.32996/jcsts.2024.6.5.7

[8] Song, T., Yang, F., and Dutta, J. (2021). *Noise2void: unsupervised denoising of pet images.* Physics in Medicine and Biology, 66(21), 214002. https://doi.org/10.1088/1361-6560/ac30a0

[9] Özkan, E., Orhan, K., Soydal, Ç., Kahya, Y., Tunç, S., Çelik, Ö., and Cangır, A. (2022). *Combined clinical and specific positron emission tomography/computed tomography-based radiomic features and machine-learning model in prediction of thymoma risk groups*. Nuclear Medicine Communications, 43(5), 529-539. https://doi.org/10.1097/mnm.0000000000001547

[10] Zhao, X., Yin, Y., and Bu, X. (2022). *Resilient iterative learning control for a class of discrete-time nonlinear systems under hybrid attacks*. Asian Journal of Control, 25(2), 1167-1179. https://doi.org/10.1002/asjc.2898

[11] Li, G., Ma, X., and Yang, H. (2018). *A hybrid model for monthly precipitation time series forecasting based on variational mode decomposition with extreme learning machine.* Information, 9(7), 177. https://doi.org/10.3390/info9070177

[12] Askaruly, B. and Abitova, G. (2023). *Hybrid information systems modeling technology for business process analysis based on the internet of things*. Bulletin of Shakarim University Technical Sciences, (3(11)), 19-28. https://doi.org/10.53360/2788-7995-2023-3(11)-2

[13] Wang, W. and Pai, T. (2023). *Enhancing small tabular clinical trial dataset through hybrid data augmentation: combining smote and wcgan-gp*. Data, 8(9), 135. https://doi.org/10.3390/data8090135

[14] Afshar, P., Heidarian, S., Naderkhani, F., Rafiee, M., Oikonomou, A., Plataniotis, K., and Mohammadi, A. (2021). *Hybrid deep learning model for diagnosis of covid-19 using ct scans and clinical/demographic data*., IEEE International Conference on Image Processing (ICIP), 180-184. https://doi.org/10.1109/icip42928.2021.9506661

[15] Kavakiotis, I., Tsave, O., Salifoglou, A., Maglaveras, N., Vlahavas, I., and Chouvarda, I. (2017). *Machine learning and data mining methods in diabetes research*. Computational and Structural Biotechnology Journal, 15, 104-116. https://doi.org/10.1016/j.csbj.2016.12.005

[16] Thomsen, C., Hangaard, S., Kronborg, T., Vestergaard, P., Hejlesen, O., and Jensen, M. (2022). *Time for using machine learning for dose guidance in titration of people with type 2 diabetes? a systematic review of basal insulin dose guidance*. Journal of Diabetes Science and Technology, 18(5), 1185-1197. https://doi.org/10.1177/19322968221145964

[17] Dai, F., Meng, Y., Tan, S., Liu, P., Zhao, C., Qian, Y., and Yu, S. (2020). *Artificial intelligence applications in allergic rhinitis diagnosis: focus on ensemble learning*. Asia Pacific Allergy, 14(2), 56-62. https://doi.org/10.22541/au.159373328.85037548

[18] Kamnitsas, K., Bai, W., Ferrante, E., McDonagh, S., Sinclair, M., Pawlowski, N., and Glocker, B. (2018). *Ensembles of multiple models and architectures for robust brain tumour segmentation*. (pp. 450-462). Springer International Publishing. https://doi.org/10.1007/978-3-319-75238-9_38

[19] Sukegawa, S., Fujimura, A., Taguchi, A., Yamamoto, *N., Kitamura, A., Goto, R., and Furuki, Y. (2021). Identification of osteoporosis using ensemble deep learning model with panoramic radiographs and clinical covariates*. Scientific reports, 12(1), 6088. https://doi.org/10.21203/rs.3.rs-956619/v1

[20] Yamamoto, N., Sukegawa, S., Kitamura, A., Goto, R., Noda, T., Nakano, K., and Ozaki, T. (2020). *Deep learning for osteoporosis classification using hip radiographs and patient clinical covariates*. Biomolecules, 10(11), 1534. https://doi.org/10.3390/biom10111534

[21] Badgeley, M., Zech, J., Oakden-Rayner, L., Glicksberg, B., Liu, M., Gale, W., and Dudley, J. (2019). *Deep learning predicts hip fracture using confounding patient and healthcare variables*. NPJ Digital Medicine, 2(1). https://doi.org/10.1038/s41746-019-0105-1

[22] Famoye, F. and Singh, K. (2021). *Zero-inflated generalized poisson regression model with an application to domestic violence data*. Journal of Data Science, 4(1), 117-130. https://doi.org/10.6339/jds.2006.04(1).257

[23] Obasohan, P., Walters, S., Jacques, R., and Khatab, K. (2020). A scoping review of the risk factors associated with anaemia among children under five years in sub-saharan african countries. International Journal of Environmental Research and Public Health, 17(23), 8829. https://doi.org/10.3390/ijerph17238829

[24] Habibov, N., Auchynnikava, A., and Luo, R. (2019). Poverty does make us sick. Annals of Global Health, 85(1). https://doi.org/10.5334/aogh.2357

[25] Li, K., Daniels, J., Liu, C., Herrero, P., and Georgiou, P. (2020). *Convolutional recurrent neural networks for glucose prediction*. IEEE Journal of Biomedical and Health Informatics, 24(2), 603-613. https://doi.org/10.1109/jbhi.2019.2908488

[26] Fujihara, K., Matsubayashi, Y., YAMADA, M., Yamamoto, M., Iizuka, T., Miyamura, K., and Sone, H. (2021). *Machine learning approach to decision making for insulin initiation in japanese patients with type 2 diabetes (jddm 58): model development and validation study*. Jmir Medical Informatics, 9(1), e22148. https://doi.org/10.2196/22148

[27] Lee, W. (2020). *Machine learning for the diagnosis of early stage diabetes using temporal glucose profiles*. Journal of the Korean Physical Society, 78(5), 373-378 https://doi.org/10.48550/arxiv.2005.08701

[28] Muñoz-Organero, M., Queipo-Álvarez, P., and García, B. (2021*). Learning carbohydrate digestion and insulin absorption curves using blood glucose level prediction and deep learning models*. Sensors, 21(14), 4926. https://doi.org/10.3390/s21144926

[29] Tang, B., Yuan, Y., Yang, J., Qiu, L., Zhang, S., and Shi, J. (2022). *Predicting blood glucose concentration after short-acting insulin injection using discontinuous injection records*. Sensors, 22(21), 8454. https://doi.org/10.3390/s22218454

[30] Nagaraj, S., Sidorenkov, G., Boven, J., and Denig, P. (2019). *Predicting short- and long-term glycated haemoglobin response after insulin initiation in patients with type 2 diabetes mellitus using machine-learning algorithms*. Diabetes Obesity and Metabolism, 21(12), 2704-2711. https://doi.org/10.1111/dom.13860

[31] Mortazavi, B., Downing, N., Bucholz, E., Dharmarajan, K., Manhapra, A., Li, S., and Krumholz, H. (2016). *Analysis of machine learning techniques for heart failure readmissions*. Circulation Cardiovascular Quality and Outcomes, 9(6), 629-640. https://doi.org/10.1161/circoutcomes.116.003039

[32] Uyttendaele, V., Knopp, J., Stewart, K., Desaive, T., Benyó, B., Szabó-Némedi, N., and Chase, J. (2018). *A 3d insulin sensitivity prediction model enables more patient-specific prediction and model-based glycaemic control*. Biomedical Signal Processing and Control, 46, 192-200. https://doi.org/10.1016/j.bspc.2018.05.032

[33] Li, Y., Wang, H., Ye, Z., and Zhou, H. (2023). *Diabetes prediction and analysis using machine learning models*. In International Conference on Mechatronics Engineering and Artificial Intelligence (MEAI 2022) (Vol. 12596, pp. 277-283). SPIE. https://doi.org/10.1117/12.2672671

[34] Pushpavathi, K. (2024). *Diabetic drug ontology mapping for individual diabetic person and predict insulin dosage on daily basis*. Journal of Electrical Systems, 20(5s), 1801-1813. https://doi.org/10.52783/jes.2515

[35] Jung, C., Lee, M., Hwang, J., Jang, J., Leem, J., Park, J., and Lee, W. (2013). *Elevated serum ferritin level is associated with the incident type 2 diabetes in healthy korean men: a 4 year longitudinal study*. Plos One, 8(9), e75250. https://doi.org/10.1371/journal.pone.0075250

[36] Carvalho, D. V., Pereira, E. M., & Cardoso, J. S. (2019). Machine Learning Interpretability: A Survey on Methods and Metrics. Electronics, 8(8), 832. https://doi.org/10.3390/electronics8080832

[37] Rudin, C. (2019). Stop explaining black box machine learning models for high stakes decisions and use interpretable models instead. Nat Mach Intell 1, 206–215. https://doi.org/10.1038/s42256-019-0048-x

[38] Lundberg, S. M., & Lee, S. I. (2017). A unified approach to interpreting model predictions. Advances in neural information processing systems, 30.

[39] Tonekaboni, S., Joshi, S., McCradden, M. D., & Goldenberg, A. (2019). What clinicians want: Contextualizing explainable machine learning for clinical end use. arXiv preprint arXiv:1905.05134. https://arxiv.org/abs/1905.05134

[40] Ghassemi, M., Oakden-Rayner, L., & Beam, A. L. (2021). The false hope of current approaches to explainable artificial intelligence in health care. The Lancet Digital Health, 3(11), e745–e750. https://doi.org/10.1016/S2589-7500(21)00208-9

[41] Ribeiro, M. T., Singh, S., & Guestrin, C. (2016, August). " Why should i trust you?" Explaining the predictions of any classifier. In Proceedings of the 22nd ACM SIGKDD international conference on knowledge discovery and data mining (pp. 1135-1144).

Appendix - Model Architectures and Hyperparameters Used in the Study

Model Name	Layer Structure/Architecture	Activation Functions	Optimization Algorithm	Learning Rate	Dropout Rate	Additional Parameters
MLP	3 Layers (128-64-32-1)	ReLU (Hidden Layers) Linear (Output Layer)	Adam	0.001	0.2	Epochs: 100 Batch Size: 32 EarlyStopping (Patience=10)
Transformer	CNN (Conv1D, filters=64, kernel=2) LSTM (50 units) Dense (1 unit)	ReLU (CNN Layer) Tanh (LSTM Layer) Linear (Output)	Adam	0.001	0.2	Epochs: 50 Batch Size: 32
Baseline Transformer	Embedding: Dense (32 dimensions) 2 Transformer Encoder Blocks (Head Size=16, Num Heads=4, FFN=64) GlobalAveragePooling Dense (64-1)	ReLU (Hidden Layers) Linear (Output Layer)	Adam	0.001	0.1	Epochs: 100 Batch Size: 32 EarlyStopping (Patience=10)
Transformer + Positional Encoding	Embedding: Dense (64 dimensions) 3 Transformer Encoder Blocks (Head Size=32, Num Heads=4, FFN=128) GlobalAveragePooling Dense (64-1)	ReLU (Hidden Layers) Linear (Output Layer)	Adam	0.0001	0.2	Epochs: 100 Batch Size: 16 EarlyStopping (Patience=10)
Optimized Transformer	Auto-tuned: embed_dim=[32,64,128] head_size=[16,32,64] num_heads=[2,4,8] ff_dim=[64,128,256] dropout=[0.1-0.5] learning_rate=[1e-3,1e-4,1e-5]	ReLU (Hidden Layers) Linear (Output Layer)	Adam	Tuned (Best Selected)	Tuned (Best Selected)	Epochs: 50 Batch Size: 32 RandomSearch (max_trials=10) EarlyStopping (Patience=10)
Keras Tuner Optimized Model	**Base Models:** - MLP (64-32 units) - Optimized Transformer (Embedding=64, Heads=4, FFN=128) **Meta-model:** Dense (16-8-1)	ReLU (Hidden Layers) Linear (Output Layer)	Adam	0.001	0.2 (Meta-model)	5-Fold Cross Validation Epochs: 20 (per model) Batch Size: 32

Dicle University
Journal of Engineering
https://dergipark.org.tr/tr/pub/dumf
duje.dicle.edu.tr

Research Article

Investigation of Geometric Invariance Properties of Hu Moments for Image Processing Applications

Ethem Sefa KÜÇÜKYILMAZ[1*], Erhan AKIN[2]

[1] Firat University, Management İnformation Systems Department, eskucukyilmaz@firat.edu.tr, Orcid No: 0009-0008-6912-1851
[2] Firat University, Computer Engineering Department, eakin@firat.edu.tr, Orcid No: 0000-0001-6476-9255

ARTICLE INFO

Article history:

Received 07 April 2025
Received in revised form 26 June 2025
Accepted 15 July 2025
Available online 30 September 2025

Keywords:

Image Processing, Hu Moments, Size Estimation, Scaling.

Doi: 10.24012/dumf.1670505

* Corresponding author

ABSTRACT

This research aims at estimating sizes of characters in the Turkish alphabet using techniques in image processing and Hu moments. The field of image processing is an important constituent in numerous applications, with specific examples including character recognition, for instance, in cases of optical character recognition (OCR). In this work, estimation of character "S" in terms of its sizes is performed through analysis of character images using techniques in Hu moments. Hu moments have proven effective in shape and object recognition, and through invariability in reflection, rotation, and scales, have become increasingly useful in a variety of applications. The observations derived during character size estimation involved examination of character "S" in its many sizes, following specific preprocessing protocols. Protocols included techniques in preprocessing, extraction of gradients, and sharpening techniques. After preprocessing, calculation of Hu moments took place in an attempt to evaluate character sizes in each case. Observational information showed that sizes of character "S," in its many sizes, could accurately be determined. Certain exceptional cases, in cases of uncertain borders of letters, necessitated additional refinements, though. The conclusion of this work identifies the use of Hu moments in character size estimation, in addition to its potential use in character and image processing studies. Conclusively, results validate efficiency and accuracy in proposed estimation of sizes, opening its use to complex forms in its range of applicable forms. In future studies, works could expand through incorporation of sophisticated preprocessing and analysis techniques for improvement in effectiveness of Hu moments.

Introduction

Image processing and shape analysis have an important place in today's computer science and engineering applications. Classification, analysis and interpretation of visual data has a wide range of uses, from medical diagnostic systems to autonomous vehicles, from remote sensing technologies to security applications. In particular, defining the geometric properties of objects and ensuring the invariance of these properties against different transformations is one of the main goals of many image processing techniques.

In this context, Hu moments are an important method that stands out with its stability against scale, rotation and translation changes. These moments, which represent the basic geometric properties of images, are used effectively in many applications such as object recognition, size determination, visual similarity analysis and motion tracking. Thanks to its computationally efficient structure, Hu moments enable fast and reliable analysis on large data sets. Compared to traditional methods, the invariance feature offered by Hu moments contributes to the preservation of accuracy, especially in complex and variable environments. In recent years, with the development of deep learning methods, more powerful feature extraction can be achieved by integrating Hu moments with models such as convolutional neural networks. This integration offers great advantages in areas such as object classification, medical image analysis and remote sensing. Additionally, Hu moments help achieve successful results in more specific applications such as small object detection and micro-scale surface recognition. This study aims to examine in detail the transformation invariance properties of Hu moments and their applications in various image processing fields. Additionally, its integration with modern artificial intelligence techniques will be discussed and how Hu moments can be made more effective in the future will be evaluated. The investigations show that Hu moments are a powerful tool in visual data analysis and suggest that future research should focus on further improving the performance of this method on different data types and applications. In contrast to prior works that focus primarily on theoretical or narrowly scoped uses of Hu moments, this study provides a comprehensive and experimentally supported analysis of geometric invariance properties by systematically evaluating translation, rotation, and scaling transformations through real-world implementations. The study's novelty lies in its modular Python-based framework that enables visual similarity, size estimation, and moment stability to be

tested on character data under controlled transformation conditions. This study differs from previous research by providing an explicitly application-oriented experimental setup that not only analyzes geometric invariance properties theoretically, but also validates them through custom-generated datasets, measurable metrics, and reproducible code modules.

Literature Review

Object recognition and shape analysis in the field of image processing is an important research area in artificial intelligence and machine learning applications. In this context, Hu moments provide stability against scale, rotation and translation changes by providing invariant properties that represent the geometric properties of objects. These moments, proposed by Hu (1961), are used in various fields such as optical character recognition (OCR), object tracking and medical image analysis [1]. The computationally simple structure and high efficiency of Hu moments enable them to be widely used in image processing applications. In the study conducted by Wu et al. (2020), image recall and classification performance was increased by integrating Hu moments with convolutional neural networks (CNN). Experiments have shown that Hu moments, when combined with CNNs, provide higher accuracy rates in recognition tasks [2]. In addition to traditional Hu moments, new orthogonal invariant moments developed in recent years provide higher accuracy and processing efficiency in image processing processes. Hjouji et al. (2020) revealed that these new moments are more effective, especially on large data sets, and provide better results compared to traditional methods [3]. Such developments further expand the field of use of Hu moments in object recognition and shape analysis. The effectiveness of Hu moments is not limited to large data sets; It is also used in more specific applications such as micro-scale surface recognition. In the study carried out by Rodríguez (2023), Hu moments were integrated with the micro-laser line contouring method in optical microscope systems and applied in the field of surface engineering, enabling a more precise recognition of surface textures [6]. Similarly, Gancheva and Peneva (2023) developed object comparison methodologies using Hu moments in radar satellite images. This approach has great potential, especially in fields such as remote sensing and satellite image analysis [5]. Medical imaging remains one of the most important uses of Hu moments. Setiawan et al (2023) revealed that Sobel segmentation and Hu moment feature extraction play an important role in classifying kidney diseases via CT images. It has been observed that these methods increase model performance, especially in unbalanced data sets [7]. Similarly, studies using Hu moments to diagnose acute lymphoblastic leukemia (ALL) have provided high accuracy rates in determining whether cells are benign or malignant [7]. It is known that pre-processing techniques make significant contributions to classification accuracy in image processing processes. In the study conducted by Zhao (2017), combining Hu moments and template matching methods achieved significant success in small target detection applications. This method has increased reliability rates by increasing target detection accuracy in low-resolution images [8]. As a result, Hu moments play an important role in image processing and object recognition applications. The principal moments developed by Hu (1961) provide higher accuracy when combined with CNNs and new orthogonal moments and have been successfully applied in many fields such as medical imaging, satellite image analysis and micro surface recognition. In particular, its integration with deep learning models can increase the effectiveness of Hu moments on larger datasets in the future. Additionally, the development of more advanced preprocessing techniques and hybrid methods to optimize performance in low-resolution and noisy environments will provide important direction for future research. While Hu moments and their derivatives are a powerful tool for many applications, they have some limitations. For example, the performance of moment-based methods may decrease in high-noise data, which necessitates optimization. In addition, it is emphasized that more flexible and dynamic methods should be preferred instead of Hu moments in objects with complex geometries. However, the development of Hu moments with hybrid approaches is another important research area suggested for future work in the literature. For example, combining deep learning with moment-based methods can provide improvements in both accuracy and generalization ability.

Methodology

Image processing is a series of analysis and manipulation processes performed to transform digital images into meaningful features. In this study, multiple image processing techniques were applied to perform visual analysis based on Hu moments. Basic steps were determined and a systematic process was followed to make the images suitable for analysis and feature extraction. This process includes pre-processing, segmentation and feature extraction stages. First of all, various preprocessing methods were applied to make the raw image data suitable for analysis. In this study, the visual dataset was manually constructed using character images of the letter "S" in the Turkish alphabet. These images were synthetically generated using Python's OpenCV library in grayscale format with a resolution of 256×256 pixels. The dataset includes various versions of the letter "S" with systematic variations in size (e.g., 300 px to 700 px), rotation (0° to 330° at 30° intervals), and translation (e.g., ±30 px on both axes).In the experimental design of this study, the geometric transformations—namely rotation, scaling, and translation—were applied independently to the reference images in order to examine their isolated impact on Hu moments. Specifically, rotation angles ranging from 0° to 330° (in 30° steps), scaling factors from 0.5x to 1.5x, and pixel translations of ±30 and ±50 pixels in both x and y directions were used. Each transformation type was tested separately on the same set of reference images to avoid confounding effects. This ensured that the invariant behavior of Hu moments could be reliably attributed to the specific transformation under analysis. In total, the dataset consists of 36 rotation-based images, 9 scale-based

samples, and 5 translated versions, all created in a controlled and repeatable environment. The ground truth labels (such as exact size, rotation angle, or translation offset) were recorded manually during image generation. The image files were named accordingly (e.g., s_90_derece.png, S_650.png) to encode their transformation parameters. All image generation, preprocessing, segmentation, and moment calculation processes were implemented in Python 3.10 using OpenCV, NumPy, Matplotlib, and SciPy libraries. The structure of the dataset and code modules have been designed to ensure reproducibility, and the experiments can be repeated with consistent outputs using the shared pipeline. Color images were converted to grayscale format so that each pixel was represented only by its intensity value. This process reduced the computational load and provided a simpler data structure. The histogram equalization method was used to improve image quality and to determine the regions to be analyzed more clearly. This method increased the contrast by rearranging the brightness distribution in the image and made the features more prominent. Additionally, the noise in the images was cleaned with low pass filters such as the Gaussian filter. The noise removal process provided more stable results, especially on low-resolution or distorted images. In the segmentation stage, different methods have been applied to highlight objects or areas of interest in the image. First, Otsu's thresholding method was used. This method determined an optimal threshold value by analyzing the grayscale histogram of the image and provided a clear separation between objects and the background [9]. Thanks to the thresholding method, objects are made independent of the background and a structure that can be analyzed more easily is obtained. In addition, object edges are highlighted using the Canny edge detection algorithm. The Canny method ensures accurate and stable detection of object boundaries with its structure that is resistant to translation and noise [10]. Following these preprocessing and segmentation steps, Hu moments representing the basic geometric features of the images were calculated. Hu moments are mathematical descriptors that are invariant to translation, rotation and scale changes [1]. Within the scope of this study, seven Hu moments were extracted for each image and these moments were used as basic features in analytical processes. In calculating the Hu moments, the pixel density distribution of the image was taken into account and the mathematical expressions of the moments were taken as basis. Especially normalized moments were calculated using the formula and then features were extracted with the invariant moment formulas derived by Hu. These moments offered distinct mathematical representations that encapsulate the geometrical structure and morphology of visual content. Hu moments extracted during the image processing phase of the study were used in visual similarity analysis and allowed the comparison of geometric structures between images. In addition, considering that Hu moments provide information about object sizes, size determination was also made. Thanks to these methods, structural differences and similarities between images could be expressed numerically and the visual analysis process was successfully completed. As a result, the methods applied in the image processing phase enabled the preparation of images for analytical processes and increased the accuracy of visual analyzes based on Hu moments. This process directly contributed to the overall success of the study and increased the reliability of the results obtained. To provide a clearer overview of the methodological steps carried out throughout the study, an algorithmic flowchart was created. This diagram presents the sequential process of data generation, preprocessing, feature extraction using Hu moments, similarity and size classification, and performance evaluation. The visual layout highlights the conditional structure of the similarity analysis and how it integrates into the overall pipeline. The step-by-step methodological flow is illustrated in Figure 1.

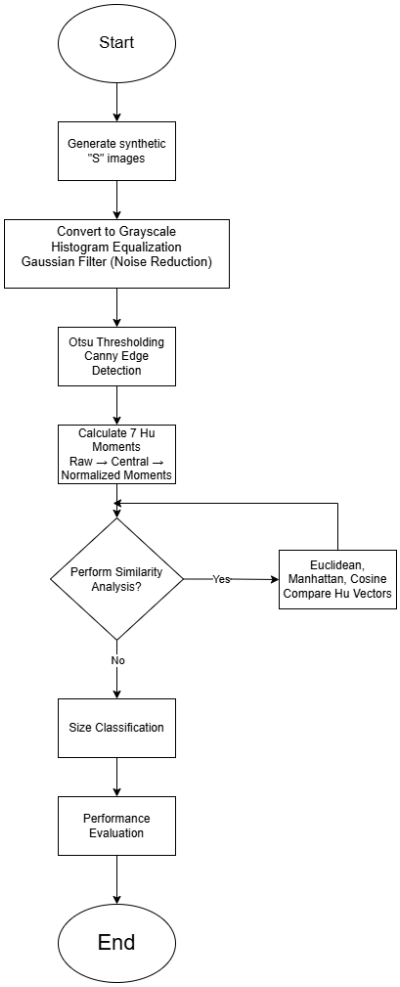


Figure 1. Flowchart illustrating the algorithmic steps of the Hu moment-based visual size estimation and classification methodology

Hu moments include seven features that mathematically represent the geometric properties of images and provide invariance against translation, rotation and scale changes. These moments, first described by Hu (1961), are widely used in image-based analysis and object recognition applications [1]. In this study, Hu moments were calculated to represent the shape features of the images and to perform visual similarity analysis. In order to calculate the Hu

moments, the spatial moments of an image are first obtained. Spatial moments are defined as the position-weighted sum of pixel values in the image. Mathematically, the moment m_{pq} is expressed as:

$$m_{pq} = \sum_x \sum_y x^p y^q f(x,y) \quad (1)$$

Where:

- m_{pq}: Raw moment of order $p+q$
- x, y : Pixel coordinates in the image domain
- $f(x,y)$: Intensity value of the pixel at position (x,y)
- p,q : Non-negative integers indicating the order of the moment

In this equation, p and q represent the degrees of the moment, while f(x,y) represents the intensity value of the image at a particular pixel. While spatial moments reflect the general characteristics of the image, normalized central moments are calculated to make these moments scale independent. The central moments are defined as u_pq and are formulated as follows, taking into account the center of gravity of the image:

$$u_{pq} = \sum_x \sum_y (x - \bar{x})^p (y - \bar{y})^p f(x,y) \quad (2)$$

Here $x' = \frac{m_{10}}{m_{00}}$ and $y' = \frac{m_{01}}{m_{00}}$ It refers to the coordinates of the center of gravity of the image. The normalized central moments are obtained by the formula:

$$n_{pq} = \frac{u_{pq}}{u_{00}^{\gamma}}, \gamma = \frac{p+q}{2} + 1 \quad (3)$$

The third formula represents the normalized central moment of order $p+q$ denoted as n_{pq} It is calculated by dividing the central moment u_{pq} by u_{00}^{γ}, where $\gamma = \frac{p+q}{2} + 1$. This normalization makes the moment invariant to scale changes, enabling consistent comparison of shapes regardless of their size. By removing the dependency on the object's absolute size, n_{pq} plays a crucial role in achieving scale invariance in image analysis tasks.

Normalized central moments provide invariance to translation and scale changes. Based on these moments, the seven invariant moments derived by Hu are calculated. Hu moments are defined mathematically by the following expressions:

$$\phi_1 = m_{20} + m_{02} \quad (4)$$

$$\phi_2 = (m_{20} - m_{02})^2 + 4m_{11}^2 \quad (5)$$

$$\phi_3 = (m_{30} - 3m_{12})^2 + (3m_{21} - m_{03})^2 \quad (6)$$

$$\phi_4 = (m_{20}m_{02} - m_{11}^2)^2 + (m_{30}m_{03} - 3m_{12}m_{21})^2 \quad (7)$$

$$\phi_5 = (m_{20} + m_{02})^2 + 4m_{11}^2 \quad (8)$$

$$\phi_6 = (m_{30} + m_{12})^2 + (m_{21} + m_{03})^2 \quad (9)$$

$$\phi_7 = (m_{20}m_{02} - m_{11}^2)^2 + (m_{30}m_{03} - 3m_{12}m_{21})^2 \quad (10)$$

The seven Hu moments (ϕ_1 to ϕ_7) are derived from raw image moments and are used to characterize the geometric properties of shapes in a manner invariant to translation, scaling, and rotation. The first Hu moment, ϕ_1, is calculated as the sum of the second-order raw moments along the x and y axes, $\phi_1 = m_{20} + m_{02}$ and represents the overall variance or spatial spread of the intensity distribution. The second moment, ϕ_2, expressed as $\phi_2 = (m_{20} - m_{02})^2 + 4m_{11}^2$ quantifies the difference in variance along the principal axes and includes a mixed moment term to account for correlation between the axes. ϕ_3 and ϕ_4 incorporate third-order and product terms to measure skewness and shape asymmetry. Specifically, ϕ_3 detects deviations from symmetry along the x and y directions using the expression $\phi_3 = (m_{30} - 3m_{12})^2 + (3m_{21} - m_{03})^2$while ϕ_4, given by $\phi_4 = (m_{20}m_{02} - m_{11}^2)^2 + (m_{30}m_{03} - 3m_{12}m_{21})^2$, captures complex interactions related to elongation and nonlinearity of the shape. ϕ_5, computed as $\phi_5 = (m_{20} + m_{02})^2 + 4m_{11}^2$, reinforces global symmetry information and provides additional robustness to noise. The sixth moment, ϕ_6, expressed as $\phi_6 = (m_{30} + m_{12})^2 + (m_{21} + m_{03})^2$, aggregates third-order spatial features, emphasizing asymmetries in diagonal directions. Lastly, ϕ_7, which shares structural similarities with ϕ_4, measures the most complex patterns of shape distribution through combinations of second- and third-order moments, and is particularly useful in distinguishing closely resembling patterns.

These moments are extremely powerful in representing the shape properties of images and provide invariance to translation, rotation and scale changes. In the study, these seven Hu moments were calculated for each image and used as feature vectors. Python programming language was preferred during feature extraction and calculation processes were supported by open source libraries. Obtaining these moments created a mathematical representation of the images and made it possible to quantitatively analyze the similarities and differences between different images. As a result, Hu moments were the main tool used for the extraction and analysis of basic visual features in this study. The invariance properties of moments enabled accurate comparison of images with different scales and transformations and contributed greatly to the general purpose of the study.

Similarity analysis is a method frequently used in the fields of image processing and computer vision to classify, recognize or match objects by comparing their features. In this study, various similarity metrics were used to evaluate the similarities between the feature vectors obtained with Hu moments and to compare the visual contents. The similarity analysis process is specifically designed to reveal the effectiveness of moments that are not affected by translation, rotation and scale changes. Similarity measures

mathematically express the level of similarity or dissimilarity between two feature vectors. In this study, Euclidean, Manhattan and Cosine distance, among the most commonly used distance measures, were preferred. These metrics are defined as follows:

Euclidean Distance: Euclidean distance measures the linear distance between two vectors and is calculated as:

$$d_E(u,v) = \sqrt{\sum_{i=1}^{n}(u_i - v_i)^2} \quad (11)$$

$u = [u_1, u_2, \ldots . u_n]$ and $v = [v_1, v_2, \ldots \ldots v_n]$ are feature vectors of dimensionality n, typically representing descriptors extracted from images. u_i and v_i denote the i-th components of vectors u and v respectively. The expression $(u_i - v_i)^2$ calculates the squared difference between corresponding components. The summation $\sum_{i=1}^{n}$ accumulates these squared differences across all dimensions. Finally, the square root is applied to obtain the actual Euclidean distance.

Manhattan Distance: Manhattan distance calculates the sum of coordinate differences between two vectors and is expressed as:

$$d_M(u,v) = \sum_{i=1}^{n} |u_i - v_i| \quad (12)$$

Here:

$|u_i - v_i|$ represents the absolute difference between the *i*-th components of vectors *u* and *v*. This metric has an approach that specifically emphasizes individual feature differences.

Cosine Similarity: Cosine similarity evaluates the angular similarity between two vectors and is defined as:

$$sim_{cos}(u,v) = \frac{u \,.\, v}{||u||\,||v||} \quad (13)$$

Here . refers vector multiplication, ||.|| refers to the vector size. Cosine similarity evaluates the directional similarity of vectors regardless of their size and is particularly insensitive to scale changes. These metrics used in similarity analysis have played a critical role in detecting shape similarities or differences between different images. In the study, the feature vectors obtained from the Hu moments of each image were compared with other images in the dataset and subjected to similarity analysis. This process was implemented using the Python programming language and libraries such as NumPy and SciPy were preferred for calculation processes. The data obtained as a result of similarity analysis provides important information, especially in tasks such as classification or grouping. Within the scope of the study, the results of similarity metrics were compared and it was analyzed which metric performed better in different image pairs. As a result, similarity analysis enabled the effective evaluation of the features obtained with Hu moments and allowed the shape similarities between different images to be expressed mathematically. The findings of the study revealed how the selected similarity metrics gave different results in certain tasks and provided important clues on how these metrics can be optimized in future applications.

Size analysis is an important method used to detect and evaluate the physical properties of an object, especially its sizes. In the context of image processing, size analysis allows objects to be scaled, compared, and their physical size accurately estimated based on certain metrics. In this study, the size analysis process was carried out using features derived from Hu moments. During the size analysis phase, the following steps were followed to determine the sizes of the objects in the image:

Object Extraction from Image: Separating objects in the image from the background is a critical prerequisite for size analysis. For this purpose, a boundary was determined between the object and the background using the Otsu thresholding method. This method automatically calculates the optimal threshold value based on the histogram of pixel intensities.

Moment-Based Size Measurements: Properties derived from Hu moments allow the sizes of objects to be estimated independently of translation, rotation, and scale changes. In this context, feature vectors obtained from moments represent the general geometric structure of the object and are used as the main source of information in size analysis.

Actual Size Calculation: Size information in an image is generally pixel-based and does not represent actual sizes in the physical world. Therefore, a scale factor was determined during the analysis process. The scale factor is derived from the physical sizes of a known object in the image and is used to calculate the actual sizes of other objects.

Size Comparison and Normalization: Size measurements obtained during the size analysis process are normalized for comparative analysis. Normalization enabled more accurate comparison, especially between images of different resolutions. In addition, the proportional relationships between the sizes of the objects were evaluated and the effect of scale changes was observed. These methods used during size analysis not only determined the physical sizes of the objects in the image precisely, but also contributed to revealing the size relationships between the objects. In the study, the size data obtained was used especially in classifying and categorizing objects. In conclusion, size analysis in this study demonstrated how Hu moments-based features can accurately represent size information. In particular, the correct application of scale factors and normalization techniques ensured consistency between different images. This approach provides a flexible and scalable solution for future applications.

Translational analysis is a method that examines the effect of this change on image properties when objects on the image are moved to different positions. Although translation does not change the geometric shapes or sizes of objects, it can lead to misleading results in feature extraction if they are placed at different coordinates on the image. Therefore, translational analysis is critical to test the

stability of Hu moments against such positional changes. In this study, translational analysis was carried out through the following steps in order to verify the invariance of Hu moments against translational effects:

Preprocessing and Translation Application: Images of each object are normalized in a determined reference coordinate system. Then, the objects were shifted a certain amount in different directions on the image and these translations were systematically recorded. In this process, the amount of translation was expressed in pixels and the shifts in the horizontal and vertical axes were examined separately.

Calculation of Hu Moments: Hu moments were recalculated for each translational configuration and possible changes that may occur due to translation were observed. It has been mathematically proven that Hu moments are completely independent of translational changes [1]. This feature is one of the main factors that make Hu moments stand out in image processing applications.

Feature Stability Analysis: The Hu moments obtained after translation were compared with the moments in the original position. By using metrics such as Mean Squared Error (MSE) for comparison, it was evaluated whether there was any significant deviation in the post-translational moments. Analysis results showed that Hu moments have high stability against translational effects.

Visualization and Interpretation of Results: Findings from the translational analysis are visualized graphically. It has been clearly observed that the moments calculated depending on the amount of translation remain constant, and therefore translation effects do not cause any deterioration in the extraction of object properties.

Application Areas and Importance: The results of translational analysis confirmed the usability of Hu moments in applications such as visual similarity, size detection and object recognition. Invariance against translation effects offers a great advantage, especially when moving objects are analyzed or the location of objects is unknown. In conclusion, the translational analysis clearly demonstrated the mathematical stability of Hu moments against translational changes and the practical benefits of this property. This study has shown that Hu moments can provide reliable results regardless of position change, further strengthening the use of this feature in the context of image processing.

Experimental Results

Image similarity analysis involves detecting visual similarities between different objects using Hu moments and expressing these similarities numerically. Experimental studies have revealed that similar objects have similar Hu moment values, while different objects present significantly different moment values. In the experiments, an image dataset representing different objects was used and comparisons were made between the Hu moments obtained from these images. Methods such as Euclidean distance and cosine similarity were used as comparison metrics. These methods have provided both sensitivity and reliability in moment-based visual similarity analysis. These observations highlight Hu moments' capability in effectively capturing structural similarities between visual objects. For example, while the Euclidean distance values between Hu moments of objects in the same category were found at a low level, these values increased significantly for objects in different categories. This underscores the discriminative strength of Hu moments in identifying subtle visual differences. The experimental results are also presented graphically, as seen in figures 2 and 3. While Figure 1 shows the similarity of the letters K and S to each other as 0.6394, Figure 2 shows the similarity of the normal version of the letter S and its 90 degree rotated version as 0, that is, exactly similar. These findings confirm the rotation-invariant properties of Hu moments as well as their ability to precisely detect shape similarity of objects. Visual similarity analysis has shown that Hu moments can be used effectively in a wide range of applications, such as object recognition, category identification, and visual classification.

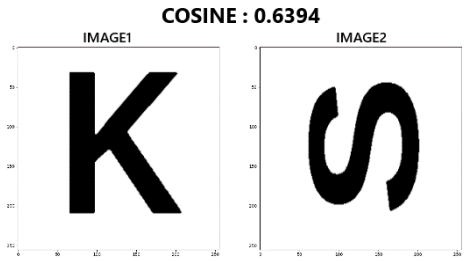


Figure 2. Visual comparison between the letter K and letter S using Hu moment similarity. The dataset includes synthetically generated images of both letters, normalized in size and position.

- Cosine Similarity Score: 0.6394
- Observation: Despite the visual and structural differences between the characters, a moderate similarity score is observed.
- Interpretation: This result indicates that Hu moments can capture shared geometric characteristics even between distinct shapes.

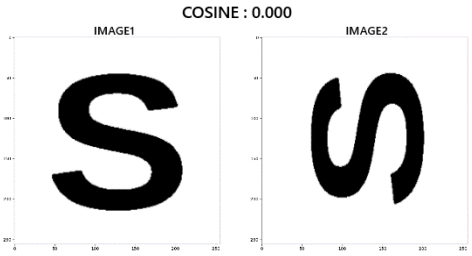


Figure 3. Similarity comparison between the original letter S and its 90-degree rotated version.

- Cosine Similarity Score: 0.000

- Observation: The complete lack of similarity score indicates a strong geometric dissimilarity after rotation.
- Interpretation: Despite Hu moments being theoretically rotation-invariant, this result reveals their limitations when applied to complex or asymmetric shapes.

To complement the visual comparisons presented in Figures 2 through 5, a numerical evaluation of similarity metrics was conducted. Table 1 summarizes the Euclidean distance and cosine similarity values calculated between the original letter S and its various rotated forms, as well as an unrelated character (K). As shown in the results, Hu moments preserved low distance values and high angular similarity for transformations such as 180°, 210°, and 330°, indicating invariance under these specific rotations. On the other hand, rotations like 90°, 120°, and 150° resulted in significantly higher distance values due to the change in perceived symmetry of the letter S. The comparison with the unrelated K character yielded the highest distance and cosine dissimilarity, as expected. The average Euclidean distance across all tested rotations was 6.5183 ± 6.9851, and cosine similarity was 0.1919 ± 0.2236, demonstrating the discriminatory capability of Hu moments while also highlighting their stability under rotational transformations.

Table 1. Euclidean distance and cosine similarity between original S and transformed images

Image Pair	Euclidean Distance	Cosine Similarity
S_Original vs S_90deg	12.0000	0.3199
S_Original vs S_120deg	12.0001	0.3197
S_Original vs S_150deg	12.0001	0.3196
S_Original vs S_180deg	0.0266	0.0000
S_Original vs S_210deg	0.0357	0.0000
S_Original vs S_240deg	0.0557	0.0000
S_Original vs S_270deg	12.0000	0.3198
S_Original vs S_300deg	0.0727	0.0000
S_Original vs S_330deg	0.0218	0.0000
S_Original vs K_Letter	16.9706	0.6396

- The cosine metric appears insensitive to small symmetric distortions (even 180° rotations), while Euclidean distance better captures fine-grained changes.
- However, both metrics fail to fully discriminate between dissimilar shapes like “S” and “K”, indicating a need for complementary or learned descriptors in future studies.

Size determination involves the process of determining the physical sizes of an object using Hu moments. In this study, object sizes were represented computably and accuracy analysis was performed between images at different scales. Experimental observations confirm that the Hu moment descriptors remain stable across different scaling transformations, validating their scale invariance. In the experiments, object images of different sizes were analysed and the relationships between the Hu moments obtained from these images were examined. In the analyses, the linear relationship between the actual physical sizes of the object and the moment values was calculated. Notably, the second- and third-order moments demonstrated superior sensitivity in the precise estimation of object dimensions. The obtained results confirm that Hu moments successfully maintain their scale invariance feature during the size determination process. For example, it has been determined that the differences between Hu moment values calculated for images of an object at different scales are negligible. This shows that Hu moments are a suitable tool for size determination applications. The experimental results are presented in figure 4. Figure 4 is selected from the dataset consisting of letters S at different scales, and in the relevant dataset, as shown in Figure 5, Hu compares the moment values and these values during the size determination and predicts the letter s closest to it, even if it is rotated to a different degree. These findings underscore the efficacy of Hu moments in enabling rapid and precise size estimation, especially in automated inspection and classification tasks. The scale invariance of Hu moments during the size determination process proves that this method provides advantages over other traditional methods.

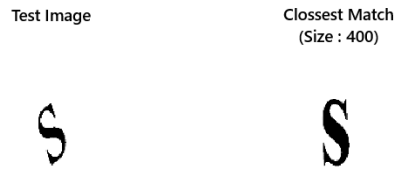


Figure 4. Size classification process for the letter S using Hu moments. Sample images at varying sizes were analyzed to determine moment-based size estimation accuracy.

- The system correctly identified the 400-pixel version as the nearest match.
- This suggests that the moment-based representation captures size-dependent shape structure reliably.

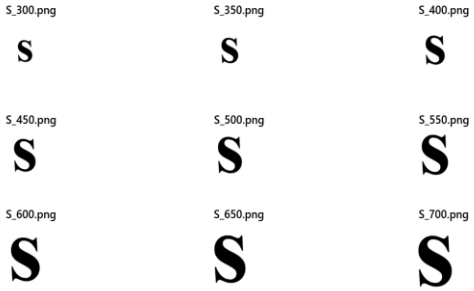


Figure 5. Dataset constructed for the size analysis of the letter S. Each image represents a specific scale class (e.g., S_300, S_400, ..., S_700) with normalized rotation and translation parameters to isolate scale as the only variable.

In addition to the geometric transformation experiments, a classification study was conducted to quantitatively evaluate the performance of Hu moment features in predicting the font size of a given character. For this purpose, a reference dataset was created by synthetically generating images of the letter "S" at nine different font sizes ranging from 300 to 700 pixels, with 100 samples per class. A KDTree-based classification method was employed to identify the most similar reference sample based on Hu moment vectors. The results of this classification task are presented in Figure 6 as a confusion matrix, which visually represents the model's prediction accuracy across all size classes. As can be seen, the majority of predictions fall along the diagonal of the matrix, indicating that the classifier successfully distinguished between different font sizes with minimal confusion, especially for the classes S_300, S_450, S_600, and S_650. To provide a more comprehensive performance evaluation, standard statistical metrics such as precision, recall, and F1-score were calculated for each class. These metrics, shown in Table 2, reveal that the model achieved a macro-averaged F1-score of 0.914 and an overall accuracy of 91.5% across 270 test samples. The precision values for the majority of the classes exceeded 0.90, and particularly high recall scores were observed for classes like S_450 and S_650, where perfect classification (recall = 1.0) was achieved. These findings demonstrate the robustness and discriminative power of Hu moments in capturing scale-specific shape characteristics even in the presence of minor distortions and augmentations. While minor misclassifications occurred between adjacent size groups (e.g., S_400 being predicted as S_300 or S_500), the model consistently maintained high classification performance, suggesting that Hu moments effectively preserve global shape patterns across transformations. These results also emphasize the potential of combining classical moment-based descriptors with efficient nearest-neighbor techniques such as KDTree for lightweight and interpretable image classification tasks. The use of confusion matrix visualization further supports the interpretability of the classifier, offering insights into class-wise performance discrepancies and helping to identify boundaries where size similarity introduces ambiguity.

Table 2. Classification Report for Hu Moment-Based KDTree Classifier

Class	Precision	Recall	F1-score	Support
S_300	0.906	0.967	0.935	30
S_350	1.000	0.933	0.966	30
S_400	0.786	0.733	0.759	30
S_450	0.857	1.000	0.923	30
S_500	0.879	0.967	0.921	30
S_550	0.893	0.833	0.862	30
S_600	1.000	0.900	0.947	30
S_650	0.968	1.000	0.984	30
S_700	0.964	0.900	0.931	30
Total				**270**

- The classifier performed consistently across classes, with minor performance dips observed in S_400 and S_550, likely due to visual similarity to adjacent size categories.

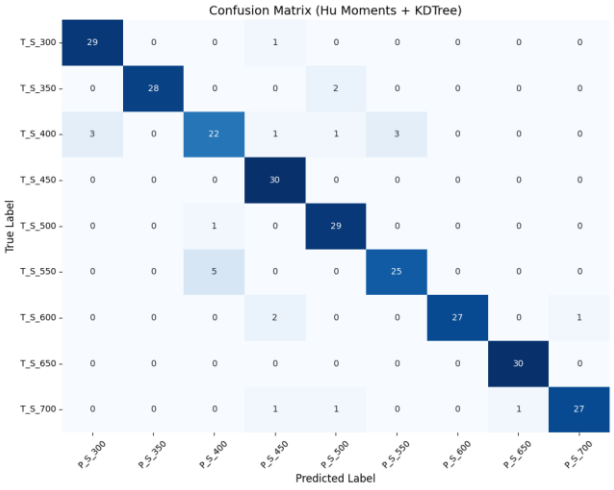


Figure 6. Confusion matrix showing classification results for Hu moment-based KDTree classifier over 9 different font sizes of the letter "S" (100 samples per class).

- The confusion matrix reveals high overall accuracy across most size classes.
- However, classes such as S_400 and S_550 demonstrate relatively higher confusion with neighboring classes, suggesting close moment similarity between adjacent sizes.
- In contrast, S_450 and S_650 exhibited perfect classification, indicating clear moment separability.

Translational analysis aims to examine the effect of moving the image of an object to different locations on Hu moments. In this study, experiments were carried out to evaluate whether the Hu moments, which provide translational invariance, maintain the same values even though the images are located in different positions. Within the scope of the analysis, imaging operations were performed by moving an object to different x and y coordinates. Hu moments were calculated for each image and examined whether there was any change between these values. Experimental results show that the translation process does not have a significant effect on the Hu moment values. This validates the translational invariance of Hu moments under varying positional displacements. The results obtained in the experiments revealed that the Hu moments remained constant, especially when the center of the image of an object was shifted to different points. For example, the image of an object was moved to various positions on both the horizontal and vertical axes, and the same moment values were obtained in each case. Such findings reinforce the suitability of Hu moments for precise size estimation tasks. The results obtained are presented in figure 4. Figure 7 shows comparatively the effects on Hu moments of images created by moving an object to different positions. Figure 8 shows the dataset consisting of the letters s used for translational analysis. The heat map visually demonstrates the translational invariance feature of Hu moments and emphasizes the importance of this feature for object recognition and analysis applications. These insights confirm that Hu moments maintain consistency across displacement scenarios, especially in moving object recognition, image fusion and tracking applications. The translational invariance property of Hu moments makes this method a reliable tool that is not sensitive to position changes.

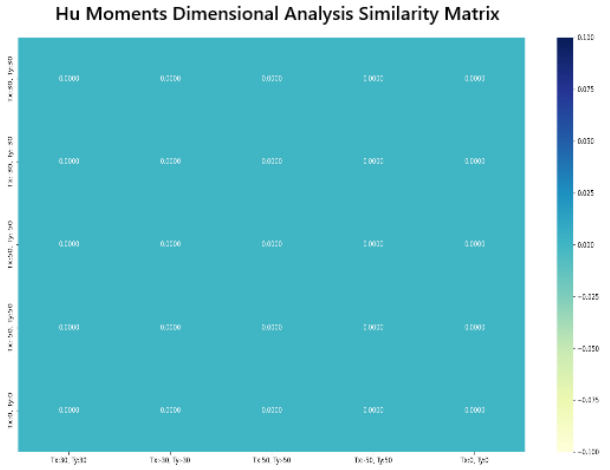


Figure 7. Heat map of pairwise similarity values for the letter S subjected to various translational shifts along the x and y axes (±30 and ±50 pixels). The matrix demonstrates Hu moments' stability across all translation configurations.

- These findings support the theoretical expectation that Hu moments are invariant under translational shifts.
- The heat map visually affirms that translations in either direction (positive or negative) do not alter the moment-based descriptor space significantly.

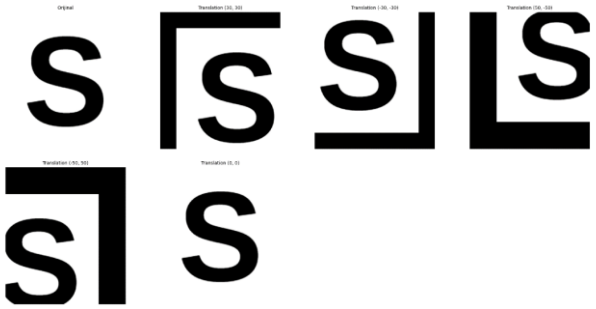


Figure 8. Synthetic dataset used in translational analysis of the letter S. Each image represents a different (x, y) offset to evaluate the translation invariance of Hu moments under controlled displacement scenarios.

Conclusion

Unlike traditional studies that only demonstrate invariance theoretically, this study develops an application-oriented structure that directly tests the transformation resilience of Hu moments using custom-generated datasets and measurable metrics. This structured experimental framework contributes to the field by

providing practical insights into the robustness of Hu moments in scalable systems. In comparison with previous studies, the results of this work align with and extend current findings in the literature. For example, Wu et al. (2020) demonstrated that integrating Hu moments with CNNs improved recognition accuracy in visual tasks, which supports our findings on the high classification success of Hu-based features for scaled images. Hjouji et al. (2020) proposed a remediation method for improving Hu invariants, emphasizing their stability under geometric distortions, which our experimental outcomes also confirm through rotation and translation robustness. Gancheva and Peneva (2023) applied Hu moments in radar satellite images and showed their utility in detecting spatial consistency; this parallels our success in translational analysis where Hu moments remained invariant despite position changes. Additionally, Rodríguez (2023) highlighted their effectiveness in micro-scale surface recognition, which resonates with our size determination experiments showing sensitivity to fine-grained scale changes. Therefore, this study not only confirms prior theoretical assertions about the invariance of Hu moments but also provides an empirical framework that enhances their practical validation and interpretability in visual classification tasks. In summary, the findings demonstrate that Hu moments serve as a reliable feature descriptor under various geometric transformations, including rotation, scaling, and translation. The results suggest several promising application domains where Hu moments can be effectively utilized. These include real-time object tracking in autonomous systems, automated quality control in manufacturing pipelines, and text recognition in OCR-based security frameworks. Future work can explore the integration of Hu moments with more advanced learning architectures such as transformer-based models to enhance performance in noisy or complex environments. Additionally, real-time deployment on embedded systems and testing on larger, multi-class datasets would provide deeper insights into scalability and generalizability. Investigating the hybrid use of Hu moments with frequency-domain descriptors (e.g., Zernike moments or Fourier transforms) may also yield improved robustness. These directions will further strengthen the role of Hu moments as a lightweight yet powerful feature descriptor in practical image processing applications. Future work may include comparative studies between Hu moments and other moment-based descriptors such as Zernike or Legendre moments, especially in terms of computational efficiency and robustness under complex geometric distortions.

References

[1] Hu, M. K. (1961). Visual pattern recognition by moment invariants. Proc. IRE, 49, 1428.

[2] Wu, Z., Jiang, S., Zhou, X., Wang, Y., Zuo, Y., Wu, Z., Liang, L., & Liu, Q. (2020). Application of image retrieval based on convolutional neural networks and Hu invariant moment algorithm in computer telecommunications. Comput. Commun., 150, 729-738.

[3] Hjouji, A., El-Mekkaoui, J., & Jourhmane, M. (2020). Rotation scaling and translation invariants by a remediation of Hu's invariant moments. Multimedia Tools and Applications, 79, 14225 - 14263.

[4] Aburass, S., Huneiti, A., & Al-Zoubi, M. (2020). Enhancing Convolutional Neural Network using Hu's Moments. International Journal of Advanced Computer Science and Applications.

[5] Gancheva, I., & Peneva, E. (2023). Methodology based on the Hu moment invariants for object comparison on radar satellite imagery. Journal of Physics: Conference Series, 2668.

[6] Rodríguez, J. (2023). Micro-Scale Surface Recognition via Microscope System Based on Hu Moments Pattern and Micro Laser Line Projection. Metals.

[7] Setiawan, R., Parewe, A., Latipah, A., Astuti, N., Murdiyanto, A., & Putra, F. (2023). Assessing Bagging-meta Estimator in Imbalanced CT Kidney Disease Classification: A Focus on Sobel and Hu Moment Techniques. International Journal of Artificial Intelligence in Medical Issues.

[8] Zhao, T. (2017, January). Small target detection and recognition based on template matching. In 2016 4th International Conference on Machinery, Materials and Information Technology Applications (pp. 964-968). Atlantis Press.

Dicle University
Journal of Engineering
https://dergipark.org.tr/tr/pub/dumf
duje.dicle.edu.tr

Research Article

Improving Fish Weight Estimation with Quantile and Box-Cox Transforms: Comparative Machine Learning Models

Hatice ESEN[1], Havvanur TAŞDELEN[2], Sefa KÜÇÜK[3], Işıl KARABEY AKSAKALLI[4]

[1] Erzurum Technical University, Department of Electrical-Electronics Engineering, hatice.esen96@erzurum.edu.tr, Orcid: 0009-0008-9805-829X
[2] Erzurum Technical University, Department of Electrical-Electronics Engineering, havvanur.tasdelen20@erzurum.edu.tr, Orcid: 0009-0000-8222-2093
[3] Erzurum Technical University, Department of Electrical-Electronics Engineering, sefa.kucuk@erzurum.edu.tr, Orcid: 0000-0002-0279-3185
[4*]Erzurum Technical University, Department of Computer Engineering, isil.karabey@erzurum.edu.tr, Orcid: 0000-0002-4156-9098

ARTICLE INFO

Article history:

Received 11 April 2025
Received in revised form 22 August 2025
Accepted 26 August 2025
Available online 30 September 2025

Keywords:

Machine learning, Quantile transformation, Box-cox transformation, Fish weight estimation.

Doi: 10.24012/dumf.1674123

* Corresponding author

ABSTRACT

Fish weight estimation using machine learning ensures that fish are fed appropriately, reduces labor, prevents physical harm to the fish, and saves time. In this study, Quantile and Box-Cox transformations are applied to improve the accuracy of fish weight predictions. These transformations correct the asymmetric distribution of the data and enable machine learning algorithms to generalize more effectively and produce more accurate results. CatBoost, Random Forest, Polynomial Regression, and Support Vector Regression methods were evaluated for fish weight estimation both before and after applying the transformations. The experimental results show that both the Quantile and Box-Cox transformations effectively reduce model error rates, particularly by normalizing the dataset distribution. Notably, models without transformation exhibit significant improvements in error rates after transformation is applied. The lowest Mean Absolute Error (MAE) without transformation was obtained using the CatBoost model, yielding a value of 14.002. After applying the Quantile transformation, the MAE decreased to 0.0171, while the Box-Cox transformation resulted in an MAE of 0.3302. Although both transformations contribute to error reduction, the Quantile transformation has a more substantial impact on fish weight estimation. These findings underscore the importance of data transformations in the preprocessing stage and highlight that transformation techniques are as crucial as selecting the appropriate machine learning model.

Introduction

Accurately estimating fish weight is crucial for nutrition planning and effective aquaculture management, as it facilitates the efficient regulation of feeding processes. Traditionally, fish weight is measured using weighing scales. However, these methods not only increase labor requirements but also fail to save time and may cause physical harm to the fish. Consequently, there is a growing demand for more accurate, non-invasive, and sustainable estimation techniques. Nonetheless, estimating weight in underwater environments remains a highly challenging task due to factors such as the continuous movement of fish, fluctuating lighting conditions, and variable water quality.

A review of recent literature reveals that machine learning (ML) and artificial intelligence (AI) have been extensively explored in academic research across various domains. For example, Wai Lok Woo et al. conducted a study that estimated the weight of Tilapia in turbid water using a low-cost single-channel video camera combined with a Mask R-CNN detection method, and subsequently employed regression models (Linear, Random Forest, SVR) to achieve high predictive accuracy [30]. For instance, Kazemi et al. conducted a comprehensive evaluation of ML algorithms used to predict the mechanical properties of fiber-reinforced polymers (FRPs), assessing model performance in detail [16]. Similarly, von Bülow et al. reviewed recent advances in ML-based approaches for investigating sequence–structure–function relationships in disordered proteins, emphasizing their relevance to biophysical functions [17]. In another study, Liu et al. developed a quantitative structure–property relationship (QSPR) model using ML techniques to predict CO_2 solubility in aqueous amine solutions. The study demonstrated high predictive accuracy and validated model interpretability through SHAP analyses [18]. D'Orazio and Pham examined the effects of climate-related financial policies on decarbonization and the renewable energy transition across 87 countries from 2000 to 2023, using ML to account for contextual differences and policy effectiveness [19]. Furthermore, Tuerxun et al. proposed an ML framework that integrates spectral indices and geospatial data to accurately estimate leaf chlorophyll

content (LCC), achieving high accuracy with the GWLS-Support Vector Regression (SVR) model [20].

For example, in a recent study, Tianye Zhang and colleagues combined fish posture recognition using deep learning technology with biomass estimation, developing a stereo vision-based fast, accurate, and fully automated system for free-swimming fish, and demonstrated that the method provides an effective approach for real production and the investigation of fish growth mechanisms [33]. Recent studies have demonstrated that image processing and machine learning techniques can be effectively applied to estimate fish weight. For instance, Gutzmann et al. proposed a method for estimating the weight of large whitefish species in the lower Mackenzie River Basin using photographic image analysis [1]. Another recent study by SV Jansi Rani et al. aimed to estimate fish biomass in highly turbid water using a deep learning-based object detection and regression approach. This study presents a non-invasive and automated method [34]. In another study, Moseli Mots'oehli et al. developed FishNet, which achieved 89% classification accuracy and a 2.3 cm MAE in fish length estimation using a dataset of 1.2 million fish images from 163 species [32]. Similarly, Konovalov et al. conducted a study on automatic weight estimation by collecting both images and weight measurements of approximately 2,500 individuals of Lates calcarifer (Asian sea bass or barramundi) harvested from three different locations in Queensland, Australia [2]. Additionally, Islamadina et al. utilized digital camera images converted to grayscale for fish weight estimation, applying segmentation techniques to remove irrelevant objects from the images. During the feature extraction phase, length, width, and height were calculated using calibration values, and these features were used to estimate fish weight [3]. A similar approach was adopted by Suwannakhun and Daungmala in their study on pig weight estimation. They extracted features such as color, texture, center of gravity, axis lengths, eccentricity, and area from digital images [4]. Neural network analyses in both studies confirmed the effectiveness of non-contact estimation methods. Collectively, these findings suggest that image processing and AI-based techniques provide faster, more accurate, and more sustainable alternatives to traditional weight measurement methods.

Quantile Transformation (QT) and Box-Cox Transformation (BCT) are widely used techniques that have demonstrated effectiveness across various fields. For instance, Bogner et al. employed the Normal Quantile Transform to normalize river flow data, thereby improving the accuracy and reliability of flood forecasting models [21]. In another study, Buchinsky applied Quantile Regression (QT) to analyze changes in returns to education and experience across different points of the wage distribution, as well as within-group wage inequality. The Box-Cox Transformation (BCT) was also incorporated in this analysis to appropriately transform the data for improved model fit [22]. Xie et al. used BCT as an early warning indicator for detecting abrupt climate changes [23], while Nagendra et al. utilized BCT to evaluate surface roughness in material science applications [24]. Similarly, Al Abbasi et al. applied QT to investigate the effects of rural transformation—specifically, high-value agricultural and non-agricultural employment—on income and poverty in Bangladesh [25].

Quantile transformation (QT) and Box-Cox transformation (BCT) improve prediction accuracy by regularizing the distribution of the dataset. In this study, QT and BCT methods are used to improve the accuracy of weight estimation. In literature, some studies that use these methods are summarized as follows: Peterson and Cavanaugh proposed a method that effectively transforms data into a normal distribution by introducing Ordered Quantile (ORQ) normalization. ORQ works consistently regardless of the underlying distribution and can be easily applied to new data. Its effectiveness is compared with other methods and the role of cross-validation in determining the best transformation is investigated. The technique was implemented on a car pricing dataset with the best Normalize R package [5]. Peng et al. highlighted the importance of transformations for mapping quantitative feature loci, and the empirical normal QT proved to be an effective method for normalizing feature values. In their study, they showed through extensive simulations that this transformation provides good control over power and type I error [6]. Rayner and MacGillivray studied the effects of Quantile-based methods in fitting g-and-k and adapted g-and-h distributions and showed that weighted methods perform better for small and medium-sized [7]. In another study, Hamzaoui et al. (2023) achieved a very high R^2 accuracy of 99.94% for different fish species by employing the SFI-XGBoost method, which combines VIF, Pearson correlation, and XGBoost [31]. Atkinson et al. (2021) examined the relationship between BCT power transformation and generalized linear models and proposed transformation models for positive and negative observations. In the study, normality, and variance homogeneity of the data were tried to be ensured by using methods that include the transformation of both sides. Zhang and Yang proposed new methods and algorithms for more efficient application of BCT on big data. This method aims to speed up transformation and model parameter estimation by scanning the data only once [8]. In Osborne's study, the relationship of the BCT transformation with traditional normalization transformations was discussed and how it was developed was discussed. Osborne stated that BCT offers better applications than traditional methods and provided examples of how this transformation can be applied using software such as SPSS and SAS [9].

In this study, fish weight estimation using ML methods using fish images is discussed. CatBoost, Random Forest, Polynomial Regression, and Support Vector Regression (SVR) models are used to accurately estimate fish weight. The success of each model was compared by applying different ML methods and to improve the accuracy, the improvements from the above QT and BCT studies were applied to the fish weight estimation project and a successful improvement was achieved. QT and BCT significantly improved the prediction accuracy by

significantly reducing the error rate in all models. The contributions of this study can be summarized as follows:

- To the best of our knowledge, Quantile Transformation (QT) and Box-Cox Transformation (BCT) have not previously been applied to the task of fish weight estimation. In this study, we incorporate these transformations into a novel fish weight estimation framework to evaluate their effectiveness.
- Machine learning methods are employed to estimate fish weight based on their morphological characteristics, and the error rates are further improved through the application of QT and BCT.
- Finally, we conducted a comparative analysis of weight estimation methods with and without transformations, evaluated the impact of the applied transformations, and assessed the improvements achieved.

The rest of the paper is organized as follows. The second section describes the dataset used and the evaluation metrics. In the third section, the methods applied in the preprocessing phase, machine learning models, and the experimental results and findings obtained from these models are presented in a comparative manner. Finally, the study ends with conclusions and future studies section.

Materials and Methods

In this study, CatBoost, Random Forest, Polynomial Regression and SVR machine learning methods were used to estimate weight from morphological features of fish and their performances were evaluated. In addition, the effects of Box-Cox Transformation (BCT) and Quantile Transformation (QT) on these methods were analyzed, and their impact on estimation performance was compared. The method with the lowest error rate was determined by making improvements and comparisons with different parameters. In total, 12 different models such as CatBoost, Random Forest, Polynomial Regression, SVR, and their versions with QT and BCT were tested. The results were analyzed among methods, especially for the effect of transformations. The dataset was divided into 80% training and 20% test data. The general progression of the steps followed in the study is presented in the method flowchart in Fig. 1. The figure the overall workflow of the study, which employs machine learning techniques to estimate fish weight based on morphological characteristics.

Dataset

This study utilizes the Fish Market dataset [10], which includes morphological measurements of fish. The dataset comprises 159 samples spanning seven species: Bream, Perch, Roach, Pike, Smelt, Parkki, and Whitefish. For each sample, seven morphological characteristics are recorded: Species, weight, length1, length2, length3, height and width. The weight estimation of fish is performed by utilizing various morphological characteristics. The meanings of these morphological features are given below and Fig. 2 shows the representation of these features on the fish. In this study, weight estimation was performed using the relationships and ratios between these features.

- Species: *Bream*, *Perch*, *Roach*, *Pike*, *Smelt*, *Parkki,* and *Whitefish*.
- Weight: Weight of the fish (in grams)
- Length1: Length from the nose to the beginning of the tail (in cm)
- Length2: Length from the nose to the notch of the tail (in cm)
- Length3: Length from the nose to the end of the tail (in cm)
- Height: % Maximal height as % of Length3Width: % Maximal width as % of Length3

Implementation Details

All experiments were conducted on a personal computer equipped with an Intel Core i5-13500HX CPU (2.5 GHz) and 16 GB of RAM.

Evaluation Metrics

In this study, Mean Absolute Error (MAE) and the Coefficient of Determination (R2) were used as evaluation metrics. MAE is defined as the average of the absolute differences between the predicted and actual values. Lower MAE values indicate that the model's predictions are closer to the true values. One of the key advantages of this metric is that it expresses the prediction error in the same unit as the target variable, which facilitates interpretability. Moreover, MAE is more robust to outliers compared to squared-error metrics, as it considers absolute deviations and does not disproportionately penalize large errors. In the literature, MAE is highlighted as a reliable and widely used metric for assessing regression performance [28]. The mathematical formulation of MAE is given in Equation (1).

$$MAE = \frac{1}{n}\sum_{i=1}^{n}|y_i - \hat{y}_i| \quad (1)$$

In this equation, n is the total number of data, yi indicates the actual values, and ŷi represents the predicted values. The R^2 metric was used to assess how well the independent variables in a regression model explain the variability of the dependent variable. It represents the proportion of variance in the dependent variable that can be predicted from the independent variables. An R^2 value of 1 indicates that the model explains the data perfectly, 0 indicates that it has no explanatory power, and negative values imply that the model performs worse than a simple mean-based prediction. In general, the closer the R^2 value is to 1, the stronger the explanatory power of the model. However, recent studies have emphasized that R^2, especially in linear regression, may sometimes overestimate the explained variance, which can lead to misleading interpretations [29]. The mathematical representation of R^2 is shown in Equation (2).

$$R^2 = 1 - \frac{\sum(y_i - \hat{y}_i)^2}{\sum(y_i - \bar{y})^2} \quad (2)$$

Within the scope of this study, the Box-Cox Transformation (BCT) was applied to adjust the distribution of variables toward normality. BCT is a parametric transformation method widely used for variance stabilization and approximation of normality in continuous and positive valued variables. The general formula of the transformation is shown in Equation (3).

$$y(\lambda) = \begin{cases} y^{\lambda} - 1, & \lambda \neq 0 \\ \log(y), & \lambda = 0 \end{cases} \quad (3)$$

here, y is the original data values to be transformed, λ is a parameter that determines the intensity and direction of the transformation. The λ values used in the study were determined by optimizing with the maximum log-likelihood method. In this method, the log-likelihood function for the transformed data set is as follows.

$$\log L(\lambda) = \frac{\pi}{2}\log(\mathrm{SSE})(\lambda) \quad (4)$$

where, SSE(λ) represents the sum of squared errors of the transformed data and n represents the number of observations. The parameter λ, which provides the maximum log-likelihood value, is used as the optimal transformation coefficient that ensures that the data set is distributed closest to normality. This method determines the transformation parameters systematically and objectively, increasing the reproducibility and statistical reliability of the analysis results.

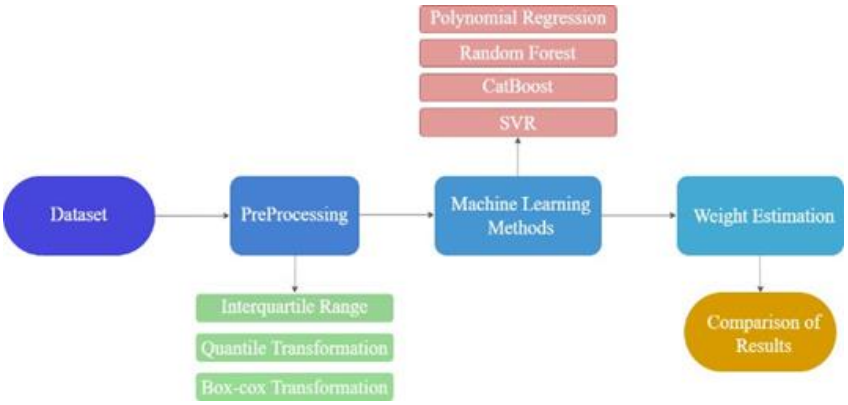


Figure 1. Flowchart of the proposed method.

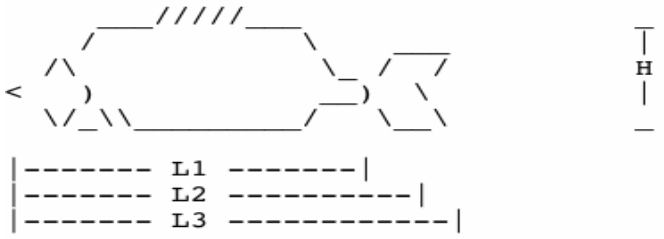


Figure 2. Illustration of the morphological features measured on fish, including Length1 (L1), Length2 (L2), Length3 (L3), Height (H), and Width (W) [11].

Experimental Results and Findings

This section outlines three key aspects: changes in preprocessing steps before and after applying QT and BCT, performance variations of machine learning algorithms under each condition, and the effect of these transformations on prediction outputs.

Preprocessing Steps

Several data-related challenges hinder the reliable and effective performance of machine learning and data analysis processes. These problems can be identified and corrected with the data preprocessing step. In the data preprocessing phase, the relationships of morphological features with each other, especially with weight, are analyzed, outliers are identified, and missing data are removed. When the data preprocessing phase is skipped, the model's learning process is adversely affected, prediction accuracy decreases, the model tends to learn biasedly, and its generalization ability may be weakened, leading to erroneous results. Data preprocessing steps should be implemented to reduce the impact of such problems.

In this study, all preprocessing steps are kept identical except for the QT, BCT, and method components. This approach allows for a more accurate comparison of

prediction errors and isolates the effects of the QT and BCT transformations on weight estimation.

Attribute Representation

To analyze the value distribution of each morphological feature in the dataset, bar charts were generated. Fig. 3 presents the column plots for species, weight, width, height, length1, length2, and length3. In the distribution of these graphs, species are clustered in certain index ranges, indicating categorical distinctions in the dataset. Fig. 3(a) shows the species distribution in the dataset. In Fig. 3(b), the weight variable shows sharp increases and decreases in certain index ranges, indicating that some fish species are much heavier. The width and height plots in Fig. 3(c) and Fig. 3(d) show that different species are more dominant in certain ranges, while the length variables (length1, length2, length3) in Fig. 3(e), Fig. 3(f) and Fig. 3(g) show similar distributional trends and increase on the horizontal axis. Overall, the variables exhibit different distributions within specific index ranges, indicating that the dataset has distinct clustering by species, reflecting measurable differences between fish species. The fact that fish exhibit different distributions within specific index ranges directly affects weight estimation, requiring consideration of species-based differences. Since each fish species has its weight range, their relationships with measurements such as length, width, and height also differ. When the graphs are analyzed, it is seen that some variables show a right-skewed (positive skewness) distribution. The distribution of weight and height variables exhibits a right-skewed character with a long tail structure extending from small to large values. Length1, length2, and length3 variables are skewed to the right with a distribution of low values and decreasing towards large values. The effect was observed when QT and BCT were applied to remove these skews.

Quantile Transformation (QT)

QT is a pre-processing step used to transform distributions of data. Instead of creating a new dataset, this transformation creates a transformed version of the original dataset. In this transformation, the data is rescaled according to a given probability distribution. It is especially preferred for data with different distributions to achieve a more homogeneous distribution. QT is usually performed by placing the order of each observation into the corresponding Quantile in the target distribution.

There are two common approaches to this transformation: uniform distribution and normal distribution. The uniform distribution is a type of distribution where each value is chosen with equal probability, and with this method, the data is redistributed with equal probabilities between 0 and 1. In this distribution, the data only lie between 0 and 1 and do not take negative values. In the normal distribution, the data are symmetrically distributed around the mean and can also take negative values. The uniform distribution was used in the study. This process ensures that the values are evenly distributed between 0 and 1, without any negative values. Furthermore, by leveraging the Box-Cox Transformation's ability to approximate a normal distribution, the study aims to compare the results obtained through this alternative transformation approach. QT has been applied to all columns except the Species column. The other columns were rearranged according to a specific probability distribution and subjected to QT to ensure a homogeneous distribution of the data. Fig. 4 shows the original distribution of the dataset and its distribution via QT. As shown in the figure, the dataset exhibits a more homogeneous distribution after the application of QT.

Before the QT transformation, the data exhibited substantial right skewness, with most values clustered near the lower end and a long tail extending toward higher values. To address this issue, QT was applied, transforming the data into a uniform distribution. After the transformation, the values were evenly distributed within the [0, 1] range, reducing skewness and the influence of outliers, and producing a more balanced dataset suitable for machine learning models.

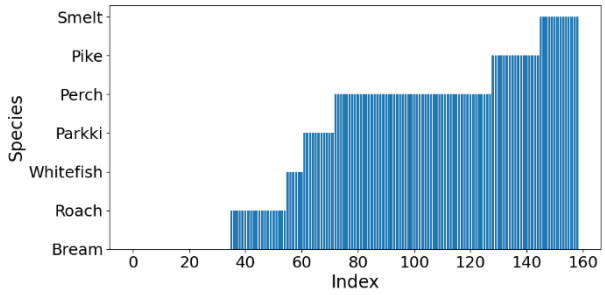
Box-Cox Transformation (BCT)

In regression analysis, the accuracy of most models increases when the data resemble a normal distribution. BCT is a mathematical method used to bring the distribution of the data closer to a normal distribution. This transformation attempts to transform the data into a normal distribution by applying functions such as a logarithm or square root to the data. BCT is widely used to improve the accuracy of the model, especially when working with volatile and skewed data, the Fish Market dataset is skewed to the right as can be seen in the bar charts in Fig. 3. This transformation aims to flatten the distribution of the data, make it symmetric, and perform a better regression analysis. BCT does not work with negative values, since there are no negative values in the Fish Market dataset, it is suitable for BCT. Fig. 5 shows the original dataset distribution, the distribution of the dataset after BCT, and the Kernel Density Estimation (KDE) curve of this distribution. By obtaining a continuous probability density function with the KDE curve, it can be observed in which intervals the data is concentrated. The graphs indicate that the data distribution after BCT is closer to the normal distribution.

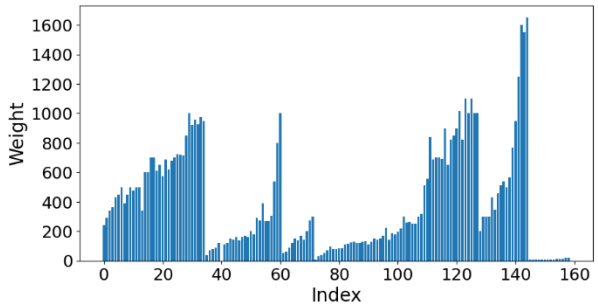
BCT proved highly effective in converting the right-skewed and potentially multimodal distributions into more symmetric, near-normal forms. This transformation serves as a critical preprocessing step for enhancing the performance of parametric statistical tests and machine learning models. Additionally, BCT alters the scale of the data, making it more compact and facilitating more stable and interpretable model training.

Interquartile Range (IQR)

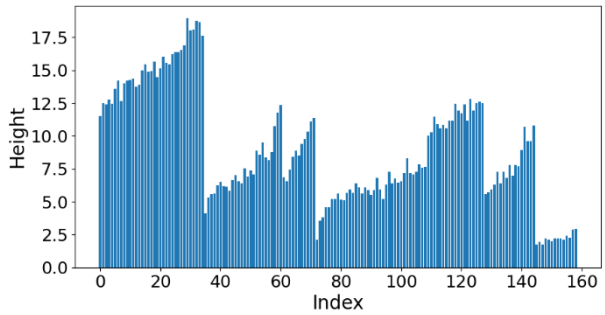
The IQR method is a statistical method used to identify outliers in a data set. This method detects and visualizes unusually low or high values based on the difference between the 25% quartile of Q1 and the 75% quartile of Q3. To identify outliers, a threshold of 1.5 times the difference between Q1 and Q3 was set. In this way, outliers in the data



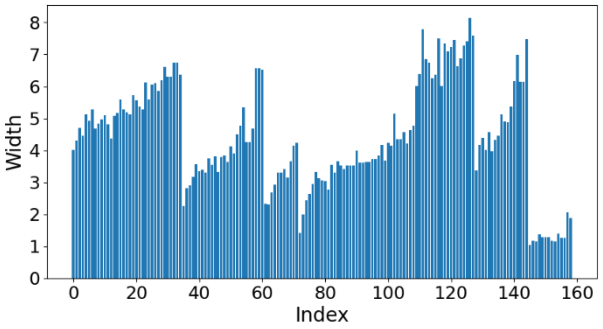
(a) Species



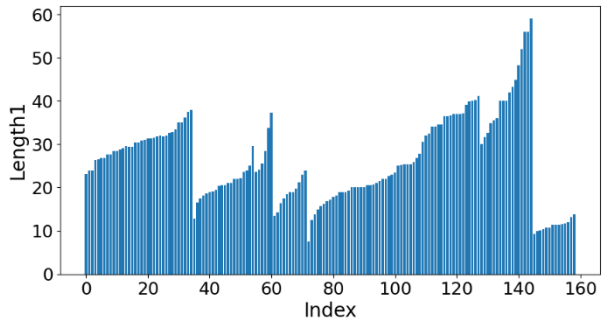
(b) Weight



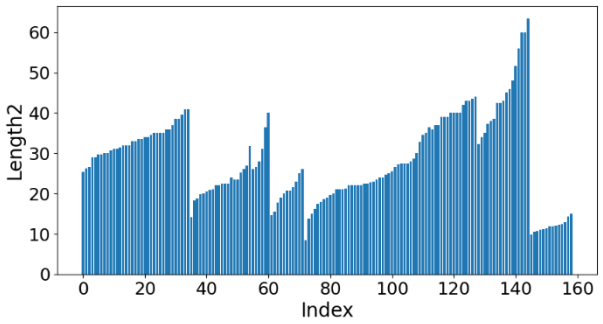
(c) Height



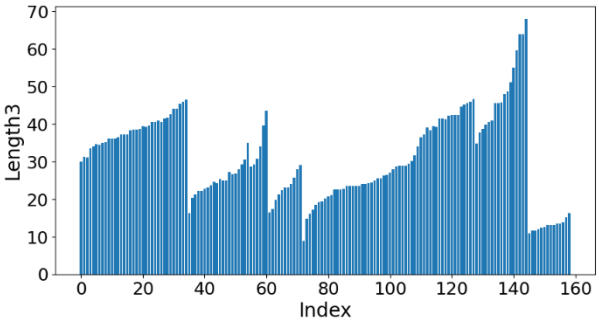
(d) Width



(e) Length1



(f) Length2



(g) Length3

Figure 3. Distribution of morphological features in the dataset.

set that could affect the analysis results were identified, resulting in more reliable and consistent results. The lower bound is shown in Equation (4) and the upper bound is shown in Equation (5).

$$L_b = \text{Q1} - 1.5 * \text{IQR} \quad (4)$$

$$U_b = \text{Q3} + 1.5 * \text{IQR} \quad (5)$$

Fig. 6(a) shows the plot of outliers detected by the IQR method before the transformation is applied, there are outliers because the raw data has a skewed distribution. Fig. 6(b) presents the results of the outliers detected with the IQR method after QT, while Fig. 6(c) shows the effect of the IQR method on the outliers after BCT. When the graphs were analyzed, outliers were detected in length1, length2, and length3 before the transformation. However, QT and BCT eliminate these outliers.

Correlation Matrix

The correlation matrix is used to analyze and interpret the relationships between variables. It is a matrix showing the linear relationship between variables. It is used in statistics and data analysis processes to understand how variables are related to each other. This matrix contains the correlation coefficients between pairs of variables. This correlation coefficient takes values between -1 and 1. Negative values mean that there is a negative correlation between the variables, i.e. one increases while the other decreases, while positive values mean that there is a positive correlation between the variables, i.e. one increases while the other increases or one decreases while the other decreases. 0 indicates that there is no linear relationship between them. In the scope of this study, we observed the correlation between morphological features in the absence of transformations, the correlation between morphological features after QT, and the correlation between morphological features after BCT, and how transformations affect the relationships between features. Fig. 7(a) shows the correlation matrix without transformation, Fig. 7(b) shows the correlation matrix after QT and Fig. 7(c) shows the changes in the correlation matrix after BCT. When the correlation matrices are analyzed, generally positive correlations are detected between the features before any transformation is applied. In particular, a strong positive correlation is observed among the features Length1, Length2, and Length3. This suggests that these features are highly interrelated and likely convey overlapping or redundant information. After applying QT and BCT, the correlation between the features generally increased at similar rates. However, this increase was found to be more pronounced in QT. This suggests that QT reveals the relationships between features more strongly and may be more effective in the process of normalizing the data distribution.

Principal Component Analysis (PCA)

PCA is a dimensionality reduction technique used to identify the components that explain the highest variability in the data. Given the relationships in the correlation matrix, applying dimensionality reduction techniques on highly correlated features can minimize the risk of overlearning by reducing the complexity of the model. Moreover, this approach can contribute to improved model generalizability and reduced error rates, thereby enhancing overall model performance. Fig. 8(a) shows the variance explained for each principal component in the absence of transformation, Fig. 8(b) shows the variance explained for each principal component after QT and Fig. 8(c) shows the changes in the variance explained for each principal component after BCT.

These graphs show that in the absence of transformation, the first principal component explains a large proportion of the total variance. This shows that the data is highly correlated and PCA can represent a large portion of the data with a single component. After the transformations, the transformations provide a more even distribution of variance, increasing the contribution of the second and third components, but the first component is still dominant.

Machine Learning Methods

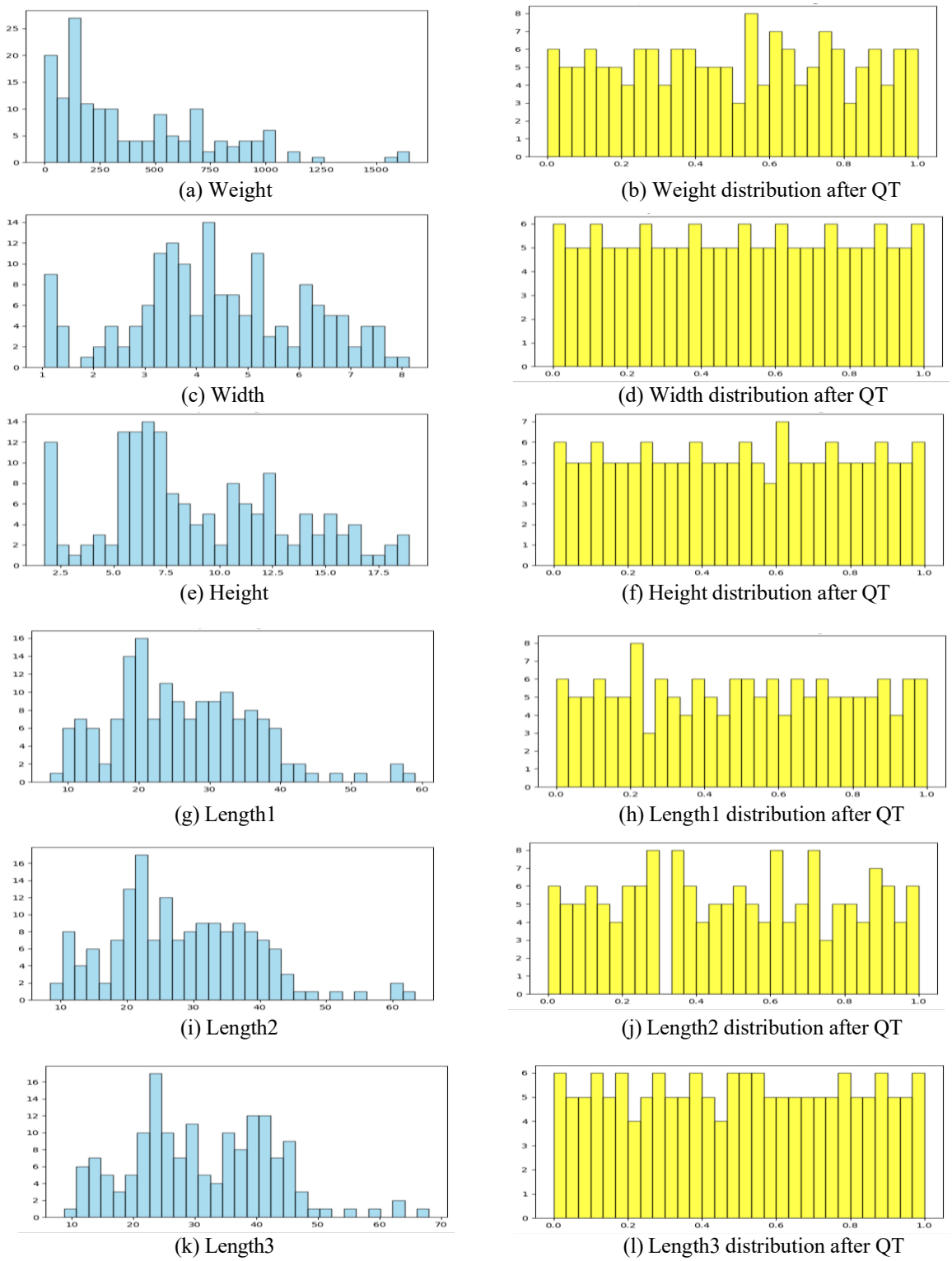
In studies involving structured datasets with multiple features, machine learning (ML) approaches offer powerful alternatives to traditional statistical methods, particularly when developing prediction models using high-dimensional data [12]. In this study, the performance of four ML methods including, CatBoost, Random Forest, Polynomial Regression, and Support Vector Regression (SVR) is compared across three data versions: untransformed, QT-transformed, and BCT-transformed. The results and the impact of these transformations on model performance are discussed in detail.

CatBoost

CatBoost has emerged as a powerful tool for ML tasks involving big data [13]. It is a machine learning algorithm belonging to the Gradient Incremental Decision Trees (GADT) family. In this study, it was used for a small dataset. CatBoost can be used in both classification and regression problems. CatBoost Regression is the version of CatBoost used in weight estimation problems. One of the most important features of CatBoost is that it can work directly with categorical variables and process these variables effectively. In the Fish Market dataset, the species column is a categorical variable. CatBoost applies several methods to deal with categorical features. For one-hot encoded features, no special processing is required, and the histogram-based approach used for partition search can be easily adapted to this case [14]. When using CatBoost, there is no need to convert this column into numerical data. CatBoost is a method that aims to build a strong model by successively building weak models, usually decision trees. At each step, it focuses on correcting the prediction errors of the previous model. The process starts with a simple model, and each new tree is trained to minimize the errors of the previous model over gradients. This process improves the performance of the model step by step. The training process of the CatBoost model is shown in Fig. 9(a) before applying the transformation, Fig. 9(b) after QT, and Figure 9 (c) after applying BCT. In the graphs, it is observed that

the error value in the test data decreases more than the training data. MAE values decrease significantly after QT and BCT. The lowest MAE value is obtained after Quantile transformation as seen in the graphs. The error values of the training data show a better reduction than the error values of the test data. However, as the model becomes more complex, the risk of overfitting arises.

A lower error was observed in the train data compared to the validation data, and this was evaluated in terms of the possibility of overfitting. However, after hyper parameter optimization and multi-level validation, the difference between training and validation errors decreased, which



(a) Weight (b) Weight distribution after QT

(c) Width (d) Width distribution after QT

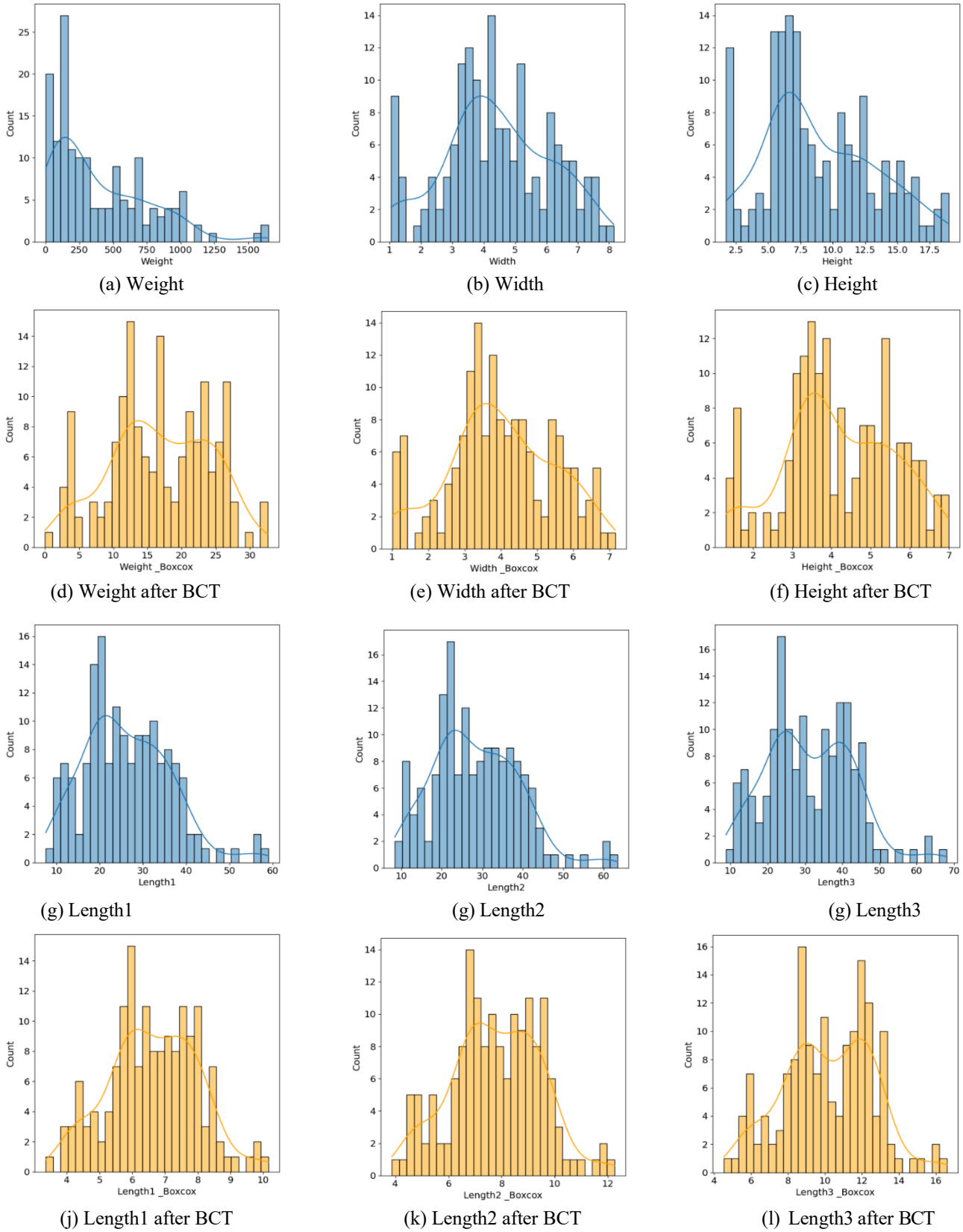
(e) Height (f) Height distribution after QT

(g) Length1 (h) Length1 distribution after QT

(i) Length2 (j) Length2 distribution after QT

(k) Length3 (l) Length3 distribution after QT

Figure 4. Original and Quantile Transformed (QT) distributions of fish morphological features: (a)-(l) show before and after QT transformations for Weight, Width, Height, Length1, Length2, and Length3, respectively.



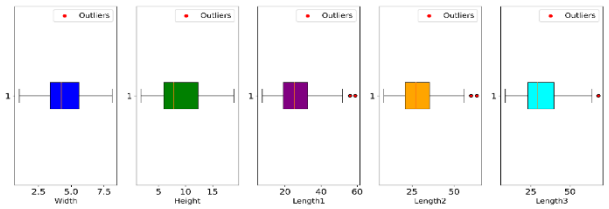
(a) Weight (b) Width (c) Height

(d) Weight after BCT (e) Width after BCT (f) Height after BCT

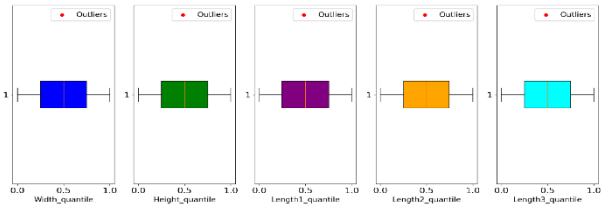
(g) Length1 (g) Length2 (g) Length3

(j) Length1 after BCT (k) Length2 after BCT (l) Length3 after BCT

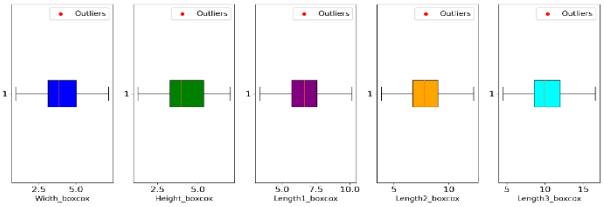
Figure 5. Original and Box-Cox Transformed (BCT) distributions of fish morphological features with Kernel Density Estimation (KDE) curves: (a)-(l) show before and after BCT transformations for Weight, Width, Height, Length1, Length2, and Length3, respectively



(a) Outliers detected by IQR method in the absence of transformation

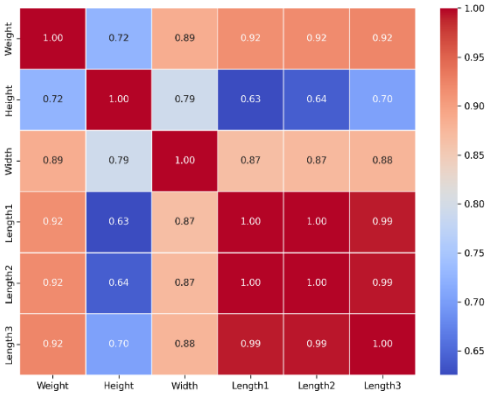


(b) Outliers detected by IQR method after QT

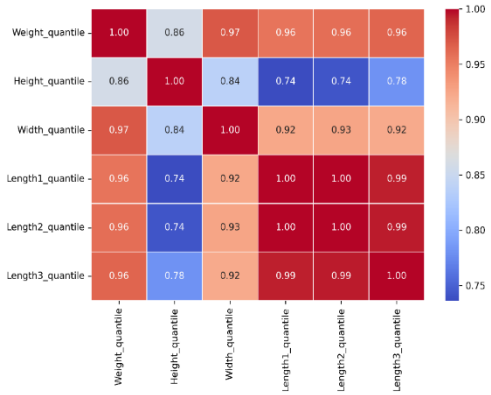


(c) Outliers detected by IQR after BCT

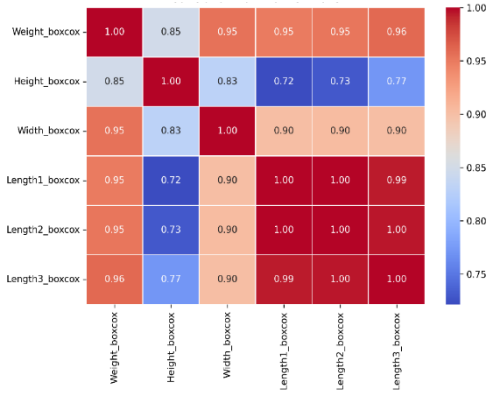
Figure 6. Outliers detected by IQR in the absence of conversion, after QT and after BCT.



(a) Correlation matrix without transformation



(b) Correlation matrix after QT



(c) Correlation matrix after BCT

Figure 7. Correlation matrices of morphological features.

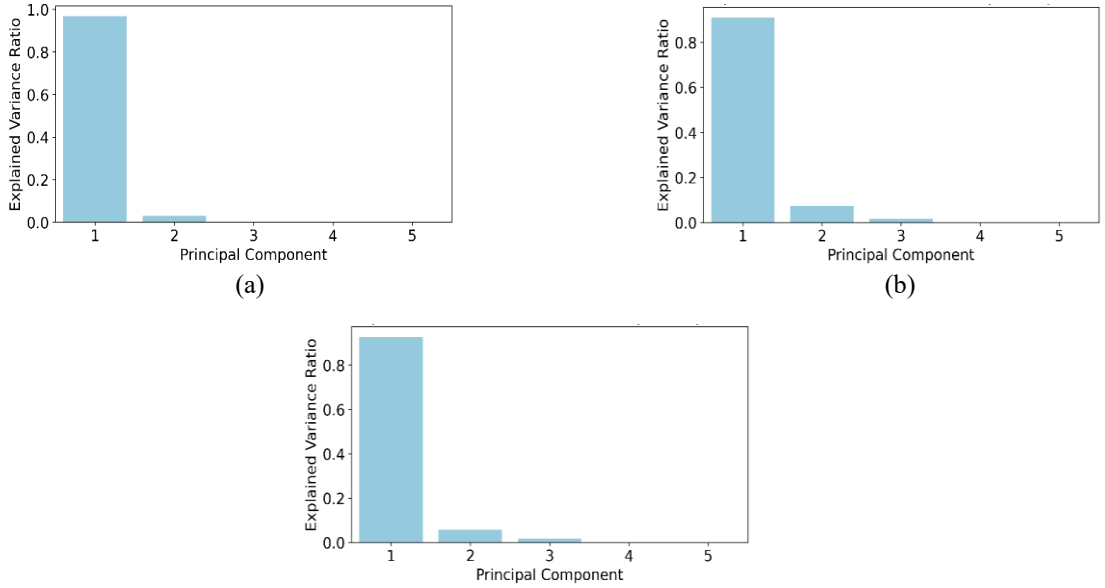


Figure 8. Variance explained by principal components: (a) Without transformation, (b) After QT, (c) After BCT.

reduced the risk of overfitting and improved the model's generalization performance.

CatBoost

Grid search is used to improve the performance of the model for hyper parameter optimization and to determine the best combination of hyper parameters. Using cross-validation with Grid search, different combinations of iterations, learning rate, depth and fold count hyper parameters were tested, and the MAE values of the combinations without transformation in Fig. 10(a), after QT in Fig. 10(b) and after BCT in Fig. 10(c) are shown graphically. In this process, the performance of the model was evaluated according to the MAE metric, and the hyper-

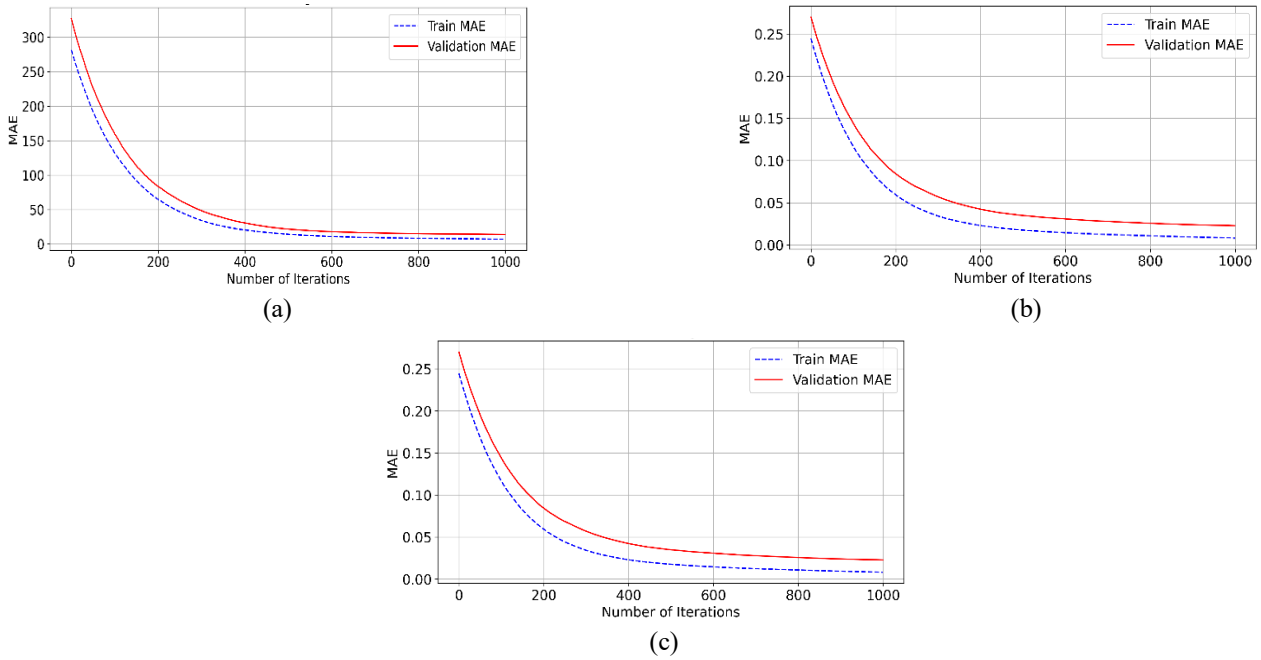


Figure 9. CatBoost model training process graphs: (a) Without transformation, (b) After QT, (c) After BCT.

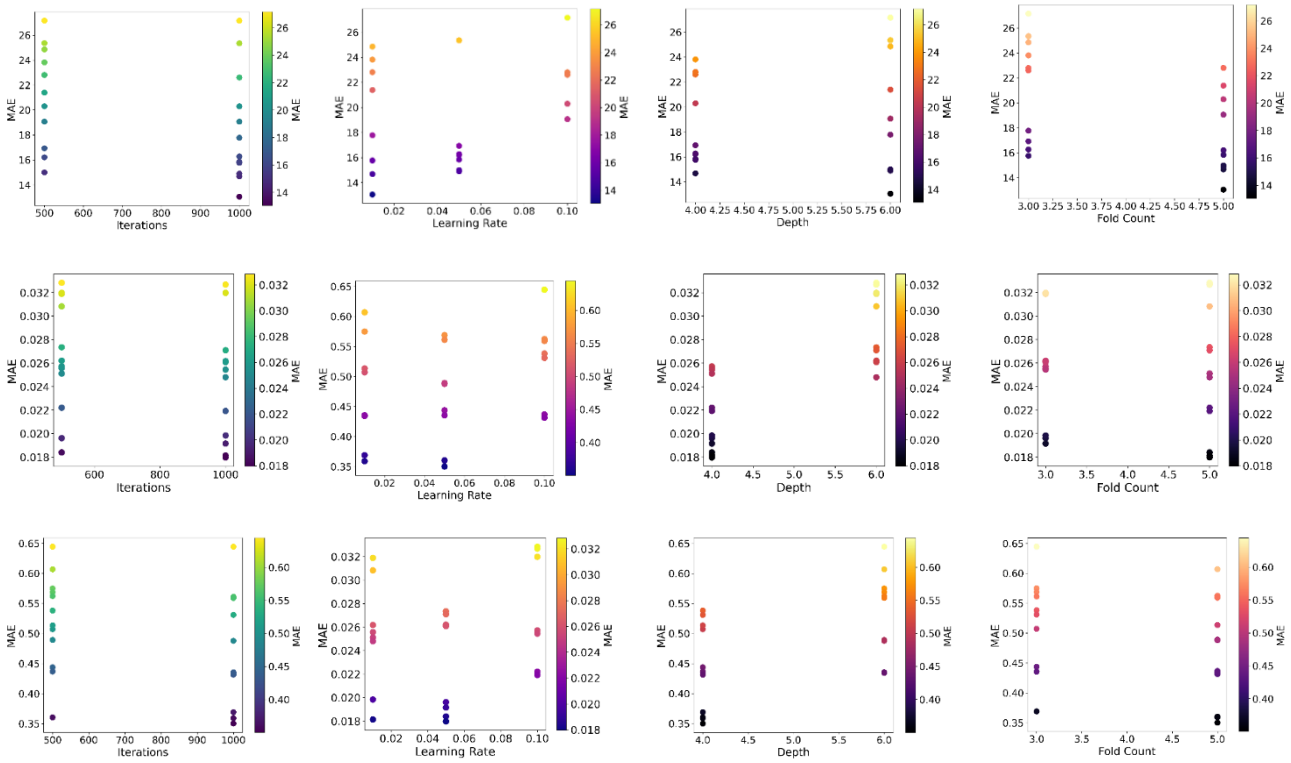


Figure 10. Grid search results showing MAE values for different combinations of CatBoost hyperparameters (iterations, learning rate, depth, and number of layers). The first column corresponds to the original data (untransformed), the second column to the data with QT applied, and the third column to the data with BCT applied.

parameters with the lowest MAE values without transformation, after QT and after BCT were selected. Thus, it was aimed to generalize the model better and to prevent overlearning and overfitting. Values giving the lowest error rate in the absence of transformation: iterations: 1000, learning rate: 0.01, depth: 6, fold count: 5. Values giving the least error rate after QT: iterations: 1000, learning rate: 0.05, depth: 4, fold count: 5 Values giving the least error rate after BCT: iterations: 1000, learning rate: 0.01, depth: 4, fold count:3. These values are different due to the transformation of the dataset after the transformations.

Random Forest

Random Forest is an ML method that can be used in both classification and weight estimation models. One study examines the historical development of Random Forest, its successful applications, and comparisons with other classifiers [15]. This method is used for a regression problem and compared with other ML methods in this study. It is an ensemble of decision trees, generates multiple decision trees, and makes a final prediction by taking predictions from these trees and averaging these predictions. This method uses the bagging technique to reduce overfitting and increase the model's generalization ability. This technique allows the model to produce more balanced and reliable results by training each decision tree on different subsets of data. It cannot work with categorical data, so categorical data was converted into numerical data using the label encoder method.

Polynomial Regression

Polynomial regression is a modeling method used to understand the relationship between independent and dependent variables. It is a preferred ML method when the link between variables is not linear.

$$y = b_0 + b_1 x + b_2 x^2 + \cdots + b_n x^n + \epsilon \qquad (5)$$

here, b_0, b_1, b_2, b_n are the coefficients of the independent variable x, x^2 is its square, ϵ is the error term. In polynomial regression, more complex and flexible models were created by adding higher-order terms of the independent variable. For example, fish length (x) as an independent variable presented a certain linear relationship when included in the model alone, while the square of length (x^2) helped to better capture growth trends and make weight estimation more accurate. Although this method allows for more successful modeling of nonlinear relationships, the optimum model complexity was determined to avoid overfitting, as polynomials of very high degree can lead to overfitting.

Support Vector Regression (SVR)

Support Vector Regression (SVR) is a machine learning method commonly applied to regression problems and has been utilized across various domains. For instance, a study

by [27] examined treatment processes and the management of patients who achieved Sustained Virologic Response (SVR), while [26] explored the application of hybrid machine learning techniques, particularly SVR, for wind forecasting and the management of ramp events. In this study, SVR is employed for the estimation of fish weight. SVR is an effective method for regression problems with non-linear relationships such as fish weight estimation. Its goal is to find the best hyperplane by ignoring the data within the specified error tolerance (ε). It builds models with support vectors only, thus avoiding overlearning and improving generalization performance. Non-linear relationships can be captured by using morphological characteristics of the fish as independent variables and weight as dependent variable. In this model, the Grid Search method was used in hyper parameter optimization to improve the performance of the model and to determine the most appropriate hyper parameter combination. C, epsilon, and gamma values were determined by the Grid search method for non- transformed, after QT and after BCT. These parameters significantly affect the learning process and performance of the SVR model. The C parameter determines the error tolerance of the model. A high C value leads to a tighter fit of the model to the training data, but increases the risk of overfitting. A low C value creates a more flexible model, but may not fit the training data perfectly. The epsilon parameter determines the acceptable amount of error in the model's predictions. A small epsilon value produces more accurate predictions, while a large epsilon value produces a more general model and accepts more errors. The gamma parameter determines the complexity of the kernel function. When 'scale' is selected, the gamma value is calculated automatically according to the characteristics of the data. When 'auto' is selected, the gamma is set to a fixed value. Setting these hyper parameters correctly improves the overall performance of the model, leading to more reliable and accurate predictions and reducing the risk of overfitting. Fig. 11(a) shows the MAE vs. MAE values of the combinations of “C”, “Epsilon” and “Gamma” parameters in the absence of transformation, in Fig. 11(b) after QT and in Fig. 11(c) after BCT. 'C' in Fig. 11(a): 1000, 'epsilon': 1, 'gamma': 'scale' and 'C': 100, 'epsilon': 0.01, 'gamma': 'auto' in Fig. 11(b): 100, 'epsilon': 0.01, 'gamma': 'auto' in Fig. 11(b), and 'C': 1000, 'epsilon': 0.01, 'gamma': 'scale' gives the lowest MAE value.

Quantitative Comparison

The values obtained with Catboost, Random Forest, Polynomial Regression and SVR methods without transformation, after QT, and after BCT are given in Table 1. As shown in Table, among the models applied without transformation, CatBoost yielded the lowest Mean Absolute Error (MAE), with a value of 14.0020. The highest MAE value was obtained in the SVR model with a value of 45.49. In general, it is observed that the average absolute error in the models decreases significantly after QT and BCT. This shows that the transformations significantly reduce the error rate and increase the success of the model. There is a greater reduction in the error value after QT than BCT, indicating that QT gives better results for the dataset. The CatBoost+QT experiment had the lowest average absolute error in these 12 runs. In the R^2 values, the highest value is obtained in the SVR + BCT method, which means that the model explains all the data almost perfectly, and the R^2 values are generally close to 1, which shows that it successfully explains a large part of the data in all methods and provides a good fit. Fig. 12 shows the boxplot of weight prediction with CatBoost model without transformation, weight prediction with CatBoost model after QT and weight prediction with CatBoost model after BCT. Fig. 13 shows the box plot of weight estimation with the Random Forest model after QT, and weight estimation with the Random Forest model after BCT. Fig. 14 shows the box plot of weight prediction with the Polynomial Regression model without transformation, weight prediction with the Polynomial Regression model after QT, and weight prediction with the Polynomial Regression model after BCT. Fig. 15 shows the box plot of weight prediction with the SVR model without transformation, after QT, and BCT, respectively.

An analysis of Figs. 12 through 15 clearly demonstrates the impact of the applied transformations on the distribution of the data. In the graphs without transformation, it is seen that the weight values are distributed in a wide range and the data set exhibits a high degree of variability. This shows that the data distribution has a skewed structure, especially with the effect of extreme values. In the graphs obtained after QT, the distribution is made more symmetric by scaling the weight values between 0 and 1. This transformation significantly reduced the effect of outliers and increased the homogeneity of the data. In graphs obtained after BCT, the weight values were scaled between 0 and 30, closer to their original units. This transformation reduced, but did not completely eliminate, the effect of outliers by bringing the data closer to a normal distribution.

Limitations of the proposed work

The Fish Market dataset used in this study is one of the rare open-access resources that provides both morphological features of different fish species and their corresponding weight measurements. In the literature, there is a limited number of reliable datasets that include both physical measurements and validated weight information, making this dataset the most suitable option for our study. However, the dataset consists of only 159 samples, which limits the generalization capability of the applied machine-learning algorithms. Additionally, due to the imbalanced representation of certain species, the models may perform poorly on underrepresented classes. The small sample size also increases the risk of overfitting, where the model performs well on training data but fails to produce accurate predictions on unseen data.

To address these limitations, future work will focus on constructing larger datasets with more representative samples, thereby improving both the accuracy and generalizability of the models. In addition, synthetic data generation techniques based on the statistical characteristics

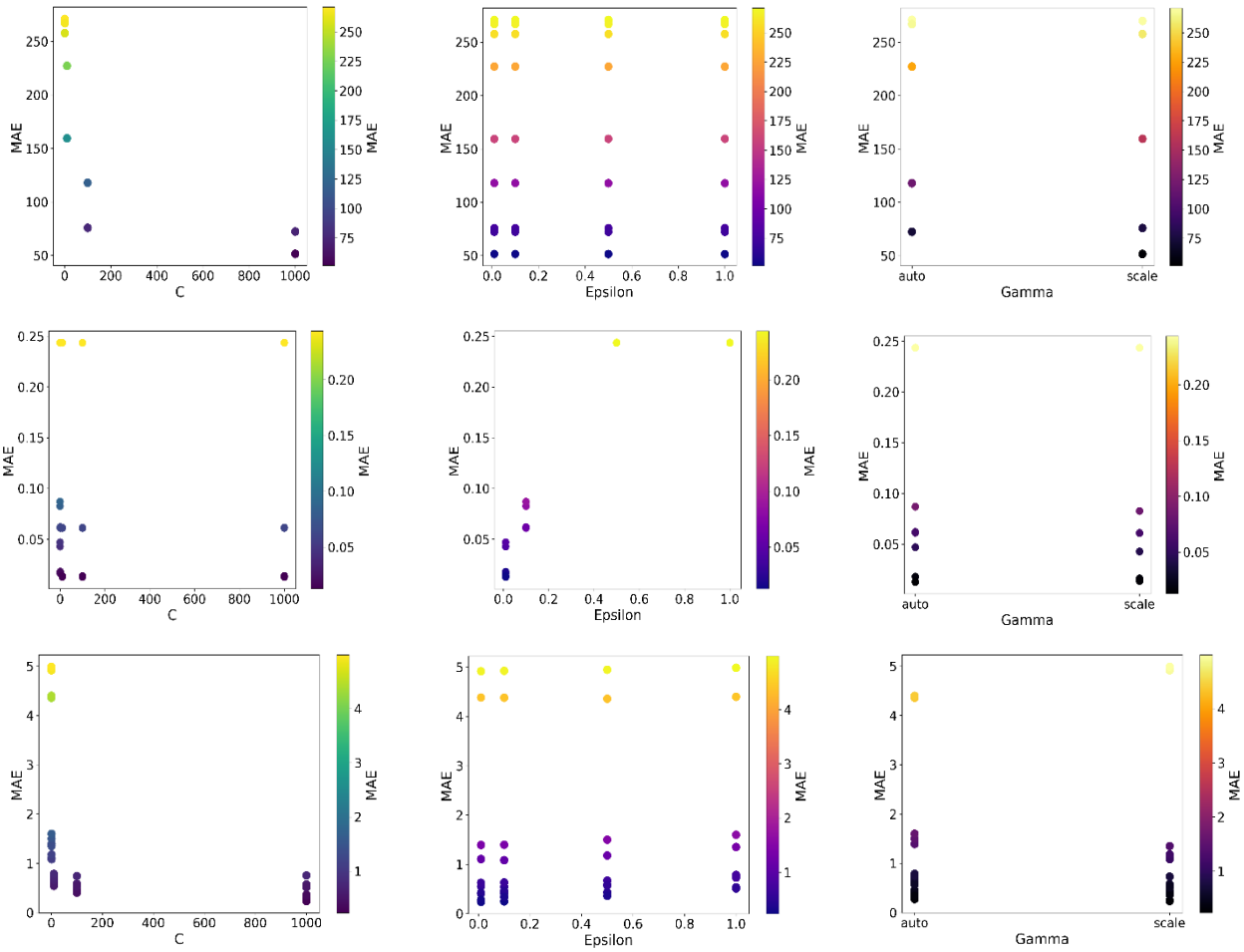


Figure 11. MAE values for Support Vector Regression (SVR) with different combinations of hyper parameters (C, epsilon, gamma). The first row corresponds to the original data (no transformation), the second row to QT-applied data, and the third row to BCT-applied data.

Table 1. Performance Comparison of Models with and Without Data Transformations

Method	MAE	R^2
CatBoost	14.0020	0.9958
CatBoost + QT	0.0171	0.9947
CatBoost + BCT	0.3302	0.9971
Random Forest	44.53	0.9692
Random Forest + QT	0.03	0.9815
Random Forest + BCT	0.77	0.9834
Polynomial Regression	42.8059	0.9732
Polynomial Regression + QT	0.0306	0.9847
Polynomial Regression+ BCT	0.6533	0.9882
SVR	45.49	0.9622
SVR + QT	0.01	0.9981
SVR + BCT	0.22	0.9986

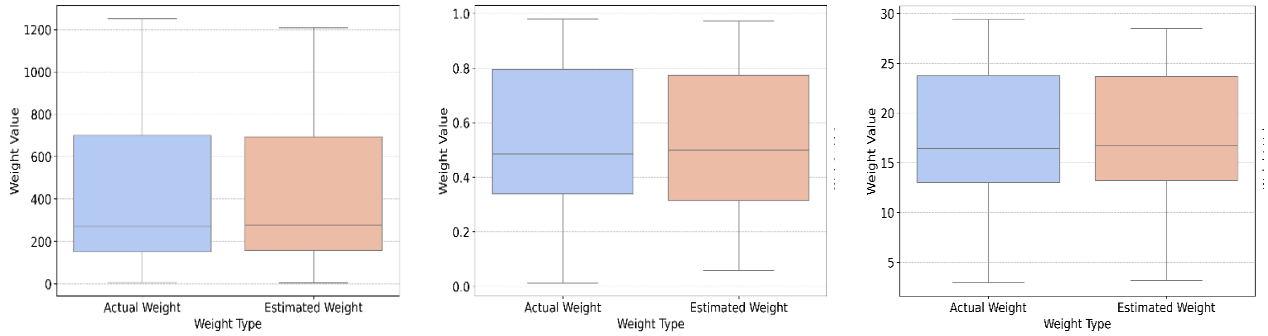


Figure 12. Box plot comparison of actual and predicted fish weight using CatBoost. From left to right, the columns correspond to the original data (no transformation), QT-applied data, and BCT-applied data.

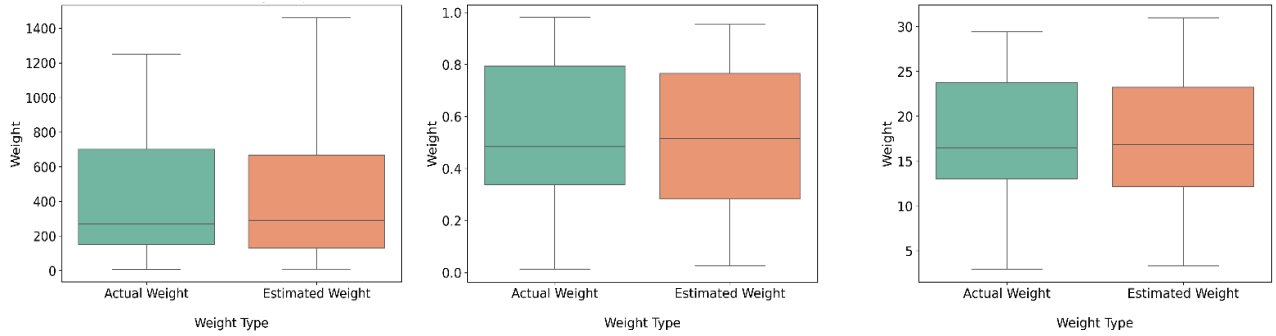


Figure 13. Box plot comparison of actual and predicted fish weight using Random Forest. From left to right, the columns correspond to the original data (no transformation), QT-applied data, and BCT-applied data.

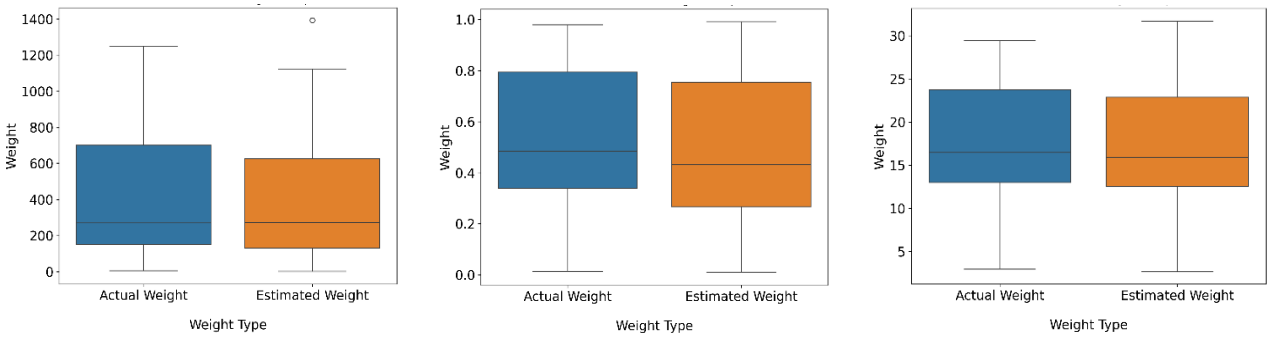


Figure 14. Box plot comparison of actual and predicted fish weight using Polynomial Regression. From left to right, the columns correspond to the original data (no transformation), QT-applied data, and BCT-applied data.

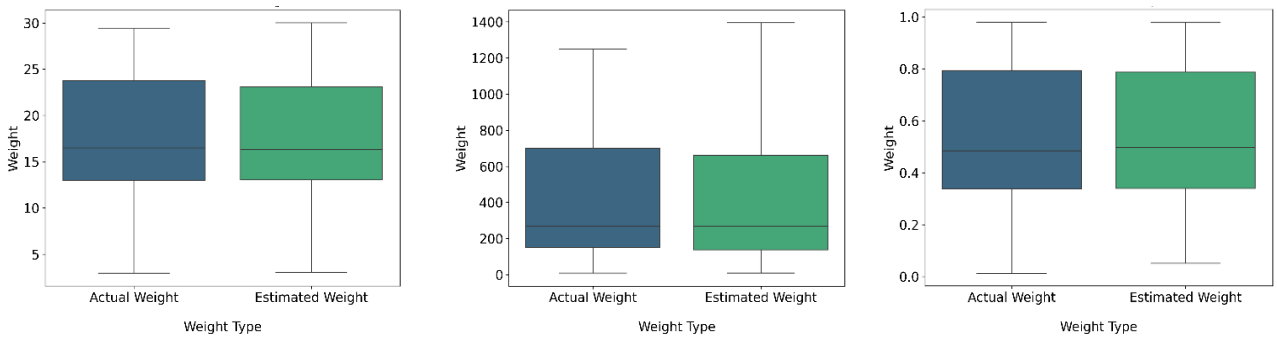


Figure 15. Box plot comparison of actual and predicted fish weight using SVR. From left to right, the columns correspond to the original data (no transformation), QT-applied data, and BCT-applied data.

of the existing data may be explored to enhance data diversity. If visual data is incorporated in subsequent phases, image-based data augmentation techniques could also be employed to improve model robustness. Expanding the dataset in these ways will significantly enhance the statistical reliability of the findings and their potential applicability in real-world scenarios.

Conclusions and Future Works

This study investigates the effects of data transformation methods on improving the fish weight estimation model's accuracy. The QT and BCT transformation methods applied to the input data as a preprocessing step appear to significantly reduce weight estimation errors by reconstructing the fish weight distribution closer to normal form. These transformations, which are applied as a preprocessing step, correct the skewed distribution in the dataset and enable machine learning models such as CatBoost, Random Forest, Polynomial Regression, and SVR to generalize better and perform better than the weight estimation results obtained without preprocessing on the raw dataset. Among the QT and BCT transformation methods, QT outperforms BCT by giving the lowest MAE value in all machine learning models. QT applied on the original dataset dramatically improves by reducing the MAE value from 14.002 to 0.017 with the CatBoost model, which gives the best accuracy, while BCT achieves an MAE value of 0.330 in the same model. The experimental results demonstrate that not only machine learning model selection has a significant impact on accuracy, but also a well-chosen transformation has a significant impact on error reduction.

The findings show that proper transformation and data normalization are important factors in maximizing model prediction performance. Future studies aim to learn more complex features from image or video frames using advanced deep learning architectures such as Convolutional Neural Networks (CNNs) for fish weight estimation and to make real-time fish weight estimation using camera and sensor-based technologies. Moreover, the model's performance on fish weight estimation using many parameters will be examined with multi-model data fusion, such as the use of image data together with sensor readings on water quality, temperature, and sonar- based measurements of fish size.

Ethics committee approval and conflict of interest statement

There is no conflict of interest with any person / institution in the article prepared.

Authors' Contributions

Esen H: Methodology, Software, Visualization, Data extraction, Writing – original draft.

Taşdelen H: Methodology, Data extraction, Writing – original draft.

Küçük S: Conceptualization, Data curation, Methodology, Validation, Supervision, Writing – review & editing.

Aksakallı IK: Conceptualization, Data curation, Methodology, Supervision, Writing – review & editing.

All authors have read and agreed to the published version of the manuscript.

References

[1] S. B. Gutzmann, E. E. Hodgson, D. Braun, J. W. Moore, and R. A. Hovel, "Predicting fish weight using photographic image analysis: a case study of broad whitefish in the lower Mackenzie River watershed," *Arct. Sci.*, vol. 8, no. 4, pp. 1356–1361, Dec. 2022. Accessed on: Jun. 30, 2025. doi: 10.1139/AS-2021-0017.

[2] D. A. Konovalov, A. Saleh, D. B. Efremova, J. A. Domingos, and D. R. Jerry, "Automatic weight estimation of harvested fish from images," in *Proc. 2019 Digital Image Computing: Techniques and Applications (DICTA)*, Dec. 2019, doi: 10.1109/DICTA47822.2019.8945971.

[3] R. Islamadina, N. Pramita, F. Arnia, and K. Munadi, "Estimating fish weight based on visual captured," in *Proc. 2018 Int. Conf. Inf. Commun. Technol. (ICOIACT)*, vol. 2018-January, pp. 366–372, Apr. 2018, doi: 10.1109/ICOIACT.2018.8350762.

[4] S. Suwannakhun and P. Daungmala, "Estimating pig weight with digital image processing using deep learning," in *Proc. 14th Int. Conf. Signal Image Technol. Internet Based Syst. (SITIS)*, pp. 320–326, Jul. 2018, doi: 10.1109/SITIS.2018.00056.

[5] R. A. Peterson and J. E. Cavanaugh, "Ordered quantile normalization: a semiparametric transformation built for the cross-validation era," *J. Appl. Stat.*, vol. 47, no. 13–15, pp. 2312–2327, Nov. 2020, doi: 10.1080/02664763.2019.1630372.

[6] B. Peng, R. K. Yu, K. L. DeHoff, and C. I. Amos, "Normalizing a large number of quantitative traits using empirical normal quantile transformation," *BMC Proc.*, vol. 1, no. S1, pp. 1–5, Dec. 2007, doi: 10.1186/1753-6561-1-S1-S156.

[7] G. D. Rayner and H. L. MacGillivray, "Weighted quantile-based estimation for a class of transformation distributions," *Comput. Stat. Data Anal.*, vol. 39, no. 4, pp. 401–433, Jun. 2002, doi: 10.1016/S0167-9473(01)00090-1.

[8] T. Zhang and B. Yang, "Box–Cox transformation in big data," *Technometrics*, vol. 59, no. 2, pp. 189–201, Apr. 2017, doi: 10.1080/00401706.2016.1156025.

[9] J. W. Osborne, "Improving your data transformations: Applying the Box–Cox transformation," *Pract. Assess. Res. Eval.*, vol. 15, no. 1, Jan. 2010, doi: 10.7275/QBPC-GK17.

[10] Fish Market. Accessed: Feb. 26, 2025. [Online]. Available:https://www.kaggle.com/datasets/vipullrathod/fish-market.

[11] *Models and test, we have used.* [Online]. Available: http://jse.amstat.org/datasets/fishcatch.txt.

[12] J. Hu and S. Szymczak, "A review on longitudinal data analysis with random forest," *Brief Bioinform.*, vol. 24, no. 2, pp. 1–11, Mar. 2023, doi: 10.1093/bib/bbad002.

[13] J. T. Hancock and T. M. Khoshgoftaar, "CatBoost for big data: an interdisciplinary review," *J. Big Data*, vol. 7, no. 1, pp. 1–45, Dec. 2020, doi: 10.1186/s40537-020-00369-8.

[14] A. V. Dorogush, V. Ershov, and A. Gulin, "CatBoost: Gradient boosting with categorical features support," *arXiv preprint*, Oct. 2018. Accessed: Mar. 1, 2025.

[15] A. Parmar, R. Katariya, and V. Patel, "A review on random forest: An ensemble classifier," in *Lecture Notes on Data Engineering and Communications Technologies*, vol. 26, pp. 758–763, 2019, doi: 10.1007/978-3-030-03146-6_86.

[16] F. Kazemi, N. Asgarkhani, T. Shafighfard, R. Jankowski, and D. Y. Yoo, "Machine-learning methods for estimating performance of structural concrete members reinforced with fiber-reinforced polymers," *Arch. Comput. Methods Eng.*, vol. 32, no. 1, pp. 571–603, Jan. 2024, doi: 10.1007/s11831-024-10143-1.

[17] S. von Bülow, G. Tesei, and K. Lindorff-Larsen, "Machine learning methods to study sequence–ensemble–function relationships in disordered proteins," *Curr. Opin. Struct. Biol.*, vol. 92, p. 103028, Jun. 2025, doi: 10.1016/j.sbi.2025.103028.

[18] B. Liu, Y. Yu, Z. Liu, Z. Cui, and W. Tian, "Prediction of CO_2 solubility in aqueous amine solutions using machine learning method," *Sep. Purif. Technol.*, vol. 354, p. 129306, Feb. 2025, doi: 10.1016/j.seppur.2024.129306.

[19] P. D'Orazio and A. D. Pham, "Evaluating climate-related financial policies' impact on decarbonization with machine learning methods," *Sci. Rep.*, vol. 15, no. 1, p. 1694, Dec. 2025, doi: 10.1038/s41598-025-85127-7.

[20] N. Tuerxun *et al*., "Accurate estimation of jujube leaf chlorophyll content using optimized spectral indices and machine learning methods integrating geospatial information," *Ecol. Inform.*, vol. 85, p. 102980, Mar. 2025, doi: 10.1016/j.ecoinf.2024.102980.

[21] K. Bogner, F. Pappenberger, and H. L. Cloke, "Technical note: The normal quantile transformation and its application in a flood forecasting system," *Hydrol. Earth Syst. Sci.*, vol. 16, no. 4, pp. 1085–1094, 2012, doi: 10.5194/hess-16-1085-2012.

[22] M. Buchinsky, "Quantile regression, Box–Cox transformation model, and the U.S. wage structure, 1963–1987," *J. Econom.*, vol. 65, no. 1, pp. 109–154, Jan. 1995, doi: 10.1016/0304-4076(94)01599-U.

[23] X. Xie, Y. Mei, B. Gu, and W. He, "Changing Box–Cox transformation parameter as an early warning signal for abrupt climate change," *Clim. Dyn.*, vol. 60, no. 11–12, pp. 4133–4143, Jun. 2023, doi: 10.1007/s00382-022-06563-z.

[24] J. Nagendra *et al*., "Evaluation of surface roughness of novel Al-based MMCs using Box–Cox transformation," *Int. J. Interact. Des. Manuf.*, vol. 18, no. 5, pp. 3369–3382, Jul. 2024, doi: 10.1007/s12008-023-01561-9.

[25] A. A. Al Abbasi, M. J. Alam, S. Saha, I. A. Begum, and M. F. Rola-Rubzen, "Impact of rural transformation on rural income and poverty for sustainable development in Bangladesh: A moments-quantile regression with fixed-effects models approach," *Sustain. Dev.*, vol. 33, no. 2, pp. 2951–2974, Apr. 2024, doi: 10.1002/sd.3276.

[26] Dhiman, H. S., Deb, D., & Guerrero, J. M. (2019). Hybrid machine intelligent SVR variants for wind forecasting and ramp events. *Renewable and Sustainable Energy Reviews*, *108*, pp. 369-379.

[27] Terrault, N. A., & Hassanein, T. I. (2016). Management of the patient with SVR. *Journal of hepatology*, *65*(1), pp. 120-129.

[28] Robeson, S. M., & Willmott, C. J. (2023). Decomposition of the mean absolute error (MAE) into systematic and unsystematic components. *PloS one*, *18*(2), e0279774.

[29] Gao, J. (2024). R-Squared (R2)–How much variation is explained?. *Research Methods in Medicine & Health Sciences*, *5*(4), 104-109.

[30] Tengtrairat, N., Woo, W. L., Parathai, P., Rinchumphu, D., & Chaichana, C. (2022). Non-intrusive fish weight estimation in turbid water using deep learning and regression models. *Sensors*, *22*(14), 5161.

[31] Hamzaoui, M., Aoueileyine, M. O. E., Romdhani, L., & Bouallegue, R. (2023). Optimizing XGBoost performance for fish weight prediction through parameter pre-selection. *Fishes*, *8*(10), 505.

[32] Mots' oehli, M., Nikolaev, A., IGede, W. B., Lynham, J., Mous, P. J., & Sadowski, P. (2024, July). Fishnet: Deep neural networks for low-cost fish stock estimation. In *2024 IEEE International Conference on Omni-layer Intelligent Systems (COINS)* (pp. 1-7). IEEE.

[33] Zhang, T., Yang, Y., Liu, Y., Liu, C., Zhao, R., Li, D., & Shi, C. (2024). Fully automatic system for fish biomass estimation based on deep neural network. *Ecological Informatics*, *79*, 102399.

[34] Rani, S. J., Ioannou, I., Swetha, R., Lakshmi, R. D., & Vassiliou, V. (2024). A novel automated approach for fish biomass estimation in turbid environments through deep learning, object detection, and regression. *Ecological Informatics*, *81*, 102663.

Dicle University
Journal of Engineering
https://dergipark.org.tr/tr/pub/dumf
duje.dicle.edu.tr

Research Article

EEG-Based Comparative Study of Brain Activity during Imagined Natural and Induced Water and Saliva Swallowing

Sevgi GÖKÇE ASLAN[1*]

[1] Inonu University, Biomedical Engineering Department, sevgigokce38@gmail.com, Orcid No: 0000-0001-9425-1916

ARTICLE INFO

Article history:

Received 13 April 2025
Received in revised form 23 June 2025
Accepted 6 August 2025
Available online 30 September 2025

Keywords:

EEG, Dysphagia, Swallowing, Imagination, Statistical Analysis

Doi: 10.24012/dumf.1675408

* Corresponding author

ABSTRACT

Dysphagia often makes eating and drinking painful, stressful, and socially isolating, potentially leading to malnutrition, dehydration, weight loss, and respiratory infections. In this study, the relationship between swallowing and brain signals was examined to contribute to the electrophysiological understanding of the imagination of swallowing and rehabilitation of dysphagia patients. To examine the swallowing event, three different experiments were conducted. The experiments included (i) natural water swallowing, (ii) swallowing saliva in an induced manner, and (iii) swallowing a sip of water in an induced manner. Visual cues on a computer monitor were used to induce the perception of swallowing and imagination. EEG data from 16 channels obtained during 15 trials of these experimental paradigms from 30 subjects (15 men) were subjected to different processes such as noise removal, selection of signal segments corresponding to the imagination of swallowing, extraction of frequency domain features, and statistical analysis. Eleven features such as spectral centroid, mean and median frequency, delta, theta, alpha and beta band powers, and relative band powers obtained from 16 channels (a total of 176 features) were first subjected to the Shapiro-Wilks normality test individually. As a result of this test, the statistical analyses were carried out with the help of repeated measures one-way ANOVA test for the features with normal distribution (spectral centroid from 11 channels), and the Friedman test for the features with non-normal distribution (spectral centroid from the remaining 5 channels and all other features from 16 channels). As a result of these tests, it is seen that 76.7% of all features yield statistically significant differences between 3 different swallowing approaches. We suggest that identifying discriminative EEG-based features could significantly contribute to the development of novel brain-machine interface applications for dysphagia rehabilitation.

1. Introduction

Swallowing is a fundamental physiological function essential for nutrition and hydration. However, for individuals with dysphagia, this simple act becomes a daily challenge, leading to significant physiological, psychological, and social difficulties [1]. Although dysphagia itself is not immediately life-threatening if left untreated, it can result in severe complications such as malnutrition, dehydration, and pneumonia due to impaired swallowing function [2], [3], [4]. Therefore, early and accurate diagnosis is crucial to improving patients' quality of life and preventing potentially life-threatening consequences.

Conventional methods, such as nasopharyngeal endoscopy and video fluoroscopy, are commonly used to assess swallowing function [5], [6]. While effective, these techniques can be invasive, uncomfortable, and require specialized clinical settings. As a result, there is an increasing demand for non-invasive and accessible alternatives for dysphagia detection and monitoring. Recent research highlights brain activity analysis as a promising approach for identifying swallowing-related impairments without direct intervention.

Among these methods, EEG stands out due to its non-invasiveness, high temporal resolution, affordability, and ease of application in clinical settings [7]. EEG records electrical brain activity through scalp electrodes, capturing voltage fluctuations associated with neuronal activity. Modern EEG systems can detect signals exceeding 1 kHz, enabling the recording of rapid neural changes critical for analyzing phenomena like epileptiform spike waves [8], [9], [10], [11] .

EEG has been used to diagnose various neurological and psychiatric disorders, including schizophrenia, Alzheimer's disease, depression, and epilepsy [12], [13], [14], [15]. In recent years, significant progress has also been made in utilizing EEG to analyze brain activity related to motor control [16]. In particular, motor imagery (MI) has emerged as a valuable paradigm for exploring cortical mechanisms involved in voluntary movement and for developing brain-computer interface (BCI) applications in neurorehabilitation [17].

Within the domain of swallowing research, MI has been effectively used to examine the cortical dynamics underlying swallowing control and to design EEG-based BCI systems for dysphagia rehabilitation [18]. In addition to these recent advancements, earlier foundational studies have offered critical insights into the neural basis of swallowing [19]. Yang et al. proposed that swallowing is initiated by tongue movement and suggested that gaps in

brain activity could indicate the absence of swallowing initiation[20], [21]. Jestrovic et al. explored how distractions influence brain activity during swallowing [22], while Huckabee et al. investigated the role of the cerebral cortex in motor planning and initiation of swallowing [23].

Building upon these developments, a recent systematic review by Alexandropoulou et al. emphasized that EEG-based studies on swallowing have increasingly revealed the cortical involvement not only during the preparatory but also during pharyngeal and esophageal phases of swallowing, challenging the earlier notion of these phases as purely reflexive. The review also highlighted using motor imagery (MI) paradigms in eliciting movement-related cortical potentials (MRCPs), mu rhythm desynchronization, and distinct connectivity patterns within sensorimotor networks. Moreover, swallowing-related EEG activity is modulated by factors such as stimulus type, bolus volume, and task complexity, and exhibits non-stationary dynamics and lateralized activation, which are relevant for developing brain-computer interfaces for dysphagia rehabilitation [24].

However, many previous studies have focused either on spontaneous swallowing or single-task MI protocols without clearly distinguishing among different imagined swallowing types, such as natural vs. induced swallowing or saliva vs. water. Furthermore, most existing EEG studies have been limited to narrow feature sets or few electrode sites, lacking comprehensive multichannel frequency-domain analysis.

In contrast to prior work limited to spontaneous or distraction-based swallowing tasks, this study aims to explore the relationship between brain function and swallowing through multichannel EEG recordings using controlled experimental paradigms. Specifically, swallowing was examined under three distinct conditions: natural water swallowing, induced water swallowing, and saliva swallowing. The study involved thirty right-handed participants of varying ages, all of whom had no history of neurological disorders or speech and swallowing impairments. EEG signals recorded from 16 channels underwent preprocessing, noise reduction, selection of swallowing imagination segments, and frequency-domain feature extraction before statistical analysis. We hypothesize that imagining swallowing water and saliva under different conditions exhibits distinct electrophysiological characteristics. Identifying discriminative EEG-based features may contribute to the development of novel brain-machine interface applications for dysphagia rehabilitation, offering a non-invasive and effective alternative for clinical assessment and treatment.

2. Materials And Methods

2.1 Participants

Our experiments were conducted with 30 participants (15 men and 15 women) aged between 19 and 56, with an average age of 30 and a standard deviation of 12. All participants were free from any swallowing disorders or related medical conditions. The study utilized three experimental paradigms approved by the Erciyes University Ethics Committee on July 12, 2023, under approval number 2023/461.

2.2 Materials

In our experiments, we utilized a 16-channel Nautilus research-grade wearable EEG headset (g.tec medical engineering, Schiedlberg, Austria) to acquire EEG signals (Figure 1). Due to its wearable design, the headset with dry electrodes was comfortably fitted onto the participant's head. The EEG electrodes were positioned following the International 10-20 system, and the signals were recorded at a sampling frequency of 500 Hz. The electrode placements on the participants' skulls are illustrated in Figure 2. EEG data were collected within 0.5–200 Hz. range using MATLAB Simulink on a Windows operating system.



Figure 1. Nautilus research-grade wearable EEG headset.

2.3 Experimental Procedure

In this study, no additional devices or sensors were attached to the neck or other body parts to detect swallowing; all analyses were conducted solely using EEG signals. To examine brain activity associated with swallowing, we not only focused on the swallowing process itself but also incorporated conditions that could potentially influence neural activity, such as pre-swallowing rest and imagined swallowing, into our experimental protocols. Consequently, our analyses were carried out across three distinct experimental conditions.

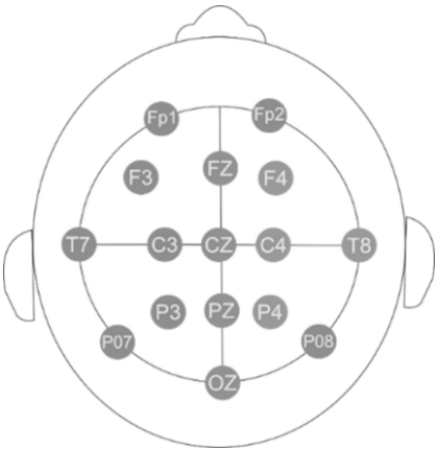


Figure 2. International 10-20 electrode placement system.

2.3.1 Paradigm 1: Natural Water Swallowing

Our first experimental paradigm aimed to examine the EEG signals of the spontaneous and natural imagination state in the brain before swallowing, without giving the subject an imagined swallowing warning (no induced swallowing). The subject was seated in front of the computer for the experiment, and the EEG electrodes were placed over the subject's skull. The subject was given a bottle of water and a straw and asked to follow the warnings/cues that appeared on the screen at regular intervals to draw a sip of water from the bottle and drink. This experiment started with the beep sound, and 2 seconds after the beep sound, the water inscription appeared on the screen for 5 seconds, and the subject drank the water in the bottle using a straw in his/her mouth during this time without any further visual cue, with minimal or no movement. Then, the subject was asked not to perform any activity for 3 seconds. This experiment consisted of 15 trials and took 150 seconds in total. The graphic showing a trace of our first experiment, which we call natural swallowing, can be seen in Figure 3.

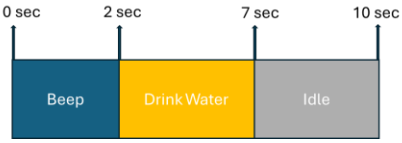


Figure 3. Natural swallowing test procedure with corresponding timing information.

2.3.2 Paradigm 2: Induced Saliva Swallowing

In contrast to the first paradigm, this experiment required participants to first rest, then imagine swallowing, and finally swallow without consuming any food or liquid. Referred to as the saliva swallowing experiment, its objective was to examine the effects of swallowing without ingestion on EEG signals. The experiment consisted of three phases: resting, imagination, and swallowing. During the resting phase, participants focused on a plus symbol displayed on the screen for 2 seconds. Following this, a beep sound signaled the start of the imagination phase, where participants envisioned swallowing for 3 seconds while viewing the prompt "imagination." In the final stage, the word "swallow" appeared on the screen, prompting participants to perform actual saliva swallowing. Each trial in this experiment lasted 9 seconds, with 15 trials totaling 135 seconds. Figure 4 illustrates a graphical representation of a 9-second segment of the dry swallowing test.

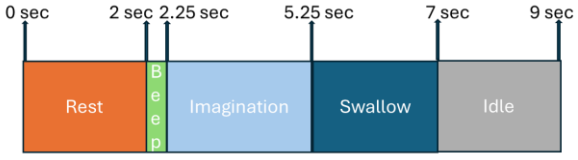


Figure 4. Saliva swallowing test procedure with corresponding timing information.

2.3.3 Paradigm 3: Induced Water Swallowing

In our final experimental paradigm, referred to as induced water swallowing, we aimed to investigate the impact of imagining the act of swallowing a sip of water held in the mouth on EEG signals. This experiment comprised four stages: water intake, resting, imagination, and actual swallowing. Participants were provided with a bottle of water and a straw and instructed to follow the cues displayed on the screen. Unlike the previous experiments, this paradigm involved the presence of water in the mouth during the imagination phase.

In the first stage, upon seeing the cue "draw water" on the screen, participants took a sip of water using the straw. Next, a plus symbol appeared for 2 seconds, during which participants engaged in the resting phase by focusing on the symbol. In the third stage, the screen displayed the word "imagination," prompting participants to mentally simulate swallowing the water for 3 seconds. Finally, in the last stage, they were instructed to perform an actual swallow. Each trial lasted 13 seconds, with a total of 15 trials, amounting to 195 seconds. Figure 5 illustrates a 13-second segment of this experiment.

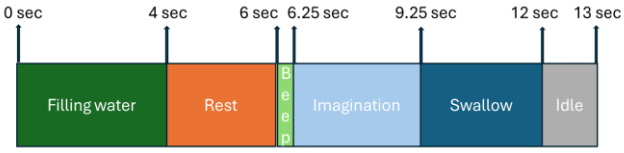


Figure 5. Water swallowing test procedure with corresponding timing information.

3. Data Analysis

3.1 Filtering

First, we performed denoising on the EEG data obtained from each subject since swallowing may cause different artifacts. We filtered EEG signals with a bandpass filter in the range of 2-30 Hz to remove low-frequency motion artifacts and high-frequency muscle artifacts. The 2–30 Hz band was selected to minimize the effects of swallowing-related artifacts. Swallowing-induced movement artifacts typically dominate frequencies below 2 Hz due to head and neck motions, while muscle activity artifacts often affect frequencies above 30 Hz. Therefore, this bandpass range was chosen to retain cortical activity while suppressing peripheral noise.

Artifact removal was performed using Independent Component Analysis (ICA), implemented via the FastICA algorithm with the 'gauss' nonlinearity function, where the number of independent components was set equal to the number of EEG channels. After ICA decomposition, each independent component (IC) was subjected to Continuous Wavelet Transform (CWT) analysis to detect abrupt high-frequency fluctuations (spikes) associated with ocular and muscle artifacts (e.g., eye blinks, facial movements). Peaks identified on CWT coefficient curves were used to automatically mark artifact-contaminated time intervals. These segments were suppressed (set to zero), and the cleaned EEG signals were reconstructed by recombining the remaining ICs through the mixing matrix A.

As a result of these processes, we have cleaned our EEG signals from artifacts. An example of filtered and unfiltered EEG signals can be seen in Figure 6.

The signal shown in Figure 6a represents a one-channel raw EEG signal (Channel 13) from one subject during 15 trials of an induced saliva swallow experiment. Figure 6b shows the filtered version of the same signal depicted in Figure 6a.

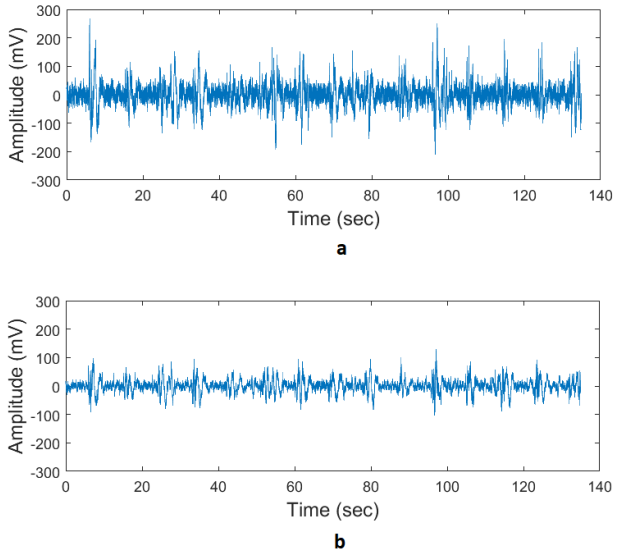


Figure 6. a) Raw signal and b) filtered signal after bandpass filtering and ICA.

3.2 Selection of Signal Segments Corresponding to Imagination

In our first experiment, natural water swallowing, the subjects were not shown any imagination-related commands and were not given specific imagination onset time information. In the natural water swallowing experiment, we aimed to analyze our data regarding how subjects imagine spontaneous swallowing before the actual swallowing movement. Since each subject's swallowing onset and finishing time instants differed from each other while performing the experiments, we examined the EEG signals from 30 people individually. Considering that each person's reaction time to actions was different in each trial, we decided to manually determine the dynamic onset time for swallowing using the motion and muscle artifacts on the EEG signals. Each person had different pre-swallow times in each trial. We considered the signal segments from our individually analyzed signals to the actual swallowing onset time manually as the imagination segment. We selected and recorded the part of the imagination that we determined from our EEG signals. We thought that the signal values with an imagination time of less than 0.5 seconds did not represent a valid signal for the Fourier analysis, which we have employed in the feature selection part of the study. Therefore, we did not include the trials whose imagination durations were less than 0.5 seconds for further analysis. Figure 7 shows the signals from different channels and different trials of 4 different subjects acquired during the natural water swallowing experiment. We included the signals shown in Figures 7a, b, and c, but not d, which had an imagination duration of less than 0.5 seconds. After this selection and elimination process, we were left with 190 trials and 3040 (190x16, number of trials x number of channels) imagination segments.

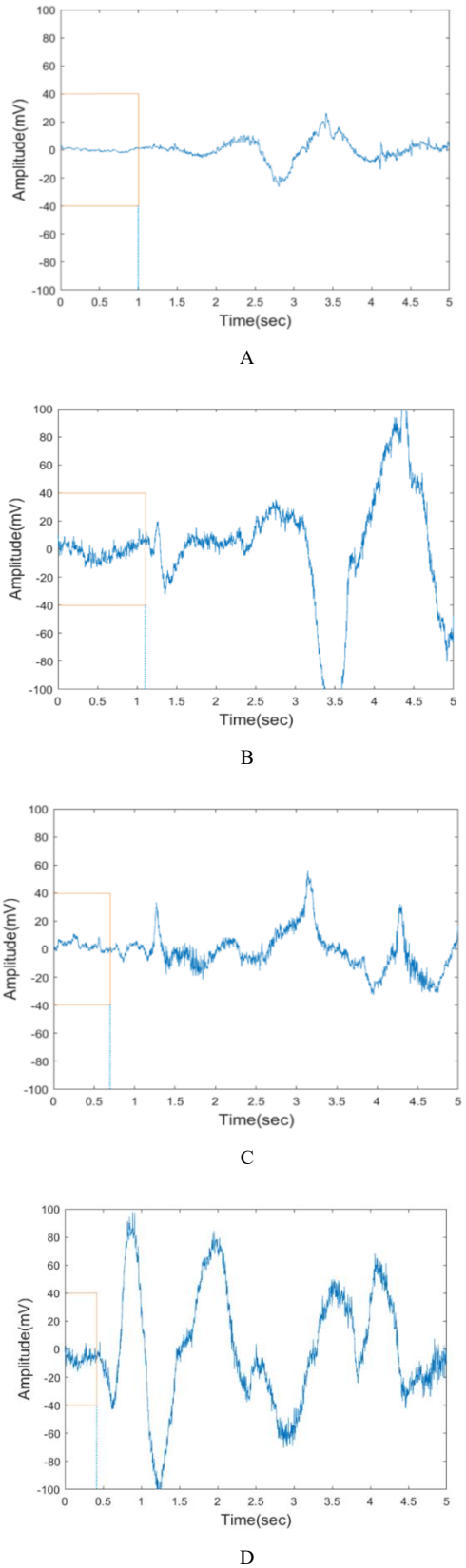


Figure 7. The selected segments corresponding to the imagination process from 4 different subjects, from different channels, and trials. Imagination durations were 1 second in (A), 1.2 seconds in (B), 0.6 seconds in (C), and 0.4 seconds in (D).

In the other two experiments, induced saliva and induced water swallowing experiments, the subjects were shown the visual cue on the screen to initiate and end the imagination of swallowing, unlike the first experiment. The imagination segments of these two experiments, of which we were certain about the imagination onset and finishing time instants, were selected and recorded. After this selection process, we obtained 450 trials and 7200 imagination segments (30 subjects x 15 trials x 16 channels).

Finally, for a consistent comparison and statistical analysis, if the imagination segments from a trial obtained during a natural water swallowing experiment for a subject were eliminated due to short signal duration, we eliminated the segments from the same trial number obtained during induced saliva and induced water swallowing experiments for the same subject. Therefore, 190 trials and 3040 imagination segments were also left for the induced saliva and induced water swallowing experimental paradigms individually.

3.3 Feature Extraction

We extracted the features from the EEG signals corresponding to the imagination of different swallowing approaches/paradigms. The feature extraction approach was based on the frequency domain. The frequency-domain features were mean frequency (in the power spectrum), median frequency (in the power spectrum), spectral centroid, band power in the delta band, band power in the theta band, band power in the alpha band, band power in the beta band, relative power in delta band, relative power in the theta band, relative power in the alpha band, and relative power in the beta band.

The mean frequency of a spectrum is calculated using Equation (1). In this equation, n is the number of frequency bins in the spectrum, f_i is the spectrum frequency in the ith bin, and I_i represents the intensity of the spectrum (in dB scale) in the ith bin.

$$f_{mean} = \frac{\sum_{i=0}^{n} I_i \cdot f_i}{\sum_{i=0}^{n} I_i} \quad (1)$$

The median frequency of a spectrum is calculated in two steps. First, the intensity in the signal across the entire spectrum is summed and divided by two. Next, a frequency is chosen where the cumulative intensity (i.e., all intensity values for lower frequencies, including focal intensity) exceeds the value calculated in the first step for the first time.

The spectral centroid is a measure used to characterize a spectrum and indicates where the center of mass of the spectrum is. As shown in equation (2), mi represents the magnitude of the bin number, and fi represents the center frequency of the bin.

$$\mu = \frac{\sum_{i=1}^{N} f_i \cdot m_i}{\sum_{i=1}^{N} m_i} \quad (2)$$

Powers in delta (0-3.9 Hz), theta (3.9-7.8 Hz), alpha (7.8-15.63 Hz), and beta (15.63-31.25 Hz) bands were calculated using a 6-level decomposition of the discrete wavelet transform. The relative power of bands was derived using the power values in each band divided by the power summed over these frequency bands. To obtain a percentage, we multiplied the ratios by 100. Thus, the relative power values were computed using the ratio of a specific band power to the total spectral power in the signal under consideration.

We extracted these 11 features in the frequency domain for 16 channels for each imagination segment. Therefore, for each segment, we obtained a total of 176 features (11 x 16).

3.4 Statistical Tests

The aim of the final stage of this research was to investigate which of these features were significantly different from each other in these different experiments using appropriate statistical tests. For values with a p-value greater than 0.05, the difference between groups is considered not significant. p-values less than 0.05 are categorized as significant, p-values less than 0.01 as very significant, and p-values less than 0.001 as highly significant.

3.4.1 Normality Check for Features

It is possible to use various normality tests to reveal whether the feature we are interested in is suitable for a normal distribution. The most well-known tests are the Chi-Square, Kolmogorov-Smirnov, Lilliefors, and Shapiro-Wilk normality tests. We decided to use the Shapiro-Wilk test because it is the most powerful test of the normality assumption [25]. We conducted our experiments with less than 50 subjects. First of all, with the Shapiro-Wilk test, we determined which features have normal or non-normal distribution among 176 features. Then, we performed a parametric test (repeated measures one-way analysis of variance, ANOVA) for normally distributed variables and a non-parametric test (Friedman test) for variables that have non-normal distribution.

3.4.2 Analysis of Features with Normal Distribution

ANOVA is a tool used to test whether there is a statistically significant difference between the means of independent groups. Repeated measures ANOVA is the extension of the dependent t-test and is the counterpart of the one-way ANOVA, but for related groups. We used the repeated measures ANOVA test to analyze the features that had a normal distribution. As a result of this test, we were able to find the features that had statistical significance, including the level of significance (according to the p-value) between three swallowing approaches/paradigms.

3.4.3 Analysis of Features with Non-normal Distribution

The Friedman test is the non-parametric equivalent of the one-way repeated ANOVA test. The Friedman test is used if the data are not normally distributed, the number of groups/conditions is three or more, and the same subjects are used in all groups/conditions. We subjected features with non-normal distribution to the Friedman test and were able to find the features that had statistical significance

including the level of significance between three swallowing approaches/paradigms.

3.5 Classification

Classification analysis was performed using a set of 135 significant features selected from the original dataset. Feature matrices corresponding to the three classes were concatenated for each paradigm, and the resulting data were standardized using z-score normalization to ensure comparable scales across features.

To evaluate classification performance, both binary and multi-class tasks were considered. Specifically, class combinations included binary pairs (Paradigm 1 vs 2, Paradigm 2 vs 3, and Paradigm 1 vs 3) as well as a multi-class scenario involving all three paradigms simultaneously.

For each class combination, the relevant subset of data was extracted. In binary classification cases, class labels were relabeled as 1 and 2 for consistency. A 10-fold cross-validation strategy was employed to assess model generalizability and prevent overfitting.

Four different classifiers were evaluated: Random Forest, Support Vector Machine (SVM) with Radial Basis Function (RBF) kernel, K-Nearest Neighbors (KNN), and Decision Tree. To optimize classifier performance, a grid search was conducted over relevant hyperparameters for each model:

- Random Forest: Number of learning cycles (100, 200, 300) and maximum number of splits per tree (20, 50, 100).
- SVM: Kernel scale parameters ([0.1, 0.5, 1, 2, 5, 10]) for the RBF kernel.
- KNN: Number of neighbors ([3, 5, 7, 9]).
- Decision Tree: Maximum number of splits ([10, 20, 50]) and minimum leaf size ([1, 5, 10]) within an ensemble framework using 100 learning cycles.

During each fold of cross-validation, classifiers were trained on the training subset and evaluated on the test subset. The best accuracy across hyperparameter combinations was recorded per fold for each classifier. Final reported accuracies represent the average performance over all folds.

The combined use of cross-validation and hyperparameter tuning ensured robust and unbiased estimates of classification accuracy across different class combinations and models.

4. Results

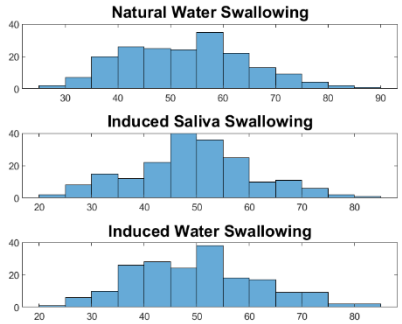
As the outcome of the normality test, we determined that 11 of 176 features have a normal distribution, and the rest have a non-normal distribution. These 11 features were spectral centroid values from 11 channels. The remaining spectral centroid features from 5 channels and all other frequency domain features from 16 channels followed a non-normal distribution. Figure 8 shows the distribution of 4 sample features, 2 of which had normal distribution, and 2 of which had non-normal distribution.

When the spectral centroid features from 11 channels with normal distribution were subjected to a one-way repeated measures ANOVA test, 10 features were found to be very significant, and 1 value was found to be significant. In other words, this result means that all p-values were less than 0.05. This indicates that there is statistical significance between the three different paradigms for the imagination of swallowing in terms of spectral centroid features from 11 channels.

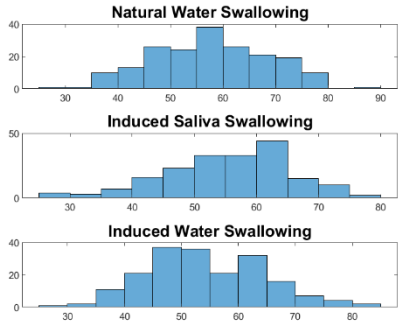
When we examined the features with non-normal distribution using the Friedman test, features such as mean frequency, median frequency, spectral centroid, delta band power, and beta band showed statistically significant differences between imagination paradigms in all 16 channels. On the contrary, a feature such as the power of the theta band showed non-significant differences in all channels. Features such as the power of the alpha band, the relative power of theta band, the relative power of the alpha band, and the relative power of the beta band showed significant and non-significant differences. Table 1 shows how many channels for each feature with a non-normal distribution have which level of statistical significance.

The p-values in the ANOVA and Friedman tests, which we applied for our features with normal and non-normal distributions, show that the group mean differences are not significant or significant. In these test results, 11 features with normal distribution and 124 with non-normal distribution seem statistically significant. We also performed multiple comparison tests to determine which groups were groups with different means for the 41 non-normally distributed and non-significant features. As a result of the test, we calculated the mean and standard deviation values between the groups. The comparison results of 41 non-significant features that we obtained are shown in Table 2. Although the features in Table 2 did not reach statistical significance, the observed trends in mean values across paradigms reveal subtle but potentially meaningful neural differences. These trends, particularly in frontal and parietal regions, suggest differentiated cortical engagement during various swallowing imagination conditions. Such latent patterns may contribute to classification success, highlighting the utility of multivariate approaches beyond univariate statistical thresholds.

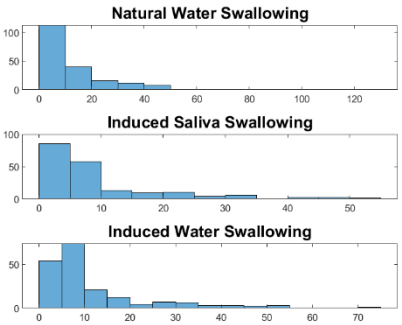
The classification results for different class combinations using 135 significant features and various classifiers are summarized in Table 3. The binary classification tasks involving pairs of paradigms (Paradigm 1 vs 2, Paradigm 2 vs 3, and Paradigm 1 vs 3) consistently achieved higher accuracies compared to the multi-class classification involving all three paradigms simultaneously (Paradigms 1 vs 2 vs 3). Among the classifiers, Random Forest demonstrated the best overall performance, achieving the highest average accuracy in all binary tasks, with accuracies of 75.26%, 71.58%, and 76.58% for Paradigm 1 vs 2, Paradigm 2 vs 3, and Paradigm 1 vs 3 classifications, respectively. Similarly, Decision Tree showed competitive results, particularly in the Paradigm 1 vs 3 classification with an accuracy of 77.11%.



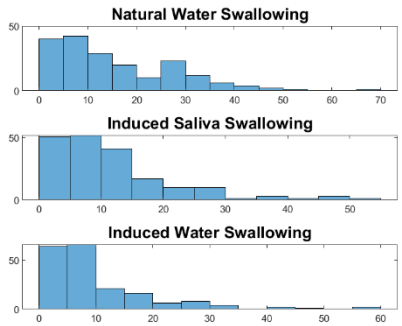
A



B



C



D

Figure 8. Histograms of two features with normal distributions (A and B) and two features with non-normal distributions (C and D). A) the Spectral centroid of channel 5, B) the spectral centroid of channel 15, C) the band power in the delta band of channel 11, and D) the mean frequency of channel 14.

The multi-class classification involving all three paradigms simultaneously yielded lower accuracy values across all classifiers, with the highest accuracy being 60.18% for Random Forest. This decrease is expected due to the increased complexity of distinguishing among three classes instead of two.

Support Vector Machine (SVM) with RBF kernel and K-Nearest Neighbors (KNN) classifiers showed moderate performance in all cases, with SVM slightly outperforming KNN in most tasks.

Overall, these results indicate that binary classification between pairs of paradigms is more reliable for this dataset, and ensemble methods like Random Forest are well-suited for the task. The reduced accuracy in multi-class classification suggests that further feature engineering or more advanced classification methods may be needed to improve performance when distinguishing among all three paradigms simultaneously.

5. Conclusions and Discussion

In this study, we tried to determine the relationship between swallowing and brain signals to contribute to the treatment of dysphagia patients with swallowing difficulties. While examining this relationship, we not only depended on the act of swallowing but also applied different paradigms before and after each experiment. We collected EEG signals of imagination of swallowing, waiting for swallowing, and actual swallowing events from 3 different experiments. By filtering each of the EEG signals from 16 channels in these experiments, we removed noise and unwanted components. In this article, we have focused specifically on the imagination states of the filtered signals. We extracted 176 features from the EEG signal segments corresponding to the imagination of swallowing. As a result of statistical analysis, we observed that 135 of 176 features (76.7%) revealed significant differences between the three experiments. We obtained these results from 30 subjects, clearly showing the relationship between the imagination of swallowing events and brain signals. One of the key novelties of this study is the integration of statistical analysis with machine learning, where significant features were used to classify the three swallowing paradigms with over 77% accuracy in binary settings.

To address dysphagia effectively, it is essential to examine swallowing from an electrophysiological perspective. Investigating electrophysiological processes enhances our understanding of swallowing control networks and provides a valuable tool for assessing the effects of various treatments on pharyngeal sensory function. In the literature, [26]. ERPs are signals derived from EEG recordings that measure time-dependent neural activity in response to sensory, motor, or cognitive events [27]. The swallowing process involves the neural transmission and cerebral integration of oropharyngeal sensory inputs, which can be investigated through ERP studies [26].

Table 1. Friedman test results for features with non-normal distribution. NS: Non-significant, S: Significant, HS: Highly Significant, VHS: Very Highly Significant.

Feature	NS	S	HS	VHS	Total
Mean Frequency				**16** Cz, Fp2, F3, Fz, F4, T7, C3, Fp1, C4, T8, P3, Pz, P4, Po7, Po8, Oz	**16**
Median Frequency				**16** Cz, Fp2, F3, Fz, F4, T7, C3, Fp1, C4, T8, P3, Pz, P4, Po7, Po8, Oz	**16**
Centroid Fft		**1** Oz	**2** Fp1, C4	**2** T8, P3	**5**
Power Delta		**4** Cz, Fz, F4, Oz	**11** Fp2, F3, T7, C3, Fp1, C4, T8, P3, Pz, P4, Po8	**1** Po7	**16**
Power Theta	**16**				**16**
Power Alpha	**5**	**5** Fz, C4, T8, P3, P4	**6** Fp2, F3, Pz, Po7, Po8, Oz		**16**
Power Beta				**16** Cz, Fp2, F3, Fz, F4, T7, C3, Fp1, C4, T8, P3, Pz, P4, Po7, Po8, Oz	**16**
Relative Power Delta		**1** Cz		**15** Fp2, F3, Fz, F4, T7, C3, Fp1, C4, T8, P3, Pz, P4, Po7, Po8, Oz	**16**
Relative Power Theta	**6**	**9** Cz, Fp2, F3, Fz, T7, C3, Fp1, C4, T8	**1** F4		**16**
Relative Power Alpha	**12**	**4** Pz, P4, Po7, Po8			**16**
Relative Power Beta	**2**	**5** F3, Fz, F4, T7, C3	**1** Fp1	**8** C4, T8, P3, Pz, P4, Po7, Po8, Oz	**16**
Total	**41**	**29**	**21**	**74**	**165**

Additionally, electrophysiological research on swallowing provides crucial insights into dysphagia. For instance, one study was conducted to evaluate dysphagia at the oropharyngeal stage of swallowing and to investigate the underlying pathophysiological mechanisms in patients with myasthenia gravis [28]. Another study explored the relationship between multiple sclerosis (MS) and dysphagia using electrophysiological methods [29]. Furthermore, research examining stroke patients and individuals with swallowing difficulties helped establish a connection between these conditions [30].

Considering these findings, we believe that EEG-based motor imagery can help identify distinct electrophysiological features, potentially advancing brain-machine interface applications for dysphagia rehabilitation. The unique neural patterns observed during motor imagery—such as imagining swallowing water versus saliva—highlight the significance of EEG-based feature extraction. These findings emphasize the crucial role of mental practice and physical therapy in motor rehabilitation, illustrating the interplay between brain activity, treatment approaches, and recovery in dysphagia patients.

Numerous studies have been conducted on the rehabilitation of swallowing disorders; however, research specifically focusing on the potential of motor imagery (MI) as a standalone approach for improving swallowing rehabilitation remains limited. Existing studies suggest that motor imagery can elicit neural responses and that mentally simulating swallowing-related actions may enhance swallowing motor performance [18].

This study used different experimental protocols to explore the relationship between motor imagery and swallowing. By examining whether motor imagery of swallowing varies across different conditions, we aimed to identify practical, cost-effective, and accessible applications that could enhance the effectiveness of active exercises in dysphagia rehabilitation. While motor imagery exercises cannot fully replace active exercises, they are recommended as a complementary approach to enhance motor learning and performance, particularly following neurological impairment. The most effective rehabilitation outcomes are achieved when physiotherapy is combined with motor imagery [31], [32], [33].

Furthermore, while previous studies have investigated various methodologies of swallow motor imagery [19], [34], [35]. They often lacked statistical analyses of the data. One of the key contributions of this study is the systematic statistical analysis of EEG signals obtained from different experimental paradigms. The results indicate that the neural responses associated with swallowing motor imagery differ significantly across experimental conditions.

In previous studies, several aspects of swallowing-related brain activity have been explored. For instance, Yang et al. demonstrated that motor imagery of swallowing activates motor-related cortical areas and suggested that gaps in brain activity may reflect the absence of swallow initiation [20], [21], [34], [36], [37], [38]. Similarly, Huckabee et al. highlighted the role of the supplementary motor area in the preparatory phase of voluntary swallowing [23].

Table 2. The mean estimates, standard errors, and corresponding channel and feature names for comparisons.

Channel	Feature name	Paradigm 1 (Mean ± STD)	Paradigm 2 (Mean ± STD)	Paradigm 3 (Mean ± STD)
CZ	theta band power	$5.22\times10^{-5} \pm 2.68\times10^{-4}$	$5.22\times10^{-5} \pm 2.68\times10^{-4}$	$5.22\times10^{-5} \pm 2.68\times10^{-4}$
CZ	alpha band power [c]	$3.28\times10^{-5} \pm 1.36\times10^{-4}$	$3.28\times10^{-5} \pm 1.36\times10^{-4}$	$3.28\times10^{-5} \pm 1.36\times10^{-4}$
CZ	relative alpha band power	0.20±0.12	0.23±0.11	0.22±0.14
CZ	relative beta band power	0.23±0.16	0.21±0.13	0.19±0.13
Fp2	theta band power	0.00±0.01	0.00±0.01	0.00±0.00
Fp3	relative alpha band power	0.19±0.12	0.20±0.11	0.19±0.13
Fp4	relative beta band power	0.22±0.16	0.19±0.13	0.17±0.13
F3	theta band power	0.04±0.16	0.02±0.07	0.02±0.06
F3	relative alpha band power	0.18±0.12	0.18±0.11	0.17±0.12
FZ	theta band power	0.29±0.84	0.16±0.34	0.19±0.34
FZ	relative alpha band power	0.18±0.12	0.16±0.11	0.16±0.12
F4	theta band power	1.16±2.71	0.69±1.09	0.84±1.33
F4	alpha band power [b]	0.53±1.11	0.30±0.27	0.50±1.45
F4	relative alpha band power	0.17±0.12	0.16±0.11	0.15±0.12
T7	theta band power	3.22±6.38	2.00±2.61	2.52±3.81
T7	alpha band power	1.41±2.30	0.87±0.78	1.40±3.61
T7	relative alpha band power	0.17±0.12	0.15±0.11	0.15±0.11
C3	theta band power	6.79±12.08	4.40±5.05	5.63±8.43
C3	alpha band power	2.94±3.79	1.95±1.76	3.04±7.40
C3	relative alpha band power	0.17±0.12	0.15±0.11	0.15±0.11
Fp1	theta band power	11.60±19.30	7.76±8.27	10.04±15.17
Fp1	alpha band power	5.07±5.39	3.57±3.27	5.46±13.07
Fp1	relative alpha band power	0.18±0.12	0.15±0.11	0.15±0.11
C4	theta band power	16.90±27.17	11.59±11.84	15.24±23.45
C4	relative alpha band power	0.18±0.12	0.15±0.11	0.15±0.11
T8	theta band power	21.88±35.10	15.33±15.34	20.20±31.74
T8	relative alpha band power	0.18±0.12	0.15±0.11	0.15±0.10
P3	theta band power [c]	25.76±42.23	18.30±18.21	24.09±38.70
P3	relative theta band power [b]	0.24±0.14	0.22±0.11	0.20±0.11
P3	relative alpha band power	0.18±0.13	0.15±0.10	0.15±0.10
PZ	theta band power	27.76±47.01	19.82±19.74	26.01±42.79
PZ	relative theta band power	0.24±0.14	0.21±0.11	0.20±0.11

Channel	Feature name	Paradigm 1 (Mean ± STD)	Paradigm 2 (Mean ± STD)	Paradigm 3 (Mean ± STD)
P4	theta band power	27.43±48.32	19.48±19.46	25.42±43.00
P4	relative theta band power	0.23±0.14	0.21±0.11	0.20±0.10
PO7	theta band power	25.02±46.90	17.39±17.46	22.61±39.66
PO7	relative theta band power	0.23±0.13	0.20±0.11	0.19±0.10
PO8	theta band power	21.50±45.68	14.13±14.33	18.92±37.49
PO8	relative theta band power	0.22±0.13	0.20±0.10	0.19±0.10
OZ	theta band power [c]	18.28±48.10	10.77±11.53	16.41±52.06
OZ	relative theta band power	0.21±0.12	0.19±0.09	0.19±0.09
OZ	relative alpha band power	0.19±0.11	0.16±0.09	0.17±0.10

a: p-value <0.05 for paradigm 1 vs. paradigm 2,

b: p-value <0.05 for paradigm 1 vs. paradigm 3,

c: p-value <0.05 for paradigm 2 vs. paradigm 3.

Table 3. Classification accuracies (%) of different classifier paradigms for various class combinations using 135 significant features.

Classifier/Paradigm	**1 vs 2**	**2 vs 3**	**1 vs 3**	**1 vs 2 vs 3**
Random Forest	75.26%	71.58%	76.58%	60.18%
SVM (RBF)	70.79%	63.95%	70.00%	51.40%
KNN	69.21%	62.37%	68.16%	51.75%
Decision Tree	74.74%	70.26%	77.11%	59.47%

Our findings are consistent with these observations, as we also identified significant differences in spectral centroid and frequency band powers during the imagination of swallowing under different conditions, reflecting distinct cortical engagement.

Jestrovic et al. reported that attentional modulation can influence EEG activity during swallowing tasks, indicating that task design may affect cortical activation patterns [22]. In our study, the use of visual cues for imagination phases (in induced saliva and induced water paradigms) allowed us to observe more temporally controlled cortical responses compared to the natural swallowing condition, where imagination onset was more spontaneous.

Furthermore, previous studies, such as those by Kober et al., primarily used hemodynamic measurements (e.g., NIRS) or did not provide detailed statistical analyses of motor imagery EEG data [39]. In contrast, our study employed comprehensive frequency-domain feature extraction combined with statistical evaluation (ANOVA and Friedman tests), which revealed that 76.7% of features exhibited significant differences across conditions. This systematic analysis contributes novel insights into the electrophysiological characterization of swallowing motor imagery and supports the feasibility of using EEG-based biomarkers for dysphagia rehabilitation.

As a novel approach to swallowing rehabilitation, this study was conducted on healthy individuals. We chose this approach based on the rationale that an initial focus on healthy participants would provide a clearer understanding of the natural swallowing process before extending the research to individuals with dysphagia. Including individuals with swallowing disorders at this stage could introduce confounding factors that might obscure the fundamental characteristics of motor imagery-related neural activity.

Overall, the findings of this study contribute to the growing body of knowledge on dysphagia rehabilitation and provide a foundation for developing more effective motor imagery-based therapeutic strategies. This research offers promising insights that may help optimize dysphagia rehabilitation programs and improve educational approaches for both clinicians and patients.

The primary limitation of this study was the variability in the timing of motor imagery across individuals. As a result, we had to analyze each trial separately, which made it challenging to establish a generalized structure with high external validity. Additionally, since the act of swallowing introduces significant noise in EEG signals, denoising the data proved to be a major challenge. However, the statistical analyses performed in this study have contributed to a better understanding of the neural mechanisms underlying the swallowing process. One limitation of the natural water swallowing paradigm was the absence of externally

provided cues for motor imagery onset, which may introduce subjective variability in determining the imagination periods. Although segment selection was based on visual inspection of muscle artifacts to identify pre-swallowing periods, potential inter-observer variability may affect the consistency of these segments.

For future studies, we aim to further improve the distinction between swallowing, rest, and imagination states by employing advanced classification methods. Moreover, we plan to expand our experimental design by incorporating additional experimental paradigms that allow for a clearer comparison between different conditions. Another crucial direction for future research is to extend this work to individuals with dysphagia, allowing for a comparative analysis between healthy participants and patients. This will provide a deeper insight into the motor imagery of swallowing and its potential applications in rehabilitation. Additionally, in future studies, we would like to use additional objective measurements such as electromyography (EMG) or laryngeal sensors to more accurately detect pre-swallow onset during natural swallowing paradigms.

Additionally, we intend to develop a novel brain-machine interface (BMI) based EEG decoding approach specifically tailored for dysphagia patients. Such advancements may facilitate the creation of more effective motor imagery-based rehabilitation strategies, ultimately improving therapeutic outcomes for individuals with swallowing disorders.

Funding Statement: The authors received no financial support for the research, authorship, and/or publication of this article.

Conflict of Interest Statement: The authors declare no conflict of interest.

Ethical Statement: The Declaration of Helsinki conducted all study procedures. This study was approved by the Erciyes University Ethics Committee on July 12, 2023, under approval number 2023/461.

References

[1] D. G. Smithard, P. A. O'Neill, R. E. England, C. L. Park, R. Wyatt, D. F. Martin, and J. Morris, "Complications and outcome after acute stroke: Does dysphagia matter?," Stroke, vol. 27, no. 7, pp. 1200–1204, 1996, doi: 10.1161/01.STR.27.7.1200.

[2] J. M. Dudik, A. Kurosu, J. L. Coyle, and E. Sejdić, "Dysphagia and its effects on swallowing sounds and vibrations in adults," Biomed. Eng. Online, vol. 17, no. 1, 2018, doi: 10.1186/s12938-018-0501-9.

[3] P. M. Bath, H. S. Lee, and L. F. Everton, "Swallowing therapy for dysphagia in acute and subacute stroke," Stroke, 2019, doi: 10.1161/STROKEAHA.118.024299.

[4] P. Leslie, M. J. Drinnan, I. Zammit-Maempel, J. L. Coyle, G. A. Ford, and J. A. Wilson, "Cervical auscultation synchronized with images from endoscopy swallow evaluations," Dysphagia, vol. 22, no. 4, pp. 290–298, 2007, doi: 10.1007/s00455-007-9084-5.

[5] S. E. Langmore, "Evaluation of oropharyngeal dysphagia: Which diagnostic tool is superior?," Curr. Opin. Otolaryngol. Head Neck Surg., vol. 11, no. 6, pp. 485–489, 2003, doi: 10.1097/00020840-200312000-00014.

[6] J. L. Coyle et al., "Oropharyngeal dysphagia assessment and treatment efficacy: Setting the record straight (Response to Campbell-Taylor)," J. Am. Med. Dir. Assoc., vol. 10, no. 1, pp. 62–66, 2009, doi: 10.1016/j.jamda.2008.10.003.

[7] C. D. Binnie and P. F. Prior, "Electroencephalography," J. Neurol. Neurosurg. Psychiatry, vol. 57, no. 11, pp. 1308–1319, 1994, doi: 10.1136/jnnp.57.11.1308.

[8] M. Proudfoot, M. W. Woolrich, A. C. Nobre, and M. R. Turner, "Magnetoencephalography," Pract. Neurol., vol. 14, no. 5, pp. 336–343, 2014, doi: 10.1136/practneurol-2013-000768.

[9] G. Muehllehner and J. S. Karp, "Positron emission tomography," Phys. Med. Biol., vol. 51, no. 13, pp. R117–R137, 2006, doi: 10.1088/0031-9155/51/13/R08.

[10] G. Niso, E. Romero, J. T. Moreau, A. Araujo, and L. R. Krol, "Wireless EEG: A survey of systems and studies," Neuroimage, vol. 269, 2023, Art. no. 119774, doi: 10.1016/j.neuroimage.2022.119774.

[11] C. Yen, C. L. Lin, and M. C. Chiang, "Exploring the frontiers of neuroimaging: A review of recent advances in understanding brain functioning and disorders," Life, vol. 13, no. 7, p. 1472, 2023, doi: 10.3390/life13071472.

[12] H. Namazi, E. Aghasian, and T. S. Ala, "Fractal-based classification of electroencephalography (EEG) signals in healthy adolescents and adolescents with symptoms of schizophrenia," Technol. Health Care, vol. 27, no. 3, pp. 231–242, 2019, doi: 10.3233/THC-181497.

[13] J. Chouinard, "Dysphagia in Alzheimer disease: A review," J. Nutr. Health Aging, vol. 4, no. 4, pp. 214–217, 2000.

[14] H. Azuma and T. Akechi, "EEG correlates of quality of life and associations with seizure without awareness and depression in patients with epilepsy," Neuropsychopharmacol. Rep., vol. 42, no. 3, pp. 281–289, 2022, doi: 10.1002/npr2.12276.

[15] Ö. Türk and M. S. Özerdem, "Epilepsy detection by using scalogram based convolutional neural network from EEG signals," Brain Sci., vol. 9, no. 5, p. 115, 2019, doi: 10.3390/brainsci9050115.

[16] S. Abenna, M. Nahid, H. Bouyghf, and B. Ouacha, "An enhanced motor imagery EEG signals prediction system in real-time based on delta rhythm," Biomed. Signal Process. Control, vol. 79, 2023, Art. no. 104210, doi: 10.1016/j.bspc.2022.104210.

[17] A. Al-Saegh, S. A. Dawwd, and J. M. Abdul-Jabbar, "Deep learning for motor imagery EEG-based classification: A review," Biomed. Signal Process. Control, vol. 63, p. 102172, 2021, doi: 10.1016/j.bspc.2020.102172.

[18] A. S. C. Caldas et al., "Motor imagery and swallowing: a systematic literature review," Rev. CEFAC, vol. 20, no. 2,

pp. 249–258, 2018, doi: 10.1590/1982-0216201820214317.

[19] S. SH, N. CV, and D. CRO, "Motor imagery and swallowing: Introduction to literature and discussion of research needs in dysphagia," Health Care Curr. Rev., vol. 6, no. 1, 2018, doi: 10.4172/2375-4273.1000218.

[20] H. Yang et al., "Detection of motor imagery of swallow with model adaptation: Swallow or tongue?," in Proc. 5th Int. Brain-Computer Interface Meeting, 2013, doi: 10.3217/978-3-85125-260-6-56.

[21] H. Yang et al., "On the correlations of motor imagery of swallow with motor imagery of tongue movements and actual swallow," in Proc. Int. Conf. Neural Inf. Process., 2016, pp. 481–488, doi: 10.1007/978-981-10-0207-6_55.

[22] I. Jestrović, J. L. Coyle, S. Perera, and E. Sejdić, "Influence of attention and bolus volume on brain organization during swallowing," Brain Struct. Funct., vol. 223, no. 2, pp. 749–761, 2018, doi: 10.1007/s00429-017-1535-7.

[23] M. L. Huckabee, L. Deecke, M. P. Cannito, H. J. Gould, and W. Mayr, "Cortical control mechanisms in volitional swallowing: The Bereitschaftspotential," Brain Topogr., vol. 16, no. 1, pp. 3–17, 2003, doi: 10.1023/A:1025671914949.

[24] A. Alexandropoulou, E. Magkouti, A. Despoti, N. Leventakis, and S. Nanas, "Studying the swallow using surface electroencephalography: A systematic review," Health Res. J., vol. 9, no. 2, pp. 63–75, 2023, doi: 10.12681/healthresj.33617.

[25] N. M. Y. B. W. Razali, "Power comparison of Shapiro-Wilk, Kolmogorov-Smirnov, Lilliefors, and Anderson-Darling tests," J. Stat. Model. Anal., vol. 2, no. 1, pp. 21–33, 2011.

[26] I. Jestrović, J. L. Coyle, and E. Sejdić, "Decoding human swallowing via electroencephalography: A state-of-the-art review," J. Neural Eng., vol. 12, no. 5, p. 051001, 2015, doi: 10.1088/1741-2560/12/5/051001.

[27] S. McWeeny and E. S. Norton, "Understanding event-related potentials (ERPs) in clinical and basic language and communication disorders research: A tutorial," Int. J. Lang. Commun. Disord., vol. 55, no. 5, pp. 649–663, 2020, doi: 10.1111/1460-6984.12535.

[28] C. Ertekin, N. Yüceyar, and I. Aydoğdu, "Clinical and electrophysiological evaluation of dysphagia in myasthenia gravis," J. Neurol. Neurosurg. Psychiatry, vol. 65, no. 6, pp. 848–856, 1998, doi: 10.1136/jnnp.65.6.848.

[29] Y. Beckmann et al., "Electrophysiological evaluation of dysphagia in the mild or moderate patients with multiple sclerosis: A concept of subclinical dysphagia," Dysphagia, vol. 30, no. 3, pp. 331–338, 2015, doi: 10.1007/s00455-015-9598-1.

[30] B. Labeit et al., "The assessment of dysphagia after stroke: State of the art and future directions," Lancet Neurol., vol. 22, no. 7, pp. 590–600, 2023, doi: 10.1016/S1474-4422(23)00153-9.

[31] C. G. Ashley Fox, "Using motor imagery therapy to improve movement efficiency and reduce fall injury risk," J. Nov. Physiother., vol. 3, no. 6, p. 186, 2013, doi: 10.4172/2165-7025.1000186.

[32] T. Singer, P. Fahey, and K. P. Y. Liu, "The efficacy of imagery in the rehabilitation of people with Parkinson's disease: Protocol for a systematic review and meta-analysis," Syst. Rev., vol. 11, no. 1, p. 47, 2022, doi: 10.1186/s13643-022-02041-z.

[33] A. M. Ladda, F. Lebon, and M. Lotze, "Using motor imagery practice for improving motor performance – A review," Brain Cogn., vol. 150, p. 105705, 2021, doi: 10.1016/j.bandc.2021.105705.

[34] H. Yang et al., "Detection of motor imagery of swallow EEG signals based on the dual-tree complex wavelet transform and adaptive model selection," J. Neural Eng., vol. 11, no. 3, p. 035016, 2014, doi: 10.1088/1741-2560/11/3/035016.

[35] S. E. Kober and G. Wood, "Changes in hemodynamic signals accompanying motor imagery and motor execution of swallowing: A near-infrared spectroscopy study," Neuroimage, vol. 93, no. Pt 1, pp. 1–10, 2014, doi: 10.1016/j.neuroimage.2014.02.019.

[36] H. Yang, K. K. Ang, C. Wang, K. S. Phua, and C. Guan, "Neural and cortical analysis of swallowing and detection of motor imagery of swallow for dysphagia rehabilitation—A review," in Prog. Brain Res., vol. 228, pp. 271–295, 2016, doi: 10.1016/bs.pbr.2016.03.014.

[37] H. Yang, C. Guan, K. K. Ang, C. C. Wang, K. S. Phua, and J. Yu, "Dynamic initiation and dual-tree complex wavelet feature-based classification of motor imagery of swallow EEG signals," in Proc. Int. Joint Conf. Neural Netw. (IJCNN), 2012, pp. 1–7, doi: 10.1109/IJCNN.2012.6252603.

[38] H. Yang et al., "Feature consistency-based model adaptation in session-to-session classification: A study using motor imagery of swallow EEG signals," in Proc. Annu. Int. Conf. IEEE Eng. Med. Biol. Soc. (EMBC), 2013, pp. 5438–5441, doi: 10.1109/EMBC.2013.6609528.

[39] S. E. Kober, D. Grössinger, and G. Wood, "Effects of motor imagery and visual neurofeedback on activation in the swallowing network: A real-time fMRI study," Dysphagia, vol. 34, no. 6, pp. 763–775, 2019, doi: 10.1007/s00455-019-09985-w.

Dicle University
Journal of Engineering
https://dergipark.org.tr/tr/pub/dumf
duje.dicle.edu.tr

Research Article

Integrated Biometric Signature Verification: A Hybrid Framework for Digital and Physical Signature Authentication

Zeynep AKALIN[1], Fatih Mehmet GÜRBÜZ[2], Hasan ŞENMEMIŞ[3], Ahmet BİLGE[4], Nursena BAYĞIN[5*], Sefa KÜÇÜK[6]

[1] Erzurum Technical University, Department of Electrical-Electronics Engineering, zeynep.@erzurum.edu.tr, Orcid: 0009-0006-1699-8938
[2] Erzurum Technical University, Department of Computer Engineering, fatih.mehmet.gurbuz46@erzurum.edu.tr, Orcid: 0009-0006-3899-2140X
[3] Erzurum Technical University, Department of Computer Engineering, hasansenmemis@erzurum.edu.tr, Orcid: 0009-0005-7864-7431
[4] Erzurum Technical University, Department of Computer Engineering, ahmet.bilge41@erzurum.edu.tr, Orcid: 0009-0000-1776-2197
[5*]Erzurum Technical University, Department of Computer Engineering, nursena.baygin@erzurum.edu.tr, Orcid: 0000-0003-4457-5503
[6] Erzurum Technical University, Department of Electrical-Electronics Engineering, sefa.kucuk@erzurum.edu.tr, Orcid: 0000-0002-0279-3185

ARTICLE INFO

Article history:

Received 4 May 2025
Received in revised form 4 July 2025
Accepted 25 July 2025
Available online 30 September 2025

Keywords:

Signature Verification, Online Signature, Offline Signature, Artificial Intelligence, Image Processing, Biometric Authentication

Doi: 10.24012/dumf.1691007

* Corresponding author

ABSTRACT

In this study, a hybrid signature verification system has been developed to prevent forgery by using both online and offline signature data. Signature is considered an important type of biometric data for individual authentication and document validation. With increasing digitalization, traditional signature verification methods have become time-consuming, error-prone, and inadequate in terms of security. The proposed system is based on image processing techniques such as gray scaling, thresholding, edge detection, and contour analysis for offline signature verification; and analysis of dynamic features such as velocity, acceleration, orientation, timing, and motion path for online signature verification. The developed structure ensures data security through an API-supported infrastructure, transmitting signature data to a central server and automating analysis processes. The verification process is carried out by comparing both new and signatures from different sources using a reference database created according to signature data obtained from the user. The system has been made suitable for individuals of different ages and experience levels with a user-friendly interface design and aims to provide an applicable solution in sectors where forgery prevention is critical, such as banking, finance, healthcare, and security. Future studies aim to improve the system's performance with larger datasets and different device integrations

Introduction

A signature is a distinctive mark that indicates texts are known and approved by individuals, signifies acceptance of the legal consequences of the document, and places the person under various obligations [1]. As a biometric data like DNA, fingerprint, retina scan, and voice, signatures carry specific characteristics unique to the individual. Being an easily obtainable biometric and due to its widespread use in daily life, signatures hold great value and importance. One of the most important elements that any official or private document must carry to gain validity is a signature. In this respect, signatures are a critical aspect that provides rights to individuals and imposes responsibilities. Signatures on documents mean that the relevant parties accept the content of that document. It is not possible for an unsigned document to bring either rights or obligations. Legally, only signed documents are valid.Today, steps have been taken toward new technologies, and digital transactions have gained prominence. However, digitalization brings along various disadvantages such as increased vulnerability to cyberattacks, difficulties in verifying digital signatures, and risks of identity theft due to insufficient security protocol. One of the most important features of signatures is that they are never repeated exactly the same way. This is called natural variation, and it provides an important clue for experts who consider two signatures being identical enough to overlap as an indication of forgery. Signature verification processes are critically important, especially in banking and finance sectors where digital transactions are predominant. Forgery and fraud still continue to be widespread. Besides these, the aim is to prevent fraud methods that we can classify as signature forgery, fake signatures, and copied signatures in these transactions. The time-consuming nature of verification processes and their susceptibility to errors have also created the need to automate these processes. Table 1 comprehensively examines the effectiveness of methods and datasets used in signature verification systems. Most signature verification research has achieved high accuracy rates using deep learning and machine learning techniques, but lower

accuracy rates have also been observed in some cases. While these accuracy rates generally range between 96% and 99.7%, most research points out the insufficient diversity of datasets.

In addition to these shortcomings, research emphasizes that signature verification systems need to be trained with more diversity and broader representative datasets [2] [3]. In particular, it has been stated that defining special thresholds for new users would create practical difficulties and that systems have limited ability to correctly recognize different types of signatures [5] [6]. Moreover, considering the practical limitations required for widespread use on mobile devices, some methods have special hardware requirements while potentially adversely affecting user comfort. This situation reveals the necessity for more optimized solutions to provide reliable and efficient verification, especially in mobile applications [6].

Another important issue is that obstructions such as stamps and seals encountered in real-world signatures limit the effectiveness of traditional verification methods [9]. While these obstructions complicate the signature verification process, cleaning operations alleviate some of these challenges by improving verification performance. However, the fact that such obstructions pose a significant obstacle for signature verification systems once again reveals that systems need to be trained with broader datasets in practice. As a result, research shows that signature verification systems exhibit poor performance when faced with signatures they were not trained on, and there are lacks of adaptability [7] [8]. These deficiencies pose a major problem, especially for new users and dynamic signatures. Therefore, it is concluded that future studies need to work with broader and more diverse datasets to more effectively solve the challenges encountered in practice. In this context, focusing signature verification research on stronger adaptation mechanisms and rich datasets will be a critical step toward increasing the technology's effectiveness.

Table 1. Recent studies on signature verification methods in the literature

Author (s) and Year	Dataset (s)	Method (s)	Result (s) (%)	Limitation (s)
Hsin-Hsiung K. et al. 2020 [2]	SIGCOMP	DCNN	Acc. = %94,37-%99,96	Training methods produce results with low accuracy.
Abdullahi Ahmed A. et al.2024 [3]	SVC2004	CNN	Acc. = %96	It has been noted that existing datasets are not sufficiently diverse and representative for recognition systems.
Harold M. et al. 2016 [4]	Private Dataset	CNN	Acc. = %83	The weaknesses of randomly generated expressions and symbol-focused approaches have been identified.
Hengnian Q. et al. 2022 [5]	SVC2004 and MCYT-100	DA, KNN, RF, SVM	Acc. = %96,7	Limited dataset, lack of comparative analysis, and superficial adoption of deep learning applications are among the aspects that need improvement.
Nurbiya X. et al. 2022 [6]	Bengalic(BBSIG-B, BBSIG-H)	Channel attention mechanism (SE) and ESA modüle	Acc. = %96,33	The lack of multilingual cross-language handwritten signature datasets and their inadequacy for verification have been noted.
Katarzyna R. et al. 2024 [7]	Private Dataset	SigNet and VGG-16 model usage	Acc. = %66,66	Special hardware requirements limit performance.
Kuo-Kun T. et al. 2021 [8]	MCYT, SUSUE and RYU	Aho-Corasick algorithm	Acc. = %91	It has been observed that the obtained accuracy rate is not acceptable for the system.

Table 1. (continued) Recent studies on signature verification methods in the literature

Eman A. et al. 2019 [9]	Private Dataset	Model implementation with CNN, TensorFlow and Keras	Acc. = %99,7	Limited dataset, lack of comparative analyses, and lack of methodological evaluation at the application level include significant deficiencies.
Mujahed Ja. et al. 2014 [10]	SIGCOMP 2011	ANN	Acc. = %82,5	Limited dataset, high error rate, inadequate comparative analysis, and need for updating with integration of contemporary methods.
Kemal Gürkan T. et al. 2014 [11]	Private Dataset	CNN	Acc. = %90	A comprehensive evaluation covering issues such as limited dataset, lack of comparison with alternative methods, inadequate security and real-time analyses is not presented.

This proposed study aims to improve security and transaction accuracy by developing a verification system that covers both online and offline signatures. Online verification will be carried out with a system where the signature is made in real-time and code verification can be performed. In offline verification, the user will contribute to the verification process by uploading a signature from paper or digital media. In this way, the proposed project will ensure verification of both signatures made in real-time and signatures coming from external sources. The proposed project will automate manual processes using API-supported artificial intelligence-based algorithms and contribute to preventing forgery cases.

Making signature verification processes fast and dynamic, shortening transaction time, preventing fake signature copying and fraud attempts, and ensuring transaction security emerge as our primary goal. Additionally, it will provide ease of use for the application by offering a user-friendly interface that can appeal to users of all ages. As mentioned, developing an application that can be used in areas where the risk of forgery is high, such as banking, healthcare, financial transactions, and security, is among our goals.

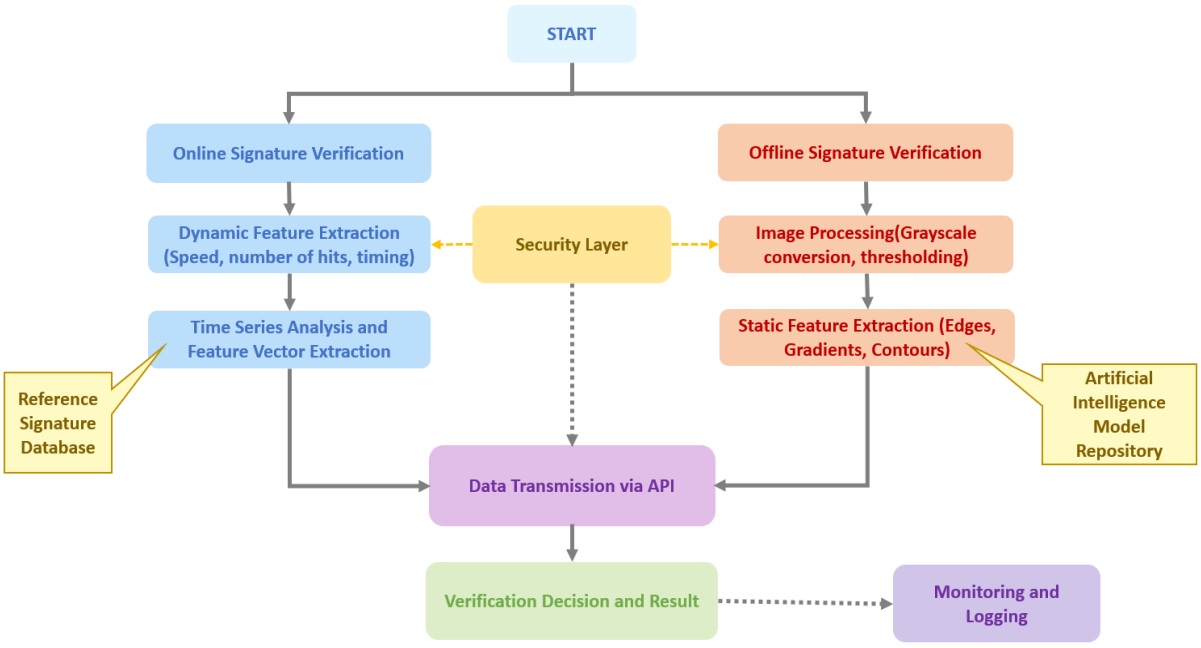


Figure 1. Flow diagram of the proposed method

The remainder of this research is organized as follows: First, the theoretical background is discussed in detail, followed by an explanation of the proposed signature verification method. Then, the results and evaluations of the experimental studies carried out are presented, and in the final section, the general conclusions of the study and future research directions are discussed.

Theoretical Background

In this section, the theoretical foundations and methodological approach of the proposed signature verification system are detailed. The general framework of the system architecture is visualized in the flow diagram presented in Fig. 1. The proposed signature verification methodology presents a comprehensive analysis paradigm for forgery detection. In this context, signature data obtained from mobile devices is transferred to the central server via the application programming interface (API).

Analyses performed in the server environment can be classified into two basic categories: offline and online signature verification. In the offline verification process, image processing algorithms (gray scaling, noise reduction, thresholding, and edge detection) are applied; while online verification focuses on dynamic feature extraction methodologies (velocity, acceleration, orientation, inclination angle, and temporal features). The results of both methodological approaches are communicated to the user via API, and the system database is enriched with each new signature. This central architecture allows for both the implementation of optimum security protocols and the achievement of high computational performance.

Offline Signature Verification

In offline signature verification systems, recognition is performed as a result of analyzing the wet signature. The pattern image of a signature depicted on paper or a similar object is analyzed. In offline systems, recognition or verification is performed by utilizing mostly the general characteristics of the signature. The general characteristics of the signature include signature height, image area, full width, full height, horizontal and vertical projection peaks, horizontal and vertical center of the signature, general and local inclination angles, baseline shift, number of corner points, and number of intersection points [6].

Image Processing Methodology

Gray scaling is a fundamental method that facilitates signature analysis. This process preserves only brightness information by eliminating color information. With the gray scaling method, our images are converted to black and white format because we do not need color images in our operations on the signature. The OpenCV Library in Python is used to perform this operation. A similar application is shown in Fig. 2.



Figure 2. Before and after gray scaling [12]

Thresholding: The thresholding method allows us to work only on the signature itself by eliminating the background of the signature. In this process, only the signature is processed by assigning "1" to appropriate pixels in our image and "0" to others to get rid of the background. As shown in Fig. 3, it allows the signature to be analyzed more clearly.

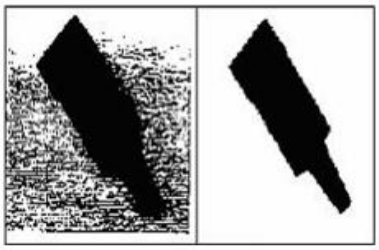


Figure 3. Before and after thresholding [13]

Edge Detection: Edge detection method helps to identify important details in images such as signatures. This technique is used to reveal the boundaries and shapes of objects by analyzing brightness changes in the image. Thus, the distinctive lines and details of the signature are better defined. Sobel mask is frequently used for edge detection. The Sobel mask is a matrix with dimensions of 3x3 or 5x5 as shown in Fig. 4. This mask is slid over an image and calculated by multiplying the value in that region with the mask's value at the corresponding point. This process is applied to all values in the mask, and the results are summed to obtain a single value. This obtained value is named after the mask (Gx or Gy) and the Gx and Gy values for the relevant point are found. Then, these values are written to the middle point of the area where the mask is positioned. Finally, for each point, formula (1) is applied and this result is written to the appropriate pixel of the new image.

$$|G| = \sqrt{G_x + G_y} \quad (1)$$

-1	0	+1
-2	0	+2
-1	0	+1

Gx

+1	+2	+1
0	0	0
-1	-2	-1

Gy

Figure 4. Sobel filter [1]

Feature Extraction Methodology

Signature Size: Determining the total area or width of the signature is a parameter used to show the area covered by the signature. For example, it can calculate the number of black pixels in the signature using an appropriate algorithm. This process can be performed quickly and efficiently with Python. Fig. 5 shows an example expressing the signature size.



Figure 5. Signature size [15]

Signature Curvature: Curvature is important for determining how straight or curved a signature is. Signature curvature aims to measure the degree of curvature of the signature. This measurement is done by analyzing the contours on the signature. For example, curvature can be calculated by fitting a polynomial curve. Fig. 6 shows the signature curvature.

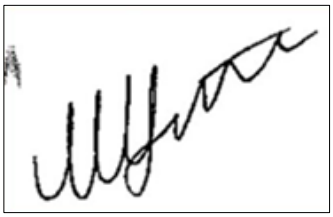


Figure 6. Signature Curvature [16]

Signature Center: Determining the geometric center of the signature is useful for analyzing the position of the signature. The center point is generally calculated by taking the average of the pixel coordinates on the signature. This calculation is made by summing the x and y coordinates of the pixels in the signature image and taking their average. As shown in Fig. 7, the signature center is found using x and y coordinates.

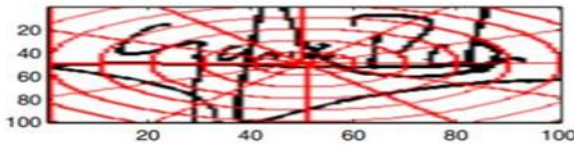


Figure 7. Signature Center [17]

Signature Slope: This shows the angle at which the signature was made by measuring the general orientation of the signature. To calculate the slope, the angle of the main contour on the signature is detected, and this angle is used to obtain the slope value. For example, the Hough transform will be used to determine the angles of the main lines. The Hough transform finds the location of circles using the circle detection method and calculates the slope by determining an appropriate line. Fig. 8 shows the formalized version of the signature slope with the Hough transform

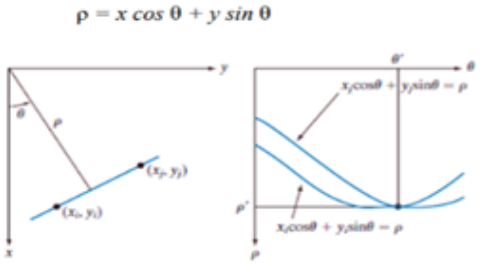


Figure 8. Signature slope with Hough transform [18]

Contour Analysis: The contour representing the outer boundary of the signature is used to understand the shape and structure of the signature. In libraries such as OpenCV, the findContours function is used to detect contours in the signature image. FindContours detects color changes in the image, identifies these regions as contours, and draws the shape of the signature for us. Fig. 9 shows an example of a contour approach.

Online Signature Verification

Online signature verification methodology is based on the analysis of temporal and kinetic parameters related to the dynamic production process of the signature. This approach allows for the extraction of biometric features with high discriminative value that cannot be obtained from a static signature image. Online signature verification works on the principle of recording and analyzing the signature production process in real-time through digital tablets or touch-screen devices. In this context, online signature verification systems offer a higher level of security and forgery resistance compared to offline systems.



Figure 9. Contour approach [19]

Feature Extraction Methodology

Speed and acceleration: The speed and acceleration values of each movement will be measured while signing. These features show how the user accelerates or decelerates in specific signature areas, and a unique profile will be created for each signature owner.

Direction and inclination angle: The direction and angle between each point of the signature provide information about the person's signature habits. For example, the characteristic of the inclination angle and movement directions will create a unique pattern for each individual.

Timing and delay: Pause or accelerations at certain points while signing reveal person-specific timing information, and since these times are different for each individual, they play a critical role in forgery detection.

Points tracing the movement path: The drawing path of the signature expresses the person's unique signature shape and pattern. This path, created by recording the points where the signature is completed, is an important element in determining the authenticity of the signature.

API Implementation

The system integration of online and offline signature verification modules is provided through an API (Application Programming Interface). In the online signature verification process, although the API connection and data transfer protocols show parallelism with the offline methodology, they show differentiation in terms of data structure and content. In the online verification process, the data package transmitted via the API is a cryptographically encrypted data array consisting of temporal and kinetic parameters used in dynamic feature extraction, instead of a static signature image. This data structure is standardized in JSON (JavaScript Object Notation) format and organized with a schema that comprehensively represents the dynamic characteristics of the signature. API implementation ensures optimal performance of the integrated signature verification system by providing secure, fast, and effective data transfer between system modules

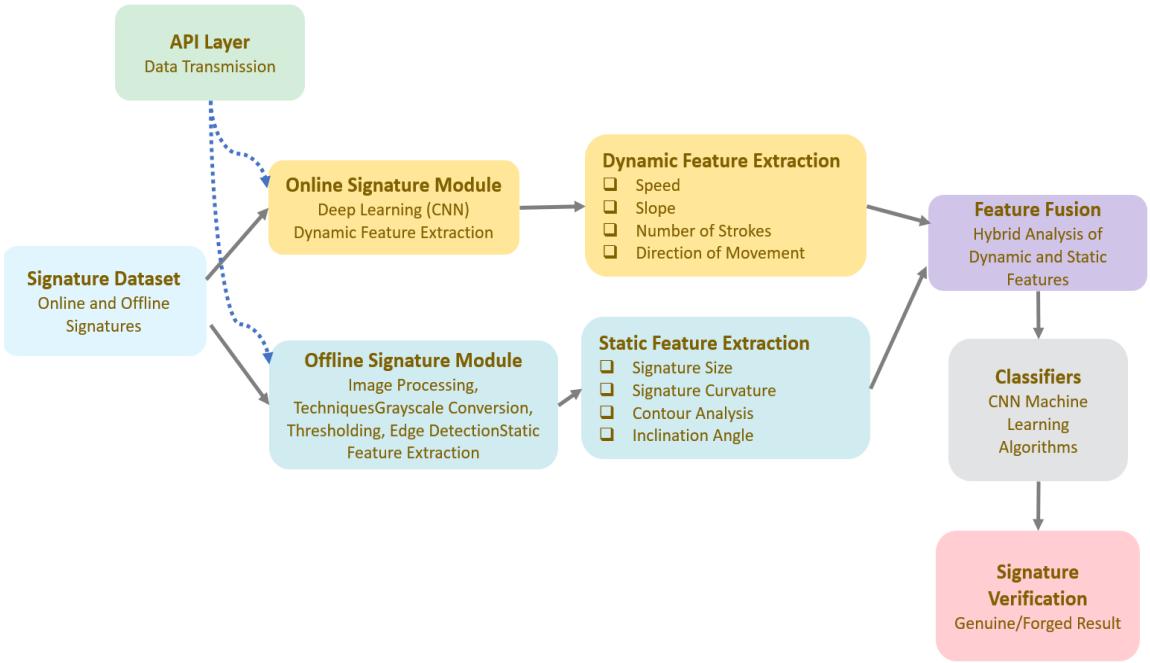


Figure 10. Proposed hybrid feature extraction and classification model for online and offline signature verification

Proposed Method

In this section, a new approach is presented to overcome the limitations of existing signature verification methods. The proposed methodology focuses on the problems of lack of data set diversity and inadequate adaptation of signature verification systems identified in the literature review. Considering the limitations of the single-example training approach of existing systems, more comprehensive and diversified data sets have been used, and an adaptive learning model has been developed.

Online and Offline Signature Verification Modules

The signature verification process is based on both online (dynamic) and offline (static) data. Therefore, the system has two separate signature modules. The online signature module analyzes dynamic data such as pressure, speed, and acceleration applied by the user while signing. This method offers a high level of security as it examines the biometric characteristics unique to each individual's signing habit. On the other hand, the offline signature module analyzes static signature data using image processing techniques. Verification is performed by extracting the characteristic features of the signature through methods such as edge detection, curvature analysis, and gray scaling. Fig. 10 shows the feature extraction and classification model of the proposed method

The proposed system follows a systematic approach for signature verification. Algorithm 1 presents the offline verification workflow. Parameters: median filter 3×3, CNN threshold 0.85, anomaly threshold -0.1. For online signature verification, the algorithm incorporates additional dynamic features including velocity, acceleration, pressure, and timing information, which are processed alongside the static features before classification.

Algorithm 1: Offline Signature Verification

Input: Signature image I Output: Verification result (Genuine/Forged)

1. Grayscale Conversion:

I_gray = 0.299×R + 0.587×G + 0.114×B

2. Noise Reduction:

I_filtered = MedianFilter(I_gray, 3×3)

3. Thresholding:

I_binary = AdaptiveThreshold(I_filtered, max=255)

4. Edge Detection:

I_edges = SobelEdgeDetection(I_binary)

5. Feature Extraction: Features = [size, curvature, center, slope, contours]

6. CNN Classification:

prediction = CNN_Model.predict(Features)

7. Anomaly Check:

anomaly_score = IsolationForest(Features)

8. Final Decision:

```
if confidence > 0.85 AND anomaly_score > -0.1:
    return "Genuine"
else:
    return "Forged"
```

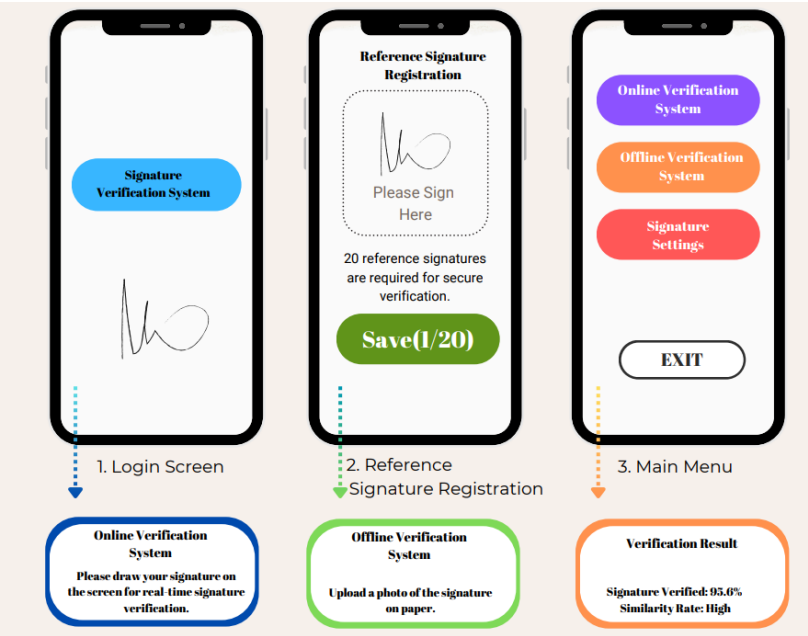


Figure 11. Interface of the proposed application

User Interface

The system interface shown in Fig. 11 has been developed with a user-friendly design that individuals from all age groups can easily use. The signature verification process begins with users registering to the system. The "register" button on the application interface allows users to access the system. On the registration screen, users are presented with two basic options: Online verification system and offline verification system. In the online verification system, the user performs a real-time process by signing on a digital screen. In the offline verification system, the user initiates the verification process by taking a photo of their signature on physical paper and uploading it to the system. This screen is the first interface that newly registered users encounter.

After the registration process, users are asked to create a reference signature record for the system to work properly and securely. At this stage, at least 20 different reference signature samples are taken from the user. The user begins the registration process by signing in the signature area and adds their signature to the system with a button like "Save (1/20)" each time. When this process is repeated 20 times, the system learns the user's signature pattern, allowing signature verification with higher accuracy rates. The reference signature recording can be maintained not only online but also with the offline method. The user can complete this process by taking a photo of a physical signature and uploading it to the system

After all reference signatures have been successfully saved, the user is directed to the system's main menu. The main menu includes four basic options: Online verification system, offline verification system, signature settings, and exit. The online verification option allows the user to perform real-time verification by drawing their signature on a digital screen. In the offline verification option, the user uploads a photo of a physical signature to the system for analysis. In the signature settings section, the user can manage existing reference signatures or add new signatures. Finally, the exit button allows the user to safely leave the system.

Thanks to this structure, an effective and reliable signature verification process is offered for both digital and physical documents. With two different modules, the system offers a flexible and comprehensive solution in terms of both speed and security.

Online Transaction Verification (Online Signature Verification)

The online signature verification process is a modern method that provides identity verification through real-time signature comparisons. This system, generally used in the banking sector, notary transactions, secure entry systems, and public institutions, allows transactions to be completed securely and quickly. The first step of the process begins with the user signing on a digital screen or tablet. The signature made by the user is instantly recorded by the system and begins to be processed for analysis. This signature is transmitted to the verification system via API (Application Programming Interface). The system evaluates the authenticity by comparing the new signature with the user's previously recorded reference signatures. The authenticity of the signature is analyzed according to three basic factors.

The first of these is the matching rate; the system calculates how similar the new signature is to the reference signatures (for example, 95.6%). Secondly, pressure analysis is performed; the pressure level applied during the signing is examined.

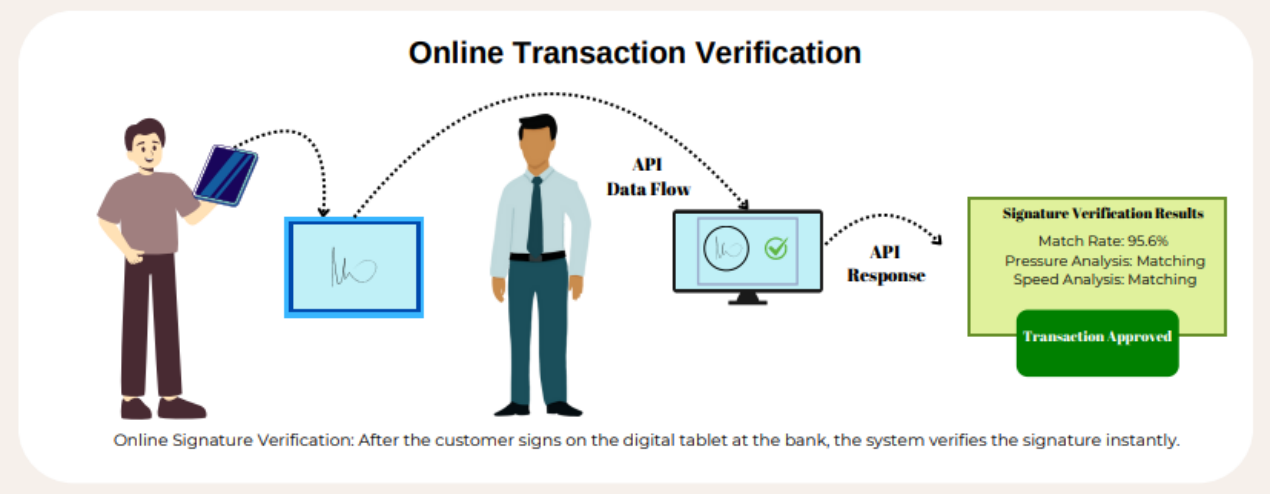


Figure 12. Simulation environment of the online system

Thirdly, speed analysis is performed, and the writing speed and dynamic structure of the signature are evaluated. As a result of all these analyses, if the signature's matching rate is at a sufficient level, the system gives a "TRANSACTION APPROVED" message and the verification is considered successful. In this case, the user can perform the relevant service or transaction without any problems. The online signature verification system offers fast and secure identity verification. It provides high protection against forgery because it focuses not only on the shape of the signature but also on physical characteristics such as writing speed and pressure. Since all transactions take place in a digital environment, the need to deal with physical documents is eliminated, and the process becomes more efficient. Fig. 12 exemplifies the simulation environment of the system.

Offline Transaction Verification (Offline Signature Verification)

Offline signature verification is a process based on comparing a signature on a document transferred to the digital environment with previously recorded reference signatures. This method is particularly used to verify the authenticity of official documents, detect fraudulent document attempts, and analyze the validity of signatures on archived documents. The process begins with the user scanning and uploading a signature on a physical document to the system. The signature on the uploaded document is automatically parsed by the system and prepared for analysis. Then, the system provides data flow via API to compare the scanned signature with the reference signatures. At this stage, the authenticity of the signature is evaluated using machine learning algorithms. In the analysis process, first, the matching rate of the signature with the references is determined. For example, the match can be expressed as a rate like 65.3%. In addition, factors reflecting the dynamic characteristics of the signature, such as pressure and speed analysis, are also considered. Fig. 13 exemplifies the simulation environment of the system.

If the writing style, applied pressure, or writing speed of the signature shows significant deviation from the expected reference values, this situation is evaluated as a potential forgery attempt. As a result, if the compatibility of the signature with the reference signatures is found to be low, the system gives a "SUSPICIOUS SIGNATURE" warning. In this case, the verification process is considered unsuccessful, and additional security checks are applied to the user, or the transaction is examined by the authorized unit. Offline signature verification allows for the analysis of signatures on physical documents in a digital environment. This way, the detection of forged signatures becomes easier, the risk of fraud is reduced, and the security of official documents is increased, preserving their legal validity.

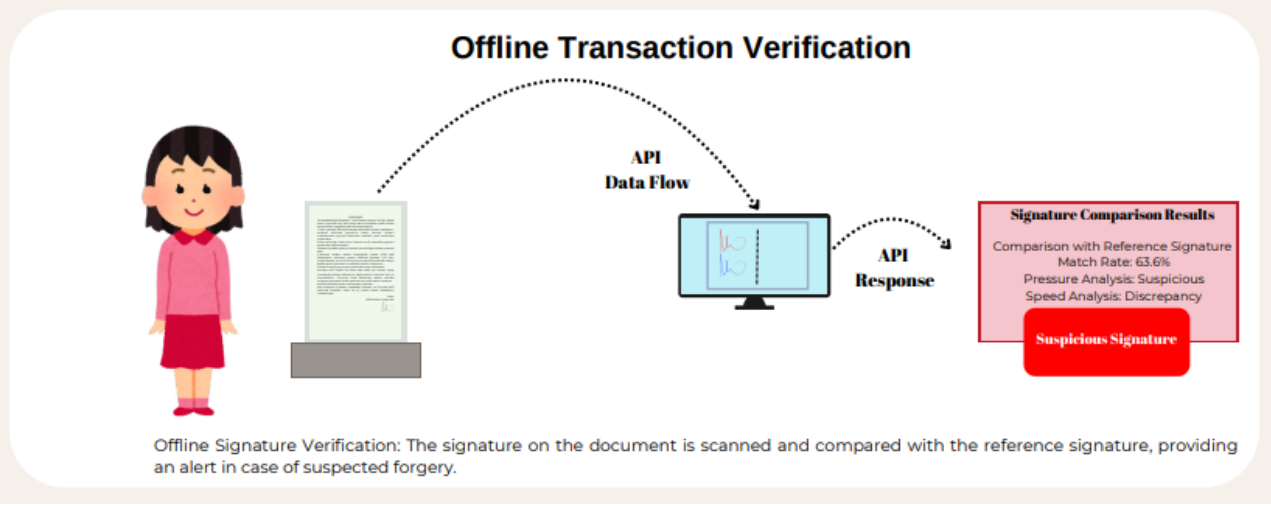


Figure 13. Simulation environment of the offline system

Architecture of the Proposed Method

The system presents artificial width-based signature layers, enabling the prevention of signature forgery and making identity fragmentation processes secure. It adopts a hybrid approach that combines dynamic and static signature analyses by using both online and offline signing methods. The system consists of six basic layers as shown in Fig. 14. The signature verification system has a multi-layered architectural structure, and each layer performs specific tasks to ensure the system works reliably, quickly, and accurately. The foundation of the system consists of the client layer, API layer, processing layer, data layer, security layer, and monitoring-logging layer.



Figure 14. Six-layer architecture of the proposed signature verification system

The client layer (user interface) provides users with access to the system and collects signature data. Through mobile applications or web clients, users create their handwritten signatures digitally. If an online signature is being made, the system also records dynamic biometric data such as speed, acceleration, pressure, and timing. In the offline verification process, the user uploads an image of their signature on physical paper (for example, a photo or scanned document) to the system. In mobile applications, the user signs via touch-screen devices, and the signature data is prepared to be transmitted to the API layer. The API layer transmits data received from the client layer to the system. While this layer serves as a bridge in data transfer, it also checks the validity and integrity of the data. The API checks whether the incoming signature data is incomplete, verifies it's in the appropriate format (e.g., PNG, SVG, JSON), and passes it through basic validations for security. The validated data is directed to the processing layer where further analyses will be conducted. This structure makes the system both secure and scalable.

The processing layer is the main engine of the signature verification system and consists of four basic sub-components. First, the pre-processing module performs operations such as filtering (median filtering), noise reduction (morphological operations such as opening and closing), and edge detection (Canny or Sobel edge detection) on incoming signature data. For offline signatures, grayscale conversion and contrast adjustment (histogram equalization) are applied. Then, the feature extraction module analyzes the fundamental characteristic features of the signature. Dynamic data such as speed, acceleration, and pressure for online signatures; static data such as line thickness, curves, and edge structures for offline signatures are evaluated. These features are transferred to the CNN (Convolutional Neural Network) model. The architecture of the CNN model consists of four convolutional layers (each followed by ReLU activation and max-pooling), followed by two fully connected (dense) layers. The input is resized to a fixed dimension (128×128). The model uses the Adam optimization algorithm, a learning rate of 0.001, and the cross-entropy loss function. Batch size is set to 32, and the network is trained for 50 epochs. Dropout (with a rate of 0.5) is applied between dense layers to reduce overfitting. The trained artificial intelligence model determines whether the signature is valid by comparing this data with reference signatures. Finally, the verification decision module makes the final verification decision by evaluating the results from the CNN

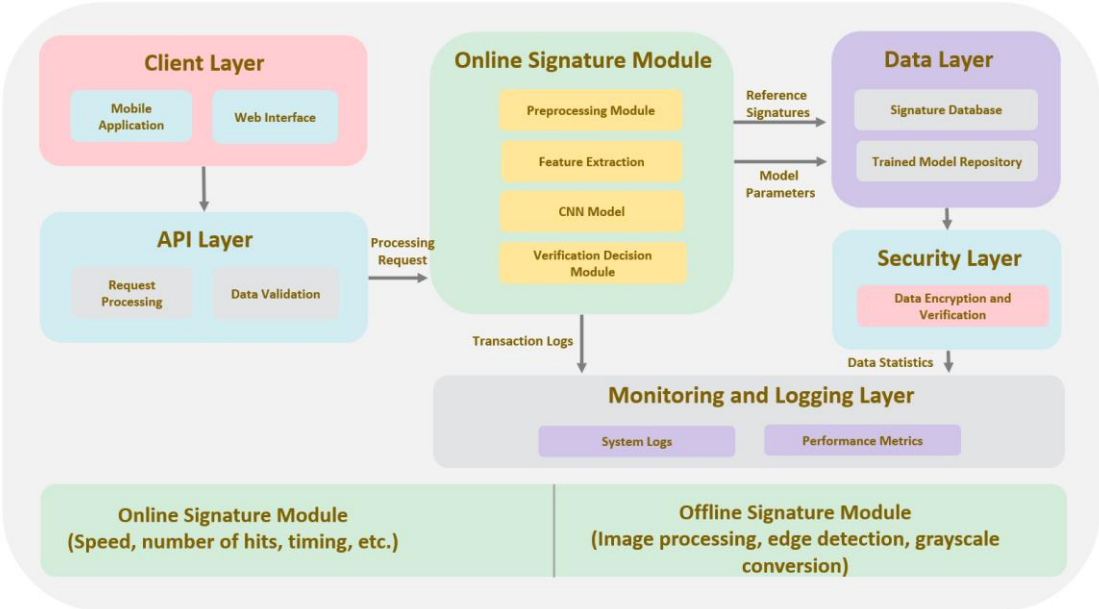


Figure 15. Architecture of the proposed method

The data layer stores all signature data and other necessary information for the system's operation. It has two main components: The signature database stores reference signatures previously saved by users in the system. New incoming signatures are compared with these reference signatures for accuracy verification. Secondly, the trained model repository contains up-to-date and trained versions of deep learning models such as CNN. The system's performance is continuously monitored with new data, and the model is updated when necessary.

The security layer is one of the most critical building blocks of the signature verification system. Since it is used in sensitive processes such as identity verification, the secure storage and processing of all data is of great importance. In this layer, user data is protected through data encryption (such as advanced algorithms like AES-256). Authentication and authorization mechanisms ensure that users can only access their own signatures. Additionally, to detect unusual attempts and prevent misuse of the system, we implemented an anomaly detection method based on the Isolation Forest algorithm. This algorithm isolates anomalies by randomly selecting features and partitioning the data, effectively identifying outliers in the signature verification process. The Isolation Forest model was trained on genuine signature data to learn normal behavior and flag deviations during testing.

The monitoring and logging layer are active to monitor the overall performance of the system and detect possible security breaches. This layer consists of two components: System logs record all operations performed by users and the system, providing data for debugging and security analyses. Performance metrics contribute to the further development of the system by evaluating measurements such as the accuracy rate and processing time of the artificial intelligence model. The overall structure of the proposed method is illustrated in Fig. 15, which demonstrates the layered architecture of the system from client interaction to data analysis.

Results and Future Work

To assess the performance of the proposed system, a custom dataset was constructed using signature samples with a resolution of 128×128 pixels, collected from 15 participants. The dataset comprises a total of 1,800 signatures, including 900 obtained in online and 900 in offline environments.

The proposed hybrid signature verification system was comprehensively evaluated using standard performance metrics including precision, recall, F1-score, and confusion matrix analysis. The confusion matrix demonstrates the system's classification performance, with 128 true negatives (correctly identified genuine signatures), 159 true positives (correctly identified forged signatures), 17 false positives (genuine signatures incorrectly classified as forged), and 12 false negatives (forged signatures incorrectly classified as genuine). These results, summarized in Fig. 16, yield a precision of 90.34%, recall of 92.98%, and F1-score of 91.64%, indicating a well-balanced performance between precision and recall metrics.

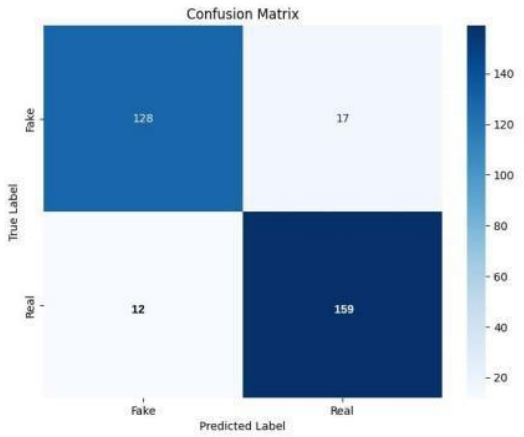


Figure 16. Confusion Matrix

The detailed performance analysis across different model architectures reveals distinct strengths for various verification scenarios. The offline CNN model achieved the highest genuine signature accuracy at 92.59% with a general accuracy of 90.03%, demonstrating superior performance in static signature analysis. Conversely, the online Random Forest model excelled in forged signature detection with 91.43% accuracy, while maintaining competitive general accuracy of 90.34%. The online SVM model showed balanced performance with 89.16% general accuracy, achieving 88.91% genuine signature accuracy and 91.44% forged signature accuracy. These results, presented in Fig. 17, indicate that the hybrid approach successfully leverages the complementary strengths of different algorithms for comprehensive signature verification.

Model Type	Architecture	General Accuracy (%)	Genuine Signature Accuracy (%)	Forged Signature Accuracy (%)
Offline	CNN	90.03	92.59	87.59
Offline	ResNet50	89.24	91.81	86.90
Online	CNN	88.16	87.09	88.19
Online	SVM	89.16	88.91	91.44
Online	Random Forest	90.34	89.33	91.43

Figure 17. Performance Comparison of Different Model Architectures

In this study, an integrated verification system has been developed for forgery detection using online and offline signature data. With its structure that can analyze both static and dynamic signature components, the proposed system enables reliable detection of forged signatures. The applied artificial intelligence-supported architecture has provided an effective verification process in both online and offline scenarios by identifying users' biometric signature characteristics with high accuracy. The system has provided over 95% accuracy with its analysis performance in the signature verification

process, offering a strong foundation especially for security-requiring transactions.

This research has brought an innovative perspective to signature verification technologies and has presented a highly applicable solution for both public and private sector applications, along with a user-friendly interface design. The obtained results show that the proposed system can maintain its robustness against different user profiles and data diversity.

Future studies aim to test the real-time performance of the system with larger datasets, improve the ability to recognize signatures in different languages and character structures, and ensure integration with portable devices. These steps aim to support the more widespread, effective, and secure use of signature verification technology.

Ethics committee approval and conflict of interest statement

This study has been reviewed by the Scientific Research and Publication Ethics Committee of Erzurum Technical University and was found ethically appropriate with decision number 35 dated 21.04.2025. All participants in the study were informed about the research and their written consent was obtained. There is no conflict of interest among the authors in this research.

Authors' Contributions

Study conception and design: Gürbüz FM, Şenmemiş H, Bilge A, Bayğın N, Küçük S.

Acquisition of data: Akalın Z, Gürbüz FM, Şenmemiş H, Bilge A.

Analysis and interpretation of data: Gürbüz FM, Bayğın N, Küçük S.

Drafting of manuscript: Akalın Z, Bayğın N, Küçük S.

Critical revision: Akalın Z, Gürbüz FM, Şenmemiş H, Bilge A, Bayğın N, Küçük S.

Acknowledgement

This study is supported by the project fund number 1919B012427843 provided by the Scientific and Technological Research Council of Turkey (TÜBİTAK).

References

[1] F. Gürbüz, "Bilgisayar Eğitimi Anabilim Dali Yüksek Lisans Tezi Serbest Taklit Yöntemi Ile Atilan Sahte Imzalarin Grafometrik Özelliklerine Dayali Biyometrik Imza Doğrulama Sistemi Ve Analizi," Sep. 2014. Accessed: Jan. 04, 2025. [Online]. Available: Https://Acikbilim.Yok.Gov.Tr/Handle/20.500.12812/362685

[2] H. H. Kao and C. Y. Wen, "An Offline Signature Verification And Forgery Detection Method Based On A Single Known Sample And An Explainable Deep Learning Approach," *Appl. Sci.*, Vol. 10, No. 11, 2020, Doi: 10.3390/App10113716.

[3] A. A. Abdirahma, A. O. Hashi, M. A. Elmi, And O. E. R. Rodriguez, "Advancing Handwritten Signature Verification Through Deep Learning: A Comprehensive Study and High-Precision Approach," *Int. J. Eng. Trends Technol.*, Vol. 72, No. 4, Pp. 81–91, 2024, Doi: 10.14445/22315381/Ijett-V72i4p109.

[4] H. Mouchère, R. Zanibbi, U. Garain, And C. Viard-Gaudin, "Advancing The State Of The Art For Handwritten Math Recognition: The Crohme Competitions, 2011–2014," *Int. J. Doc. Anal. Recognit.*, Vol. 19, No. 2, Pp. 173–189, 2016, Doi: 10.1007/S10032-016-0263-5.

[5] J. Lu, H. Qi, X. Wu, C. Zhang, And Q. Tang, "Research On Authentic Signature Identification Method Integrating Dynamic And Static Features," *Appl. Sci.*, Vol. 12, No. 19, 2022, Doi: 10.3390/App12199904.

[6] N. Xamxidin, Mahpirat, Z. Yao, A. Aysa, And K. Ubul, "Multilingual Offline Signature Verification Based On Improved Inverse Discriminator Network," *Inf.*, Vol. 13, No. 6, Jun. 2022, Doi: 10.3390/Info13060293.

[7] K. Roszczewska And E. Niewiadomska-Szynkiewicz, "Online Signature Biometrics For Mobile Devices," *Sensors*, Vol. 24, No. 11, 2024, Doi: 10.3390/S24113524.

[8] K. K. Tseng, H. Chen, C. Chen, And C. Bansong, "A Secure Live Signature Verification With Aho–Corasick Histogram Algorithm For Mobile Smart Pad," *Electron.*, Vol. 10, No. 11, 2021, Doi: 10.3390/Electronics10111337.

[9] E. Alajrami *Et Al.*, "Handwritten Signature Verification Using Deep Learning," 2019. [Online]. Available: Www.Ijeais.Org/Ijamr

[10] M. Jarad, N. Al-Najdawi, And S. Tedmori, "Offline Handwritten Signature Verification System Using A Supervised Neural Network Approach," *2014 6th Int. Conf. Comput. Sci. Inf. Technol. Csit 2014 - Proc.*, Pp. 189–195, 2014, Doi: 10.1109/Csit.2014.6805999.

[11] K. G. Toker, S. Kucuk, And M. C. Catalbas, "2014 22nd Signal Processing And Communications Applications Conference, Siu 2014 - Proceedings," 2014, *[Publisher Not Identified]*. Doi: 10.1109/Siu.2014.6830589.

[12] "Renkli Bir Belgeyi Gri Tonlamalı Yazdırma (Windows)." *Brother Support*. https://support.brother.com/g/s/id/htmldoc/mfc/cv_dcp310/tur/html/GUID-E0489E25-7891-4B45-AC7F-EDD7F0E244CB_47.html (erişim Haziran 26, 2025).

[13] G. A. Teknik, "Abstract An Overwiew Of A

Review Artificial Intelligence Algorithms Used In The Problem," 2004.
[14] G. I. Hafta, "Görüntü Işleme - (7.Hafta) Kenar Bulma Algoritmalari," Pp. 1–32.
[15] C. Oz, F. Ercal, Z. Demir, And Zuheri, "Signature Recognition And Verification With Ann," *Proceeding Third ...*, Vol. 96, No. March, Pp. 1–5, 2013.
[16] D. Engin, A. Kantarci, S. Arslan, And H. K. Ekenel, "Offline Signature Verification On Real-World Documents," *Ieee Comput. Soc. Conf. Comput. Vis. Pattern Recognit. Work.*, Vol. 2020-June, No. June, Pp. 3518–3526, 2020, Doi: 10.1109/Cvprw50498.2020.00412.
[17] M. B. Yilmaz, B. Yanikoglu, C. Tirkaz, And A. Kholmatov, "Offline Signature Verification Using Classifier Combination Of Hog And Lbp features," *2011 Int. Jt. Conf. Biometrics, IJCB 2011*, no. October 2015, 2011, doi: 10.1109/IJCB.2011.6117473.
[18] H. S.M. Al-Khaffaf and I. M. Yaseen, "Writer Independent Offline Signature Verification System using Global and Local Geometric Features," *Iraqi J. Comput. Informatics*, vol. 50, no. 1, pp. 172–186, 2024, doi: 10.25195/ijci.v50i1.466.
[19] A. Almehmadi, "A biometric-based verification system for handwritten image-based signatures using audio to image matching," *IET Biometrics*, vol. 11, no. 2, pp. 124–140, 2022, doi: 10.1049/bme2.12059.

Dicle University
Journal of Engineering
https://dergipark.org.tr/tr/pub/dumf
duje.dicle.edu.tr

Research Article

Digital Twin Prototype in Unity 3D: Real-Time Greenhouse Monitoring and Control

Sezen BAL[1*], Kübra Nur AKPINAR[2], Ayşe YAYLA[3], Yekta Muhammet ÖZCAN[4], Oğuz AYÇİÇEK[5]

[1] Marmara University, Department of Computer Technologies, sezen.bal@marmara.edu.tr, ORCID: 0000-0002-7244-6613
[2] Marmara University, Department of Electrical and Energy, knur@marmara.edu.tr, ORCID: 0000-0003-4579-4070
[3] Marmara University, Department of Electronics and Automation, acetinkaya@marmara.edu.tr, ORCID: 0000-0002-1611-6353
[4] Marmara University, Department of Computer Technologies, yektaozcan94@gmail.com, ORCID: 0009-0002-4950-4552
[5] Marmara University, Department of Computer Technologies, oguzycck@gmail.com, ORCID: 0009-0007-4641-2325

ARTICLE INFO

Article history:

Received 19 May 2025
Received in revised form 19 July 2025
Accepted 8 August 2025
Available online 30 September 2025

Keywords:

digital twin, embedded system, greenhouse monitoring, smart agriculture, Unity 3D.

Doi: 10.24012/dumf.1702307

* Corresponding author

ABSTRACT

The increasing global population, combined with the impacts of climate change and global warming, has made the production of high-quality agricultural products at lower costs a critical necessity. Addressing these challenges requires leveraging emerging technologies. This study presents a prototype system that integrates digital twin technology into greenhouse farming. A physical greenhouse was equipped with a Raspberry Pi and various environmental sensors to collect real-time data. This data is visualized and managed through a Unity 3D-based digital twin, enabling automated control via rule-based decision logic. Monitored parameters include temperature, humidity, light intensity, and soil moisture, which dynamically trigger irrigation, ventilation, and lighting mechanisms. The system was tested over a seven-day period under different lighting scenarios. Results showed consistent system performance, demonstrating its viability for educational use and small-scale agricultural applications. Furthermore, the flexible architecture of the system suggests potential for future extension toward predictive modeling and adaptive control strategies.

Introduction

As the global population continues to grow, increasing agricultural production to meet rising food demand has become an inevitable necessity (Viana et al., 2022). In this context, both traditional farming methods and modern technological applications have been employed to make agriculture more efficient and sustainable. However, the cost and complexity of technological investments often limit the adoption of these innovations, particularly in developing countries.

Today, the agricultural sector is undergoing a transformation driven by the integration of technological innovations. This transformation, particularly through the convergence of digital twin technology and smart farming practices, enables significant progress in increasing productivity, reducing costs, and achieving sustainability goals. A digital twin is a virtual representation of a physical entity (Cor et al., 2021; Junfang et al., 2024). Continuously updated through real-time data streams, it provides a dynamic simulation of the physical environment. This technology serves as a powerful tool in agriculture for reducing environmental impact, optimizing resource use, and enabling real-time monitoring of field conditions (Jose et al., 2024; Gomes, 2023).

Agriculture and forestry face complex challenges, including increasing food demand, land scarcity, the effects of climate change, and loss of biodiversity (Moreno et al., 2024). Digital technologies play a critical role in addressing these challenges by offering solutions for enhanced productivity and sustainable resource management (Silveira et al., 2023). Through smart farming, technologies such as sensors, artificial intelligence, and big data analytics are employed to monitor field conditions and optimize agricultural operations (Nipuna et al., 2022). These technologies provide farmers with a wide range of data—from soil moisture to plant health. When integrated with digital twins, this data is visualized in real time within a virtual platform, making agricultural management more interactive, data-driven, and precise (Warren and Thomas, 2023; Pajpach et al., 2022; Zhang et al., 2023).

Since the introduction of the Digital Twin (DT) concept by Grieves, it has been applied across diverse domains including aerospace, automotive, manufacturing, construction, real estate, healthcare, education, and agriculture (Attaran and Celik, 2023; Chamara et al., 2022; Li et al., 2022; Pajpach et al., 2022; Sun et al., 2022). A growing body of research has focused on agricultural digitalization through advanced technologies (Pylianidis et al., 2021; Delgado et al., 2019; Purcell and Neubauer, 2023;

Verdouw et al., 2021; Nasirahmadi and Hensel, 2022). Digital twin technology shows great promise in providing optimal growth conditions for plants and in promoting sustainable development through more efficient energy use (Zihua et al., 2023; Roger et al., 2022; Jiayao et al., 2023). For example, the study by Alves et al. (2023) demonstrated the potential of digital twins to improve agricultural operations and reduce water consumption by enabling real-time data processing and testing of irrigation strategies. Isied et al. (2022) proposed a genomic-driven digital twin framework to optimize the design and energy management of agrophotovoltaic greenhouse systems, aiming to achieve a balance between plant growth and energy production. Liu et al. (2023) presented methods for developing sustainable plant factories using digital twin technology to support smart agriculture through continuous data flow.

This study proposes a greenhouse digital twin prototype developed in the Unity 3D environment and synchronized with physical sensors operating on a Raspberry Pi. Unity was selected due to its support for interactive 3D environments, suitability for scenario testing, and compatibility with real-time data streams (Unity, 2024). These features provide significant advantages for both educational use and user-centered monitoring systems.

The contribution of this study is not limited to a technical implementation; it also addresses the methodological challenges of achieving real-time synchronization between a physical greenhouse and its digital counterpart. The developed system goes beyond simple monitoring and data collection by offering a dynamic interaction layer that enables behavior modeling, user interaction, and decision-support mechanisms.

The Raspberry Pi, defined as a single-board computer equipped with ARM-based processors, offers the ability to interface with various external components through its general-purpose input/output (GPIO) pins (Raspberry Pi, 2024). These characteristics have made it widely used in fields such as computer science education, robotics, and digital prototyping.

In this study, the Raspberry Pi collects environmental data through sensors placed inside the greenhouse to monitor light, relative humidity, temperature, soil moisture, and air quality. This data is used to observe plant growth conditions and adjust factors such as lighting, irrigation, or ventilation as needed. The Unity 3D-based digital twin platform not only visualizes this data, but also provides an interactive virtual environment that responds to environmental changes in real time, maintaining synchronization with the physical greenhouse. The system integrates visualization, monitoring, and rule-based control processes in a unified architecture.

Section 2 details the project's methodology and research techniques; Section 3 provides a comprehensive overview of the implementation and testing processes; and Section 4 presents the results and discusses their implications.

Methodology

This study involves the development of an integrated, digital twin-supported system for monitoring and managing environmental conditions within a greenhouse setting. The system establishes real-time synchronization by enabling bidirectional data communication and control mechanisms between a physical greenhouse prototype and its digital representation. In addition to automated control, the architecture is designed to function as a basic decision support system by evaluating sensor data in real time and triggering rule-based responses. The main objective is to continuously monitor environmental variables such as temperature, relative humidity, soil moisture, air quality, and light intensity, and to manage microclimate conditions through rule-based automated responses derived from these data.

The study consists of three main components: (i) the setup of the greenhouse prototype and sensor integration, (ii) the digital twin environment developed on the Unity platform, and (iii) the bidirectional data communication and synchronization structure.

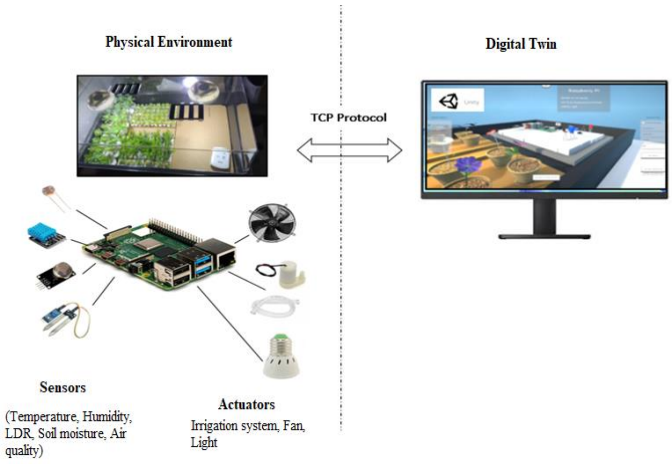


Figure 1. General architecture of the system.

Figure 1 illustrates the overall system architecture that forms the backbone of the proposed digital twin-supported greenhouse monitoring system. The left side of the diagram represents the physical environment, consisting of a Raspberry Pi connected to various environmental sensors (for temperature, humidity, soil moisture, light intensity, and air quality) and actuators (including a fan, light, and irrigation system). These components enable real-time data collection, environmental control, and data-driven decision making. The right side shows the digital twin developed in the Unity 3D environment, which mirrors the physical greenhouse and supports user interaction, behavior modeling, and scenario testing. Bidirectional data communication between the physical and virtual systems is provided through the TCP protocol, enabling synchronized operation, visualization and rule-based control decisions, and forms the basis of the system's decision support function.

Table 1. Types of sensors used and their purposes

	Sensor name	Features	Usage purpose
Temperature sensor	DHT11	- Measurement range: 0-50°C - Accuracy: ±2°C	Used to monitor temperature levels indoors.
Humidity sensor	DHT11	- Measurement range: 20-90% RH - Accuracy: ±5% RH	Used to monitor humidity levels indoors.
Light sensor	LDR	- Resistance varies with light exposure - High resistance in low light, low resistance in high light	Used to measure light levels and for applications dependent on daylight.
Air quality measurement sensor	MQ-135	- Detectable gases: NH3, NOx, alcohol, benzene, smoke - High sensitivity and fast response time	Used to measure environmental air quality and detect hazardous gases.
Soil moisture sensor	FC-28	- Measurement range: Typically from dry to wet soil -Output: Digital (High/Low) and Analog voltage that varies with moisture level	Used to monitor soil moisture levels to optimize irrigation in gardening and agriculture.

Greenhouse Prototype Setup and Sensor Integration

In this study, a small-scale greenhouse prototype was constructed, and various environmental factors such as soil moisture, relative humidity, air quality, temperature, and light intensity were measured using sensors configured on a Raspberry Pi. The types of sensors used and their corresponding purposes are presented in Table 1.

he FC-28 soil moisture sensor used in this study was configured to automatically trigger irrigation when soil moisture levels fall below a predefined threshold. This sensor provides both analog and digital outputs, with the digital mode selected for the current implementation. In digital mode, the output is either 0 or 1, depending on whether the soil moisture is below or above the user-defined threshold set via a built-in potentiometer. If the soil moisture level falls below the threshold, the sensor outputs a low signal (0), indicating insufficient moisture and the need for irrigation.

Monitoring environmental conditions such as temperature, relative humidity, and air quality inside the greenhouse is critical for maintaining optimal conditions for plant growth. When these factors exceed predefined thresholds, integrated ventilation systems are automatically activated. These systems operate to maintain environmental variables within ideal ranges. For instance, if the internal temperature or humidity is too high, or if air quality drops below acceptable levels, ventilation fans are automatically triggered. This process helps stabilize the internal environment, allowing plants to grow healthily without stress.

In addition, LDR (Light Dependent Resistor) sensors were used to measure light intensity within the greenhouse. These sensors detect changes in resistance based on ambient light levels. When light intensity falls below a specified threshold—potentially affecting plant development—supplemental light sources (LEDs) are automatically activated based on the input from the LDR sensors. This ensures that optimal lighting conditions are maintained inside the greenhouse, creating an ideal environment for plant growth while also optimizing energy consumption.

Finally, the physical greenhouse environment that houses all the technological components described above is shown in Figure 2. Through this integrated system, environmental variables within the greenhouse are continuously monitored and appropriate interventions are made when necessary.



Figure 2. Greenhouse prototype

Development of the digital twin environment

The digital twin environment developed on the Unity platform represents a virtual counterpart of the physical greenhouse prototype. Through this interface, users can monitor real-time environmental conditions, observe system responses, and conduct scenario-based experiments. Unity not only provides a visual representation but also processes real-time data streams to run a synchronized simulation that reflects the physical system within the virtual environment.

The system operates through bidirectional communication established between Unity's TCP client and the Raspberry Pi's TCP server. The Raspberry Pi collects environmental sensor data every 2 seconds and

transmits it to Unity in JSON format. The Unity application processes this incoming data, visualizes it on the interface, and, if necessary, generates and sends control commands back to the Raspberry Pi. This continuous exchange ensures real-time synchronization between the digital twin environment and the physical greenhouse system. The digital twin scene shown in Figure 3 is an example of this interactive simulation.



Figure 3. Interactive digital twin scene developed in Unity 3D for real-time greenhouse monitoring and control

Data Communication and Synchronization

At this stage, bidirectional data communication is established between a TCP server running on the Raspberry Pi and a TCP client configured within the Unity environment. The Raspberry Pi is configured as a TCP server and periodically transmits sensor data representing environmental parameters—such as temperature, humidity, light intensity, and air quality—to the digital twin environment. The data are formatted in JSON and sent to the Unity application, where they are processed. Based on the processed data, Unity generates control commands that are sent back to the Raspberry Pi via the TCP client. The Raspberry Pi then interprets these commands and converts them into physical output signals to activate relevant hardware components (e.g., fan, LED, irrigation system).

To better illustrate this interaction, a flow diagram showing the step-by-step data exchange and communication between system components is presented in Figure 4.

Figure 5 displays the latest improvements made to the user interface of the digital scene designed in Unity. These interface enhancements simplify system usability and improve the accuracy and realism of the virtual simulation of the physical environment. The improvements also help users better understand the system while supporting seamless and effective data exchange between the physical and digital domains.

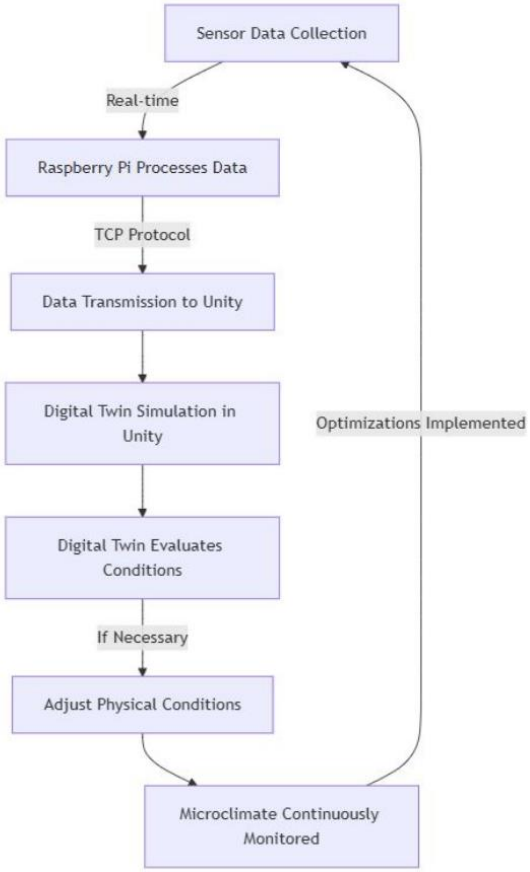


Figure 4. Bidirectional data flow between physical and virtual systems

The system is primarily designed to operate autonomously based on environmental parameters. However, the developed Unity interface also provides users with the ability to actively interact with the system. Through the graphical interface, users can dynamically modify threshold values for temperature, humidity, light, and soil moisture, thereby altering the system's behavior in real time. Additionally, users can manually trigger physical components such as the fan, LED light, or irrigation system, allowing for the testing of different scenarios.

This bidirectional control mechanism transforms the digital twin from a passive visualization tool into an interactive experimentation platform. Such flexibility is particularly valuable for educational and research purposes, as it not only allows users to observe the system’s behavior visually but also to intervene directly and immediately observe the effects. This capability enables the system to be adapted to various user profiles—such as students, engineers, and farmers—and enhances its potential as a learning and development tool.

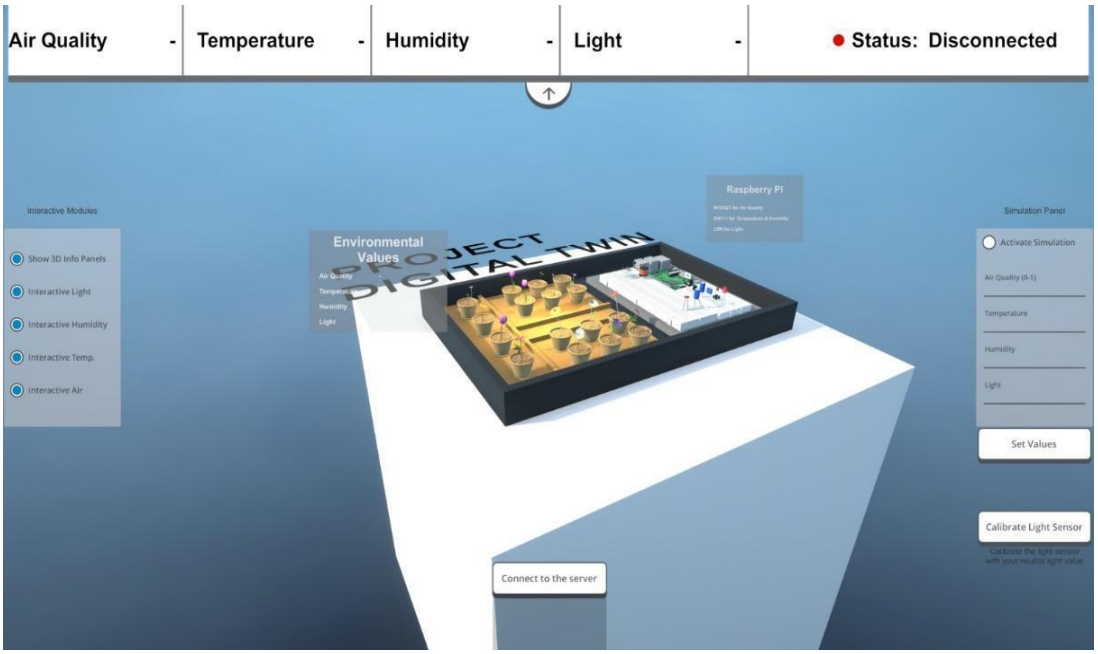


Figure 5. Unity digital twin interface with user control functions

Implementation and testing processes

In this study, the simulation and management of the environmental parameters of the physical greenhouse has been successfully realized through a digital twin developed on the Unity platform. The research is based on one-day data obtained in June conditions in Turkey, which were used to evaluate the effectiveness of the greenhouse lighting control mechanisms. In particular, during time periods of low natural light intensity, such as early morning and late evening, the LEDs were automatically switched on based on high readings from the LDR sensor. The graph in Figure 6 shows how the readings from the LDR sensor change throughout the day and how the LEDs are activated when they are above the threshold value set at 800.

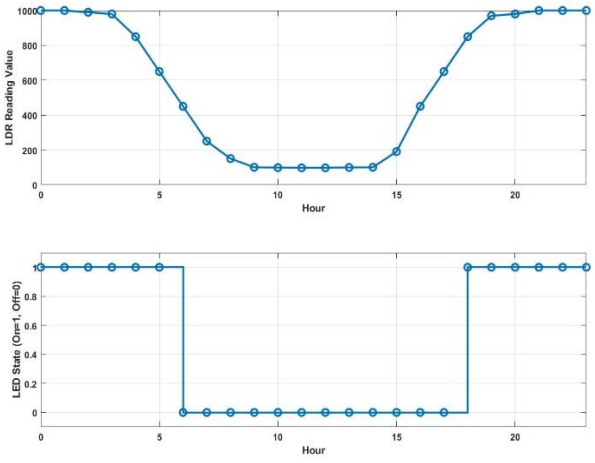


Figure 6. LDR Sensor Readings and LED Activation Based on Light Intensity Throughout the Day

This successfully demonstrates the capacity of the LEDs to provide the required light level for the plants, especially between 00:00 and 06:00 at night and after 20:00 in the evening.

In Figure 7, Unity 3D visually displays the moments when the LEDs are active in the digital twin environment. This simulation screen provides an interactive experience for the user to observe in real time when the LEDs are activated in the digital twin and the effect of this situation on the plants inside the greenhouse.

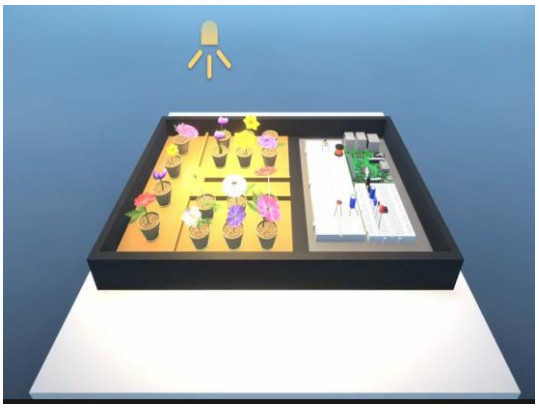


Figure 7. Real-Time LED Activation in the Digital Twin Environment Displayed in Unity 3D

In this study, data from temperature, relative humidity and air quality sensors were analyzed every hour for 24 hours and these data are presented in Figure 8. During the day, the temperature generally tended to increase, while the humidity showed a reverse trend and an increase was observed during the night hours. Air quality remained constant throughout the day. In the study, air quality is defined as a digital variable, where '0' indicates good air quality and '1' indicates poor air quality. The threshold values were used to analyses the changes in temperature and humidity.

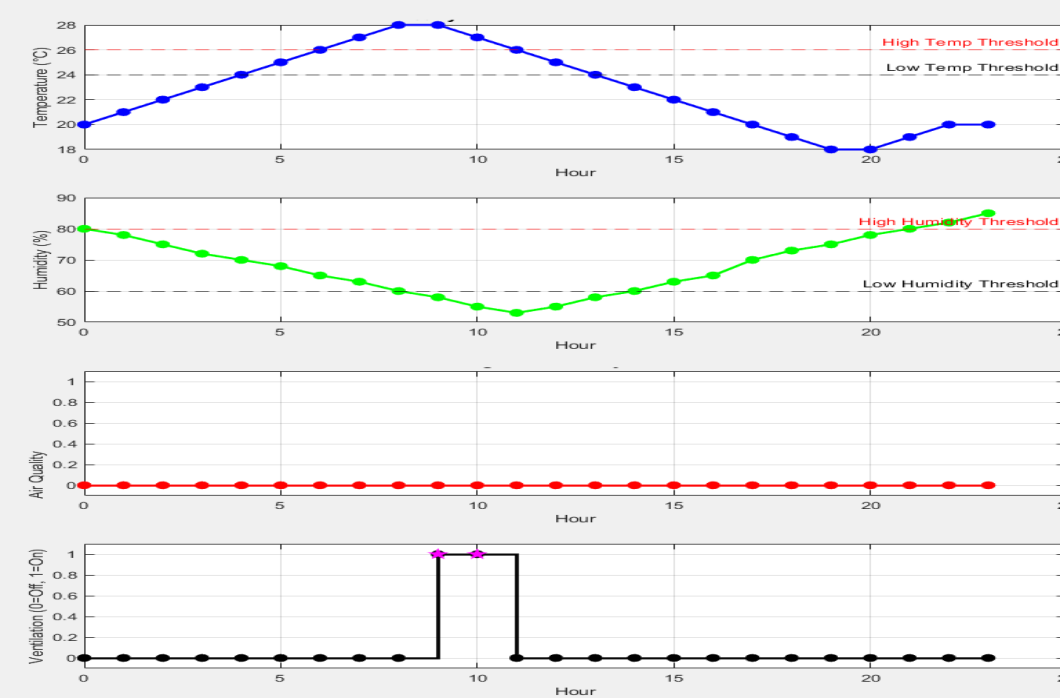


Figure 8. Hourly variation of temperature, humidity, air quality, and ventilation status over a 24-hour period

The low threshold value for temperature was set as 24°C and the high threshold value was set as 26°C. For humidity, the low threshold value was defined as 60% and the high threshold value was defined as 80%. As can be seen in Figure 8, the ventilation system was activated during the hours when the temperature and humidity threshold values exceeded the specified limits at the same time. The four sub-graphs in Figure 8 show the following: The first graph shows the temperature variations and their high and low threshold values. The second graph presents the relative humidity variations and the set high-low humidity limits. The third graph shows how the air quality changes in a digital form throughout the day. Here, an air quality of '0' represents a good condition, while '1' represents poor air quality. The fourth graph shows the activation status of the ventilation system. Ventilation is only activated when the temperature is above the high threshold and the humidity is below the low threshold. The purple markers highlight the times when these conditions are met and the ventilation is activated.

The measurements obtained from the soil moisture sensor show that the irrigation system is automatically activated and irrigation is performed for one minute for experimental purposes in case of moisture levels below the set threshold value.

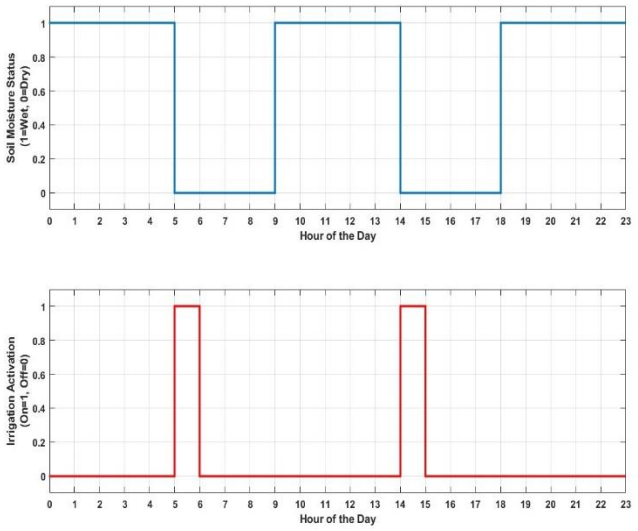


Figure 9. Irrigation System Activation Based on Soil Moisture Sensor Readings Below Threshold

Figure 9. visually presents the activation times of the irrigation system and how these activations are triggered when the moisture level falls below the threshold value. The irrigation system is activated as soon as the moisture level passes below the threshold value and remains activated for one minute, which is the specified experimental time, to maintain the moisture balance of the soil.

These control mechanisms, which are automatically triggered based on predefined sensor thresholds, demonstrate the system's functionality as a basic decision support system. By analyzing real-time environmental data and applying rule-based logic, the system can autonomously determine when and how to intervene, thus assisting in efficient greenhouse management.



Figure 10. Visualization of the Physical Greenhouse Environment and its Digital Twin

Finally, a visualization of the physical greenhouse environment and its digital twin is presented in Figure 10. Thanks to this integrated system, the variables inside the greenhouse are continuously monitored and interventions can be made when necessary.

Conclusions

This study presents the design and implementation of a real-time, interactive digital twin system developed on the Unity 3D platform for monitoring and managing environmental conditions in a greenhouse environment. The system processes real-time data from multiple sensors—including temperature, humidity, soil moisture, light intensity, and air quality—and simultaneously manages physical actuators such as fans, LEDs, and the irrigation system in both automatic and user-controlled modes.

Scenario-based experiments showed that the LEDs were automatically activated under low light conditions, the ventilation system was triggered when the temperature and humidity thresholds exceeded critical levels, and the irrigation system was activated when the soil moisture fell below a predefined limit. These applications indicate that the system effectively executes rule-based environmental control. Additionally, users were able to adjust threshold values dynamically and manually trigger physical components via the Unity interface, demonstrating that the system functions not only autonomously but also interactively.

The study presents a digital twin architecture that combines real-time environmental sensing, automated decision-making, and user-interactive control. The integration of a general-purpose game engine like Unity 3D with a physical greenhouse system in a synchronized and interactive manner offers a noteworthy example in terms of user experience, visualization capability, and educational usability. The system allows users to modify threshold values, perform scenario-based interventions, and observe the results in both the digital and physical environments simultaneously. Through its real-time sensor evaluation and rule-based control logic, the system also operates as a basic decision support system, assisting users in making timely and informed decisions for greenhouse management.

Thanks to its reusable, low-cost, and education-oriented design, the developed platform is not only a functional prototype but also a tool with potential for teaching, experimentation, and advanced research. The study demonstrates the feasibility of establishing an interactive closed-loop between simulation and the physical environment, and it offers a foundation that can be extended with AI-based decision support systems, cloud-supported data analytics, and large-scale agricultural applications.

Ethics committee approval and conflict of interest statement

There is no need to obtain permission from the ethics committee for the article prepared.

There is no conflict of interest with any person / institution in the article prepared.

Authors' Contributions

The conceptualization and design of the study were carried out by Ayçiçek and Özcan. Data collection was conducted by Ayçiçek and Özcan. Data analysis and interpretation were performed by Bal, Akpınar, and Yayla. The manuscript was drafted by Bal, and critical revisions were made by Bal, Akpınar, and Yayla.

Acknowledgment

References

[1] Alves, G., Maia, R., & Lima, F. (2023). Development of a Digital Twin for smart farming: Irrigation management system for water saving. Journal of Cleaner Production, 388, 135920. https://doi.org/10.1016/j.jclepro.2023.135920

[2] Attaran, M., & Celik, B. G. (2023). Digital twin: benefits, use cases, challenges, and opportunities. Decision Analysis Journal, 6, 100165.

[3] Chamara, N., Islam, M. D., Bai, G., Shi, Y., & Ge, Y. (2022). Ag-IoT for crop and environment monitoring: Past, present, and future. Agricultural Systems, 203, 103497. https://doi.org/10.1016/j.agsy.2022.103497

[4] Isied, R., Mengi, E., & Zohdi, T. (2022). A digital-twin framework for genomic-based optimization of an agrophotovoltaic greenhouse system. Proceedings of the Royal Society A: Mathematical, Physical and

Engineering Sciences, 478. https://doi.org/10.1098/rspa.2022.0414

[5] Li, L., Aslam, S., Wileman, A., & Perinpanayagam, S. (2022). Digital twin in aerospace industry: a gentle introduction. IEEE Access, 10, 9543–9562.

[6] Liu, J., Wang, L., Wang, Y., Xu, S., & Liu, Y. (2023). Research on the Interface of Sustainable Plant Factory Based on Digital Twin. Sustainability, 15, 5010. https://doi.org/10.3390/su15065010

[7] Moreno, J. C., Berenguel, M., Donaire, J. G., Rodríguez, F., Sánchez-Molina, J. A., Guzmán, J. L., & Giagnocavo, C. L. (2024). A pending task for the digitalisation of agriculture: A general framework for technologies classification in agriculture. Agricultural Systems, 213, 103794.

[8] Pajpach, M., Drahoš, P., Pribiš, R., & Kučera, E. (2022). Educational-development Workplace for Digital Twins using the OPC UA and Unity 3D. 2022 Cybernetics & Informatics (K&I), Visegrád, Hungary, pp. 1-6. https://doi.org/10.1109/KI55792.2022.9925933

[9] Paruelo, J. M., Texeira, M., & Tomasel, F. (2024). Hybrid modeling for grassland productivity prediction: A parametric and machine learning technique for grazing management with applicability to digital twin decision systems. Agricultural Systems, 214, 103847. https://doi.org/10.1016/j.agsy.2023.103847

[10] Purcell, W., & Neubauer, T. (2022). Digital Twins in Agriculture: A State-of-the-art review. Smart Agricultural Technology, 3, 100094. https://doi.org/10.1016/j.atech.2022.100094

[11]Raspberry Pi. Retrieved from https://www.raspberrypi.com/ (accessed 10 March 2024)

[12] Silveira, F., Silva, S. L. C., Machado, F. M., Barbedo, J. G. A., & Amaral, F. G. (2023). Farmers' perception of the barriers that hinder the implementation of agriculture 4.0. Agricultural Systems, 208, 103656.

[13] Sun, T., He, X., Song, X., Shu, L., & Li, Z. (2022). The digital twin in medicine: a key to the future of healthcare? Frontiers in Medicine, 9, 907066.

[14] Unity, Introduction to Digital Twins with Unity. Retrieved from https://learn.unity.com/tutorial/introduction-to-digital-twins-with-unity (accessed 30 March 2024))

[15]Verdouw, C., Tekinerdogan, B., Beulens, A., & Wolfert, S. (2021). Digital twins in smart farming. Agricultural Systems, 189, 103046. https://doi.org/10.1016/j.agsy.2020.103046

[16] Viana, C. M., Freire, D., Abrantes, P., Rocha, J., & Pereira, P. (2022). Agricultural land systems importance for supporting food security and sustainable development goals: A systematic review. Science of the Total Environment, 806, 150718.

[17] Zhang, Z., Zhu, Z., Gao, G., Qu, D., Zhong, J., Jia, D., Du, X., Yang, X., & Pan, S. (2023). Design and research of digital twin system for multi-environmental variable mapping in plant factory. Computers and Electronics in Agriculture, 213, 108243.

Dicle University
Journal of Engineering
https://dergipark.org.tr/tr/pub/dumf
duje.dicle.edu.tr

Araştırma Makalesi/Research Article

Chen Kaotik Sisteminin Adaptif Kontrolü

Adaptive Control of Chen Chaotic System

Mehmet GÜZEL[1*], Muhittin BAYRAM[2]

[1] Dicle University, Electrical-Electronics Engineering Department, mehmetguzel_21@.com, Orcid No: 0009-0006-4128-8225
[2] Dicle University, Electrical-Electronics Engineering Department, muba@dicle.edu.tr, Orcid No 0000-0002-9941-4347

MAKALE BİLGİLERİ

Makale Geçmişi:

Geliş 4 Haziran 2025
Revizyon 30 Ağustos 2025
Kabul 6 Eylül 2025
Online 30 Eylül 2025

Anahtar Kelimeler:

Kaos, Kaotik Sistemler, Chen Kaotik Sistemi, Adaptif Kontrol

ÖZ

Bu çalışmada, Chen kaotik sisteminin dinamik davranışları incelenmiş ve bu sistem için adaptif bir kontrol stratejisi geliştirilmiştir. Adaptif kontrol teknikleri, sistem parametrelerindeki belirsizlikleri ve dış bozucuları telafi ederek sistemin kararlı bir duruma ulaşmasını sağlar. Kontrol algoritması Chen kaotik sisteminin başlangıç parametlerinde oynama yaparak sistemi istenilen referans durumlarına yönlendirir. Chen kaotik sisteminde adaptif kontrol, sistemin kaotik dinamiklerini bastırmak veya belirli bir referans durumuna yönlendirmek amacıyla kullanılan etkili bir yöntemdir. Böylece Chen sisteminin kaotik davranışı kontrol altına alınarak mühendislik ve güvenlik uygulamalarında kullanılmak üzere daha kararlı bir yapı elde edilir. Geliştirilen adaptif kontrol algoritması ile x, y ve z durum değişkenleri belirlenen referans noktalarında stabilize edilmiştir. Başlangıçta yüksek genlikli ve düzensiz salınımlar sergileyen sistem, zamanla adaptif kontrol etkisiyle sönümlenmiş ve her üç durum değişkeni referans değer seçilen sıfıra doğru yönelmiştir. Bu durum, sistemin kaotik davranışının bastırıldığını ve kontrol algoritmasının etkin biçimde çalıştığını göstermektedir. Simülasyon sonuçlarında, geliştirilen adaptif kontrol yapısı, Chen sistemini kararlı hale getirmiş ve istenilen dinamik davranışı başarıyla sağlamıştır.

ARTICLE INFO

Article history:

Received 4 June 2025
Received in revised form 30 August 2025
Accepted 6 September 2025
Available online 30 September 2025

Keywords:

Chaos, Chaotic Systems, Chen Chaotic System, Adaptive Control

Doi: 10.24012/dumf.1713168

* Sorumlu Yazar

ABSTRACT

In this study, the dynamic behavior of the Chen chaotic system is investigated and an adaptive control strategy is developed for this system. Adaptive control techniques compensate for uncertainties in the system parameters and external disturbances to achieve a steady state. The control algorithm manipulates the initial parameters of the Chen chaotic system to steer the system to the desired reference states. Adaptive control in the Chen chaotic system is an effective method to suppress the chaotic dynamics of the system or to steer it to a specific reference state. Thus, the chaotic behavior of the Chen system is controlled and a more stable structure is obtained for use in engineering and security applications. With the developed adaptive control algorithm, the state variables x, y and z are stabilized at specified reference points. The system, which initially exhibits high amplitude and irregular oscillations, is damped over time by the adaptive control effect and all three state variables tend towards zero, which is chosen as the reference value. This shows that the chaotic behavior of the system is suppressed and the control algorithm works effectively. In the simulation results, the developed adaptive control structure stabilized the Chen system and successfully achieved the desired dynamic behavior.

Giriş

Kaotik sistemlerin kontrolü her geçen gün önem kazanmakta ve bu alanda literatüre yeni boyut kazandırılmaktadır. Kontrol çeşitlerinden ise adaptif (uyarlanır) kontrol güncelliğini korumakta ve farklı alanlara uygulanma ihtiyacı bulmaktadır. Kaosun ilk keşfiyle birlikte bu tür dinamikler olumsuz bir özellik olarak görülmüş ve başlangıçta kaotik davranış sergileyen doğrusal olmayan sistemlerin parametreleri değiştirilerek kararlı bir yapı elde edilmiş, kontrol tasarımı bu doğrultuda gerçekleştirilmiştir. Ancak zamanla, kaotik sinyallerin dikkat çekici özelliklerinden yararlanarak olumlu amaçlara yönelik çeşitli çalışmalar da geliştirilmiştir.

Kaotik sistemleri içeren literatür çalışmalarının [1-3] yanında, adaptif kontrol içeren çalışmalar [4-10] popülerliğini her geçen gün daha da artırmaktadır.

Kaotik sistemlerin kontrolü, denge noktasında kararlılığı sağlama amacını güder. Bu amaçla OGY (Ott, Grebogi, Yorke) kontrolü, doğrusal ve doğrusal olmayan geri besleme, zaman gecikmeli geri besleme, kayma kipli, adaptif ve pasif kontrol yöntemleri geliştirilmiştir.

Başlangıçta, kaotik sistemlerin başlangıç koşullarına hassasiyetleri nedeniyle kontrol edilemez oldukları düşünülse de Ott, Grebogi ve Yorke [11] kapalı döngü metodu ile bu engeli aşarak OGY kaos kontrol yöntemini ortaya koymuşlardır. Kaos kontrolünde yaygın olarak kullanılan yöntemlerden biri, basitliği ve etkinliği nedeniyle doğrusal geri-beslemeli kontroldür. Bu yöntem, Lorenz, Rössler, Duffing ve Liu gibi kaotik sistemlerde başarıyla uygulanmıştır. Sistemin (x, y, z) durum değerleri, katsayılarla geri beslenerek kararsız periyodik salınımlar sıfıra yaklaştırılır. Ayrıca, Lyapunov kararlılık teoremi kullanılarak kaotik sistemler farklı denge noktalarında stabilize edilebilir. Doğrusal olmayan geri-beslemeli kontrol ise, lineer olmayan sinyallerin durum değişkenlerine eklenmesiyle kaotik sistemlerin kontrolünü sağlayarak ve çok sayıda kaotik sistemde kullanılmıştır. Lyapunov kararlılık teoremi, dinamik sistemlerin kararlılığını inceleyen bir matematiksel yöntemdir ve özellikle diferansiyel denklemlerle tanımlanan sistemlerin zaman içindeki davranışlarını analiz etmek için kullanılır. Bu teorem, bir sistemin denge noktasına olan yakınlığında zamanla ne olacağını belirlemeye yardımcı olur. Pyragas [12] tarafından geliştirilen zaman gecikmeli geri besleme kontrolü, dinamik sistemlerdeki kararsız yörüngeleri dengelemek için kullanılan sade ve etkili bir yöntem olarak öne çıkmaktadır. Bu yöntemde, kontrol sinyali, sistemin mevcut durumu ile geçmişteki durumu arasındaki farkla hesaplanır.

Kayma kipli kontrol, Emelyanov [13] tarafından ikinci dereceden sistemlerde faz uzayında özel bir doğru tanımlanarak, başlangıç koşullarından bağımsız olarak sistemin durumlarının bu doğruya yönlendirilmesi amacıyla geliştirilmiştir. Bu yöntemin yüksek performans gösterdiği gözlemlenerek üzerinde daha fazla çalışma yapılmıştır. Adaptif kontrol, kaotik sistemlerin davranışlarını ortadan kaldırmak için sistem parametrelerini değiştirmeye odaklanır. Parametre değişimlerinin sistemin asimptotik davranışı üzerindeki etkisi, çatallaşma diyagramları kullanılarak analiz edilebilir. Bu diyagramlar, sistemin hangi parametre değerlerinde kaotik bölgeye geçtiğini veya dallanma gerçekleştirdiğini gösterir. Kararlı sabitleştirilmiş noktalar, periyot-1 veya daha yüksek periyotlu yörüngeler elde etmek için uygun parametre değerleri belirlenebilir.

Hua ve Guan çalışmalarında, kaotik sistemlerin kontrolü için adaptif bir yöntem geliştirmeyi amaçlayarak kaotik sistemleri kararsız sabit noktalara yönlendirebilen bir adaptif kontrolör önermişlerdir. Bu kontrolör, yalnızca sabit noktaların ve kaotik sistemlerin boyutlarının bilinmesi gerektiğini vurgulamakta ve kesin matematiksel modellere ihtiyaç duymadan çalışabilmektedir [14].

Khan ve Prasad, uyarlamalı kontrolün kaotik sistemlerde güvenilir senkronizasyon sağlamada önemli bir araç olduğunu ortaya koymakta ve gelecekte daha karmaşık sistemlerde uygulanabilirliği konusunda yeni perspektifler sunmaktadır [15].

Vaidyanathan ve Volos çalışmalarında, gizli çekicilere sahip sistemlerin incelenmesinin hem pratik hem de teorik önem taşıdığına dikkat çekmektedir. Ayrıca kaos literatürüne değerli bir katkı sunup adaptif kontrol yöntemleri ile kaotik sistemlerin kontrol edilebilirliğini ortaya koymaktadır [16].

Eshaghi ve arkadaşları, Lorenz–Haken denklemlerinden türetilmiş yeni bir fraksiyonel lazer kaotik sistemini tanıtmaktadır. Geri besleme kontrol yönteminin uygulanması ile sistemin kaotik davranışlarının ortadan kaldırılması ve belirli bir denge noktasında stabilizasyonu sağlanmaktadır. Ayrıca, fraksiyonel türev derecesinin azaltılması ile sistemin kararlılığının artırılabileceği gösterilmektedir [17].

Ding ve arkadaşları, sistem parametrelerindeki belirsizlikleri ve dış bozucuları çevrim içi olarak tahmin edebilen norm tabanlı bir uyarlanabilir kazanç yapısı oluşturmuşlardır. Chen sistemi ve çok kanatlı Lu kaotik sistemleri üzerinde gerçekleştirilen sayısal simülasyonlar, önerilen yöntemin üstün hızda yakınsama, yüksek hassasiyet ve güçlü bozucu reddetme kabiliyeti sağladığını göstermektedir [18].

Bu çalışmada, Chen kaotik sisteminin dinamiklerini kontrol etmek amacıyla adaptif kontrol algoritması geliştirilmiştir. Simülasyon sonucunda, bu algoritmaların kaotik davranışı başarılı bir şekilde stabilize ettiği gözlemlenmiştir. Kontrol öncesinde düzensiz olan sistem dinamikleri, adaptif kontrol sayesinde belirli bir denge noktasına yönlendirilmiş ve kararlı bir yapı elde edilmiştir. Çalışmanın literatüre özgün katkısı, kaotik sistemlerin adaptif kontrolünü, Python ortamında uygulamalı olarak gerçekleştirmesi ve bu kontrol yapısını Lorenz, Chua, Chen ve Rössler gibi farklı kaotik dinamik sistemlere entegre etmesidir. Bu yönüyle çalışma, literatürde yaygın olan tek sistem ve Matlab odaklı yaklaşımların ötesine geçmekte, açık kaynaklı yazılımlar ile yeniden üretilebilir ve üzerine eklemeler yapılarak geliştirilebilir bir kontrol altyapısı sunmaktadır.

Materyal ve Metot

Bu bölümde, çalışmada kullanılacak temel kavramlar arasında yer alan kaos bilimi ve kaotik sistemler, Chen kaotik sisteminin zaman serileri, Chen kaotik sisteminin faz uzayları ve adaptif kontrol konuları üzerinde durulacaktır.

Kaos Bilimi ve Kaotik Sistemler

Kaos Bilimi; başlangıç koşullarına son derece hassas bağlı olan, düzensizliğin içinden düzen oluşturan ve geleceği öngörülemeyen sistemleri inceleyen bilim dalıdır. Kaos bir sistemin zaman içinde nasıl değiştiğini, nasıl karmaşıklaştığını, kendi içindeki düzende nasıl dağılım gösterdiğini inceler. Matematik ve fen bilimleriyle başlayıp, mühendislik, sosyal bilimler, kuantum fiziği ve astrofizik gibi alanlarda gelişimi devam etmektedir [19].

Kaotik sistemler; fraktal geometrilere sahip kendini tekrarlayan, kendi içinde düzen oluşturan karmaşık sistemlerdir. Kaotik sistemlerin gelecekteki davranışlarını doğru bir şekilde tahmin edebilmek için başlangıç koşullarının son derece hassas bir biçimde belirlenmesi gerekmektedir [20].

Günlük yaşamda karşılaşabileceğimiz bazı kaotik sistemlere; hava durumu, borsa ve diğer finansal piyasalar, okyanus akıntıları, nüfus dinamikleri, ekonomik değişimler, kalp atışları gibi örnekler verilebilir.

Kaos teorisi, elektrik şebekelerinin ve güç sistemlerinin stabilitesini artırmada, ani güç dalgalanmalarını ve sistem çökmelerini önlemede, elektronik devrelerin çıkışlarını senkronize etmede, ileri seviye elektronik cihazların geliştirilmesinde, yüksek performanslı elektrik devrelerinin geliştirilmesinde, bilgi ve iletişim teknolojileri alanında güvenliğin artırmasında, enerji sistemlerinin kesintisiz çalışmasında, piyasa karmaşıklığını anlamada ve modellemede, büyük veri analizinde, beyin dalgalarının incelenmesi için biyomedikal sinyallerin analizinde ve pek çok alanda uygulama bularak önemli faydalar sağlamaktadır. Bu durum bilimsel ve mühendislik alanlarında yeni keşiflere ve inovasyonlara kapı aralamaktadır. Kaos teorisinin, gelecekte beynin karmaşık işlevlerini modellemede önemli bir araç olarak kullanılacağı öngörülmektedir. Çünkü beyin, evrimin ve yaşam süreci boyunca çevresel etkileşimlerin etkisiyle şekillenen, karmaşık ve fraktal bir yapıya sahiptir. Öğrenme, hatırlama ve fikir yürütme gibi üst düzey bilişsel süreçlerin kaotik dinamiklerle modellenmesi, beyin işlevlerinin daha iyi anlaşılmasını ve nörobilim alanında yeni keşiflerin yapılmasını sağlayabilir. Bu bakış açısı, kaos teorisi ve fraktal yapıların, biyolojik sistemlerdeki karmaşıklığı ve öngörülemezliği anlamada ne denli kritik bir rol oynadığını ortaya koymaktadır [21].

Kaos tabanlı şifreleme, iletişim güvenliği için güçlü bir yöntem olarak kullanılır. Kaotik sinyallerin karmaşıklığı ve öngörülemezliği, veri (görüntü, ses, data) transferi sırasında verilerin güvenliğini sağlar, yetkisiz kişilerin veriyi çözmesini oldukça zorlaştırır. Gönderilen verinin kaotik sinyal üzerine bindirilmesi, veriyi şifreler ve sadece doğru anahtara sahip olanlar tarafından çözülebilir. Bu teknik, veri iletişimi sürecinde kaotik bir sinyalin üzerine bilginin bindirilmesiyle çalışır. Askeri ve diplomatik iletişimde yüksek güvenlikli veri transferi için kullanılır.

Kaos teorisi, yıldızların ve gezegenlerin yörüngelerindeki küçük değişikliklerin uzun vadede büyük etkiler yaratabileceğini gösterir. Uydular ve kuyruklu yıldızlar gibi Güneş Sistemi'ndeki objelerin hareketleri de kaotik olabilir. Kaos teorisi, bu objelerin yörüngelerindeki öngörülemez değişimleri anlamamıza yardımcı olur.

Kaos, rastgele faktörler içermeyen, tamamen deterministik kurallara dayalı bir süreçtir. Geçmişten geleceğe kadar olan sistem davranışları, olasılık yerine belirli kurallar tarafından yönlendirilir. Ancak, deterministik ve olasılıksal sistemler arasındaki sınır, bazen rastgele gibi görünen süreçlerin henüz keşfedilmemiş temel kurallarından dolayı belirsiz olabilir. Başlangıç koşullarına hassas bağımlılık, kaosun belirgin özelliklerinden biri olup, literatürde 'kelebek etkisi' olarak bilinir. Bu durum, başlangıç koşullarındaki çok küçük bir değişikliğin, zaman içinde büyük ve öngörülemez sonuçlara yol açabileceğini ifade eder [22].

Chen Kaotik Sistemi

Chen kaotik sistemi, doğadaki karmaşık ve öngörülemez davranışları matematiksel olarak modellemek amacıyla geliştirilmiş üç boyutlu dinamik sistemlerden biridir. Bu sistem, belirli başlangıç koşulları ve parametre değerleri altında düzensiz ama deterministik bir yapı sergiler. Chen sistemi, özellikle Lorenz sistemi ile benzerlik gösterse de kendine özgü denklemleri ve kaotik çekicisi sayesinde farklı dinamik özellikleri sunar. Sistem, başlangıç koşullarına oldukça duyarlı olması nedeniyle, küçük değişimlerin zamanla büyük farklılıklara yol açtığı karmaşık süreçleri incelemek için elverişli bir yapı sunar. Bu yönüyle Chen kaotik sistemi, hem teorik araştırmalarda hem de uygulamalı bilimlerde, özellikle kontrol mühendisliği, güvenlik sistemleri ve sinyal işleme gibi alanlarda önemli bir yere sahiptir [23].

Chen kaotik sistemi, Guanrong Chen tarafından tanıtılan bir kaotik dinamik sistemdir. Chen sistemi, kaos teorisi ve nonlineer dinamiklerin incelenmesinde önemli bir modeldir [24].

Chen kaotik sistemi aşağıdaki Denklem 1, 2 ve 3 ile gösterilir [1].

$$\dot{x} = \frac{\mathrm{dx}}{\mathrm{dt}} = a(y - x) \quad (1)$$

$$\dot{y} = \frac{\mathrm{dy}}{\mathrm{dt}} = (c - a)x - xz + cy \quad (2)$$

$$\dot{z} = \frac{\mathrm{dz}}{\mathrm{dt}} = xy - bz \quad (3)$$

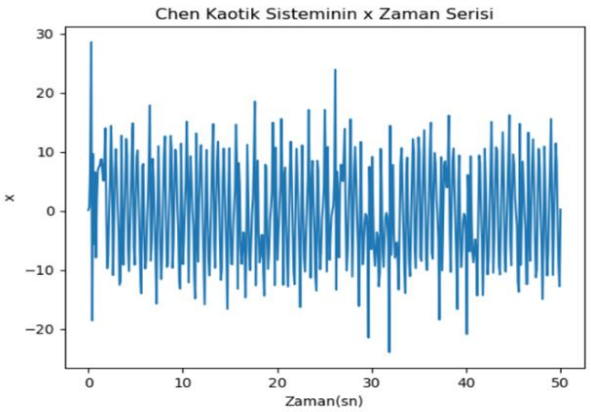
x, y, z durum değişkenleridir.

a, b, c sistemin parametreleridir.

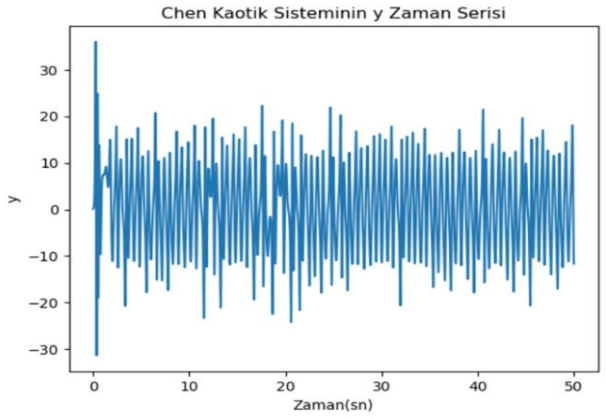
Chen kaotik sistemi için yaygın olarak kullanılan parametre değerleri a=35, b=3 ve c=28 şeklindedir. Sistemin parametreleri bu değerlerde kaotik davranış gösterir. Bu sistem, Lorenz sisteminin yapısıyla benzerlik gösteren bir eşleniği olup, daha karmaşık dinamik özelliklere sahiptir.

Kaotik sistemlerde zaman serisi; sistemin belirli bir durum değişkeninin (örneğin konum, hız, sıcaklık, voltaj vb.) zamanla değişimini gösteren bir veri dizisidir. Zaman serisi, kaotik sistemin dinamik davranışlarını incelemek, analiz etmek ve modellemek için kritik bir rol oynar.

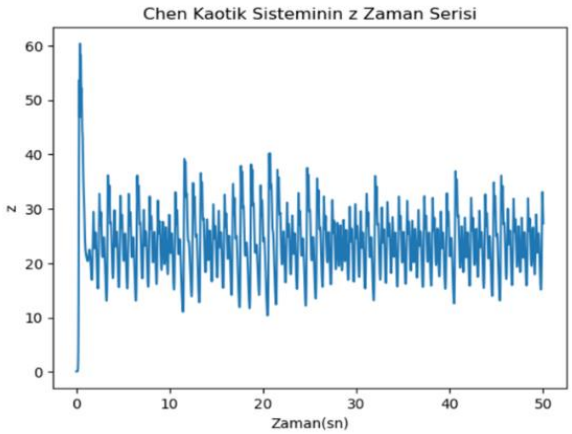
Aşağıdaki Şekil 1, Şekil 2, Şekil 3 ve Şekil 4'te Chen Kaotik Sisteminin x, y ve z zaman serisi grafikleri gösterilmiştir.



Şekil 1. Chen kaotik sisteminin x zaman serisi grafiği



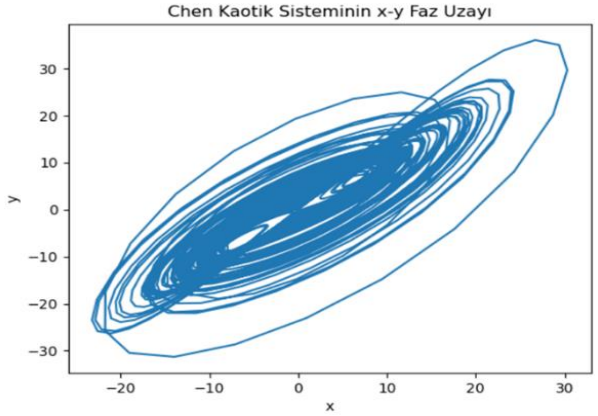
Şekil 2. Chen kaotik sisteminin y zaman serisi grafiği



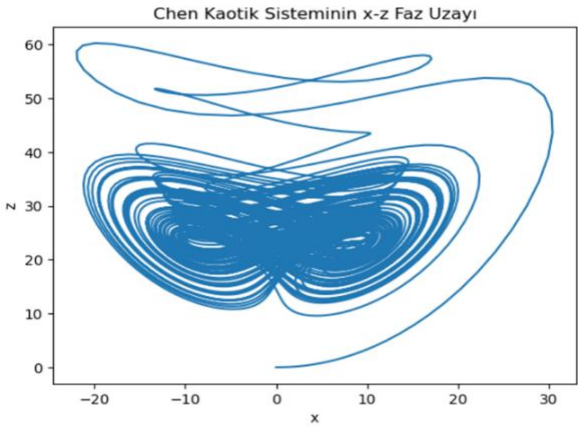
Şekil 3. Chen kaotik sisteminin z zaman serisi grafiği

Kaotik sistemlerde faz uzayı; sistemin tüm durum değişkenlerinin birlikte gösterildiği çok boyutlu bir yapıdır. Bu uzayda, sistemin zamanla nasıl evrildiği yörünge şeklinde takip edilir ve uzun vadeli davranışları, genellikle fraktal yapıya sahip çekiciler aracılığıyla temsil edilir. Faz uzayı analizi, tek bir zaman serisinden sistemin dinamik özelliklerini ortaya çıkarmak için kullanılan önemli bir yöntemdir ve kaotik davranışların anlaşılmasında temel bir araçtır.

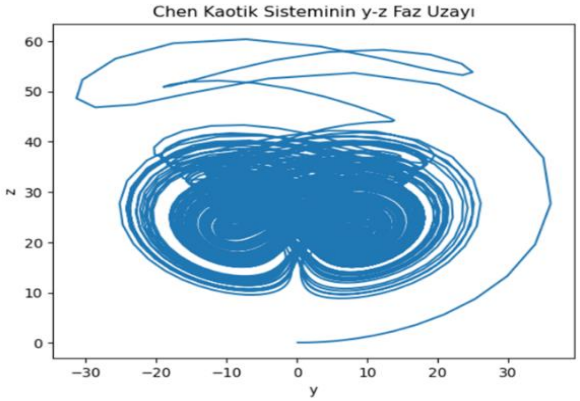
Aşağıdaki Şekil 4, Şekil 5 ve Şekil 6'da Chen Kaotik Sisteminin iki boyutlu faz uzay grafikleri, Şekil 8 ise üç boyutlu faz uzayı grafiği gösterilmiştir.



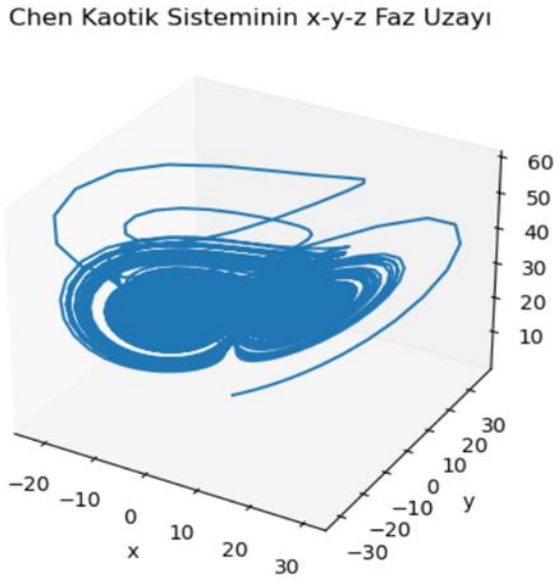
Şekil 4. Chen kaotik sisteminin x-y faz uzayı



Şekil 5. Chen kaotik sisteminin x-z faz uzayı



Şekil 6. Chen kaotik sisteminin y-z faz uzayı



Şekil 7. Chen kaotik sisteminin x-y-z faz uzayı

Chen kaotik sistemine ait zaman serileri ve faz uzay grafikleri incelendiğinde faz uzay grafiklerinde ilginç çekicilerin (attractor) oluştuğu gözlemlenmiştir. Bu da kaotikliğin göstergesidir.

Kontrol

Bir sistemin davranışını düzenlemek, izlemek ve yönlendirmek amacıyla kullanılan bir süreçtir. Bu süreç, bir mühendislik sisteminin belirli bir hedefe ulaşmasını sağlamak için çeşitli ölçüm ve geri bildirim mekanizmaları kullanarak sistemi yönlendirmeyi amaçlar. Kontrol, genellikle otomatik kontrol olarak bilinen ve sistemlerin otomatik olarak çalışmasını sağlayan yöntemlerle ilgilidir. Mühendislikte kontrolün temel amacı, belirli bir sistemin istenilen performansı sağlamasını ve kararlı bir şekilde çalışmasını garanti altına almaktır [25].

Adaptif Kontrol

Bir sistemin kontrolünü, çevresel değişiklikler veya sistem parametrelerindeki belirsizlikler gibi durumlara uyum sağlayacak şekilde dinamik olarak değiştiren bir kontrol yöntemidir. Bu yöntem, özellikle sistemin davranışlarının zaman içinde değişebileceği veya tam olarak bilinmediği durumlarda kullanılır. Adaptif kontrol, sistemin parametrelerini veya dinamiklerini izleyerek, zamanla daha iyi performans gösteren bir kontrol stratejisi geliştirmeyi amaçlar. Adaptif kontrol, sistemin parametreleri veya çevresel koşulları değiştikçe, kontrol stratejisini buna göre ayarlayarak çalışır.

Sistemlerin bazı parametreleri zamanla değişebilir veya başlangıçta tam olarak bilinmeyebilir. Adaptif kontrol, bu tür belirsizliklerle başa çıkmak için uygundur. Adaptif kontrol, değişken veya belirsiz sistemlerde istenilen performansı sağlamak için güçlü bir araçtır. Dinamik çevresel koşullara ve parametre değişikliklerine uyum sağlayabilme yeteneği, adaptif kontrolün önemli bir avantajıdır.

Adaptif Kontrolün Kullanılabilme Alanları

Adaptif kontrol sayesinde kaotik sistemlerin öngörülemezliği minimize edilerek sistem kararlılığı sağlanabilir [26]. Özellikle, Havacılık, otomasyon, elektrik güç sistemleri, robotik, iletişim ağları, biyomedikal sinyallerin kontrolü ve mekanik sistemlerde kaotik davranışların düzenlenmesi amacıyla yaygın olarak uygulanabilir. Kaotik sinyallerle veri şifreleme uygulamalarında sistem performansının iyileştirilmesi için tercih edilebilir. Güç elektroniğinde çıkış voltajının stabilize edilmesi, biyomedikal alanda EEG yani elektroensefalograf sinyalleri ile uyarlanabilir nöro-modülasyon tekniklerinde, kalp ritmi (EKG) gibi kaotik yapıya sahip sinyallerin denetlenmesi ve kaotik görüntü kodlama ile çözme sistemlerinde de önemli rol oynayabilir. Savunma ve havacılık alanlarından insansız hava araçları (İHA) stabilizasyonu ile uydu ve uzay sistemlerinin yörünge kontrolünde adaptif kontrol yöntemleri kullanılabilir. Robot kollarda hassasiyet kontrolünün sağlanması ve yapay zeka ile birlikte öğrenen kontrolcü sistemlerin geliştirilmesinde kaotik sistemlerde adaptif kontrolün yaygın uygulama alanları arasında yer alabilir. Bunların yanı sıra pek çok alanda adaptif kontrol kullanılarak kaotik sistemlerin karmaşık dinamikleri yönetilebilir.

Araştırma Sonuçları ve Tartışma

Chen Kaotik Sisteminin Adaptif Kontrolü

Chen kaotik sisteminde adaptif kontrol, sistemin kaotik dinamiklerini bastırmak veya belirli bir referans duruma yönlendirmek amacıyla kullanılan bir yöntemdir. Chen sistemi, Lorenz ve Lü sistemleri gibi yüksek derecede duyarlılığa sahip olup, kontrol edilmediğinde kaotik yörüngelerde hareket eder. Adaptif kontrol teknikleri, sistem parametrelerindeki belirsizlikleri ve dış bozucuları telafi ederek sistemin kararlı bir duruma getirilmesini sağlar. Bu sayede, Chen sisteminin kaotik davranışı kontrol edilerek, mühendislik ve güvenlik uygulamalarında daha kararlı bir yapı elde edilebilir.

Chen kaotik sisteminde adaptif kontrol durum denklemleri denklem 4, 5 ve 6'da gösterilmiştir.

$$\dot{x} = \frac{dx}{dt} = \alpha(y - x) + \mu_x \quad (4)$$

$$\dot{y} = \frac{dy}{dt} = (c - a)x - xz + cy + \mu_y \quad (5)$$

$$\dot{z} = \frac{dz}{dt} = xy - bz + \mu_z \quad (6)$$

x, y ve z durum değişkenleridir.

a, b ve c sistemin parametreleridir.

μ_x, μ_y ve μ_z; adaptif kontrol sinyalleridir ve sistemin dinamiklerini değiştirmek için eklenmiştir. Adaptif kontrol sinyalleri denklem 7, 8 ve 9 ile gösterilmiştir.

$$\mu_x = -k_1 x \quad (7)$$

$$\mu_y = -k_2 y \quad (8)$$

$$\mu_z = -k_3 z \quad (9)$$

Burada k_1, k_2 ve k_3 başlangıçta bilinmeyen adaptif kazançlardır ve zamanla değişir.

Daha gelişmiş bir kontrol yaklaşımıyla, adaptif kazançlar denklem 10, 11 ve 12 ile gösterilmiştir.

$$\frac{dk1}{dt} = \gamma_1 x^2 \quad (10)$$

$$\frac{dk2}{dt} = \gamma_2 y^2 \quad (11)$$

$$\frac{dk3}{dt} = \gamma_3 z^2 \quad (12)$$

k_1, k_2, k_3; adaptif kazanç olup, zamanla değişerek sistemi kaotik hareketlerini kontrol altına almaya çalışır.

$\gamma_1, \gamma_2, \gamma_3$; adaptasyon hızlarını belirleyen pozitif sabitlerdir.

k_i değerleri, sistemin durum değişkenleri (x, y ve z) büyüdükçe artar.

Gamma (γ_i) Katsayıları:

Gamma katsayıları: adaptasyon hızını belirler. Matematiksel olarak sabit pozitif değerlerdir ve sistemin kararlılığına göre tasarımcı tarafından seçilir**.** Her adaptif kazanç değişimi her zaman pozitif katkı yapar.

Büyük (γ_i) adaptif kazanç daha hızlı artar, sistem hızlı tepki verir.

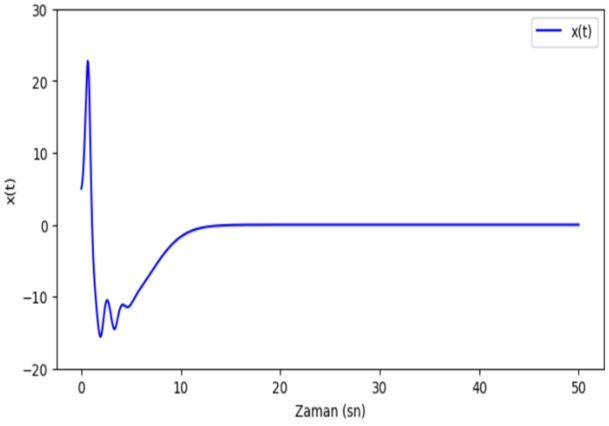
Küçük (γ_i) adaptif kazanç daha yavaş artar, sistem daha yumuşak tepki verir.

Adaptif kontrol katsayılarının hesaplanması Lyapunov fonksiyonu seçimi ile yapılır. Örnek olarak aşağıdaki Lyapunov fonksiyonu alınır [4]:

$$V = 1/2\ (x^2 + y^2 + z^2) + (1/(2\gamma_1))k_1^2 + (1/(2\gamma_2))k_2^2 + (1/(2\gamma_3))k_3^2 \quad (13)$$

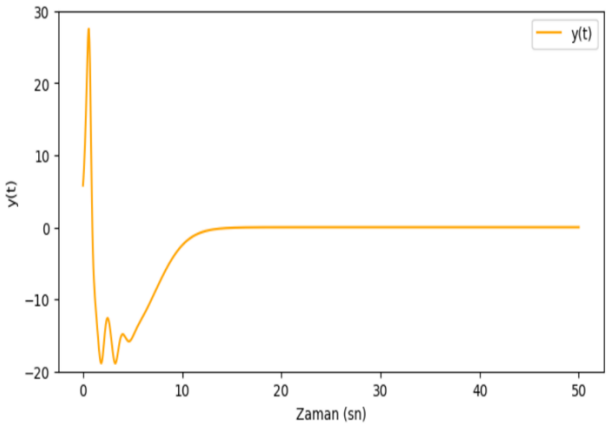
Buradan türev alınarak sistemin kapalı çevrim kararlılığı için gerekli şartlar elde edilir. Adaptasyon yasaları denklem (10)-(12) seçilerek Lyapunov türevinde belirsiz terimler yok edilir. Bu nedenle γ katsayıları sistem tasarımcısı tarafından pozitif sabitler olarak belirlenir. Büyük γ değerleri hızlı adaptasyona, küçük γ değerleri ise yumuşak adaptasyona yol açar. Sonuç olarak, k katsayıları zamanla artarak sistemin kaotik davranışlarını bastırır. γ katsayıları ise adaptasyon hızını kontrol eder. Bu katsayılar analitik olarak Lyapunov fonksiyonunun negatif tanımlı olmasını sağlayacak şekilde seçilir [1].

Chen Kaotik Sisteminin x zaman serisinde adaptif kontrol Şekil 8'de grafiksel olarak gösterilmiştir.



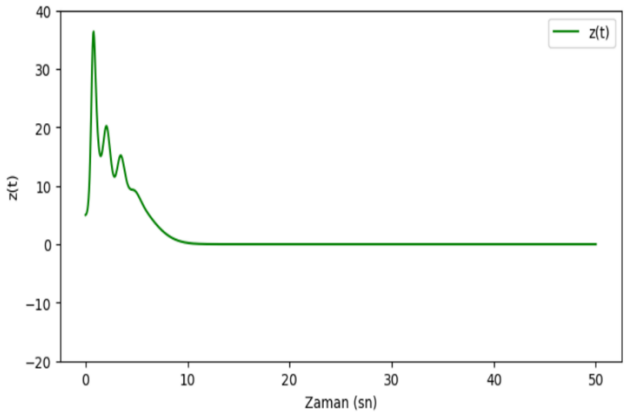
Şekil 8. Chen kaotik sisteminin x zaman serisinde adaptif kontrol

Chen Kaotik Sisteminin y zaman serisinde adaptif kontrol Şekil 9'da grafiksel olarak gösterilmiştir.



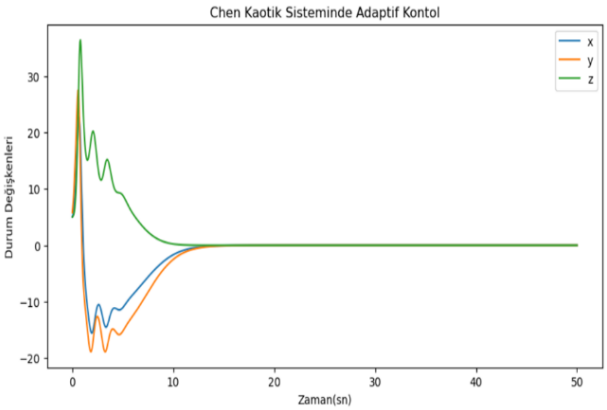
Şekil 9. Chen kaotik sisteminin y zaman serisinde adaptif kontrol

Chen Kaotik Sisteminin z zaman serisinde adaptif kontrol Şekil 10'da grafiksel olarak gösterilmiştir.



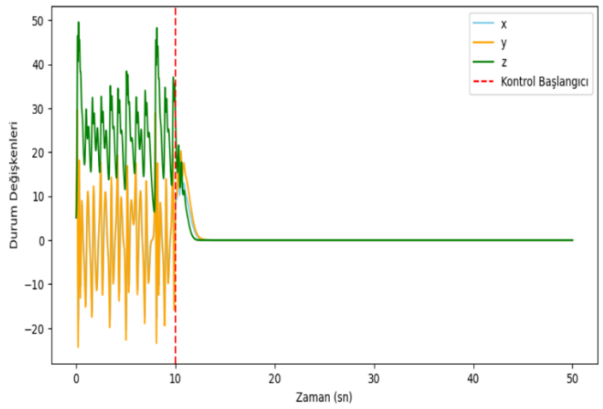
Şekil 10. Chen kaotik sisteminin z zaman serisinde adaptif kontrol

Chen Kaotik Sisteminin x- y- z zaman serilerinde adaptif kontrol 0. saniyeden itibaren Şekil 11'de '0' noktası referans alınarak grafiksel olarak gösterilmiştir.



Şekil 11. Chen kaotik sisteminde adaptif kontrol

Chen Kaotik Sisteminin x- y- z zaman serilerinde adaptif kontrol 10. saniyeden itibaren Şekil 12'de '0' noktası referans alınarak grafiksel olarak gösterilmiştir.



Şekil 12. Chen kaotik sisteminde adaptif kontrol

Chen kaotik sistemine uygulanan adaptif kontrol algoritmasının x, y ve z durum değişkenleri üzerindeki etkisini göstermektedir. Başlangıçta yüksek genlikli ve düzensiz salınımlar sergileyen sistem, zamanla adaptif kontrol etkisiyle sönümlenmiş ve her üç durum değişkeni de referans değer olan sıfıra doğru yönelmiştir. Bu durum, sistemin kaotik davranışının başarıyla bastırıldığını ve kontrol algoritmasının etkin biçimde çalıştığını göstermektedir. Kontrol algoritması, sistem hatalarını sürekli ölçerek kazançları dinamik olarak güncellemiş ve kontrol girişlerini buna göre uyarlamıştır. Bu sayede sistemin farklı evrelerinde değişen dinamiklerine uyum sağlanmış ve kararlı bir yapı elde edilmiştir. Özellikle Chen sistemi gibi güçlü kaotik karaktere sahip bir yapının kısa sürede dengeye ulaşması, kullanılan adaptif kontrol yapısının esneklik ve doğruluk bakımından güçlü bir performans sergilediğini göstermektedir.

Chen Kaotik Sisteminin Adaptif Kontrolünde Parametre Belirsizliği ve Bozucu Etkiler

Adaptif kontrol tasarımında parametre belirsizliği, sistem parametrelerinin tam olarak bilinmemesi veya zamanla değişmesidir. Chen sisteminde a, b, c parametreleri kesin olarak bilinmeyebilir. Bu durumda adaptif kontrol tasarımında denklem 14, 15 ve 16 elde edilir [6]:

$$a=a_0+\Delta_a \quad (14)$$

$$b=b_0+\Delta_b \quad (15)$$

$$c=c_0+\Delta_c \quad (16)$$

Burada $a_0 + b_0 + c_0$ nominal (bilinen) değerler.

Burada Δ_a, Δ_b, Δ_c parametre hatalarını ifade eder. Belirsizlikler, kontrol performansını doğrudan etkiler ve sistemin kararlılığını bozabilir.

Bozucu etkiler, sistem üzerinde kontrol dışı meydana gelen dışsal girişler veya gürültülerdir.

Dış bozucu giriş d(t) sisteme eklenirse denklem 17, 18 ve 19 elde edilir [6]:

$$\dot{x} = \frac{dx}{dt} = \alpha(y - x) + \mu_x + d_1(t) \quad (17)$$

$$\dot{y} = \frac{dy}{dt} = (c - a)x - xz + cy + \mu_y + d_2(t) \quad (18)$$

$$\dot{z} = \frac{dz}{dt} = xy - bz + \mu_z + d_3(t) \quad (19)$$

$d_1(t)$, $d_2(t)$, $d_3(t)$ dışsal Bozucu etkiler, rastgele veya deterministik olabilir. Bunlar kontrolün etkisini azaltabilir ve kaotik sistemin kararlılığını bozabilir.

Bu durumda sistem genel formda denklem 20 deki gibi yazılır:

$$\dot{x} = f(x, \theta) + d(t) \quad (20)$$

Burada $\theta=[a, b, c]^T$ parametre vektörüdür.

Sistemin denge noktasına ($x^* = 0$) yönlendirilmesi durumunda kontrol hedeflenir.

Kontrol edilmek istenen sisteme bir kontrol girişi u(t) eklenirse denklem 21 elde edilir [6]:

$$\dot{x} = f(x, \theta) + B\mu + d(t) \quad (21)$$

Burada B, kontrol giriş matrisidir.

Lyapunov tabanlı adaptif kontrol yaklaşımıyla kontrol yasası denklem 22 elde edilir. Bu denklemin amacı sistemi kararlı hale getirmketir [6]:

$$u = -Kx - \hat{\theta}^T \varphi(x) \quad (22)$$

K: geri besleme kazancı (kararlılığı sağlar)

K'nın amacı durum değişkenlerini denge noktasına ($x \rightarrow 0$) yönlendirmektir.

$\phi(x)$: regresyon vektörü

$\hat{\theta}$:parametrelerin tahmini

Bozucu etkiler güçlü ise (denklem 23) kayma kipli kontrol kullanılır:

$$u = -Kx - \hat{\theta}^T \varphi(x) - \eta\, \mathrm{sgn}(x) \quad (23)$$

Sonuçlar

Yapılan simülasyonlar sonucunda, kullanılan adaptif kontrol algoritmasının sistemin kaotik davranışını başarılı bir şekilde düzenlediği gözlemlenmiştir. Kontrol öncesinde öngörülemez ve düzensiz olan sistem dinamikleri, adaptif kontrol sayesinde belirli bir denge noktasına yönlendirilmiş ve sistemin kararlı bir yapıya ulaşması sağlanmıştır.

Simülasyon ortamında elde edilen başarılı sonuçların fiziksel sistemler üzerinde test edilmesi de büyük önem taşımaktadır. Özellikle robotik, biyomedikal ve finansal sistemler gibi kaotik davranış gösteren alanlarda adaptif kontrolün uygulanabilirliği değerlendirilmelidir. Ayrıca, endüstriyel süreçlerde ve enerji sistemlerinde kaotik dalgalanmaların kontrolü için geliştirilen yöntemlerin test edilmesi, teorik çalışmaların pratik uygulamalarla desteklenmesini sağlayacaktır.

Adaptif kontrolün yapay zekâ temelli yöntemler, örneğin yapay sinir ağları ve bulanık mantık ile desteklenmesi, sistemin daha hızlı uyum sağlamasına ve performansının gelişmesine yardımcı olabilir. Özellikle derin öğrenme ve pekiştirmeli öğrenme tekniklerinin adaptif kontrol stratejilerine entegre edilmesi, daha öngörülebilir ve

kararlı sistem dinamikleri elde edilmesini mümkün kılabilir. Kontrol parametrelerinin otomatik ayarlanmasını sağlayan adaptif algoritmaların geliştirilmesi, sistemin farklı koşullara daha hızlı yanıt vermesini sağlayabilir.

Gelecek çalışmalar açısından, adaptif kontrol yöntemlerinin daha karmaşık ve yüksek boyutlu kaotik sistemlerde uygulanabilirliği araştırılmalı, klasik kontrol teorisi ile yapay zekâ tabanlı yaklaşımların birlikte kullanıldığı hibrit yaklaşımlar geliştirilmelidir.

Etik kurul onayı ve çıkar çatışması beyanı

Hazırlanan makalede etik kurul izni alınmasına gerek yoktur. Hazırlanan makalede herhangi bir kişi/kurum ile çıkar çatışması bulunmamaktadır.

Kaynaklar

[1] G. Chen and T. Ueta, "Yet another chaotic attractor," *Int. J. Bifurcation Chaos*, vol. 9, no. 7, pp. 1465–1466, Jul. 1999.

[2] X. P. She, "Two synchronization schemes for Chen chaotic system," in *Appl. Mech. Mater.*, vols. 385–386, pp. 915–918, Aug. 2013, doi: 10.4028/www.scientific.net/AMM.385-386.915.

[3] T. Liu and T. Chen, "Network synchronization with an adaptive coupling strength," arXiv preprint, Oct. 2006.

[4] H.-T. Yau and C.-L. Chen, "Adaptive sliding mode control for uncertain chaotic systems," *Chaos, Solitons and Fractals*, vol. 32, no. 4, pp. 1453–1461, May 2007, doi: 10.1016/j.chaos.2005.11.092.

[5] X. Zhang, X. Li, and X. Han, "Design of hybrid controller for synchronization control of Chen chaotic system," *J. Nonlinear Sci. Appl.*, vol. 10, no. 6, pp. 3320–3327, Jun. 2017. en.wikipedia.org+6isr-publications.com+6scientific.net+6

[6] H.-T. Yau, "Design of adaptive sliding mode controller for chaos synchronization with uncertainties," *Chaos Solitons & Fractals*, vol. 22, no. 2, pp. 341–347, Oct. 2004, doi: 10.1016/j.chaos.2004.02.004.

[7] P. Guang and W. Jing, "Design of an adaptive sliding mode controller for synchronization of fractional-order chaotic systems," *Acta Phys. Sin.*, vol. 64, no. 4, Apr. 2015, doi:10.7498/aps.64.040505.

[8] L. Du, F. Wang, J. Pian, and Z. Han, "Adaptive switching control for projected synchronization of chaotic systems with uncertainties," *Adv. Mater. Res.*, vol. 499, pp. 360–365, Apr. 2012, doi:10.4028/www.scientific.net/AMR.499.360.

[9] Q. Ye *et al.*, "Adaptive feedback control for synchronization of chaotic neural systems with parameter mismatches," *Complexity*, vol. 2018, Article 5431987, Jan. 2018.

[10] T. Yang, C. M. Yang, and L.-B. Yang, "A detailed study of adaptive control of chaotic systems with unknown parameters," *Dynamics and Control*, vol. 8, pp. 255–267, Jul. 1998, doi:10.1023/A:1008258403620.

[11] E. Ott, C. Grebogi, and J.A. Yorke, Controlling Chaos. Physical Review Letters, 64, 1196-1199, 1990.

[12] K. Pyragas, Continuous control of chaos by self-controlling feedback. *Physics letters A*, *170*(6), 421-428, 1992.

[13] G. V. Emel'yanov, a queuing system with apparatus which can go out of service and be restored. *Problemy Peredachi Informatsii*, *3*(3), 59-63, 1967.

[14] C. Hua and X. Guan, "Adaptive control for chaotic systems," Chaos, Solitons & Fractals, vol. 22, no. 1, pp. 55–60, 2004, doi: 10.1016/j.chaos.2003.12.071.

[15] Khan, Ayub, and Ram Prasad, "Adaptive Control for Synchronization of Identical and Non-Identical Chaotic Systems with Unknown Parameters," *J. Eng. Technol. Appl. Sci.*, vol. 5, no. 2, pp. 77–92, 2020, doi: 10.30931/jetas.756968.

[16] S. Vaidyanathan and C. Volos, "Analysis and adaptive control of a novel 3-D conservative no-equilibrium chaotic system," *Archives of Control Sciences*, vol. 25, no. 3, pp. 333–353, 2015, doi: 10.1515/acsc-2015-0022.

[17] S. Eshaghi, N. Kadkhoda, and M. Inc, "Chaos control and synchronization of a new fractional laser chaotic system," *Qualitative Theory of Dynamical Systems*, vol. 23, no. 5, 2024, doi: 10.1007/s12346-024-01097-7.

[18] H. Ding, J. Qian, D. Tian, & Y. Zeng, Norm-Based Adaptive Control with a Novel Practical Predefined-Time Sliding Mode for Chaotic System Synchronization. Mathematics (2227-7390), 13(5), 2025.

[19] J. Gleick, *Chaos: Making a New Science*. New York, NY, USA: Penguin Books, 1987.

[20] G. Boeing, "Visual Analysis of Nonlinear Dynamical Systems: Chaos, Fractals, Self-Similarity and the Limits of Prediction," *Systems*, vol. 4, no. 4, pp. 1–15, Nov. 2016, doi: 10.3390/systems4040037.

[21] A.-B. A. Al-Hussein, "Chaos phenomenon in power systems: A review," *Iraqi Journal for Electrical and Electronic Engineering*, vol. 17, no. 2, pp. 219–240, 2021.

[22] E. N. Lorenz, "Deterministic nonperiodic flow," *J. Atmos. Sci.*, vol. 20, no. 2, pp. 130–141, 1963.

[23] L. E. X. Zhou, “Chen system: relations with Lorenz and dynamic properties,” *Chaos*, vol. XX, no. Y, pp. ZZ–ZZ, 20AA.

[24] G. Qi, G. Chen, S. Du, Z. Chen, and Z. Yuan, "Analysis of a new chaotic system," *Physica A: Statistical Mechanics and its Applications*, vol. 352, no. 2, pp. 295–308, 2005.

25] K. Ogata, *Modern Control Engineering*, 5th ed. Upper Saddle River, NJ, USA: Prentice Hall, 2010.

[26] K. J. Åström and B. Wittenmark, *Adaptive Control*, 2nd ed. Mineola, NY, USA: Dover Publications, 2013.

Dicle University
Journal of Engineering
https://dergipark.org.tr/tr/pub/dumf
duje.dicle.edu.tr

Research Article

NeuroHybridNet: A Hybrid EEG Classification Model with Autoencoder-Enhanced Fractal-Wavelet Features

Hazret TEKİN

Şırnak University, Vocational School of Technical Sciences, hazrettekin@sirnak.edu.tr, Orcid No: 0000-0002-9379-721X

ARTICLE INFO

Article history:

Received 3 June 2025
Received in revised form 16 September 2025
Accepted 21 September 2025
Available online 30 September 2025

Keywords:

Autoencoder, CWT, EEG, Fractal Dimension, Machine Learning.

Doi: 10.24012/dumf.1713314

* Corresponding author

ABSTRACT

Electroencephalography (EEG) signals offer a rich but complex source of information for assessing cognitive states, particularly in dynamic and high-stakes environments such as driver attention monitoring, where rapid and accurate detection of mental fatigue or distraction is critical for safety and performance.This study proposes WaveFrac-AE, a hybrid EEG classification model that combines time-frequency analysis, fractal dynamics, and nonlinear descriptors with Autoencoder-based dimensionality reduction. EEG signals representing three cognitive states—focused, distracted, and drowsy—are transformed into a compact latent space capturing both temporal and structural complexity. By fusing Continuous Wavelet Transform features with fractal measures (Petrosian, Hurst, DFA), the model achieves robust representation of non-stationary EEG dynamics. The Autoencoder component enhances generalizability by filtering noise and redundancy, enabling accurate and scalable mental state classification for real-time neuroergonomic applications. This hybrid approach has been tested with various machine learning algorithms—namely XGBoost, LightGBM, CatBoost, Random Forest, and Support Vector Machines (SVM). In subject-specific analyses, SVM achieved an average accuracy exceeding 97%, while the aggregated dataset—combining all subjects—yielded an accuracy surpassing 92%. Comparisons with contemporary studies suggest that this method occupies a competitive position and, in numerous cases, demonstrates higher performance. Consequently, the proposed model offers high-performance solution in driver attentiveness monitoring systems, thereby showing substantial potential for the development of early warning systems integrated into smart automobiles.

Introduction

In contemporary intelligent transportation systems, the real-time monitoring of driver attention levels has become a critical component for ensuring both road safety and passenger well-being. Particularly under prolonged and monotonous driving conditions, transitions in the driver's cognitive state—ranging from focused to distracted or drowsy—can significantly increase the risk of serious, and often fatal, traffic accidents [1]. To proactively detect and mitigate such high-risk scenarios, next-generation smart vehicles demand the integration of advanced technologies capable of continuously tracking and interpreting the driver's neural activity with precision and reliability [2]. At this point, portable EEG acquisition systems—either embedded into in-vehicle interfaces or designed as wearable devices for ergonomic use—offer a promising solution for uninterrupted assessment of attentional states, thereby contributing to enhanced situational awareness and driving safety [3]. Electroencephalography (EEG) signals are widely preferred for real-time observation of human brain activity due to their non-invasive nature and high temporal resolution. However, the inherently noisy structure, non-stationary behavior, and nonlinear dynamics of EEG signals pose significant challenges for accurate analysis and hinder the reliable detection of rapidly fluctuating attentional states in drivers [4]. Traditional approaches based on unidimensional or narrowband frequency analysis fail to fully capture this complexity, often overlooking transient fluctuations in attention [5]. Moreover, most feature extraction techniques reported in the literature rely on single-type and single-domain descriptors, typically constrained to either the time or frequency domain, while disregarding the fractal and chaotic properties inherently present in EEG signals [6]. This uni-dimensional perspective considerably limits the representational capacity of extracted features and constrains the ability of classification models to accurately distinguish between complex and overlapping cognitive states [7]. Consequently, hybrid models that integrate multiple complementary feature types—spanning time, frequency, and complexity domains—are increasingly favored alongside deep learning and advanced machine learning approaches, as they offer a more comprehensive characterization of EEG signals and improve the effectiveness of feature extraction. This enriched representation enhances the fidelity of mental state classification, particularly in real-time driver monitoring scenarios where nuanced cognitive dynamics must be reliably detected.

In the literature, subject-specific approaches are commonly employed in EEG-based mental state classification tasks, primarily due to the pronounced structural and functional variability of EEG signals across individuals [8]. These inter-individual differences are primarily attributed to factors such as cranial anatomy, electrode placement variability, and individual cognitive response patterns [9]. Although individually tailored models can capture subtle variations in EEG signals more effectively and thus achieve higher classification accuracy, the need to retrain the model for each new user imposes a significant cost in terms of time and computational resources—particularly in real-time applications [10]. To address these limitations, common-subject approaches have been developed, aiming to minimize the need for subject-specific calibration by training generalized models on EEG data collected from multiple individuals [11]. However, due to substantial inter-individual variability in EEG signals, the classification performance of these approaches is generally lower compared to subject-specific models [12]. This underscores the necessity of establishing a delicate balance between generalizability and classification accuracy in EEG-based attention monitoring systems.

This study introduces a novel hybrid framework for driver attention classification based on EEG signals, integrating diverse feature extraction techniques with deep representational learning through Autoencoder-driven dimensionality reduction. The proposed approach has been systematically assessed under both subject-specific and common-subject evaluation schemes, facilitating a rigorous comparison of the model's responsiveness to inter-individual variability and its capacity for cross-subject generalization. By leveraging this dual-paradigm assessment, the framework not only demonstrates adaptability to personalized neural patterns but also exhibits robustness in broader, population-level applications. The proposed approach—referred to as WaveFrac—aims to capture the complex patterns associated with varying levels of driver attention by holistically integrating features derived from multiple domains, including Continuous Wavelet Transform (CWT) and fractal descriptors such as Petrosian Fractal Dimension, Hurst Exponent, and Detrended Fluctuation Analysis (DFA). In this hybrid framework, the high-dimensional and noise-prone nature of EEG data is further addressed through an Autoencoder (AE) architecture, which transforms the input into a more compact and semantically meaningful latent representation. This dimensionality reduction not only enhances computational efficiency but also substantially improves the model's generalization capability. To comprehensively assess the classification performance of the proposed framework, a diverse set of machine learning algorithms—namely XGBoost, LightGBM, CatBoost, Random Forest, and Support Vector Machines (SVM) was utilized to discriminate between focused, distracted, and drowsy mental states. By validating the model across multiple classifiers and data variations, this strategy enhances the methodological rigor and demonstrates the adaptability, reliability, and robustness of the hybrid system in real-world driver attention analysis scenarios.

The originality of the proposed hybrid model lies in its integrative strategy that captures the structural complexity of EEG signals through the fusion of time-frequency, fractal, and statistical features—rather than relying on single-domain analyses, as commonly observed in prior studies [13]. By leveraging CWT for transient spectral dynamics, fractal measures (e.g., Petrosian, Hurst, DFA) for long-range signal dependencies, and Autoencoder-based dimensionality reduction to condense high-dimensional, noisy data into a more coherent latent space, the model preserves the strengths of each technique while mitigating their individual limitations. Furthermore, the framework has been rigorously evaluated under both subject-specific and common-subject paradigms using EEG data from five individuals, allowing for a comprehensive assessment of both personalization accuracy and cross-subject generalizability. This integrative and methodologically rigorous design distinguishes WaveFrac-AE as a novel and robust solution, capable of capturing the multidimensional nature of EEG signals while ensuring reliable performance across varying users and cognitive states.

The structure of this article unfolds across six integral sections. Following the introduction, the second section synthesizes key contributions from the literature on EEG-based mental state classification, critically examining the methodologies employed and the performance outcomes reported. The third section elaborates on the experimental framework, detailing the characteristics of the EEG dataset, participant demographics, and the data acquisition protocol. The fourth section presents the methodological core of the study, delineating the proposed hybrid classification architecture, which integrates time-frequency analysis via CWT, fractal dimension–based descriptors, Autoencoder-driven dimensionality reduction, and multiple machine learning classifiers. The fifth section reports the empirical findings under both subject-specific and common-subject paradigms, supported by performance metrics including classification accuracy, confusion matrices, and ROC analyses. The final section offers a holistic interpretation of the results, situates the study within the broader scientific context, and outlines prospective avenues for future exploration**.**

Literature Studies

In recent years, EEG-based mental state classification has attracted considerable attention due to its broad applications in monitoring driver fatigue, assessing mental workload, and detecting human stress. Researchers have explored various time-frequency analysis techniques, advanced feature-selection strategies, and deep-learning pipelines to address the complex, non-stationary nature of EEG signals. The following section reviews a series of representative studies, each contributing distinct insights into data preprocessing, feature extraction, or classification methodologies.

Acı et al. distinguished three cognitive conditions—focused, unfocused, and drowsy—by combining short-time Fourier transform (STFT) with an SVM classifier, surpassing 96% accuracy [14]. Building on similar aims in

driver drowsiness detection, Alreshidi et al. proposed a multimodal framework for detecting pilots' mental states using EEG signals, combining automated preprocessing, Riemannian geometry-based feature extraction, and hybrid ensemble learning. Their method achieved 86% accuracy on EEG data collected from 18 pilots in flight simulations [15]. Nuamah and Seong likewise achieved high accuracy in detecting multiple cognitive load levels in a driving-simulator environment by leveraging well-labeled tasks and advanced EEG features, consistently surpassing 90% [16]. Hag et al. developed a stress detection framework using frontal EEG signals, salivary alpha-amylase levels, and machine learning classifiers under two induced stress levels. Their SVM-based model achieved a classification accuracy of 93.2%, utilizing optimal features from functional connectivity and temporal-spectral EEG domains [17]. Rahman et al. analyzed EEG signals to classify mental states using ten different machine learning algorithms, with hyperparameter tuning via RandomSearchCV. Among the models, SVM achieved the highest accuracy of 95.36%, followed closely by Gradient Boosting and XGBoost classifiers [18]. Zeng et al. proposed a cross-subject fatigue detection model (GDANN) that integrates Domain-Adversarial Neural Networks with GANs to overcome inter-subject variability in EEG signals. Their model achieved an average accuracy of 91.63%, outperforming traditional classifiers in EEG-based fatigue detection tasks [19]. Kimmatkar and Babu developed an EEG-based emotion detection system to classify 12 subtle emotional states and evaluated the impact of meditation music therapy on mental state regulation. Using Chirplet transform features and a multimodel classifier approach, their system achieved successful emotion recognition and demonstrated a 75% positive emotional shift with music therapy intervention [20]. Sharma et al. proposed a stress detection method based on short-duration EEG signals, utilizing entropy features extracted via stationary wavelet transformation. Their SVM model, optimized using the Whale Optimization Algorithm, achieved a high classification accuracy of 97.26%, demonstrating the method's reliability for timely stress recognition [21]. Kamińska et al. investigated EEG-based stress classification in a virtual reality environment using relaxing and stressful VR scenes, monitored via the EMOTIV EPOC Flex system. Among several classifiers tested, MLP and SVM achieved the highest accuracy of 96.42% when all EEG frequency bands were used [22]. Rajendran et al. analyzed EEG signals from 25 subjects under stress and non-stress conditions using DWT-based sub-band energy features and statistical validation via the Wilcoxon signed-rank test. Their cubic SVM classifier achieved 95.83% accuracy and maintained 89.74% accuracy when validated on an external EEG dataset [23].

Dataset and Experimental Material

In this study, EEG recordings were collected from five neurologically healthy adults across seven experimental sessions per participant, with the first two serving as acclimatization and the remaining five for data collection [14]. On average, each participant contributed five sessions, totaling approximately 25 hours of EEG data. During each 35–55-minute session, participants engaged in a passive task using Microsoft Train Simulator, aiming to maintain train speed within set limits with minimal control input. Three cognitive states—focused (0–10 min), unfocused (10–20 min), and drowsy (20–30 min)—were defined based on temporal segments. EEG signals were recorded using the Emotiv Epoc neuroheadset from seven active electrodes (F7, F3, P7, O1, O2, P8, AF4), sampled at 128 Hz, and wirelessly transmitted via Bluetooth. One sample per second was labeled according to cognitive state, yielding segmented data across the three conditions. Table 1 summarizes dataset specifications, and Figure 1 shows a representative raw EEG waveform from one channel.

Table 1. Overview of the EEG dataset characteristics [14]

Feature	**Description**
Number of Participants	5 (Healthy, voluntary students)
Number of Sessions (Experiments)	7 per participant (first 2 for training/adaptation, last 5 for actual data collection)
Duration of Each Session (min)	35–55 min (average ~40 min)
Total Recording Duration	Approximately 25 hours (5 participants × 5 sessions × ~1 hour)
EEG Device	Emotiv Epoc (128 Hz sampling rate, 0.2–43 Hz frequency band)
Electrodes Used	7 main electrodes: F7, F3, P7, O1, O2, P8, AF4 (modified placement)
Mental States	1) Focused 2) Unfocused 3) Drowsy

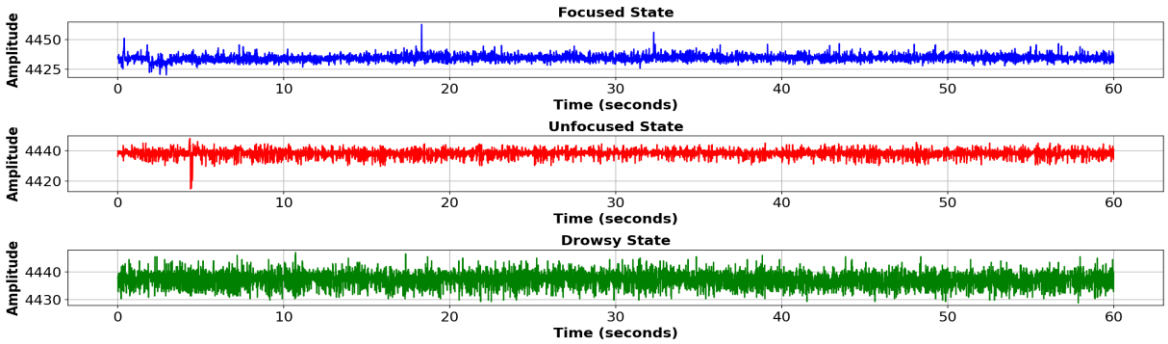


Figure 1. Raw EEG waveforms associated with three cognitive conditions

Methodology

This study presents WaveFrac-AE, a hybrid EEG classification framework that integrates handcrafted multiscale features with deep representation learning. The model fuses CWT–based time-frequency descriptors and nonlinear fractal metrics to construct a robust representation of cognitive states. CWT enables high-resolution, scale-continuous analysis, capturing localized EEG oscillations with statistical and energy-based measures such as mean, standard deviation, skewness, kurtosis, and wavelet entropy variants (Shannon, Rényi) [24]. The choice of CWT over the more conventional Discrete Wavelet Transform (DWT) is motivated by its superior ability to provide continuous, high-resolution analysis across all time and scale levels [25]. CWT is preferred in this study over DWT due to its finer spectral sensitivity, which is crucial for capturing the transient dynamics and subtle cognitive fluctuations in nonstationary EEG signals [26]. To capture EEG's long-range and scale-invariant dynamics, this study employs PFD, Hurst Exponent, and DFA as fractal analysis complements CWT by quantifying global nonlinear patterns and persistent temporal structures, enriching the model's representation for cognitive state classification [27].

To enhance classification accuracy and reduce complexity, all extracted features are compressed into a compact latent space using an Autoencoder. Unlike traditional reduction methods, the Autoencoder preserves key discriminative patterns while suppressing noise and redundancy, making it essential for refining the hybrid wavelet-fractal feature set. This integration not only strengthens generalization but also complements the dual-domain representation, enabling more robust EEG-based attention state classification. To evaluate classification performance, the proposed model was tested using multiple algorithms (SVM, Random Forest, XGBoost, LightGBM, CatBoost), enabling a comprehensive assessment of its robustness and generalizability across learning paradigms. This strategy highlights how the hybrid feature set interacts with diverse classifiers, revealing consistent gains in accuracy and adaptability. The integration of deep features encoding traditional classifiers significantly boosts discriminative power, validating the model's effectiveness for EEG-based mental state classification. The study's multi-classifier evaluation reveals the model's strong adaptability and enhanced discriminative power, resulting in improved accuracy and generalization for EEG-based mental state classification. The overall structure of the proposed hybrid model is illustrated in Figure 2, detailing each stage of the framework with concise process descriptions.

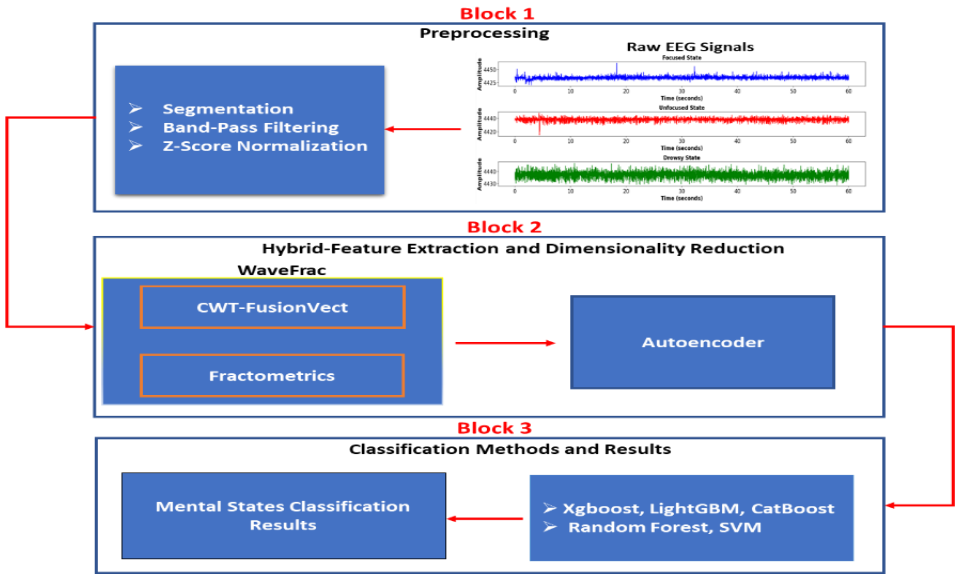


Figure 2. Block diagram of the proposed EEG-based classification pipeline

➢ **Block 1 (Preprocessing):** Raw EEG signals are segmented, band-pass filtered (0.5–45 Hz) to remove noise, and then normalized using Z-score to standardize amplitudes, ensuring clean and consistent input for analysis.

➢ **Block 2 (Feature Extraction & Dimensionality Reduction):** In the proposed WaveFrac architecture, two complementary feature sets—CWT-FusionVect (derived from time-frequency coefficients via statistical moments, energy measures, and entropy-based descriptors) and Fractometrics (capturing fractal complexity via PFD, Hurst, and DFA)—are extracted from EEG signals. These high-dimensional descriptors are then fused and compressed using an Autoencoder to generate a compact latent representation, enabling robust and scalable mental state classification.

➢ **Block 3 (Classification Methods and Results):** Autoencoder-derived features are classified into cognitive states (focused, unfocused, drowsy) using algorithms like SVM, Random Forest, and boosting methods. Performance is evaluated via 5-fold cross-validation using accuracy, confusion matrices, and ROC curves.

Preprocessing

During the preprocessing stage, raw EEG signals are first segmented into fixed-length time windows to structure the analysis of temporal dynamics. Each segment is treated independently, enabling localized examination of cognitive patterns. After segmentation, a band-pass filter (0.5–45 Hz) is applied to remove irrelevant frequency components and retain those associated with cognitive activity. A fifth-order Butterworth filter with zero-phase distortion is employed to preserve signal integrity during this step. Finally, Z-score normalization is performed to reduce inter-channel variability and standardize signal amplitudes, ensuring that the model is not biased by differences in magnitude across channels or recording sessions. All preprocessing operations—including segmentation, filtering, and normalization—are applied uniformly across all subjects and EEG channels to guarantee methodological consistency. These steps enhance the quality and relevance of the data, preparing it for reliable feature extraction. Figure 3 illustrates sample EEG signals before and after preprocessing, highlighting the effectiveness of the pipeline in isolating clean signal components across different cognitive states.

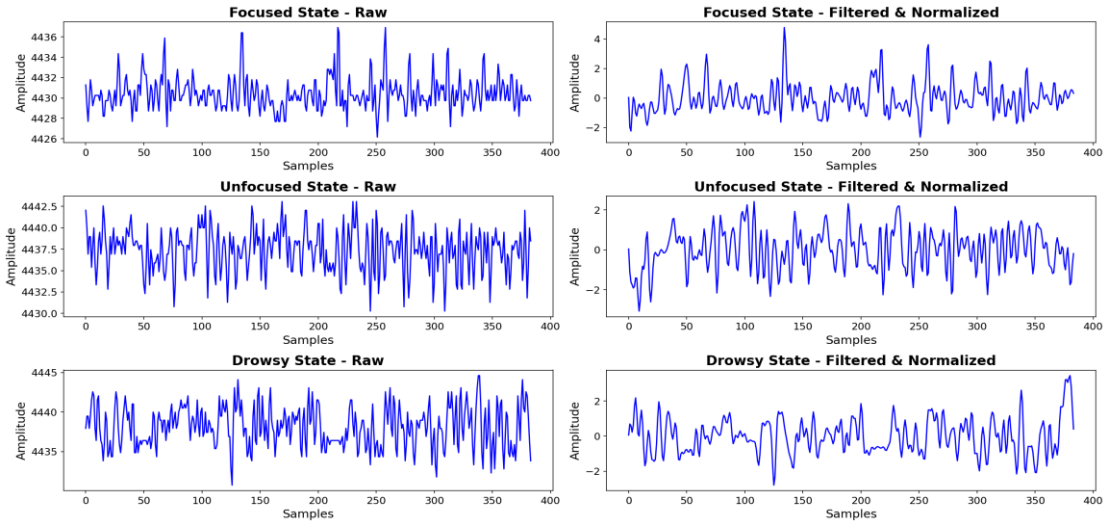


Figure 3. EEG signal raw vs. filtered-normalized

Hybrid Feature Extraction and Dimensionality Reduction

CWT-derived multiscale features for EEG dynamics

EEG is a powerful non-invasive method for tracking brain activity, but its complex, dynamic nature requires time-frequency analysis to accurately capture neural oscillations linked to cognitive and clinical states [28]. Unlike the Fourier Transform, which provides only global frequency content, and the STFT, which suffers from fixed resolution, CWT offers multi-resolution analysis—making it ideal for capturing transient, time-varying neural patterns in EEG signals [29]. While CWT is traditionally employed to compute time-frequency coefficients, this study emphasizes a more advanced usage: extracting diverse statistical, energy-based, and entropy-driven features from the wavelet coefficients to map subtle neural dynamics. These descriptors—mean, standard deviation, skewness, kurtosis, and entropy measures—complement fractal features such as Petrosian, Hurst, and DFA, which capture structural irregularity and self-similarity in EEG signals. This fusion creates a synergistic feature space, where CWT highlights transient patterns and fractals model inherent complexity. To extract CWT coefficients, the Continuous Wavelet Transform is applied to EEG signals as formulated in Equation (1), enabling a multi-scale decomposition that captures localized time-frequency patterns essential for feature derivation.

$$\mathrm{CWT}(a,b) = \int_{-\infty}^{\infty} x(t)\psi_{a,b}^{*}(t)\,dt \qquad (1)$$

In Equation (1), x(t) denotes the input signal, $\psi_{a,b}^*(t)$ represents the scaled and shifted wavelet function, a is the scale parameter, and b corresponds to the time-shift parameter. The wavelet coefficients obtained through the CWT encapsulate the time-frequency characteristics of EEG signals and serve as a rich source for extracting informative features. To capture cognitive-related neural dynamics, various features were extracted from CWT coefficients, including statistical (mean, std, skewness, kurtosis), energy-based, and entropy measures (Wavelet, Rényi, Shannon). Together, they provide a rich representation of signal amplitude and spectral complexity, enhancing mental state classification. The corresponding mathematical formulations and notations for these features are presented in the equations below. The mean represents the arithmetic average of the wavelet coefficients. In the mathematical expression provided in Equation (2), μ denotes the mean value, N is the total number of samples in the signal and, C_i refers to the individual wavelet coefficients.

$$\mu = \frac{1}{N}\sum_{i=1}^{N} C_i \tag{2}$$

The standard deviation quantifies the extent to which the wavelet coefficients deviate from their mean, reflecting the dispersion of the data around the average value. In Equation (3), σ denotes the standard deviation, N represents the total number of samples in the signal, C_i corresponds to the individual wavelet coefficients, and μ is the mean of the coefficients.

$$\sigma = \sqrt{\frac{1}{N}\sum_{i=0}^{n} (C_i - \mu)^2} \tag{3}$$

Skewness is utilized to assess the asymmetry in the distribution of wavelet coefficients, while kurtosis captures the presence of extreme values in the EEG signal, thereby enabling the detection of abrupt changes in neural activity. The mathematical formulations corresponding to these two measures are provided in Equations (4) and (5), respectively. In these equations, Sk denotes the skewness, Ku represents the kurtosis, σ is the standard deviation, N is the total number of samples in the signal, C_i indicates the wavelet coefficients and μ refers to their mean value.

$$Sk = \frac{1}{N}\sum_{i=1}^{N} \left(\frac{C_i - \mu}{\sigma}\right)^3 \tag{4}$$

$$Ku = \frac{1}{N}\sum_{i=1}^{N} \left(\frac{C_i - \mu}{\sigma}\right)^4 - 3 \tag{5}$$

Energy-based features offer a powerful means of analyzing the distribution of energy across different frequency bands in EEG signals, serving as key indicators in the identification of cognitive processes and neurological disorders. Wavelet energy quantifies the energy concentration of the EEG signal at various scales, while relative wavelet energy computes the proportion of energy at each scale, thereby facilitating the interpretation of EEG activity within specific frequency bands. The corresponding mathematical formulations for wavelet energy and relative energy are provided in Equations (6) and (7), respectively.

$$E = \sum_{i=1}^{N} C_i^2 \tag{6}$$

$$RE = \frac{E_{scale}}{\sum_{all_scales} E} \tag{7}$$

In Equations (6) and (7), N denotes the total number of signal samples, C_i represents the wavelet coefficients, E corresponds to the wavelet energy, and RE denotes the relative wavelet energy. The RE value is calculated as the ratio of the energy at each scale (Escale) to the total energy across all scales.

Entropy-based features derived from the CWT are employed to quantify the complexity and irregularity of EEG signals, with Wavelet Entropy specifically serving as a measure of signal disorder and proving useful in the detection of events such as epileptic seizures and alterations in consciousness levels [30]. Rényi Entropy is utilized to analyze the information density and uncertainty embedded within EEG signals, providing a generalized framework for quantifying signal complexity beyond traditional entropy measures [31]. Shannon Entropy, on the other hand, is employed to characterize the relationship between EEG dynamics and underlying cognitive processes [32]. The following equations present the mathematical formulations corresponding to Wavelet Entropy, Rényi Entropy, and Shannon Entropy, respectively.

$$E_i = \sum_{i=1}^{N} |C_i(t)|^2 \quad , \quad p_i = \frac{E_i}{\sum_{j=1}^{N} E_j} \quad , \quad H = -\sum_{i=1}^{N} p_i \log p_i \tag{8}$$

In Equation (8) E_i represents the energy distribution of the wavelet coefficients obtained through the CWT. This energy distribution is normalized to form a probability distribution denoted by pi representation. The symbol H denotes the wavelet entropy, which is computed by taking the logarithm of the probability distribution components to quantify the signal's degree of disorder.

$$p_i = \frac{|C_i|^\alpha}{\sum_{j=1}^{N} |C_j|^\alpha} \quad , \quad H_\alpha = \frac{1}{1-\alpha} \log \sum_{i=1}^{N} p_i^\alpha \tag{9}$$

In Equation (9) p_i denotes the normalized probability distribution derived from the wavelet coefficients. The parameter α defines the order of the entropy and controls the sensitivity of the measure to the distribution's structure. H_α represents the Rényi entropy, which is computed by applying a logarithmic function to the probability distribution, with its value influenced by the chosen α parameter.

$$p_i = \frac{|C_i|}{\sum_{j=1}^{N}|C_j|}, H_s = -\sum_{i=1}^{N} p_i \log_2 p_i \quad (10)$$

Equation (10) presents the mathematical formulation of Shannon entropy, utilizing the same notations as described in the previous entropy measures. The logarithmic expression with base 2 is employed to quantify information in bits. Shannon entropy evaluates the information content of EEG signals by analyzing the distribution of CWT coefficients: higher entropy values indicate a more homogeneous and complex signal distribution, whereas lower entropy values suggest that the energy is concentrated in fewer coefficients, reflecting a more regular and less complex signal structure. The Morlet wavelet was used in this study for its balanced time-frequency resolution, ideal for transient EEG analysis [33]. Figure X displays the CWT scalograms of EEG signals corresponding to focused, unfocused, and drowsy cognitive states. EEG signals across different cognitive states show noticeable diversity in their time-frequency energy patterns. These variations emphasize the non-stationary and dynamic nature of EEG signals. Given the diversity and temporal evolution observed in the scalograms, it is insufficient to rely solely on raw CWT coefficients. Instead, we extract higher-order statistical (mean, standard deviation, skewness, kurtosis), energy-based, and entropy features (Shannon, Rényi, Wavelet entropy) that effectively summarize the signal's structural and spectral behavior over time. This approach enables the model to capture both transient activations and underlying complexity, providing a discriminative feature space well-suited for mental state classification. The use of CWT-derived features is thus not arbitrary but grounded in the visually evident variability across cognitive conditions, as exemplified by the scalograms.

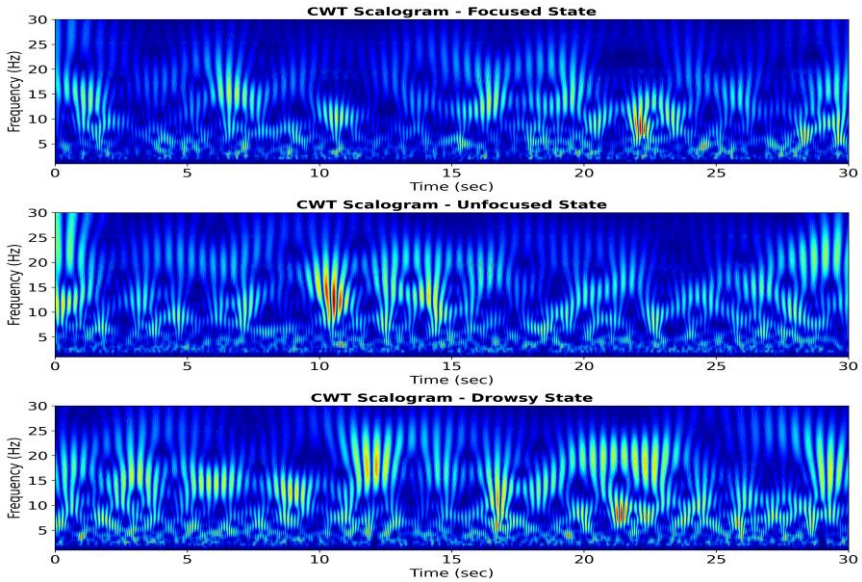


Figure 4. CWT-based scalograms of EEG signals for different mental states

Fractal Features

Fractal dimension analysis is a widely employed technique for quantifying the complexity and irregularity of biomedical signals, and it plays a critical role in uncovering the underlying dynamics of EEG data, which inherently exhibit nonlinear and fractal characteristics [34]. While the CWT is highly effective for performing time-frequency analysis of EEG signals, it does not directly quantify intrinsic properties such as signal irregularity, complexity, or long-range temporal dependencies [35]. Fractal features are employed in this study to capture the nonlinear, self-similar, and scale-invariant properties inherent in EEG signals—characteristics that conventional linear methods often fail to represent. These features provide critical insight into the long-term dependencies and complex temporal dynamics of brain activity, which are essential for distinguishing cognitive states. Among them, PFD offers a compact yet sensitive measure of signal irregularity by quantifying zero-crossings, making it particularly effective in detecting subtle, transient changes in neural activity. The mathematical formulation of PFD is given in Equation (11).

$$\mathrm{PFD} = \frac{\log \mathrm{N}}{\log \mathrm{N} + \log\left(\frac{\mathrm{N}}{\mathrm{N} + 0.4\mathrm{N}_\delta}\right)} \quad (11)$$

In Equation (11), *N* denotes the total number of signal samples, N_δ represents the number of sign changes (zero-crossings) in the first derivative of the signal. This method is directly linked to signal regularity: a signal exhibiting high variability and frequent fluctuations (i.e., high-frequency components) will result in a lower PFD value, whereas a more regular and structured signal will yield a higher PFD. The Hurst exponent is a statistical measure used to evaluate the long-term dependency and predictability of a time series. It yields a value within the range of $0 \leq H \leq 1$, where the magnitude of *H* indicates the

degree of persistence or anti-persistence in the signal. The mathematical formulation of the Hurst exponent is provided in Equation (12).

$$H = \lim_{N\to\infty} \frac{\log\left(\frac{R}{S}\right)}{\log N} \tag{12}$$

In Equation (12), N denotes the length of the time series, R represents the range between the maximum and minimum values within the cumulative signal, and S refers to the standard deviation of the series. The ideal range of the Hurst exponent depends on the intrinsic characteristics of the EEG signal under analysis, as different cognitive or physiological states may manifest varying degrees of long-term temporal correlation. DFA is a robust technique used to evaluate long-range correlations and scale-dependent dynamics within time series data. It quantifies how the residual variance evolves after removing local trends from the signal, thereby capturing the underlying self-similarity and temporal organization. The mathematical formulation of the DFA method is presented in the equations below.

$$Y(k) = \sum_{i=1}^{k} (x_i - \bar{x}) \tag{13}$$

In Equation (13), *Y(k)* represents the cumulative sum of the signal, where, x_i denotes the original signal values and $\bar{x}$ is the mean of the series. In the subsequent step, the integrated signal is divided into non-overlapping segments of equal length *n*, and a linear trend is fitted to each segment. After detrending each window, the fluctuation function *F(n)* is computed as shown in Equation (14), which quantifies the variance of the residuals from the local trends across all segments.

$$F(n) = \sqrt{\frac{1}{N}\sum_{k=1}^{N} (Y(k) - Y_n(k))^2} \tag{14}$$

In Equation (14), $Y_n(k)$ denotes the local trend estimated within each segment, and *N* represents the total number of segments. The fluctuation function *F(n)* is computed for various window sizes *n*, and the scaling behavior of the signal is characterized by plotting *F(n)* against *n* in a log-log plot. The slope of this plot defines the DFA exponent, which serves as a quantitative indicator of long-range correlations. This exponent has been widely employed in EEG studies for applications such as sleep stage analysis, epilepsy detection, and the classification of consciousness levels [36].

Fractal features—PFD, Hurst Exponent, and DFA—complement CWT by capturing nonlinear dynamics and long-range correlations that time-frequency analysis alone may overlook. Each metric targets a distinct aspect of signal complexity: PFD reflects structural irregularity, Hurst indicates long-term memory, and DFA captures scale-invariant fluctuations. Figure 5 provides a visual comparison of three fractal-based features—PFD, Hurst Exponent, and DFA Exponent—across different mental states. The violin plots display the overall distribution and variability of each feature for the three classes (focused, unfocused, and drowsy), while the KDE plots illustrate their density profiles, revealing how these features vary between cognitive conditions. Among the three, PFD shows the most noticeable separation between mental states, suggesting it is particularly effective at capturing signal irregularities related to attentional changes. The DFA Exponent also demonstrates distinct class-dependent patterns, especially in the focused condition, while the Hurst Exponent provides additional insight into long-term signal trends, albeit with more overlap between classes. The integration of PFD, Hurst, and DFA provides a richer, physiologically grounded EEG representation, enhancing the model's ability to detect subtle cognitive transitions. This strengthens the overall accuracy and generalizability of the WaveFrac-AE framework, especially in real-time applications like driver monitoring

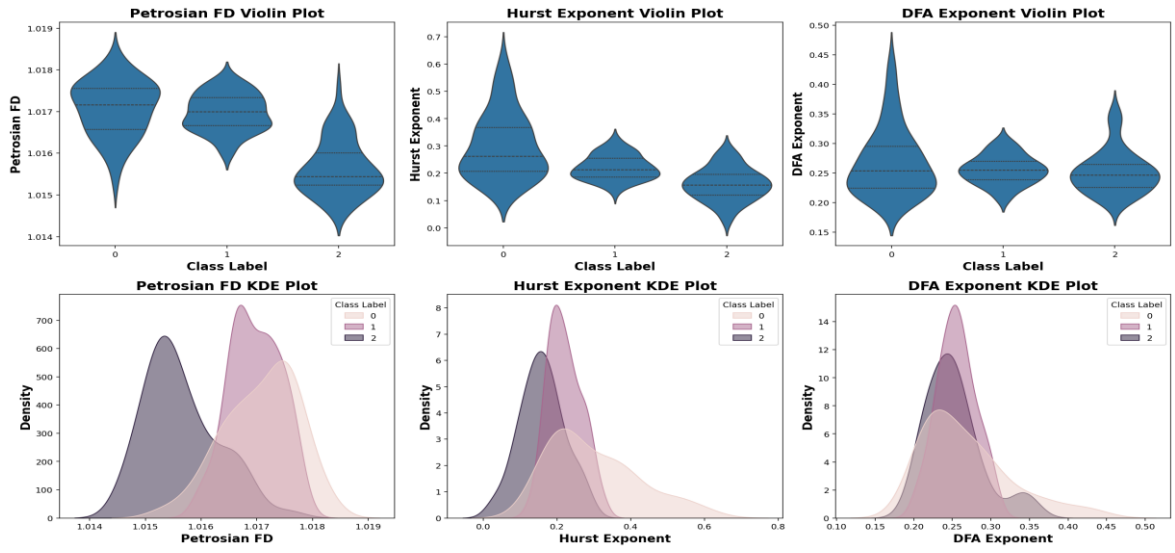


Figure 5. Class-wise distributions of EEG nonlinear features: Petrosian FD, Hurst, and DFA measures

Feature Dimensionality Reduction (Autoencoder)

EEG signals, owing to the inherent complexity of underlying biological processes, are characterized by high dimensionality, substantial noise, and multi-component structure. To enhance classification accuracy and computational efficiency in EEG-based mental state recognition, this study employs an Autoencoder-based dimensionality reduction technique that compresses the data into a more compact and information-dense latent representation by capturing its intrinsic patterns through a neural network architecture [37]. Unlike traditional dimensionality reduction techniques, Autoencoders not only reduce data dimensionality but also generate latent representations that preserve salient patterns, thereby enabling the extraction of more discriminative features for downstream classification tasks [38]. In this study, an Autoencoder is used to compress the high-dimensional feature space—derived from CWT and fractal descriptors (PFD, Hurst, DFA)—into a lower-dimensional, informative representation. This process reduces noise and redundancy while preserving key features essential for classification. The model's architecture and parameters are detailed in Table 2 and Figure 6, respectively.

Table 2. Hyperparameters of the proposed Autoencoder model

Structural Element	Details
Encoder	Three fully connected layers: 1024 → 512 → 256 (latent space)
Decoder	Two fully connected layers: 512 → 1024 → input_dim
Normalization & Regularization	Batch Normalization after each layer Dropout rate: 0.35
Output Layer	Linear activation to reconstruct original input
Optimization	AdamW optimizer Learning rate: 0.0005 Weight decay: 1e-4
Training Strategy	MAE loss Early Stopping based on validation error stagnation

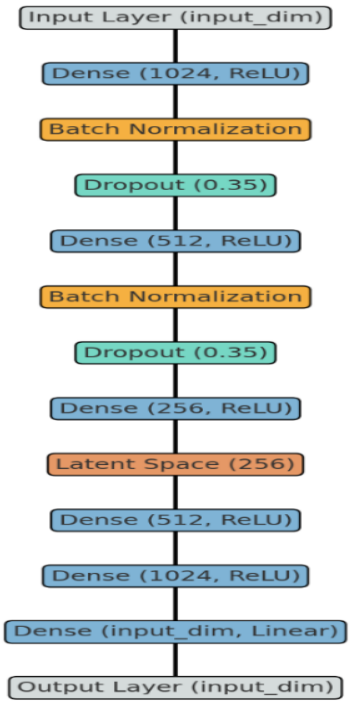


Figure 6. Autoencoder structural diagram

The proposed Autoencoder uniquely integrates time-frequency and fractal EEG features into a low-dimensional latent space, enhancing feature discriminability. Its architecture employs progressive compression—from 1024 to 256 units—combined with Batch Normalization and Dropout (rate = 0.35) to enhance training stability and prevent overfitting. The use of the AdamW optimizer with weight decay (1e-4) is a deliberate choice to improve convergence and prevent weight explosion, while the learning rate (0.0005) balances convergence speed and stability. MAE loss minimizes reconstruction error, and Early Stopping avoids overtraining. Together, these design choices support a more generalizable and efficient model, distinguishing WaveFrac-AE from standard Autoencoder applications in EEG analysis.

Machine Learning Algorithms Employed in the Classification Framework

EEG signals are highly complex, nonlinear, and non-stationary, making them difficult to model with traditional statistical methods. Their dynamic structure requires advanced learning algorithms to effectively capture temporal and structural variations [39]. In this context, tree-Tree-based models like Random Forest, XGBoost, LightGBM, and CatBoost use hierarchical partitioning and ensemble learning to capture complex decision boundaries and improve classification. In contrast, SVM maps data to higher-dimensional spaces to identify optimal hyperplanes, enabling precise separation of cognitive states.

Support Vector Machines (SVM)

Support Vector Machines (SVM) are widely adopted supervised classifiers in statistical learning due to their high accuracy and effectiveness in handling complex, high-dimensional data structures. This method constructs an optimal separating hyperplane by projecting samples into a higher-dimensional feature space to maximize the margin between classes, and it remains effective on non-linearly separable datasets through the use of kernel functions. To enhance generalizability and mitigate overfitting, careful tuning of hyperparameters such as C and gamma is essential; C controls the trade-off between margin maximization and classification error, while gamma defines the influence of individual data points on the decision boundary. Moreover, by relying solely on support vectors during the classification process, the algorithm enhances computational efficiency and significantly reduces processing costs.

Random Forest

Random Forest is a robust ensemble learning algorithm that constructs multiple decision trees using randomly selected data subsets and features via bootstrap aggregation (bagging), combining their outputs through majority voting or averaging for final prediction. This structure enhances generalization and reduces overfitting by promoting model robustness against data variability. The *n_estimators* parameter, which defines the number of trees, plays a crucial role in model accuracy; however, increasing it may lead to higher computational costs. The high channel-wise variability in EEG signals makes Random Forest's random feature selection advantageous for identifying salient attributes; however, its reliance on numerous independent decision trees can result in prolonged computation times when applied to large-scale EEG datasets.

XGBoost (Extreme Gradient Boosting)

XGBoost, a gradient boosting-based decision tree algorithm, is widely recognized for its exceptional computational efficiency and predictive accuracy, particularly when dealing with large-scale datasets [41]. It iteratively builds decision trees that correct the residuals of previous ones, thereby progressively minimizing prediction errors through a stepwise optimization process. Its application in biomedical signal classification—especially EEG—is largely attributed to its advanced branch and leaf optimization mechanisms, which significantly enhance class separability within complex signal patterns [42]. Moreover, the incorporation of both L1 and L2 based ensemble models and kernel-based classifiers—particularly Support Vector Machines (SVM)—have emerged as powerful modeling alternatives for EEG-based mental state classification, owing to their ability to handle complex decision boundaries and capture non-linear patterns within high-dimensional neurophysiological data [40].

regularization techniques mitigates overfitting and reinforces generalizability, while its histogram-based processing architecture enables scalable modeling with reduced computational overhead in high-dimensional EEG datasets [43].

LightGBM (Light Gradient Boosting Machine)

LightGBM is a gradient boosting framework that functions similarly to XGBoost but achieves greater computational efficiency and reduced memory usage, making it particularly well-suited for large-scale biomedical data analysis [44]. By adopting a leaf-wise tree growth strategy, LightGBM enhances the precision of decision boundaries, thereby facilitating a more nuanced interpretation of complex medical signals such as EEG [45]. One of its most prominent advantages lies in the use of Gradient-based One-Side Sampling (GOSS), which selectively discards low-gradient instances during training [46]. This approach not only improves generalization but also significantly reduces training time especially when modeling the non-stationary and high-dimensional nature of EEG signals

CatBoost (Categorical Boosting)

CatBoost is a gradient boosting algorithm specifically designed to handle categorical data more effectively, making it a robust choice for modeling inter-subject variability in EEG signals [47]. One of its key strengths lies in its ability to automatically encode categorical features, enabling the model to optimize decision boundaries without extensive preprocessing. Furthermore, CatBoost employs symmetric tree structures during training, allowing for more balanced learning. This architectural feature enhances the model's ability to generalize across diverse individuals, capturing subtle variations in EEG patterns while maintaining classification consistency and robustness [48].

Experimental Results

To systematically evaluate the classification performance, adaptability, and generalization capability of the proposed WaveFrac-AE framework, the study implements two distinct experimental paradigms: the subject-specific and common-subject approaches. In the subject-specific setting, independent models are trained and evaluated for each participant, enabling the assessment of personalized classification performance and the model's suitability for individual-level applications. Conversely, the common-subject paradigm involves pooling EEG data from all participants to train a single unified model, allowing the evaluation of inter-subject generalization and the model's scalability in broader, real-world contexts. In both paradigms, the unified feature set—comprising time-frequency descriptors (via CWT) and nonlinear complexity measures (PFD, Hurst, DFA)—is reduced using an Autoencoder to extract the most salient and discriminative components while minimizing noise and redundancy.

To ensure a comprehensive and unbiased performance evaluation, five state-of-the-art machine learning classifiers—XGBoost, LightGBM, CatBoost, Random Forest, and SVM—were employed. For each model, predefined search spaces were established, and systematic hyperparameter optimization was carried out using a grid search procedure combined with five-fold stratified cross-validation. A fixed random seed was applied during all experiments to preserve class balance, reduce the risk of overfitting, and guarantee reproducibility. Importantly, all classifiers were evaluated under the same cross-validation framework, which enabled a fair and systematic comparison of adaptability, stability, and generalization capacity across different learning algorithms. The final hyperparameter configurations obtained through this optimization process are summarized in detail in Table 3.

Table 3. Hyperparameter configurations of the classification models used in the study

Classifier	Main Parameters
XGBoost	n_estimators=200 learning_rate=0.02 max_depth=4 subsample=0.6 colsample_bytree=0.6
LightGBM	n_estimators=200 learning_rate=0.02 num_leaves=31 max_depth=4 subsample=0.6 colsample_bytree=0.6
CatBoost	iterations=200 learning_rate=0.02 depth=4 verbose=0
Random Forest	n_estimators=100 max_depth=3
SVM	kernel='rbf' C=2 gamma='scale' probability=True

Table 4 summarizes the subject-specific classification results using the WaveFrac+AE framework across five participants and five machine learning algorithms. The findings clearly underscore the strength of personalized modeling in EEG-based attention classification. Support Vector Machines (SVM) consistently delivered the highest accuracies—for example, 97.52% for Subject 1 and 97.33% for Subject 4—demonstrating its superior ability to capture subject-specific EEG dynamics. SVM achieved the best performance since the RBF kernel can effectively model complex non-linear decision boundaries, while the margin maximization principle provides strong generalization across different subjects. XGBoost and LightGBM also performed well, with XGBoost achieving 91.67% for Subject 5, highlighting the effectiveness of gradient boosting in handling high-dimensional EEG features. CatBoost yielded moderate results, performing best for Subject 5 (85.60%) but showing reduced accuracy for others, especially Subject 3 (73.96%). Random Forest recorded the lowest performance overall, with particularly poor results for Subject 3 (67.35%), indicating its limited capability to model complex EEG structures. These results confirm that WaveFrac+AE, particularly when paired with SVM, offers high accuracy and robustness in subject-specific settings—making it a strong candidate for individualized EEG-based mental state monitoring.

Table 4. 5-Fold subject-specific accuracies of WaveFrac-AE across machine learning models

Subject	XGBoost		LightGBM		CatBoost		Random Forest		SVM	
	Mean (%)	± SD (%)	Mean (%)	± SD (%)	Mean (%)	± SD (%)	Mean (%)	± SD (%)	Mean (%)	± SD (%)
S1	91.43	2.25	90.95	2.72	82.19	5.15	79.52	2.12	97.52	0.85
S2	89.62	3.11	88.86	3.45	79.62	3.37	73.52	3.58	96.95	1.54
S3	81.93	4.79	83.19	3.97	73.96	4.94	67.35	5.43	90.00	1.97
S4	90.19	2.93	90.19	1.52	81.33	2.88	77.43	1.22	97.33	0.65
S5	91.67	1.66	91.31	1.97	85.60	3.94	83.21	2.45	96.19	1.23
Average (Mean± SD)	**88.97**	**2.95**	**88.90**	**2.73**	**80.54**	**4.06**	**76.21**	**2.96**	**95.60**	**1.25**

Figure 7 presents subject-specific confusion matrices, offering a detailed class-level view of each classifier's ability to distinguish between focused, distracted, and drowsy states. These visualizations support the accuracy results in Table 4, further emphasizing the advantages of SVM. SVM stands out with consistently high precision and balanced classification across all classes, particularly for Subjects S1, S2, and S4, where true positive rates are notably strong and inter-class confusion is minimal. In comparison, XGBoost and LightGBM maintain strong overall performance but show occasional confusion in detecting the distracted state, often misclassifying it as focused or drowsy—indicating less distinct decision boundaries for intermediate cognitive states. CatBoost performs moderately, while Random Forest shows clear limitations, with frequent misclassifications between distracted and drowsy states. This suggests a lower capacity to model the nonlinear, non-stationary nature of EEG data. Overall, Figure 7 reinforces the superiority of SVM in subject-specific EEG classification, highlighting its robustness and class-wise balance—making it particularly suitable for applications requiring accurate and fine-grained mental state differentiation.

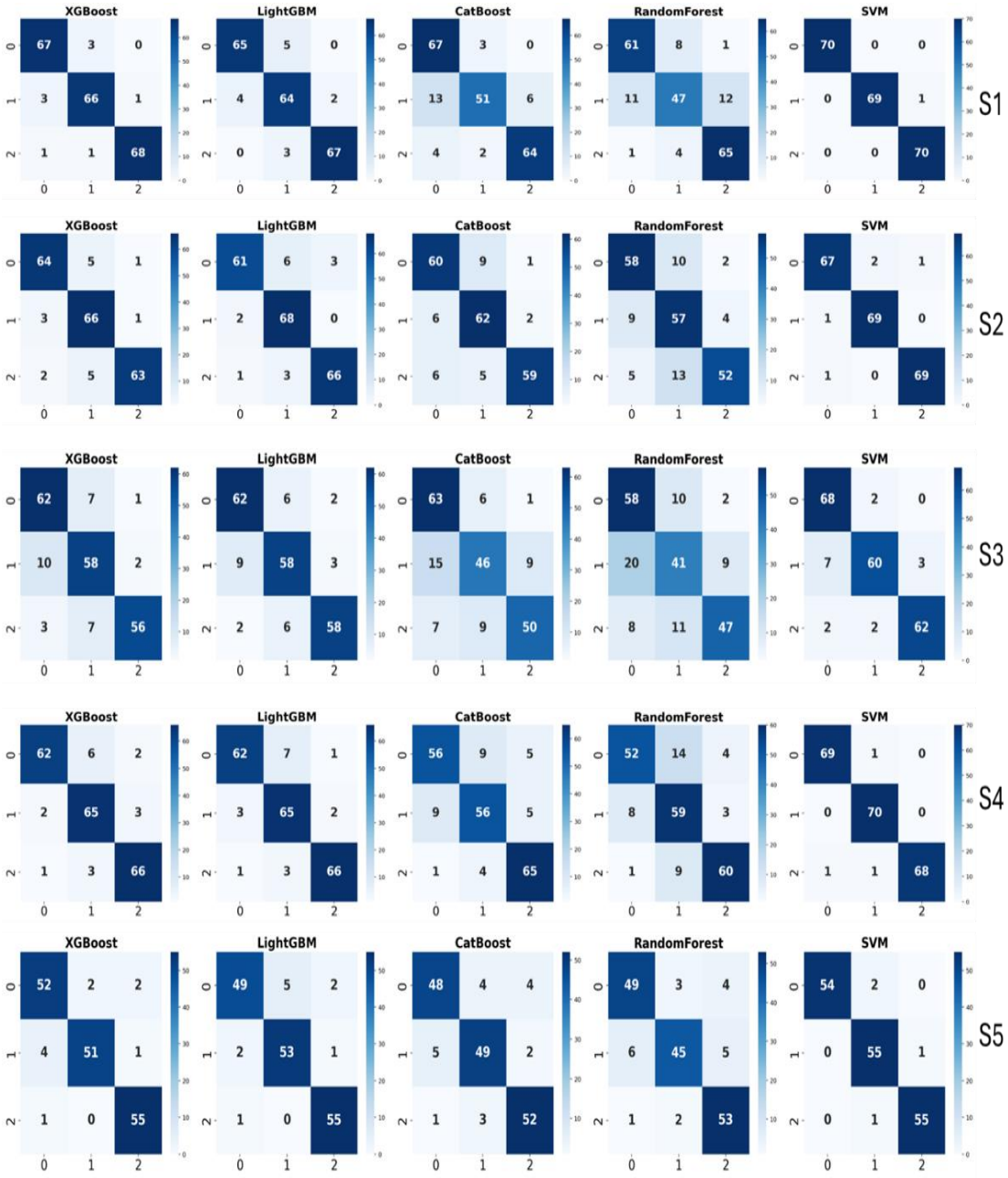


Figure 7. Confusion matrices of subject-specific classification results for each machine learning model across five subjects (S1–S5)

To provide a more comprehensive evaluation beyond overall accuracy, Figure 8 presents ROC curves and AUC scores to assess classifier performance beyond overall accuracy, focusing on sensitivity-specificity trade-offs across subjects (S1–S5) and classifiers. SVM achieved near-perfect AUCs (1.00 for four subjects, 0.98 for S3), confirming its superior precision and generalizability in modeling nonlinear EEG patterns. XGBoost and LightGBM also showed strong performance (AUCs 0.95–0.99), while CatBoost and Random Forest lagged slightly (AUCs 0.90–0.95 and 0.85–0.92, respectively), indicating lower class discrimination. Overall, ROC analysis reaffirms SVM as the most reliable model for EEG-based mental state classification.

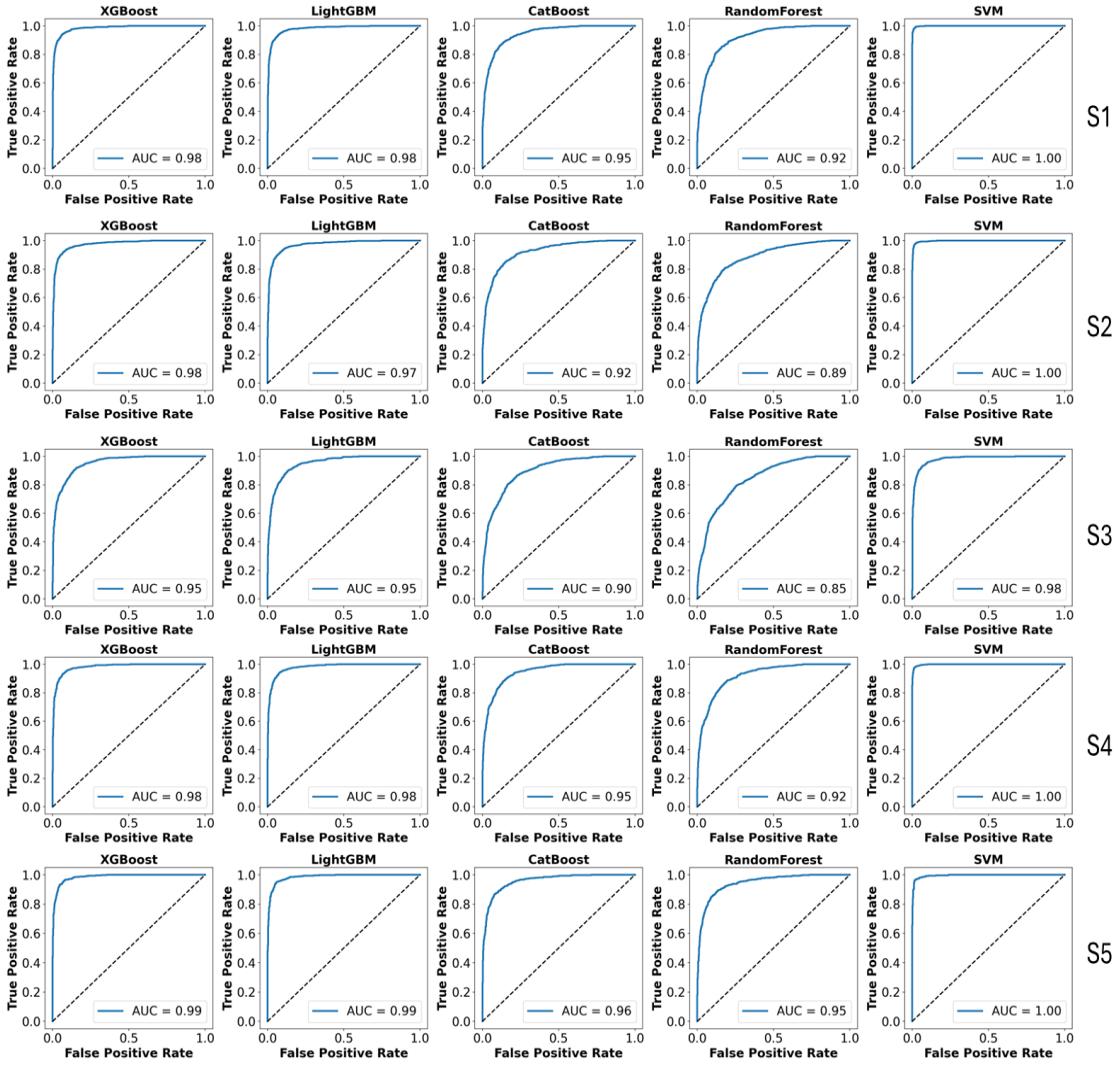


Figure 8. ROC curves and corresponding AUC values for subject-specific classification across five subjects and five classifiers.

To rigorously evaluate the WaveFrac+AE framework, its components—CWT-only features, fractal-only features, and hybrid features without Autoencoder—were tested separately. Results showed that models using isolated feature sets or omitting dimensionality reduction performed significantly worse. As shown in Table 5 and Figure 9, WaveFrac+AE + SVM outperformed all other configurations, achieving an average accuracy of 95.6%. This represents a 5.7% improvement over WaveFrac without Autoencoder, 14.5% over CWT-only, and 30.1% over fractal-only models. Importantly, the model's standard deviation decreased from 4.84 to 3.10, indicating better cross-subject consistency. These findings confirm that fusing CWT's time-frequency features with fractal metrics, and compressing them via an Autoencoder, yields a more robust, discriminative, and generalizable EEG representation—making WaveFrac-AE + SVM the most effective and reliable solution for multi-class mental state classification.

Table 5. Subject-wise test accuracies (%) of competing EEG pipelines (Fractal + SVM, CWT + SVM, WaveFrac + SVM, WaveFrac-AE + SVM)

Subject	Fractal+SVM	CWT+SVM	WaveFrac+SVM	WaveFrac + AE +SVM
S1	69.52	88.48	94.09	97.52
S2	66.38	81.52	90.24	96.95
S3	60.93	70.56	80.55	89.92
S4	67.69	84.29	93.11	97.33
S5	63.02	80.76	91.31	96.19
Mean ± SD	65.51 ± 3.26	81.12 ± 6.66	89.87 ± 4.84	95.60 ± 3.10

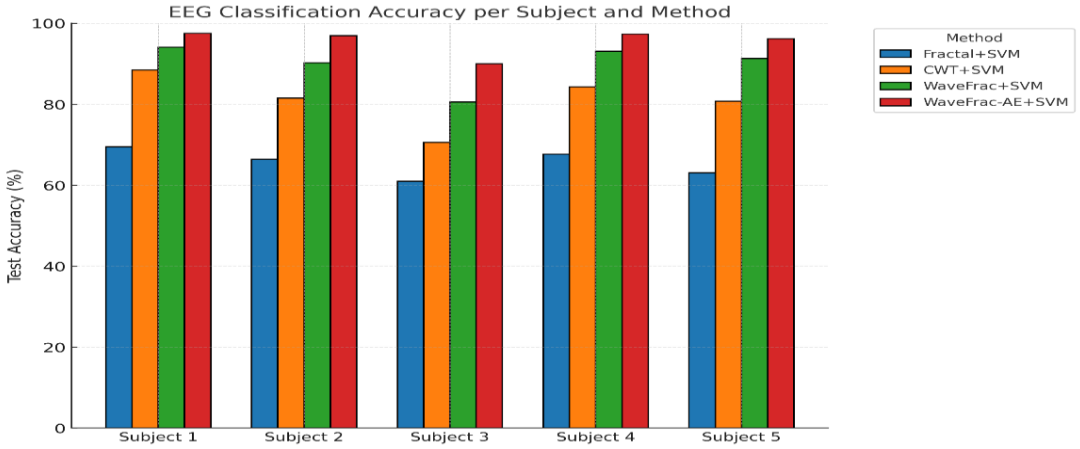


Figure 9. Per-subject accuracy profile highlighting the superiority of the proposed WaveFrac-AE + SVM over baseline methods

Figure 10 illustrates the benchmarking results obtained by comparing the proposed hybrid feature extraction method (WaveFrac-AE) with its individual components, namely fractal-based and time–frequency (CWT, WaveFrac) representations. For each feature type, classification accuracies were computed across all five subjects using five-fold cross-validation, and the mean values were subsequently averaged to provide a comprehensive comparison. The bar graph presents the performance of all classifiers (XGBoost, LightGBM, CatBoost, Random Forest, and SVM), thereby enabling a systematic evaluation of how different learning algorithms respond to alternative feature representations. The results clearly demonstrate that the hybrid WaveFrac-AE features consistently outperform their individual counterparts across classifiers, with SVM achieving the highest accuracy levels. This confirms the effectiveness of combining fractal and time–frequency information under an autoencoder-based dimensionality reduction framework, resulting in more discriminative and robust representations of EEG signals.

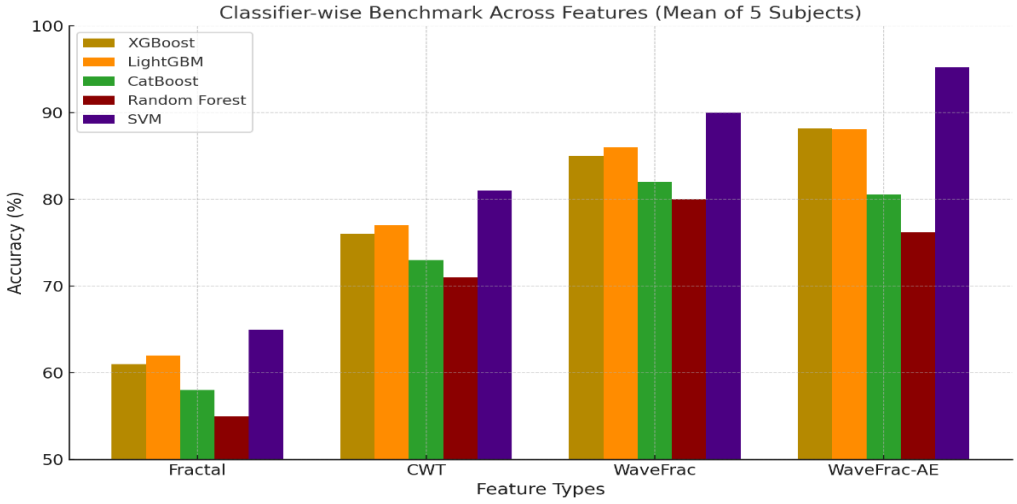


Figure 10. Benchmarking of feature sets across classifiers (Mean of 5 subjects)

All previous analyses were performed on a subject-specific basis, assessing classification performance individually. However, to evaluate the generalizability of the proposed WaveFrac-AE framework, additional experiments were conducted under a common-subject paradigm, where EEG data from all five subjects were combined to train a single, unified model. In this approach, the aggregated dataset was partitioned into five folds for stratified cross-validation. In each iteration, four folds were used for training and the remaining fold for testing, ensuring that all subjects contributed to both the training and testing phases. This setup provides a more rigorous test of the model's robustness against inter-subject variability. As shown in Table 6, SVM achieved the highest accuracy at 92.03%, significantly outperforming other classifiers—XGBoost (78.67%), LightGBM (78.54%), CatBoost (71.36%), and Random Forest (69.17%). These results demonstrate SVM's strong ability to handle the complex, nonlinear structure of EEG data across diverse individuals. The consistently high performance of WaveFrac-AE + SVM confirms its capacity to generalize well, despite challenges posed by inter-individual differences in EEG signals, making it a robust solution for real-world, population-wide cognitive monitoring.

Table 6. 5-Fold average accuracy of the proposed WaveFrac-AE model for common-subject attention state classification

Models	**Mean Accuracy (%)**	**± SD (%)**
XGBoost	78.67	3.29
LightGBM	78.54	2.47
CatBoost	71.36	3.93
RandomForest	69.17	4.76
SVM	92.03	1.78

Figure 11 displays confusion matrices from the best-performing folds of each classifier under the common-subject paradigm, illustrating class-wise performance across the three attention states: focused, unfocused, and drowsy. SVM stands out with the most balanced performance—achieving 95% accuracy for classes 0 and 1, and 91% for class 2—aligning with its top overall accuracy of 92.03% (Table 6). XGBoost and LightGBM also performed reasonably well, particularly for class 2 (84%), but showed confusion between focused and unfocused states, suggesting less clear decision boundaries. CatBoost delivered moderate results, especially struggling with class 1 (66% accuracy), while Random Forest performed weakest overall, achieving only 58% for class 1 and displaying frequent misclassification between unfocused and drowsy states. Overall, Figure 10 reinforces that SVM not only leads in accuracy but also provides superior class-wise precision and balance, making it the most robust and generalizable model for EEG-based mental state classification across individuals.

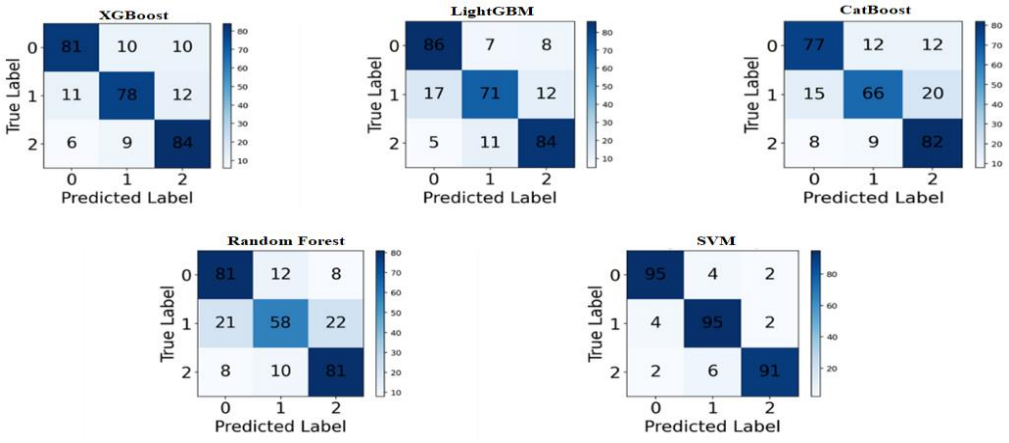


Figure 11. Confusion matrices of each classifier in the common-subject paradigm

Figure 12 presents ROC curves for all classifiers under the common-subject EEG modeling setup, offering a detailed view of each model's class discriminability. The SVM classifier achieved the highest AUC (0.98), confirming its strong ability to separate classes with minimal error, even amidst inter-subject variability. XGBoost and LightGBM also performed well, each with AUCs of 0.92, indicating effective pattern recognition and reliable class separation. In contrast, CatBoost (AUC = 0.89) and especially Random Forest (AUC = 0.87) showed reduced discriminative capability, with Random Forest's curve indicating higher misclassification. Overall, the ROC analysis confirms that SVM not only leads in accuracy but also excels in sensitivity and specificity, reaffirming its robustness and reliability for generalized EEG-based mental state classification

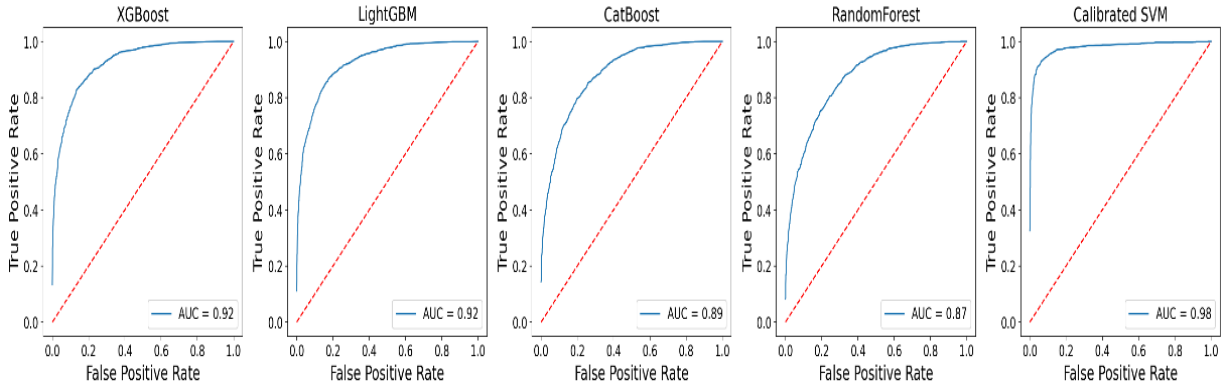


Figure 12. ROC curves and AUC scores of classifiers in the common-subject paradigm.

As summarized in Table 7, reported accuracies in EEG-based mental state classification vary considerably across studies, ranging from 83% to 97.2%, largely due to differences in datasets, number of classes, and evaluation strategies. In particular, Li et al. [51] achieved 97.2% using CWSTR-Net, which is numerically very close to the accuracy obtained in this study (97.52%). Although the numerical gain of 0.3% should not be overstated in the absence of identical datasets and train–test partitions, it is important to note that our study addresses the same number of mental state classes as Li et al. [51]. Under this comparable setting, the proposed method achieves performance that is highly competitive with, and in some cases slightly superior to, state-of-the-art approaches, highlighting its robustness and reliability. The significance of our contribution lies not merely in the numerical accuracy but in the methodological framework. Unlike prior works that rely exclusively on deep learning architectures (e.g., Wu et al. [50]) or kernel-based models (e.g., Wang et al. [52]), our approach integrates hybrid feature representations (WaveFrac-AE) with a robust SVM classifier. This combination effectively balances handcrafted signal characteristics with representation learning, leading to consistently high accuracies across all subjects. These findings confirm that the proposed methodology is both competitive and reliable within the current landscape of EEG-based mental state classification. While absolute superiority cannot be claimed without standardized benchmarking across datasets, the results clearly demonstrate that our framework provides a strong alternative to existing methods. In this respect, the study makes a meaningful contribution by achieving accuracy levels that are competitive with, and in some instances exceed, the best-reported results in the literature, while offering methodological novelty that enhances robustness and interpretability.

Tablo 7. Comparative analysis of mental state classification methods in EEG studies

Literature Studies	**Dataset**	**Number of Mental State Classes**	**Method**	**Accuracy (%)**
Zhang et al. [49]	EEG	2	Recurrent 3D-CNN	89.0
Wu et al. [50]	EEG	3	Deep Stacked Contractive Autoencoder	91.6
Li et al. [51]	EEG	3	CWSTR-Net	97.2
Wang et al. [52]	EEG	2	Multiple Kernel Learning (MKL)+SVM	84.3
Zeng et al. [53]	EEG	2	Generative-Domain-Adversarial Neural Network(GDANN)	91.63
Sonnleitner et al. [54]	EEG	2	Regularized Linear Discriminant Analysis (LDA)	92.0
Cao et al. [55]	EEG–fNIRS	3	SVM	83.0
Venkat and Chinara [56]	EEG	2	Wavelet Packet Transform+ Extra Trees Classifier	85.3-94.45
This study	**EEG**	**3**	**WaveFrac-AE + SVM**	**97.52**

Discussing and Conclusion

This study provides both theoretical and practical insights into EEG-based mental state classification. The proposed WaveFrac-AE framework integrates time–frequency features (via CWT) and fractal measures (PFD, Hurst, DFA), which are subsequently compressed using an Autoencoder to capture both short-term fluctuations and long-term dependencies. This hybrid design addresses the limitations of traditional narrow-band analyses by better modeling the complex, nonlinear, and non-stationary nature of EEG signals, thus offering a more comprehensive and interpretable representation of brain activity.

From a practical perspective, the study demonstrates that high-dimensional EEG features can be efficiently reduced while preserving critical information. This reduction significantly lowers computational complexity, which is a valuable step toward real-time feasibility. In particular, the consistently strong performance of SVM indicates that such hybrid representations are well-suited for classification tasks under constrained settings. While the accuracies achieved (over 97% for subject-specific and ~92% for common-subject evaluations) are promising, they should be interpreted with caution given the limited number of participants and the use of a controlled simulator environment. These results therefore serve as an encouraging proof of concept rather than a definitive claim of readiness for deployment in safety-critical systems.

Several limitations remain. The small participant pool restricts generalizability, as EEG signals are highly subject-dependent. More diverse populations are needed to validate robustness across users. Moreover, simulator-based recordings may not capture external artifacts and behavioral variations observed in real-world driving, where motion artifacts, fatigue, and environmental noise can degrade signal quality. While leave-one-subject-out validation would offer stronger insights into inter-subject generalization, the dataset size prevented its application; instead, a common-subject paradigm was adopted as a practical compromise.

Future work should extend this framework through multimodal integration (e.g., combining EEG with ECG, eye-tracking, or fNIRS) to enhance the robustness of cognitive state detection. In addition, expanding evaluations to larger, multi-subject datasets will be essential for improving the generalizability of the findings across diverse populations. Beyond the current hybrid WaveFrac-AE design, future studies will also investigate the integration of entropy-based measures and the use of alternative dimensionality reduction and compression techniques (in addition to Autoencoder), thereby enriching feature representations and reducing redundancy. Transfer learning strategies could further facilitate rapid adaptation to new users with minimal calibration. Finally, testing the framework in real-world driving and industrial environments will provide critical insights into its feasibility and practical deployment within advanced driver-assistance and neuroergonomic systems.

In summary, the study contributes a novel hybrid framework that demonstrates competitive performance and methodological robustness, while acknowledging the need for further validation before drawing strong conclusions regarding safety-critical applications.

Research funding: None.

Author contributions: Author have accepted responsibility for the entire content of this manuscript and approved its submission.

Competing interests: Authors state no conflict of interest.

Informed consent: Not applicable.

Ethical approval: Not applicable

References

[1] M. Yousaf, M. Farhan, Y. Saeed, M. J. Iqbal, F. Ullah, and G. Srivastava, “Enhancing driver attention and road safety through EEG-informed deep reinforcement learning and soft computing,” *Appl Soft Comput*, vol. 167, p. 112320, Dec. 2024, doi: 10.1016/J.ASOC.2024.112320.

[2] T. Zhang, J. Yang, M. Chen, Z. Li, J. Zang, and X. Qu, “EEG-based assessment of driver trust in automated vehicles,” *Expert Syst Appl*, vol. 246, p. 123196, Jul. 2024, doi: 10.1016/J.ESWA.2024.123196.

[3] J. Min, C. Xiong, Y. Zhang, and M. Cai, “Driver fatigue detection based on prefrontal EEG using multi-entropy measures and hybrid model,” *Biomed Signal Process Control*, vol. 69, p. 102857, Aug. 2021, doi: 10.1016/J.BSPC.2021.102857.

[4] A. Khosla, P. Khandnor, and T. Chand, “Automated diagnosis of depression from EEG signals using traditional and deep learning approaches: A comparative analysis,” *Biocybern Biomed Eng*, vol. 42, no. 1, pp. 108–142, Jan. 2022, doi: 10.1016/J.BBE.2021.12.005.

[5] Y. Xie and S. Oniga, “Classification of Motor Imagery EEG Signals Based on Data Augmentation and Convolutional Neural Networks,” *Sensors 2023, Vol. 23, Page 1932*, vol. 23, no. 4, p. 1932, Feb. 2023, doi: 10.3390/S23041932.

[6] S. Morales and M. E. Bowers, “Time-frequency analysis methods and their application in developmental EEG data,” *Dev Cogn Neurosci*, vol. 54, p. 101067, Apr. 2022, doi: 10.1016/J.DCN.2022.101067.

[7] C. Uyulan and T. T. Erguzel, “Analysis of Time — Frequency EEG Feature Extraction Methods for Mental Task Classification,” *International Journal of Computational Intelligence Systems*, vol. 10, no. 1, pp. 1280–1288, Jan. 2017, doi: 10.2991/IJCIS.10.1.87/METRICS.

[8] H. Steiner, I. Mikheev, and O. Martynova, “Cross-Subject Classification of Effectiveness in Performing Cognitive Tasks Using Resting-State EEG,” *Applied Sciences 2023, Vol. 13, Page 6606*, vol. 13, no. 11, p. 6606, May 2023, doi: 10.3390/APP13116606.

[9] E. Guttmann-Flury, X. Sheng, and X. Zhu, “Channel selection from source localization: A review of four EEG-based brain–computer interfaces paradigms,” *Behav Res Methods*, vol. 55, no. 4, pp. 1980–2003, Jun. 2023, doi: 10.3758/S13428-022-01897-2/METRICS.

[10] E. Gibson, N. J. Lobaugh, S. Joordens, and A. R. McIntosh, "EEG variability: Task-driven or subject-driven signal of interest?," *Neuroimage*, vol. 252, p. 119034, May 2022, doi: 10.1016/J.NEUROIMAGE.2022.119034.

[11] Y. Hadad, M. Bensimon, Y. Ben-Shimol, and S. Greenberg, "Situational Awareness Classification Based on EEG Signals and Spiking Neural Network," *Applied Sciences 2024, Vol. 14, Page 8911*, vol. 14, no. 19, p. 8911, Oct. 2024, doi: 10.3390/APP14198911.

[12] A. Al-Nafjan and M. Aldayel, "Predict Students' Attention in Online Learning Using EEG Data," *Sustainability 2022, Vol. 14, Page 6553*, vol. 14, no. 11, p. 6553, May 2022, doi: 10.3390/SU14116553.

[13] S. Morales and M. E. Bowers, "Time-frequency analysis methods and their application in developmental EEG data," *Dev Cogn Neurosci*, vol. 54, p. 101067, Apr. 2022, doi: 10.1016/J.DCN.2022.101067.

[14] Ç. İ. Acı, M. Kaya, and Y. Mishchenko, "Distinguishing mental attention states of humans via an EEG-based passive BCI using machine learning methods," *Expert Syst Appl*, vol. 134, pp. 153–166, Nov. 2019, doi: 10.1016/J.ESWA.2019.05.057.

[15] I. Alreshidi, I. Moulitsas, and K. W. Jenkins, "Multimodal Approach for Pilot Mental State Detection Based on EEG," *Sensors 2023, Vol. 23, Page 7350*, vol. 23, no. 17, p. 7350, Aug. 2023, doi: 10.3390/S23177350.

[16] J. K. Nuamah and Y. Seong, "Support vector machine (SVM) classification of cognitive tasks based on electroencephalography (EEG) engagement index," *Brain-Computer Interfaces*, vol. 5, no. 1, pp. 1–12, Jan. 2018, doi: 10.1080/2326263X.2017.1338012.

[17] A. Hag, D. Handayani, T. Pillai, T. Mantoro, M. H. Kit, and F. Al-Shargie, "EEG Mental Stress Assessment Using Hybrid Multi-Domain Feature Sets of Functional Connectivity Network and Time-Frequency Features," *Sensors 2021, Vol. 21, Page 6300*, vol. 21, no. 18, p. 6300, Sep. 2021, doi: 10.3390/S21186300.

[18] A. A. Rahman *et al.*, "Detection of Mental State from EEG Signal Data: An Investigation with Machine Learning Classifiers," *KST 2022 - 2022 14th International Conference on Knowledge and Smart Technology*, pp. 152–166, 2022, doi: 10.1109/KST53302.2022.9729084.

[19] H. Zeng *et al.*, "An EEG-Based Transfer Learning Method for Cross-Subject Fatigue Mental State Prediction," *Sensors 2021, Vol. 21, Page 2369*, vol. 21, no. 7, p. 2369, Mar. 2021, doi: 10.3390/S21072369.

[20] N. V. Kimmatkar and B. Vijaya Babu, "Novel Approach for Emotion Detection and Stabilizing Mental State by Using Machine Learning Techniques," *Computers 2021, Vol. 10, Page 37*, vol. 10, no. 3, p. 37, Mar. 2021, doi: 10.3390/COMPUTERS10030037.

[21] L. D. Sharma, V. K. Bohat, M. Habib, A. M. Al-Zoubi, H. Faris, and I. Aljarah, "Evolutionary inspired approach for mental stress detection using EEG signal," *Expert Syst Appl*, vol. 197, p. 116634, Jul. 2022, doi: 10.1016/J.ESWA.2022.116634.

[22] D. Kamińska, K. Smółka, and G. Zwoliński, "Detection of Mental Stress through EEG Signal in Virtual Reality Environment," *Electronics 2021, Vol. 10, Page 2840*, vol. 10, no. 22, p. 2840, Nov. 2021, doi: 10.3390/ELECTRONICS10222840.

[23] V. G. Rajendran, S. Jayalalitha, K. Adalarasu, and R. Mathi, "Machine learning based human mental state classification using wavelet packet decomposition-an EEG study," *Multimed Tools Appl*, vol. 83, no. 35, pp. 83093–83112, Oct. 2024, doi: 10.1007/S11042-024-18725-8/TABLES/8.

[24] O. Faust, R. Acharya U, S. M. Krishnan, and L. C. Min, "Analysis of cardiac signals using spatial filling index and time-frequency domain," *Biomed Eng Online*, vol. 3, no. 1, pp. 1–11, Sep. 2004, doi: 10.1186/1475-925X-3-30/FIGURES/8.

[25] P. Ghorbanian, D. M. Devilbiss, T. Hess, A. Bernstein, A. J. Simon, and H. Ashrafiuon, "Exploration of EEG features of Alzheimer's disease using continuous wavelet transform," *Med Biol Eng Comput*, vol. 53, no. 9, pp. 843–855, Sep. 2015, doi: 10.1007/S11517-015-1298-3/FIGURES/4.

[26] A. K. Maddirala and K. C. Veluvolu, "SSA with CWT and k-Means for Eye-Blink Artifact Removal from Single-Channel EEG Signals," *Sensors 2022, Vol. 22, Page 931*, vol. 22, no. 3, p. 931, Jan. 2022, doi: 10.3390/S22030931.

[27] A. M. John, O. Elfanagely, C. A. Ayala, M. Cohen, and C. J. Prestigiacomo, "The utility of fractal analysis in clinical neuroscience," *Rev Neurosci*, vol. 26, no. 6, pp. 633–645, Dec. 2015, doi: 10.1515/REVNEURO-2015-0011/MACHINEREADABLECITATION/RIS.

[28] S. Morales and M. E. Bowers, "Time-frequency analysis methods and their application in developmental EEG data," *Dev Cogn Neurosci*, vol. 54, p. 101067, Apr. 2022, doi: 10.1016/J.DCN.2022.101067.

[29] M. Pal, P. Manimaran, and P. K. Panigrahi, "A multi scale time–frequency analysis on Electroencephalogram signals," *Physica A: Statistical Mechanics and its Applications*, vol. 586, p. 126516, Jan. 2022, doi: 10.1016/J.PHYSA.2021.126516.

[30] M. A. Rahman, F. Khanam, M. Ahmad, and M. S. Uddin, "Multiclass EEG signal classification utilizing Rényi min-entropy-based feature selection from wavelet packet transformation," *Brain Inform*, vol. 7, no. 1, pp. 1–11, Dec. 2020, doi: 10.1186/S40708-020-00108-Y/TABLES/3.

[31] U. R. Acharya, H. Fujita, V. K. Sudarshan, S. Bhat, and J. E. W. Koh, "Application of entropies for automated diagnosis of epilepsy using EEG signals: A review," *Knowl Based Syst*, vol. 88, pp. 85–96, Nov. 2015, doi: 10.1016/J.KNOSYS.2015.08.004.

[32] P. Patel, R. Raghunandan, and R. N. Annavarapu, "EEG-based human emotion recognition using entropy as a feature extraction measure," *Brain Inform*, vol. 8, no. 1, pp. 1–13, Dec. 2021, doi: 10.1186/S40708-021-00141-5/FIGURES/4.

[33] M. A. Belcher, I. C. Hwang, S. Bhattacharya, W. D. Hairston, and J. S. Metcalfe, "EEG-based prediction of driving events from passenger cognitive state using Morlet Wavelet and Evoked Responses," *Transportation Engineering*, vol. 8, p. 100107, Jun. 2022, doi: 10.1016/J.TRENG.2022.100107.

[34] S. A. David, J. A. T. Machado, C. M. C. Inácio, and C. A. Valentim, "A combined measure to differentiate EEG signals using fractal dimension and MFDFA-Hurst," *Commun*

Nonlinear Sci Numer Simul, vol. 84, p. 105170, May 2020, doi: 10.1016/J.CNSNS.2020.105170.

[35] P. Chattopadhyay and P. Konar, "Feature Extraction using Wavelet Transform for Multi-class Fault Detection of Induction Motor," *Journal of The Institution of Engineers (India): Series B*, vol. 95, no. 1, pp. 73–81, Jan. 2014, doi: 10.1007/S40031-014-0076-1/TABLES/11.

[36] A. F. Farag, S. M. El-Metwally, and A. A. A. Morsy, "Automated Sleep Staging Using Detrended Fluctuation Analysis of Sleep EEG," *Advances in Intelligent Systems and Computing*, vol. 195 AISC, pp. 501–510, 2013, doi: 10.1007/978-3-642-33941-7_44.

[37] Y. Wang, H. Yao, and S. Zhao, "Auto-encoder based dimensionality reduction," *Neurocomputing*, vol. 184, pp. 232–242, Apr. 2016, doi: 10.1016/J.NEUCOM.2015.08.104.

[38] Y. Liu, B. Jiang, J. Feng, J. Hu, and H. Zhang, "Classification of EEG Signals for Epileptic Seizures Using Feature Dimension Reduction Algorithm based on LPP," *Multimed Tools Appl*, vol. 80, no. 20, pp. 30261–30282, Aug. 2021, doi: 10.1007/S11042-020-09135-7/FIGURES/10.

[39] R. Sharma and H. K. Meena, "Emerging Trends in EEG Signal Processing: A Systematic Review," *SN Comput Sci*, vol. 5, no. 4, pp. 1–14, Apr. 2024, doi: 10.1007/S42979-024-02773-W/TABLES/5.

[40] R. Mandal, S. Pal, and U. Maji, "Importance of Activity and Emotion Detection in the Field of Ambient Assisted Living," *Studies in Computational Intelligence*, vol. 1175, pp. 209–240, 2024, doi: 10.1007/978-3-031-71821-2_7.

[41] S. K. Kiangala and Z. Wang, "An effective adaptive customization framework for small manufacturing plants using extreme gradient boosting-XGBoost and random forest ensemble learning algorithms in an Industry 4.0 environment," *Machine Learning with Applications*, vol. 4, p. 100024, Jun. 2021, doi: 10.1016/J.MLWA.2021.100024.

[42] B. L. Radhakrishnan, K. Ezra, I. J. Jebadurai, I. Selvakumar, and P. Karthikeyan, "An Autonomous Sleep-Stage Detection Technique in Disruptive Technology Environment," *Sensors*, vol. 24, no. 4, p. 1197, Feb. 2024, doi: 10.3390/S24041197/S1.

[43] S. Singh, H. Jadli, R. Padma Priya, and V. B. Surya Prasath, "KDTL: knowledge-distilled transfer learning framework for diagnosing mental disorders using EEG spectrograms," *Neural Comput Appl*, vol. 36, no. 30, pp. 18919–18934, Oct. 2024, doi: 10.1007/S00521-024-10207-0/TABLES/5.

[44] T. O. Omotehinwa, D. O. Oyewola, and E. G. Moung, "Optimizing the light gradient-boosting machine algorithm for an efficient early detection of coronary heart disease," *Informatics and Health*, vol. 1, no. 2, pp. 70–81, Sep. 2024, doi: 10.1016/J.INFOH.2024.06.001.

[45] B. K. Swain, S. Mohapatra, M. Mishra, and R. Sharma, "A unified approach for Parkinson's disease recognition: imbalance mitigation and grid search optimized boosting with LightGBM," *Med Biol Eng Comput*, vol. 62, no. 11, pp. 3471–3491, Nov. 2024, doi: 10.1007/S11517-024-03139-3/TABLES/12.

[46] T. O. Omotehinwa, D. O. Oyewola, and E. G. Moung, "Optimizing the light gradient-boosting machine algorithm for an efficient early detection of coronary heart disease," *Informatics and Health*, vol. 1, no. 2, pp. 70–81, Sep. 2024, doi: 10.1016/J.INFOH.2024.06.001.

[47] S. K. Pemmada, J. Nayak, and A. R. Routray, "A Photoplethysmography Based Mental Workload Evaluation Using Ensembled CatBoost Approach," *Journal of The Institution of Engineers (India): Series B*, vol. 106, no. 1, pp. 165–180, Jun. 2024, doi: 10.1007/S40031-024-01092-1/FIGURES/12.

[48] M. Bałdyga, K. Barański, J. Belter, M. Kalinowski, and P. Weichbroth, "Anomaly Detection in Railway Sensor Data Environments: State-of-the-Art Methods and Empirical Performance Evaluation," *Sensors 2024, Vol. 24, Page 2633*, vol. 24, no. 8, p. 2633, Apr. 2024, doi: 10.3390/S24082633.

[49] P. Zhang, X. Wang, W. Zhang, and J. Chen, "Learning Spatial-Spectral-Temporal EEG Features With Recurrent 3D Convolutional Neural Networks for Cross-Task Mental Workload Assessment," *IEEE Transactions on Neural Systems and Rehabilitation Engineering*, vol. 27, no. 1, pp. 31–42, Jan. 2019, doi: 10.1109/TNSRE.2018.2884641.

[50] E. Q. Wu, X. Y. Peng, C. Z. Zhang, J. X. Lin, and R. S. F. Sheng, "Pilots' fatigue status recognition using deep contractive autoencoder network," *IEEE Trans Instrum Meas*, vol. 68, no. 10, pp. 3907–3919, Oct. 2019, doi: 10.1109/TIM.2018.2885608.

[51] X. Li, J. Tang, X. Li, and Y. Yang, "CWSTR-Net: A Channel-Weighted Spatial–Temporal Residual Network based on nonsmooth nonnegative matrix factorization for fatigue detection using EEG signals," *Biomed Signal Process Control*, vol. 97, p. 106685, Nov. 2024, doi: 10.1016/J.BSPC.2024.106685.

[52] F. Wang, S. Wu, W. Zhang, Z. Xu, Y. Zhang, and H. Chu, "Multiple nonlinear features fusion based driving fatigue detection," *Biomed Signal Process Control*, vol. 62, p. 102075, Sep. 2020, doi: 10.1016/J.BSPC.2020.102075.

[53] H. Zeng *et al.*, "An EEG-Based Transfer Learning Method for Cross-Subject Fatigue Mental State Prediction," *Sensors 2021, Vol. 21, Page 2369*, vol. 21, no. 7, p. 2369, Mar. 2021, doi: 10.3390/S21072369.

[54] A. Sonnleitner *et al.*, "EEG alpha spindles and prolonged brake reaction times during auditory distraction in an on-road driving study," *Accid Anal Prev*, vol. 62, pp. 110–118, Jan. 2014, doi: 10.1016/J.AAP.2013.08.026.

[55] J. Cao, E. M. Garro, and Y. Zhao, "EEG/fNIRS Based Workload Classification Using Functional Brain Connectivity and Machine Learning," *Sensors*, vol. 22, no. 19, p. 7623, Oct. 2022, doi: 10.3390/S22197623/S1.

[56] V. P. B and S. Chinara, "Automatic classification methods for detecting drowsiness using wavelet packet transform extracted time-domain features from single-channel EEG signal," *J Neurosci Methods*, vol. 347, p. 108927, Jan. 2021, doi: 10.1016/J.JNEUMETH.2020.108927

Dicle University
Journal of Engineering
https://dergipark.org.tr/tr/pub/dumf
duje.dicle.edu.tr

Research Article

Investigation of the Effect of Notches Opened on the Stator Shoe on the Cogging Torque by Parametric Analysis in Inner Rotor Single-Phase BLDC Motors

Sedat YILDIZ[1*], Ahmet ORHAN[2]

[1] Fırat University, Electrical-Electronics Engineering Department, sedattyldzz@gmail.com, Orcid No: 0009-0009-3820-6665
[2] Fırat University, Electrical-Electronics Engineering Department, aorhan@firat.edu.tr, Orcid No: 0000-0003-1994-4661

ARTICLE INFO

Article history:

Received 30 June 2025
Received in revised form 9 August 2025
Accepted 13 August 2025
Available online 30 September 2025

Keywords:

Asymmetric air gap, Asymmetric position notch, Cogging torque, Single-phase brushless DC motor, Ansys Maxwell 2D

Doi: 10.24012/dumf.1730805

* Corresponding author

ABSTRACT

An asymmetric air gap is required for the self-starting capability of BLDC motors; however, this condition causes an increase in cogging torque, which negatively affects motor performance. In this study, a parametric analysis of notches opened on the stator legs was conducted to reduce cogging torque in inner rotor single-phase brushless DC (BLDC) motors. In the finite element analyses performed using Ansys Maxwell 2D software, notches with different positions and geometries were modeled on the stator legs in the air gap region. Within the scope of the parametric studies, the effects of the notches were examined in regions where the air gap is both at its minimum and maximum, and the optimum position was determined to be the region with the minimum air gap. During the production phase, a notched stator was manufactured, and the impact of these notches on the production processes and manufacturability was evaluated. According to the simulation results, the newly created notched stator model achieved approximately a 28.5% reduction in cogging torque.

Introduction

Increasing sensitivity to energy efficiency has led to the preference of high-performance three-phase BLDC motors instead of low-efficiency induction motors. In this context, research and development activities in single-phase BLDC motors have also come to the forefront due to cost advantages [1]. Single-phase BLDC motors are widely used in low-power applications thanks to their simple structures, low production costs, and easy manufacturing processes. They have lower efficiency and response time compared to three-phase BLDC motors. However, due to their lower costs, they are preferred in low-power applications such as computer fans, boiler fans, the automotive industry, and household appliances. Especially, the number of transistors and position sensors used in single-phase BLDC motors is significantly less compared to three-phase motors; this ratio is generally around one-third. This situation, along with the reduction in the number of components, significantly reduces costs and makes single-phase BLDC motors a strong alternative to multiphase motors in applications where economic efficiency is prioritized over performance [2-6]. Additionally, their compact size, reliable structures, low maintenance requirements, precise speed control, and potentially high efficiency are other advantages that make these motors attractive [7].

One of the most significant disadvantages of single-phase BLDC motors is the risk of the rotor stopping at dead spots where no torque is produced. To prevent this situation, the air gap between the stator poles must be asymmetric. Otherwise, if the rotor is positioned at a dead spot, the motor may not be able to start. To enable the motor to start on its own, an asymmetric air gap design is preferred to shift the torque position from zero to a non-zero point. However, this asymmetric structure causes the motor to operate in only one direction. While this provides an advantage in applications such as fans that operate unidirectionally, it can lead to torque fluctuations and a decrease in overall efficiency [8-11].

Asymmetric air gap causes the formation of cogging torque within the motor; this situation leads to undesirable effects such as vibration, noise, and torque fluctuations. Various methods have been proposed in the literature to reduce cogging torque. These methods include changing the size of the air gap, applying skew to the rotor or stator structure, redesigning the stator tooth geometry, and opening notches on the stator teeth [12-13].

In this study, the analysis of the inner rotor single-phase brushless direct current (BLDC) motor, whose technical specifications are given in Table 1, was carried out using Ansys Maxwell 2D software. Notches were opened on the stator teeth to reduce the cogging torque, and parametric analyses were conducted on this structure. As a result of the literature review, it was determined that similar studies have largely focused on outer rotor single-phase BLDC motors; no studies aiming to reduce cogging torque in inner rotor single-phase BLDC motors were found. Additionally, existing studies show that notches have been placed in both minimum and maximum air gap regions. In this study, an inner rotor motor model was considered, and the effect of applying notches to both positions as well as placing them only in the minimum air gap region on reducing cogging torque was investigated, and the parametric analysis process carried out in the Ansys Maxwell environment was explained.

Table 1. Specifications of the Single-Phase BLDC Motor.

Parameters	Value	Unit
Input Voltage	300	V_{DC}
Rated Speed	7200	rpm
Rated Current	0.8	A
Stator outer diameter	71	mm
Rotor outer diameter	36.5	mm
Stack length	12	mm
Slot depth	8.5	mm
Minimum air gap	0.5	mm
Maximum air gap	1	mm
Number of magnet poles	4	
Number of stator poles	4	

Cogging Torque

Cogging torque originates from the variations in magnetic permeability and reluctance between the slots and tooth tips of the rotor and stator during the rotor's rotational motion. An increase in the magnitude of this torque raises the amount of torque required for motor startup, which negatively affects the motor's operational performance and efficiency [14].

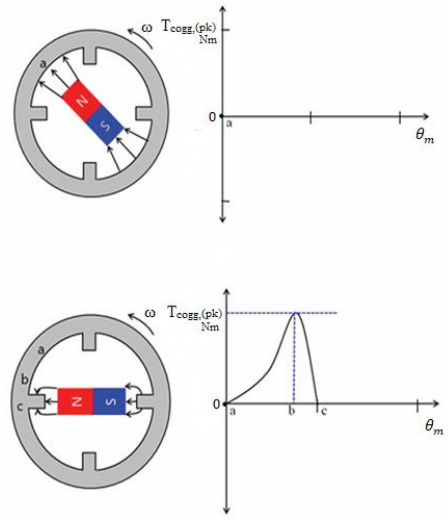


Figure 1. First half cycle of cogging torque

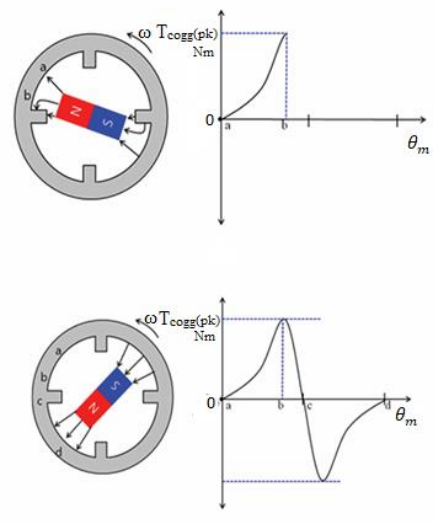


Figure 2. Last half cycle of cogging torque

Figure 1 and 2 shows the distribution of cogging torque at different angular positions of the rotor. Cogging torque is a periodic torque component in permanent magnet synchronous motors, especially brushless direct current (BLDC) motors, caused by variations in magnetic permeability occurring in the air gap between the rotor and stator. This torque arises from the imbalance of magnetic attraction forces resulting from the alignment of the rotor with the stator teeth at certain angles and has direct negative effects on the motor's operational stability at low speeds, noise levels, and efficiency.

The formation of cogging torque can be explained by the change in the system's magnetic energy during the rotor's movement. Even if the motor is not operating, when the rotor is moved, an energy fluctuation occurs in the system due to its relative position with the stator. This energy fluctuation produces a torque that varies depending on the rotor's position. Theoretically, cogging torque is expressed as the derivative of the motor's magnetic energy with respect to the rotor's angular position. This relationship is expressed in Equation 1.

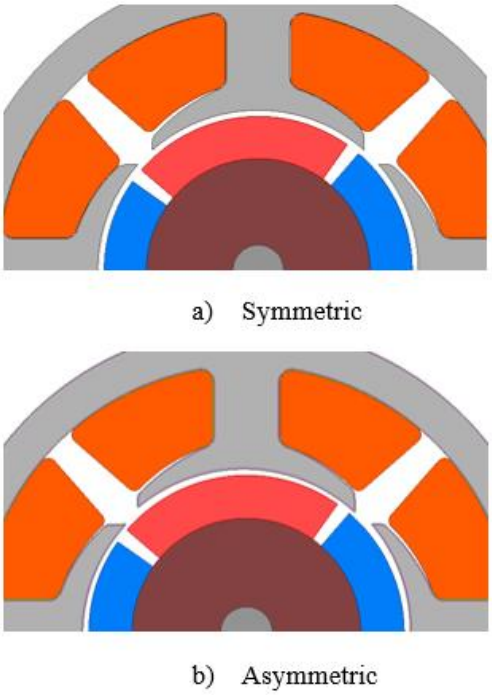
$$T_{cogg}(\alpha) = \frac{\partial W(\alpha)}{\partial \alpha} \quad (1)$$

In this equation, $T_{cogg}(\alpha)$ represents the cogging torque that arises depending on the rotor's angular position; $W(\alpha)$ denotes the amount of magnetic energy possessed by the motor at the given rotor position; and α represents the rotor's mechanical angular position [15].

This equation reveals that cogging torque is entirely of electromagnetic origin. Specifically, parameters such as tooth structure, slot geometry, and air gap distribution affect the position-dependent variation of this energy, determining the magnitude of the cogging torque. Therefore, approaches to reduce cogging torque in motor design, including air gap optimization, changing the tooth angle, or applying notches, aim to regulate this energy variation.

Asymmetric Air Gap in Single-Phase BLDC Motor

Three-phase BLDC motors inherently have a characteristic where torque production is continuous, and therefore, no dead-point problem occurs during startup. In contrast, single-phase BLDC motors experience a dead point when the rotor aligns with the stator at a certain position, resulting in no torque generation. This situation especially causes the rotor to remain stationary at the initial startup moment and prevents the motor from starting on its own.



a) Symmetric

b) Asymmetric

Figure 3. Symmetric and asymmetric geometries of the stator shape

Figure 3(a) shows the structure with a symmetric air gap. In this configuration, when the rotor aligns at an unexpected position, the phases in which the back electromotive force (EMF) and cogging torque both cross zero may coincide. In such a case, since the current flowing through the motor windings approaches zero, electromagnetic torque cannot be generated, which may lead to startup failure. As seen in Figure 4, due to the symmetric design of the air gap in a four-pole single-phase BLDC motor, the torque drops to zero every 90 degrees [16]. Any delay in current during switching may also result in the generation of negative torque.

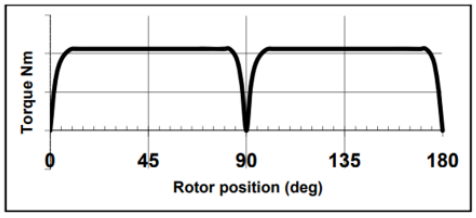


Figure 4. Excitation torque of a symmetric 4-pole single-phase BLDC motor

One of the methods proposed in the literature to solve the startup problem of the motor is to create structural asymmetry by introducing varying air gaps between the stator teeth and the rotor, as shown in Figure 3b. With this method, the possibility of the rotor aligning at a dead point is eliminated, and an initial torque can be generated under all conditions. In designs with an asymmetric air gap, the points at which the back EMF and cogging torque become zero can be separated to prevent their overlap. In this way, the rotor is always aligned in a position where torque generation is possible. This approach enables the generation of initial torque in single-phase BLDC motors, thereby improving startup performance. However, although such asymmetric air gap designs eliminate the dead-point problem, they may lead to an increase in cogging torque and a decrease in average torque, resulting in undesirable effects on motor performance.

Notch Creation and Parametric Analysis in Ansys Maxwell

The amount of variation in magnetic reluctance is a parameter that directly affects the cogging torque. In single-phase brushless direct current (BLDC) motors, the use of an asymmetric air gap increases the reluctance, which in turn leads to an increase in cogging torque. Therefore, reducing the cogging torque is of great importance for the performance of such motors. Another expression related to cogging torque is given in Equation (2). As can be seen, in order to minimize cogging torque, the rate of variation in magnetic reluctance must be minimized [17].

$$T_{cogg} = -\frac{1}{2}\emptyset_g{}^2 \frac{dR}{d\theta} \tag{2}$$

Thanks to the accurate association of variables with geometry in the Ansys Maxwell software, optimization, parametric analysis, and many other engineering applications can be effectively performed. In this study, with an approach not previously found in the literature, an approximate parabolic function was first defined to fit the geometry of the stator shoe. The parabola was expressed as a second-degree polynomial and is given in Equation (3).

$$y = ax^2 + bx + c \tag{3}$$

In Equation (3), the coefficients a, b, and c are parameters that determine the slope, position, and shape of the parabola. If the given curve passes through three known points on a plane, these coefficients can be determined by relating them to the coordinates of the corresponding points. Three different points on the arc of the stator shoe shown in Figure 2 have been selected. These points are defined as follows:

$$(x_1, y_1), (x_2, y_2), (x_3, y_3)$$

If these points lie on the parabola, three equations that satisfy the parabolic expression for each point are given in Equation (4).

$$\begin{cases} y_1 = a{x_1}^2 + bx_1 + c \\ y_2 = a{x_2}^2 + bx_2 + c \\ y_3 = a{x_3}^2 + bx_3 + c \end{cases} \tag{4}$$

Equation (4) forms a system of linear equations containing the coefficients a, b, and c. By solving this system, the coefficients in question are determined, and thus the equation of the parabolic function is obtained.

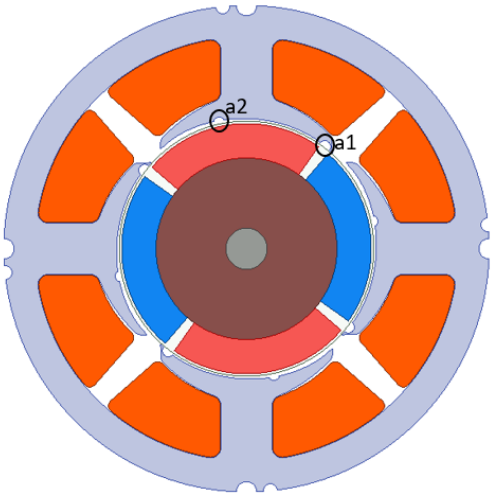


Figure 5. Opening of Two Notches on the Stator Shoe

The number of notches to be placed on the stator shoe is determined based on the suitability of the available area and can be optimized according to system requirements and the results of the analyses conducted. In the Ansys Maxwell environment, the positions of the notches created were parameterized using the derived parabolic equation. The diameters of these notches were defined as variables and used as control parameters during the analysis process.

The diameters of the notches shown in Figure 4 are denoted as a1 and a2, respectively; and two different position parameters, X1 and X2, were defined to determine the locations of these notches on the stator. Here, the parameter X1 is used for the position of notch a1, while X2 is used for the position of notch a2. Specific ranges were defined for these four variables, and a parametric analysis was conducted based on multiple combinations. The analysis parameters were determined as follows:

- X1 and X2: in the range of 2 mm to 12 mm, with a step size of 0.5 mm,
- a1 and a2: in the range of 0.5 mm to 2 mm, with a step size of 0.3 mm.

In line with these definitions, a total of 15876 different combinations were analyzed. As a result of the analyses conducted, the findings related to some combinations with the lowest values in terms of cogging torque are presented in Table 2.

Table 2. Parameter Combinations with the Lowest Cogging Torque

a1 (mm)	**a2** (mm)	**X1**	**X2**	**Cogging Torque** (mNm)
1.7	1.1	11.5	11.5	7.7456
1.7	1.7	11.5	9	7.7669
1.7	1.4	11.5	10	7.7674
1.7	1.1	11.5	12	7.7692
1.7	1.7	11.5	8.5	7.7696
1.7	2	11.5	7.5	7.7839
1.7	1.4	11.5	9.5	7.7844
1.7	1.4	11.5	10.5	7.7904
1.7	1.7	11.5	9.5	7.7918

When the manufacturability and positions of the notches were evaluated, it was observed that opening notches in regions with a wide air gap was not necessary. This is due to the limited effect of the notch in areas with low magnetic flux density. Therefore, it was deemed sufficient to open only one notch in the region where the air gap is narrow. A parametric analysis was conducted for the newly opened notch using only the parameters a1 and X1.

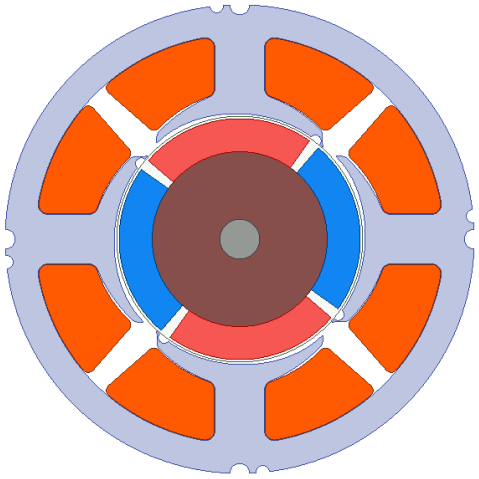


Figure 6. Opening of a Single Notch on the Stator Shoe

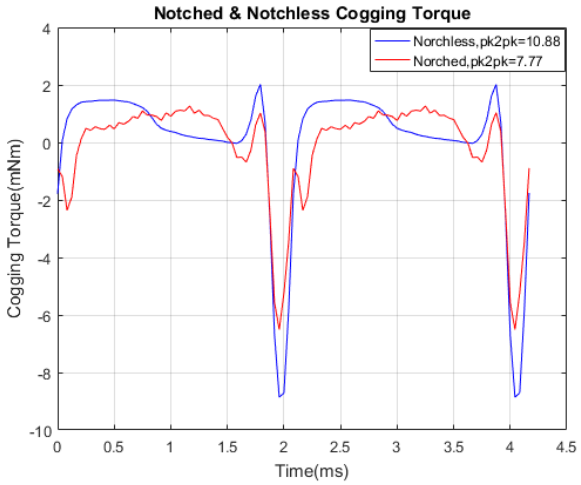


Figure 7. Cogging torque obtained before and after introducing notchesin the stator shoe

As a result of the conducted parametric analyses, the notched stator structure shown in Figure 6 was obtained. This structure was achieved with the notch parameters a1 = 1.7 mm and X1 = 11.4. In Figure 7, the cogging torque values obtained from this notched structure and the unnotched structure are presented comparatively. Upon examining the graph, it can be seen that the peak-to-peak cogging torque in the unnotched structure was 10.88 mNm, while it was reduced to 7.77 mNm in the notched structure.

Examination of the Manufacturability of the Notched Stator Structure

In order to evaluate the possible effects of the notches on the stator sheet shown in the Ansys 2D drawing in Figure 6 such as distance, fracture, bending, or slipping during the manufacturing process the stator sheet was manufactured using the laser cutting method, as seen in Figure 8. Subsequently, the sheet underwent the stacking process, was placed in the winding plastic, and wound. As a result of these applications, it was determined that the opened notches did not cause any mechanical issues or manufacturability obstacles during the production process.

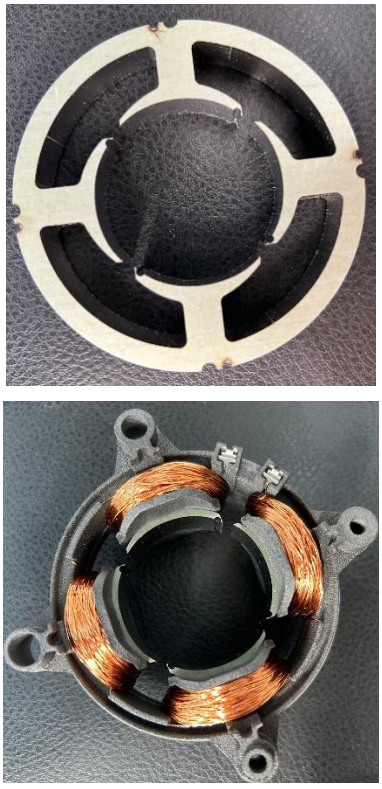


Figure 7. Notched stator in its stacked and wound state

Conclusion

In this paper, the stator geometry of an inner rotor single-phase brushless direct current (BLDC) motor was examined, and a method to reduce cogging torque was developed. As a result of analyses conducted in the Ansys Maxwell 2D environment, an approximate reduction of 3.11 mNm in cogging torque was achieved compared to the initial model, corresponding to an improvement of 28.5%. It was observed that the designed notch structure did not cause any structural issues during the manufacturing process, and its manufacturability was successfully evaluated. The presented method is considered an applicable and effective alternative for reducing cogging torque in single-phase BLDC motors.

Ethics committee approval and conflict of interest statement

There is no conflict of interest with any person / institution in the article prepared.

Authors' Contributions

Both authors contributed equally to the research and manuscript preparation.

Acknowledgement

The authors would like to thank Bader Motor Technologies for manufacturing the designed stator used in this study.

References

[1] Y.-U. Park et al., "Optimal Design of Stator Shape for Cogging Torque Reduction of Single-phase BLDC Motor," The Transactions of The Korean Institute of Electrical Engineers, vol. 62, no. 11, pp. 1528–1534, Nov. 2013, doi: 10.5370/KIEE.2013.62.11.1528.

[2] Y. S. Lee, N. R. Jo, H. J. Pyo, D. H. Jung, and W. H. Kim, "Study on Single-Phase BLDC Motor Design through Drive IC Integration Analysis," Machines, vol. 11, no. 11, 2023, doi: 10.3390/machines11111003.

[3] Y. T. Chen, C. L. Chiu, Y. R. Jhang, Z. H. Tang, and R. H. Liang, "A driver for the single-phase brushless DC fan motor with hybrid winding structure," IEEE Transactions on Industrial Electronics, vol. 60, no. 10, pp. 4369–4375, 2013, doi: 10.1109/TIE.2012.2209619.

[4] L. I. Iepure, I. Boldea, and F. Blaabjerg, "Hybrid I-f starting and observer-based sensorless control of single-phase BLDC-PM motor drives," IEEE Transactions on Industrial Electronics, vol. 59, no. 9, pp. 3436–3444, 2012, doi: 10.1109/TIE.2011.2172176.

[5] S. Lizhi, F. Qi, and S. Jing, "Drive of single-phase brushless DC motors based on torque analysis," IEEE Transactions on Magnetics, vol. 43, no. 1, pp. 46–50, 2007, doi: 10.1109/TMAG.2006.886965.

[6] B. Il Kwon, B. Y. Yang, S. C. Park, and Y. S. Jin, "Novel topology of unequal air gap in a single-phase brushless DC motor," IEEE Transactions on Magnetics, vol. 37, no. 5 I, pp. 3723–3726, 2001, doi: 10.1109/20.952699.

[7] J. S. Mayer and O. Wasynczuk, "Analysis and modeling of a single-phase brushless DC motor drive system," IEEE Transactions on Energy Conversion, vol. 4, no. 3, pp. 473–479, 1989, doi: 10.1109/60.43251.

[8] Y. Byeong-Ryeol, B.-I. Gwon, and P. Seung-Chan, "Design of Air Gap for Reducing Torque Ripple in a Single-Phase BLDC Motor," KoreaScience, vol. 51, no. 2, pp. 49–54, 2002.

[9] M. Fazil and K. R. Rajagopal, "A novel air-gap profile of single-phase permanent-magnet brushless DC motor for starting torque improvement and cogging torque reduction," IEEE Transactions on Magnetics, vol. 46, no. 11, pp. 3928–3932, 2010, doi: 10.1109/TMAG.2010.2057514.

[10] A. Hamler and B. Hribernik, "Impact of shape of stator pole of one phase brushless motor on cogging torque," *IEEE Transactions on Magnetics*, vol. 32, no. 3, pp. 1545–1548, May 1996, doi: 10.1109/20.497545.

[11] D. K. Hong, B. C. Woo, D. H. Koo, and U. J. Seo, "A single-phase brushless DC motor with improved high efficiency for water cooling pump systems," IEEE Transactions on Magnetics, vol. 47, no. 10, pp. 4250–4253, 2011, doi: 10.1109/TMAG.2011.2157482.

[12] Y.-U. Park, J.-H. Cho, S.-H. Rhyu, and D.-K. Kim, "A Novel Cogging Torque Reduction Method for Single-Phase Brushless DC Motor," Journal of Magnetics, vol. 18, no. 2, pp. 117–124, Jun. 2013, doi: 10.4283/JMAG.2013.18.2.117.

[13] J.-D. Seo, J.-H. Yoo, and T.-U. Jung, "Design on notch structure of stator tooth to reduce of cogging torque of single-phase BLDC motor," in 2015 18th International Conference on Electrical Machines and Systems (ICEMS), IEEE, Oct. 2015, pp. 1475–1478. doi: 10.1109/ICEMS.2015.7385273.

[14] K. Sitapati and R. Krishnan, "Performance comparisons of radial and axial field, permanent-magnet, brushless machines," IEEE Transactions on Industry Applications, vol. 37, no. 5, pp. 1219–1226, 2001, doi: 10.1109/28.952495.

[15] K. Seung-Han and T.-U. Jung, "A Study of Cogging Torque Reduction depending on Notch Position of Single Phase BLDC Motor Stator," Journal of the Korean Society of Industry Convergence, vol. 17, no. 3, pp. 113–121, 2014, doi: 10.21289/KSIC.2014.17.3.113.

[16] P. Lefley and S. Ahmed, "Development of a single phase PM BLDC motor from a novel generic model," in 2009 11th Spanish Portuguese Conference on Electrical Engineering–11CHLIE, 2009.

[17] Y.-U. Park, H.-G. Jeong, J.-H. Cho, J.-Y. So, D.-H. Jung, and D.-K. Kim, "Development of Single-phase Brushless DC Motor with Outer Rotor for Ventilation Fan," Journal of the Korean Institute of Illuminating and Electrical Installation Engineers, vol. 27, no. 8, pp. 36–41, Aug. 2013, doi: 10.5207/JIEIE.2013.27.8.036.

Dicle University
Journal of Engineering
https://dergipark.org.tr/tr/pub/dumf
duje.dicle.edu.tr

Research Article

Classification of Lumbar Spine Degenerative Diseases Using Deep Learning Techniques

Bora BİNGÖL[1], İbrahim ÖZTÜRK[2], Zeynep Çağla DÖNMEZ[3], Ahmet SAYGILI[4*]

[1] Tekirdağ Namık Kemal University, Faculty of Çorlu Engineering, Department of Computer Engineering, 1220606801@nku.edu.tr, Orcid No 0009-0009-2499-7566
[2] Tekirdağ Namık Kemal University, Faculty of Çorlu Engineering, Department of Computer Engineering, 2210656007@nku.edu.tr, Orcid No 0009-0009-9224-5518
[3] Tekirdağ Namık Kemal University, Faculty of Çorlu Engineering, Department of Computer Engineering, 1210606011@nku.edu.tr, Orcid No 0009-0002-0441-8386
[4] Tekirdağ Namık Kemal University, Faculty of Çorlu Engineering, Department of Computer Engineering, asaygili@nku.edu.tr, Orcid No 0000-0001-8625-4842

ARTICLE INFO

Article history:

Received 19 July 2025
Received in revised form 6 August 2025
Accepted 4 September 2025
Available online 30 September 2025

Keywords:

Degenerative Disc Disease, Medical Imaging, Data Augmentation, CNN, Ensemble Learning.

Doi: 10.24012/dumf.1744856

* Corresponding author

ABSTRACT

This study investigates the use of deep learning (DL) techniques for the classification of lumbar spine degenerative diseases. In particular, Magnetic Resonance (MR) images used for the detection of spinal canal stenosis are evaluated. The potential of deep learning models to accelerate diagnostic processes through their capability for automatic analysis of radiological images is demonstrated. Various deep learning models were employed in the study; however, the lowest loss value was achieved with the EfficientNetV2-Large architecture. Advanced data augmentation techniques, especially targeted approaches for rare cases, and the use of high-resolution (512x512) images significantly improved the model's performance. As a result of architectural updates and data processing strategies, the test log-loss value was reduced to as low as 0.69. Additionally, the results obtained by combining the predictions of different models through ensemble learning with a soft voting method are also presented. This approach yielded a low log-loss value of 0.604510 on the public test dataset. The results demonstrate that the model is capable of distinguishing clinically critical "severe" cases and maintains its generalization ability even in an expanded class structure.

Introduction

Degenerative disc diseases of the lumbar spine are among the most common health problems worldwide, severely impacting quality of life. Accurate and rapid diagnosis of these conditions is critical for effective treatment planning [1-3]. Today, medical imaging, especially Magnetic Resonance (MRI) images, is widely used to diagnose such degenerations [4, 5]. In recent years, deep learning (DL) techniques have attracted significant attention due to their potential to accelerate disease diagnosis and increase accuracy in medical imaging. Convolutional neural networks (CNNs), in particular, play an active role in the automatic analysis and classification of medical images. Various deep learning-based approaches have been developed in the literature for spinal degeneration and other related medical imaging tasks. For example,

- Borisagar et al. classified lumbar spine degeneration diseases using transfer learning methods and reported that Spine-CNN achieved 92% F1 consistency, better than AlexNet, VGG-16, and ResNet50 [6].
- Wang and colleagues improved the U-Net++ model used in spinal MRI segmentation compared to traditional methods; it was reported that U-Net++ provided more effective segmentation with a Dice score of 88% compared to U-Net's 86% Dice score. Furthermore, U-Net++ was found to have higher accuracy in sensitivity and PPV (Positive Predictive Value) values than U-Net [7].
- Pal et al.'s study emphasized that the Modified Attention U-Net model demonstrated significant success in segmenting and labeling lumbar vertebrae, with a 99.5% accuracy rate. This model also attracted attention for its ability to cope with data deficiencies in medical imaging [8].
- Milletari and colleagues reported that V-Net achieved high success rates, such as a Dice coefficient of 86.9%, on prostate MRI images. These accuracy rates are impressive, considering its ability to accurately segment small, subtle structures [9].

The primary objective of this study is to examine how degenerative disc diseases of the lumbar spine, particularly spinal canal stenosis, can be classified using artificial intelligence-supported algorithms. The study used deep learning models such as CNN to classify spinal stenosis at different levels. Training processes and test results were evaluated, and recommendations were developed based on the results.

Medical approach to lumbar spine degenerative disc disease

The lumbar vertebrae, along with the cervical and thoracic sections of the spine, are the fundamental building blocks that support the head and support the weight of the entire body. They also transfer body weight from the upper body to the legs and bear the load when lifting objects. The L4 and L5 vertebrae, in particular, are responsible for movements such as bending, rotating, and extending the lower back. The spinal cord begins at the base of the skull and terminates at the L1 level, and the lumbar vertebra at this level provides a protective structure for the nerve roots at the end of the spinal cord, called the cauda equina (CE). These nerves travel down to the legs and feet, controlling movement and sensation.

Each lumbar vertebra performs different functions:

• L1: The first and smallest vertebra of the lumbar spine, responsible for providing balance and acting as a transition between the thoracic and lumbar regions.

• L2: Carries more weight and resists vertical compression.

• L3: Located in the middle of the lumbar vertebrae and has a high weight-bearing capacity.

• L4: Carries greater body weight and plays a key role in the bending and rotation of the spine.

• L5: The largest and lowest vertebra of the lumbar spine, it carries the greatest body weight and plays a critical role in spinal movement and load bearing.

This study examined five major degenerative conditions that cause low back pain:

• Left Neural Foraminal Stenosis

• Right Neural Foraminal Stenosis

• Left Subarticular Stenosis

• Right Subarticular Stenosis

• Spinal Canal Stenosis

Lumbar foraminal stenosis, or lumbar neuroforaminal stenosis, is defined as the narrowing of the neural exit foramina (spaces). Spinal stenosis is a condition that can cause pressure on nerves due to narrowing of the spinal canal. It typically occurs in the low back and neck and is most common in individuals over the age of 50. Symptoms can include leg pain, numbness, tingling, and muscle weakness. This condition is usually caused by spinal disc degeneration, joint osteoarthritis, or connective tissue thickening. Anatomical locations of lumbar vertebrae L1 through L5 are shown in Figure 1. These vertebrae form the lower part of the spine and are responsible for supporting body weight, enabling motion, and protecting the spinal cord and nerve roots. L1 to L5 each have distinct biomechanical functions and are common sites for degenerative changes that can lead to spinal stenosis.

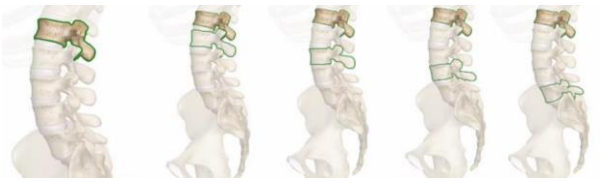


Figure 1. L1, L2, L3, L4, L5 vertebras

Material and methods

Dataset

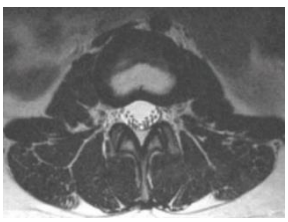
This study used the database submitted for the Kaggle competition "RSNA 2024 Lumbar Spine Degenerative Classification Challenge" organized by the Radiological Society of North America (RSNA) [10]. This dataset contains MRI (Magnetic Resonance) images shared by various research hospitals. MRI images are typically stored in DICOM format and are widely used in musculoskeletal imaging. Table 1 shows sample images from different cross-sections.

Table 1. Image Samples from Different Planes



a) Sagittal T1 Image Sample [11]

b) Sagittal T2/STIR Image Sample [13]



c) Axial T2 Image Sample [12]

The dataset contains many patients, comprising approximately 48,600 images. MRI images were acquired in three different planes: Sagittal T2/STIR, Sagittal T1, and Axial T2. The images represent five different degenerative

conditions (Left Neural Foramen Narrowing, Right Neural Foramen Narrowing, Left Subarticular Stenosis, Right Subarticular Stenosis, and Spinal Canal Stenosis) and were categorized into three classes: normal/mild, moderate, and severe. The model was trained using only visual data. Significant disparities were observed in the number of samples across classes, making learning difficult for the models.

The dataset consists of 30 slices of volumetric data obtained from three different MRI sequences for each patient. Ten slices were carefully selected from each of the Sagittal T1, Sagittal T2/STIR, and Axial T2 sequences. Each slice was stored as a single-channel (grayscale) image with a resolution of 512x512 pixels. The slices were stacked, preserving their original order, to create a volumetric tensor of size 512x512x30. This structure allowed the model to capture detailed features by combining contrast variations and depth information. The raw images were subjected to histogram equalization, normalization, and resizing.

Data augmentation methods

To increase the model's robustness and generalizability, eight different augmentation techniques were applied to magnetic resonance images:

• Motion Blur: Simulates patient or device movement during acquisition.

• Median Filtering: Provides noise reduction and mild smoothing, particularly suppressing salt-and-pepper noise.

• Gaussian Blur: Increases model robustness by simulating out-of-focus acquisition artifacts.

• Gaussian Noise: Simulates real-world noise that can occur in MRI devices with low signal-to-noise ratios.

• Optical Distortion: Simulates device-material misalignments and lens-related artifacts (e.g., fisheye effect).

• Grid Distortion: Represents localized distortions caused by magnetic field irregularities.

• Elastic Transform: This aims to improve model generalization across different patient anatomies by mimicking the natural anatomical variations of organs and surrounding tissues.

These techniques make the model more robust against patient motion, imaging artifacts, noise, and anatomical variability. Especially in medical applications where data is limited, these methods strengthen the model's resistance to overfitting.

Cross-validation (k-Fold Cross-Validation)

Five-fold cross-validation was applied to improve the model's generalization ability and performance reliability. The dataset was divided into five equally sized subsets (folds) by preserving patient-based samples and preserving the class distribution (stratified). In each iteration, one-fold was allocated as the validation set, while the remaining four folds were used as training data. This method ensures that each sample is used in both training and validation and is critical for more accurate prediction of the model's generalization to real-world, limited medical datasets.

Models used

Multiple deep learning models were used and compared in the study:

• InceptionNeXt_small: This is an efficient CNN architecture that separates the depth-adjusted convolution with a large kernel into four parallel branches, offering a good balance between practical speed and performance.

• Vgg_19_bn: This is a 19-layer deep convolutional neural network that follows a repetitive strategy of using small (3x3) convolution kernels. Compared to the original VGG19, it increases robustness to changes in the distribution of the input data by adding Batch Normalization after each convolution layer.

• tf_efficientnetv2_l: This is an improved and faster-training version of EfficientNetV1. It uses Fused-MBConv blocks in the early layers and parameter-efficient MBConv blocks in the deep layers. Techniques such as progressive learning both increase accuracy and reduce training time.

• resnext101_32x8d: Like the ResNet architecture, it uses residual connections, but each block contains multiple parallel narrow convolutional paths called "cardinality." "32x8d" means that each block has 32 8-channel paths, enabling rich feature extraction with computational efficiency.

• Convnext_large: A modernized version of ResNet; it is a fully convolutional structure developed with transformer-like ideas. It contains large (7x7) ConvNeXt blocks with depthwise convolution.

• Mobilenetv2_100: A lightweight deep learning model developed for mobile and embedded devices. It provides balanced performance between speed and accuracy with its inverted residual blocks and depthwise separable convolution structure.

• Densenet121: A 121-layer CNN; It strengthens the gradient flow by combining the outputs of all previous layers in Dense Blocks, saves parameters with bottleneck (1×1→3×3) convolutions and inter-block compression layers, and provides efficient learning by limiting the number of new features with the growth rate.

Training Procedure

The models mentioned were trained using architecture that allows for multiple training sessions within each model. The individual predictions of the four best models were then combined using soft voting within the framework of ensemble learning. Ensemble learning is a machine learning technique that uses multiple base learners to create an ensemble learner for a given learning problem. Soft voting, on the other hand, is a technique that makes the final decision by weighting and normalizing the probability predictions generated by each base model for a given sample.

Experimental Results

The performance of various deep learning models used in the study was examined during the training and validation processes. The models' metrics (Loss, F1 score, Precision,

Recall, Validation WLL) provide information about their general learning trends and generalization capabilities:

• InceptionNeXt_small: As shown in Figure 2, Training and validation losses were steadily reduced; F1, precision, and recall values showed significant improvement in the first 4-5 epochs and then stabilized around 0.75-0.77. The closeness of the losses indicates a low risk of overfitting.

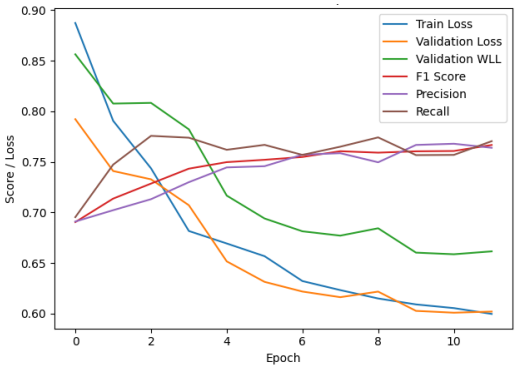


Figure 2. Best fold metrics for InceptionNeXt_small

- Vgg_19_bn: As shown in Figure 3, While training and validation losses steadily decreased, Validation WLL remained generally stable. F1 score and Recall fluctuated, suggesting inconsistency in classification success.

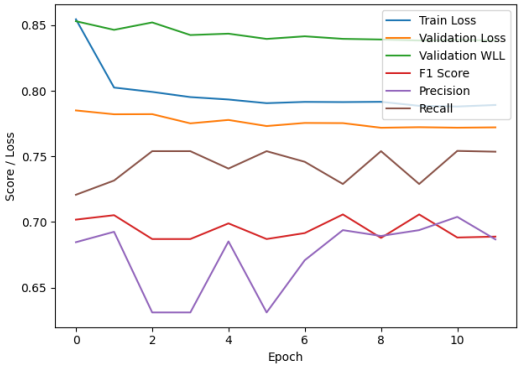


Figure 3. Best fold metrics for vgg_19_bn

- tf_efficientnetv2_l: As shown in Figure 4, While training loss is steadily decreasing, validation loss, despite initially declining, has begun to increase slightly in recent epochs. This may be a sign of overfitting risk. However, validation WLL generally remained on a decreasing trend. F1 score, precision, and recall values stabilized at a high and stable level from epoch 4 onward.

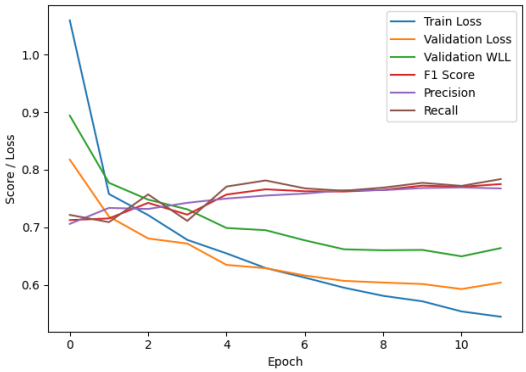


Figure 4. Best fold metrics for tf_efficientnetv2_l

- resnext101_32x8d: As shown in Figure 5, All losses (Train Loss, Validation Loss, Validation WLL), which were high in the first epoch, experienced a sharp decrease in the second epoch and stabilized in subsequent epochs. F1 score, precision, and recall values also remained stable throughout the training period, and overlearning was not observed.

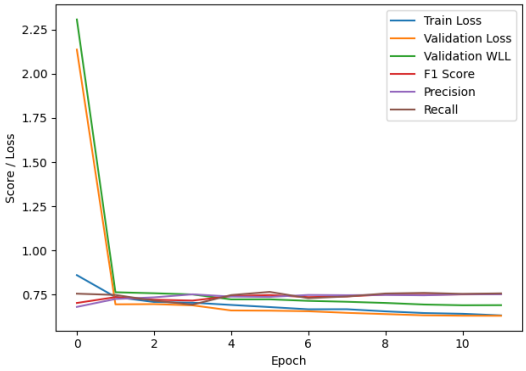


Figure 5. Best fold metrics for resnext101_32x8d

- Convnext_large: As shown in Figure 6, Training and validation loss values decreased slightly but steadily across epochs; however, these decreases were limited, indicating slower learning. Validation WLL remained high and stable, suggesting that the model was not fully reducing the uncertainties in the validation data. Overall, no overfitting was observed.

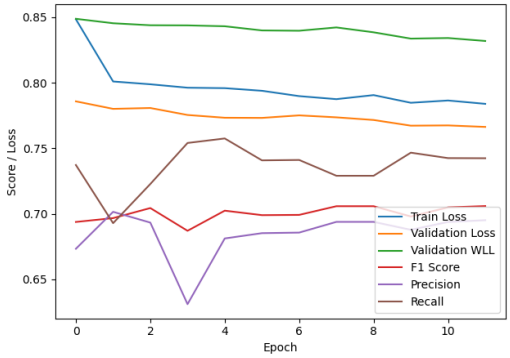


Figure 6. Best fold metrics for Convnext_large

• Mobilenetv2_100: As shown in Figure 7, Training and validation loss decreased steadily across epochs, and the Validation WLL metric also decreased significantly. F1 score, precision, and recall values initially increased slowly, then stabilized after the fifth epoch; there was no sign of overfitting.

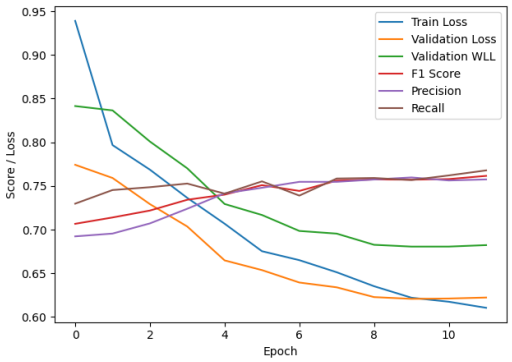


Figure 7. Best fold metrics for mobilenetv2_100

- Mobilenetv2_100 (no augmentation): As shown in Figure 8, While training loss is constantly decreasing, verification loss, although fluctuating, has not increased significantly, and the risk of overfitting is limited. F1 score, precision, and recall values remained constant and close to each other throughout the training.

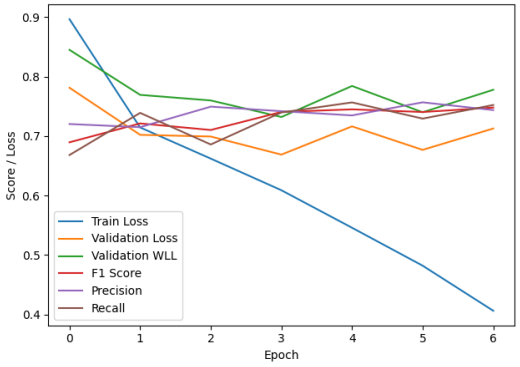


Figure 8. Best fold metrics for mobilenetv2_100 (no augmentation)

- Mobilenetv2_100 (with previous augmentation techniques): The Figure 9 shows that the previously used augmentation methods (horizontal flip, vertical flip, random rotate, random crop, random scale) reduced the model's training and validation losses and stabilized at a certain level, while performance metrics such as accuracy, F1 score, precision, and recall stabilized at approximately 70-75%. This indicates that the model's generalization capacity was limited at a certain point due to limited data diversity, and further performance improvements were not achieved.

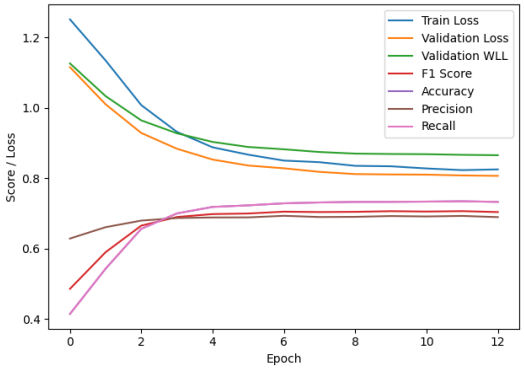


Figure 9. Best fold metrics for mobilenetv2_100 with previous augmentation techniques

- Densenet121: As shown in Figure 10, While training and validation losses decreased steadily, Validation WLL also exhibited a similar downward trend. F1 Score, Precision, and Recall values increased and became more stable over time, demonstrating a balanced and successful performance without overfitting.

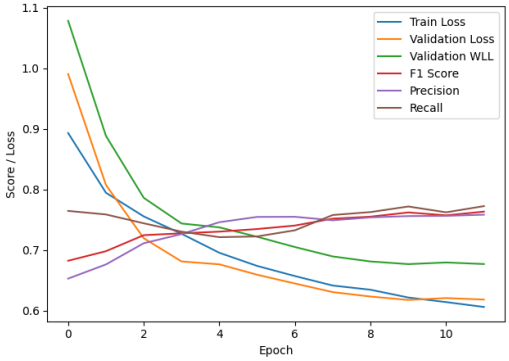


Figure 10. Best fold metrics for densenet121

Initially, the EfficientNet-B5 model was used to classify MRI images. However, to capture more complex patterns and improve generalization success, the EfficientNetV2 architecture was reviewed, and the EfficientNetV2-Large model was adopted. EfficientNetV2 reduces training time using techniques such as fused convolution and progressive learning, while its deeper and broader architecture allows it to extract more information from the data. Furthermore, by reducing overfitting with advanced regularization methods, it provides more stable results, especially on high-variance data such as medical images. Following this transition, a decrease in validation loss values was observed, and more successful results were achieved, especially in the classification of fine details such as spinal canal stenosis.

As a result of the architectural updates and data processing strategies, the test log-loss value, measured at 1.006 in previous studies, was reduced to 0.69. This significant advancement: This was achieved through the combined effects of multiple innovations, including expanding the number of classes, enabling more precise pathological and anatomical distinctions, targeted data augmentation

techniques for rare cases, and the transition to the EfficientNetV2-Large architecture. Furthermore, omitting cropping and working with high-resolution (512x512) images allowed the model to better utilize contextual information, resulting in increased accuracy, particularly in the recognition of complex cases. The model's successful learning of this high complexity in a 75-class structure was made possible by the advanced regularization and optimization strategies used. The log-loss decrease below 0.70 demonstrates that the model maintains its generalization power even with the expanded class structure, in addition to its ability to distinguish clinically critical "severe" cases.

The performance of the models developed in this study was evaluated on two different subsets of the test data. Approximately 20% of the test data was used to provide feedback during the model development process (public leaderboard), while the remaining approximately 80% was reserved for final evaluation (private leaderboard). RSNA Lumbar Metric 71549 was used to measure performance. This metric is the combination of the average of the weighted multiclass log-loss values for the Normal/Mild (weight = 1), Moderate (weight = 2), and Severe (weight = 4) classes for five different lumbar degenerative conditions and the log-loss for the "any_severe_spinal" binary classification. Final model evaluation was performed only on the private leaderboard.

The following values were obtained from the ensemble learning method using the top four models:

- Private Score: 0.700984
- Public Score: 0.604510

The average F1-score and average accuracy values obtained using the values obtained for each fold of the individual models are summarized in the table below:

Table 2. Average F1-Score and Accuracy Table of the Used Models

Models	F1-score (μ)	Accuracy (μ)
tf_efficientnetv2_l	0.7719	0.7741
densenet121	0.7599	0.7662
mobilenetv2_100	0.7535	0.7541
inception_next_small	0.7521	0.7578
resnext101_32x8d	0.7449	0.7605
mobilenetv2_100 (no aug)	0.7370	0.7380
vgg19_bn	0.7247	0.7556
convnext_large	0.6914	0.7400

The table shows that the tf_efficientnetv2_l architecture exhibits the highest average performance with an F1-score of 0.7719 and an accuracy of 0.7741. This is followed by the DenseNet121 and MobileNetV2_100 models, respectively. It is noted that the unaugmented MobileNetV2_100 (F1-score of 0.7370) achieves the lowest averages, highlighting the critical contribution of data diversity to model generalization. The Public and Private scores of the individual models and the ensemble learning approach are presented in the table below:

Table 3. Public and Private Scores of the Used Models

Models	Public Score	Private Score
ensemble_learning	0.604510	0.700984
tf_efficientnetv2_l	0.683606	0.596394
resnext101_32x8d	0.695268	0.597387
inception_next_small	0.704435	0.604568
convnext_large	0.718956	0.617964
densenet121	0.723002	0.611939
mobilenetv2_100	0.758519	0.656926
vgg19_bn	0.837269	0.778723
mobilenetv2_100 (no aug)	0.931379	0.875920

This table shows that Ensemble_learning achieves the best overall performance, offering the lowest loss on the Public set (0.6045), demonstrating that the combined weighted average of errors across different models can outperform individual architectures. On the other hand, tf_efficientnetv2_l (0.5964) achieves the lowest loss on the Private set, demonstrating the strongest generalization ability on the test set. These results indicate that the Ensemble strategy provides optimal performance on the public data due to its variance reduction effect, while EfficientNet provides optimal performance on the private data due to its regularization and deep learning hierarchy.

Results and Discussion

This study successfully demonstrated the high potential of deep learning techniques, particularly CNN-based models and ensemble learning, for the classification of lumbar spine degenerative diseases. The low log-loss value of 0.69 and the success in distinguishing severe cases demonstrate that this approach can make significant contributions to clinical applications.

The use of advanced architectures such as EfficientNetV2-Large, increased data diversity (data augmentation techniques), the evaluation of high-resolution images, and the expanded classification framework played a critical role in improving the model's generalization ability and accuracy. Ensemble learning has proven its ability to provide more stable and reliable predictions by combining the strengths of different models.

Based on the results obtained, future studies require further development. Validating the model on a larger scale in real-world clinical settings and potentially integrating it into radiologists' diagnostic processes will be important steps. Furthermore, training on more balanced datasets or using more sophisticated balancing algorithms could further improve performance in rare disease classes.

Although data augmentation and cross-validation techniques were employed to mitigate class imbalance, these approaches have limitations. Data augmentation does not create new pathological information and may not fully address the under-representation of rare classes such as severe spinal canal stenosis. Consequently, the model may still exhibit bias toward majority classes, which can affect its sensitivity in detecting clinically critical but less frequent

conditions. In future work, advanced rebalancing strategies such as class-aware sampling or synthetic data generation (e.g., GAN-based augmentation) could be explored to further improve performance in rare categories.

Ethics committee approval and conflict of interest statement

This study does not involve any human participants, interventions, or any personally identifiable information. Therefore, ethics committee approval is not applicable. The dataset utilized in this research was sourced from an open-access medical imaging challenge (RSNA 2024 Lumbar Spine Degenerative Classification) and comprises fully anonymized MRI scans shared by clinical institutions for public research purposes. There is no conflict of interest with any person or organization related to this study.

Acknowledgement

This study was supported by the Scientific and Technological Research Council of Türkiye (TÜBİTAK) 2209-A University Students Research Projects Support Program. Project No: 1919B012410067

References

[1] K. Hoffeld *et al.*, "Patient-related risk factors and lifestyle factors for lumbar degenerative disc disease: a systematic review," *Neurochirurgie,* vol. 69, no. 5, p. 101482, 2023.

[2] W. Liawrungrueang, J.-B. Park, W. Cholamjiak, P. Sarasombath, and K. D. Riew, "Artificial intelligence-assisted MRI diagnosis in lumbar degenerative disc disease: a systematic review," *Global Spine Journal,* vol. 15, no. 2, pp. 1405-1418, 2025.

[3] L. Scarcia *et al.*, "Degenerative disc disease of the spine: from anatomy to pathophysiology and radiological appearance, with morphological and functional considerations," *Journal of Personalized Medicine,* vol. 12, no. 11, p. 1810, 2022.

[4] R. U. Din, X. Cheng, and H. Yang, "Diagnostic role of magnetic resonance imaging in low back pain caused by vertebral endplate degeneration," *Journal of Magnetic Resonance Imaging,* vol. 55, no. 3, pp. 755-771, 2022.

[5] M. Hussain, D. Koundal, and J. Manhas, "Deep learning-based diagnosis of disc degenerative diseases using MRI: a comprehensive review," *Computers and Electrical Engineering,* vol. 105, p. 108524, 2023.

[6] H. B. Viral, "Advanced Classification of Lumbar Spine Degenerative Disorders Using Spine-CNN Attenuation Model," *International Journal of Intelligent Systems and Applications in Engineering,* vol. 12, no. 3, pp. 3687 – 3694, 03/24 2024. [Online]. Available: https://ijisae.org/index.php/IJISAE/article/view/6045.

[7] Z. Wang, P. Xiao, and H. Tan, "Spinal magnetic resonance image segmentation based on U-net," *Journal of Radiation Research and Applied Sciences,* vol. 16, no. 3, p. 100627, 2023.

[8] R. Pal, P. Saha, S. Ghoshal, A. Chakrabarti, and S. Sur-Kolay, "Panoptic Segmentation and Labelling of Lumbar Spine Vertebrae using Modified Attention Unet," *arXiv preprint arXiv:2404.18291,* 2024.

[9] F. Milletari, N. Navab, and S.-A. Ahmadi, "V-net: Fully convolutional neural networks for volumetric medical image segmentation," in *2016 fourth international conference on 3D vision (3DV)*, 2016: Ieee, pp. 565-571.

[10] J. T. Tyler Richards, Robyn Ball, Errol Colak, Adam Flanders, Felipe Kitamura, John Mongan, Luciano Prevedello, and Maryam Vazirabad, "RSNA 2024 Lumbar Spine Degenerative Classification," *Kaggle,* 2024. [Online]. Available: https://kaggle.com/competitions/rsna-2024-lumbar-spine-degenerative-classification.

[11] D. C. Preston, "Normal mid sagittal MRI scans of the lumbar spine (T1

and T2 weighted images)," *Case Western Reserve University.,* 2006. [Online]. Available: https://case.edu/med/neurology/NR/MRI_Spine/NormalSagittalMRI.htm.

[12] D. C. Preston, "Axial MRI of the lumbar spine – T2 weighted image at the L4 level [Image]. Case Western Reserve University," 2006. [Online]. Available: https://case.edu/med/neurology/NR/MRI_Spine/nl%20ls%20anatomy.htm.

[13] Radiopaedia, "Sagittal STIR MRI of the lumbar spine [Magnetic resonance imaging]. Radiopaedia.org.," 2023. [Online]. Available: https://radiopaedia.org/images/53402207.

Dicle University
Journal of Engineering
https://dergipark.org.tr/tr/pub/dumf
duje.dicle.edu.tr

Research Article

Advancing Welding Quality through Intelligent TIG Welding: A Hybrid Deep Learning Approach for Defect Detection and Quality Monitoring

Emre GORGUN[1*]

[1] Sivas Cumhuriyet University, *Sivas Technical Sciences Vocational School, Railway Systems Department*, emregorgun@cumhuriyet.edu.tr, Orcid No: 0000-0002-1971-456X

ARTICLE INFO

Article history:

Received 19 February 2025
Received in revised form 13 March 2025
Accepted 20 March 2025
Available online 30 September 2025

Keywords:

Artificial Intelligence, Convolutional Neural Networks, Deep Learning, Tungsten Inert Gas, Welding)

Doi: 10.24012/dumf.1642978

* Corresponding author

ABSTRACT

Modern welding procedures are intricate, requiring a variety of variables and occasionally lacking a complete understanding of their underlying mechanics. Despite the adoption of intelligent welding processes in a few applications, there are still several obstacles. By combining advanced search, combinatorial optimisation, geometric reasoning techniques, and comprehensive Artificial Intelligence (AI) modelling cognitive capabilities, the proposed research aims to build intelligent welding. The three main scientific foci of the research are feature correlation to forecast process performance and facilitate corrective actions, feature extraction utilising intense signal analysis, and the use of simulated or supplied data for analysis. Previous research led to the development of an intelligent Tungsten Inert Gas (TIG) welding platform for materials made of aluminium. On the other hand, TIG welding is susceptible to fluctuations in the root gap, which affect the quality of the weld and could result in electrode contamination. Common welding errors include excessive heat-affected zone width, fusion width, bead height, and inadequate penetration. These errors directly affect the strength and load-bearing capacity of the joint while also making it more susceptible to stress and fracture propagation. The proposed AI-powered welding tool is made to overcome common weld imperfections. Therefore, the research's objective is to develop a hybrid deep learning-powered platform for TIG welding. Convolutional Neural Networks (CNNs) will be employed to extract discrete visual characteristics linked to each type of weld defect, establish correlations between these features, and give weld images to identify the types of defects or their absence. The objective of the research is to create a neural network model that can determine whether a given weld image is good or bad due to contamination, burn-through, or lack of fusion. These findings will make precise weld quality monitoring and process improvement possible.

Introduction

Tungsten Inert Gas (TIG) welding is a crucial process in the industrial sector that calls for qualified and experienced welders, which entails high costs and potential health concerns [1]. However, with the introduction of big data and Industry 4.0, efforts have been made to discover weld flaws in several other welding procedures in addition to TIG welding [2]. Therefore, this research has the potential to ease problems related to using human labour in the TIG welding process if weld automation when successfully implemented. The ability of a worker to make intelligent decisions based on cursory investigations is crucial for welding. Making these choices is essential for figuring out and altering process parameters to meet requirements. The choice of these parameters directly affects product quality, underscoring the significance of this decision.

However, the introduction of machine learning algorithms that can mimic human cognitive capacities offers a potential substitute by reproducing abilities like learning, image classification, and feature identification. The ResNet-50 and ResNet-18 networks are examined and compared in this research as they have shown potential in the past such as [3], [4], [5]. These neural networks are trained to correlate characteristics from a verification dataset after extracting them from a training dataset [6]. The objective is to categorise a given weld image as either a good weld or a particular type of defective weld, taking into account common TIG weld faults [7] [8] [9]. Therefore, the main goal is to create a neural network that can categorise post-weld images of TIG welds into different groups, such as weld quality, burn-through, contamination, lack of fusion, misalignment, and lack of penetration. However, data accessibility determines this research's scope. The TIG welding process on 5083 aluminium will be represented in the ResNet model exclusively as post-weld images taken with High Dynamic Range (HDR) camera. It's crucial to remember that numerous weld flaws can exist in a single piece in real-world applications. However, occurrences containing many flaws in a single sample will not be taken into consideration in this research due to the limits of the training data [7]. Therefore, the main contributions of this paper are as follows:

Development of an Intelligent TIG Welding Platform

The research contributes to the field of welding technology by developing an intelligent TIG welding platform. This platform is designed to enhance the welding process for materials made of aluminum, which is known to be particularly challenging due to its susceptibility to common welding errors [9] [10] [11]. The development of this platform showcases the application of advanced search, combinatorial optimization, geometric reasoning techniques, and comprehensive AI modeling cognitive capabilities to address real-world welding challenges.

Hybrid Deep Learning-Powered Welding Tool

The research introduces a novel approach by leveraging CNNs to extract discrete visual characteristics associated with various types of weld defects. By establishing correlations between these features and using weld images as input, a hybrid deep learning-powered platform is developed. This platform has the ability to identify common weld imperfections such as contamination, burn-through, or lack of fusion. This contribution holds significant promise for precise weld quality monitoring and process improvement, ultimately leading to enhanced weld quality and reliability.

Advancements in Welding Defect Detection

The research significantly advances the capabilities of defect detection in welding processes [12]. By training a neural network model to analyze weld images and determine whether a given weld is of good or bad quality, the study introduces a new level of automation and accuracy to the inspection and assessment of welds. This contribution not only enables real-time quality control but also facilitates rapid corrective actions in response to welding errors, thereby improving the overall efficiency and reliability of welding operations in various industries.

These contributions collectively represent a substantial step forward in the integration of AI and deep learning techniques into the welding domain, addressing critical issues related to weld quality and performance prediction while paving the way for more intelligent and efficient welding processes.

Background

The common welding method known as TIG creates welds of excellent quality. This process employs a non-consumable tungsten electrode, Argon shielding gas, and an electric arc as the heat source to melt the weld pool. The accuracy and superior quality of the welds produced are enhanced by the intense and small size of the arc. The quality of the welded connection is significantly influenced by the operator's control of crucial welding parameters such as arc current, arc voltage, travel speed, and gas flow rate [8]. Numerous weld faults may develop when any of these variables depart from their ideal ranges, endangering the connection's structural integrity. One such issue that develops when there is insufficient penetration into the base metal is “burn-through”. This issue is frequently brought on by an excessively high arc current or voltage and/or a slow enough travel speed, which produces too much extra heat in comparison to what is needed for melting and fusing. A key factor in understanding this phenomenon is the specific heat input, which may be calculated using Equation (1) [9]. These factors highlight the complexity and importance of precise control over welding settings in preserving the quality and integrity of TIG welding.

$$\text{Specific Heat Input} = (\text{Voltage} * \text{Amperage})/(\text{Travel speed} * \text{mass}) \quad (1)$$

In welding, “contamination” is the presence of foreign particles in or close to the weld zone. On the surface of base metals, these particles—which can be anything from dust to oil to metal shavings—are frequently observed. Contamination can be efficiently reduced during pre-welding procedures by wiping, chemical cleaning, or mechanical cleaning techniques. Whereas, “lack of fusion” in welding describes an inadequate bond between the weld and the base metals. This occurrence is commonly attributed to insufficient heat input, which happens when there is not enough energy given to allow for proper melting and fusing. When welding, low voltage or current, as well as an incredibly fast travel speed, can all result in insufficient heat input. The link between these parameters is seen in Equation (1). Fusion failure can also happen in circumstances when the surface isn't properly prepared before welding. When two base metals are not precisely aligned in their appropriate dimensions (“misalignment”), the necessary degree of interaction between them cannot be maintained. However, when the welding process fails to fill the target connection, this is known as a “lack of penetration”. This results from improper management or inadequate control of welding parameters including arc current, voltage, or travel speed. As a result, the joint is weaker than necessary, raising the possibility of structural issues.

Related Works

The goal of this research is to integrate AI into welding systems. Although numerous studies examine AI and welding sciences individually such as [13], [14], [15], there is a noteworthy dearth of research on the development of intelligent welding systems. Robots have achieved significant gains in several production processes [18], [19], including machining [16], [17], thanks to the quick development of intelligent systems. The welding industry, particularly in the field of process automation, has been hesitant to adopt new technological advancements. Critical TIG welding process variables including current, voltage, welding speed, and gas flow rate directly affect the shape of the weld bead and, consequently, the joint's Ultimate Tensile Strength (UTS). The UTS of AISI 4340 low alloy steel underwent a considerable 57MPa change as a result of changing production conditions [12], [20]. Even though there has been advancement in automating process parameter determination, it is still limited to online programming and large batch sizes. Robotic welding arms' actuation and control systems have been shown to work such as[21], [22], [23], but sophisticated sensing and decision-making systems still need to be improved.

The ability of AI to make decisions is still significantly lacking, despite attempts to replicate human brain cognitive processes. Humans are better than machines at making the appropriate decisions at the right time while exhibiting ingenuity and resourcefulness in problem-solving [24], [25]. The strength of AI, on the other hand, is in its capacity to perform lower-level human judgements with outstanding speed, efficiency, and cost-effectiveness. Each of the divisions of AI has its collection of algorithms created to solve particular problem sets. Notably, GoogleNet and ResNet-50 have proven effective at classifying images, identifying objects, recognising faces, and classifying objects [26]. Layers may be disregarded if they do not bring value to the network thanks to ResNet-50's addition of residual blocks. Utilising inception modules, GoogleNet's convolutional operations are affordable and free from the risk of overfitting. Despite the dearth of research on AI-based welding systems, significant advancements have been made. Notably, this research gathers visual data with an emphasis on either weld feature extraction or weld problem identification for intelligent systems to handle. A weld geometric feature monitoring system is developed in [27] to assist welders in selecting the best welding settings by calculating the bead width that will be produced based on input data. Another study i.e. [28] predicts welding parameters based on desired weld penetration and vice versa, showing prediction accuracies reached with different approaches. Another critical step in the welding process is non-destructive testing for weld defect detection and image-based defect sensing devices that have been proposed and put into use by [29]. For instance, researchers employed ResNet with 18 convolutional layers for image classification to accurately identify a variety of weld flaws [30]. Another study in the same spirit emphasises the potential benefit of CNNs for image classification [31].

Emiprical study

Dataset

The enormous amount of data required for successfully training a CNN is a key factor in this endeavour. The difficulty, though, is that substantial testing and data collection are difficult due to the inherent limitations of the available internal resources. To address this, it was determined that the necessary data would be obtained from outside sources, mainly online archives, ensuring a large and varied dataset suitable for training and validation. The requirement for a dataset that precisely replicates the wide range of real-world welding circumstances, a prerequisite for training and verifying the CNN model, led to the choice to obtain data externally. The goal was to gather a dataset that would include various welding circumstances and faults, which made access to a variety of images necessary. Leveraging other sources became a practical strategy to alleviate resource shortages given the enormous volume required. Given its depth and clear connection with the research's goals, the TIG Aluminium 5083 dataset from Kaggle was specifically chosen as the fundamental corpus for training the CNN. This effort was greatly helped by the dataset, a treasure trove of 33,254 images painstakingly categorised into separate classifications. The collection is intelligently divided into several groups that correspond to important welding circumstances and flaws. The following subcategories are included in this list: "Good Weld", "Burn Through", "Contamination", "Lack of Fusion", "Misalignment", and "Lack of Penetration". This dataset's extensiveness offered a solid foundation for training the CNN and attaining the research's objectives. The provenance of the dataset adds to its legitimacy. The Department of Metallurgy and Materials at the University of Birmingham in the UK and TWI Ltd in Abington, Cambridge, were the organisations responsible for taking the images in this collection. These organisations captured images using cutting-edge technology, particularly HDR cameras. The dataset's diversity and quality were greatly increased by the HDR cameras' high-fidelity capture of welding settings.

The dataset is then organised into designated subfolders, which is an essential step for speeding up data processing. Then, image augmentation is carried out to increase dataset diversity and efficiency. The ResNet-50 and ResNet-18 models are then imported and adjusted as necessary to meet the research's specifications. The main stage in the process is to train these modified ResNet models using the collected TIG Aluminium 5083 dataset, which is essential for the models. The models' ability to recognise welding conditions and flaws accurately depends on this training step. Following training, the effectiveness of the models in identifying and categorising welding instances is evaluated in detail by utilising confusion matrices and Grad-CAM to examine network performance. With the use of these analytical tools, models may be thoroughly evaluated, directing future model improvements and optimisations for better performance.

Dataset Preprocessing

As they pass through several convolutional layers, filters, and the neural network in this research, the images undergo significant processing. Red, Green, or Blue (RGB) channels correspond to the dimensions of each image's three-dimensional array [13]. Each component of a dimension corresponds to a pixel in the image and has a value between 0 and 255 that represents the brightness of the corresponding pixel. Neural network training is a computationally demanding process that uses a lot of memory, especially on the GPU. As a result, the processing time varies greatly depending on the image resolution. Image sizes are minimised to the greatest extent possible to speed up processing and lower computational load. The images in the dataset are initially cropped from their original size of 1280*1024 pixels to 800*974 pixels to remove extraneous black pixels. The images are then changed to grayscale, which further shrinks them to an array of 800*974*1 pixels each. The dataset is, however, extended and altered to meet this criterion for compatibility with the ResNet-50 model, which analyses RGB images with 224 pixels in height and 224 pixels in width. For the network to perform better with unseen images, gained by augmentation, the dataset must be diverse. Each image is given a 50% probability of being either vertically mirrored or rotated by 20 degrees in either a clockwise or

anticlockwise direction during the augmentation process. The data must be arranged in a specified folder structure with a subfolder for each class of image to enable effective training with the MATLAB network training tool. The initial dataset, though, did not follow this structure. A Python script was used to properly reorganise the dataset. By comparing image names to a JSON file that comprised image names and their corresponding classifications, this script iterated over each file in the folder, transferred images to the appropriate subfolder, and assured accurate labelling for supervised learning. By carefully processing the data, it is ensured that the dataset is formatted and enhanced to fulfil the needs for effective training and validation of the AI-based welding system.

Model architecture

The layer count and its ramifications are the most important factors to take into account when choosing a suitable CNN architecture. In this decision-making process, we place special emphasis on the convolutional layers because they extract features from the input images. In the TIG dataset, these layers are crucial for identifying the digital properties connected to each unique weld class. The CNN's earliest layers are tasked with identifying basic features including the borders of the weld zone and colour gradients coming from the Heat-Affected Zone (HAZ). The network can distinguish increasingly complicated traits as the information moves through succeeding layers. It has been demonstrated that an architecture with more layers can find complex and sophisticated features in the dataset. While improving feature extraction capabilities, this increase in layer count does present some questions. When dealing with deep architectures that have a high layer count, the overfitting issue must be taken into account. When a model is overturned to the complexities of the training data, it captures highly specific features, even subtleties like scratches on the base metal used in the training dataset. As a result, the model predicts the training data with remarkable accuracy but fails when attempting to predict the unknown data. Finding the right number of layers to avoid overfitting and guaranteeing the network's generalizability presents a complex task in this case. The risk of overfitting in large networks reduces the model's capacity to generalise effectively to new data.

Finding the ideal balance between the number of layers is a difficult undertaking that calls for a practical strategy incorporating testing. To find the ideal configuration that strikes the ideal balance between complexity and generalisation ability, it is essential to experiment and assess the model's performance with a range of layer counts. Given this, we incorporate the ResNet-18 architecture into our experimental framework to compare its performance to that of the ResNet-50 model. This methodical comparison will show how an 18-layer deep network compares to its 50-layer counterpart in terms of effectiveness and efficiency for our particular goals. As we move from the domain of network parameters to the domain of training the ResNet-50 model on the dataset, it becomes clear that careful changes and fine-tuning are required. These variables have a significant impact on the network's learning dynamics, successfully guiding it in the direction of optimal convergence and reliable predictions. The output layer's number of neurons is a crucial parameter to configure, to start. The model's ability to accurately describe the classes found in the dataset depends on this parameter.

To guarantee that the model can recognise the varied welding circumstances and faults in the dataset, the proper balance must be struck here. The learning rate, which affects how big of a step to take throughout the optimisation process, is another key component. The network's capacity to settle into an ideal solution and the speed at which it converges are both greatly impacted by the learning rate. To promote effective training and avoid problems like overshooting or slow convergence, a well-calibrated learning rate is essential. Another important component of the network parameters is momentum, which can be written as a constant. During optimisation, it affects how the weights are updated. Smoother convergence and escape from local minima can result from proper tuning of the momentum constant. Another crucial setting to choose is the maximum number of iterations, which determines how many times the algorithm will run through the full dataset during training. This parameter affects how long the model is trained for and how much of the dataset it is exposed to as a result. The bias value, which affects the model's adaptability and capacity to precisely capture the underlying patterns in the dataset, is the final crucial parameter to adjust. Table I lists the hyperparameter that has been used.

Table 1. Hyperparameters value.

Hyperparameter	Value
Momentum	0.9
Initial learning rate	0.001
Learning rate drop factor	0.1
Learning rate drop period	10
Gradient Threshold method	‘12norm’
Gradient threshold	Inf
Maximum epochs	30
Mini batch size	32
Verbose	1
Verbose frequency	50
Validation frequency	50
Sequence padding direction	‘right’
Sequence padding value	0
Batch normalisation statistics	‘Population’

Experiments

Fig. 1 shows a large dataset sample and highlights the notable differences in appearance between images within each class. It should be noted that the "contamination" class exhibits substantial variability, making it difficult to pinpoint a typical image for feature extraction. As a result, an individual technique is required, in which unique features are extracted from each image within a class. This guarantees that each class is accurately characterised by the CNN by capturing all pertinent information related to that class. The goal of network training is to create a network

capable of using convolutional layers to extract distinctive properties for each class. The CNN should then compare these characteristics to any given image and determine which class it belongs to. Although deeper networks are capable of extracting more complex characteristics, they run a higher risk of overfitting the training set.

The performance of the ResNet-50 model is contrasted with that of the shallower ResNet-18 model to establish the ideal depth of the network. Both models go through training on 1000 images from each class, followed by validation on 200 images from each class. The ResNet-50 model was trained for 257 minutes and 30 seconds, with a validation accuracy of 99.75% and a validation loss of 0.0144 at the end. While the ResNet-18 model took 106 minutes and 49 seconds to train, it finished with a validation accuracy of 99.67% and a loss of 0.0081. ResNet-18 was more effective in terms of training time and loss value, despite the ResNet-50 model showing a 0.8% greater prediction accuracy. Because of its 18 layers and quicker training time, the ResNet-18 model is recommended for training. It also has a lower loss value. It is clear from examining Figs. 2 and 3's training progression that both prediction accuracy and loss have peaked. The training procedure should have been finished after 1000 iterations, but it took 5610 instead. Both networks are ready to classify the test dataset after the training is finished, and a variety of analytical methods are used to assess their performance. Figs. 4 and 5 shows that ResNet-50 almost precisely predicts the classes of images in the test dataset, except for one misclassification in which an image tagged as "good weld" is wrongly predicted as "lack of penetration". Despite the excellent forecast accuracy, this misclassification calls for further inquiry.

The Grad-CAM algorithm is applied to investigate the prediction process of the network and maybe to comprehend the misclassification. Fig. 6 shows the Grad-CAM visualisation for each class of images. There aren't many distinguishing characteristics in the images from the "good weld" and "lack of fusion" classes, which could confuse these classes. Grad-CAM heat maps show that the network is highlighting features on the left and right sides instead of the "good weld" class, which is an improper focus for the network. Other classes like "lack of fusion" and "misalignment" also show this pattern. Instead of concentrating on the basic weld aspects that are essential for classification, the majority of images from each class come from the same experiment and share some experiment-specific data that the model employs for identification. As a result, the model is outstanding at categorising images from this particular dataset but less effective for more general industrial applications. This shows overfitting to the training data. Surprisingly, the ResNet-18 model's prediction accuracy with the test dataset matches that of ResNet-50 with only one misclassification: an image tagged "contamination" was projected mistakenly to be "lack of penetration". The Grad-CAM visualisations for each image class using ResNet-18 are shown in Fig. 6. It becomes clear that due to their visual resemblance, classifications like "contamination" and "lack of fusion" could be mistaken for one another. According to the Grad-CAM explanation, the network concentrates on comparable areas of the images (upper right corner), which have nothing to do with the weld quality itself. The ResNet-18 model also demonstrates a propensity to focus on characteristics unrelated to weld quality, as observed in the ResNet-50 model. This indicates that overfitting is still an issue in both 50-layer and 18-layer deep CNNs. The models, ResNet-50 and ResNet-18, exhibit great prediction accuracy but also show evidence of overfitting, making them most useful on this particular dataset.

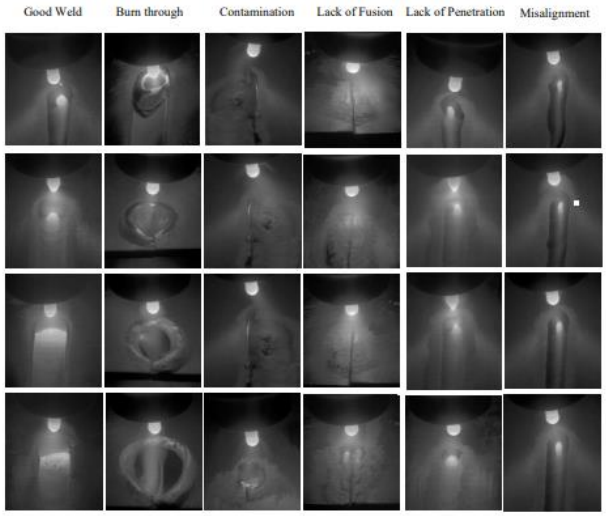


Figure 1. Dataset sample. [18]

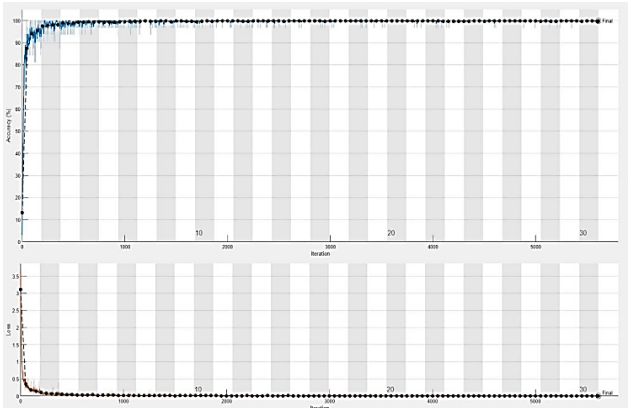


Figure 2. ResNet-18 accuracy vs loss.

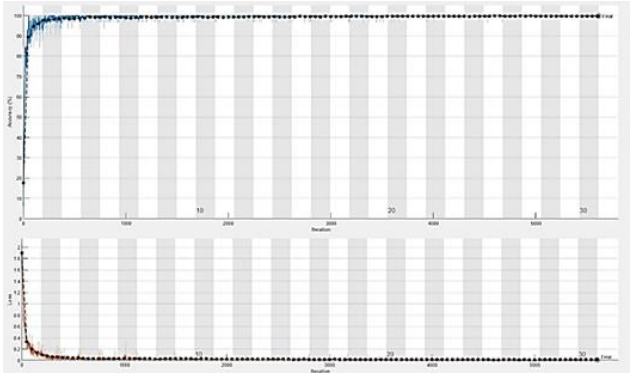


Figure 3. ResNet-50 accuracy vs loss.

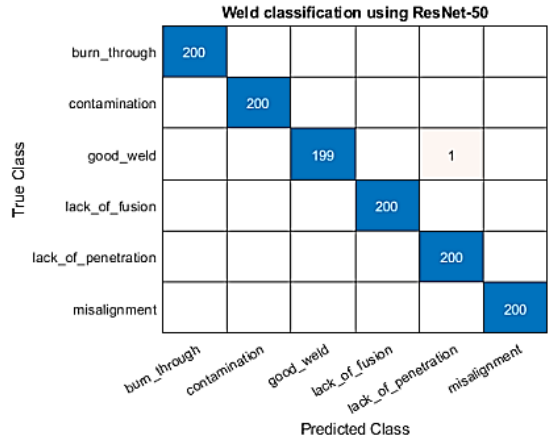


Figure 4. Confusion matrix chart- ResNet-50.

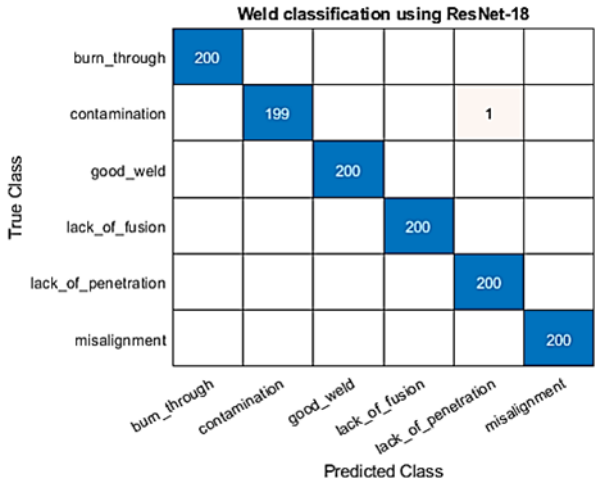


Figure 5. Confusion matrix chart- ResNet-18.

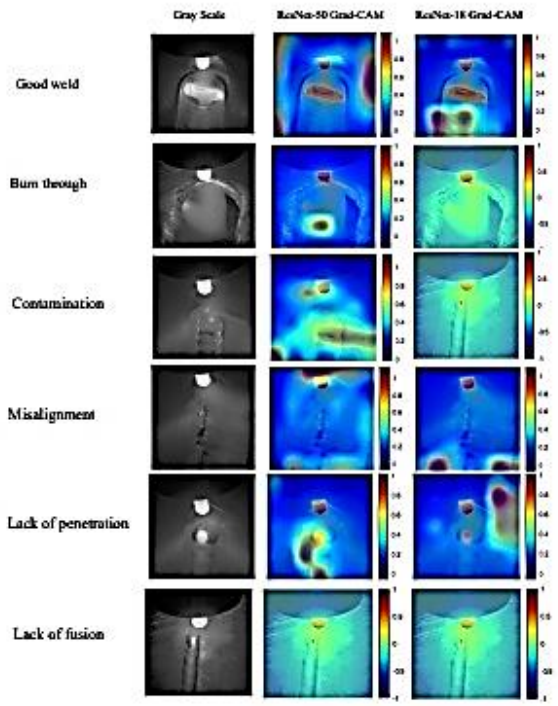


Figure 6. Grad-CAM ResNet-50 and ResNet-18. [18]

Result analysis

The effectiveness of both models in extracting distinctive properties for each class is evaluated through a thorough examination. A comparison research is also done to see how these features may be defined digitally manually as opposed to automatically using a neural network. On a scale of 0 to 1, the heat map serves as a crucial tool for highlighting the importance of the features that CNN used to digitally designate each class. A score of 1 denotes the most prominence, whereas a score of 0 denotes the least significance in terms of feature representation.

Good weld

An important finding from the heat map is that the ResNet-50 model's emphasis is too narrow. It shows that the ResNet-50 model is highlighting aspects of the image that have nothing to do with the weldment. These components may include base metal-specific patterns or gradients that the deeper network wrongly classified as defining characteristics of the "good weld" class. On the other hand, the heat map's prominent focus on the weldment area shows that the ResNet-18 model has acquired characteristics associated with a good weld. In real-world terms, this means that the ResNet-50 model is expected to produce extremely precise predictions only for the photos in this dataset. In contrast, the ResNet-18 model is anticipated to produce precise predictions for both images within and outside of this dataset. If we were to describe these features digitally, we would use a 5*5 filter to flatten colour gradients by averaging the pixel values. The image would therefore be labelled as having a "good weld" if there is a rectangular area of pixels that is lighter (pixels with lower values) between two darker (base metal-representing) areas.

Burn through

A noteworthy finding is highlighted by the heat map analysis of the burn-through class: neither the ResNet-50 model nor the ResNet-18 model was able to successfully learn the characteristics of this class. The heat map shows that contrary to what was initially thought, the ResNet-50 model emphasises a specific area at the burn-through's middle rather than its outskirts. On the other hand, the ResNet-18 model did not learn any specific aspects of the image, as seen by the green mask over its heat map (green corresponds to a value of 0). Although the models learned false features for this class, their burn-through prediction accuracy topped 98%. This implies that the models perform exceptionally well in predicting images of this class inside this dataset but may fail to predict images of this class precisely from additional datasets. If this class were to be defined digitally, the procedure would entail averaging the pixel values with a 5*5 filter to balance out the colour gradients. A darker rectangular section of pixels (pixels with higher values) of the same value is present between two lighter portions (indicating the base metal), and the image is afterwards categorised as "burn through" if this is the case.

Contamination

The green mask on the heat map shows that, like the "burn through" class, the ResNet-18 model has trouble distinguishing the distinctive characteristics of the "contamination" class. On the other hand, the heat map for the ResNet-50 model provides information: the light red zones covering the weld area show that specific areas of the actual weld are receiving focus. However, a dark red area in the heat map's corner implies that the deeper model is picking up elements that are both connected to and unconnected from the actual weld. This suggests that the ResNet-50 model might outperform the shallower 18-layer model in terms of image prediction from outside the dataset. Identifying foreign particles based on their pixel values may be necessary to define this class. Contamination is when a group of pixels considerably differs (by more than 50%) from the pixels around it. Additionally, if more than 20% of the image's pixels comprise foreign particles, the image may be labelled as "contaminated".

Misalignment

The heatmaps unmistakably show that both models are emphasising the bottom half of the image, which has little to do with the weld's specifics. Surprisingly, this is the only situation in which the shallower and deeper networks concentrate on the same image regions. Despite both models' remarkable prediction accuracy within this dataset, they are unlikely to correctly categorise images belonging to this class outside of it. A procedure utilising pixel value averaging with a 2*2 filter and finding vertical lines of higher pixel values might be used to manually establish this image class. The image might be correctly categorised as "misalignment" if it has several misaligned lines running vertically across the middle of it.

Lack of penetration

The deeper design of the ResNet-50 model demonstrates that it is more effective at extracting the distinguishing characteristics of this particular class. The heatmap demonstrates that although the 18-layer CNN tends to emphasise information around the weld, the 50-layer CNN nearly entirely concentrates on the fine weld details. This distinction strongly implies that the ResNet-50 model is likely to show a better prediction accuracy for this particular image class than it did on the training dataset. A method that uses a 5*5 filter size to average all pixel values can be used for digital classification. The core of the image, where the weld bead should be, should show a gradient shift; if it doesn't, the image can be correctly categorised as having a "lack of penetration".

Lack of Fusion

Both models fail to accurately capture particular characteristics of the "lack of fusion" class, as seen by the green mask overlaid on the images. Therefore, it seems that CNN's performance in this situation may not be primarily influenced by the depth of the network. To ensure that both networks can correctly categorise images of this class outside the boundaries of this dataset, changes to other CNN parameters are likely needed. In a digital setting, defining the characteristics of this class requires a vertical scan through the image. If a vertical matrix of pixels in the centre of the image is discovered to be 50% darker than the surrounding pixels, the weld can be safely categorised as having a "lack of fusion".

Discussion

Carefully separating the dataset into training and validation images is a crucial step in starting the model training and evaluation phase. This division is necessary to ensure a complete assessment of the model's performance. Additionally, it is crucial to estimate the volume of data used for training with caution; given the size of the TIG Aluminium 5083 dataset. When the model is too suited to the training data, overfitting can lead to overfitting, which weakens the model's generalisation skills. During the training phase, the network is intensively trained and features are retrieved using the designated training images. The performance of the model is then scrutinised using the validation images. This evaluation consists of guessing the class to which each validation image belongs and contrasting those predictions with the actual labels attached to each image. Such a comparison research offers valuable insight into the accuracy and effectiveness of the model. The training and validation data are meticulously plotted in various ways to thoroughly examine the network's performance as shown in Section 6. Critical performance measures are represented graphically, which aids in understanding the behaviour of the model. This thorough analysis points up potential areas for enhancement and optimisation, opening the door to well-informed decisions on how to improve the model's performance and accuracy in locating and classifying welding errors in the dataset. To achieve the goals of using AI for better welding defect identification and categorization, this ongoing process of training, evaluating, and refining is essential. The prediction accuracy is evaluated graphically and quantitatively (as a percentage) to give a thorough analysis of the neural network's performance as shown in Section 6. This comprehensive graphic allows for a quick assessment of incorrect classifications and offers important insights into both correct and incorrect image classifications. If a particular class is regularly misclassified, a thorough investigation is necessary to ascertain the underlying causes. However, it takes a lot of work to manually go through the output of each convolutional layer and find the crucial traits that the model thought were important. In this case, automated algorithms save the day by providing a clear and comprehensive explanation of the model's decision-making process. One such incredible algorithm is the directed Gradient-Class Activation Mapping (Grad-CAM). Grad-CAM generates a heat map that successfully highlights the portions of the image that the network considers crucial for prediction. By shedding light on the model's inner workings, assisting in the identification of crucial components, and permitting potential model alterations, this representation enhances understanding. Grad-CAM is employed in this way to add a crucial layer of interpretability and transparency to the model, improving the evaluation procedure and ultimately increasing the

model's expected accuracy and efficiency in identifying and categorising welding defects in the dataset.

Conclusion and future works

To create the framework for the later development of a specific AI deep learning system, this research started with an examination of AI applications in the welding industry. The major objective was to develop an algorithm capable of correctly determining if a weld image represented a "good weld", "burn through", "contamination", "lack of fusion", "lack of penetration", or "misalignment". The successful installation and alterations of the ResNet-50 and ResNet-18 CNN models were among this research's accomplishments. The acquisition and improvement of a TIG on the Aluminium 5083 dataset, which was necessary for effectively training the models, was a significant component. Through the training process, both models showed exceptional prediction accuracy, reaching 98%. Despite the excellent forecast accuracy, a further investigation utilising the Grad-CAM approach identified a significant issue. It was shown that, in most situations, neither model was able to adequately extract the critical characteristics that distinguished each type of weld. More study is needed to address the risk of overfitting, which was cited as the cause of this disadvantage. Potential methods for reducing overfitting include using a more varied dataset to expose the models to a wider variety of features, modifying the learning rate to encourage efficient convergence during training, and investigating different CNN architectures that might enhance feature extraction and generalisation. Future iterations of this AI deep learning algorithm are anticipated to produce predictions that are even more accurate by resolving these shortcomings, and as a result, will be more widely used in the sector.

References

[1] A. W. Fande, R. V. Taiwade, and L. Raut, 'Development of activated tungsten inert gas welding and its current status: A review', Jun. 11, 2022, *Taylor & Francis*. doi: 10.1080/10426914.2022.2039695.

[2] E. A. Gyasi, H. Handroos, and P. Kah, 'Survey on artificial intelligence (AI) applied in welding: A future scenario of the influence of AI on technological, economic, educational and social changes', in *Procedia Manufacturing*, Elsevier, Jan. 2019, pp. 702–714. doi: 10.1016/j.promfg.2020.01.095.

[3] D. Sarwinda, R. H. Paradisa, A. Bustamam, and P. Anggia, 'Deep Learning in Image Classification using Residual Network (ResNet) Variants for Detection of Colorectal Cancer', in *Procedia Computer Science*, Elsevier, Jan. 2021, pp. 423–431. doi: 10.1016/j.procs.2021.01.025.

[4] A. Sirco, A. Almisreb, N. M. Tahir, and J. Bakri, 'Liver Tumour Segmentation based on ResNet Technique', in *ICCSCE 2022 - Proceedings: 2022 12th IEEE International Conference on Control System, Computing and Engineering*, Institute of Electrical and Electronics Engineers Inc., 2022, pp. 203–208. doi: 10.1109/ICCSCE54767.2022.9935636.

[5] N. Saleem, J. Gao, M. Irfan, E. Verdu, and J. P. Fuente, 'E2E-V2SResNet: Deep residual convolutional neural networks for end-to-end video driven speech synthesis', *Image and Vision Computing*, vol. 119, p. 104389, Mar. 2022, doi: 10.1016/j.imavis.2022.104389.

[6] M. H. R. Sobuz, M. K. I. Kabbo, T. S. Alahmari, J. Ashraf, E. Gorgun, and M. M. H. Khan, *'Microstructural behavior and explainable machine learning aided mechanical strength prediction and optimization of recycled glass-based solid waste concrete'*, Case Studies in Construction Materials, p. e04305, 2025.

[7] A. Mayr, M. Weigelt, M. Masuch, M. Meiners, F. Hüttel, and J. Franke, 'Application Scenarios of Artificial Intelligence in Electric Drives Production', in *Procedia Manufacturing*, Elsevier, Jan. 2018, pp. 40–47. doi: 10.1016/j.promfg.2018.06.006.

[8] E. Gorgun, *'Numerical analysis of inflow turbulence intensity impact on the stress and fatigue life of vertical axis hydrokinetic turbine'*, Physics of Fluids, vol. 36, no. 1, 2024, Accessed: Mar. 06, 2024. [Online]. Available: https://pubs.aip.org/aip/pof/article/36/1/015111/2932752.

[9] E. Görgün, *'Çoklu Yükleme Koşulları Altında Yük Vagonu Şasisinin Topoloji Optimizasyonu'*, Karadeniz Fen Bilimleri Dergisi, vol. 12, no. 2, pp. 593–604, Dec. 2022, doi: 10.31466/kfbd.1078425.

[10] E. Görgün, *'Ultrasonik Muayene Prob Çaplarının Darbe Yankı Değerine Etkisinin Araştırılması'*, Karadeniz Fen Bilimleri Dergisi, vol. 12, no. 1, pp. 381–389, 2022.

[11] E. Görgün, *'Investigation of The Effect of SMAW Parameters On Properties of AH36 Joints and The Chemical Composition of Seawater'*, International Journal of Innovative Engineering Applications, vol. 8, no. 1, pp. 28–36, 2024.

[12] E. Gorgun, *'Ultrasonic testing and surface conditioning techniques for enhanced thermoplastic adhesive bonds'*, J Mech Sci Technol, vol. 38, no. 3, pp. 1227–1236, Mar. 2024, doi: 10.1007/s12206-024-0218-6.

[13] E. Gorgun, A. Ali, and Md. S. Islam, *'Biocomposites of Poly(Lactic Acid) and Microcrystalline Cellulose: Influence of the Coupling Agent on Thermomechanical and Absorption Characteristics'*, ACS Omega, vol. 9, no. 10, pp. 11523–11533, Mar. 2024, doi: 10.1021/acsomega.3c08448..

[14] D. Vijayan and V. Seshagiri Rao, 'Process Parameter Optimization in TIG Welding of AISI 4340 Low Alloy Steel Welds by Genetic Algorithm', in *IOP Conference Series: Materials Science and Engineering*, IOP Publishing, Jul. 2018, p. 012066. doi: 10.1088/1757-899X/390/1/012066.

[15] TWI, 'What is Tungsten Inert Gas (GTAW or TIG) Welding?', Job Knowledge 6. Accessed: Sep. 28, 2023. [Online]. Available: https://www.twi-global.com/technical-knowledge/job-knowledge/tungsten-inert-gas-tig-or-gta-welding-006

[16] Z. Abbasi *et al.*, 'The Detection of Burn-Through Weld Defects Using Noncontact Ultrasonics', *Materials 2018, Vol. 11, Page 128*, vol. 11, no. 1, p. 128, Jan. 2018, doi: 10.3390/MA11010128.

[17] B. Wang, S. J. Hu, L. Sun, and T. Freiheit, 'Intelligent welding system technologies: State-of-the-art review and perspectives', Jul. 01, 2020, *Elsevier*. doi: 10.1016/j.jmsy.2020.06.020.

[18] R. Tsuzuki, 'Development of automation and artificial intelligence technology for welding and inspection process in aircraft industry', Jan. 01, 2022, *Springer Science and Business Media Deutschland GmbH*. doi: 10.1007/s40194-021-01210-3.

[19] M. A. Kesse, E. Buah, H. Handroos, and G. K. Ayetor, 'Development of an artificial intelligence powered tig welding algorithm for the prediction of bead geometry for tig welding processes using hybrid deep learning', *Metals*, vol. 10, no. 4, p. 451, Mar. 2020, doi: 10.3390/met10040451.

[20] S. Wazir, G. S. Kashyap, and P. Saxena, 'MLOps: A Review', Aug. 2023.

[21] N. Marwah, V. K. Singh, G. S. Kashyap, and S. Wazir, 'An analysis of the robustness of UAV agriculture field coverage using multi-agent reinforcement learning', *International Journal of Information Technology (Singapore)*, vol. 15, no. 4, pp. 2317–2327, May 2023, doi: 10.1007/s41870-023-01264-0.

[22] W. Ji and L. Wang, 'Industrial robotic machining: a review', *International Journal of Advanced Manufacturing Technology*, vol. 103, no. 1–4, pp. 1239–1255, Apr. 2019, doi: 10.1007/s00170-019-03403-z.

[23] S. H. Kim *et al.*, 'Robotic Machining: A Review of Recent Progress', *International Journal of Precision Engineering and Manufacturing*, vol. 20, no. 9, pp. 1629–1642, Sep. 2019, doi: 10.1007/S12541-019-00187-W/FIGURES/12.

[24] M. H. M. Ali and M. R. Atia, 'A lead through approach for programming a welding arm robot using machine vision', *Robotica*, vol. 40, no. 3, pp. 464–474, Mar. 2022, doi: 10.1017/S026357472100059X.

[25] N. Oh and H. Rodrigue, 'Toward the Development of Large-Scale Inflatable Robotic Arms Using Hot Air Welding', *Soft Robotics*, vol. 10, no. 1, pp. 88–96, Feb. 2023, doi: 10.1089/soro.2021.0134.

[26] A. Ghosh, D. Chakraborty, and A. Law, 'Artificial intelligence in Internet of things', Dec. 01, 2018, *The Institution of Engineering and Technology*. doi: 10.1049/trit.2018.1008.

[27] G. S. Kashyap, K. Malik, S. Wazir, and R. Khan, 'Using Machine Learning to Quantify the Multimedia Risk Due to Fuzzing', *Multimedia Tools and Applications*, vol. 81, no. 25, pp. 36685–36698, Oct. 2022, doi: 10.1007/s11042-021-11558-9.

[28] Z. Guo, Y. Sun, M. Jian, and X. Zhang, 'Deep residual network with sparse feedback for image restoration', *Applied Sciences (Switzerland)*, vol. 8, no. 12, p. 2417, Nov. 2018, doi: 10.3390/app8122417.

[29] D. Das, D. K. Pratihar, G. G. Roy, and A. R. Pal, 'Phenomenological model-based study on electron beam welding process, and input-output modeling using neural networks trained by back-propagation algorithm, genetic algorithms, particle swarm optimization algorithm and bat algorithm', *Applied Intelligence*, vol. 48, no. 9, pp. 2698–2718, Sep. 2018, doi: 10.1007/s10489-017-1101-2.

[30] C. Xia, Z. Pan, Z. Fei, S. Zhang, and H. Li, 'Vision based defects detection for Keyhole TIG welding using deep learning with visual explanation', *Journal of Manufacturing Processes*, vol. 56, pp. 845–855, Aug. 2020, doi: 10.1016/j.jmapro.2020.05.033.

[31] D. Bacioiu, G. Melton, M. Papaelias, and R. Shaw, 'Automated defect classification of Aluminium 5083 TIG welding using HDR camera and neural networks', *Journal of Manufacturing Processes*, vol. 45, pp. 603–613, Sep. 2019, doi: 10.1016/j.jmapro.2019.07.020.

Dicle University
Journal of Engineering
https://dergipark.org.tr/tr/pub/dumf
duje.dicle.edu.tr

Research Article

An Investigation of Driver Brake Pedal Stroke Input on Regenerated Braking Energy in Electric Vehicles via Dynamic Programming

Nurettin Okan Çaycı[1*], Erkin Dinçmen[2], İlyas İstif[3]

[1] Amasya University, Tasova Yüksek Akin Vocational School, Motor Vehicles And Transportation Technologies Department, Railroad Construction Program, nurettin.cayci@amasya.edu.tr
ORCID: https://orcid.org/0009-0002-0060-531X

[2] Yildiz Technical University, Control And Automation Engineering Department, erkin.dincmen@yildiz.edu.tr
ORCID: https://orcid.org/0000-0002-3234-281X

[3] Yildiz Technical University, Mechanical Engineering Deparment, istif@yildiz.edu.tr
ORCID: https://orcid.org/0000-0003-0792-249X

ARTICLE INFO

Article history:

Received 12 March 2025
Received in revised form 13 August 2025
Accepted 25 August 2025
Available online 30 September 2025

Keywords:

Fully electric vehicle, pedal stroke, regenerative braking, torque distribution, dynamic programming, energy efficiency

Doi: 10.24012/dumf.1655409

* Corresponding author

ABSTRACT

The rising popularity of electric vehicles increases the need for advanced techniques to improve driving efficiency. One such method is regenerative braking, which captures kinetic energy from the wheels—energy that would otherwise be lost as in traditional braking systems. In this study, a fully electric vehicle model which is three degrees of freedom was created with a fixed pedal-feel brake pedal and electric motors on both axles. The brake torque produced by pedal stroke input in different braking scenarios was allocated to the electric motors on the front and rear axles via dynamic programming in MATLAB/Simulink. It was compared to the case where the distribution ratio is fixed. More energy was gained with dynamic programming compared to the fixed allocation, and it is concluded that the duration of pressing the pedal and the repetition of pressing are effective parameters on energy recovery.

Introduction

Growing concerns over environmental pollution and greenhouse gas emissions from fossil fuels have increased interest in electric vehicles. Additionally, fossil fuel reserves are finite, making alternative energy sources essential. Among these, electric cars stand out as the most viable option, partly due to their lack of noise pollution. However, challenges remain, such as limited battery energy density, short driving ranges, and long charging times. These issues highlight the need for maximizing battery efficiency, with regenerative braking playing a key role in energy conservation. Regenerative braking allows a DC motor to function as a generator, producing current that can recharge the battery. The efficiency of this process depends on several key factors, including the motor's torque and speed-dependent efficiency, battery internal resistance, open circuit voltage, temperature, charge level, and torque distribution between axles.

Studies in the literature on regenerative braking are as follows: Investigation [1] examined the self-reported behaviors of 36 Parisian drivers using an electric MINI E prototype for six months. The study found that EV operation requires a learning phase where drivers adapt to range limitations, establish charging routines, and modify trip planning habits. Work [2] developed a driver model to control vehicle speed and mimic human driving behavior. A regenerative braking strategy using a series brake system was implemented to replicate real-world braking performance. Analysis [3] focused on electric motor control strategies, including Sliding Mode, H2/H∞, Adaptive, and Fuzzy Logic Controllers, along with Artificial Neural Networks and Neuro-Fuzzy systems integrated with PID controllers. In contribution [4], an optimized braking force

distribution approach was presented, maximizing regenerative energy recovery while ensuring braking efficiency by utilizing ground adhesion on both front and rear wheels. Research [5] performed a mathematical analysis of batteries and supercapacitors, evaluating their regenerative braking performance and system characteristics using MATLAB/SIMULINK. The authors of [6] explored the feasibility of fully relying on regenerative braking for all deceleration scenarios, employing multiple generators with different gear ratios to achieve this goal. Publication [7] investigated control strategies for regenerative braking in electric vehicles powered by brushless DC motors, proposing and comparing two control methods. In [8] introduced a braking torque allocation strategy optimized with a particle swarm algorithm for an electro-hydraulic compound braking system in a dual-motor, dual-axle electric vehicle. Article [9] presented a new braking torque allocation strategy to in-wheel motor EVs, prioritizing both safety and energy recovery. Model Predictive Control (MPC) was used to handle multi-objective constraints effectively. Paper [10] proposed a vehicle stability control system for a all-wheel-drive hybrid electric vehicle, optimizing braking torque distribution between regenerative braking and an electrohydraulic brake (EHB) using a genetic algorithm. Efforts in [11] focused on enhancing distributed torque control via Direct Torque Control (DTC) during regenerative braking. A Fuzzy Logic Controller for the BLDC motor was implemented and compared with a PI controller using MATLAB/Simulink. Research presented in [12] detailed the Energy-Optimal Deceleration Planning System (EDPS) for connected and autonomous EVs, utilizing a polynomial-based model to optimize regenerative braking based on real-time driving data. Study [13] proposed a downshifting strategy based on cluster-based stochastic dynamic programming (SDP). The method categorized driving conditions using the K-means algorithm and modeled braking torque transitions with Markov chains. A support vector machine (SVM) enabled real-time application of SDP-based commands. In [14] developed a predictive control method integrating adaptive cubic exponential prediction and dynamic programming to enhance regenerative braking energy recovery. The model optimized motor braking torque and wheel cylinder pressures while considering electro-hydraulic braking dynamics. Lastly, work [15] examined the distribution of friction and electrical braking forces, introducing key parameters to evaluate braking energy recovery efficiency while ensuring vehicle safety under critical driving conditions.

In this study, depending on the driver's behavior, the distribution of the torque amount produced depending on the pedal stroke that occurs when the pedal is pressed and the pressing speed, which is the result of the change in the pedal stroke depending on time, to the electric motors located on the front and rear axles and also to the hydraulic brakes was done and regenerated energy into the battery was found in Matlab/Simulink environment via dynamic programming and Simulink model. Briefly, the effect of pedal pressing behavior on the amount of regenerative energy was investigated.

Electric Vehicle Model

Brake pedal model

Pedal stroke x_p pedal-dependent deceleration is utilized according to the fixed pedal feel [16]. The brake pedal displacement x_p and deceleration a_{dec} described as follow:

$$a_{dec} = \begin{cases} -(0.01x_p)g, & x_p \le 20mm \\ -(0.02x_p - 0.2)g, & 20mm \le x_p \le 80mm \end{cases} \quad (1)$$

Total brake torque produced by pedal stroke T_b^{tot} is calculated as:

$$T_b^{tot} = m.a_{dec}.r_{eff} \quad (2)$$

where vehicle mass is m and wheel effective radius is r_{eff}.

Vehicle Dynamics

The three-degree-of-freedom single track vehicle dynamics model is utilized in this paper. The longitudinal vehicle dynamics equation is given as follows:

$$ma_x = \sum F_x = F_{xf}cos\ \delta_f + F_{xr} - F_{yf}sin\ \delta_f - F_g - F_{aero} - F_{roll} \quad (3)$$

where, aerodynamic resistance is F_{aero}, rolling resistance is F_{roll} , ma_x inertial resistance, F_g is the grade of the road and F_{xf} , F_{xr} are the longitudinal and F_{yf} , F_{yr} are the lateral forces on the front and rear wheels, respectively. Steering angle is denoted by δ_f. The lateral vehicle dynamics is described as follows:

$$ma_y = \sum F_y = F_{xf}sin\ \delta_f + F_{yf}cos\ \delta_f + F_{yr} \quad (4)$$

The yaw motion dynamics is given as follows:

$$I_z\dot{r} = (F_{xf}sin\ \delta_f)l_f + (F_{yf}cos\ \delta_f)l_f - F_{yr}l_r \quad (5)$$

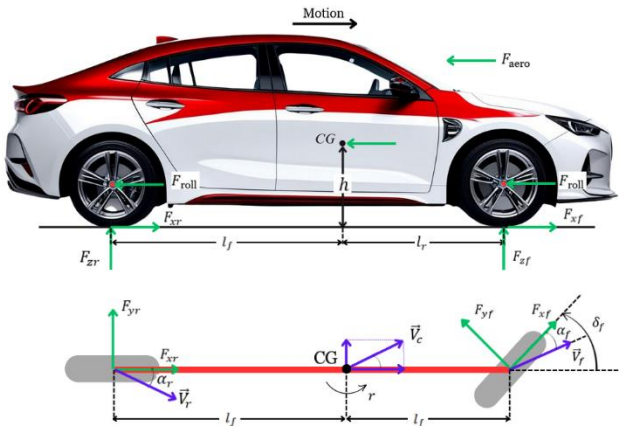


Figure 1. Distances, forces and angles.

I_z is the vehicle inertia in yaw motion. Figure 1 displays the forces, angels and dimensions which is defined in equation

3, 4 and 5. Because lateral dynamics will be considered in future studies, the Simulink model created has three degrees of freedom. However, steering input was not provided in the braking scenarios covered in this article.

Tire Model

Dugoff tire model is utilized to compute tire forces. This model enables the calculation of forces considering both lateral and longitudinal force generation simultaneously [17]. As per the Dugoff model, the longitudinal forces of the front and rear tires are determined using equation (6).

$$F_{x(f,r)} = C_{x(f,r)} \frac{\sigma_{(f,r)}}{1+\sigma_{(f,r)}} f\left(\lambda_{(f,r)}\right) \tag{6}$$

For the front and rear lateral tire forces, (7) is used,

$$F_{y(f,r)} = C_{\alpha(f,r)} \frac{tan\ \alpha_{(f,r)}}{1+\sigma_{(f,r)}} f\left(\lambda_{(f,r)}\right) \tag{7}$$

where, σ_f and σ_r represent the longitudinal slip ratios, while α_f and α_r denote the side slip angles of the front and rear tires, respectively. The cornering stiffness of the front and rear tires is denoted by $C_{\alpha f}$ and $C_{\alpha r}$, whereas the longitudinal tire stiffness of the front and rear tires are represented as $C_{x,f}$ and $C_{x,r}$. The values of $f(\lambda_f)$ and $f(\lambda_r)$ are determined using equations (8), μ is tire-road friction coefficient.

$$f\left(\lambda_{(f,r)}\right) = \begin{cases} (2-\lambda_{(f,r)})\lambda_{(f,r)} & \text{when } \lambda_{(f,r)} < 1 \\ 1 & \text{when } \lambda_{(f,r)} \geq 1 \end{cases}$$
$$\lambda_{(f,r)} = \frac{\mu F_{z(f,r)}\left(1+\sigma_{(f,r)}\right)}{2\sqrt{\left(C_{x(f,r)}\sigma_{(f,r)}\right)^2 + \left(C_{\alpha(f,r)} tan\ \alpha_{(f,r)}\right)^2}}. \tag{8}$$

Braking Standards

To guarantee vehicle braking safety, the UN/ECE has established specific regulations. As per the ECE R13-H brake standards, passenger cars must comply with defined brake force allocation criteria between the front and rear axles, [18]:

1. In all vehicle load conditions, the braking ratio is defined as the ratio of deceleration to gravitational acceleration, and when this ratio expressed by z is in the range z=0.15~0.8, the traction-use curve of the rear axle should not be greater than that of the front axle::

$$k_f \geq k_r \tag{9}$$

2.When the adhesion coefficient k is in the range of 0.2 ~ 0.8, the braking ratio must satisfy the following condition:

$$z \geq 0.1 + 0.7(k - 0.2) \tag{10}$$

If the values $k = 0.15 \sim 0.8$ are substituted into inequality 10, respectively, the range of variation of z is found to be $0.1 \leq z \leq 0.61$. In this case, the adhesion coefficients of the front and rear wheels satisfy the following conditions:

$$k_f \leq \frac{z+0.04}{0.7} \tag{11}$$

$$k_r \leq \frac{z+0.04}{0.7} \tag{12}$$

where k_f and k_r are the theoretical adhesion coefficients on the front and rear axles, respectively, that is, the coefficients showing how effectively the wheels use road grip during braking, and they are calculated with the following formulas:

$$k_f = \frac{F_{x,f}}{F_{z,f}} = \frac{\beta z L}{l_r cos\ (\alpha) + zh} \tag{13}$$

$$k_r = \frac{F_{x,r}}{F_{z,r}} = \frac{(1-\beta) z L}{l_f cos\ (\alpha) - zh} \tag{14}$$

where; $F_{z,f}$ and $F_{z,r}$ are the normal forces acting on the front and rear axles from the road surface during braking, respectively, l_f is the distance between the front axle and the center of gravity (CG), l_r is the distance between the rear axle and the center of gravity, L is the total axle distance, α is the road slope, h is the center of gravity height, and β is the braking torque allocation ratio. β is defined as follows:

$$\beta = \frac{T_f}{T_b^{tot}} \tag{15}$$

where T_f is the front axle torque. Substituting equations 13 and 14 into 9, 11 and 12 respectively, we obtain the following inequalities related to the torque allocation ratio:

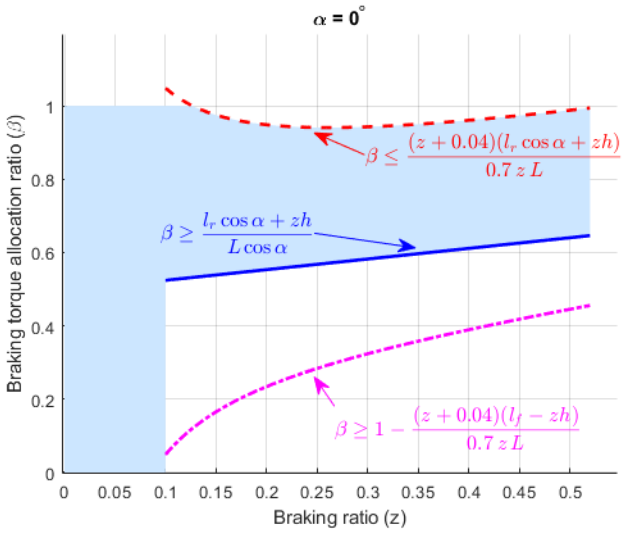


Figure 2.

The graph of the inequalities in (16),(17),(18) is plotted in figure (2). Under ECE regulations, the front wheels always maintain a higher adhesion coefficient than the rear wheels, ensuring braking stability. However, for optimal braking, the wheels' usage coefficients should remain below the road's adhesion coefficient (μ). Given the inequality in Equation 9, it is sufficient to ensure that only the front wheels' usage coefficient stays below μ.

Table 1. Vehicle Parameters.

Symbol	Values
m	1623 kg
l_f	1.09 m
l_r	1.07 m
h	0.627 m
I_z	2166 kg.m^2
r_{eff}	0.327 m
J	0.563 kg.m^2

$$\beta < \frac{\mu(zh + l_r)}{zL} \tag{19}$$

Electrical Motor Model

After determining the braking torque limits at both axles while accounting for the β value, the generated torques during braking, based on the pedal stroke, are utilized to compute the wheel's angular acceleration using the following equation:

$$\dot{\omega} = \frac{-T_b^{tot} - r_{eff}\left(m \cdot \alpha_x + F_{\text{aero}} + F_{\text{roll}} + F_g\right)}{J} \tag{20}$$

where J represents the wheel's inertia. Electric motor's efficiency is determined by using the efficiency map shown in Fig. 2. The power generated from both axles' EM as follows:

$$P_{EM,f} = T_b^{tot}.\beta \cdot \omega_{EM,f}.\eta_{EM,f} \tag{21}$$

$$P_{EM,r} = T_b^{tot}.(1-\beta) \cdot \omega_{EM,r}.\eta_{EM,r} \tag{22}$$

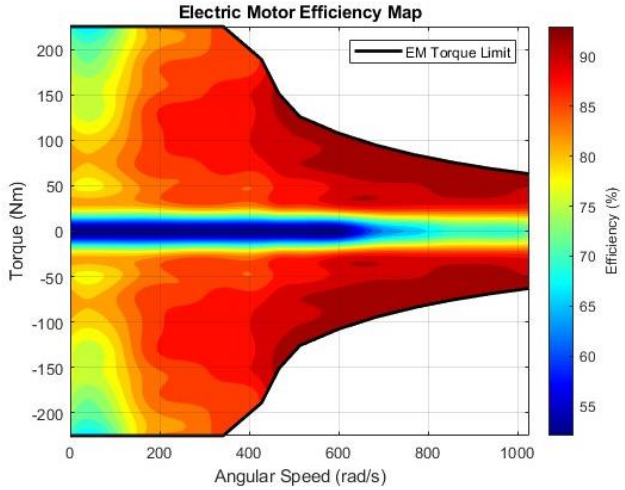


Figure 3. Electrical motor (EM) efficiency map

where $\omega_{EM,f}$ and $\omega_{EM,r}$ represent the angular speeds of the front and rear electric motors (EM), respectively, while $\eta_{EM,f}$ and $\eta_{EM,r}$ denote their efficiencies, as determined from the efficiency map in Figure 3. The total EM power, which can subsequently be used to determine the total energy stored in the battery, is calculated as follows:

$$P_{EM}^{tot} = P_{EM,f} + P_{EM,r} \tag{23}$$

Battery Model

The equations necessary for calculating the power charged into the battery are given as follows [19]:

$$I_{chg} = \frac{-U_{oc} + \sqrt{Uoc^2 - 4R_{chg}P_{EM}^{tot}}}{2 * R_{chg}} \tag{24}$$

$$\eta_{bat} = U_{oc}/\left(U_{oc} + R_{chg}I_{chg}\right) \tag{25}$$

$$P_{bat} = \eta_{bat}P_{EM}^{tot} \tag{26}$$

here, U_{oc} represents the open-circuit voltage of the battery, R_{chg} is the battery's charging resistance, I_{chg} denotes the charging current, η_{bat} refers to the battery efficiency, and P_{bat} is the power stored in the battery.

Dynamic Programming

Dynamic programming (DP) optimally distributes power by solving sequential sub-problems backward from the last to the first stage, significantly reducing calculations. However, since it requires prior knowledge of the entire driving scenario, it cannot be applied in real-time control. Instead, DP is used offline to evaluate the performance of instantaneous control algorithms. For the basic principle of the DP algorithm see also [20].

As observed, this process follows a backward calculation approach. In dynamic programming, this method requires fewer computations than forward one.

Where, 225×20 matrix is constructed for DP. The front axle (EM) torque levels are represented on the vertical axis, while the horizontal axis denotes the simulation time which is shown in Figure 4. The EM torque is segmented into 225 equal steps, ranging from zero to its maximum limit. The simulation runs with a step size of half second Δt , with braking concluding at T_{end} , the 10th second, making the total duration 10 seconds.

Δt second before T_{end}, at the highest torque level, there are four possible transitions to the next state. These transitions are illustrated in Figure 4 with black arrows.

For instance, if the torque variation is restricted to a maximum of three levels owing to EM's response time, a change of four levels downward within Δt is not feasible.

Throughout this process, the amount of battery charge for each torque change is calculated. The optimal choice is the one that charges the battery the most.

$$J^*_{(Tend-1)}(1) = max\{J^{Tend}_{(Tend-1)}(1,1), J^{Tend}_{(Tend-1)}(1,2), J^{Tend}_{(Tend-1)}(1,3), \quad J^{Tend}_{(Tend-1)}(1,4) \ \} \tag{27}$$

The alternative torque levels after Δt second, corresponding to the second torque level, The procedure is described as follows:

$$J^*_{(Tend-1)}(2) = max\{J^{Tend}_{(Tend-1)}(2,1), J^{Tend}_{(Tend-1)}(2,2), J^{Tend}_{(Tend-1)}(2,3), J^{Tend}_{(Tend-1)}(2,4), J^{Tend}_{(Tend-1)}(2,5)\} \quad (28)$$

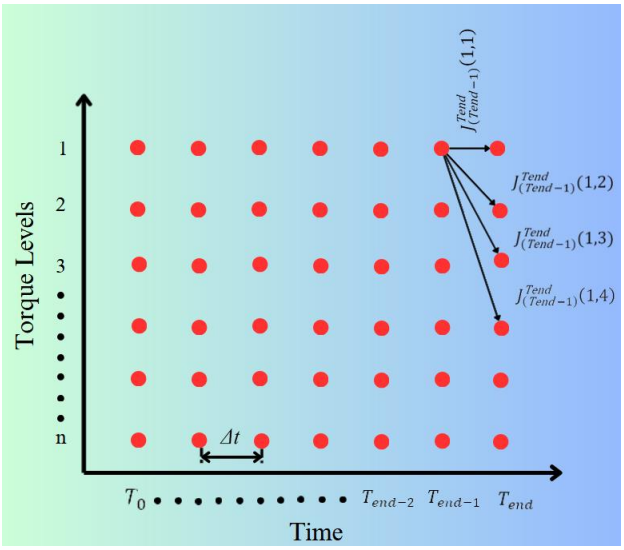


Figure 4. The first level alternatives of the DP.

Similarly, at the moment $T_{end} - 2\Delta t$, the possible alternatives are written, and calculations are then performed for the state transitions at $T_{end} - 2\Delta t$ for the first torque level as follow:

$$J^*_{(Tend-2)}(1) = max\{J^{Tend-1}_{Tend-2}(1,1) + J^*_{Tend-1}(1), J^{Tend-1}_{Tend-2}(1,2) + J^*_{Tend-1}(2), J^{Tend-1}_{Tend-2}(1,3) + J^*_{Tend-1}(3), J^{Tend-1}_{Tend-2}(1,4) + J^*_{Tend-1}(4)\} \quad (29)$$

This process continues backward through the time steps $T_{end} - 3\Delta t$, $T_{end} - 4\Delta t$, $T_{end} - 5\Delta t$, $T_{end} - 6\Delta t$ and so on. Upon completing the calculations, the torque distribution ratios that optimize battery charging during braking are found.

Meanwhile, rear EM's torque is calculated by using that $T_r = T_b^{tot} - T_f$. Using T_r, the power generated by the rear EM to charge the battery is calculated.

The flowchart of both the Simulink model and dynamic programming is given in Figure 5.

Simulation Study and Results

Where three different braking scenarios of a vehicle traveling at a constant speed of 28 m/s in all scenarios were considered within 10 seconds. In the first scenario, the brake pedal is pressed slowly, the change in pedal stroke from zero to 30 mm and the torque amount generated accordingly are seen in Figure 6. The amount of energy recovered during braking is given in Figure 7. Accordingly, the continuous line represents the amount of energy gained via dynamic programming, while the amount of energy given with the dashed line represents the situation where β is constant. In both cases, the amount of energy gained when torque is shared with dynamic programming is greater than the amount of energy gained when β is taken as constant. The maximum amount of energy gained in the situation where

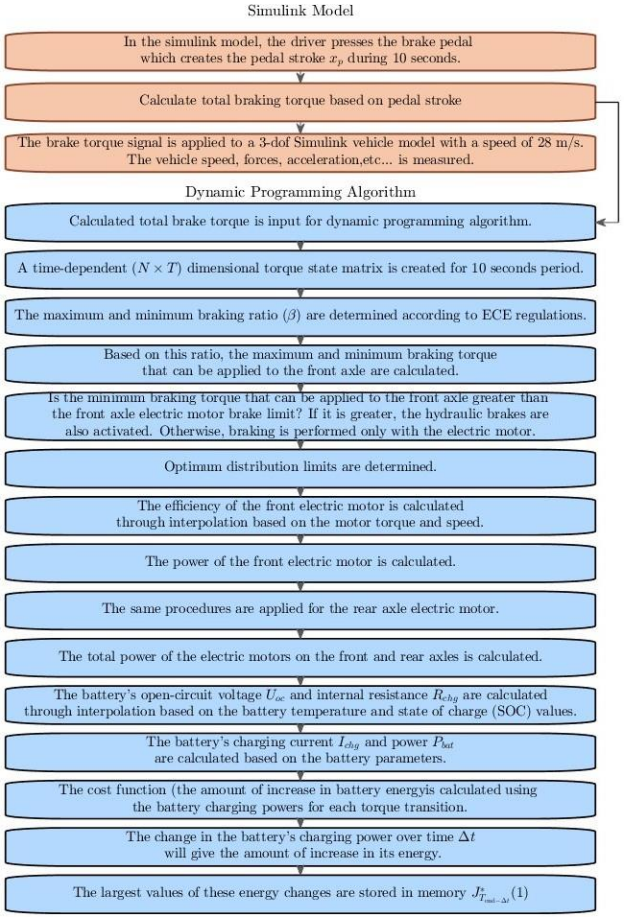


Figure 5. Flowchart.

β is constant is 570.334 kJ, and the amount of energy gained in dynamic programming is 586.952 kJ. In this scenario, 2.91% more gain was achieved with dynamic programming.

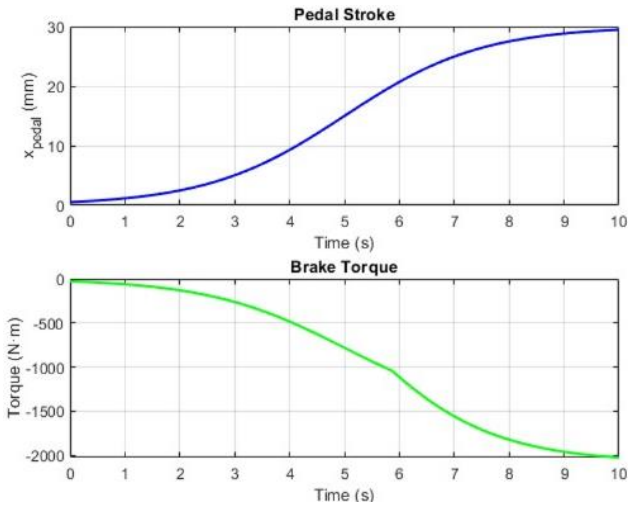


Figure 6. Change in pedal stroke with time and amount of torque generated for scenario 1

Figure 8 shows the graph of the time-dependent change of the pedal stroke applied in the second scenario and the torque amount generated accordingly. Here, the time-dependent change of the pedal stroke applied is greater than in the first scenario, and the pedal stroke is kept constant after the 6th second. Figure 9 shows the result of the amount of energy gained in this scenario. The maximum amount of energy gained in the case where β is constant is 580.442 kJ, and the amount of energy gained via dynamic programming is 598.995 kJ. This indicates that 3.196% more energy is gained thanks to dynamic programming.

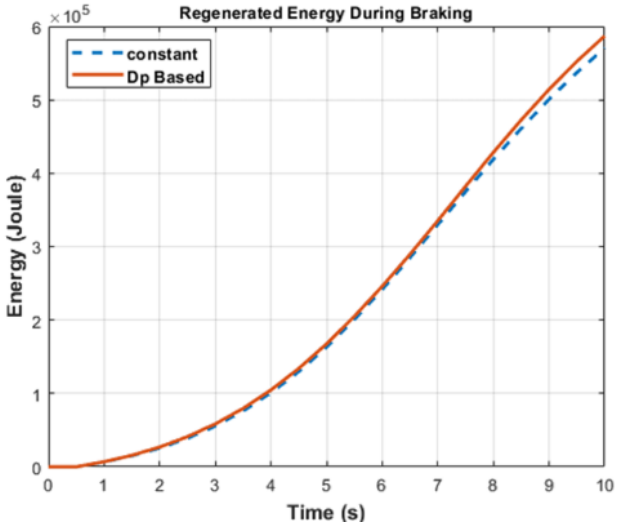


Figure 7. The amount of energy gained in scenario 1

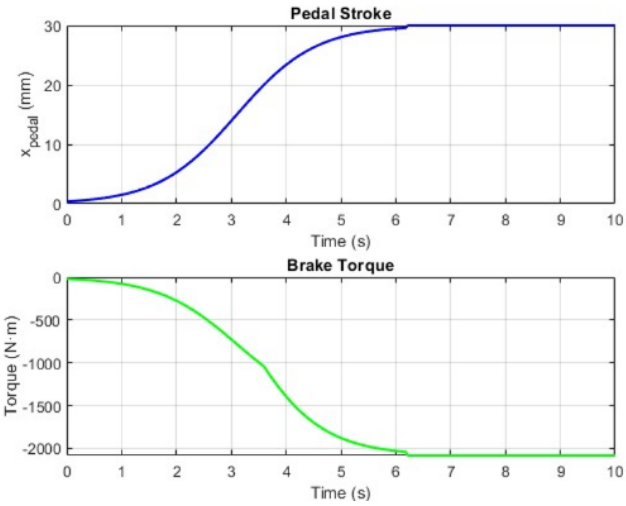


Figure 8. Pedal stroke and torque variation in ten sec. for scenario 2

Figure 10 shows the time-dependent change of the pedal stroke applied in the third scenario and the torque amount generated accordingly. The difference of the pedal stroke applied here from the previous two scenarios is that it considers the situation of pressing and releasing the pedal twice within a period of 10 seconds. Pressing the pedal takes longer than releasing the pedal. Figure 11 shows the result of the amount of energy gained in this scenario. The maximum amount of energy gained in the case where β is constant is 603.787 kJ, and the amount of energy gained in dynamic programming is 621.935 kJ. This indicates that there is 3% more energy gain in terms of dynamic programming.

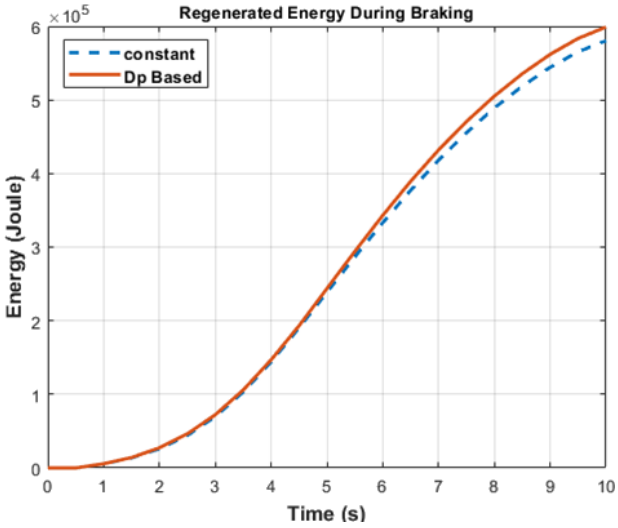


Figure 9. The amount of energy gained in scenario 2

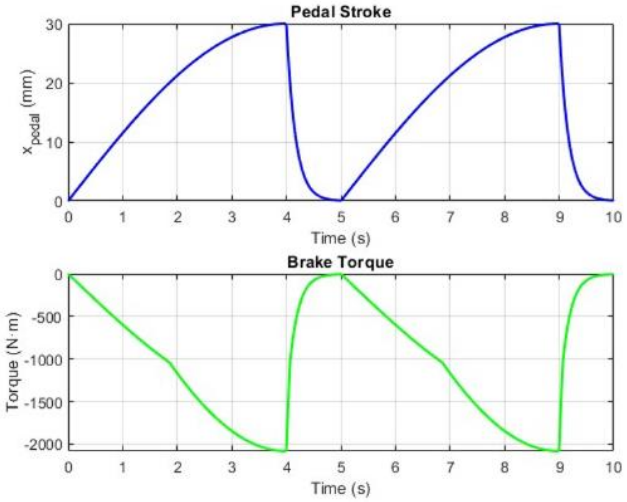


Figure 10. Pedal stroke and torque variation in ten sec. for scenario 3

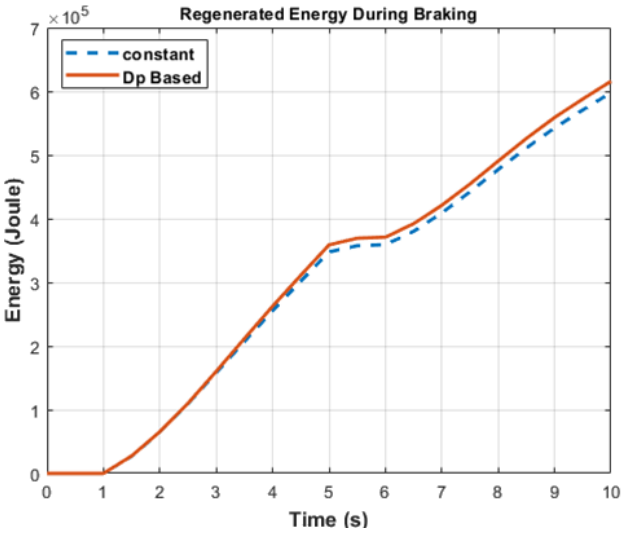


Figure 11. The amount of energy gained in scenario 3

Table 2. Results.

Scenarios	Regenerated Energy via DP (kWh)	Regenerated Energy by constant β (kWh)	Gain (%)
1	0.163	0.158	2.91
2	0.166	0.161	3.196
3	0.173	0.168	3

In all 3 simulations, the energy amounts gained via dynamic programming provide approximately 3% more gain than the energy gains in cases where β is constant. In addition, the pedal stroke is taken as 30 mm in all 3 simulations. As seen in the graph in Figure 10, the highest total energy is obtained in the third scenario. The change in vehicle speed in 10 seconds is given in Figure 10. Since the vehicle speed does not drop to zero in a braking as in scenario 1, the total energy gained is lower than in scenario 2. However, if the simulation period is extended and the brake is applied to reduce the speed to zero, it is certain that the amount of energy gained in scenario 1 will exceed scenario 2. The real gain here is in scenario 3. As a result, there is more energy gain in pressing and releasing the brake. In Table 2, the amount of energy gained is given in kWh.

Conclusion

Dynamic programming provides 3% approximately more energy recovery than using a constant β in all braking scenarios. The highest energy gain occurs in the third scenario with variable pedal application, showing that press-release braking is more efficient for regenerative systems. It appears that pedal behavior is crucial for energy recovery. Future studies could include a frequency that maximizes energy recovery after determining the braking torque requirement and yaw motion could be taken in to account. In addition, the data obtained here will be used to train artificial neural network and the torque distribution process will be undertaken by it.

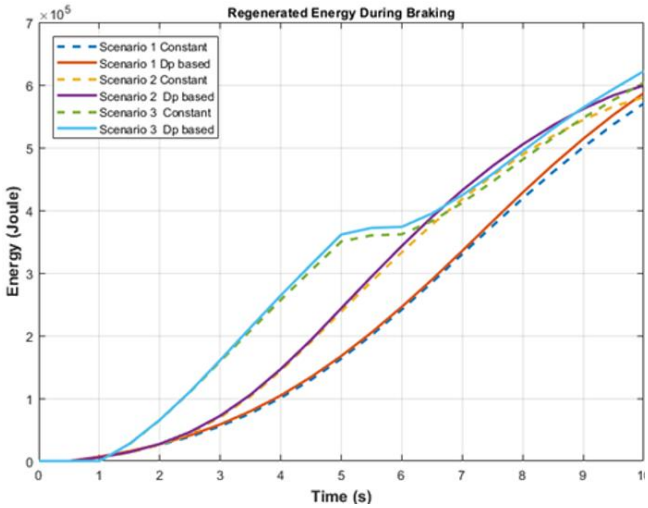


Figure 12. The amount of energy gained for all scenarios

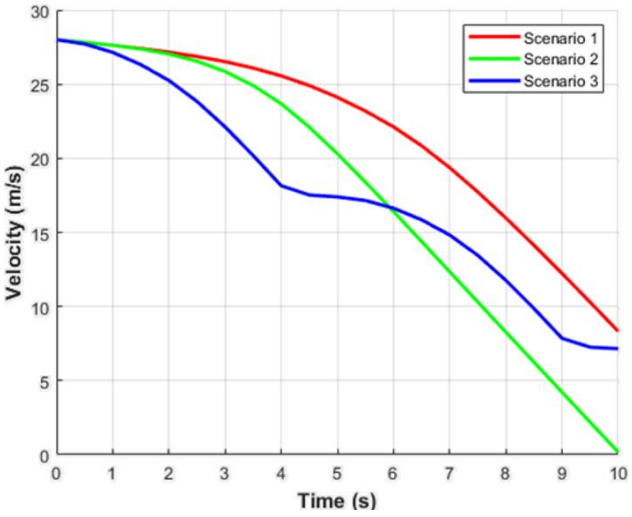


Figure 13. Velocities for all scenarios

Aknowledgement

The authors extend their heartfelt gratitude to the Turkish National Research Council (TUBITAK) for its generous support under grant no: 122M994.

References

[1] E. Labeye, M. Hugot, C. Brusque, and M. A. Regan, "The electric vehicle: A new driving experience involving specific skills and rules, "Transportation Research Part F: Traffic Psychology and Behaviour", vol. 37, pp. 27–40, Feb. 2016.

[2] Miri, I., Fotouhi, A., and Ewin, N., "Electric vehicle energy consumption modelling and estimation—A case study," International Journal of Energy Research, vol. 45, no. 1, pp. 501-520, Jan. 2021.

[3] G. A. Chandak and A. A. Bhole, "A review on regenerative braking in electric vehicle," 2017 Innovations in Power and Advanced Computing Technologies (i-PACT), pp. 1-5, 2017.

[4] J. Zhiming, R. Dianbo, S. Baoyu, C. Shumei, and S. Gang, "The research of regenerative braking control strategy for advanced braking force distribution," in 2009 Fifth International Conference on Natural Computation, vol. 6, Aug. 2009, pp. 458–462. IEEE

[5] Bogineni, J., & Nakka, J. (2022, January). Battery and supercapacitor performance analysis during regenerative braking in electric vehicles. In 2022 International Conference on Computing,

Communication and Power Technology (IC3P) (pp. 108-112). IEEE.

[6] W. J. Melis and O. Chishty, “Fully regenerative braking and improved acceleration for electrical vehicles,” Int. J. Sustain. Energy Dev. (IJSED), vol. 2, no. 1, pp. 75–80, 2013.

[7] P. S. Shenil, “Novel regenerative braking controllers for electric vehicle driven by BLDC motor,” in 2021 Fourth International Conference on Electrical, Computer and Communication Technologies (ICECCT), 2021.

[8] W. Jiang, R. Zheng, G. Zhang, Z. Zhu, W. Wang, C. Li, and Q. Tong, “Optimal torque distribution strategy for electric vehicles with electro-hydraulic compound braking system,” in 2023 7th CAA International Conference on Vehicular Control and Intelligence (CVCI), Oct. 2023, pp. 1–6. IEEE.

[9] W. Xu, H. Chen, H. Zhao, and B. Ren, “Torque optimization control for electric vehicles with four in-wheel motors equipped with regenerative braking system,” Mechatronics, vol. 57, pp. 95–108, 2019.

[10] D. H. Kim, J. M. Kim, S. H. Hwang, and H. S. Kim, “Optimal brake torque distribution for a four-wheel-drive hybrid electric vehicle stability enhancement,” Proc. Inst. Mech. Eng., Part D: J. Automob. Eng., vol. 221, no. 11, pp. 1357–1366, 2007.

[11] G. BhaskarRao, N. Mounika, K. Chandana, A. DileepKumar, G. AshokBabu, and S. HimaVarshini, "Control strategy for regenerative braking in electric vehicles," International Journal of Scientific Research in Engineering and Management, 2023, doi: 10.55041/ijsrem18484

[12] D. Kim, J. SooEo, and K.-K. K. Kim, "Parameterized energy-optimal regenerative braking strategy for connected and autonomous electrified vehicles: A real-time dynamic programming approach," *IEEE Access*, 2021. DOI: 10.1109/access.2021.3098807

[13] B. Liu, L. Li, X. Wang, and S. Cheng, "Hybrid electric vehicle downshifting strategy based on stochastic dynamic programming during regenerative braking process," IEEE Transactions on Vehicular Technology, 2018. [Online]. Available: DOI: 10.1109/TVT.2018.2815518.

[14] J. Zhang, Y. Yang, D. Qin, C. Fu, and Z. Cong, "Regenerative braking control method based on predictive optimization for four-wheel drive pure electric vehicle," IEEE Access, vol. 9, pp. 1-10, 2021. DOI: 10.1109/ACCESS.2020.3046853.

[15] C. Qiu, G. Wang, M. Meng, and Y. Shen, “A novel control strategy of regenerative braking system for electric vehicles under safety critical driving situations,” Energy, vol. 149, pp. 329–340, Apr. 2018, doi:10.1016/j.energy.2018.02.046.

[16] U. Caliskan and V. Patoglu, "Efficacy of haptic pedal feel compensation on driving with regenerative braking," IEEE Transactions on Haptics, vol. 13, no. 1, pp. 175-182, 2020.

[17] Rajamani, R.: Vehicle Dynamics and Control. Springer, New York (2012)

[18] Regulation No 13 of the Economic Commission for Europe of the United Nations (UN/ECE) — Uniform provisions concerning the approval of vehicles of categories M, N and O regarding braking, (OJ L 257 30.9.2010, p. 1) [Online]. Available: https://op.europa.eu/s/y1QM

[19] E. Dincmen, B. Güvenç, "A control strategy for parallel hybrid electric vehicles based on extremum seeking," Vehicle System Dynamics, vol. 50, pp. 199-227, 2012, doi: 10.1080/00423114.2011.577224.

[20] O. Ergun, N. O. Cayci, E. Dincmen, and I. Istif, "Optimum torque distribution during regenerative braking in a fully electrical vehicle via dynamic

[21] programming," in 2023 7th International Symposium on Multidisciplinary Studies and Innovative Technologies (ISMSIT), Oct. 2023, pp. 1-6.

Appendix A

Nomenclature

Symbol	Description
α	Road slope angle (rad)
a_{dec}	Pedal-dependent vehicle deceleration
a_x	Longitudinal acceleration (m/s^2)
a_y	Lateral acceleration (m/s ^{2})
$\alpha_{(f,r)}$	Side slip angle (front/rear)
β	Braking torque distribution ratio
$C_{\alpha(f,r)}$	Cornering stiffness (front/rear tires)
$C_{x(f,r)}$	Longitudinal stiffness (front/rear tires)
F_{aero}	Aerodynamic drag force
$f(\lambda_{(f,r)})$	Dugoff friction function
F_g	Gravitational force due to road slope
F_{roll}	Rolling resistance force
F_{xf}, F_{xr}	Longitudinal tire forces (front/rear)
F_{yf}, F_{yr}	Lateral tire forces (front/rear)
$F_{z(f,r)}$	Normal force on front/rear tires
h	Height of CG from ground (m)
I_{chg}	Battery charging current (A)

I_z	Yaw moment of inertia of vehicle ($\mathrm{kg \cdot m^2}$)
J	Wheel inertia ($\mathrm{kg \cdot m^2}$)
k_f, k_r	Adhesion utilization coefficient (front/rear)
L	Wheelbase (distance between axles) (m)
l_f	Distance from CG to front axle (m)
l_r	Distance from CG to rear axle (m)
m	Vehicle mass (kg)
μ	Tire-road friction coefficient
η_{bat}	Battery charging etticiency
$\eta_{EM(f,r)}$	Efficiency of front/rear electric motor
P_{bat}	Power charged into the battery
$P_{EM(f,r)}$	Power generated from front/rear electric motor
P_{EM}^{tot}	Total power generated by electric motors
r	Yaw rate (rad/s)
r_{eff}	Effective wheel radius (m)
R_{chg}	Internal resistance during charging (Ω)
$\sigma_{(f,r)}$	Longitudinal slip ratio (front/rear)
T_b^{tot}	Total brake torque generated by the pedal stroke
U_{oc}	Open-circuit voltage of battery (V)
δ_f	Front wheel steering angle (rad)
$\omega_{EM(f,r)}$	Angular speed of front/rear electric motor (rad/s)
$\dot{\omega}$	Angular acceleration of wheel ($\mathrm{rad/s^2}$)
x_p	Brake pedal stroke (mm)
z	Braking intensity (deceleration/gravity)
$\vec{V}_f$	Front axle velocity (m/s)
$\vec{V}_r$	Rear axle velocity (m/s)
$\vec{V}_c$	Velocity of the CG (m/s)
$\lambda_{(f,r)}$	Combined slip function (front/rear)
CG	Center of gravity

Dicle University
Journal of Engineering
https://dergipark.org.tr/tr/pub/dumf
duje.dicle.edu.tr

Araştırma Makalesi/Research Article

CTP kompozit plakaların çoklu cıvata bağlantı davranışlarının incelenmesi

Investigation of multi-bolted connection behaviors of GFRP composite plates

Çağdaş Şen[1], Fırat Aydın[1], Mehmet Emin Deniz[2]

[1]Lisansüstü Eğitim Enstitüsü, Batman Üniversitesi, cagdassen1994@gmail.com, ORCID: https://orcid.org/0009-0003-4604-2521

[1]Lisansüstü Eğitim Enstitüsü, Batman Üniversitesi, firat.aydin.192@gmail.com, ORCID: https://orcid.org/0000-0002-0211-9756

[2]Makine Mühendisliği Bölümü, Batman Üniversitesi, mehmetemin.deniz@batman.edu.tr, ORCID: https://orcid.org/0000-0003-1898-1161

MAKALE BİLGİLERİ

Makale Geçmişi:

Geliş 21 Mart 2025
Revizyon 27 Temmuz 2025
Kabul 7 Ağustos 2025
Online 30 Eylül 2025

Anahtar Kelimeler:

Pultrüzyon ile üretilmiş cam fiber takviyeli polimer (CTP), çoklu cıvata bağlantısı, delik, hasar modları

ÖZ

Pultrüzyon ile üretilmiş cam fiber takviyeli polimer (CTP) esaslı kompozit plakaların bağlantı kapasitesi genellikle kompozit yapının tasarımında önemli bir faktör olarak kabul edilir. Bu çalışmada, farklı sıkma momentleri (M = 0–2–4 N.m), farklı delik sayıları (2–4–5) ve farklı E/D (2–3–4) oranları dikkate alınarak 0° ve 90° fiber yönelim açılarına sahip polimer matris esaslı cam fiber takviyeli kompozit plakaların cıvatalı bağlantı davranışları tartışılmıştır. Bağlantı cıvatalarına yeterli sıkma momenti uygulanması, numunelerin yük taşıma kapasitesini artırmaktadır. Ancak delik sayısının artışı, kesit kaybına neden olduğu için malzemenin mukavemetini olumsuz etkileyebilmektedir. Bu yüzden mühendislik uygulamalarında, optimum sıkma momenti ve delik düzenlemesi dikkatlice seçilmelidir. Çekme yükleri altında mekanik olarak sabitlenmiş tabakalı kompozitler genellikle, yatak (bearing) hasar modu, kesme (shear-out) hasar modu ve yırtılma (net-tension) hasar modu olarak üç temel mod şeklinde hasarlanırlar. 0° fiber yönelim açılarına sahip numunelerde bu üç hasar modu oluşurken 90° fiber yönelim açılı numunelerde ise yatak/net-gerilim (bearing/net-tension) hasar modları belirgin şekilde gerçekleşmiştir.

ARTICLE INFO

Article history:

Received 21 March 2025
Received in revised form 27 July 2025
Accepted 7 August 2025
Available online 30 September 2025

Keywords:

Glass fiber reinforced polymer (GFRP) produced by pultrusion, multiple bolt joint, hole, damage modes

Doi: 10.24012/dumf.1662259

*Sorumlu Yazar

ABSTRACT

The connection capacity of pultruded glass fiber reinforced polymer based composite plates is generally considered as an important factor in the design of composite structures. In this study, the bolt connection behaviors of polymer matrix based glass fiber reinforced composite plates with 0° and 90° fiber orientation angles were discussed by considering different tightening torques (M = 0–2–4 N.m), different hole numbers (2–4–5) and different E/D (2–3–4) ratios. Applying sufficient tightening torque to the connection bolts increases the load carrying capacity of the samples. However, increasing the number of holes may negatively affect the strength of the material since it causes cross-section loss. Therefore, in engineering applications, the optimum tightening torque and hole arrangement should be carefully selected. Mechanically restrained laminated composites under tensile loads generally fail in three basic modes as bearing, shear-out and net-tension damage modes. While these three damage modes occurred in samples with 0° fiber orientation angles, bearing/net-tension damage modes occurred significantly in samples with 90° fiber orientation angles.

Giriş

Genellikle pek çok makine parçası sökülüp tekrar bağlanmaya imkân verecek şekilde tasarlanmaktadır. Bu makine parçalarının ya da bağlantıda kullanılan bağlantı elemanlarının, sökme ve bağlama durumunda hasara uğramaması gerekir. Bu nedenle istenilen şartları sağlayan değişik şekil ve özelliklere sahip çok sayıda bağlama elemanı geliştirilmiştir [1]. Bu bağlantı elemanları yalnızca makine mühendisliği ve havacılıkta değil, aynı zamanda inşaat mühendisliği yapılarında da kullanılmaktadır. Yapı uygulamalarında kullanılan pultrüzyon işlemi ile üretilen cam elyaf takviyeli polimer (CTP) kompozit cıvatalı bağlantılarının davranışı, 1990'ların başından beri bir dizi çalışmanın araştırma konusu olmuştur [2]. Mekanik bağlantılar yüksek gerilme dağılımlarından ötürü kompozit yapılarda kopma, yırtılma ve yataklanma hasarlarına yol açmaktadırlar. Mekanik bağlantıların neden olduğu bu gerilmeler, bağlayıcı-delik boşluğuna, levha ve mekanik bağlayıcı arasındaki sürtünme katsayısına, bağlayıcı malzemesinin esnekliğine, bağlantı malzemesinin geometrik yapısına ve yükleme durumlarına bağlı olarak değişmektedir. Bu nedenle kompozit malzeme tasarımında mekanik bağlantıların bağlayıcı delik etrafında oluşturduğu gerilme dağılımının doğru tahmini, güvenilir mukavemet değerlendirmesi için önem arz etmektedir [3]. Mekanik bağlantı elemanları, yapıyı tahrip etmeden çıkarılabilme avantajı sunmaktadır. Fakat yüzey onarımına, servis sıcaklığına veya neme karşı hassas değildirler. Kompozit malzemelerde mekanik olarak tutturulmuş birleşimleri tasarlama prosedürü ağırlıklı olarak deneysel verilere dayanmaktadır ve analitik modeller büyük ölçüde deneysel niteliktedir. Kompozit yapılarda yapısal bütünlük ve güvenilirliği elde etmek için uygun geometrik parametrelerin ve malzemelerin seçimi esastır. Çünkü kompozitlerdeki cıvatalı bağlantılar, mükemmel elastik veya mükemmel plastik varsayımlarla öngörülmeyen yüklerde hasara uğrayabilirler. Kompozit bir yapıdaki herhangi bir bağlantı, uygun şekilde tasarlanmazsa, bir hasar başlatma noktası görevi görebilir ve bileşenin o konumda nihai hasarına sebep olabilmektedir [4].

Literatür çalışmaları göz önüne alındığında, elyaf takviyeli kompozit yapıların mekanik bağlantı davranışları, elyaf tipi ve şekli, kompozitin malzeme özellikleri, bağlantı malzemesinin geometrisi, bağlayıcı tipi ve yükleme şeklini içeren parametrelerin bağlantı hasar mukavemetlerine ve hasar oluşum şekillerine etkileri üzerine çalışmaları içermektedir. Araştırmacıların büyük çoğunluğu mekanik bağlantıların bağlantı davranışlarını deneysel çalışmalarda elde ettikleri sonuçların sayısal ve analitik çözümlemelerin sonuçlarıyla karşılaştırarak değerlendirmişlerdir.

Crews [5] cıvata sıkıştırma torku uygulanan numunelerin, statik ve yorulma yüklemeleri altında cıvata yatak yüklerini ciddi şekilde etkilemiştir. Wang ve ark. [6] cıvatalı bağlantıların yatak tepkisini ve yatak mukavemetini, yatak hasar mekanizmasını sıkıştırma basıncına bağlı olarak incelediler. Yazarlar çalışmalarında, yatak hasarını değerlendirmek için pim yüklü bir yatak (yanal sıkıştırma olmadan) ve cıvatalı bir yatak (yanal sıkıştırma ile) gibi iki farklı test gerçekleştirmişlerdir. Aktas ve Karakuzu [7], karbon/epoksi esaslı kompozit plakaların pim bağlantıları üzerine yaptıkları çalışmada, bağlantılarda hasara neden olan yükleri ve meydana gelen hasar tiplerini deneysel ve sayısal olarak incelemiştir. Chang ve Scott [8], farklı fiber yönelim ve tabakalama tiplerine sahip elyaf takviyeli plakaların bağlantı dayanımlarını incelemiştir. Collings [9, 10] yaptığı çalışmalarında, tabakalama fiber yönelimi, tabaka kalınlığı ve cıvata sıkıştırma basıncı gibi parametreleri dikkate alarak kompozitlerin bağlantı mukavemetini belirlemeye çalışmıştır. Fan ve Qiu [11], sürtünme ve montaj toleransının dört bağlantı elemanlı bir bağlantının yük dağılımı üzerindeki etkilerini incelenmişlerdir. Yazarlar çalışmalarında, çoklu bağlantı elemanı bağlantısının yük dağılımı üzerine montaj toleransı etkisinin önemli olduğunu belirtmişlerdir. Montaj toleransı ne kadar büyük olursa bu etkinin o kadar belirgin olduğu belirtilmiştir. Başlangıçtaki montaj toleransı sabitlendiğinde, dış yük P'nin artışıyla, çoklu bağlantı elemanı bağlantısının yük dağılımı daha fazla olma eğiliminde olduğu görülmüştür. Ayrıca sürtünme katsayısının küçük değerlerinde yük dağılımı etkisinin fazla olmadığı fakat sürtünmenin varlığından dolayı yük dağılımının daha dengeli oluştuğu belirlenmiştir.

Kim [12] çalışmasında, bir delikte gevşek bir cıvata ileri-geri kaydırıldığında, deliğin artan bir oranda uzadığını ve hasarın meydana geldiğini belirtmiştir. Ayrıca, kompozitlerdeki tüm cıvataların düzgün bir şekilde oturmasının önemli olduğunu belirtmiştir. Eriksson [13] yaptığı çalışma ile yatak mukavemetinin yanal kısıtlama koşulları ve tabakalama yönelimleri dahil olmak üzere birkaç önemli parametreden etkilendiğini belirlemiştir. Wu ve Sun [14] kompozit tabakaların deliklerinde pim teması hasarının davranışını araştırmış ve kompozitin 0^o fiber yönelim tabakalarındaki elyaf mikro burkulmasının yatak hasarının başlamasında önemli bir rol oynadığını belirtmiştir. Camanho ve ark. [15] bir bağlantının üç temel hasar modu için ayrıntılı bir deneysel çalışma gerçekleştirmişlerdir. Çalışma sonuçları, yatak hasarının ana mekanizmasının birikmiş delaminasyon hasarı olduğunu göstermiştir. Meola ve ark. [16], mekanik bağlantıların mukavemetini ve davranışını karakterize etmek amacıyla cam elyaf takviyeli metal tabakalı hibrit (Glare) kompozitlerin üzerine deneysel bir araştırma yürütmüşlerdir. Yazarlar çalışmalarında, farklı genişlik ve delik-kenar mesafesi için hazırlanan numunelerin mekanik bağlantıların simülasyonunda en kritik test prosedürü olan yanal kısıtlamalar olmaksızın pim yataklama yöntemi testleri gerçekleştirilmiştir. Tosh ve Kelly [17] yapmış oldukları çalışmada, elyaf takviyeli kompozit levhalardaki pimli bağlantıların davranışlarına delik etrafındaki elyafların yönelim açılarının ve kompozit malzemenin imalat metotlarının etkisini deneysel olarak incelemişlerdir. Fiber yönelim açısı [0/±60]s olan grafit elyaf kullanan araştırmacılar, kompozit plakaları otoklavda 177°C sıcaklıkta ve 630 kPa basınç altında üretmiştir. Yazarlar çalışmalarının sonucunda, mukavemet değerinin açık bir delik konfigürasyonu için %62'ye kadar ve pim bağlantılı delik konfigürasyonunda ise %85'e kadar geliştirdiğini tespit etmişlerdir. Cıvata bağlantılı tabakalı T800/3900-2 grafit/epoxy prepreg kompozit plakaların yırtılma hasarı

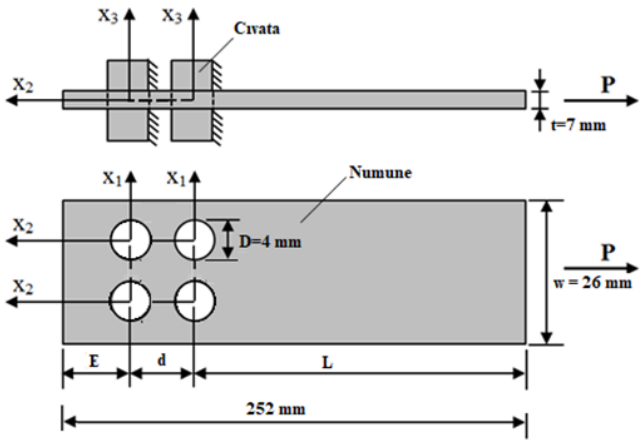
üzerine cıvata sıkma etkisini değerlendirmek için deneysel bir çalışma yapılmıştır [18]. Yazarlar çalışmalarında, cıvatasız ve cıvatalı numunelerin çekme mukavemeti ve hasar direncini incelemiştir. Deneysel sonuçlar, cıvata sıkma kuvvetinin kompozit plakaların çekme mukavemetini önemli ölçüde azaltabildiğini (%20'ye varan bir azalma) göstermiştir. Daha yüksek sıkma basıncı, numunelerin çekme mukavemetini daha çok düşürmüştür.

Pultrüde CTP kompozit levha ve geniş flanş (GF) kesitleri üzerinde, bağlantı geometrisinin, kenar mesafesinin (E) ve genişliğin (W), cıvata delik çapına (D) olan etkilerini ölçmek amacıyla tek cıvatalı çekme bağlantı testleri gerçekleştirilmiştir [19-20-21]. Hassan ve ark. [22], pultrüde CTP kompozit numunelerdeki çok cıvatalı bağlantılar için hasar yüklerini ve gerilimlerini, numune genişliği, kenar mesafesi, cıvata sayısı, cıvata düzeni, numune kalınlığı ve fiber yönü gibi çeşitli parametreleri dikkate alarak belirlemiştir. Tüm bağlantı tipleri için yük-deformasyon eğrileri hasar oluşana kadar doğrusal ilerlediği belirlenmiştir. Ayrıca, tek sıra cıvatalı bağlantılar için yükün cıvatalar arasında eşit olarak paylaşıldığı ve 2 ya da 3 sıra cıvatalı bağlantılar için yük dağılımının eşit olmadığı sonucuna varılmıştır. Pultrüde CTP yapılardaki cıvatalı bağlantıları üzerine yapılan çalışmalar, araştırmacılar için ilham verici bir konu haline gelmiştir [23, 24]. Bazı araştırmacılar tarafından yapılan çalışmalar ile numunelerin geometri etkisi, pultrüzyon yönü, bağlantı elemanı tipi gibi birçok parametre araştırılmıştır. [25-27]. Liang ve ark. [28], çok yönlü pultrüzyonla üretilmiş elyaf takviyeli polimer (CTP) bağlantılarının çekme özellikleri üzerine yükleme yönünün etkisini belirlemek için sayısal bir çalışma yapmışlardır. Yazarlar, çoklu cıvata bağlantılı modellerin tekli cıvata bağlantılı modellere göre daha fazla yırtılma hasarına uğradıkları belirlemişlerdir. Liu ve ark. [29], cıvatalı bazalt kompozit bağlantıların çekme-çekme yorulma özellikleri üzerine tek yönlü ve çok yönlü fiber örgü tipinin etkisini araştırmak için deneysel bir çalışma yapmışlardır. Çok yönlü fiber numunelerin hasar yükü tek yönlü fiber numunelerin hasar yükünün neredeyse iki katı elde edilmiştir. Çok cıvatalı bağlantı en tipik bağlantı elemanı tipi olduğundan, pultrüde CTP kompozitlerin bağlantı performansının bağlantı yoluyla güçlendirilmesi gerekmektedir. Çoklu cıvata bağlantılı pultrüde cam elyaf takviyeli polimer esaslı kompozitlerin güçlendirme etkilerini ve hasar modunu belirlemek için Duc ve ark. [30] tarafından bir çalışma yapılmıştır. Elde edilen sonuçlar, numuneler üzerindeki güçlendirme etkileri yapıların hasar davranışlarını ve hasar modunu önemli şekilde değiştirdiğini göstermiştir.

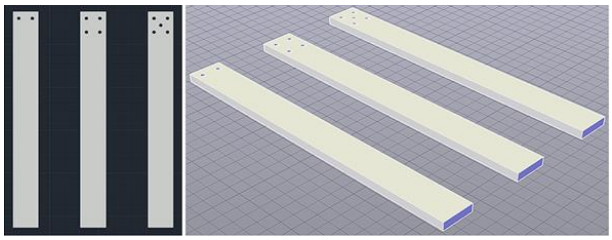
Bu çalışmada, farklı sıkma momentleri (M = 0–2–4 N.m), farklı delik sayıları (2–4–5) ve farklı E/D (2–3–4) oranları dikkate alınarak 0° ve 90° fiber yönelim açılarına sahip polimer matris esaslı cam elyaf takviyeli kompozit plakaların cıvatalı bağlantı davranışları araştırılmıştır. Kompozit bağlantıların cıvatalardan hasarlanacak şekilde tasarlanması durumunda, önerilen cıvataların kullanılmasının, hasar anındaki kararlılık platoları kullanılarak bu bağlantıların kırılgan hasarının üstesinden gelebileceğini göstermektedir (yani, kompozit bağlantıların sünek bir şekilde hasarlanması). Bu nedenle, özellikle sünek hasarın güvenlik açısından büyük önem taşıdığı uçak yapılarında uygulama için bu olasılığı araştırmak üzere daha fazla çalışma önerilmektedir.

Materyal ve Metot

Bu çalışmada, Pul-Tech FRP Kompozit Yapı Teknolojileri İmalat Sanayi ve Tic. A.Ş. tarafından pultrüzyon yöntemi ile üretilmiş polimer matrisli cam elyaf takviyeli kompozit U profilden test parametrelerine uygun olarak hazırlanan numuneler kullanılmıştır. U profil üretiminde, takviye malzeme olarak cam elyaf sürekli keçe (450 gr/m^2) ve 4800 Tex cam elyaf fitiller ve matris olarak ise PV 300 vinilester reçine kullanılmıştır [27]. U profilden 252 mm x 26 mm x 7 mm boyutlarında hazırlanan 0° ve 90° fiber yönelimlerine sahip numuneler üzerine 4 mm çapında belli konumlarda 2, 4 ve 5 adet olmak üzere cıvata delikleri açılmıştır (Şekil 1-2). Tüm test parametreleri için yaklaşık 162 numune hazırlanmıştır (Tablo 1). Delik ve pim çapı D, uç mesafesi E ve uç mesafesinin pim çapına oranı E/D olarak belirtilmiştir. E/D = 2 (8/4), E/D = 3 (12/4), E/D = 4 (16/4) olan her bir numune için 3 adet olacak şekilde testler yapılmıştır. Böylece deliklerin farklı E/D oranları için hasar durumları incelenmiştir. Ayrıca cıvata bağlantıları M=2 N.m ve M=4 N.m döndürme momenti ile sıkılmıştır. Daha sonra numuneler, bu çalışma için tasarlanmış bir aparat yardımıyla cıvata deliklerinden çekme yüküne maruz bırakılmıştır (Şekil 3). Böylece farklı ön yükler altındaki cıvata bağlantılarının çekme yükü altındaki davranışlarının delik sayısı ve yeri, fiber yönelim açısı etkileri incelenmiştir. Deneyler, 250 kN yük kapasiteli Shimazdu AG-IC marka üniversal test cihazı kullanılarak 1 mm/dak çene hızında gerçekleştirilmiştir. Cihaz, bilgisayar yardımı ile kuvvet-uzama verileri kayıt etmektedir.



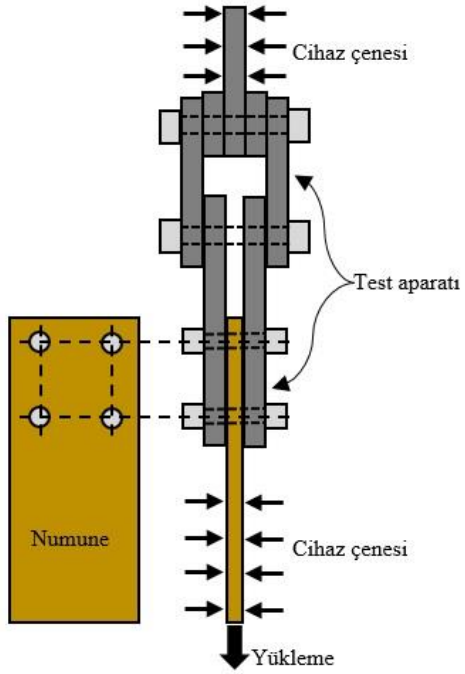
Şekil 1. Dairesel delik bulunduran pultrüzyon yöntemiyle üretilmiş CTP numune detayı.



Şekil 2. Numuneler üzerine açılan üç farklı cıvata delik biçimi.

Tablo 1. Test parametreleri ve numune sayıları.

Fiber yönelim açısı	Cıvata ve delik sayısı	E/D oranı	Moment M=0, 2 ve 4 N.m	Numune sayısı
0°	2	2	3x3x3	9
		3	3x3x3	9
		4	3x3x3	9
	4	2	3x3x3	9
		3	3x3x3	9
		4	3x3x3	9
	5	2	3x3x3	9
		3	3x3x3	9
		4	3x3x3	9
90°	2	2	3x3x3	9
		3	3x3x3	9
		4	3x3x3	9
	4	2	3x3x3	9
		3	3x3x3	9
		4	3x3x3	9
	5	2	3x3x3	9
		3	3x3x3	9
		4	3x3x3	9
			Toplam numune sayısı	162



Şekil 3. Test aparatı ve numune.

Sonuçlar ve Tartışma

Bu çalışmada, farklı sıkma momentleri (M=0–2–4 N.m), farklı delik sayıları (2–4–5) ve farklı E/D (2–3–4) oranları dikkate alınarak 0° ve 90° fiber yönelim açılarına sahip polimer matris esaslı cam elyaf takviyeli kompozit plakaların cıvatalı bağlantı davranışları incelenmiştir.

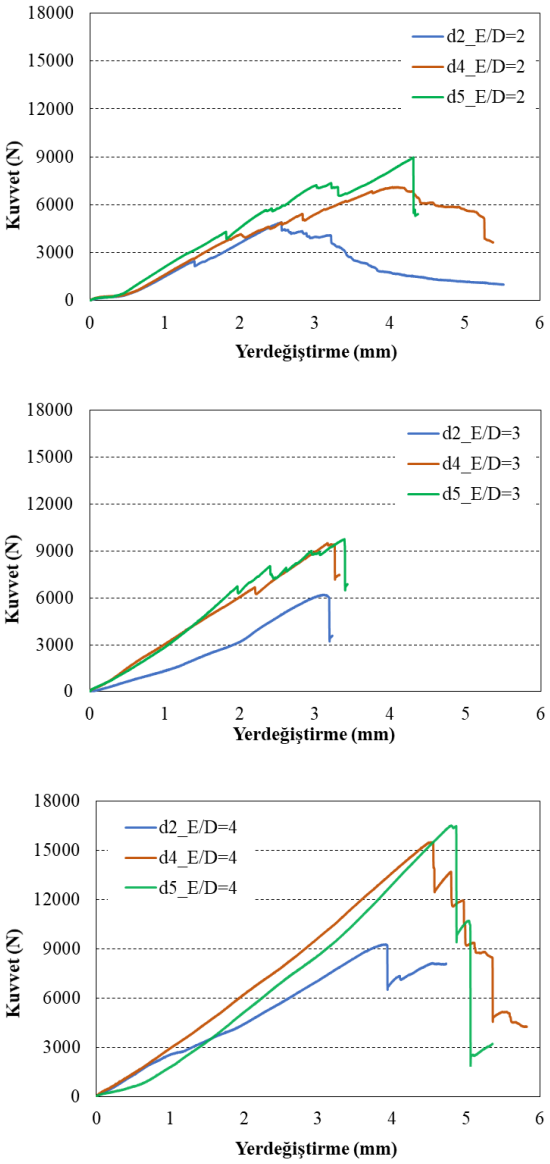
Çekme yükleri altında mekanik olarak sabitlenmiş tabakalı kompozitler genellikle, yataklanma (bearing) hasar modu, kesme (shear-out) hasar modu ve yırtılma (net-tension) hasar modu olarak üç temel modda hasarlanırlar. Karma mod olarak ise yataklanma/kesme, yataklanma/yırtılma/kesme hasar modu ve yırtılma/kesme hasar modları oluşmaktadır. Cıvata bağlantılı numuneler için Şekil 4-9'da verilen kuvvet–yer değiştirme eğrileri iki bölgeden oluşmaktadır. Birinci bölge için delik sayısı, E/D oranı ve moment değerine bağlı olarak yataklanma hasarı oluşana kadar yüksek başlangıç sertliğine sahip doğrusaldır, ardından kesme veya yırtılma hasar noktasına ulaşana kadar doğrusal olmayan davranış izlemektedir. Kırılma noktasının ötesinde, numuneler bir veya birden fazla hasar moduna sahip olmasından dolayı bağlantı yükleme kapasitesini kaybetmeye başlamaktadır.

Kesme hasar modu, gerilmelerden kaynaklanır ve delik kenarındaki kesme düzlemleri boyunca meydana gelmektedir. Delik ve kenar mesafesi E'nin kısa olmasından dolayı tipik bir hasar modu olarak adlandırılır. Yırtılma hasar modu, deliğin kenarındaki teğetsel çekme veya basma gerilimlerinden kaynaklanmaktadır. Tek eksenli yükleme koşulları için delik sayısı ve moment değerinin yüksek olduğu durumda oluşmaktadır. Yataklanma hasar modu, basma gerilmelerinden dolayı temas alanında büyüme meydana gelmektedir. Cıvatalı bağlantılarda meydana gelen ilk hasar modu olarak tanımlanmaktadır.

Aynı test parametresi için numunelerinin üç tekrar verisi kullanılarak kuvvet–yer değiştirme eğrileri oluşturulmuştur. Kuvvet–yer değiştirme eğrilerinin başlangıcında, uygulanan yükte belirgin bir artış olmadan yer değiştirmede bir artış olduğu görülmektedir. Bu davranış, cıvatalar ve delikler arasındaki boşluktan kaynaklanan göreceli kaymaya yorumlanabilir. Daha sonra, cıvataların deliklerle tam teması nedeniyle kuvvet–yer değiştirme eğrisinin eğimi, yataklanma hasar modu nedeniyle bir düşüşün meydana geldiği nihai kuvvet değerine ulaşana kadar artmaktadır. Şekil 4 ve Şekil 5'te görüldüğü gibi, 0° fiber yönelim açısına sahip numunelerde, hasar yükü değerinin yaklaşık %50'sinden sonra kuvvet–yer değiştirme eğrisinin eğiminde bir değişiklik gözlemlenmiştir. Bu değişiklik, yatak hasarının başlamasına yorumlanabilir, çünkü bu değişikliğe her zaman matris veya matris-elyaf ara yüzey hasarı eşlik etmektedir.

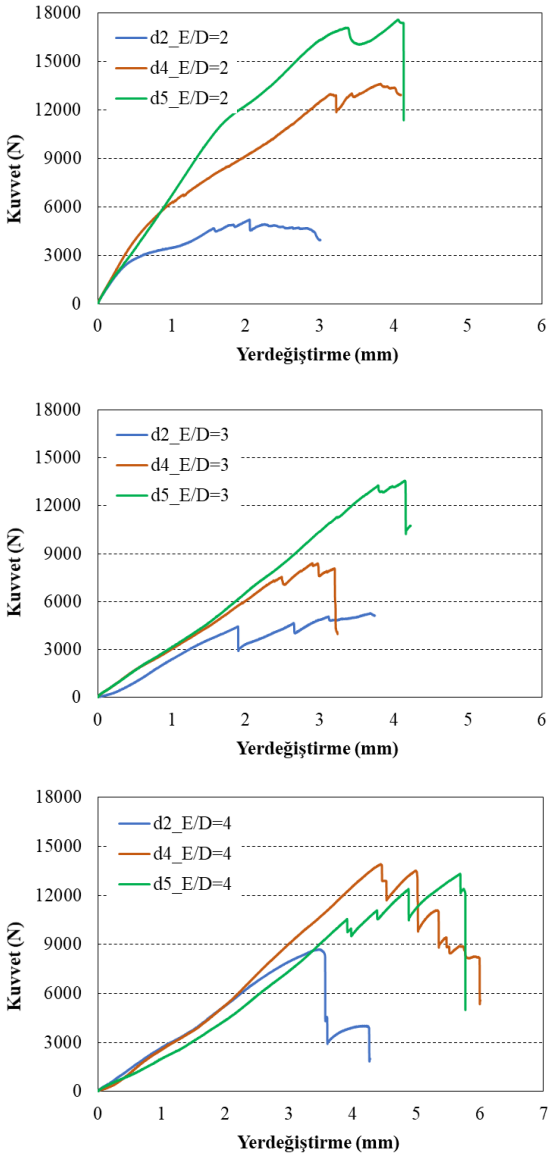
Şekil 4'de moment uygulanmamış (M=0 N.m) 2–4–5 cıvatadan çekme yüklemesine maruz bırakılmış numunelerin kuvvet–yer değiştirme eğrileri verilmiştir. Şekil 4 eğrileri

incelendiğinde, E/D oranı 2–3–4 olarak alındığında en düşük kuvvet değeri 4779 N 2 delik için elde edilirken en yüksek kuvvet değeri 16400 N ise 5 delik için elde edilmiştir. Delik sayısının artmasıyla numunelerin maksimum kuvvet taşıma kapasitesinde artış görülmektedir. Yani daha fazla delik, bağlantının daha fazla kuvvet taşımasına olanak sağlamaktadır. Ayrıca E/D oranı 2'den 4'e çıkarıldığında tüm delik tipleri için numunelerin kuvvet taşıma kapasitelerinde artış oluştuğu belirlenmiştir.



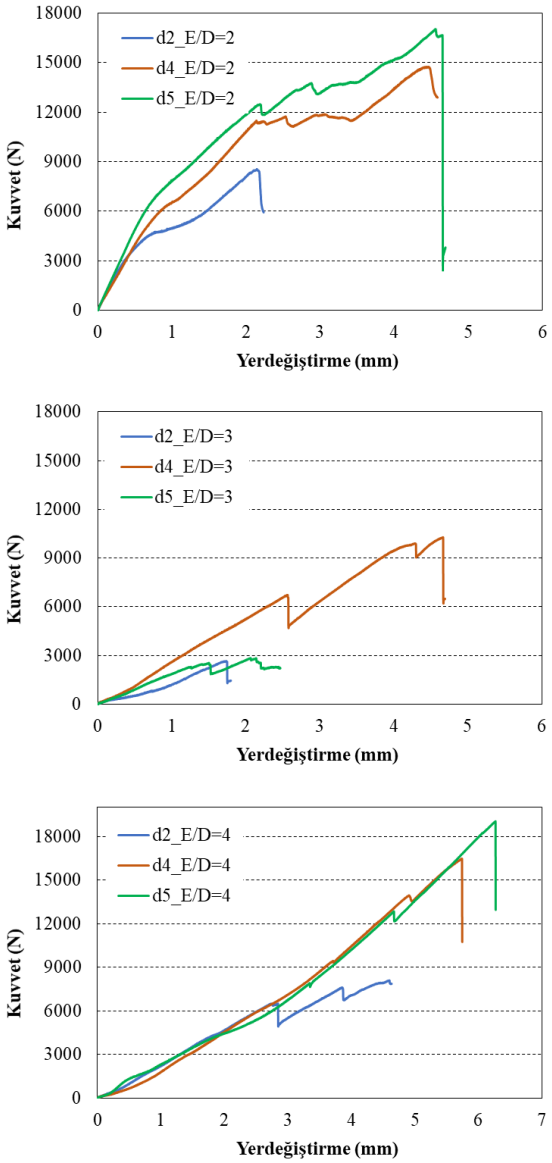
Şekil 4. Moment uygulanmamış (M=0 N.m) numunelere ait kuvvet–yer değiştirme eğrileri.

M=2 N.m moment uygulanmış ve 2–4–5 cıvatalardan çekme yüklemesine maruz bırakılmış numunelerin kuvvet–yer değiştirme eğrileri Şekil 5'te verilmiştir. E/D oranı 2–3–4 ele alındığında, en düşük kuvvet değeri 4781 N 2 delik için elde edilirken en yüksek kuvvet değeri 17383 N ise 5 delik için elde edilmiştir. Momentin varlığı ve delik sayısının artışı numunelerin kuvvet taşıma kapasitesinde artışa sebep olmuştur.

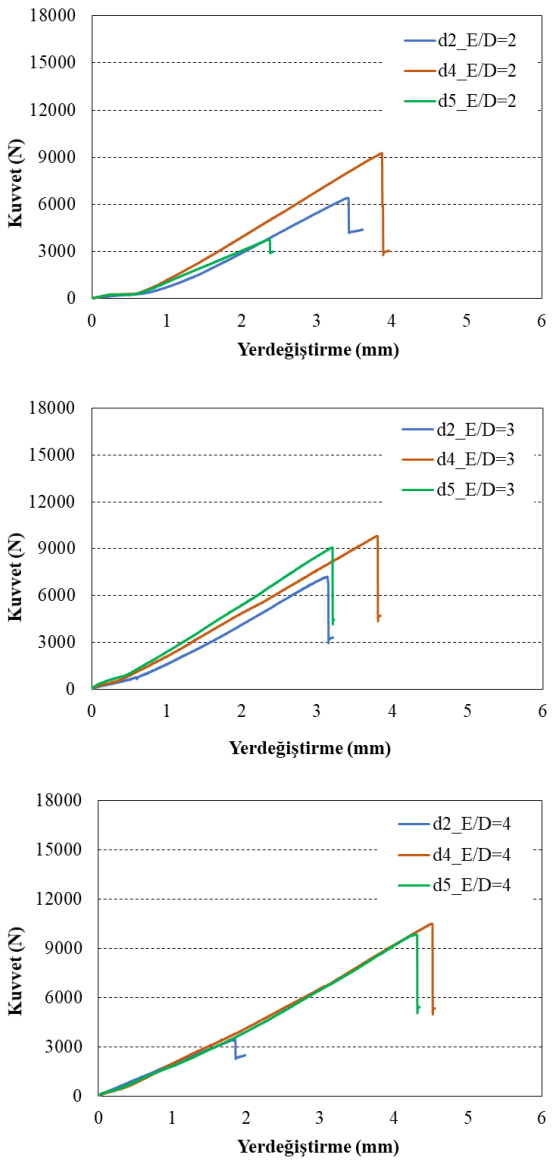


Şekil 5. 2 N.m moment uygulanmış numunelere ait kuvvet–yer değiştirme eğrileri.

Şekil 6'da verilen kuvvet–yer değiştirme eğrileri incelendiğinde cıvata sıkma momentinin artışı ile eğri eğimlerinde değişiklikler gözlemlenmiştir. E/D oranı 2 için Şekil 4, Şekil 5 ve Şekil 6'da verilen eğrilerinde ikinci bölge eğri eğimlerinde azalma görülürken diğer eğrilerin eğiminde artış olmuştur. E/D oranı 3 için Şekil 6'nin 2 ve 5 delikli numunelerin kuvvet değeri diğer numunelerden daha düşük elde edilmiştir. Bunun sebebinin numune hazırlanması esnasındaki bazı kusurlardan kaynaklı olabileceği düşünülmektedir.



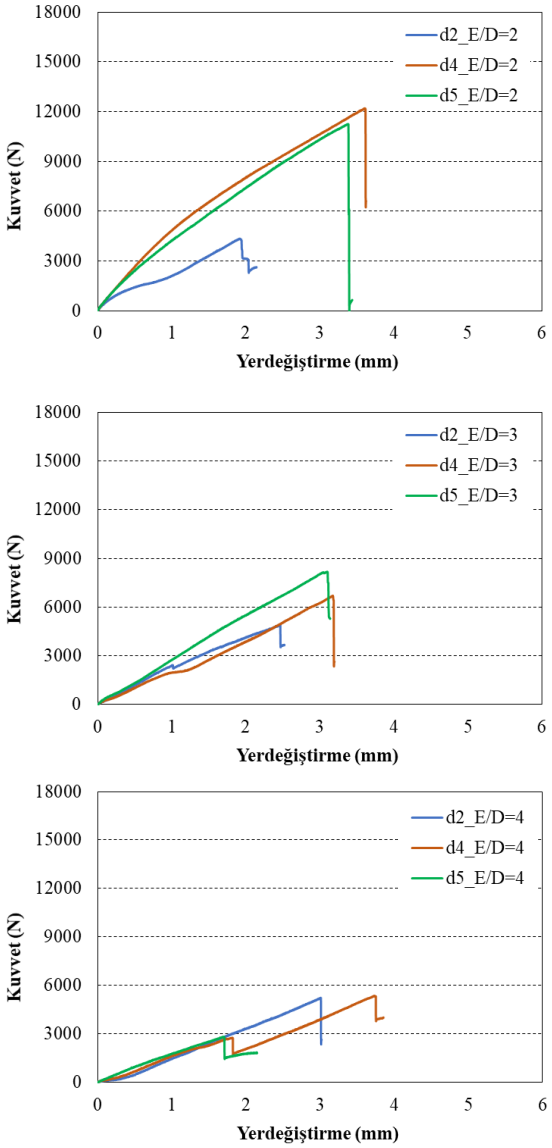
Şekil 6. 4 N.m moment uygulanmış numunelere ait kuvvet–yer değiştirme eğrileri.



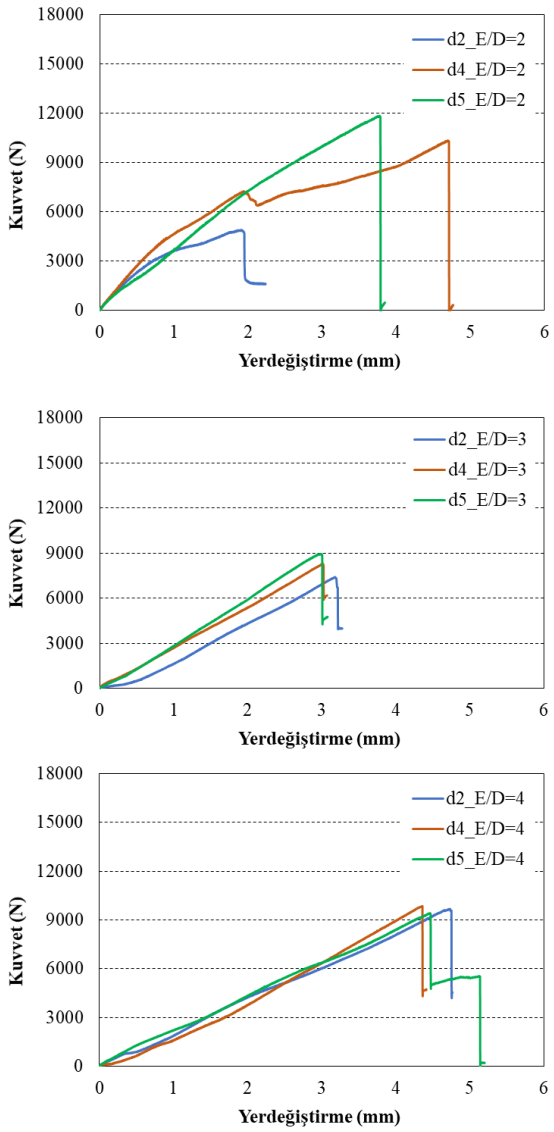
Şekil 7. Moment uygulanmamış (M=0 N.m) 90° fiber yönelimine sahip numuneler için kuvvet–yer değiştirme eğrilerinin değişimi.

90° fiber yönelim açılı numuneler, moment (M=0 N.m) uygulanmamış durum için çoklu cıvata ile çekme yüklemesine maruz bırakılmıştır. Bu numuneler, hasar yüklerine ulaşana kadar doğrusal davranış sergilemiştir (Şekil 7). Eğriler incelendiğinde, en yüksek kuvvet değeri 10414 N E/D oranı 4 ve 2 deliğe sahip numuneler için belirlenirken en düşük kuvvet değeri 3605 N ise E/D oranı 4 ve 4 deliğe sahip numuneler için belirlenmiştir. Numuneler, yataklanma ve yırtılma hasar modları şeklinde hasarlanmıştır.

Şekil 8'de moment uygulanmış (M=2 N.m) 2–4–5 cıvata bağlantısından çekme yüklemesine maruz bırakılmış numunelerin kuvvet–yer değiştirme eğrileri verilmiştir. Şekil eğrileri incelendiğinde, E/D oranı 2–3–4 olarak alındığında en düşük kuvvet taşıma değeri 2765 N E/D=4 oranı ve 5 delik için elde edilirken en yüksek kuvvet taşıma değeri 12156 N ise 4 delik ve E/D oranı 2 için elde edilmiştir. Delik sayısının artırılmasıyla maksimum kuvvet taşıma kapasitesinde değişiklikler olmuştur. Yani daha fazla delik, bağlantının E/D oranına bağlı olarak daha düşük veya daha fazla kuvvet taşımasına olanak sağlamaktadır. Ayrıca E/D oranı 2'den 4'e çıkarıldığında tüm delik tipleri için kuvvet taşıma kapasitesinde değişiklikler belirlenmiştir.



Şekil 8. 2 N.m moment uygulanmış 90° fiber yönelimine sahip numuneler için kuvvet–yer değiştirme eğrilerinin değişimi.



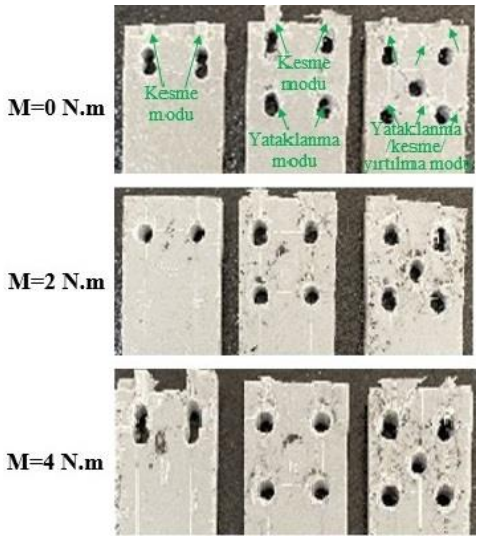
Şekil 9. 4 N.m cıvata sıkma momenti uygulanmış 90° fiber yönelimine sahip numuneler için kuvvet–yer değiştirme eğrilerinin değişimi.

4 N.m cıvata sıkma momenti uygulanmış 90° fiber yönelim açısına sahip numuneler için kuvvet–yer değiştirme eğrilerinin değişimi Şekil 9'da verilmiştir. E/D oranı 2 olan numunelerin eğrilerindeki eğim E/D oranı 3 ve 4 olan numunelerin eğrilerindeki eğimden daha farklıdır. E/D oranı 2 olan numune eğrilerinde iki eğim oluşurken diğer E/D oranlarına sahip numune eğrilerinde tek eğim oluşmuştur. En yüksek kuvvet değeri 11726 N E/D oranı 2 ve 5 deliğe sahip numuneler için belirlenmiştir. En düşük kuvvet değeri 4711 N E/D oranı 2 ve 2 deliğe sahip numunelerde görülmüştür.

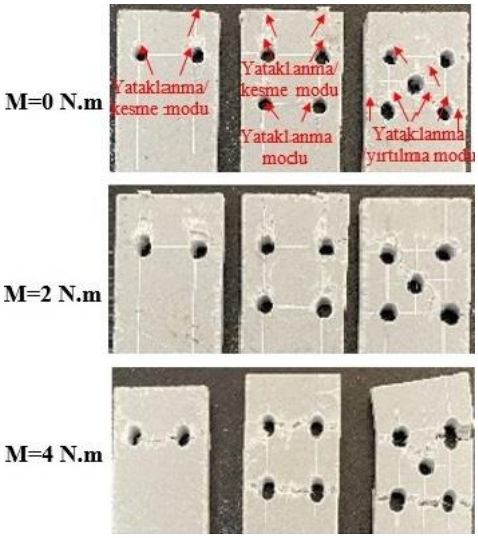
Temel hasar modları, deneylerde elde edilen Şekil 4 ve Şekil 9'da verilen kuvvet-yer değiştirme verilerine ve Şekil 10 ve Şekil 11'de verilen görsellere dayanarak, hasar modları Şekil 10 ve Şekil 11'de gösterildiği gibi listelenmiş ve aşağıdaki gibi tanımlanmıştır:

Fiber yönelim açısı 0° olan numunelerin M=0 N.m ve E/D oranı 2 olan bağlantılar ve E/D oranı 3 ve 4 olan bağlantılarda 2 delikli numunelerde kesme ve yataklanma hasar modları gözlemlenmiştir. E/D oranı 3 ve 4 olan çoklu bağlantılarda ise yataklanma ve yırtılma hasar modları oluşmuştur. Öte yandan, M=2 N.m ve M=4 N.m, E/D oranı 2 olan bağlantılar için kesme ve yataklanma hasar modları meydana gelmiştir. E/D oranı 3 ve 4 olan bağlantılarda ise yataklanma ve yırtılma hasar modları belirlenmiştir. Şekil 10'da verilen görseller incelendiğinde, M=0 N.m durumu için E/D oranı 2 olan 2 delikli numunelerin ve çoklu delikli numunelerin sıralı ilk iki deliğinde önce yatak sonra kesme hasar modları gerçekleşmiştir. Pultrüzyon ile üretilmiş CTP

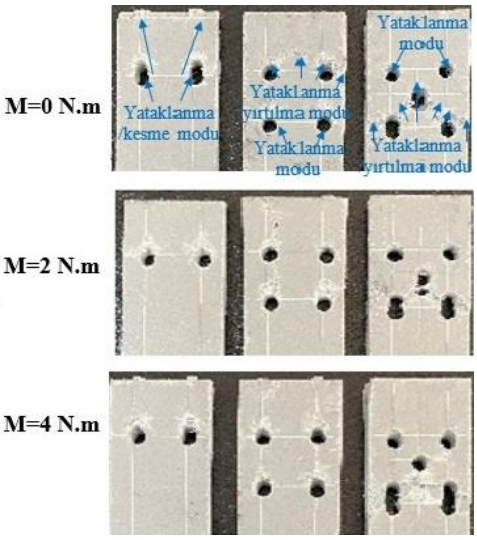
numunelerdeki cıvatalı bağlantıların yırtılma hasar modu, moment miktarı ve delik sayısının artışı ile önemli ölçüde artacağı iyi bilinmektedir, çünkü cıvataları barındıran delikler yalnızca cam elyaf fitillerinin sürekliliğini bozmakla kalmaz, aynı zamanda deliklerin kenarlarında gerilim yoğunlaşmaları da üretir. Pultrüde edilmiş CTP yapılarda cıvatalı bağlantıların tasarımı üzerine çalışan araştırmacıların ayrıntılı bağlantı tasarımına başlamadan önce, belirli bir durum için kırılma gerilimindeki olası azalmanın ne olabileceğine dair bir fikre sahip olunması faydalı olacaktır.



(a)



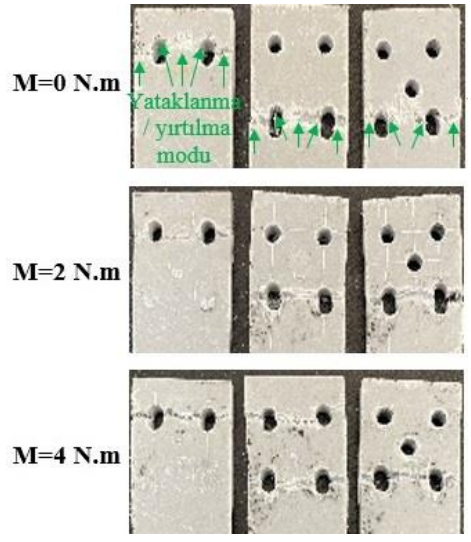
(b)



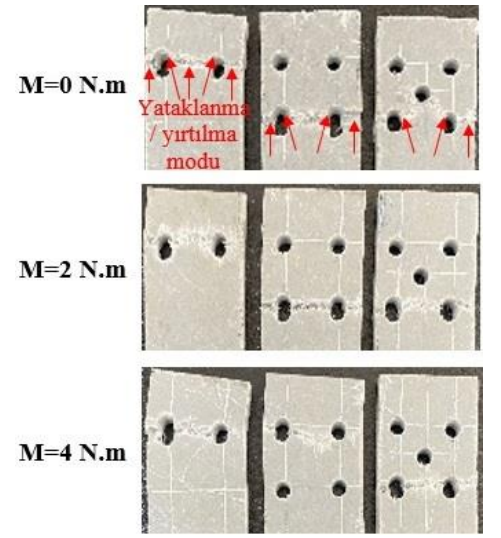
(c)

Şekil 10. Deneyden sonra fiber yönelim açısı 0º olan tüm numunelerde görülen hasarlar: (a) E/D=2, (b) E/D=3 ve (c) E/D=4.

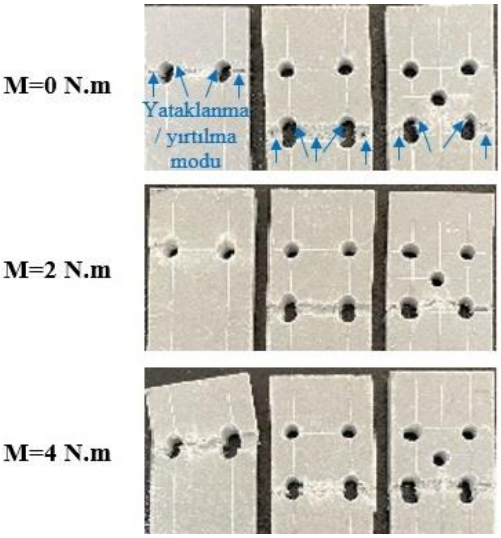
Şekil 11'de verilen hasarlı numunelerin görüntüleri incelendiğinde yataklanma hasarının önce meydana geldiği sonrasında yükün uygulanmaya devam edilmesiyle hasarın yırtılma hasarına dönüştüğü görülmüştür. Fiber yönelim açısının 90º olması numune hasarlarının yatak ve yatak/yırtılma şeklinde oluşmasını sağlamıştır. Bu durum özellikle M=0 N.m ve M=2 N.m moment durumları ve E/D oranları için iki delikli numunelerde ve çoklu delikli numunelerin dip kısmında sıralı ilk iki deliklerinde meydana gelmiştir. M=4 N.m durumunda ise hasarlar biraz farklı gerçekleşmiştir. Tüm durumlar dikkate alındığında E/D oranının 2'den 4'e artırılmasıyla hasarın geciktirildiği yani numunenin daha çok yük taşıması sağlanmıştır. Ayrıca moment etkisi de benzer durumların oluşmasını sağlamıştır.



(a)



(b)



(c)

Şekil 11. Deneyden sonra fiber yönelim açısı 90º olan tüm numunelerde görülen hasarlar: (a) E/D=2, (b) E/D=3 ve (c) E/D=4.

Bağlantı cıvatalarına yeterli sıkma momenti uygulanması, numunelerin yük taşıma kapasitesini artırmaktadır. Ancak delik sayısının artışı, kesit kaybına neden olduğu için malzemenin mukavemetini olumsuz etkilemektedir. Bu yüzden mühendislik uygulamalarında, optimum sıkma momenti ve delik düzenlemesi dikkatlice seçilmelidir.

Değerlendirme

Pultürizyon yöntemi ile üretilmiş 0º ve 90º fiber açılarına sahip kompozit plakalardan hazırlanan numunelerin cıvata bağlantı noktalarındaki çekme performansı üzerine 3 farklı moment (M=0–2–4 N.m) yükü, 3 farklı E/D (2–3–4) oranı ve 3 farklı delik (2–4–5) etkisini araştırmak için deneysel bir çalışma yürütülmüştür. Bu çalışmanın sonuçlarına ve tartışmalarına dayanarak, şu değerlendirmeler yapılmıştır:

- ✓ Delik sayısının artması genel olarak kesit alanını azalttığı için, numunelerin yük taşıma kapasitesini düşürebilmektedir. Ancak, belirli koşullarda (örneğin cıvata sıkma momentleriyle) daha iyi yük dağılımı sağlanarak numunelerin dayanımını artırdığı gözlemlenmiştir.
- ✓ 0º fiber açılarına sahip kompozit plakalardan hazırlanan numunelerin bağlantı cıvatalarına uygulanan sıkma momenti arttıkça (M=0 N.m'den M=4 N.m'e artırılması) maksimum kuvvet değeri artmaktadır. Sıkma momenti M=0 N.m olan bağlantılarda daha erken kaymalar ve ani kırılmalar gözlemlenirken, sıkma momenti M=4 N.m olduğunda yük taşınması daha verimli hale gelmekte ve numuneler daha rijit davranış sergilemektedir. Fakat bağlantı cıvatalarına uygulanan sıkma momenti değeri 90º fiber açılarına sahip numunelerin maksimum hasar kuvvet değerlerinde önemli bir değişim oluşturmamıştır.
- ✓ Fiber yönelim açısı 0º olan numunelerin temel hasar modları E/D oranlarına bağlı olarak yataklanma ve kesme, yatak/yırtılma hasar modları şeklinde gerçekleşmiştir.
- ✓ Fiber yönelim açısı 90º olan numunelerin temel hasar modları E/D oranlarına bağlı olarak yatak ve yırtılma hasar modları oluşmuştur.
- ✓ 90º fiber yönelimli numunelerde, delik sayısının artması, yük taşıma kapasitesini artırırken, sıkma momentinin değerinin artması bağlantının rijitliğini ve dayanımını artırmaktadır.
- ✓ Fiber yönelim açısı 0º olan numuneler, 90º olanlara göre daha yüksek kuvvetlere dayanabilmektedir. 90º fiber yönelim açısına sahip numuneler genellikle daha düşük yüklerde ani kırılmalar gösterirken, 0º numuneler daha yüksek dayanım davranışı göstermektedir. Aynı delik sayısına sahip 0º fiber yönelim açısına sahip numuneler bile kendi içlerinde farklı mekanik davranışlar gösterebilmektedir.

Bilgi

Bu çalışma, birinci yazarın üçüncü yazar danışmanlığında hazırladığı yüksek lisans tez çalışmasından üretilmiştir.

Kaynaklar

[1] Technical Information Staff of Industrial. (1963). The Fasteners Book Issue. Machine Design.

[2] Turvey, G. J., & Sana, A. (2016). Pultruded GFRP double-lap single-bolt tension joints – Temperature effects on mean and characteristic failure stresses and knock-down factors. Composite Structures, 153, 624–631. https://doi.org/10.1016/j.compstruct.2016.06.016

[3] Madenci, E., Shkarayev, S., Sergeev, B., Oplinger, D. W., & Shyprykevich, P. (1998). Analysis of composite laminates with multiple fasteners. International Journal of Solids and Structures, 35(15), 1793–1811. https://doi.org/10.1016/S0020-7683(97)00152-2

[4] Ghanbari, E. (2011). Bolt-Hole Tightening Effects in Singlelap Composite Bolted Joints. Dokuz Eylül University Graduate School of Natural and Applied Sciences.

[5] Crews, JHJ. (1981). Bolt-bearing fatigue of a graphite/epoxy laminate . American Society for Testing and Materials, 131–144.

[6] Wang, H.-S., Hung, C.-L., & Chang, F.-K. (1996). Bearing Failure of Bolted Composite Joints. Part I: Experimental Characterization. Journal of Composite Materials, 30(12), 1284–1313. https://doi.org/10.1177/002199839603001201

[7] Aktas, A., & Karakuzu, R. (1999). Failure Analysis of Two-Dimensional Carbon-Epoxy Composite Plate Pinned Joint. Mechanics of Advanced Materials and Structures, 6(4), 347–361. https://doi.org/10.1080/107594199305502

[8] Chang, F.-K., Scott, R. A., & Springer, G. S. (1982). Strength of Mechanically Fastened Composite Joints. Journal of Composite Materials, 16(6), 470–494. https://doi.org/10.1177/002199838201600603

[9] Collings, T. A. (1977). The strength of bolted joints in multi-directional cfrp laminates. Composites, 8(1), 43–55. https://doi.org/10.1016/0010-4361(77)90027-1

[10] Collings, T. A. (1982). On the bearing strengths of cfrp laminates. Composites, 13(3), 241–252. https://doi.org/10.1016/0010-4361(82)90006-4

[11] Wei-Xun, F., & Chun-Tu, Q. (1993). Load distribution of multi-fastener laminated composite joints. International Journal of Solids and Structures, 30(21), 3013–3023. https://doi.org/10.1016/0020-7683(93)90209-P

[12] Kim, RY. (1987). Fatigue strength. ASM Engineered Materials Handbook, 1.

[13] Eriksson, I. (1990). On the Bearing Strength of Bolted Graphite/Epoxy Laminates. Journal of Composite Materials, 24(12), 1246–1269. https://doi.org/10.1177/002199839002401201

[14] Wu, P. S., & Sun, C. T. (1998). Bearing Failure in Pin Contact of Composite Laminates. AIAA Journal, 36(11), 2124–2129. https://doi.org/10.2514/2.316

[15] Camanho, P. P., Bowron, S., & Matthews, F. L. (1998). Failure Mechanisms in Bolted CFRP. Journal of Reinforced Plastics and Composites, 17(3), 205–233. https://doi.org/10.1177/073168449801700302

[16] Meola, C. , S. A. , G. G. and N. L. (2003). Experimental Characterization of an Innovative Glare Fiber Reinforced Metal Laminate in Pin bearing. Journal of Composite Materials, 37, 1543–1553.

[17] Tosh, M. W., & Kelly, D. W. (2000). On the design, manufacture and testing of trajectorial fibre steering for carbon fibre composite laminates. Composites Part A: Applied Science and Manufacturing, 31(10), 1047–1060. https://doi.org/10.1016/S1359-835X(00)00063-4

[18] Yan, Y., Wen, W.-D., Chang, F.-K., & Shyprykevich, P. (1999). Experimental study on clamping effects on the tensile strength of composite plates with a bolt-filled hole. Composites Part A: Applied Science and Manufacturing, 30(10), 1215–1229. https://doi.org/10.1016/S1359-835X(99)00002-0

[19] Abd-El-Naby, S. F. M., & Hollaway, L. (1993). The experimental behaviour of bolted joints in pultruded glass/ polyester material. Part 1: Single-bolt joints. Composites, 24(7), 531–538. https://doi.org/10.1016/0010-4361(93)90266-B

[20] Rosner, C. N., & Rizkalla, S. H. (1995). Bolted Connections for Fiber-Reinforced Composite Structural Members: Experimental Program. Journal of Materials in Civil Engineering, 7(4), 223–231. https://doi.org/10.1061/(ASCE)0899-1561(1995)7:4(223)

[21] Cooper, C., & Turvey, G. J. (1995). Effects of joint geometry and bolt torque on the structural performance of single bolt tension joints in pultruded GRP sheet material. Composite Structures, 32(1–4), 217–226. https://doi.org/10.1016/0263-8223(95)00071-2

[22] Hassan, N. K., Mohamedien, M. A., & Rizkalla, S. H. (1997). Multibolted Joints for GFRP Structural Members. Journal of Composites for Construction, 1(1), 3–9. https://doi.org/10.1061/(ASCE)1090-0268(1997)1:1(3)

[23] Girão Coelho, A. M., & Mottram, J. T. (2015a). A review of the behaviour and analysis of bolted connections and joints in pultruded fibre reinforced polymers. Materials & Design, 74, 86–107. https://doi.org/10.1016/j.matdes.2015.02.011

[24] Girão Coelho, A. M., & Mottram, J. T. (2015b). A review of the behaviour and analysis of bolted connections and joints in pultruded fibre reinforced polymers. Materials & Design, 74, 86–107. https://doi.org/10.1016/j.matdes.2015.02.011

[25] Feo, L., Marra, G., & Mosallam, A. S. (2012). Stress analysis of multi-bolted joints for FRP pultruded composite structures. Composite Structures, 94(12), 3769–3780. https://doi.org/10.1016/j.compstruct.2012.06.017

[26] Turvey, G. J. (1998). Single-bolt tension joint tests on pultruded GRP plate — effects of tension direction relative to pultrusion direction. Composite Structures, 42(4), 341–351. https://doi.org/10.1016/S0263-8223(98)00079-8

[27] Leblebicier, B. (2022). Pultrüzyon Yöntemi ile Üretimi Yapılan Kompozit Malzemelerin Çevre Koşulları Altındaki Performanslarının İncelenmesi. Uşak Üniversitesi, Fen Bilimleri Enstitüsü.

[28] Liang, M., Wang, X., Zhong, L., Jiang, Z., Huang, H., Wu, Z. (2024). Effects of off-axis load direction on tensile properties ofpultruded fiber-reinforced polymer bolted jointswith multi-directional fiber lay-ups. Polym Compos.2024;45(11):10172-10189. doi:10.1002/pc.28465

[29] Liu, L., Wang, X., Wu, Z., Keller, T. (2023). Effect of fiber architecture ontension–tension fatigue behavior of bolted basalt compositejoints. Eng Struct. 286:116089. doi:10.1016/j.engstruct.2023.116089

[30] Duc, T., Nhut, P., Matsumoto, Y. (2022). Multi-bolted connection for pultruded glass fiber reinforced polymer's structure: A Study on Strengthening by Multiaxial Glass Fiber Sheets. Polymers. 14. doi:10.3390/polym14081561.

Dicle University
Journal of Engineering
https://dergipark.org.tr/tr/pub/dumf
duje.dicle.edu.tr

Research Article

Investigation of mechanical properties in variable oriented glass fiber reinforced insulators

Selçuk İlhan BİLGİN[1*], Hakan ÇETİNEL[2], Enver YALÇIN[3]

[1] Balıkesir University, Mechanical Engineering Department, selcukilhanbilgin@gmail.com, Orcid No: 0000-0001-9335-4307
[2] Manisa Celal Bayar University, Mechanical Engineering Department, hakan.cetinel@cbu.edu.tr, Orcid No 0000-0001-5938-1213
[3] Balıkesir University, Mechanical Engineering Department, eyalcin@balikesir.edu.tr, Orcid No: 0000-0001-6171-1955

ARTICLE INFO

Article history:

Received 7 May 2025
Received in revised form 5 June 2025
Accepted 10 June 2025
Available online 30 September 2025

Keywords:

fiber orientation, tensile test, glass fiber, electrical insulators, composite materials

Doi: 10.24012/dumf.1694736

* Corresponding author

ABSTRACT

This study investigates the influence of fiber orientation on the mechanical performance of composite insulators produced by the hand lay-up method. E-glass fiber-reinforced epoxy composites were fabricated using three types of glass fiber fabrics: unidirectional (L300), ±90° biaxial (LT600), and ±45° biaxial (X600). Additionally, silica sand-filled epoxy insulators were also evaluated—both factory-produced and commercially sourced—to benchmark performance differences with glass fiber-reinforced counterparts. The primary objective is to assess how varying fiber alignment and material configurations affect mechanical properties, particularly under tensile loading. Specimens were prepared in four distinct orientation configurations and subjected to tensile testing. The results demonstrated significant variations in tensile strength, highlighting that even minor differences in fiber orientation can substantially alter mechanical behavior. Failure mode analysis further emphasized the critical role of fiber orientation in load distribution and structural integrity. Overall, this study provides insights into enhancing the mechanical reliability of composite insulators by optimizing fiber placement and evaluating alternative filler systems such as silica sand.

Introduction

Composite materials have emerged as essential engineering materials across various industries due to their ability to provide tailored properties through the combination of different constituents. Among these, fiber-reinforced polymer (FRP) composites stand out for offering an excellent balance between strength, weight, and environmental resistance. Their versatility has led to widespread adoption in sectors such as aerospace, automotive, and energy, including high-voltage electrical systems.

In the maritime industry, glass fiber reinforced polymer (GFRP) composite panels are used on the outer surfaces of sandwich panels that form the hull coverings of vessels. A recent example of this application is the Visby Corvette, which is part of the Swedish Navy's fleet. Polymer laminates composed of hybrid carbon and glass fibers are layered around a core made of polyvinyl chloride (PVC). These sandwich composite panels have been used as exterior cladding in the construction of the corvette's hull [1].

When considering examples from the aerospace industry, rear pressure bulkhead of the Airbus A380, which plays a vital role in maintaining cabin pressure, is manufactured from carbon fiber-reinforced composite material. Given that this component separates the pressurized fuel compartment from the rear of the aircraft, it operates in a highly critical position. Similarly, the cargo door of the Airbus A400M, measuring 7 by 4 meters, is also constructed using carbon fiber-reinforced composite material[2].

GFRP composites have also found increasing applications in the automotive industry due to their favorable strength-to-weight ratio, corrosion resistance, and potential to improve fuel efficiency through weight reduction. These materials are commonly used in structural and semi-structural components, including leaf springs, bumper beams, and body panels. In a recent study on electric vehicles, GFRP was utilized in the design of a transverse composite leaf spring for the rear suspension system. Specifically, E-glass fibers were employed as reinforcement material, highlighting their suitability for load-bearing applications in lightweight vehicle platforms [3], [4].

In recent years, fiber-reinforced polymer (FRP) composites have become increasingly important in electrical insulation applications due to their excellent mechanical strength,

lightweight structure, corrosion resistance, and dielectric properties. Particularly in the production of insulators, the combination of glass fibers with thermoset resin matrices such as epoxy has proven to be a cost-effective and highly adaptable solution.

One of the most influential factors affecting the mechanical and dielectric behavior of composite insulators is fiber orientation. Different stacking sequences and fiber alignment patterns can significantly alter the stress distribution, crack propagation, and overall failure behavior under loading. This is especially critical in hand lay-up processes, where manual fiber placement can introduce variability in the final product quality. Although the hand lay-up method is known for its simplicity and low cost, it remains sensitive to inconsistencies in fiber distribution, resin saturation, and void formation.

Glass fiber reinforced polymer (GFRP) composites are widely used in electrical and mechanical applications due to their high strength-to-weight ratio and excellent dielectric properties. However, as reported by Tuncer et al. [5], the dielectric breakdown strength of GFRP significantly varies depending on the material's thickness and field orientation. In their study, FR4 and cryogenic-grade GFRP samples showed up to 14% difference in breakdown strength, and a decrease in dielectric strength with increasing thickness was observed, following a power law. This sensitivity to material structure highlights the importance of laminate quality and consistency, especially for applications involving complex field directions or manual lay-up processes. These findings support the need to further investigate both mechanical and electrical performance in GFRP composites with different fiber orientations.

The mechanical properties of composite insulators, particularly their bending stiffness and equivalent elastic modulus, are significantly influenced by fiber orientation and lay-up angles. Wang et al. [6] emphasized that skew-symmetric laminates with specific winding angles, such as ±30°, affect the mechanical response of post insulators under loading. Their study also demonstrated that theoretical predictions based on laminate theory are in close agreement with experimental results, supporting the idea that fiber alignment is critical in optimizing structural rigidity. These insights highlight the importance of precise fiber arrangement, especially in manually fabricated systems like the hand lay-up method.

Glass-fiber reinforced polymer (GFRP) composites have been widely employed in outdoor electrical insulation due to their excellent dielectric properties, high mechanical strength, and resistance to environmental degradation. As highlighted by Park et al. [7], the combination of glass fibers with epoxy resin offers enhanced durability under ultraviolet exposure, humidity, and pollution, making it a preferred choice for high-voltage insulators. However, the mechanical and insulation performance of such composites is not only dependent on the material constituents but also significantly influenced by the orientation of the fibers. Fiber alignment angles determine the load transfer efficiency, failure modes, and stiffness of the composite. Misalignment or suboptimal lay-up angles (such as deviations from 0°, ±45°, or ±90°) may lead to stress concentrations, delamination, and premature failure, particularly in hand lay-up processes where manual placement introduces variability. Therefore, understanding and optimizing fiber orientation is essential for ensuring consistent performance in both mechanical and dielectric aspects of GFRP-based insulators.

Furthermore, several studies have demonstrated that glass fiber-reinforced polymers exhibit their highest mechanical strength when the applied load is aligned parallel to the fiber direction, and the lowest when the load is applied perpendicularly. This anisotropic behavior represents both strength and a limitation of fiber-reinforced polymer (FRP) composites, depending on the intended application and loading conditions. This phenomenon is also observed in the present study, where significant differences in tensile performance were recorded depending on the fiber orientation [8], [9]. Salgar et al. [10] produced epoxy matrix composites with varying fiber volume fractions (40%, 50%, and 60%) and compared their tensile test results. The best mechanical performance was achieved at a fiber content of 50%.

Sheng et al. [11] proposed a novel mechanical model to simulate the seismic behavior of composite insulators and cylindrical electrical equipment, which was developed based on combined experimental and numerical studies. In their investigation, the failure response of composite insulators under hysteretic bending was examined, and three distinct failure types were identified: (I) cracking of the metal flange, (II) tearing of the fiberglass composite tube, and (III) bond failure between the fiberglass tube and adjoining components.

Park [12] investigated the mechanical and dielectric properties of glass cloth composites. The study revealed that as the angle between the fiber orientation and the tensile loading axis increases, the load-bearing capacity of glass–epoxy composites decrease significantly.

Previous studies [13] have shown that increasing the fiber weight fraction up to 55% enhances tensile strength and stiffness, although flexural strength may decrease due to surface imperfections and porosity.

Different lay-up sequences in GFRP composites have a significant effect on tensile performance, with mechanical properties varying according to fiber orientation and stacking arrangement. The hand lay-up method remains widely used in the fabrication of fiber-reinforced composites, and its effect on tensile performance has been evaluated in various studies [14], supporting its relevance to experimental investigations like the present one.

Recent studies have compared different manufacturing techniques such as hand lay-up and vacuum infusion, highlighting that hand lay-up GFRP laminates typically exhibit lower tensile strength due to increased porosity and lower fiber volume fraction [15]. This reinforces the

relevance of hand lay-up composites for performance benchmarking in experimental studies.

Failure mechanisms in fiber-reinforced composites can vary significantly depending on the fiber orientation, with common failure modes including matrix cracking, fiber fracture, and interlaminar delamination. These phenomena have been extensively detailed in recent literature, emphasizing their prevalence in both unidirectional and multidirectional laminates [16].

Recent research has examined the suitability of glass fiber-reinforced polymer (GFRP) composites for use as electrical insulators in power transmission lines. The study compared epoxy and polyester matrix composites by evaluating their mechanical such as tensile strength and dielectric behavior, particularly under environmental stress conditions such as moisture and acid exposure. It was found that moisture absorption negatively impacted breakdown voltage, and acid aging led to minor reductions in tensile strength. Epoxy-based GFRP composites exhibited superior resistance to chemical degradation, indicating their higher reliability for high-voltage insulation applications [17].

The main objective of this study is to investigate how different fiber orientations affect the mechanical performance of glass fiber-reinforced epoxy composite insulators. For this purpose, composite specimens were produced using the hand lay-up method with E-glass fiber fabrics in four orientation configurations: 0°, 90°, ±90°, and ±45°. Additionally, a silica sand-filled epoxy insulator—both factory-fabricated and commercially available—was included for comparison. All specimens were subjected to tensile testing to evaluate the influence of fiber alignment on their structural integrity and load-bearing capacity.

Material and Method

In this study, epoxy matrix composite insulator specimens were fabricated using different fiber orientations. The reinforcement materials included:

E-glass fiber fabrics produced by Metyx:

- L300 unidirectional (UD) glass fiber fabric (300 g/m²) for specimens with fibers oriented parallel and perpendicular to the tensile direction,



Figure 1. L300 Glass Fiber Unidirectional Fabric

- LT600 biaxial fabric (600 g/m²) for ±90° unidirectional orientation,

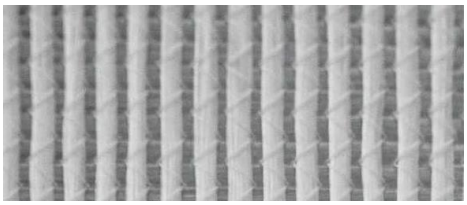


Figure 2. LT600 Glass Fiber Biaxial Fabric

- X600 biaxial fabric (600 g/m²) for ±45° orientation.

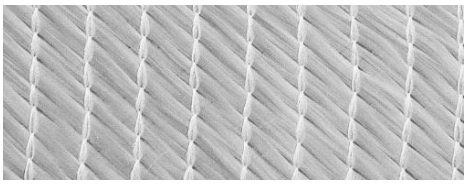


Figure 3. X600 Glass Fiber (Biaxial) Fabric

The resin system consisted of epoxy and hardener mixed at a 55:45 weight ratio, prepared and poured at 70 °C, and cured in a controlled temperature process.

Although both 300 g/m² and 600 g/m² fiber fabrics were used across the specimen types, the fiber volume fraction was kept constant at approximately 40% in all specimens, ensuring consistent material content across different laminates.

Manufacturing Process

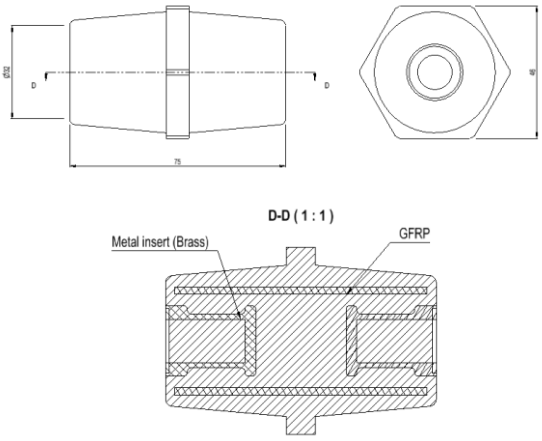


Figure 4. Specimen overview

The specimens were produced via the hand lay-up method. Glass fiber fabrics were cut and laid onto inserts, then rolled into cylindrical shapes and placed into a pre-heated mold.



Figure 5. Specimen preparation

The mold was initially heated at 70 °C for 30 minutes, followed by a staged temperature increase of 10 °C every 4 hours up to 120 °C, where it was held for a final curing period before cooling to room temperature. All specimens had a fiber volume fraction of approximately 40%, and the laminated wall thickness was ~7 mm.

Four types of fiber orientations were produced:

- Fibers perpendicular to the tensile direction,
- Fibers parallel to the tensile direction,
- ±90° unidirectional orientation,
- ±45° orientation.

Each specimen type was prepared in triplicate for mechanical testing. In addition to the four fiber-reinforced composite types, resin–silica filled insulator specimens were also fabricated. Furthermore, a commercially available insulator, commonly used in daily applications, was included in the study as a benchmark reference for performance comparison.

Tensile Testing

Tensile tests were conducted using a Zwick-Roell universal testing machine at Balıkesir University's Center for Science and Technology. Three specimens were tested for each fiber orientation; one representative force–elongation graph is presented, and mean force and strain values from all three specimens are reported in the related tables. Each specimen was mounted using M12 threaded rods and tested under a constant displacement rate of 2 mm/min, following the general principles of ISO 527-4[18] and ISO 527-5[19] , which define test conditions for fiber-reinforced plastics. Both standards refer to ISO 527-1[20] for the general principles regarding the determination of tensile properties. Although the sample geometry did not conform exactly to the ISO standard dumbbell shapes, test parameters such as speed and boundary conditions adhered to the relevant guidelines. Maximum force, strain, and failure modes were recorded for each test.

±90° fiber-reinforced specimen

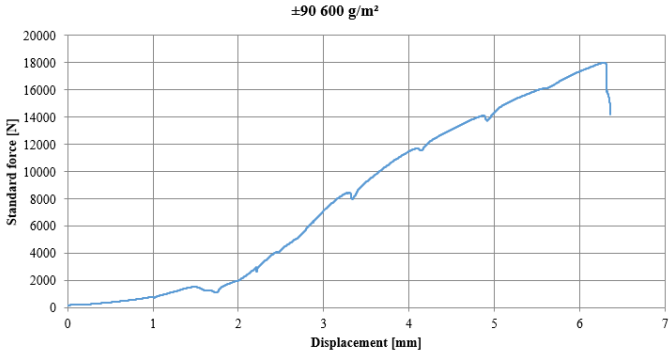


Figure 6 Test result ±90° fiber-reinforced specimen

Table 1 Summary of tensile performance of ±90° lay up

±90° specimen	Displacement (mm)	Force (N)
Mean	6,63	18333

A force–elongation diagram of a composite insulator reinforced with 600 g/m² glass fiber is presented here. While three specimens were initially tested, only one has been retained as a representative example in the figure. The table summarizes the average tensile performance across all three samples. Initially, the force increases linearly, reaching a maximum value. Following this peak, a sudden drop in the force is observed as the specimens reach their strength limits and subsequently fail. Minor drops and jumps can be seen throughout the graphs. The small force drops and recoveries, particularly noticeable in specimens 1 and 3, are likely attributed to the microstructural characteristics of the material and instantaneous effects during the testing process. These phenomena can be explained by the following reasons:

- Fiber Fracture in Glass Fibers: In glass fiber-reinforced materials, some fibers may fracture under loading. These fractures cause sudden small drops in force. However, as the remaining structure continues to carry the load, the force rises again.
- Weak Bonding at the Fiber-Matrix Interface: In composite materials, the bond between the polymer matrix and the glass fibers may not be completely uniform. Microcracks may form in regions of weak bonding, temporarily reducing the load-carrying capacity and causing small force drops.
- Load Redistribution: When some fibers break or the matrix cracks, the load is redistributed to the remaining intact regions, resulting in small recoveries observed in the graph.



Figure 7 ±90° fiber-reinforced specimen after test

When it comes to explaining the differences among specimens the second specimen shows the highest maximum force. This suggests that the second specimen is structurally more robust, has fewer discontinuities, or that the resin more uniformly infiltrated the fiber structure. The third specimen reaches a lower maximum force compared to the others and exhibits greater fluctuation. This indicates a higher number of fiber fractures or bonding issues, meaning it has more internal discontinuities. The first specimen demonstrates a moderate level of performance.

The strain value observed around 6–7 mm appears relatively high for a brittle structure. As the load is applied, the insert inside the insulator gradually detaches from the matrix at the interface. Although this internal separation is not visibly detectable from the outside, it contributes to the observed strain values of 6–7 mm.

±45° fiber-reinforced specimen

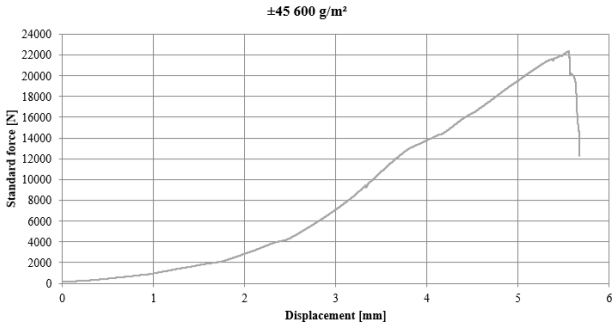


Figure 8 Test Results ±45° fiber-reinforced specimen

Table 2 Summary of tensile performance of ±45° layup

±45° specimen	Displacement (mm)	Force (N)
Mean	5,56	22604

The force–elongation diagram and test result images of a composite insulator reinforced with ±45° 600 g/m² glass fiber are presented. Although three specimens were tested, one representative curve is retained in the figure, and the table shows the average tensile results. Although the specimens exhibited similar fracture behaviors, they showed differences at certain points. Among the six types of fiber orientations tested, this insulator type demonstrated the highest fracture loads, reaching approximately 25,000 N. Examination of the fracture structure revealed the effects of the ±45° lamination, where capillary-like crack propagation was observed.



Figure 9 ±45° fiber-reinforced specimen after test

Specimen with fibers oriented parallel to the tensile direction

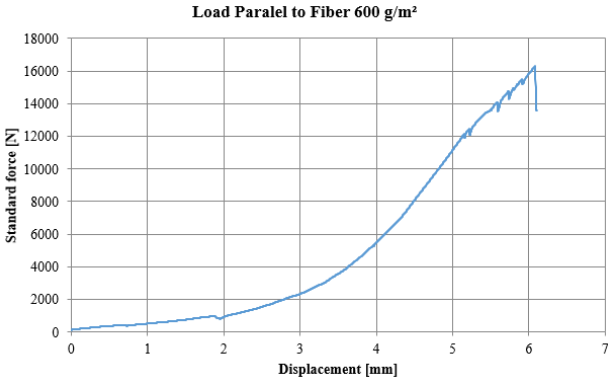


Figure 10 Load Parallel to Fiber Direction

Table 3 Summary of tensile performance of fiber parallel to load direction

Load paralel to fiber specimen	Displacement (mm)	Force (N)
Mean	5,95	15297

In this specimen type, the fibers were laminated with an orientation parallel to the tensile direction. As expected, based on the stacking structure, this group of specimens exhibited the lowest strength among all types [8]. Since the fibers were not loaded along their working direction, the matrix primarily carried the applied load, resulting in deformation at lower force levels. The fracture mode observed is like that of silica-filled insulators, which will be discussed later.

As in the first tests, minor drops and recoveries were observed in the graphs of Specimen 1 and Specimen 2. This behavior suggests that partial deformations occurred within the matrix at the microstructural level. After the failure of some bonds, the remaining structure continued to carry the load, leading to recovery in the force-displacement curve after each drop.

The strain values, again around 6–7 mm, appear relatively high for a brittle specimen structure. As the load increases, the insert inside the insulator gradually detaches from the matrix interface. Although this internal separation is not visible externally, it results in the recorded strain values around 6–7 mm.



Figure 11 Fiber direction parallel to tensile load specimens after test

In conclusion, although all specimens in this group exhibited similar structural behavior, Specimen 2 demonstrated the highest load-carrying capacity among them. For this generally weaker group, it can be stated that they were able to carry an average load of approximately 15,000 N.

Specimen with fiber-oriented perpendicular to the tensile direction

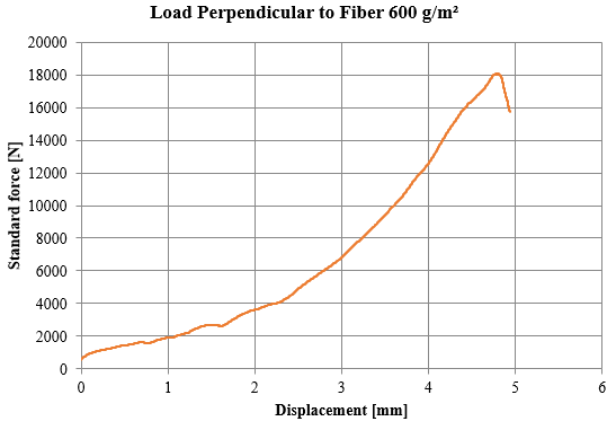


Figure 12 Load Perpendicular to Fiber Direction

Table 4 Summary of tensile performance of fiber perpendicular to load direction

Load perpendicular to fiber specimen	Displacement (mm)	Force (N)
Mean	4,4	18958

This specimen group exhibited the highest strength following the ±45° lamination configuration. As expected, since the fibers were oriented perpendicular to the loading axis, the specimens were able to withstand higher forces. Minimal surface deformation was observed; however, certain regions showed crack propagation along the matrix.



Figure 13 Fiber direction perpendicular to tensile load specimens after test

Purchased (outsourced) sand-filled specimen

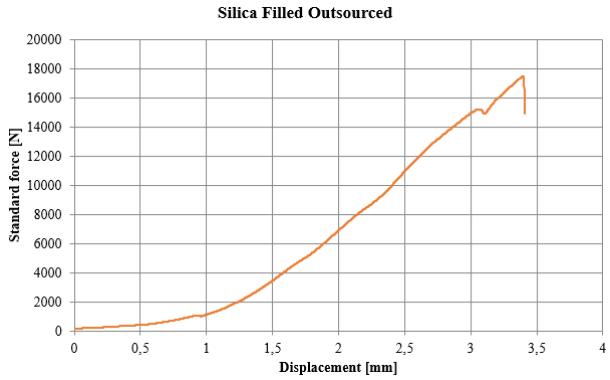


Figure 14 Silica Filled Outsourced Test Result

Table 5 Summary of tensile performance of silica filled outsourced specimens

Purchased specimen	Displacement (mm)	Force (N)
Mean	3,3	16212

The product evaluated in this study is a commercially available insulator manufactured from a sand-filled resin mixture. Similar products are produced by various domestic and international companies. Although it exhibited lower strength than the glass fiber-reinforced specimens with laminations perpendicular to the loading direction, it still demonstrated a moderate level of mechanical performance.

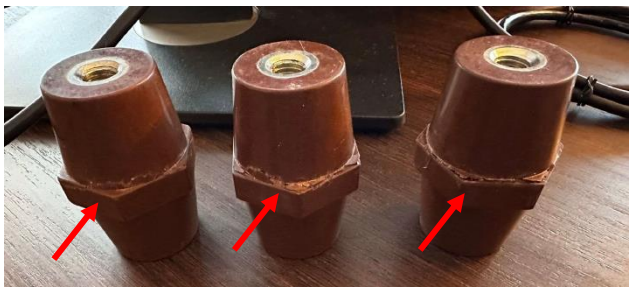


Figure 15 Silica filled purchased specimens after tensile test

While the product's datasheet claims that it can withstand a tensile load of 20,000 N, experimental tests revealed a maximum load-bearing capacity of only 18,000 N, raising concerns about the product's reliability. As expected, the specimen exhibited brittle behavior and failed at the point where the metal insert ended, due to a notch effect.

In house produced sand-filled specimen

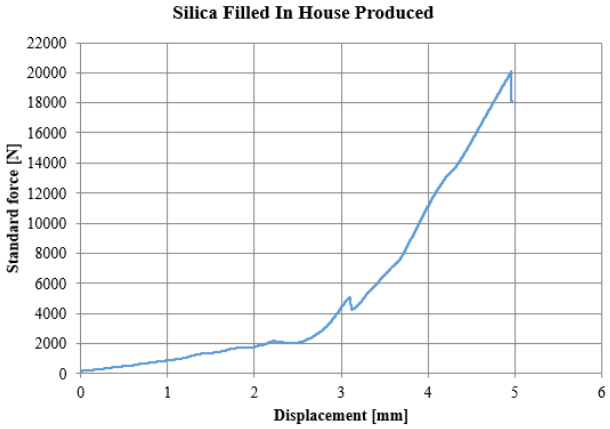


Figure 16 Silica Filled In House Produced Test Result

Table 6 Summary of tensile performance of silica filled in house produced specimens

In house produced specimen	Displacement (mm)	Force (N)
Mean	4,7	18496

It was manufactured from a mixture of sand and resin. It exhibited approximately 10% higher strength compared to the commercially available counterpart. The specimen fractured at an average load of 18,500 N. As expected, it displayed a brittle fracture behavior and failed at the point where the metal insert ended due to a notch effect.



Figure 17 Silica filled inhouse specimens after tensile test

Results and Discussion

Overall, the six types of tested specimens exhibited relatively consistent mechanical behavior without significant deviations. However, specific specimen types demonstrated clear superiority in terms of load-bearing capacity. The specimens with ±45° 600 g/m² glass fiber laminations showed the highest tensile strength among all tested groups. Following them, the specimens with fibers oriented perpendicular to the tensile direction and the unidirectional ±90° 600 g/m² fiber specimens exhibited relatively high performances, respectively. Although the literature generally suggests that specimens with fibers oriented perpendicular to the loading direction tend to exhibit the highest strength [9], [12], the present study revealed that the ±45° configuration outperformed all other types in terms of maximum tensile load. Among the sand-filled specimens, the manufactured specimen distinguished itself by achieving approximately 10% higher tensile strength compared to the commercially purchased one. This finding indicates that controlled fabrication processes can significantly enhance the mechanical performance of resin-sand composite insulators.

Overall, the results emphasize that fiber orientation has a decisive impact on the tensile behavior of composite insulators. Laminations that enable effective load transfer through fiber alignment, particularly ±45° orientations, provide superior mechanical properties. In contrast, configurations where fibers do not efficiently contribute to load bearing results in lower performance, requiring greater reliance on the matrix material.

Table 7. General Evaluation of the Results

Type	Mean Displacement (mm)	Standard Deviation (mm)	Mean Force (N)	Standard Deviation (N)	% Difference Force vs Min	% Difference Displacement vs Min
±90°	6,63	0,36	18333,33	1505,55	19,80	100,90
±45°	5,56	0,08	22603,67	2351,15	47,80	68,50
Load Paralel to Fiber 600 g/m²	5,95	0,63	15297,33	1790,80	Reference (min)	80,30
Load Perpendicular to Fiber 600 g/m²	4,40	0,74	18958,33	2787,00	23,90	33,30
Silica Filled Outsourced	3,30	0,31	16212	1495,00	6,00	Reference (min)
Silica Filled Inhouse Produced	4,70	0,82	18496,33	1331,90	20,90	42,40

Conclusion

This study demonstrated that fiber orientation plays a critical role in determining the tensile performance of epoxy matrix composite insulators manufactured using the hand lay-up method. The key findings of the study are summarized below:

- ±45° fiber-oriented specimens exhibited the highest tensile strength among all configurations tested.
- Specimens with fibers perpendicular to the tensile direction and ±90° unidirectional layups followed in performance.
- Manufactured sand-filled specimens performed approximately 10% better in tensile strength than their commercially available counterparts.
- The results emphasize the significance of precise fiber alignment and controlled manufacturing processes in improving the mechanical reliability of composite insulators.

These findings provide a foundation for further research into optimizing fiber orientation strategies in composite insulator design and improving the performance of manually fabricated polymer-based components.

Ethics committee approval and conflict of interest statement

There is no need to obtain permission from the ethics committee for the article prepared.

There is no conflict of interest with any person / institution in the article prepared.

Authors' Contributions

-Study conception and design: Bilgin, Çetinel, Yalçın

-Acquisition of data: Bilgin

-Analysis and interpretation of data: Bilgin, Çetinel, Yalçın

-Drafting of manuscript: Bilgin

-Critical revision: Çetinel, Yalçın

Acknowledgement

This article is derived from the author's doctoral dissertation titled "Investigation of mechanical and dielectric properties in variable oriented glass fiber reinforced insulators", completed at Balıkesir University, 2025.

References

[1] A. P. Mouritz, E. Gellert, P. Burchill, and K. Challis, "Review of advanced composite structures for naval ships and submarines," *Compos Struct*, vol. 53, no. 1, pp. 21–42, 2001, doi: 10.1016/S0263-8223(00)00175-6.

[2] P. Middendorf and C. Metzner, *Aerospace applications of non-crimp fabric composites*. Woodhead Publishing Limited, 2011. doi: 10.1016/B978-1-84569-762-4.50018-7.

[3] D. McLellan, "Corvette from the Inside," 2002, Accessed: Apr. 24, 2025. [Online]. Available: https://www.sae.org/publications/technical-papers/content/B-858/

[4] S. Van Hulle, "Preliminary Design of a Transverse Composite Leaf Spring for Electric Vehicles," 2023.

[5] E. Tuncer, I. Sauers, D. R. James, and A. R. Ellis, "Electrical insulation characteristics of glass fiber reinforced resins," in *IEEE Transactions on Applied Superconductivity*, Jun. 2009, pp. 2359–2362. doi: 10.1109/TASC.2009.2018748.

[6] Z. Wang, D. Zhang, M. Yang, J. Fang, S. Zhou, and W. Wang, "Study on Bending Stiffness of Solid Post Composite Insulator," in *7th IEEE International Conference on High Voltage Engineering and Application, ICHVE 2020 - Proceedings*, Institute of Electrical and Electronics Engineers Inc., Sep. 2020. doi: 10.1109/ICHVE49031.2020.9279975.

[7] H. Park, M. S. Ahn, T. JLee, and andD ILee, "Compressive Strength of FRP for Insulator," 2004.

[8] V. E. Ogbonna, A. P. I. Popoola, O. M. Popoola, and S. O. Adeosun, "A review on corrosion, mechanical, and electrical properties of glass fiber-reinforced epoxy composites for high-voltage insulator core rod applications: challenges and recommendations," Sep. 01, 2022, *Springer Science and Business Media Deutschland GmbH*. doi: 10.1007/s00289-021-03846-z.

[9] P. Mallick, "Fiber Reinforced Composites Materials, Manufacturing, and Design."

[10] A. Swapnil, B. SatheSandip, … P. C. today, and undefined 2017, "Experimental investigation of mechanical properties of glass fibre/epoxy composites with variable volume fraction," *ElsevierAS Swapnil, B SatheSandip, P ChaudhariBapu, SJ Vishalmaterials today: proceedings, 2017•Elsevier*, Accessed: Apr. 24, 2025. [Online]. Available: https://www.sciencedirect.com/science/article/pii/S2214785317310040

[11] S. Li, H. H. Tsang, Y. Cheng, and Z. Lu, "Seismic testing and modeling of cylindrical electrical equipment with GFRP composite insulators," *Compos Struct*, vol. 194, pp. 454–467, Jun. 2018, doi: 10.1016/j.compstruct.2018.02.036.

[12] C. H. Park, "A STUDY OF THE DIELECTRIC AND MECHANICAL PROPERTY INTERACTIONS OF GLASS-CLOTH/EPOXY COMPOSITES," 1987.

[13] N. Mishra, U. A. Khan, A. Srivastava, and N. Asthana, "Effect of the Glass Fiber Orientation on Mechanical Performance of Epoxy based Composites," *Prabha Materials Science Letters*, vol. 3, no. 2, pp. 175–190, Sep. 2024, doi: 10.33889/pmsl.2024.3.2.011.

[14] J. S. Kim, S. J. Kim, K. J. Min, J. C. Choi, H. S. Eun, and B. K. Song, "A Study on Tensile Behavior According to the Design Method for the CFRP/GFRP Grid for Reinforced Concrete," *Materials*, vol. 15, no. 1, Jan. 2022, doi: 10.3390/ma15010357.

[15] S. Y. Kim, C. S. Shim, C. Sturtevant, D. D. W. Kim, and H. C. Song, "Mechanical properties and production quality of hand-layup and vacuum infusion processed hybrid composite materials for GFRP marine structures," *International Journal of Naval Architecture and Ocean Engineering*, vol. 6, no. 3, pp. 723–736, Sep. 2014, doi: 10.2478/IJNAOE-2013-0208.

[16] J. ; Z. H. Li, "Failure mechanisms of fiber-reinforced composites with varied orientations," *Materials Science and Engineering: A*, vol. 789, pp. 1–20, 2020.

[17] "Evaluation of the electrical properties and mechanical behavior of".

[18] "ISO 527-4 Plastics — Determination of tensile properties — Part 4: Test conditions for isotropic and orthotropic fibre-reinforced plastic composites," Geneva, Switzerland, 1997.

[19] "ISO 527-5 Plastics — Determination of tensile properties — Part 5: Test conditions for unidirectional fibre-reinforced plastic composites," Geneva, Switzerland, 2009.

[20] "ISO 527-1 Plastics — Determination of tensile properties — Part 1: General principles," Geneva, Switzerland, 2012.

Dicle University
Journal of Engineering
https://dergipark.org.tr/tr/pub/dumf
duje.dicle.edu.tr

Research Article

Modal Analysis of Sandwich Structure Using Finite Element Approach

Kübra Çağla ÇIBIKÇI[1*]

[1] Erzincan Binali Yıldırım University, Mechanical Engineering Department, kubra.cibikci@erzincan.edu.tr, Orcid No: 0000-0002-4060-5608

ARTICLE INFO

Article history:

Received 12 May 2025
Received in revised form 26 June 2025
Accepted 14 July 2025
Available online 30 September 2025

Keywords:

Modal Analysis, Mode Shape, Natural Frequency, Sandwich Structure

Doi: 10.24012/dumf.1697649

* Corresponding author

ABSTRACT

In automotive, aviation, marine and advanced engineering applications, sandwich structures are increasingly preferred due to their superior properties such as high strength to weight ratio, wear resistance, and good surface quality. In this study, the natural frequencies and mode shapes of sandwich structures were investigated, and the effects of different boundary conditions and material combinations on their vibration characteristics were evaluated. Modal analyses were performed using the Finite Element Method (FEM) via ANSYS software, and the generated model was validated by comparing with existing literature data. In the model, carbon steel and carbon fiber reinforced plastic (CFRP) were used as the face sheet materials, while polyurethane elastomer matrix fiber and PVC foam were used as the core material. According to the results, the sandwich structure with a PVC foam core exhibited a 178.6% increase in the first natural frequency compared to the structure with a polyurethane elastomer matrix fiber core. Boundary conditions had a significant impact on natural frequencies, with the completely fixed (C–C–C–C) configuration yielding values 28.6% higher than the completely free (F–F–F–F) condition. Sandwich structures with fully CFRP face sheets showed a 27.7% higher natural frequency than those with hybrid face sheets. These findings demonstrate that the dynamic performance of sandwich structures is highly sensitive to boundary conditions as well as the types of core and face sheet materials, emphasizing the importance of appropriate material and geometric configuration in engineering design.

Introduction

Continuous advances in technology have led researchers to develop lighter, more durable and functional new material systems. In this context, sandwich structures, which offer mechanical advantages such as high strength to weight ratio, superior energy absorption capacity, and long-term durability are widely used in many engineering and industrial fields such as aviation, automotive, marine and construction [1, 2]. Sandwich structures are multilayer composite systems composed of thin, and high-strength face sheets and a low-density yet rigid core material [3]. In such structures, the face sheets primarily bear bending loads, while the core material provides shear rigidity and ensures effective load distribution. Additionally, the core material plays a crucial role in damping impacts and vibrations acting on the structure [4]. The most striking feature of sandwich structures is that the type, thickness, and geometry of both the face sheets and the core material can be optimized with great flexibility, depending on application requirements. This enables the design of high-performance structures tailored to specific engineering problems. Core materials are generally optimized for both lightness and mechanical strength [5]. Materials such as polyurethane foam, polyethylene terephthalate (PET) foam, balsa wood, cork, and PVC foam are widely preferred because they provide sufficient structural stiffness despite their low density [6]. In addition, the combination of these core materials with different face sheets significantly affects both the static and dynamic performance of sandwich structure. Accurate understanding and modeling of the mechanical characteristics of sandwich structures is of critical importance for engineering designs. In particular, understanding the vibration behavior of these structures is essential to ensure structural integrity and reliable performance under dynamic loading conditions.

Various studies have been conducted in literature on the modal analysis of sandwich structures. Manoharan et al. performed a modal analysis of hybrid laminated composite panels with viscoelastic core using ANSYS software. Their study revealed that fiber orientations, laminate stacking sequences, and boundary conditions significantly affect the natural frequencies and mode shapes of composite panels [7]. Similarly, Apalak et al. investigated the effect of fiber orientations, number of layers, and boundary conditions on natural frequency of graphite/epoxy plates and reported that these parameters have a considerable impact on vibrational behavior [8]. Kumar et al. investigated the vibration behavior of honeycomb core sandwich composite panels using the finite element method and carried out the

modeling with ANSYS APDL software. The study indicated that the surface plate thickness and core material type are key determinants of the natural frequencies and mode shapes of the structure [9]. Jalali and Doğan performed a modal analysis of laminated composite sandwich panels using ANSYS and ABAQUS software, and especially emphasized the effects of fiber orientation, layer stacking sequence, and boundary conditions on the natural frequencies [10]. Hose et al. analyzed the natural frequencies of graphene sheet reinforced polymer composite plates using ANSYS software. They showed that changes in geometry, boundary conditions, and aspect ratio significantly affect the vibration characteristics of the structure, even when the density is kept constant [11]. Prashant et al. performed a theoretical modal analysis of cantilever beams made from two different materials and experimentally determined the natural frequencies, damping ratios, and mode shapes. The experimental findings were found to be in good agreement with the theoretical results. It was also observed that, for beams with identical cross-sections and lengths, the natural frequency of aluminum was higher than that of mild steel [12]. Potluri et al. performed static structural and modal analyses using ANSYS Workbench software to investigate the effect of core and face plate thicknesses on natural frequencies of sandwich structures [13]. Lashin and El-Nady studied the effects of material selection and boundary conditions on the natural frequencies and mode shapes of sandwich beam structures which were modeled using MSC-PATRAN/NASTRAN software. The results obtained for aluminum solid beams, CPVC solid beam, and Aluminum-CPVC sandwich beam were compared with analytical data. Kheirikhah et al. investigated the effects of fundamental parameters such as groove geometry, boundary conditions, composite layer properties, and thickness ratio on the natural frequencies of corrugated sandwich structures [14]. Maraş and Yaman investigated the vibration behavior of fiber metal laminate (FML) plates using numerical and experimental methods and found a strong agreement between the two approaches. In their studies, they revealed that the location of the aluminum layers and the boundary conditions have significant effects on the natural frequencies [15]. In a separate study, Maraş and Yaman numerically analyzed the vibration behavior of sandwich syntactic foams using a finite element method based on Higher Order Shear Deformation Theory (HSDT). The numerical results were compared with experimental data, which showed a high level of agreement [16]. Maraş, investigated the free vibration and buckling behaviors of sandwich plates composed of fiber metal laminate (FML) face sheets and a balsa wood core using the Generalized Differential Quadrature (GDQ) method. The developed model demonstrated an agreement of over 97% with reference results in the literature. In addition, the effects of various design parameters on the natural frequencies and buckling loads were comprehensively evaluated [17]. In a separate study, Maraş and Yaman performed free vibration analysis of fiber-metal laminated (FML) composite plates under different boundary conditions using Differential Quadrature (DQ), Generalized DQ (GDQ) and Harmonic DQ (HDQ) methods. The numerical results showed a high level of agreement with experimental data. This is the first comprehensive study in the literature to demonstrate the reliable applicability of DQ-based methods for vibration analysis of FML structures [18].

This study aims to determine the natural frequencies and mode shapes of sandwich structures using ANSYS software. The study is structured in two main stages. In the first stage, the accuracy of the numerical model developed in the ANSYS environment was evaluated by comparison with previous studies in the literature, and the model's validity was verified. In the second stage, the effects of different boundary conditions and material combinations on the vibration characteristics of sandwich structures were systematically investigated.

The study specifically contributes to the determination of optimal layer arrangements and material selection for enhanced vibration performance. In particular, the comparative modal analysis of PVC foam and polyurethane elastomer matrix fiber cores, combined with CFRP and carbon steel face sheets, enables a direct comparison of these materials' vibration performance addressing a gap identified in the literature. Furthermore, a more comprehensive and versatile analysis of modal behavior was achieved by jointly evaluating multiple parameters (core material, face sheet configuration, and boundary conditions), thus making a novel contribution to the existing body of knowledge.

Material Properties and Finite Element Model

In this study, Finite Element Analysis (FEA) method was used to investigate the vibration behavior of sandwich structures, and the models were created using the commercial software ANSYS. The sandwich structure was modeled as consisting of two stiff face sheets and a low-density core layer in between. Carbon steel and CFRP, which offer high mechanical strength and rigidity, were preferred as the face sheet materials. The CFRP layer was defined as an orthotropic material with the fiber orientation set to [0°]. Polyurethane elastomer matrix fiber and PVC foam, which are distinguished by their lightness and energy absorption capacity, were used as core materials. The material definitions were made in the ANSYS Engineering Data module, and the elastic modulus, density, and Poisson's ratio of each material are presented in Table 1.

Table 1. Mechanical properties of core and face sheet materials used in the sandwich structures [4, 19, 20]

Properties	Carbon steel	Carbon fiber reinforced plastic	Polyurethane elastomer matrix fiber	PVC foam
E_1 (GPa)	200	120	0.90195	0.056
E_2 (GPa)	-	7.9	-	-
E_3(GPa)	-	7.9	-	-
ν_{12}	0.3	0.33	0.36	0.27
ν_{13}	-	0.33	-	-
ν_{23}	-	0.33	-	-
G_{12} (GPa)	-	5.5	-	-
G_{13} (GPa)	-	5.5	-	-
G_{23} (GPa)	-	5.5	-	-
ρ (kg/m^3)	7850	1580	1098	60

The geometry was created using ANSYS Design Modeler with dimensions of 300 x 300 x 28 mm. The core thickness was set to 20 mm, and each face sheet had a thickness of 4 mm. The model used is the same as the model in the Ariesta et al. [19] study. Figure 1 shows the three-dimensional geometric design of the sandwich structure.

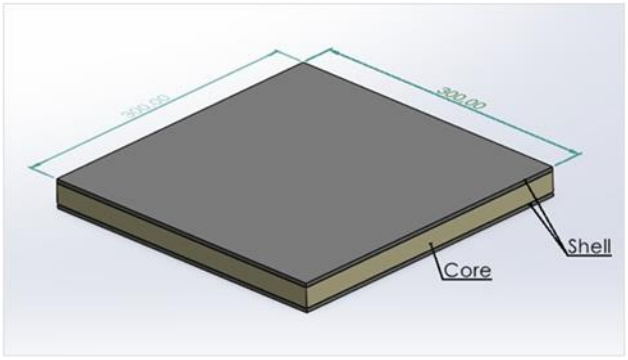


Figure 1. The three-dimensional geometric design of the sandwich structure

To ensure the accuracy and validity of the analysis results, a suitable mesh structure was created, establishing an optimal balance between mesh quality, computational accuracy, and solution time. The mesh consisted of hexahedral (brick) elements, which are suitable for structural dynamic analyses involving both layered composite and isotropic materials. The model consists of 8000 elements and 48093 nodes in total.

After generating the mesh structure, the model was configured according to the specified boundary conditions, and the Block Lanczos algorithm was preferred for the modal analysis in the free vibration analysis. As a result of the analysis, the first five natural frequencies and their corresponding mode shapes were obtained.

Figure 2 shows the modeling steps of sandwich structures; Figure 3a shows the three-dimensional model created in the ANSYS software, while Figure 3b shows the created mesh structure.

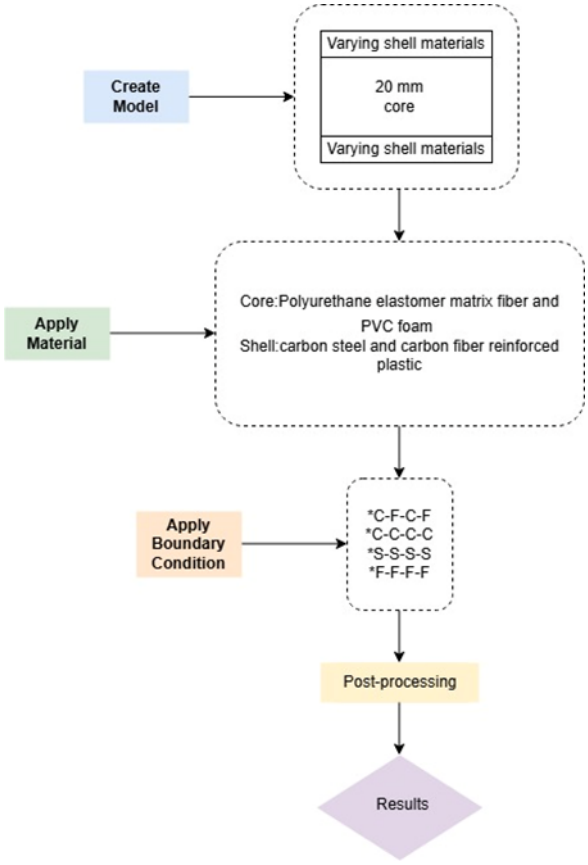


Figure 2. Flowchart of the numerical modelling steps for sandwich structures

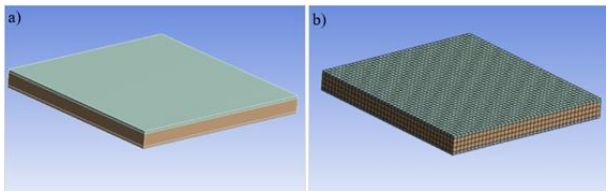


Figure 3. Geometrical model of the sandwich structure a) before meshing b) after meshing

Simulation Validation and Literature Comparison

The numerical analyses performed in this study were implemented using ANSYS software. To ensure the reliability and validity of the analysis model, the natural frequency results obtained from the simulations were compared with data from the literature. Accordingly, the material properties, layer thickness and geometric dimensions used in the modeling process were fully defined in accordance with the parameters specified in the study conducted by Ariesta et al. using ABAQUS software. Modal analysis was performed under clamped-free-clamped-free (C-F-C-F) boundary conditions. The natural frequency values and mode shapes obtained from the numerical analysis were compared with those reported by Ariesta et al.; similarities were evaluated, and the validation level of the model was revealed. The comparison of the results obtained in this study with those in the literature is presented in Figure 4.

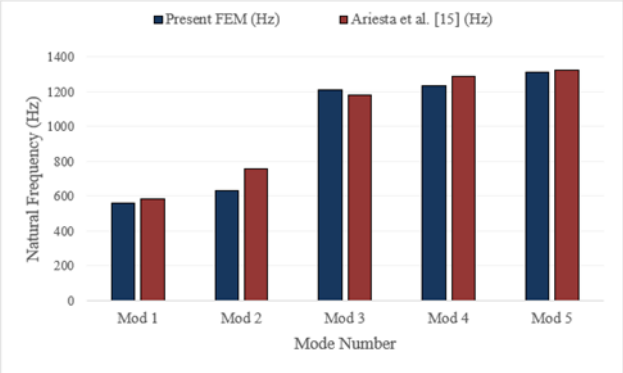


Figure 4. Comparisons of the natural frequencies of the sandwich structure obtained by the present FEM and Ariesta et al. [19]

In order to evaluate the accuracy of the numerical model, the obtained natural frequencies were compared with those reported in the study conducted by Ariesta et al. [19], which used ABAQUS software. Percentage error rates were calculated for each mode in the comparisons made. Accordingly, deviations of 4.15% for the first mode, 17.06% for the second mode, 2.77% for the third mode, 4.30% for the fourth mode, and 0.81% for the fifth mode were obtained. These results confirm that the model demonstrates a high level of agreement with literature, particularly with errors below 5% in four out of five modes, thus validating its reliability for the modal analysis of sandwich structures.

When the obtained natural frequency results are compared with those of the study conducted by Ariesta et al. [19] using ABAQUS software, both analysis results show generally similar trends. This supports the validity of the modeling approach used in the present study and increases the reliability of the parametric analyses performed in the subsequent stages. However, limited differences were observed in the natural frequency values. The main reason for these differences is the nuances that arise in the analysis algorithms, mesh generation strategies, boundary condition implementation methods, and solution methods of different finite element software such as ANSYS and ABAQUS. Although both programs are based on the finite element method principle, they have some structural differences in terms of the element types used, numerical stability of the solvers and accuracy levels. Therefore, such differences can lead to certain deviations in the natural frequency values, in higher order modes and complex boundary conditions. This situation reveals that the comparison of simulation results should focus not only on numerical values but also on the general vibration behavior and mode shapes.

Results

Case 1: Effect of change in the core material

In Case 1, the effect of varying the core material on the dynamic properties of sandwich structures was evaluated. To provide a comparative analysis, the carbon steel was used as the constant material for the top and bottom face sheets in all models and only the core material was changed. In this context, polyurethane elastomer matrix fiber and PVC foam were used as core materials, and both configurations were analyzed using the modal analysis method. The modeling process was carried out under C-F-C-F boundary conditions, and natural frequency values were obtained for each vibration mode.

The comparison of natural frequencies obtained for polyurethane elastomer matrix fiber and PVC foam core materials are presented in Figure 5. It was observed that changing the core material directly affected the total mass and stiffness of the structure; thus, it caused differences in natural frequencies. These findings are consistent with previous studies [4, 6], which reported that the total mass and stiffness of the structure caused differences in frequencies.

The analysis results indicated that the sandwich structure with a PVC foam core exhibited higher natural frequencies compared to the structure with a polyurethane elastomer matrix fiber core. This situation can be explained by the relatively lower density and higher stiffness/weight ratio of PVC foam. On the other hand, although polyurethane elastomer matrix fiber has a higher density, it results in lower natural frequencies.

When the obtained frequency values are examined in detail, it is seen that the natural frequencies increase significantly as the mode number increases for both materials. The PVC foam core structure exhibited much higher frequencies than the polyurethane elastomer matrix fiber core structure, especially in the higher modes (Mode 3, 4, 5). This difference is related to the system becoming more sensitive to stiffness and mass distribution in higher modes. For example, while the frequency value obtained for PVC foam in Mode 5 is 4826.9 Hz, this value is 1313.4 Hz for the polyurethane elastomer matrix fiber core.

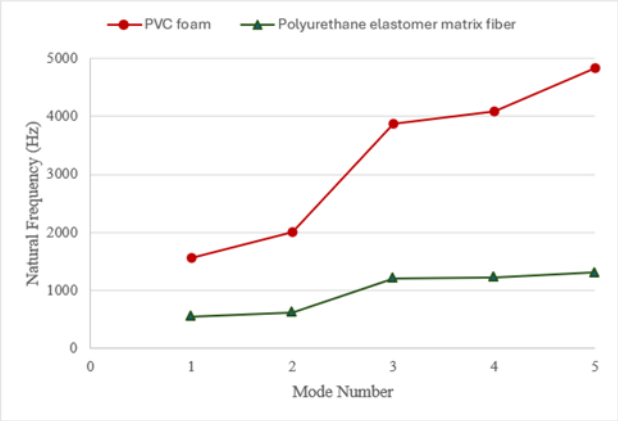


Figure 5. Effect of core material on the natural frequencies of sandwich structures

The comparison of mode shapes obtained for polyurethane elastomer matrix fiber and PVC foam core materials is presented in Figure 6. In both cases, the first mode shape shows the classical bending mode characteristic. However, differences are observed in frequency values and deformation magnitudes. The PVC foam core structure vibrates at a higher frequency, indicating a stiffer system. The larger deformation, the more energy the system can carry (high frequency oscillations) and the clearer separation of the mode shape. The polyurethane elastomer matrix fiber structure, on the other hand, reveals that the system is more flexible with lower frequency and less deformation. At higher modes, vibration behavior becomes more complex and multiple nodes appear in the mode shapes.

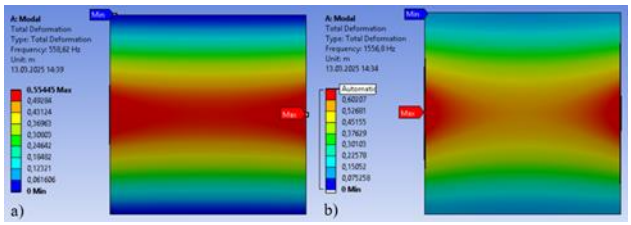


Figure 6. Contour plot of the first mode shape for a) polyurethane elastomer matrix fiber b) PVC foam as core

An important advantage of sandwich structure with PVC foam cores is the light achieved thanks to their low density. The reduction of the total mass of the structure not only allows for higher natural frequencies but also provides operational convenience in terms of transportation and assembly. In addition, PVC foam cores generally require less processing in the production process and are more cost-effective. With these features, PVC foam stands out as a preferable core material, especially in engineering applications where cost and weight sensitivity are critical.

Case 2: Effect of change in the boundary conditions

The dynamic behavior of sandwich structures with carbon steel face sheets and a polyurethane elastomer matrix fiber core was investigated under different boundary conditions. In this context, the effects of completely fixed (C–C–C–C), completely simply supported (S–S–S–S) and, completely free (F–F–F–F) boundary conditions on the natural frequencies of the structure were analyzed. The first five natural frequency values for each boundary condition are presented in Figure 7, and the corresponding first mode shapes are presented in Figure 8.

The boundary conditions applied in the model directly affect the stiffness of the sandwich structure. As shown in Figure 7, the highest natural frequency values are obtained under C–C–C–C boundary conditions. This situation is due to the fact that the mentioned boundary condition provides the most restrictions on the system and maximizes the stiffness of the structure. The natural frequencies obtained under S–S–S–S boundary conditions are lower than the C–C–C–C boundary condition, but higher than the frequencies obtained under F–F–F–F boundary conditions. This situation shows that the S–S–S–S boundary condition partially reduces the stiffness of the structure and causes a decrease in natural frequencies. On the other hand, the lowest natural frequency values are observed under F–F–F–F boundary conditions. This condition is evaluated as the configuration where the free vibration behavior of the structure occurs most dominantly by providing the least restrictions on the system.

The results show that the boundary conditions have a decisive effect on the dynamic behavior of sandwich structures. The changes observed in the frequency values depending on the boundary conditions are consistent with the studies reported in the literature [21, 22], which reveal that the boundary conditions significantly affect the vibration characteristics. While increased structural rigidity leads to higher natural frequencies, a greater degree of freedom results in a decrease in natural frequency values.

In addition, when high-order natural frequencies such as the 3rd, 4th and 5th modes are evaluated, it is clearly seen that the effect of the boundary conditions continues. Under the C–C–C–C boundary condition, thanks to the maximum restriction of the system from all sides, the structure can maintain high frequency values even in more complex mode shapes. For example, while the C–C–C–C configuration reaches a high value of 2091.1 Hz in the 5th mode, the same mode remains at 1952.5 Hz in the S–S–S–S boundary condition and only at 1211.7 Hz in the F–F–F–F condition. This clearly demonstrates that stiffness directly affects the high mode frequencies and significantly changes the resonance behavior. In addition, the equal frequency values (1211.7 Hz) observed in the 4th and 5th modes under the F–F–F–F boundary condition suggest that some symmetric modes overlap under this structure or that the structure exhibits repetitive mode characteristics. This overlap shows that mode separation becomes difficult in systems with high degrees of freedom and complex dynamic responses may arise.

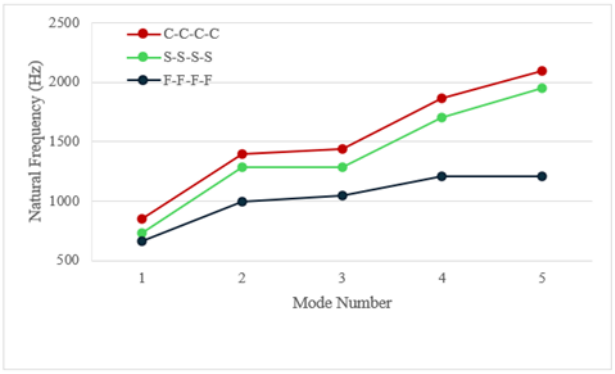


Figure 7. Effect of boundary conditions on the natural frequencies of the sandwich structure

Figure 8 presents the first mode vibration patterns of the sample under different boundary conditions. Since all edges of the sample were fixed under the C-C-C-C boundary condition, the maximum displacement occurred at the center of the structure and a symmetrical doming mode was observed. Under the S-S-S-S boundary condition, it was observed that the maximum displacement was not located exactly at the center as a result of allowing the edges to displace. In the analysis performed under the F-F-F-F boundary condition, the displacement distribution showed an asymmetrical character due to the edges of the sample being completely free. In this case, the maximum displacement shifted towards the edges. The obtained mode shapes show that the boundary conditions have a significant effect on the vibration behavior of the sandwich structure.

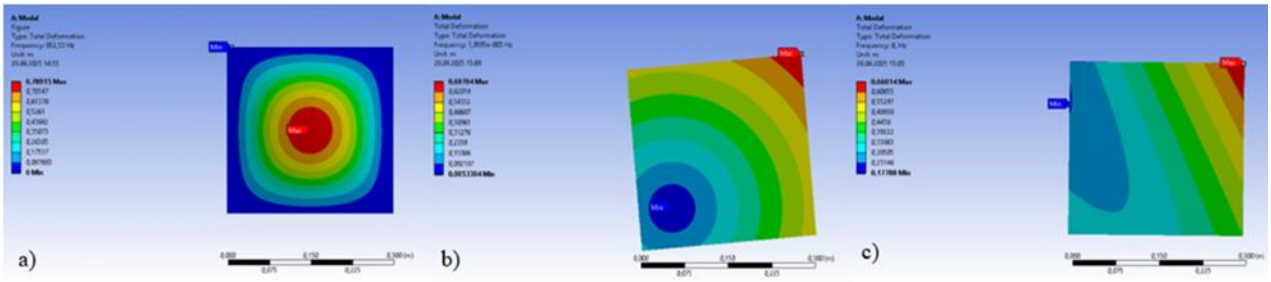


Figure 8. Contour plot of first mode shape under boundary condition a) C-C-C-C b) S-S-S-S c) F-F-F-F

Case 3: Effect of change of shell material

In this case, the dynamic behavior of the examined sandwich structures was analyzed by considering different shell material configurations. In the first configuration, both face sheets were made of CFRP, while the core layer consists of a fixed sandwich structure. In the second configuration, the upper and lower shell materials differed; one was CFRP, and the other was carbon steel. To investigate the effects of these shell material combinations on the modal characteristics of sandwich structures, the obtained natural frequency values were evaluated comparatively. Numerical analyses were carried out under C–F–C–F boundary conditions. The findings regarding the effects of shell material variation on the vibration behavior of the structures are presented in Figures 9 and 10.

When Figure 9 is examined, it is evident that the materials used in the face sheets of sandwich structures significantly influence their natural frequencies. The configuration with CFRP on both surfaces exhibits higher natural frequency values across all modes compared to the configuration with one CFRP and one carbon steel face sheet. This can be associated with the fact that the CFRP has a higher modulus of elasticity than carbon steel, thus providing greater structural rigidity. Despite its high density, carbon steel offers lower rigidity than CFRP in terms of elastic properties, and this reduces the overall rigidity of the structure, causing the natural frequencies to decrease. The difference between the natural frequencies is more pronounced, especially in the third, fourth and fifth modes. This finding shows that the effect of the shell material on high-order modes is greater. A similar trend is observed in the first and second modes, but the frequency difference becomes less pronounced. As a result, the preference of high stiffness materials in the face sheets increases the overall stiffness of sandwich structures and contributes to an increase in their natural frequencies. The findings are in line with the generally accepted trend in the literature that an increase in structural stiffness increases natural frequencies [10]. The use of CFRP on both surfaces improves the vibration performance of the sandwich structure and allows for higher frequency responses.

In sandwich structure design, the material selection for the face sheets has a direct impact on the mechanical performance of the structure. If the structure operates in a way that will receive loads from both surfaces and symmetrical vibration behavior is desired, the use of carbon fiber on both surfaces offers the optimum solution. In this case, both the bending rigidity of the structure increases, and the mode shapes become symmetrical and predictable. On the other hand in cases where the structure is subjected to loading primarily from one side—such as in applications like protective shields or cladding panels—using carbon fiber on one face and carbon steel on the other may serve as a cost-effective alternative. This hybrid structure can provide sufficient structural performance in certain applications while significantly reducing production costs.

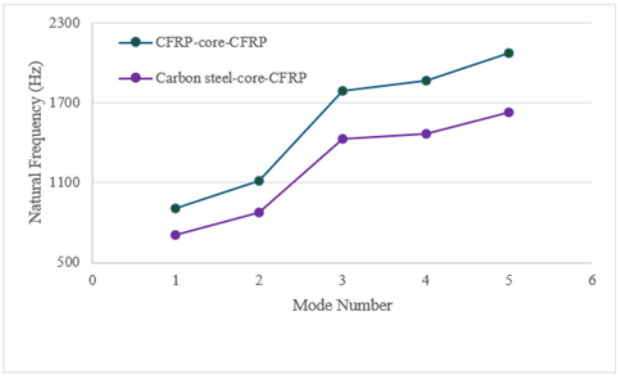


Figure 9. Effect of face sheet material on the natural frequencies of sandwich structures

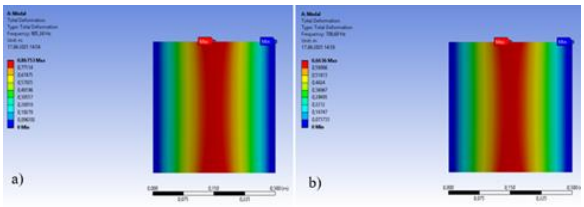


Figure 10. Contour plot of first mode shape of a) CFRP-core-CFRP b) carbon steel-core-CFRP

Conclusions

In this study, a modal analysis of sandwich structures was performed, and their natural frequencies were obtained. The results were compared with previously published studies, and after determining that the sandwich structure model was designed correctly, parametric studies were started. In these parametric studies, the effects of different boundary conditions and material combinations on the natural frequencies were found.

The main findings obtained from this study are as follows:

1. It shows that the sandwich structure with a PVC foam core has higher natural frequencies compared to the one with a polyurethane elastomer matrix fiber core material.

2. The results indicate that boundary conditions significantly affect the dynamic behavior of sandwich structures. As structural rigidity increases, natural frequency values increase, and as the degrees of freedom increase, the natural frequencies decrease. In addition, the observed isofrequencies in some modes reveal that the system has symmetric vibration modes.

3. It has been observed that changing the face sheet material has a decisive effect on the natural frequencies of sandwich structures. The use of CFRP layers increases structural stiffness and increases the natural frequency values.

In conclusion, both boundary conditions and material combinations play a critical role in the dynamic behavior of sandwich structures. Stiffer boundary conditions and higher-stiffness materials increase the natural frequencies of the system and improve its vibration resistance. Therefore, both appropriate boundary conditions and material must be carefully selected to achieve the desired dynamic performance in engineering applications.

References

[1] U. Demircioğlu & M.T. Çakır, "An investigation of the influence of various shaped cutouts on the free vibration behavior of sandwich structures," Sakarya University Journal of Science, vol. 26, no. 4, pp. 687-694, 2022. Doi: 10.16984/saufenbilder.1063422

[2] H. Elangovan & V. Rajamohan, "Numerical and experimental approach on vibration characterization of non-uniform hybrid sandwich plates," Mechanics of Advanced Materials and Structures, pp. 1-33, 2025. Doi: 10.1080/15376494.2024.2449502

[3] K. N Shivakumar, S. D. Argade, R. L. Sadler, M. M. Sharpe, L. Dunn, G. Swaminathan, & U. Sorathia, "Processing and properties of a lightweight fire resistant core material for sandwich structures," Journal of advanced materials, vol. 38, no.1, pp.32-38, 2006.

[4] V. N. Burlayenko & T. Sadowski, "Analysis of structural performance of sandwich plates with foam-filled aluminum hexagonal honeycomb core," Computational Materials Science, vol.45, no.3, pp.658-662, 2009. Doi: 10.1016/j.commatsci.2008.08.018

[5] S. Gürgen and M. A. Sofuoğlu, "Vibration attenuation of sandwich structures filled with shear thickening fluids," Compos. Part B Eng., vol. 186, no. October 2019, 2020, Doi: 10.1016/j.compositesb.2020.107831. Doi: 10.1016/j.compositesb.2020.107831

[6] D. Kumar, V. Kallannavar, S. Kattimani, & B. R. P. Reddy, "Dynamic analysis of laminated composite sandwich plates with a circular hole," In IOP Conference Series: Materials Science and Engineering, Vol. 1136, No. 1, p. 012050. IOP Publishing, 2021, June. Doi: 10.1088/1757-899X/1136/1/012050

[7] R. Manoharan, N. M. Kurhe, I. B. Shedbale, & U. D. Charapale, "Modal analysis of hybrid laminated composite sandwich plate," Mater Today Proc, vol.5, pp.1245-1246, 2018. Doi: 10.1016/j.matpr.2018.02.225

[8] Apalak, M. Kemal, M. Yildirim, and R. Ekici, "Layer optimization for maximum fundamental frequency of laminated composite plates for different edge conditions," Composite Science and Technology, vol.68, pp.537-550, 2008. Doi: 10.1016/j.compscitech.2007.06.031

[9] M. Kumar, V. R. Kar, & M. L. Chandravanshi, "Free vibration analysis of sandwich composite plate with honeycomb core," Materials Today: Proceedings, vol.56, pp.931-935, 2022. Doi: 10.1016/j.matpr.2022.02.561

[10] M. B. Jalali, & A. Doğan, "Farkli Sinir Şartlari Ve Farkli Tabaklanma Açilari İçin Tabakali Kompozit Balpeteği Sandviç Plağin Serbest Titreşim Frekanslarinin Karşilaştirilmasi," Uludağ Üniversitesi Mühendislik Fakültesi Dergisi, vol.28, no.1, pp.293-306, 2023. Doi: 10.17482/uumfd.1150777

[11] P. F. P. Hose, & D. A. Krishna, "Free vibration analysis of polymer composite plates reinforced with graphene platelets," Materials Today: Proceedings, vol.65, pp.961-968, 2022. Doi: 10.1016/j.matpr.2022.03.531

[12] S. W. Prashant, V. N. Chougule, & A. C. Mitra, "Investigation on modal parameters of rectangular cantilever beam using experimental modal analysis," Materials Today: Proceedings, vol.2, no.4-5, pp. 2121-2130, 2015. Doi: 10.1016/j.matpr.2015.07.214

[13] R. Potluri, M. N. Raju, & K. R. P. Babu, "Finite element analysis of cellular foam core sandwich structures," Materials Today: Proceedings, vol.4, no.2, pp.2501-2510, 2017. Doi: 10.1016/j.matpr.2017.02.103

[14] M. M. Lashin, & A. O. El-Nady, "Free vibration analysis of sandwich beam structure using finite element approach," IOSR Journal of Mechanical and Civil Engineering Ver. Vol.I, no.12, pp.2278-1684, 2015. Doi: 10.9790/1684-12613442

[15] S. Maraş, & M. Yaman, "Investigation of dynamic properties of GLARE and CARALL hybrid composites: Numerical and experimental results," Engineering Analysis with Boundary Elements, 155, pp. 484-499, 2023. Doi: 10.1016/j.enganabound.2023.06.026

[16] S. Maraş, & M. Yaman, "Experimental and numerical investigation of free vibration behaviours of sandwich syntactic foams," In Structures, vol. 58, pp. 105390, 2023. Doi: 10.1016/j.istruc.2023.105390

[17] S. Maraş, "Free Vibration and Buckling Analyses of Balsa Core Sandwich Composite Plates With Fiber Metal Laminate Facesheets Using the Generalized Differential Quadrature Method," Arabian Journal for Science and Engineering, vol. 50, no.12, pp. 9583-9610, 2025. Doi: 10.1007/s13369-024-09517-1

[18] S. Maraş, & M. Yaman, "Free vibration analysis of fiber-metal laminated composite plates using differential, generalized and harmonic quadrature methods: experimental and numerical studies," *Engineering Computations*, vol. *39*, no.6, pp. 2326-2349, 2022. Doi: 10.1108/EC-08-2021-0490

[19] R. C. Ariesta, A. Zubaydi, A. Ismail, & T. Tuswan, "Identification of damage size effect of natural frequency on sandwich material using free vibration analysis," NAŠE MORE: znanstveni časopis za more i pomorstvo, vol.69, no.1, pp.1-8, 2022. Doi: 10.17818/NM/2022/1.1

[20] F.A. Ghasemi, R. Paknejad and K.M. Fard, "Effects of geometrical and material parameters on free vibration analysis of fiber metal laminated plates," Mechanics and Industry, vol. 14, no. 4, pp. 229-238, 2013. Doi: 10.1051/meca/2013062.

[21] L. Hadji & M. Avcar, "Free vibration analysis of FG Porous Sandwich Plates under various boundary conditions," Journal of Applied and Computational Mechanics, vol.7, no.2, pp.505-519, 2021.

[22] S. R. Farsani, A. Ramian, R. A. Jafari-Talookolaei, P. S. Valvo, & M. Abedi, "Free vibration analysis of rectangular sandwich plates with compressible core and various boundary conditions," Journal of Sandwich Structures & Materials, vol.23, no.8, pp.4077-4106, 2021. Doi: 10.1177/1099636220979

Dicle University
Journal of Engineering
https://dergipark.org.tr/tr/pub/dumf
duje.dicle.edu.tr

Research Article

Parametric Impacts of Metabolic Rate and Occupancy on Internal Thermal Gains in Buildings

Ahmet YÜKSEL[1*]

[1] Yalova University, Electricity and Energy Department, ahmet.yuksel@yalova.edu.tr, ORCID No: 0000-0002-0472-0342

ARTICLE INFO

Article history:

Received 11 June 2025
Received in revised form 23 July 2025
Accepted 23 July 2025
Available online 30 September 2025

Keywords:

Building energy simulation, internal thermal gains, metabolic rate, occupancy level, parametric analysis

Doi: 10.24012/dumf.1717808

* Corresponding author

ABSTRACT

This study investigated the effects of varying metabolic rate (MR) and occupancy levels on indoor air temperature, interior surface temperatures, and internal thermal gains within a non-ventilated building model. The goal was to evaluate how these parameters influence thermal dynamics and determine which plays a more dominant role. Ventilation was intentionally excluded to isolate the thermal effects of occupants and eliminate external influences. The relative humidity generated by occupants accumulated, causing relative humidity to reach saturation in all scenarios. Since relative humidity showed no variation between cases, it was not included in the analysis. The results demonstrated that both MR and occupancy significantly impacted indoor thermal responses. Higher values of either parameter led to increased temperatures, though their relative influence varied. MR had a stronger effect under low-occupancy conditions, while its impact diminished as occupancy increased. For instance, in scenarios with 50 occupants, the indoor air temperature difference between MR values of 50 and 200 W/person reached 6.7°C. Conversely, increasing occupancy led to more uniform total thermal gains due to expanded heat transfer surface area, especially with 200 occupants. The study concluded that both MR and occupancy need to be considered when modeling indoor thermal comfort and energy efficiency. Additionally, the results indicated that occupancy had a more significant influence on indoor temperature dynamics, particularly due to its role in heat transfer surface area expansion. These findings underscored the critical role of occupancy density in shaping indoor temperature profiles and highlighted the need to account for metabolic activity levels when designing energy-efficient and thermally comfortable building environments.

Introduction

Energy efficiency and indoor comfort are pivotal and continuously evolving research areas that form the foundation of sustainability-focused work in buildings [1], [2]. Achieving thermal comfort conditions often requires substantial energy consumption, primarily driven by heating, ventilation, and air conditioning (HVAC) systems [3]. These systems demand considerable energy to maintain indoor comfort parameters within ideal ranges, posing a significant challenge for energy efficiency, especially in buildings with high occupancy densities. In this context, reducing energy consumption while optimizing thermal comfort conditions is a fundamental objective in sustainable building design and operation [4].

Thermal comfort is a key determinant of occupant satisfaction in indoor environments [5]. It is influenced by environmental factors such as indoor temperature, relative humidity, air velocity, and mean radiant temperature, as well as personal factors like clothing insulation and metabolic rate (MR) [6]–[8]. Among these, MR refers to the amount of heat generated by the body in proportion to an individual's physical activity level [9]. Variations in metabolic activity can lead to differing thermal comfort perceptions under the same environmental conditions [10].

Numerous studies in the literature have addressed the consideration of MR to assess individual comfort [11]–[13]. Zhang et al. [14] examined the role of MR in thermal comfort evaluation, emphasizing the importance of accurate MR measurement for enhancing thermal index models. The study highlighted that dynamic MR changes are key human factors affecting thermal regulation and underscored the need for portable, affordable, and precise MR monitoring devices. Nomoto et al. [15] investigated MR values among Japanese individuals performing typical office activities, reporting significantly lower MR values (0.8–2.6 met) compared to international standards (1.0–3.0 met). This discrepancy, particularly pronounced among female participants, suggested potential inaccuracies in thermal comfort assessments and CO_2 generation estimations when applying global standards to specific populations. Jia et al. [16] evaluated the effectiveness of the standard effective temperature in thermal comfort studies across different MR levels. They found that the traditional model failed to maintain consistent thermal sensation across MR variations. Consequently, they proposed a new standard environment incorporating clothing insulation and convective heat transfer coefficients based on actual activity levels, ensuring a linear relationship between standard effective

temperature and thermal sensation votes from 1.0 to 3.8 met.

International standards such as ASHRAE Standard 55-2020 [17] have been updated to better reflect the impact of occupant-related variables on indoor environmental quality. These standards emphasize the importance of accounting for dynamic human factors, such as activity level and occupant density, in the design and operation of HVAC systems. Accordingly, recent studies have begun integrating personalized inputs like MR and real-time occupancy levels into performance assessments, aiming to enhance comfort while optimizing energy use. Čulić et al. [18] reviewed advancements in monitoring technologies for personal thermal comfort and their implications for building energy performance. The review highlighted the significance of both environmental parameters (e.g., room temperature, humidity, mean radiant temperature) and personal factors (e.g., MR, skin temperature), with emerging technologies like wearable devices and connected sensors offering promising solutions for accurate data collection. Choi et al. [19] proposed a vision-based approach to estimate individual thermal comfort parameters, such as metabolic rate and clothing insulation, using indoor images in real time. Their intelligent model was designed to function in both single and multi-occupant spaces and achieved high accuracy through advanced computer vision techniques. The estimated parameters were integrated into a predicted mean vote (PMV) based control algorithm, which significantly improved thermal comfort compared to conventional methods. The study emphasized that using representative values for group scenarios offered a practical solution for real-time thermal regulation while maintaining energy efficiency. Yun et al. [20] developed an occupant-centric control strategy that utilizes real-time MR estimation to enhance thermal comfort and reduce energy use. Their approach combined pose classification and object interaction detection from indoor images to predict MR values, which were then integrated into a novel indoor thermal environment control algorithm. Experimental validation in real building settings demonstrated that this method significantly improved comfort levels, by up to 59% compared to fixed temperature control, and reduced energy consumption by as much as 88%. Jung et al. [21] introduced a semi-supervised multi-task learning model designed to estimate key occupant-specific parameters, namely MR and clothing insulation, for enhanced thermal comfort control. Leveraging both labeled and unlabeled image data, the proposed convolutional neural network model employed a dual-phase training method with pseudo labels to improve activity and clothing detection. Validation against existing models showed substantial accuracy gains, with a 15.8% increase in activity detection and a 25% improvement in clothing recognition. Zhang et al. [22] introduced a novel wearable sensor system designed to accurately estimate human MR, addressing the limitations of conventional bulky and intrusive measurement tools. Their model integrates physiological indicators such as heart rate, skin resistance, heat loss, and muscle composition to predict MR through a linear regression framework. Experimental validation involving various activity intensities and environmental conditions demonstrated strong agreement with reference equipment ($R^2 \approx 0.90$), achieving high accuracy and low uncertainty. Na et al. [23] proposed a deep learning-based approach to estimate individual MR for improved thermal comfort assessment. The study measured metabolic equivalents for eight common indoor activities in a diverse group of participants, analyzing the impact of gender and body mass index (BMI) on MR values. Their self-evaluation model achieved a low coefficient of variation, indicating reliable performance, while the third-party model demonstrated promising generalization across individuals. Notably, the results showed that MR values varied with both activity intensity and individual characteristics, highlighting the need for personalized comfort models in indoor environments. Yıldırım and Pekel [24] conducted a systematic review to explore how wearable sensors integrated with artificial intelligence (AI) can objectively assess physical activity levels, particularly among sedentary individuals. By screening 582 studies published between 2015 and 2024, they identified 17 relevant articles that examined AI-supported activity tracking using wearable technologies. Their findings highlighted the growing potential of such systems to monitor daily movement patterns, estimate MR, and support personalized interventions. The study emphasized that AI-enhanced wearable tools not only enable accurate and continuous activity assessment but also offer promising applications for promoting healthier behaviors in school-aged populations. Choi et al. [25] proposed a real-time MR and clothing insulation estimation method using deep learning and computer vision, alongside a comfort-focused temperature control strategy. Their system accurately predicted MR and clothing insulation with up to 100% accuracy and improved thermal comfort consistency, increasing the proportion of "no thermal change" votes by 17% compared to conventional set-point controls.

In indoor thermal environment studies, building simulations are often tailored to specific activity types to realistically assess internal heat gains and occupant comfort. The level of physical activity directly influences the MR, which in turn affects the thermal loads within space. Depending on the intended use of the building and the occupants' activity, various MR values have been utilized in literature to represent realistic internal conditions. For example, in [26], metabolic rates of 0.8, 1.0, and 1.2 met were used to represent low-activity conditions such as sitting or light movement, especially in residential settings. In [27], occupant activity was categorized into four levels, ranging from sedentary to intense, with corresponding MR values of 1.2, 2.4, 3.0, and 3.7 met, each phase lasting 20 minutes to assess the dynamic impact of different activity levels. In another study [4], thermal sensation was evaluated during sitting and two exercise conditions, associated with MR values of 1.0, 2.4, and 4.4 met. Further investigations, such as [28], simulated moderate indoor activities at 3.0, 3.5, and 4.5 met over 30-minute intervals.

In alignment with these studies, in this study, the simulation modeled a 100 m^2 space without ventilation. It varied

occupancy levels (50 to 200 people) and metabolic rates (50 to 200 W/person) to reflect a range of indoor scenarios. These combinations correspond approximately to MR values ranging from sedentary office work to moderate activity, simulating indoor environments such as waiting areas, classrooms, or high-density public zones. This modeling strategy reflects diverse use cases found in the literature while enabling a controlled parametric evaluation of occupant-induced thermal impacts.

Studies focusing on continuous or intermittent building usage scenarios examine not only MR but also varying occupancy levels [29]–[31]. This is since occupancy rate significantly affects the total heat load within indoor spaces, thereby altering thermal balance and directly influencing the distribution of indoor temperatures [32]. Aparicio-Ruiz et al. [33] evaluated adaptive thermal comfort conditions in a primary school classroom with a floor area of 50 m^2 and a capacity of 25 students. A survey conducted with 67 students revealed inconsistencies between the thermal sensation vote (TSV) and the PMV. Kumar et al. [34] investigated thermal comfort in an engineering workshop occupied by approximately 15–20 students for over 20 minutes. Post-occupancy surveys indicated that female participants reported a comfort temperature approximately 1.5°C higher than their male counterparts. Yang et al. [35] experimentally analyzed thermal comfort conditions in test rooms with floor areas of 6.3 m^2 and 17.6 m^2, each occupied by four individuals. The study found that female participants exposed to indoor temperatures of 14°C and 34°C reported feeling cooler and less comfortable at lower temperatures, whereas male participants felt warmer and less comfortable at higher temperatures. Reda et al. [36] examined thermal comfort and CO_2 concentrations in a mosque with a floor area of 1,000 m^2, accommodating 72 people during Friday prayers (1 hour), 72–117 people during Tarawih prayers (2 hours), and 20–50 people during daily noon and afternoon prayers (30 minutes). The results showed that CO_2 concentrations correlated with the duration of occupancy, reaching 480 ppm, 715 ppm, and 900 ppm for 30-minute, 1-hour, and 2-hour periods, respectively. Additionally, the predicted percentage of dissatisfied (PPD) values for these durations were 10, 41, and 28%, respectively.

MR and occupancy parameters play a pivotal role in ensuring thermal comfort and sustainable energy management, especially in high-occupancy buildings. While several studies have explored the thermal effects of MR and occupancy in buildings [4], these investigations typically focus on structures with varying floor areas, functions, and usage patterns. For instance, prior works have modeled occupant activities using a broad range of metabolic rates, such as 0.8–1.2 met for sedentary or elderly individuals, 1.2–3.7 met for staged activity simulations, and up to 5 met for higher-intensity activities under stable environmental conditions [26], [27]. These examples illustrate the relevance of MR variation across different indoor use cases and provide a foundation for selecting representative MR values in building simulations. Despite these efforts, a notable gap remains in understanding which of the two factors, MR or occupancy, has a more significant impact on indoor thermal gains. This study aims to address this gap by providing a comprehensive analysis of the effects of MR and occupancy on indoor environmental conditions. To achieve this objective, a building model was developed to simulate different activity levels and occupancy rates. In this context, internal heat gains of 50, 100, 150, and 200 W/person were used to represent metabolic activity levels ranging approximately from 0.85 to 3.4 met, in alignment with prior indoor environment research [4], [28]. The analysis focuses on variations in indoor air temperatures, interior surface temperatures, and internal thermal gains generated by occupants. The present study intentionally excluded humidity and ventilation effects to isolate the thermal gains due to occupancy alone, following the scope defined in the simulation framework. This approach allowed for controlled comparison of thermal loads arising directly from MR and occupancy density without confounding external climatic influences, despite the known importance of moisture in overall thermal comfort evaluations. The findings of this study are expected to offer critical insights into the interplay between MR and occupancy, contributing to the optimization of internal thermal gains and informing future energy efficiency strategies.

Material and Methods

Building upon the extensive literature addressing the significance of MR in assessing individual comfort [12], [13], [19], [37], this study employs EnergyPlus, a state-of-the-art building energy modeling tool, to further investigate these dynamics. EnergyPlus is a state-of-the-art building energy modeling tool developed by the U.S. Department of Energy. It is recognized for its ability to simulate various energy-related aspects of building performance, including thermal, lighting, and ventilation dynamics. The software provides a detailed analysis of energy flows, enabling simulations of both the building's energy consumption and the indoor environment. With its comprehensive set of features, EnergyPlus models the heat transfer within building materials, air movement, and internal heat gains from occupants and equipment. This makes it an ideal choice for evaluating how different levels of occupancy density and metabolic rates influence indoor temperatures and overall thermal dynamics. In this study, EnergyPlus software was employed to investigate the effects of varying MR and occupancy densities on indoor air temperatures and thermal dynamics.

The simulation was based on a 100 m^2 building model with a total volume of 300 m^3, specifically designed without natural ventilation, enabling a controlled and isolated assessment of internal thermal dynamics. Outdoor air conditions were defined using the "BSk" Koppen-Geiger climate classification, as shown in Fig. 1 [38]. This classification, which falls under the B (dry) climate group with S (steppe) indicating a semi-arid precipitation regime and k (cold) representing low mean annual temperatures, characterizes a cold semi-arid (steppe) climate. The building was assumed to be located within this BSk climate zone, exemplified by cities such as Denver, Colorado

(Latitude: 39.74°N, Longitude: 105.0°W), which experience semi-arid conditions with cold, dry winters and warm summers. The solar incidence angle in the modeled location varies throughout the day and year. At solar noon during the summer solstice, the sun reaches a maximum altitude of approximately 73°, resulting in a minimal incidence angle of about 17°. Conversely, during the winter solstice, the solar altitude at noon drops to around 27°, increasing the incidence angle to approximately 63°. This choice reflects the specific climate characteristics of the region where the modeled building is situated and ensures that the simulation results are relevant to realistic environmental conditions.

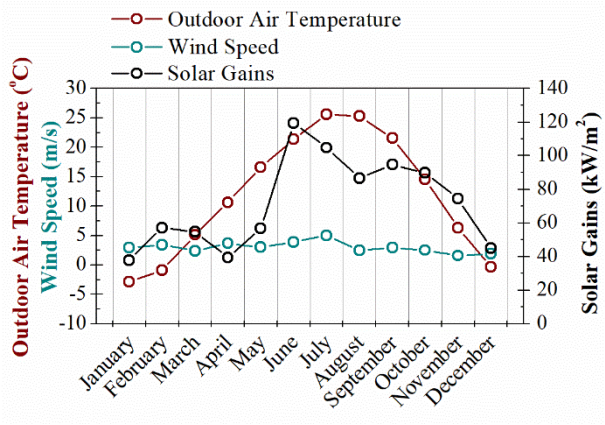


Figure 1. Monthly variations in outdoor air conditions for investigated BSk climate location.

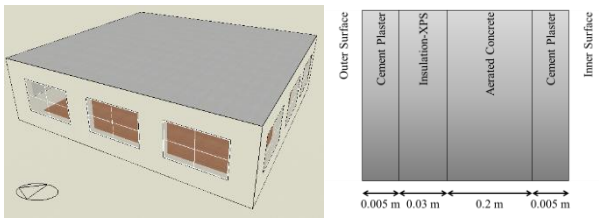


Figure 2. Building model and wall components.

The wall components of the building, as illustrated in Fig. 2 and Table 1, were constructed with materials that provided a U-value of 0.53 W/m²K, ensuring a moderate level of thermal insulation. However, this U-value was relatively high compared to the values recommended in the latest national standards. According to the revised Turkish Thermal Insulation Standard TS825, the maximum allowable U-values for external walls vary regionally and range between 0.45 and 0.20 W/m²K, depending on the severity of the local climate [39]. Although the selected U-value in the present study reflects older or less-insulated building stock still common in practice, this deviation from the latest recommendations was intentionally made to represent a more conservative and realistic scenario for thermal load analysis.

Additionally, all exterior walls were equipped with double-glazed windows, which accounted for 30% of the total wall surface area [40]. Each window used in the model was a standard double-glazing system, made up of two glass panes of 3 mm thickness, separated by a 13 mm air-filled cavity. These windows had a thermal transmittance of 2.7 W/m²K. Their overall solar energy transmittance was 62%, with 54% of direct solar radiation passing through, and 62% of visible light being transmitted into space.

In the study, it was assumed that the indoor environment was not ventilated, and that no heat losses occurred other than through the building components. Additionally, the study did not include the effects of HVAC systems, as the primary focus was on investigating the impact of occupancy density and MR on internal thermal gains. It should be noted that ventilation was intentionally excluded in this simulation to isolate the effects of internal thermal gains caused solely by human metabolic activity and occupancy rate. The study was designed as a parametric analysis, in which the number of occupants and their metabolic rates were systematically varied to evaluate their direct impact on indoor thermal dynamics. Although such a non-ventilated and densely occupied environment does not reflect typical or safe real-world conditions, this modeling approach allows for a clearer understanding of the threshold points where internal gains begin to significantly influence thermal comfort.

Internal thermal gains can be defined as the thermal energy generated by the activities of individuals present in the environment and the devices used. These gains generally include the heat produced by human metabolic activities, the operation of electrical devices, indoor heaters, various activities within the building, and other internal energy sources. Metabolic gains refer to the thermal energy produced by individuals because of their physical activities, while the occupancy rate represents the number of people and their activity level within the building. In the presented study, MR and occupancy rate were considered the primary factors influencing internal thermal gains. Other potential internal heat gain sources such as equipment and lighting were intentionally excluded to ensure that the effects of occupants' sensible heat contributions could be assessed in isolation. This approach allowed for a focused analysis of how MR and occupancy influence indoor thermal dynamics in the absence of external or non-human internal loads. Four MR values were evaluated: 50, 100, 150, and 200 W/person, representing different activity levels. Occupancy levels were varied as 50, 100, 150, and 200 occupants, resulting in total internal heat gains ranging from 2,500 W (50 occupants × 50 W) to 40,000 W (200 occupants × 200 W). This approach allowed for a focused and quantifiable analysis of how MR and occupancy influence indoor thermal dynamics under controlled internal gain conditions. The study was designed to represent a broad range of human activities, covering both low and high activity levels. Activities such as sleeping, which are associated with a metabolic rate of 0.7–0.8 met or 45–55 W/person, were considered alongside more physically demanding activities, such as heavy physical labor, which generate a higher metabolic rate of 2.5–3.5 met or 200–300 W/person. Moreover, the proportion of sensible and latent heat gains varies depending on both activity level and ambient temperature. According to ASHRAE Standard 55-2020 [17], [41], at an ambient temperature of 26°C,

approximately 42% of the total metabolic heat generated by a resting individual is sensible, while the remaining 58% is latent. This ratio can shift depending on the activity level, with higher-intensity activities leading to increased latent heat production due to elevated perspiration and respiration rates. For example, in activities exceeding 2.5 met (e.g., heavy manual labor), latent heat can surpass sensible heat gains [42]. Although this study does not separate these components explicitly in the simulation, the total metabolic rates (e.g., 200 W/person) implicitly include both latent and sensible portions as estimated by EnergyPlus's internal algorithms. In EnergyPlus, internal gains from people are specified using the "People" object, where the activity level represents the total metabolic rate. This total is then internally divided into sensible and latent heat gains based on predefined algorithms, which rely on ambient temperature and activity level. Specifically, EnergyPlus uses empirical correlations, derived from ASHRAE Standard 55-2020, to partition the total metabolic heat into dry (sensible) and moist (latent) components. Sensible heat further contributes to convective and radiative heat transfer within space, while latent heat contributes to moisture gains through respiration and perspiration. Although users do not manually enter these fractions, EnergyPlus dynamically calculates them during simulations to ensure realistic thermal and moisture load estimations under various environmental and metabolic conditions.

Table 1. Thermophysical properties of building materials.

	Material	**Thickness (m)**	**Density (kg/m^3)**	**Thermal Conductivity (W/m.K)**	**Specific heat (J/kg.K)**
Wall	Outer cement plaster	0.005	1760	0.72	840
	XPS insulation	0.03	35	0.034	1400
	Aerated concrete	0.2	750	0.24	1000
	Inner cement plaster	0.005	1760	0.72	840
Roof	Roof brick	0.1	1000	0.3	840
	Roofing felt	0.02	960	0.19	837
	Roof insulation	0.06	20	0.035	1100
Floor	Aerated concrete	0.1	750	0.24	1000
	Flooring block	0.14	650	0.14	1200

The values used in the simulations (up to 200 W/person) correspond to activities such as moderate walking, manual work, or physically active standing tasks, which might occur in emergency response centers, temporary shelters, or crowded healthcare environments during intense or stressful periods. These activities were selected to reflect not routine conditions, but highly loaded emergency-like scenarios. Additionally, the study considered a range of occupancy densities from 0.5 to 2 people/m^2 to evaluate the effects of varying population densities on thermal performance. Although these values are significantly higher than the typical standards defined by ASHRAE Standard 55-2020 [17] (5-100 m^2 per person), they were deliberately selected to simulate high-density occupancy scenarios beyond normal conditions. The simulated building was intended to represent public-use spaces such as primary healthcare waiting areas, temporary shelters, or emergency response centers, where elevated occupancy levels may temporarily occur. However, it is acknowledged that the upper-bound internal load condition (e.g., 2 people/m^2 combined with high metabolic activity leading to 200 W/m^2) exceeds the typical operational range of such facilities. This scenario does not represent passive activities like sitting or standing quietly, but rather a hypothetical worst-case scenario involving moderately active occupants (e.g., moving, queueing, or interacting) densely packed in a confined space. The goal was not to reflect average or routine usage but to explore how the indoor thermal environment responds to extreme internal load conditions. In all scenarios, occupants were assumed to be uniformly distributed throughout the 100 m^2 indoor space, ensuring consistent internal heat gain distribution. This modeling approach allowed for a comprehensive assessment of system performance under stressful conditions that could arise in overcrowded environments such as emergency shelters or waiting rooms during peak hours. Besides, it was assumed that both MR and occupancy remained constant throughout the year, maintaining steady values 24 hours a day, 7 days a week. This simplification allowed for a focused analysis, free from the complicating factors of fluctuating occupancy patterns or seasonal variations in activity levels. However, to reflect real-world conditions more accurately, clothing insulation values were assumed to vary seasonally, with different values applied for summer, transitional, and winter months. The clothing insulation was set at 0.5 clo for summer, 1.0 clo for transitional months, and 1.5 clo for winter months, corresponding to the typical clothing insulation levels expected for each season.

Validation of Simulation Model

To validate the reliability of the developed EnergyPlus-based simulation model, indoor air temperature outputs were compared with real-world data reported by Alonso et al. [43]. In reference study [43], the thermal performance of classrooms in southern Spain was monitored under specific HVAC protocols during January 2020 (pre-pandemic) and

January 2021 (pandemic period with altered ventilation strategies).

For the North Class (A6) with 100 m^2 floor area, which was selected for validation purposes, mechanical ventilation and heating were active from 7:30 a.m. to 2:00 p.m. with no manual airing in January 2020. During January 2021, the protocol changed to manual airing through one window (11:30 a.m. to 2:00 p.m.), with no mechanical ventilation and only heating being applied. These HVAC protocols were incorporated solely for model validation. In the remainder of the study, the building was modeled as a naturally non-ventilated space with no mechanical ventilation, representing a controlled scenario for investigating the impact of internal heat gains and occupancy patterns. The MR and occupancy ratio were 1.4 met and 3.85 m^2/person, respectively.

The reference study [43] reported average indoor air temperatures of 21.9°C and 18.0°C for January 2020 and January 2021, respectively. The simulated values under corresponding HVAC conditions were 22.8°C and 18.7°C. The maximum deviation was 0.9°C and 0.7°C, which fell within the acceptable range for thermal modeling [44]. Simulated temperature ranges also aligned closely with measured field data. These results confirmed that the simulation model could capture indoor thermal behavior under real-world HVAC strategies, supporting its validity for further use in thermal comfort and energy performance analysis of buildings.

Table 2. Comparison of average indoor air temperatures between the reference [43] and present study.

	Average indoor air temperatures (°C)	
	January 2020	January 2021
Reference Study [43]	21.9°C (range: 14.5-26.8)	18.0°C (range: 14.0-20.0)
Present Study (Simulation)	22.8°C (range: 14.0-27.5)	18.7°C (range: 14.5-21.2)
Difference (ΔT)	0.9°C	0.7°C

Model Limitations

In this study, mechanical ventilation and HVAC systems were intentionally excluded from the simulation model after the validation phase, with the aim of developing a simplified framework that isolates the effects of internal heat gains, occupancy rates, and metabolic activity on thermal conditions. This approach allows for a more focused analysis of thermal comfort dynamics that are often overshadowed by HVAC operation in fully conditioned spaces. However, it is important to acknowledge that the exclusion of ventilation inherently limits the model's ability to capture certain environmental parameters, such as CO_2 concentration and indoor air quality metrics. In real buildings, especially those with continuous or dense occupancy, ventilation plays a vital role in maintaining acceptable air quality and regulating humidity. The current model, by design, does not simulate these aspects, as its primary objective is to examine the thermal response of the indoor environment under passive or emergency-like conditions where ventilation may be reduced or temporarily unavailable. While scenarios involving extended high occupancy without ventilation are not intended to reflect standard operating conditions, they serve to highlight the thermal consequences and internal load behaviors in the absence of mechanical systems. Therefore, the findings should be interpreted as representing a boundary case that contributes to a better understanding of how internal factors influence thermal comfort when HVAC support is limited or selectively deactivated.

Results and Discussion

The variations in monthly average outdoor and indoor air temperatures, as well as interior surface temperatures for different occupancy and MR values, are presented in Fig. 3. As expected, an increase in MR or occupancy led to an increase in indoor air temperature and interior surface temperatures. In scenarios with 50 occupants, the impact of increasing MR on temperatures was more pronounced. However, in scenarios with 100 or more occupants, the effect of MR on monthly average indoor air and wall surface temperatures remained limited. For the case with 50 occupants, the difference between the maximum and minimum indoor temperatures was 16.8°C for MR of 50 W/person and 10.1°C for MR of 200 W/person. For 200 occupants, these values were determined as 4.4°C and 4.1°C, respectively. Additionally, with every increment of 50 people, the average indoor air temperatures increased by 3.7, 1.2, and 0.6°C, while the average interior surface temperatures increased by 2.9, 0.9, and 0.5°C, respectively. The reduction in temperature differences with increasing occupancy highlighted that the contribution of thermal gains from occupants to the total heat load was significant, making these effects more noticeable at lower occupancy levels.

On the other hand, an increase in MR significantly influenced indoor temperatures, and it was observed that at an MR value of 200 W/person, indoor air temperatures remained higher regardless of the number of occupants. This result clearly highlighted the dominant role of metabolic activity in shaping internal thermal conditions, especially under low occupancy scenarios. This indicated that the increase in heat production per person elevated the total internal heat gain, consequently raising indoor temperatures as expected. Each 50 W/person increase in MR raised the average indoor air temperatures by 5.4, 0.7, and 0.6°C for an occupancy of 50 people, and by 0.1, 0.1, and 0.2°C for an occupancy of 200 people. This non-linear trend suggested that as the internal thermal load increased, the relative impact of additional metabolic heat generation diminished, indicating a saturation effect in enclosed environments. Therefore, it was determined that the influence of MR diminished in conditions where high internal thermal gains and temperatures were achieved. Additionally, as outdoor temperatures increased, indoor temperatures reached maximum levels, indicating a potential rise in cooling loads. Although the interior surface temperatures followed a trend parallel to indoor air

temperatures, they exhibited more limited variations in response to increases in MR and occupancy. For 50 occupants and an MR of 50 W/person, the difference between the average indoor air and interior surface temperatures was 1.8°C, which increased to 3.1°C with rising MR and occupancy. In the study by Calvaresi et al. [45], an increase of approximately 50 W/person in metabolic rate during the winter months was noted to cause a rise in air temperature of up to 3°C for occupancy level of 10 people. In the present study, this increase corresponded to average temperature rises of 2.1, 0.6, 0.3, and 0.1°C for occupancy levels of 50, 100, 150, and 200 people during January, February, and December. This was attributed to the slower response of wall surfaces to heat transfer processes and the influence of thermal mass. Additionally, these findings underscored the buffering role of building envelope materials in mitigating rapid indoor temperature changes, which could be strategically utilized in passive design approaches. Kumar et al. [34] evaluated thermal comfort conditions in a university workshop located in a "Cwa" climate zone based on the Koppen–Geiger classification, involving students with an estimated metabolic rate of approximately 100 W/person. Although the floor area per person was not specified, the average indoor air temperatures during autumn, winter, and the overall experimental period were reported as 25.1°C, 18.1°C, and 20.8°C, respectively. In the present study, under a comparable metabolic rate (100 W/person) and an occupancy level of 50 individuals, the corresponding values were calculated as 30.8°C, 24.9°C, and 27.9°C. This notable difference was likely attributed to variations in building envelope configurations and regional climate characteristics. Furthermore, other factors such as differences in solar exposure levels or internal heat gains from equipment might also have contributed to the observed temperature discrepancies. These findings demonstrated that, even under similar metabolic loads, indoor thermal conditions could differ significantly depending on building and environmental parameters.

On the other hand, when MR values were kept constant and occupancy varied, the differences observed in indoor air and interior surface temperatures were more pronounced compared to scenarios where occupancy was kept constant and MR varied. This was because the increase in the heat transfer surface area associated with the number of occupants had a more significant effect than individual heat gains resulting from metabolic density. In other words, the spatial distribution and density of heat sources (people) had a greater influence on the thermal environment than the intensity of each source. Particularly, as the number of occupants increased, the heat transfer surface area of the indoor environment expanded, which led to a higher potential for heat insulation or heat loss. Consequently, it was concluded that occupancy had a much stronger impact on indoor temperature dynamics compared to MR. This conclusion aligned with the fundamental principles of internal heat gain modeling, emphasizing that both occupant density and distribution significantly affect thermal comfort outcomes.

In Fig. 4, the variation of monthly internal thermal gains from occupants (total metabolic gains) according to MR and the number of occupants is presented. It was determined that total internal thermal gains reached minimum levels during the summer months and maximum values during the winter months. This indicated that the thermal balance of the indoor environment was related to outdoor temperatures. Additionally, it was identified that due to the high outdoor temperatures in the summer, heat production from occupants had a limited impact. However, the increase in internal thermal gains during the winter months (January, February, December) was identified as a significant factor contributing to the maintenance of indoor temperatures.

A noticeable increase in thermal gains was observed with the rise in occupancy when the MR was kept constant and the number of occupants varied. This trend was particularly evident in the scenario with 200 occupants, where the total internal heat gain in January and December was significantly higher than in other scenarios. These findings emphasized the substantial impact of occupant density on indoor heat accumulation, even when individual metabolic contributions remained unchanged. This highlighted the influence of per capita metabolic heat on total thermal gains.

Internal thermal gains increased as the MR rose when the number of occupants was kept constant and the MR varied. For instance, in the scenario with 50 occupants, thermal gains generated by individuals with a MR of 200 W/person showed a significant increase compared to those with a MR of 50 W/person. This showed a saturation point where the relative contribution of additional metabolic energy per person becomes less significant in environments with already high internal heat loads.

In the findings presented thus far in this study, the increases in indoor air temperatures, interior surface temperatures, and internal thermal gains from occupants due to the rise in MR or the number of occupants were expected outcomes. However, determining which factor (MR or occupancy) had a greater influence on internal thermal gains was significant, particularly for improving energy efficiency and thermal comfort in buildings. Therefore, scenarios with different combinations of MR and the number of occupants, where the total metabolic thermal gains (MR × number of occupants) were equal, were analyzed to determine their impacts on indoor air temperature, interior surface temperature, and internal thermal gains from occupants, as shown in Fig. 5.

Despite having the same total metabolic heat production (e.g., MR: 50 W/person with 100 occupants and MR: 100 W/person with 50 occupants), notable differences in indoor air and wall surface temperatures were observed, especially during winter and transitional seasons. In scenarios with a higher number of occupants and lower MR, indoor air and surface temperatures tended to be slightly higher due to more homogeneous heat distribution and reduced local temperature gradients. Conversely, in scenarios with fewer occupants and higher MR, heat was concentrated around

fewer individuals, reducing distribution efficiency and resulting in lower average indoor temperatures.

Furthermore, while sharp peaks in thermal gains were observed in scenarios with higher MR but fewer occupants, the total thermal contribution remained limited due to local heat losses and inefficient air mixing. In contrast, scenarios with lower MR and more occupants exhibited more stable and balanced thermal gains, contributing to the stability of indoor temperatures. Notably, scenarios with a higher number of occupants demonstrated greater internal thermal gains even when the total metabolic heat production was the same, highlighting the importance of heat distribution dynamics.

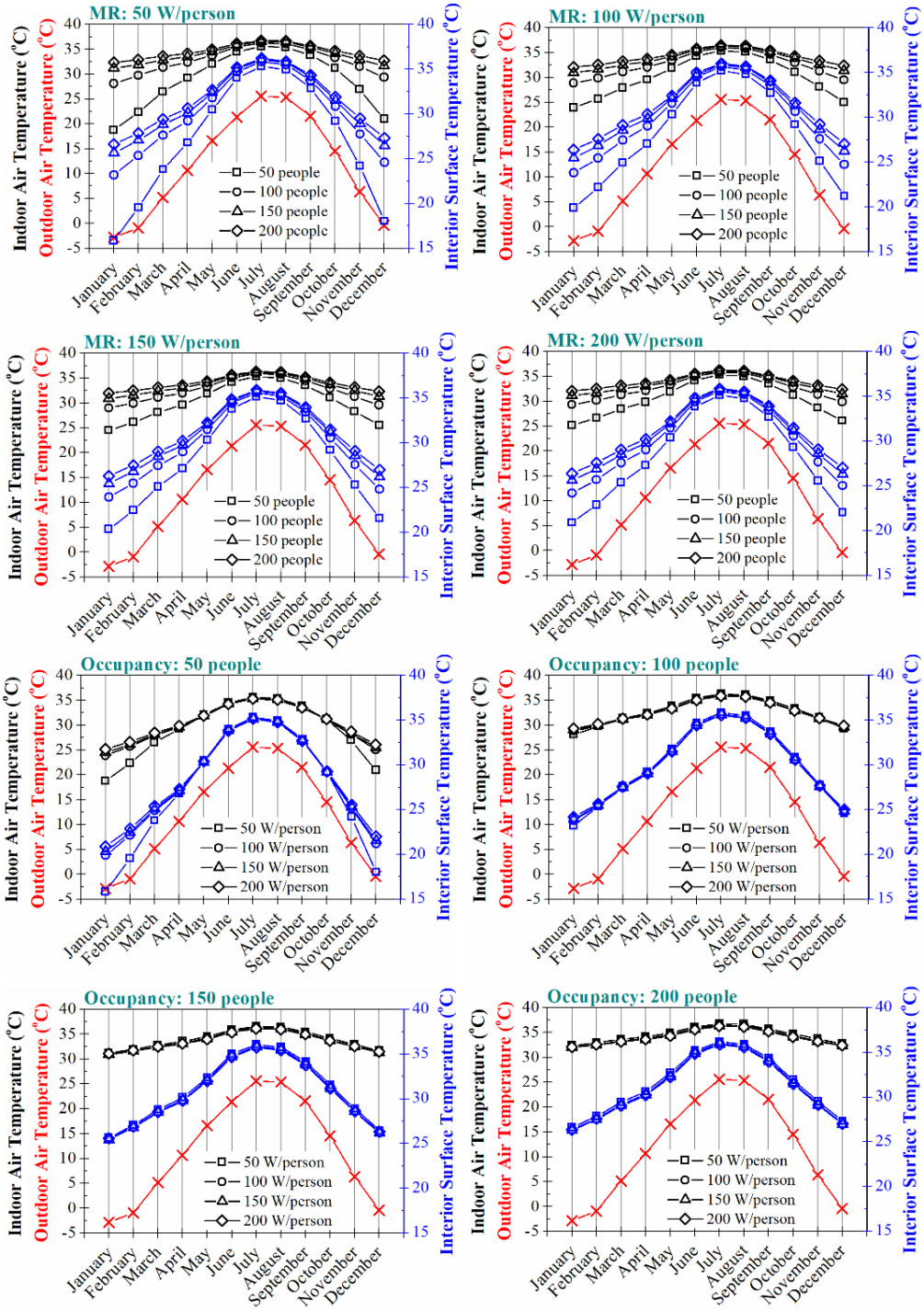


Figure 3. Indoor air and interior surface temperatures for different occupancy and MR values.

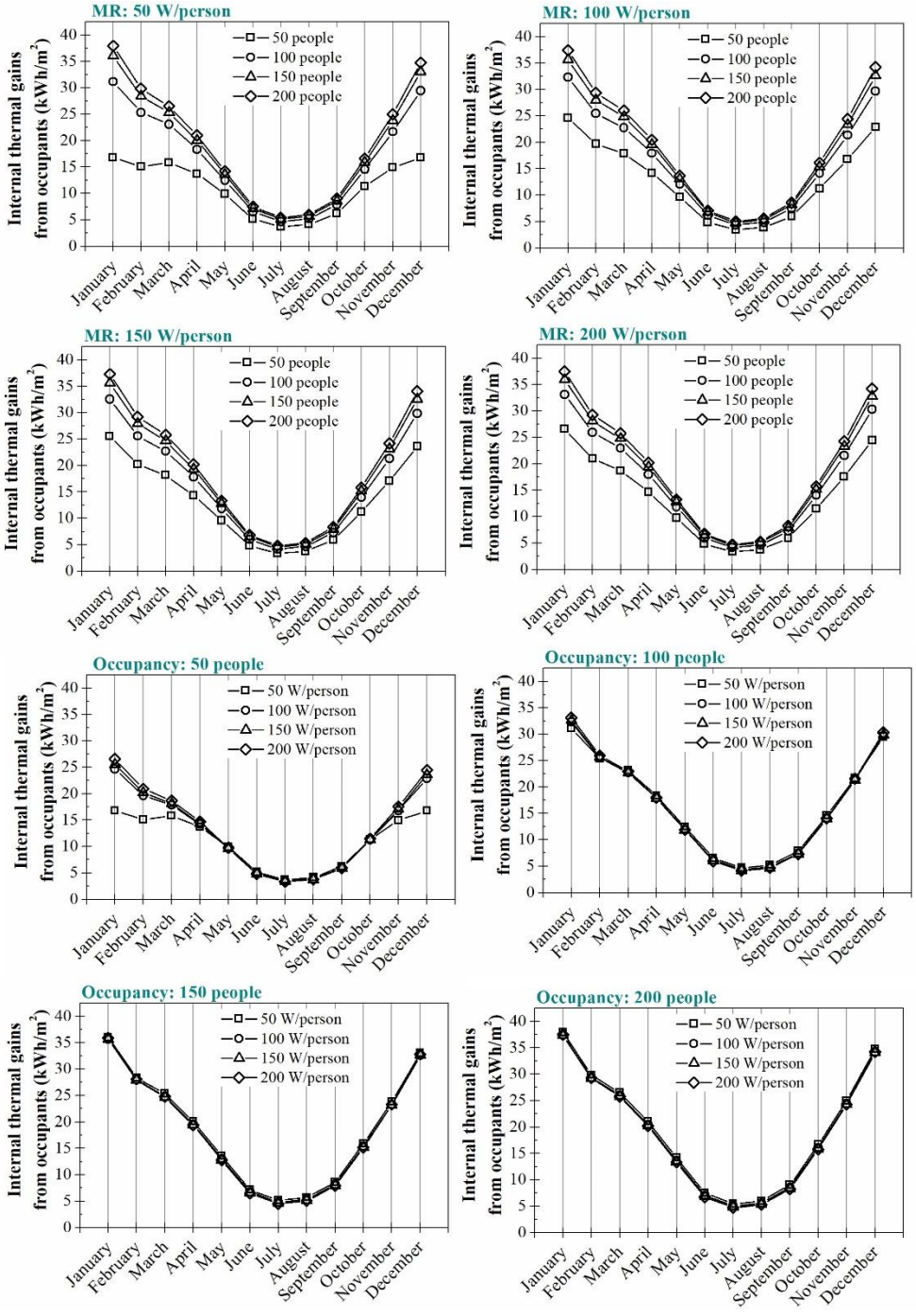


Figure 4. Internal thermal gains from occupants for different occupancy and MR values.

Seasonal variations also had a pronounced effect on indoor conditions. During winter months, the differences between scenarios became more evident, particularly in those involving a higher number of occupants, which consistently maintained elevated indoor temperatures. This contributed to a reduction in heating demand, as internal heat gains from occupancy played a more dominant role in thermal regulation.

In the summer, due to high outdoor temperatures, the influence of metabolic thermal gains diminished; however, a large number of occupants could marginally increase indoor temperatures, potentially impacting cooling loads. As in studies such as [46], which examined energy consumption and comfort under different occupancy levels, it was determined that a greater number of occupants could maintain indoor temperatures despite fluctuations in metabolic rates. Besides, it was revealed that the interaction between MR and occupancy was non-linear. Despite having the same total metabolic heat, the distribution of occupants significantly affected indoor temperatures. This finding addressed a gap in the literature, which typically focused on total heat output while overlooking the effects of spatial distribution and air mixing. Additionally, seasonal analyses highlighted the variable impacts of internal thermal gains under different climatic conditions, emphasizing the importance of context-specific strategies in building energy

design. In conclusion, even when total metabolic heat remained constant across different MR-occupancy scenarios, indoor conditions were influenced by factors such as heat distribution efficiency and occupant density. These findings contributed to a deeper understanding of thermal comfort modeling and building energy consumption, offering valuable insights for the development of more responsive and adaptive HVAC strategies.

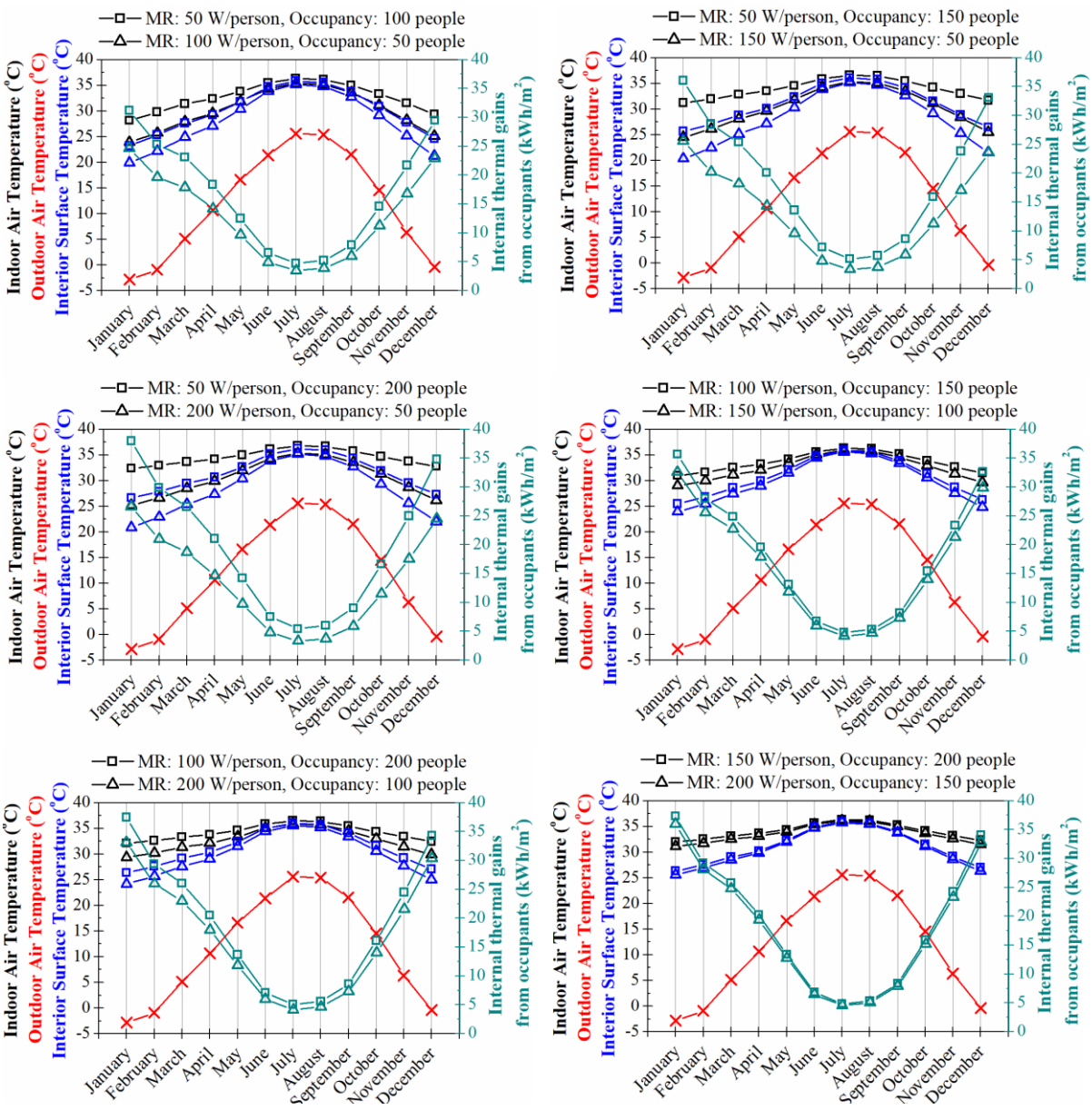


Figure 5. Monthly mean temperatures and internal thermal gains for different occupancy and MR combinations.

Conclusion

In this study, a simulation-based parametric analysis was conducted to examine the effects of different combinations of MR and occupancy on indoor air temperature, interior surface temperature, and internal thermal gains from occupants. Unlike previous studies that primarily investigated thermal effects in buildings with diverse functions, floor areas, and usage scenarios, this research specifically isolated the influence of MR and occupancy in a controlled non-ventilated building model. By systematically varying these parameters, the study provided a novel perspective on their relative impact on temperature distribution and thermal dynamics. The findings contributed to bridging the existing knowledge gap by clarifying which factor (MR or occupancy) played a more dominant role in shaping indoor thermal conditions. These insights served as a foundation for optimizing internal thermal gains and advancing energy-efficient design strategies. To eliminate external influences and isolate the thermal effects of occupants, ventilation was intentionally excluded from the simulation model. Consequently, the

humidity released by occupants accumulated over time, causing indoor relative humidity to reach saturation (100%) in all cases. Since relative humidity remained saturated and showed no variation across scenarios, it was not included in the comparative analysis.

This modeling approach is particularly relevant for temporary or transitional indoor environments where ventilation may be limited or intentionally suspended. Examples include temporary emergency shelters, high-density waiting areas (e.g., during crises or vaccination campaigns), or enclosed public spaces used for short-term occupancy, such as modular field hospitals or relief centers. In such contexts, understanding the thermal effects of occupancy and metabolic activity is critical for ensuring occupant safety, thermal resilience, and energy resource planning. By identifying the dominant role of occupant density in shaping indoor temperatures, even under conditions of constant metabolic heat, the study provides actionable insights for energy load forecasting and passive design strategies in these special-use environments.

The key findings revealed that both MR and occupancy significantly impacted indoor thermal conditions, but their effects differed depending on the scenario. While an increase in MR or occupancy generally led to higher indoor air and wall surface temperatures, the influence of MR diminished in scenarios with high occupancy. Conversely, occupancy had a stronger effect on indoor temperature dynamics, particularly due to its role in expanding the heat transfer surface area. Notably, even when total metabolic heat production was constant, scenarios with a higher number of occupants demonstrated greater internal thermal gains due to more homogeneous heat distribution. Seasonal variations played a critical role, with the impact of metabolic thermal gains being more pronounced during the winter months, thereby reducing heating demands, whereas in the summer, their influence was limited due to dominant outdoor temperatures.

In conclusion, even when total metabolic heat remained constant across different MR-occupancy scenarios, indoor conditions were influenced by factors such as heat distribution efficiency and occupant density. These findings contributed to a deeper understanding of thermal comfort modeling and building energy consumption.

In future work, it would be valuable to explore how different heating and cooling strategies, beyond traditional HVAC systems, influence the relationship between MR, occupancy, and indoor thermal conditions. Moreover, it may be beneficial to investigate the impact of smart building technologies, such as automated shading or adaptive lighting systems, on the interplay between MR, occupancy, and indoor thermal comfort. Expanding the scope of such modeling to include emergency-use scenarios and adaptive ventilation schemes may further enhance its relevance and practical applicability. This could provide insights into how responsive systems can optimize energy use while maintaining occupant comfort under varying conditions.

Ethics committee approval and conflict of interest statement

There is no need to obtain permission from the ethics committee for the article prepared.

There is no conflict of interest with any person / institution in the article prepared.

Authors' Contributions

Yüksel A.: Study conception and design, acquisition of data, analysis and interpretation of data, drafting of manuscript, and critical revision

References

[1] M. Taylor, N. C. Brown, and D. Rim, "Optimizing thermal comfort and energy use for learning environments," *Energy Build.*, vol. 248, p. 111181, 2021, doi: 10.1016/j.enbuild.2021.111181.

[2] D. Kajjoba, R. Wesonga, J. D. Lwanyaga, H. Kasedde, P. W. Olupot, and J. B. Kirabira, "Assessment of thermal comfort and its potential for energy efficiency in low-income tropical buildings: a review," *Sustain. Energy Res.*, vol. 12, no. 1, 2025, doi: 10.1186/s40807-025-00169-9.

[3] S. Bhat, "Building Thermal Comforts with Various HVAC Systems and Optimum Conditions," *Int. J. Multidiscip. Res. Sci. Eng. Technol.*, vol. 7, no. 9, 2024, doi: 10.15680/IJMRSET.2024.0709032.

[4] Z. Fang, P. Zhang, P. Wu, L. Li, and Z. Zheng, "Effects of different metabolic rates on thermal comfort in a warmer thermal environment," *J. Build. Eng.*, vol. 80, p. 108030, 2023, doi: 10.1016/j.jobe.2023.108030.

[5] A. B. Avci, "Machine learning-based prediction of thermal comfort: exploring building types, climate, ventilation strategies, and seasonal variations," *Build. Res. Inf.*, vol. 3218, pp. 1–18, 2025, doi: 10.1080/09613218.2025.2462932.

[6] J. Lee and Y. Ham, "Physiological sensing-driven personal thermal comfort modelling in consideration of human activity variations," *Build. Res. Inf.*, vol. 49, no. 5, pp. 512–524, 2021, doi: 10.1080/09613218.2020.1840328.

[7] J. Liu, I. W. Foged, and T. B. Moeslund, "Clothing Insulation Rate and Metabolic Rate Estimation for Individual Thermal Comfort Assessment in Real Life," *Sensors*, vol. 22, no. 2, pp. 1–20, 2022, doi: 10.3390/s22020619.

[8] L. Zhuang and K. Zhong, "An adaptive comfort equation of human heat balance: Based on physiological and thermosensory adaptations," *Build. Environ.*, vol. 277, p. 112951, 2025, doi: 10.1016/j.buildenv.2025.112951.

[9] L. Yang *et al.*, "Comparative analysis of indoor thermal environment characteristics and occupants' adaptability: Insights from ASHRAE RP-884 and the Chinese thermal comfort database," *Energy Build.*, vol. 309, p. 114033, 2024, doi: 10.1016/j.enbuild.2024.114033.

[10] J. Liu, I. W. Foged, and T. B. Moeslund, "Automatic estimation of clothing insulation rate and metabolic rate for dynamic thermal comfort assessment," *Pattern Anal. Appl.*, vol. 25, no. 3, pp. 619–634, 2022, doi: 10.1007/s10044-021-00961-5.

[11] C. Zhang, J. Li, and Y. Chen, "Improving the energy discharging performance of a latent heat storage (LHS) unit using fractal-tree-shaped fins," *Appl. Energy*, vol. 259, p. 114102, 2020, doi: 10.1016/j.apenergy.2019.114102.

[12] J. Y. Yun, E. J. Choi, M. H. Chung, K. W. Bae, and J. W. Moon, "Performance evaluation of an occupant metabolic rate estimation algorithm using activity classification and object detection models," *Build. Environ.*, vol. 252, p. 111299, 2024, doi: 10.1016/j.buildenv.2024.111299.

[13] T. Bajc, A. Kerčov, M. Gojak, M. Todorović, N. Pivac, and S. Nižetić, "A novel method for calculation of the CO_2 concentration impact on correlation between thermal comfort and human body exergy consumption," *Energy Build.*, vol. 294, no. 2, 2023, doi: 10.1016/j.enbuild.2023.113234.

[14] Y. Zhang, Z. Lin, Z. Zheng, S. Zhang, and Z. Fang, "A review of investigation of the metabolic rate effects on human thermal comfort," *Energy Build.*, vol. 315, p. 114300, 2024, doi: 10.1016/j.enbuild.2024.114300.

[15] A. Nomoto *et al.*, "Indirect calorimetry of metabolic rate in college-age Japanese subjects during various office activities," *Build. Environ.*, vol. 199, p. 107909, 2021, doi: 10.1016/j.buildenv.2021.107909.

[16] X. Jia, S. Li, Y. Zhu, Z. Du, and B. Cao, "Development of the Universal Standard Effective Temperature for evaluating thermal comfort across different metabolic rates," *Build. Environ.*, vol. 250, p. 111149, 2024, doi: 10.1016/j.buildenv.2023.111149.

[17] "ANSI/ASHRAE Standard 55-2020 : Thermal Environmental Conditions for Human Occupancy," *ASHRAE Inc.*, 2020, doi: ISSN 1041-2336.

[18] A. Čulić, S. Nižetić, P. Šolić, T. Perković, and V. Čongradac, "Smart monitoring technologies for personal thermal comfort: A review," *J. Clean. Prod.*, vol. 312, 2021, doi: 10.1016/j.jclepro.2021.127685.

[19] E. J. Choi, J. Y. Yun, Y. J. Choi, M. C. Seo, and J. W. Moon, "Impact of thermal control by real-time PMV using estimated occupants personal factors of metabolic rate and clothing insulation," *Energy Build.*, vol. 307, p. 113976, 2024, doi: 10.1016/j.enbuild.2024.113976.

[20] J. Y. Yun, E. J. Choi, M. H. Chung, T. W. Kim, and J. W. Moon, "Development and performance evaluation of an indoor thermal environment control algorithm incorporating MET estimation model with object detection," *Build. Environ.*, vol. 267, no. PA, p. 112217, 2025, doi: 10.1016/j.buildenv.2024.112217.

[21] S. Jung, J. Jeoung, M. Kong, and T. Hong, "Occupant activities and clothes detection based on semi-supervised learning for occupant-centric thermal control," *Build. Environ.*, vol. 267, no. PB, p. 112178, 2025, doi: 10.1016/j.buildenv.2024.112178.

[22] P. Zhang, D. Liao, H. Yu, and H. Qiu, "Innovative Metabolic Rate Sensing Approach for Probing Human Thermal Comfort," *ACS Biomater. Sci. Eng.*, vol. 9, no. 11, pp. 6504–6514, Nov. 2023, doi: 10.1021/acsbiomaterials.3c01029.

[23] H. Na, H. Choi, and T. Kim, "Metabolic rate estimation method using image deep learning," *Build. Simul.*, vol. 13, no. 5, pp. 1077–1093, 2020, doi: 10.1007/s12273-020-0707-1.

[24] F. Yıldırım and H. A. Pekel, "Wearable Artificial Intelligence Approach in Physical Activity: A Systematic Litearture Review," vol. 14, no. 1, pp. 8–17, 2025.

[25] H. Choi, B. Jeong, J. Lee, H. Na, K. Kang, and T. Kim, "Deep-vision-based metabolic rate and clothing insulation estimation for occupant-centric control," *Build. Environ.*, vol. 221, p. 109345, 2022, doi: 10.1016/j.buildenv.2022.109345.

[26] J. Zhang, J. Lu, W. Deng, P. Beccarelli, and I. Y. F. Lun, "Investigation of thermal comfort and preferred temperatures among rural elderly in Weihai, China: Considering metabolic rate effects," *J. Build. Eng.*, vol. 97, p. 110940, 2024, doi: 10.1016/j.jobe.2024.110940.

[27] Y. Bai, Y. Zhang, Z. Wei, and Y. Wang, "Experimental study on human comfort responses after simulated summer commutes with double transients of temperature and metabolic rate," *Build. Environ.*, vol. 221, no. 13, p. 109253, 2022, doi: 10.1016/j.buildenv.2022.109253.

[28] Y. Zhai *et al.*, "Preferred temperatures with and without air movement during moderate exercise," *Energy Build.*, vol. 207, p. 109565, 2020, doi: 10.1016/j.enbuild.2019.109565.

[29] M. Borowski, K. Zwolińska, and M. Czerwiński, "An Experimental Study of Thermal Comfort and Indoor Air Quality—A Case Study of a Hotel Building," *Energies*, vol. 15, no. 6, pp. 1–18, 2022, doi: 10.3390/en15062026.

[30] S. Ma, W. Deng, J. Lu, T. Zhou, and B. Liu, "Investigation of thermal comfort and preferred temperatures for healthcare staff in hospitals in Ningbo, China," *J. Build. Eng.*, vol. 80, no. May, p. 108029, 2023, doi: 10.1016/j.jobe.2023.108029.

[31] J. Lee, S. H. Cha, T. Hong, and C. Koo, "Empirical investigation of occupant-centric thermal comfort in hotel guestrooms," *Renew. Sustain. Energy Rev.*, vol. 189, no. PB, p. 114046, 2024, doi: 10.1016/j.rser.2023.114046.

[32] P. Niemann and G. Schmitz, "Impacts of occupancy on energy demand and thermal comfort for a large-sized administration building," *Build. Environ.*, vol. 182, no. March, p. 107027, 2020, doi: 10.1016/j.buildenv.2020.107027.

[33] P. Aparicio-Ruiz, E. Barbadilla-Martín, J. Guadix, and J. Muñuzuri, "A field study on adaptive thermal comfort in Spanish primary classrooms during summer season," *Build. Environ.*, vol. 203, 2021, doi: 10.1016/j.buildenv.2021.108089.

[34] S. Kumar, M. K. Singh, A. Mathur, and M. Košir, "Occupant's thermal comfort expectations in naturally ventilated engineering workshop building: A case study at high metabolic rates," *Energy Build.*, vol. 217, 2020, doi: 10.1016/j.enbuild.2020.109970.

[35] L. Yang, S. Zhao, S. Gao, H. Zhang, E. Arens, and Y. Zhai, "Gender differences in metabolic rates and thermal comfort in sedentary young males and females at various temperatures," *Energy Build.*, vol. 251, p. 111360, 2021, doi: 10.1016/j.enbuild.2021.111360.

[36] I. Reda, R. N. AbdelMessih, M. Steit, and E. M. Mina, "Experimental assessment of thermal comfort and indoor air quality in worship places: The influence of occupancy level and period," *Int. J. Therm. Sci.*, vol. 179, no. May, p. 107686, 2022, doi: 10.1016/j.ijthermalsci.2022.107686.

[37] Y. Zhang, X. Zhou, Z. Zheng, M. O. Oladokun, and Z. Fang, "Experimental investigation into the effects of different metabolic rates of body movement on thermal comfort," *Build. Environ.*, vol. 168, no. 106489, 2020, doi: 10.1016/j.buildenv.2019.106489.

[38] Britannica, "https://www.britannica.com/science/Koppen-climate-classification (accessed March 22, 2022)," 2022. https://www.britannica.com/science/Koppen-climate-classification (accessed Mar. 22, 2022).

[39] "TS 825:2024 Turkish Standard: Thermal Insulation Requirements for Buildings," 2024.

[40] H. Baş and T. Kazanasmaz, "Hybrid-Model Simulations to Equilibrate Energy Demand and Daylight Autonomy as a Function of Window-to-Wall Ratio and Orientation For a Perimeter Office in Izmir," *MEGARON / Yıldız Tech. Univ. Fac. Archit. E-Journal*, vol. 15, no. 4, pp. 537–552, 2020, doi: 10.14744/megaron.2020.42223.

[41] S. Hammerling, "2023-2024: ASHRAE Research Report," *ASHRAE J.*, vol. 66, no. 10, 2024.

[42] L. G. Ioannou *et al.*, "Occupational heat strain in outdoor workers: A comprehensive review and meta-analysis," *Temperature*, vol. 9, no. 1, pp. 67–102, 2022, doi: 10.1080/23328940.2022.2030634.

[43] A. Alonso, J. Llanos, R. Escandón, and J. J. Sendra, "Effects of the Covid-19 pandemic on indoor air quality and thermal comfort of primary schools in winter in a mediterranean climate," *Sustainability*, vol. 13, no. 5, pp. 1–17, 2021, doi: 10.3390/su13052699.

[44] N. Netam, S. Sanyal, and S. Bhowmick, "A Mathematical Model Featuring Time Lag and Decrement Factor to Assess Indoor Thermal Conditions in Low-income-group House," *J. Therm. Eng.*, vol. 6, no. 2, pp. 114–127, 2020, doi: 10.18186/THERMAL.728054.

[45] A. Calvaresi, M. Arnesano, F. Pietroni, and G. M. Revel, "Measuring metabolic rate to improve comfort management in buildings," *Environ. Eng. Manag. J.*, vol. 17, no. 10, pp. 2287–2296, 2018, doi: 10.30638/eemj.2018.227.

[46] A. Yüksel, M. Arıcı, M. Krajčík, M. Civan, and H. Karabay, "Developing a Strategy to Reduce Energy Consumption and CO_2 Emissions from Underfloor Heating Systems in Mosques: A Case Study of a Typical Neighbourhood Mosque," *Energy Build.*, p. 112984, 2023, doi: 10.1016/j.enbuild.2023.112984.

Dicle University
Journal of Engineering
https://dergipark.org.tr/tr/pub/dumf
duje.dicle.edu.tr

Research Article

Determination of the Effects of Structural Design Parameters on Dynamic Characteristics of Centrifugal Pump Systems

Murat ŞEN[1*]

[1] Fırat University, Engineering Faculty, Mechanical Engineering, msen@firat.edu.tr, Orcid No: 0000-0002-3063-5635

ARTICLE INFO

Article history:

Received 17 June 2025
Received in revised form 29 June 2025
Accepted 7 July 2025
Available online 30 September 2025

Keywords:

Campbell Diagram, Centrifugal Pump, Critical Speed, Modal Analysis, Rotordynamic Analysis

Doi: 10.24012/dumf.1721157

* Corresponding author

ABSTRACT

Pump systems are critical in engineering, and their design demands extensive calculations to achieve safety and efficiency. These dynamic systems, with components like shafts, impellers, and bearings, are exposed to various dynamic effects. Therefore, understanding how a pump's dynamic characteristics evolve during the design phase is crucial for ensuring safe, high-performance operation. In this study, modal analysis and rotordynamic analysis were performed on a rotor system, consisting of the shaft, impeller, and bearings of a centrifugal pump system. A numerical model of this system was created using MATLAB. The moving rotor of the centrifugal pump was modeled using the Euler-Bernoulli beam theory. The impeller was represented as an equivalent disk after creating its 3D solid model, taking into account its polar and diametric moments of inertia. The ball bearings supporting the rotor were modeled using linear spring and damping elements. Presented study investigates how the natural frequencies and critical speeds of the rotor system changed for different distances between the two ball bearings used for shaft support and for various bearing stiffness values. Additionally, the presence of anti-resonance frequencies in the transfer frequency response functions between the impeller and the bearings was identified, and their variations with parameter changes were analyzed. The conducted parameter variations revealed that the natural frequencies and critical speeds changed significantly, and these changes exhibited different tendencies depending on the mode shapes. The results demonstrate that constructional design parameters in pump system rotors significantly influence the system's dynamic characteristics.

Introduction

Rotor systems are designed to operate at certain rotation speeds. Dimensions of rotor systems, material properties, and design of bearing and support systems are made according to many engineering calculations. One of the most important issues to consider in rotor systems is the calculation of natural frequencies and critical rotation speeds of the rotors. Physical and mechanical properties of rotor systems, bearing conditions and operating conditions are the features that affect natural frequencies and critical speeds. The operating speeds of the rotors should be determined to be far from critical speeds. A rotor system has many critical speeds, and when any of these critical speeds is exceeded, operating conditions in this region can be considered safe until it approaches the other critical speed value. However, it is desired that the rotor exceeds critical speeds as quickly as possible and moves away from this danger zone. If possible, critical speeds should be moved as far away from the operating speed region as possible.

It is seen that rotating rotors are used in many mechanical systems in engineering applications. One of these is pump systems that enable water transfer from an area at a lower altitude to an area at a higher altitude. Although there are many types of pumps used for this purpose, all pump systems have rotating rotor elements and impellers. Therefore, it is of great importance to consider natural frequencies and critical speeds during the design phase of pumps and to take the necessary precautions at this stage. The length and diameter of the pump rotor, distances between bearings and the type of bearings used have very important effects on these features. Designers and researchers carry out many studies in this context. Huang et al. [1], have studied the rotor blade modes of the turbomolecular pump. They modeled the rotor blades with a simpler equivalent approach based on the basic invariance principle of mass and moment of inertia, and demonstrated the accuracy of this approach with experimental modal analyzes on a real pump system. Minette et al. [2], used the experimental modal analysis method to determine the natural frequency and damping parameters of an electric submersible pump installed in a test well. They used the single-input, multiple-output (SIMO) technique in their modal analysis studies. The results obtained showed that the submersible pump examined had resonance frequencies in the operational operating frequency region between 30 and 62 Hz. In such cases, resonance frequency zones in the operating range should be crossed as quickly as possible, or structural modifications can be made in the system under appropriate conditions.

In some cases, reduction of resonance frequencies or structural modifications can be desired in design studies of pumps. Mohamed and Azmir [4] carried out design modification studies to reduce the natural frequencies of a water purification pump. For this purpose, they made analyzes by making material modifications in the pump system they modeled numerically and placing flexible bearing elements under the pump body, and examined the effects of these modifications on the resonance frequencies. Ashri et al. [3] carried out numerical modal analysis studies to see the effects of the number of blades and impeller disc thickness of the centrifugal pump impeller on the natural frequency and vibration mode shapes. They determined that the increase in the number of blades of the pump impeller and the increase in the impeller disc thickness had an increasing effect on the natural frequencies. In another study, Wang et al. [17] carried out studies to determine the optimum values of the pump impeller's outlet diameter, outlet width, vane angle, number of windings and number of vanes in order to reduce vibration effects and to increase the performance of centrifugal pumps. Rad [11] examined the effects of disc thickness, blade thickness and blade profiles on the dynamic properties of a radial flow impeller with numerical and experimental modal analysis. In [12], machine learning techniques were used to increase the stability and performance of pump impellers. Efforts have been made to increase resonance safety margins and minimize wing mode deformations. Al-Obaidi and Alhamid [16], conducted numerical and experimental investigations into how transient flow conditions affect pressure pulsation phenomena in axial flow pumps. Their study specifically examined the pressure pulsation characteristics and the impeller flow field under varying flow rates and blade angles. They observed that as the flow rate decreased, pump stability diminished, leading to increased pressure pulsations.

Construction parameters and flow dynamic interactions in pump systems have significant effects on the dynamic characteristics of the system. Egusquiza et al. [15] studied experimentally and numerically the dynamic behavior of the impeller of a large pump-turbine unit. They obtained the natural frequencies and mode shapes of the impeller. In order to see the effect of the rotor and supporting structures on the dynamic behavior of the impeller, they analyzed the impeller separately. D'Addio et al. [6] performed numerical dynamic analyzes of a small-sized centrifugal pump used in automotive applications. They determined that a finite element (FE) model with a flexible shaft, concentrated masses and elastic supports made it possible to determine a more meaningful Campbell diagram and harmonic response in a relatively short time. In another study, Yong et al. [7] analyzed the natural vibration frequencies of the impeller of a horizontal flow pump in water by considering the fluid-rotor structure interaction. They determined that the natural frequencies decreased due to the water environment and the damping distribution of the water mass led to the reduction of the amplitude of the impeller in water.

In pump shaft-impeller systems, various necessary analyses can be conducted through modal tests on the actual system. Based on the obtained analysis results, essential measures can be taken or certain modifications can be implemented on the real system. For instance, Baginski et al. [5] investigated the dynamic behaviors of a vertical motor cooling compressor using experimental modal analysis and forced vibration tests. They observed the critical speeds of the rotor and the vibration amplitudes within the critical operating range. A similar study was performed for a centrifugal pump by Oza and Shah [8].

In addition, numerical methods are also used for rotor dynamics and modal analysis of many pump systems. The dynamic characteristics of pump systems with numerical models can be determined by analyzing them with numerical methods. In addition, the created numerical models can be actively used to meet the requirements such as model updating of pump systems. Briend et al. [10] performed dynamic analysis studies on a model of a vehicle rotor mounted on hydrodynamic bearings using the Timoshenko beam model. White et al. [14] performed linear and nonlinear analyses of a multistage vertical pump. They characterized the bearings in the rotor system by their stiffness and damping coefficients. In [9], stress analysis and modal analysis of a screw centrifugal pump were carried out numerically and the pressure distribution on the impeller blades and changes in natural frequencies were investigated. Guo and Du [13] investigated the dynamic characteristics of the gear pump by performing numerical modal analysis of its components and the entire structure.

In this study, FE model of a centrifugal pump was developed using MATLAB to perform dynamic analyses. The moving rotor of the centrifugal pump was modeled using the Euler-Bernoulli beam theory. The impeller was represented as an equivalent disk after creating its 3D solid model, taking into account its polar and diametric moments of inertia. The ball bearings supporting the rotor were modeled using linear spring and damping elements.

The presented research investigated how changes in distances between bearings and variations in bearing stiffness, defined as design parameters, affected the resonance frequencies and critical speeds of the pump system. Frequency Response Functions (FRFs) were calculated and plotted between selected coordinates of the rotor-impeller system to illustrate resonance peaks. Rotor critical speeds were calculated and presented using Campbell Diagrams. Additionally, the presence of anti-resonances in the transfer FRFs between bearing coordinates and the impeller was examined.

Methodology

The shaft of the pump system was modelled using the Euler Bernoulli approach. One of the Euler-Bernoulli beam element is given with Figure 1.

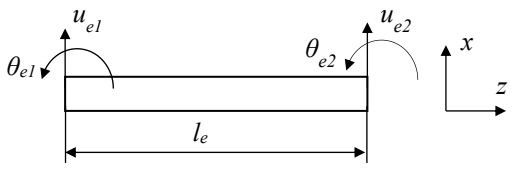


Figure 1. The coordinates of the Euler-Bernoulli beam element on *x-z* plane

In Figure 1, u_{e1} and u_{e2} represent the translational coordinates in *x-z* plane, θ_{e1} and θ_{e2} are the rotational coordinates about *y* axis and the coordinates of each element of the shaft can be written as follows:

$$\{q_e\} = \{u_{e1}, \theta_{e1}, u_{e2}, \theta_{e2}\}^T \tag{1}$$

Each node in the shaft element has 2 degrees of freedom (DoF), while each beam element possesses a total of 4 DoFs. The corresponding element-based stiffness and mass matrices are provided below.

Stiffness matrix of the beam element:

$$[k_s]^{(i)} = \begin{bmatrix} k_{11}^{(i)} & k_{12}^{(i)} & k_{13}^{(i)} & k_{14}^{(i)} \\ k_{21}^{(i)} & k_{22}^{(i)} & k_{23}^{(i)} & k_{24}^{(i)} \\ k_{31}^{(i)} & k_{32}^{(i)} & k_{33}^{(i)} & k_{34}^{(i)} \\ k_{41}^{(i)} & k_{42}^{(i)} & k_{43}^{(i)} & k_{44}^{(i)} \end{bmatrix} \tag{2}$$

$$= \frac{E_i I_i}{l_i^3} \begin{bmatrix} 12 & 6l_i & -12 & 6l_i \\ 6l & 4l_i^2 & -6l_i & 2l_i^2 \\ -12 & -6l_i & 12 & -6l_i \\ 6l_i & 2l_i^2 & -6l_i & 4l_i^2 \end{bmatrix} \quad (i = 1, 2, \ldots, n)$$

Where, E_i, I_i and l_i are the modulus of elasticity, moment of inertia and the length of the beam elements respectively and $[k_s]_{(i)}$ represents the stiffness matrix.

Mass matrix of the beam element:

$$[m_s]^{(i)} = \begin{bmatrix} m_{11}^{(i)} & m_{12}^{(i)} & m_{13}^{(i)} & m_{14}^{(i)} \\ m_{21}^{(i)} & m_{22}^{(i)} & m_{23}^{(i)} & m_{24}^{(i)} \\ m_{31}^{(i)} & m_{32}^{(i)} & m_{33}^{(i)} & m_{34}^{(i)} \\ m_{41}^{(i)} & m_{42}^{(i)} & m_{43}^{(i)} & m_{44}^{(i)} \end{bmatrix} \tag{3}$$

$$= \frac{\rho_i A_i l_i}{420} \begin{bmatrix} 156 & 22l_i & 54 & -13l_i \\ 22l_i & 4l_i^2 & 13l_i & -3l_i^2 \\ 54 & 13l_i & 156 & -22l_i \\ -13l_i & -3l_i^2 & -22l_i & 4l_i^2 \end{bmatrix} \quad (i = 1, 2, \ldots, n)$$

Where, ρ_i, A_i and $[m_s]_{(i)}$ are the mass density, cross-section area and the mass matrix of the beam element. The shaft to be modelled is given in Figure 2.

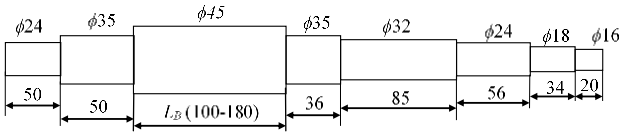


Figure 2. The shaft model of the pump system

In the rotor FE model, the shaft is divided into 8 segments with different diameters and lengths and 9 nodes are created.

For a single disk representing the impeller, its mass matrix can be formulated to account for both its mass and its diametral mass moments of inertia. This matrix captures the contributions from the translational and rotational coordinates at the specific node where the disk is connected within the rotor system.

$$[m_d] = \begin{bmatrix} m_d & 0 \\ 0 & I_d \end{bmatrix} \tag{4}$$

The mass of the disk m_d corresponds to the translational coordinate, while the mass moment of inertia I_d corresponds to the rotational coordinate and these values can be obtained as follows:

The disk's mass (m_d) is assigned to the translational coordinate, and its mass moment of inertia (I_d) corresponds to the rotational coordinate. These values are determined as follows:

$$m_d = \frac{\rho_d \pi \left(D_d^{\,2} - D_s^{\,2}\right) t_d}{4} \tag{5}$$

$$I_d = \frac{\rho_d \pi \left(D_d^{\,4} - D_s^{\,4}\right) t_d}{64} + \frac{\rho_d \pi \left(D_d^{\,2} - D_s^{\,2}\right) t_d^{\,3}}{48} \tag{6}$$

In Equations 5 and 6, ρ_d, D_d, D_s and t_d represent the mass density, the outer diameter, the inner diameter and the thickness of the disk, respectively.

After obtaining the matrices of all the elements in the shaft-impeller system, the general stiffness and mass matrices of the system can be created as given with Figure 3.

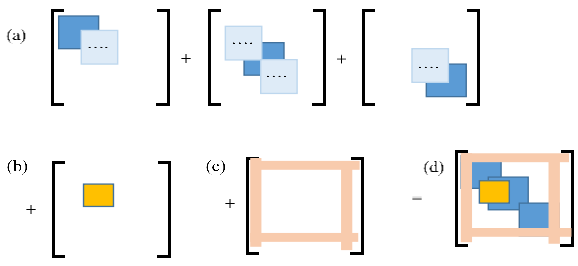


Figure 3. The matrices of the rotor system; (a) shaft, (b) disk (impeller), (c) bearings (constraints), (d) the overall system [18]

In Figure 3 (c), the illustrated section represents the constraints imposed by the bearings. Depending on the bearing type, either translational or rotational coordinates can be restricted to establish pinned or fixed boundary conditions.

However, in this study's rotor model, boundary conditions were not directly applied at the bearing coordinates. Instead, the bearings were modeled using grounded spring and damping elements. This approach, dictated by the construction's requirements, allows for a more realistic solution by incorporating the effects of these bearings into the system in this manner. Furthermore, if desired, pinned or fixed boundary conditions can still be achieved by modeling the bearings with very high spring stiffness values (Figure 4).

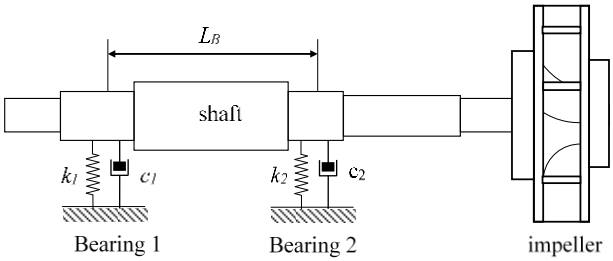


Figure 4. Shaft, impeller, bearing system

After the global mass and the stiffness matrices of the entire system are created, the equation of motion of the system can be written as follows:

$$[M]\{\ddot{q}\}+[C]\{\dot{q}\}+\Omega[G]\{\dot{q}\}+[K]\{q\}=\{f\} \qquad (7)$$

By using Equation 7 and with the eigenvalue solution, the dynamic analysis can be made for the rotor system numerically.

The 3D model of the designed pump system, including all its components, is presented as an assembled view in Figure 5 below.

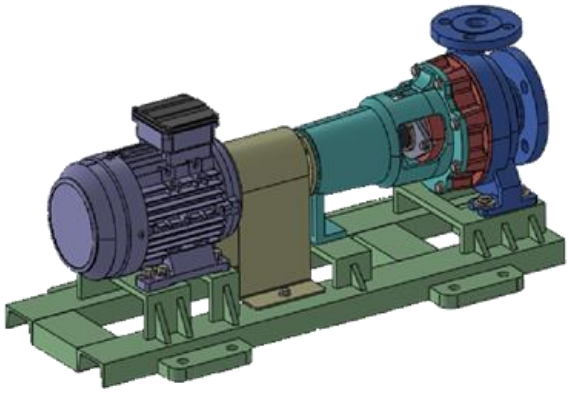


Figure 5. 3D assembly of the pump system

Typically, in such systems, the base chassis supporting the entire system also influences its dynamic characteristics. The rigidity of the areas where the electric motor, pump housing, and bearing unit casing are connected, along with the screwing and assembly techniques, directly affect the system's vibration characteristics. However, the focus of this study is the pump system's rotor group, specifically the subsystem composed of the shaft, impeller, and bearings (Figure 6).

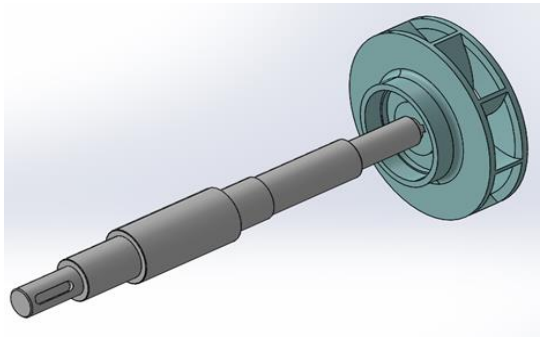


Figure 6. Shaft-impeller system of the centrifuge pump

The mechanical properties of the shaft and the impeller are given in Table 1.

Table 1. Mechanical properties of the system

Property	Shaft	Impeller
Modulus of Elasticity (GPa)	205	200
Mass Density (kg/m^3)	7850	7800
Polar Mass Moment of Inertia (kg-m^2)	5.74x 10^{-3}	0.49 x 10^{-3}
Diametral Mass Moment of Inertia (kg-m^2)	3.63x 10^{-3}	27.13 x 10^{-3}

Equation 8 was used to calculate FRFs numerically.

$$\alpha_{pq}(\omega)=\sum_{r=1}^{N}\frac{\phi_{pr}\phi_{qr}}{\left(k_r-\omega^2 m_r\right)+i\eta_r k_r} \qquad (8)$$

Here ϕ_{pr} and ϕ_{qr} are the elements of the r^{th} mode shape vector at coordinates p and q, k_r, m_r and η_r are the modal stiffness, modal mass and modal damping ratio of the r^{th} mode, respectively. ω represents the circular frequency in rad/s.

Simulation Studies

The simulation studies consist of three stages. In the first stage, the natural frequency values and critical speeds of the system were examined for different values of the distance between the bearings for which the bearing springs were modeled with equal and constant (5x10^6 N/m).

In the second stage, in the case where the distance between the bearings was constant (140 mm), how changing the stiffness of the identical bearings affected the natural

frequency values and critical speeds of the system were examined.

In the third stage, the anti-resonance frequencies in the transfer FRFs between the coordinate of the impeller and the coordinate of each shaft bearing were determined. In this way, the frequency values of the shaft bearings that will not be affected by the imbalances that may occur in the pump impeller are determined. This feature can be used in the design phase of many rotor systems in order to solve vibration problems.

For the first stage of simulations, the bearing stiffness values were $5x10^6$ N/m and identical for both bearings. For different distance between the bearings, the calculated resonance frequencies for the first 5 bending vibration mode shapes are given in Table 2.

Table 2. Natural frequencies of the shaft, impeller, bearing system for different bearing distances

L_B (mm)	Natural Frequencies (Hz)				
	Modes				
	1	2	3	4	5
100	15.09	187.13	498.41	895.66	1503.40
120	16.97	195.88	521.96	863.65	1520.99
140	18.77	204.32	540.32	838.38	1536.94
160	20.57	212.57	548.98	825.95	1542.52
180	22.44	220.69	544.74	829.52	1534.96

For the distance 140 mm, one point and one transfer FRF are given with Figure 7.

In Figure 7, the upward peaks represent the natural frequencies and the downward peaks represent the anti-resonance frequencies. Since natural frequencies are a global property of the system, they appear in all FRFs. However, since anti-resonance frequencies are a local property of the system, they may appear in some FRFs but not in others. Due to the property of point FRFs, an anti-resonance frequency appears after each natural frequency in point FRFs.

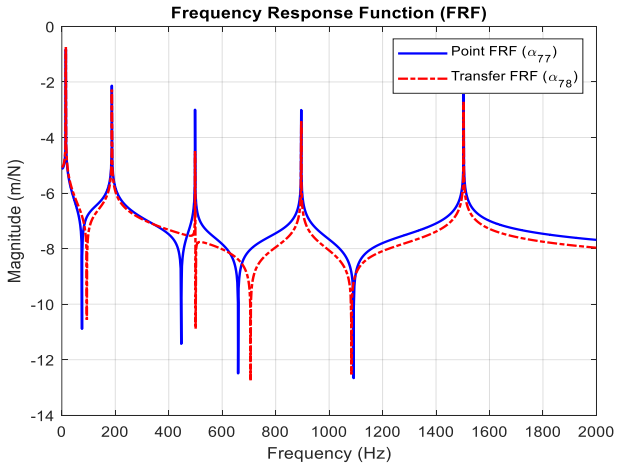


Figure 7. Point and transfer FRF samples of the system for 140 mm distance between the bearings.

For one of the simulations in Table 1, the mode shapes were obtained as given in Figure 8.

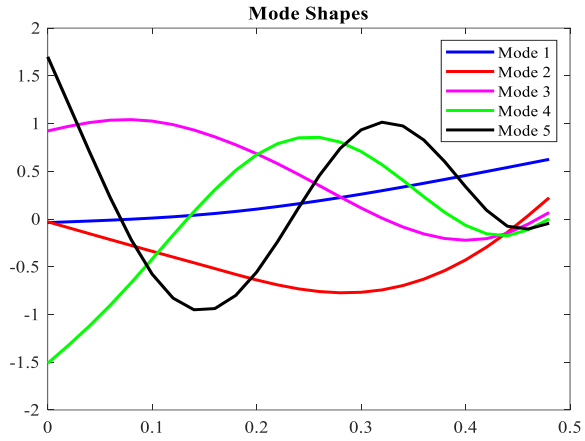


Figure 8. Mode shapes of the shaft, impeller, bearing rotor system of the pump for 140 mm bearing distance

The mode shapes illustrated in Figure 8, can differ for different configurations.

In rotor dynamics analysis, with the rotation of shaft influences the stiffness of the rotor and affects the natural frequencies. This situation can be analyzed using Campbell diagrams which indicate speed dependent damped natural frequencies and the critical speeds. The critical speeds were obtained for all simulations for the first stage of simulations. The obtained critical speed values are given in Table 3 and one of the Campbell diagram for 140 mm bearing distance is given with Figure 9. The operating speed of the designed pump was determined as 2900 rpm. Therefore, when calculating the rotor critical speeds and drawing Campbell diagrams, the speed range of 0-5000 rpm was examined. However, it should be noted that in some special pump systems, speeds can even exceed 10000 rpm. In such cases, a wider speed range should be examined.

Table 3. Critical speeds of the shaft, impeller, bearing system for different bearing distances

L_B (mm)	Critical Speeds (rpm)				
	1	2	3	4	5
100	956	978	-	-	-
120	1090	1118	-	-	-
140	1216	1252	-	-	-
160	1340	1384	-	-	-
180	1464	1520	-	-	-

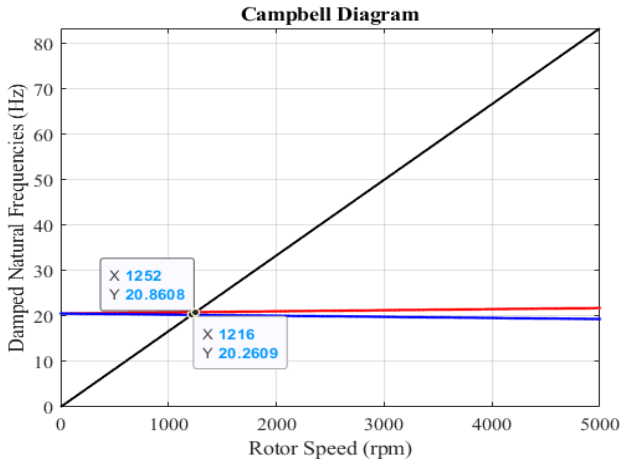


Figure 9. Campbell diagram of the system for 140 mm distance between the bearings.

In the second stage of simulations, for 140 mm distance between the bearings, the natural frequencies of different bearing stiffness values were calculated and the obtained values are given in Table 4.

Table 4. Natural frequencies of the shaft-impeller system for different bearing stiffness

Bearing Stiffness (N/m)	Natural Frequencies (Hz) Modes				
	1	2	3	4	5
$2x10^6$	15.39	184.57	414.16	667.88	1411.96
$4x10^6$	18.05	199.83	508.29	789.03	1495.84
$6x10^6$	19.30	207.77	567.15	881.79	1576.71
$8x10^6$	20.03	212.73	610.34	955.51	1650.84
$10x10^6$	20.50	216.14	643.88	1017.44	1716.58

One point and one transfer FRF are given with Figure 10 for $6x10^6$ N/m bearing stiffness.

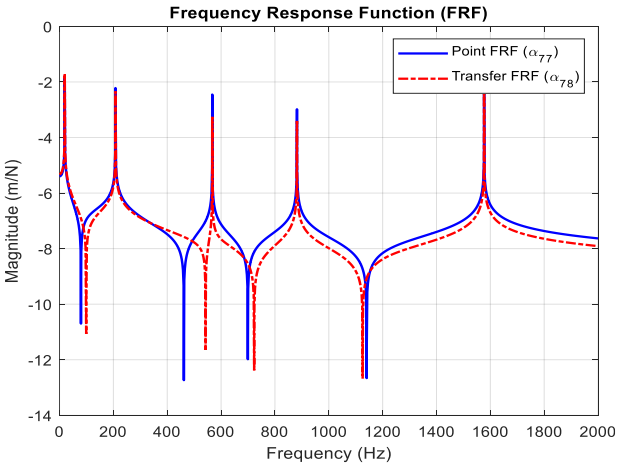


Figure 10. Point and transfer FRF samples of the system for $6x10^6$ N/m bearing stiffness.

The calculated critical speeds are tabulated in Table 5 and one of the Campbell diagrams, for $6x10^6$ N/m bearing stiffness, is illustrated with Figure 11.

Table 5. Critical Speeds of the shaft-impeller system for different bearing stiffness

Bearing Stiffness (N/m)	Critical Speeds (rpm)				
	1	2	3	4	5
$2x10^6$	950	972	-	-	-
$4x10^6$	1156	1188	-	-	-
$6x10^6$	1260	1300	-	-	-
$8x10^6$	1326	1370	-	-	-
$10x10^6$	1370	1416	-	-	-

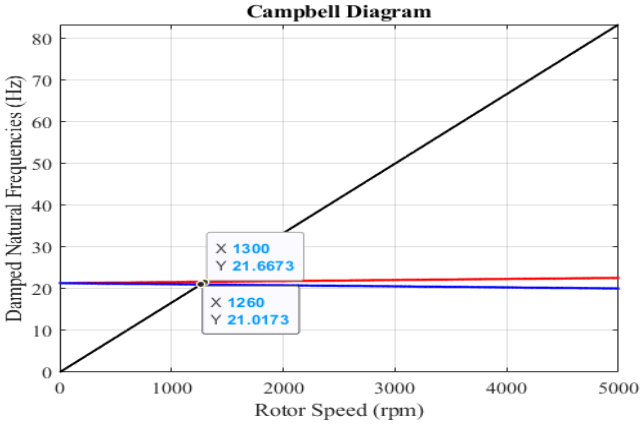


Figure 11. Campbell diagram of the system for $6x10^6$ N/m bearing stiffness.

For the third stage of the simulations, anti-resonance frequencies were investigated.

In a rotor system comprising a shaft, impeller, and bearings, the presence of anti-resonance frequencies can be crucial for enhancing the system's dynamic stability and efficiency. These frequencies provide insights into whether harmonic forces arising from imbalances are transmitted to the bearings. If an anti-resonance frequency exists in the transfer FRF between two coordinates in a mechanical system, one coordinate remains stationary despite the harmonic force excitation occurring at the other. This phenomenon can serve as a solution for many vibration problems. Consequently, in the third stage of this study, the existence of anti-resonance frequencies in the transfer FRFs between the impeller coordinate, which has a high potential for generating harmonic forces due to imbalances, and the bearing coordinates, which are the most vulnerable components in the system, was investigated in detail.

Calculated anti-resonance frequencies are presented in Table 6-9 for the coordinates between the impeller and the bearings. Specifically, these frequencies are provided for Bearing 1 (FRF: $\alpha_{3,9}$) and Bearing 2 (FRF: $\alpha_{4,9}$), considering various distances between the bearings and different bearing stiffnesses, respectively.

Table 6. Anti-resonance frequencies of the shaft-impeller system for different bearing distances for $\alpha_{3,9}$

L_B (mm)	Anti-resonance Frequencies (Hz)				
	Modes				
	1	2	3	4	5
100	-	358.22	862.88	-	-
120	-	347.16	859.89	-	-
140	-	328.65	-	859.26	-
160	-	307.92	-	861.48	-
180	-	288.33	-	866.82	-

Table 7. Anti-resonance frequencies of the shaft-impeller system for different bearing stiffness $\alpha_{3,9}$

Bearing Stiffness (N/m)	Anti-resonance Frequencies (Hz)				
	Modes				
	1	2	3	4	5
$2x10^6$	271.71	-	-	851.65	-
$4x10^6$	-	276.76	-	856.45	-
$6x10^6$	-	380.15	862.38	-	-
$8x10^6$	-	479.27	869.69	-	-
$10x10^6$	-	568.98	878.90	-	-

Table 8. Anti-resonance frequencies of the shaft-impeller system for different bearing distances $\alpha_{4,9}$

L_B (mm)	Anti-resonance Frequencies (Hz)				
	Modes				
	1	2	3	4	5
100	-	-	860.27	1198.68	-
120	-	-	859.82	1047.25	-
140	-	-	-	855.62 960.10	-
160	-	-	-	834.79 917.96	-
180	-	-	-	796.87 907.46	-

Table 9. Anti-resonance frequencies of the shaft-impeller system for different bearing stiffness $\alpha_{4,9}$

Bearing Stiffness (N/m)	Anti-resonance Frequencies (Hz)				
	Modes				
	1	2	4	4	5
$2x10^6$	-	-	657.48	883.96	-
$4x10^6$	-	-	-	827.86 911.20	-
$6x10^6$	-	-	863.81	1018.98	-
$8x10^6$	-	-	868.84	1127.10	-
$10x10^6$	-	-	870.71	1218.26	-

After the anti-resonance frequencies were calculated, as presented in Table 6-9, these computed values were populated into the relevant sections of the tables based on the natural frequencies of the total five bending modes. For instance, an anti-resonance frequency calculated to be between the first and second natural frequencies was placed in the cell corresponding to the first mode. In some cases, more than one anti-resonance frequency was calculated between two natural frequencies, and these were all entered into the cells under the same mode number in the tables.

Conclusions

In this study, the dynamic properties of the rotor system consisting of shaft, impeller and bearings of a centrifugal pump under different design parameters were investigated. The design parameters in the study were selected entirely in a constructional sense.

This study investigates the influence of the distance between two identical ball bearings and different stiffness values for constant distance, on the natural frequencies and critical speeds of the system. Additionally, anti-resonance frequencies observed in the transfer FRFs between the impeller and each of the two bearings were calculated. The significant outcomes derived from the three-stage simulation studies are as follows:

1. In the initial simulation stage, dynamic analyses were performed on a system utilizing identical bearings, each with a stiffness of $5x10^6$ N/m. The distance between these two bearings was progressively increased by 20 mm increments, from 100 mm to 180 mm (i.e., 100, 120, 140, 160, and 180 mm). The resulting natural frequencies were then compiled.

   It was observed that, generally, increasing the distance between the bearings led to an increase in natural frequency values, with the exception of mode 4. The most significant increase, at 23.75%, was noted in mode 1, while the smallest increase, 2.05%, occurred in mode 5. A different trend was observed for mode 4, where increasing bearing distances resulted in a decrease in natural frequencies, calculated at -7.97%. This inverse relationship could potentially be attributed to the specific positioning of the bearings at those distances and their corresponding zero points.

   Assuming that the pump shaft rotates at 2900 rpm, critical speeds between 0-5000 rpm were calculated and two critical speed values were determined in each simulation. It is seen that the critical speed values increase with the increase in the distance between the bearings. This increase was calculated as 34.69% in the first critical speed and 35.65% in the second critical speed.

2. In the second simulation stage, with the bearing distance held constant at 140 mm, the system's natural frequencies were calculated and listed for varying bearing stiffnesses of (2, 4, 6, 8, and 10)$x10^6$ N/m. A consistent trend was observed across all modes: as bearing stiffness increased, the natural frequency values also tended to rise. The most significant increase, at 35.67%, was found in mode 3, while the smallest increase, 14.57%, occurred in mode 2

   Additionally, two critical speed values were identified in these simulations. As bearing stiffness values increased, the critical speeds also demonstrated an

upward trend. This increase was calculated to be 30.65% for the first critical speed and 31.35% for the second critical speed.

3. In the third simulation stage, anti-resonance frequencies were investigated. The existence of anti-resonances in the transfer FRFs between the impeller and the bearings and how they are influenced by the change of the distance between the bearings and the change of the bearing stiffness values were investigated.

   In the transfer FRF ($\alpha_{3,9}$) between the impeller and the far-side bearing (the one distant from the impeller), no anti-resonance was observed following the natural frequency of the first mode. However, for the second mode, an anti-resonance was consistently present after the natural frequency across all investigated bearing distances. Furthermore, the frequency values of these anti-resonances increased as the distance between the bearings expanded. After the natural frequencies of the other modes, anti-resonances were observed in some simulations but not in others.

   As bearing stiffness values increased, a corresponding increase in the values of the observed anti-resonance frequencies was noted. It was also observed that while anti-resonances appeared after the resonance frequencies in some modes during certain simulations, they were not identified in others. The absence of an anti-resonance after the natural frequency in Mode 5 is considered normal, as the frequency response curve typically terminates in this region.

4. In the transfer FRF ($\alpha_{4,9}$) between the impeller and the central bearing (the one closer to the impeller), no anti-resonance was found following the natural frequencies of the first and second modes. However, after the natural frequency of mode 4, two anti-resonances were consistently observed across different bearing distances. Notably, as the distance between the bearings increased, the frequency values of these anti-resonances decreased. For the natural frequencies of other modes, anti-resonances were present in some simulations but absent in others.

   With an increase in bearing stiffness values, the anti-resonance frequencies observed also showed an increase. Similar to the previous findings, anti-resonances were sometimes visible after the resonance frequencies in certain modes during simulations, but not always identified in others.

In conclusion, this study demonstrates that bearing distance and bearing stiffness values can be effectively utilized as design parameters to enhance the efficiency and performance of pump systems. These parameters were found to directly and significantly influence the system's dynamic behavior. Furthermore, it was emphasized that anti-resonance frequencies are similarly affected by these parameters and can also be leveraged during the design phase of pump systems.

Ethics committee approval and conflict of interest statement

There is no conflict of interest with any person / institution in the article prepared.

Authors' Contributions

The author confirms sole responsibility for the following: Study conception and design, acquisition of data, analysis and interpretation of data, drafting of manuscript, critical revision.

References

[1] Z. Huang, B. Han, and Y. Le, "Modeling method of the modal analysis for turbomolecular pump rotor blades", Vacuum, vol. 144, pp. 145-151, 2017.

[2] R.S. Minette, S.F. SilvaNeto, L.A. Vaz, and U.A. Monteiro, "Experimental modal analysis of electrical submersible pumps", Ocean Engineering, vol. 124, pp. 168–179, 2016.

[3] M. Ashri, S. Karuppanan, S. Patil, and I. Ibrahim, "Modal Analysis of a Centrifugal Pump Impeller Using Finite Element Method", MATEC Web of Conferences, 13, 0403 0 (2014).

[4] M.F.B. Fasal Mohamed, and N.A.B. Azmir, "Study on behavior of water treatment pump before and after modification using finite element modal analysis", IOP Conf. Series: Materials Science and Engineering824 (2020) 012004.

[5] P. Bagiński, A. Andrearczyk, P. Ziółkowski, "Investigation of the dynamic behaviour of the vertical rotor of a refrigeration compressor supported by foil bearings", Renewable Energy 253 (2025) 123505.

[6] V. D'Addio, P. Forte, F. Frendo, and R. Squarcini, "Rotordynamic analysis of a centrifugal pump for automotive applications", Procedia Structural Integrity 24 (2019) 510–525.

[7] S. Yong, W. Donglei, J. Tao1, and L. Yanwei, "Modal Analysis on Impeller Rotor of the Axial Flow Pump based on Fluid-structure Interaction", IOP Conf. Series: Earth and Environmental Science 376 (2019) 012023.

[8] M.N. Oza, D.S. Shah, "Theoretical and experimental modal analysis of centrifugal pump radial flow impeller", IOP Conf. Series: Materials Science and Engineering 992 (2020) 012003 IOP Publishing, doi:10.1088/1757-899X/992/1/012003.

[9] S.Q. Yuan, T. Li, J.P. Yuan, and J.J. Zhou, "Static stress and modal analysis on the impeller of screw centrifugal pump", IOP Conf. Series: Earth and

Environmental Science, 15 (2012), 052013doi:10.1088/1755-1315/15/5/052013.

[10] Y. Briend, M. Dakel, E. Chatelet, M. Andrianoely, R. Dufour, and S. Baudin, "Effect of multi-frequency parametric excitations on the dynamics of on-board rotor-bearing systems" Mechanism and Machine Theory 145 (2020) 103660.

[11] S.Z. Rad, "Finite element, modal testing and modal analysis of a radial flow impeller", Iranian Journal of Science & Technology, Transaction B, Engineering, Vol. 29, No. B2.

[12] L. Xin, Q. Li, and Y. Liu, "Dynamic analysis of the impeller under optimized blade design for a pump-turbine", Journal of Energy Storage 107 (2025) 114900.

[13] F. Guo and H. Du, "Modal Analysis of Components and Whole of Gear Pump", IOP Conf. Series: Earth and Environmental Science 632 (2021) 032005, doi:10.1088/1755-1315/632/3/032005.

[14] M.F. White, E. Torbergsen, and V.A. Lumpkin, "Rotordynamic analysis of a vertical pump with tilting-pad journal bearings", Wear 207 (1997) 128–136.

[15] E. Egusquiza, C. Valero, A. Presas, X. Huang, A. Guardo, and U. Seidel, "Analysis of the dynamic response of pump-turbine impellers. Influence of the rotor", Mechanical Systems and Signal Processing, 68-69, (2016), 330–341.

[16] A.R. Al-Obaidi and J. Alhamid, "Analyses of the transient turbulence flow in a 3D impeller axial pump using Novel vibration signals and Inner dynamic simulation techniques", Flow Measurement and Instrumentation 102 (2025) 102779.

[17] K. Wang, G. Luo, Y. Li, R. Xia, and H. Liu, "Multi-condition optimization and experimental verification of impeller for a marine centrifugal pump", International Journal of Naval Architecture and Ocean Engineering 12 (2020) 71e84.

[18] Şen M., Çakar O., and Yiğid O., "Model reduction and dynamic analysis of a rotor system", VI-International European Conference on Interdisciplinary Scientific Research, August 26-27, 2022 / Bucharest, Romania, pp: 317-329.

Dicle University
Journal of Engineering
https://dergipark.org.tr/tr/pub/dumf
duje.dicle.edu.tr

Research Article

Worm Gear Reducer Design An Strength Analysis KissSoft-KissSys Program

Mustafa Timur*

Adnan Menderes University, Engineering Faculty, Mechanical Engineering Department, Mustafa.timur@adu.edu.tr, Orcid No: 0000-0002-4569-0450

ARTICLE INFO

Article history:

Received 01 July 2025
Received in revised form 28 August 25
Accepted 29 August 2025
Available online 30 September 2025

Keywords:

Worm gear, KissSoft , Strength

Doi: 10.24012/dumf.1731857

* Corresponding Author

ABSTRACT

This manuscript presents a comprehensive engineering approach to the design and structural analysis of worm gear reducers. The gearbox system developed with the objectives of high reduction ratio, compact structure and reliable operation is evaluated in detail using numerical analysis methods and international design standards. Accordingly, basic design parameters such as gear geometry, material selection, assembly tolerances and lubrication conditions were systematically analyzed, and simulations were performed at component and system level with a focus on performance and reliability using KISSsoft and KISSsys software. As a result of the analyses, key performance parameters such as structural stresses, fatigue strength, deflections, contact geometries and overall efficiency were evaluated, and a critical point was identified, especially in the life of a shaft bearing, and areas for improvement were identified. The overall findings show that worm gear reducer systems can be effectively investigated and optimization potentials can be revealed with theoretical modeling and CAE tools.

Introduction

In worm gear reducers used in applications requiring high torque transmission and compact design, a critical design problem arises between system efficiency and bearing life. The aim of this study is to investigate this problem through KISSsoft/KISSsys-based parametric analyses, to identify the reliability-limiting factors, and to discuss potential improvements.

Ulusoy (2024) conducted a study in which he performed a performance evaluation and backlash
analysis of the worm gear mechanism. In this context, experiments were conducted with six different values for three different reducers, and the results were compared. The specially designed worm gear mechanism for this study demonstrated better performance compared to the traditional two-value worm gear mechanism. The results revealed that the designed mechanism provides lower backlash and higher accuracy [1]. Fang and Tsay highlighted the effects of mechanical factors such as contact pressures, friction, and wear in these gear sets through mathematical modeling. This study has made significant contributions to research in worm gear design and strength analyses and has provided insights into the design of more efficient gear systems [2]. Salman (2009) conducted a comprehensive study on the mathematical modeling of worm gears and worm gear counterparts [3]. Kacalak and colleagues presented a study examining worm gear systems with improved kinematic accuracy. In this research, new design and machining techniques aimed at enhancing the kinematic accuracy of worm gear sets were discussed. The authors focused on minimizing tooth profile errors to improve the performance of the gear sets, and on methods that enhance the load-carrying capacity and efficiency of the gear systems [4].

Flexibility and accuracy provided by the CAD environment play a crucial role in optimizing the performance of gear sets. The study demonstrated that CAD-based modeling allows for a better understanding of gear systems from both kinematic and strength analysis perspectives, while also improving efficiency in the design process. This research serves as an important resource for future studies on worm gear design and strength analysis [5]. Strength analyses of the gear sets emphasized that double depth teeth enhance the durability of the gear systems, leading to longer lifespans. This study demonstrated how innovative structural modifications used in the design of worm gears provide significant advantages in terms of performance and durability, making important contributions to research in worm gear design and strength analysis [6]. Thesis demonstrated how computer-based methodologies could be effectively applied in the design of worm gear reducers and

underscored the importance of these approaches in engineering applications [7].
Recent studies emphasize the importance of coating technologies and thermal performance optimizations in reducing efficiency losses in worm gear systems [8-9].

Material Method

Worm gear reducers play an indispensable role in mechanical power transmission systems where high gear reduction ratios are required. These reducers are particularly favored in applications where low rotational speeds, high torque transmission, compact design, and quiet operation are essential. The software tools utilised, the design parameters determined according to application requirements, and the methodologies followed in selecting these parameters are systematically presented. In addition, structural analyses, material selection, and strength evaluations were conducted in accordance with international standards, including ISO/TR 14521 and DIN 3996, with the objective of assessing the mechanical performance of the reducer. In the present study, the KISSsys and KISSsoft software programmes were employed for the design and analysis of mechanical systems

Basic Data

In the “Basic Data” tab of KISSsoft, the basic geometry of the worm-worm wheel pair is initially defined by entering a modulus of 3 mm, a normal pressure angle of 20°, a center distance of 80 mm and a shaft angle of 90°. The number of teeth is then set to z1 = 2 for the worm screw and z2= 40 for the worm wheel, resulting in a gear ratio of 20:1.
In this study, a worm gear system was developed for use in an automatic garage door. An AC motor with an input speed of 600 rpm and an output torque of approximately 12–14 Nm was selected to drive the mechanism. A gear ratio of 20:1 was selected to reduce the motor speed of 600 rpm to approximately 30 rpm at the output shaft, ensuring controlled movement of the garage door. This ratio also allows sufficient torque amplification to meet the lifting requirements of an average garage door, while maintaining compactness and efficiency of the gear system. Additionally, this ratio is commonly used in similar commercial applications, which supports its practicality.
A module value of 3 mm was selected to provide sufficient strength and durability for the worm and worm gear teeth, ensuring safe transmission of torque without excessive wear. This value also maintains a balance between gear size and load capacity, and corresponds to a standard metric gear size that facilitates manufacturing and component sourcing. The number of teeth was chosen as $Z_1 = 2$ for the worm and $Z_2 = 40$ for the worm gear to achieve the desired reduction ratio of 20:1. A two-thread worm ($Z_1 = 2$) was selected to improve transmission efficiency and reduce sliding wear, while maintaining compatibility with the target speed reduction. The 40-tooth worm gear allows for a compact design and ensures sufficient output torque. The center distance was selected as 80 mm to provide sufficient spacing between the worm and worm gear while maintaining a compact design. This value also accommodates the selected module (m = 3 mm) and tooth numbers ($Z_1 = 2$, $Z_2 = 40$), ensuring proper meshing and tooth contact. A slightly extended center distance compared to the theoretical minimum (63 mm) helps reduce surface pressure and improves the durability and thermal stability of the gear set. A module value of 3 mm was selected to ensure sufficient tooth thickness and load carrying capacity for the worm gear system. This fig.1 value represents a practical balance between mechanical strength and component compactness, while also being a commonly available standard in gear manufacturing.

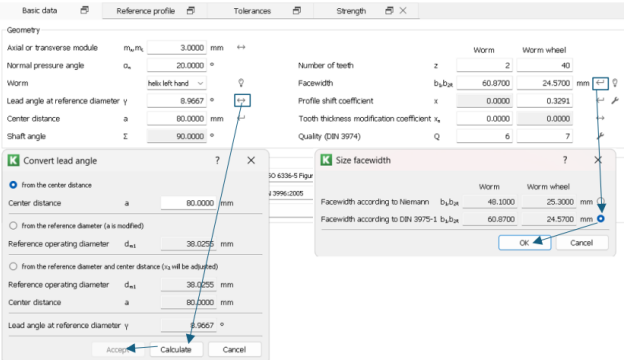


Figure 1. Convert lead angle and size facewidth tabs in 'Basic data' tab of KISSsoft software

Material Selection

Material selection in worm gear mechanisms plays a critical role in terms of efficiency, durability and long life of the system. In such mechanisms, hardenable steel (e.g. 20MnCr5) for the worm element and bronze with high tin content (e.g.CuSn12-C-GZ) for the gear wheel are generally preferred.

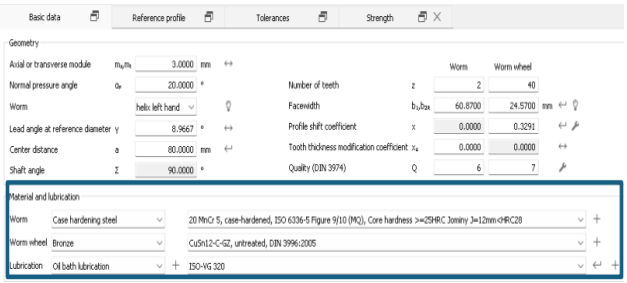


Figure 2. Material selection tab of KISSsoft software

Tolerances

The Tolerances tab in KISSsoft facilitates the precise definition of manufacturing eviations and clearance parameters for both the worm and the worm wheel.

Table 1. Niemann tolerances to DIN 3967

Proposal acc. to Niemann (tolerances acc. to DIN 3967, module > 0.5 mm)	
Casted rims	a29, a30
Rims (normal backlash)	a28
Rims (tight backlash)	bc26
Turbo gears (high temperatures)	ab25
Polymer machines	c25, cd25
Locomotive gear trains	cd 25
Standard mechanical engineering, heavy machinery, not reversing	b26
Standard mechanical engineering, heavy machinery, reversing	c25, c24, cd25, cd24, d25, d24, e25, e24
Automobiles	d26
Agricultural vehicles	e27, e28
Machine tools	f24, f25
Printing machines	f24, g24
Measuring gearboxes	g22

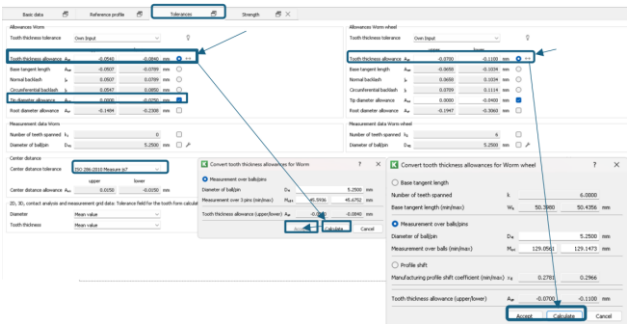


Figure 3. 'Tolerances' tab of KISSsoft software

To make this calculation, click on the double-sided arrow icon to the right of the Tooth thickness allowance option, then click Calculate and accept in the window that opens and the calculation is made. Click on the tick next to Tip diameter allowance. Tooth thickness tolerances, which directly affect the precision of the gear geometry, were determined based on “ball over pins” as the measurement method. These tolerances, defined in the range of -0.0540 / -0.0840 mm and -0.0700 / -0.1100 mm for worm and worm wheel, respectively, ensure post-production measurement and assembly precision and contribute to the efficient operation of the system by reducing backlash. End diameter tolerances, on the other hand, are not directly in the contact zone, but are important in terms of assembly fit. For this reason, 0 / -0.0250 mm for worm and 0 / -0.0400 mm for worm wheel. In addition, the center distance tolerance in the system is defined in the js7 tolerance class in accordance with the ISO 286-1 standard and is left in the range of ±0.015 mm. This choice ensures that the gear contact line is protected, creating a quiet and smooth working condition. All these tolerances have been set to optimize both the manufacturability and the longterm performance of the system.

Strength

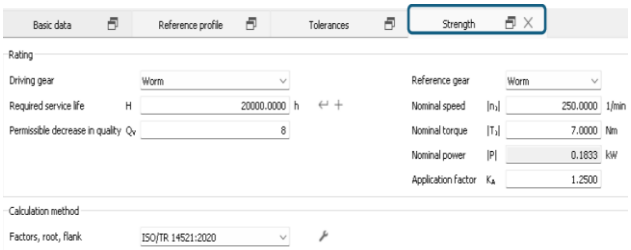


Figure 1 'Strength'' tab of KISSsoft software

The Strength section in KISSsoft is utilized for the calculation of the root and flank strength of gear systems. In this section, key operating parameters such as torque, speed, power, and service life are defined, and strength analysis is carried out according to international standards.

Bearing Selection In KISSsys

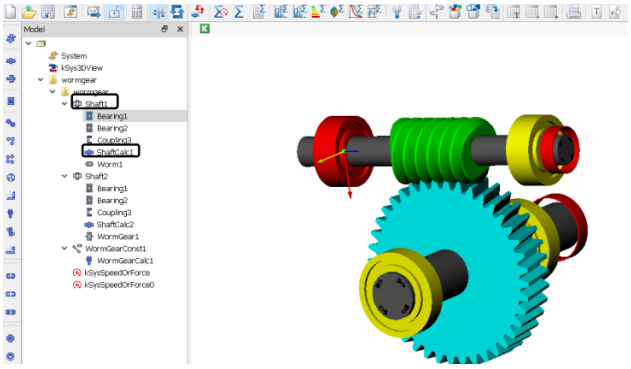


Figure 4. Bearing selection tab of KISSsys software

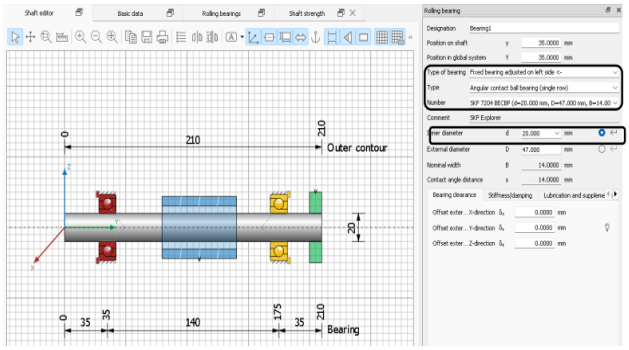


Figure 5. Worm 2D bearing selection screen ın KISSsys

For this specific design, the SKF 7204 BECBP model single-row angular contact ball bearing was selected for the worm shaft. This bearing, with standard dimensions of a 20 mm inner diameter, a 47 mm outer diameter, and a 14 mm width, features the "BECBP" designation, which indicates an approximate 40° contact angle, a robust steel cage, and universal matching capability.

When our design is finished, we must define the input speed and torque to the system. For this, some elements are added into Shaft 1 in the models section. To add this shaft element, select the element box from the Insert tab and select the 2nd element (kissSyscoupling) from the left in the shaft element and add it into Shaft1.

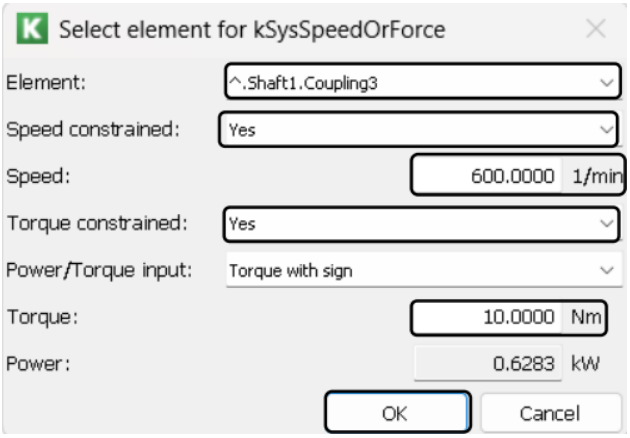


Figure 6. Speed-Torque calculation ın KISSsys

In this fig.6, we can define speed and torque for the couplings that we previously added to Shaft1 and Shaft2. In our system, since the input will be from the worm, we select the element we added to shaft1. then we must make the Speed constrained and torque constrained option yes so that we can give values. then we enter the speed =600.00rpm (1/min) and torque = 10.00Nm values we have determined, click ok and confirm.

Strength

The structural behavior of the worm shaft (Shaft1) under working loads was investigated in detail by means of deflection analysis performed by means of KISSsoft software. The shaft deformation graph presented in Figure 7 visualizes the displacement in millimeters as a result of bending and other forces to which the shaft is subjected along the axial Y direction.

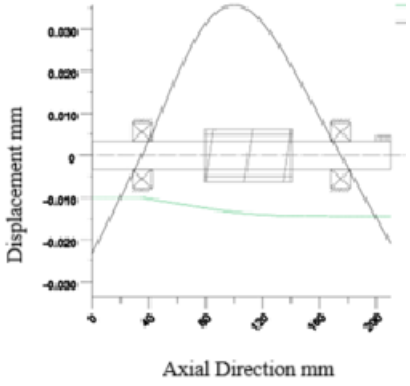
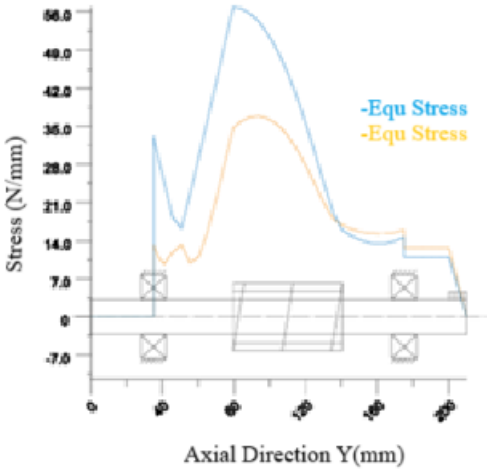


Figure 7 Deformation analysis results of worm shaft (Shaft1) under load

According to this graph and the companying numerical data, the maximum deflection on the shaft was calculated to be 35.636 µm (micrometers) and it was determined that this maximum deformation occurred at a location of approximately 98.294 mm on the shaft between the bearing points. It was also found that the shaft was subjected to a total axial load of -3333.333 N during operation and exhibited a torsion angle of 0.044 degrees under the influence of the applied torque.

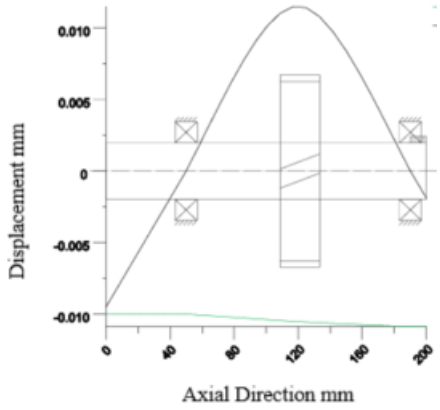
The deflection and torsion values obtained from this analysis provide important information about the geometric stability and stiffness of the worm shaft during operation. In particular, the maximum deflection of 35.636 µm is a critical parameter for maintaining the correct contact between the gears and the performance of the bearings. It is concluded that this deflection is within acceptable limits (as confirmed by the high deflection safety coefficient calculated as Sd=19.958 in the relevant section of the KISSsoft report), considering its effects on the overall operating accuracy and life of the system. Therefore, it is considered that the worm shaft has sufficient structural strength under the designed loads and the required stiffness to exhibit the expected functional performance. This is a positive indication for long life and reliable operation of the gearbox.



Graphic 8 Equivalent stress distribution along the axial direction of the worm shaft (Shaft1) calculated according to von Mises (GEH) and Tresca (SSH) criteria

In order to determine the structural adequacy of the worm shaft (Shaft1) under service loads, the distribution of equivalent stresses along the shaft was analyzed using KISSsoft software. The stress distribution graph presented in Figure 9 shows in detail the equivalent stress levels (in N/mm²) along the axial Y-direction of the shaft calculated according to both von Mises (blue curve denoted as GEH) and Tresca (orange curve denoted as SSH) criteria. By examining the graph, it is clear that the highest stress concentration occurs close to the central regions of the shaft, especially around the region where the worm gear is located (between about 80 mm and 100 mm). In this critical region, the von Mises equivalent stress reaches a peak value of just over 56 N/mm², while the Tresca equivalent stress reaches a maximum value of around 38 N/mm². The maximum equivalent stress values obtained from this analysis are compared with the mechanical properties of the C45 steel from which the shaft is manufactured, such as yield and fatigue strength, to provide a basis for concluding on the safety of the shaft. The observed maximum von Mises stress of approximately 56 N/mm² is well below the typical yield strength of C45 steel. This indicates that the

shaft has a low risk of permanent deformation under static loads and will maintain its structural integrity under operating conditions. Therefore, the stress distribution and peak values obtained indicate that the design of the worm shaft has sufficient strength for the applied loads and can operate safely.



Graphic 9 Deformation analysis results of worm wheel shaft (shaft2) under load

Conclusion

When the KISSsoft analysis make on the performance of the worm gear reducer system designed within the scope of your thesis study is evaluated in general, it is seen that the design is successful in many aspects, but there is potential for improvement in some critical points. The worm gear set analysis results show that the main power transmission elements of the gearbox meet the targeted criteria in terms of strength and life. The calculated wear safety coefficient (SW=1.264), pitting safety coefficient (SH=1.347) and tooth bottom fracture safety coefficient (SF=3.794) for the gear wheel are above the minimum requirements specified in the relevant standards. The calculated system service life of 119,613 hours for the gear set significantly exceeds the targeted service life of 20,000 hours. The deflection safety of the worm shaft (Sd=19.958) and the thermal safety of the system (ST=2.050) with a calculated oil temperature of 43.9∘C are also satisfactory. The calculated total efficiency of the gearbox was determined as 70.993%. When the structural analyses of the shafts are examined, the maximum deflections (35.636 µm and 11.505 µm, respectively) and the maximum equivalent von Mises stresses (~56 N/mm² for shaft1 and ~54 N/mm² for shaft2) occurring in both the worm shaft (shaft1) and the worm wheel shaft (shaft2) under operating loads are within acceptable limits considering the mechanical properties of the C45 shaft material used. This confirms that the shafts show sufficient stiffness and strength under load. The evaluation of bearing performances points to an area where the results require more careful scrutiny. Both of the SKF 7007 ACD/P4A bearings (Bearing1 and Bearing2) used in the worm wheel shaft (Shaft2), with their calculated L10h life (199,523 hours and 347,193 hours respectively), more than meet the targeted service life of 20,000 hours. However, of the SKF 7204 BECBP bearings used in the worm shaft (Shaft1), the calculated L10h life of the primary bearing (Bearing1) located closer to the power input is approximately 5498 hours. This is well below the targeted service life of 20,000 hours, indicating a damage rate of 363.78%. This finding suggests that the design requires a critical refinement or more detailed investigation at this particular point. It should be noted that the bearing life calculations assume an ISO-VG 220 viscosity oil at an operating temperature of 70∘C for the shaft bearings and an ISO-VG 320 viscosity oil for the gear set, with an oil bath temperature of 43.9∘C. If a single common oil bath is used in the system, updating the bearing life analysis to the actual operating conditions of the gear set with oil (ISO-VG 320) and a lower temperature (approximately 44∘C) may provide a more realistic assessment of the life of this critical bearing. Otherwise, the choice of a different bearing or a modification of the bearing arrangement may be unavoidable. The obtained efficiency value of 70.99% is reasonable when compared to the 72–75% range reported in the study of Zhao et al. (2021). However, the bearing life results (approximately 5,498 hours) are considerably lower than the lifetimes reported in the literature for similar capacities (over 20,000 hours). This indicates that the input-side bearings, in particular, represent a critical limitation for system reliability. In conclusion, it is concluded that the analyzed worm gear reducer design is generally successful and safe in terms of the gear set and shafts, but the life of the primary bearing on the worm shaft is the most important limiting factor in terms of the overall reliability and targeted service life of the system, and this issue should be further investigated or the design should be revised.

Acknowledgement

This study was carried out practically in a special gearbox enterprise and the results were manufactured correctly.

References

[1] Ulusoy, E, Diş Boşluğu Ayarlanabilen Sonsuz Dişli Mekanizmasının Tasarımı, Karabük Üniv. Müh.Fak. Mak.Müh. Fen.Bil.Enst., (Yüksek Lisans Tezi), Türkiye, 2024.

[2] Fang, H. S. ve Tsay, C. B, "Büyük boy ocak kesiciler tarafından kesilen ZN tipi sonsuz dişli setinin matematiksel modeli ve yatak kontakları. Mekanizma ve Makine Teorisi", 35(12), 1689-1708, 2000.

[3] Selman, B. (2009). Sonsuz vidalar ve sonsuz vida karşılık dişlisi helisel dişli matematik modellemesi, İTÜ Fen Bil.Enst. Mak.Müh., (Yüksek Lisans Tezi).

[4] Kacalak, W., Majewski, M., Budniak, Z. ve Ponomarenkow, J, "Geliştirilmiş kinematik hassasiyete sahip sonsuz dişli tahrikleri", Malzemeler, 14(24), 7825, 2021.

[5] Połowniak, P., Sobolak, M. ve Marciniec, A, "CAD ortamı kullanılarak çift zarflı sonsuz dişli modellemesi", Polonya Bilimler Akademisi Teknik Bilimler Bülteni, e136736-e136736, 2021.

[6] Chen, W. L., Tsay, C. B. 2011. "Mathematical Model and Tooth Surfaces of Recess Action Wormgears with Doubledepth Teeth," Mechanism and Machine Theory, vol. 46 (12), p. 1840-1853.

[7] Pak, M. (1998). Sonsuz vidalı redüktörlerin bilgisayar yardımıyla parametrik tasarımı, Sakarya Üniversitesi, Fen Bil.Enst. Mak.Müh., (Yüksek Lisans tezi).

[8] Li, X., et al. (2022). "Tribological performance of worm gears with advanced coatings." *Wear, 494–495, 204285.*

[9] Zhao, Y., et al. (2021). "Optimization of worm gear design considering efficiency and thermal performance." *Mechanism and Machine Theory, 162, 104379* .

Dicle University
Journal of Engineering
https://dergipark.org.tr/tr/pub/dumf
duje.dicle.edu.tr

Research Article

Identification of Dynamic Properties of a Fixed-Supported T-Frame Using Experimental Modal Analysis

Ali Osman YAŞA[1], Mesut HÜSEYİNOĞLU[2*]

[1] Dicle University, Mechanical Engineering Department, yasaaliosman@gmail.com, Orcid No 0009-0007-0104-0281
[2] Dicle University, Mechanical Engineering Department, mesuth@dicle.edu.tr, Orcid No: 0000-0002-6130-6658

ARTICLE INFO

Article history:

Received 28 July 2025
Received in revised form 21 August 2025
Accepted 26 August 2025
Available online 30 September 2025

Keywords:

experimental modal analysis, modal parameters, frame structures, narrowband, broadband

Doi: 10.24012/dumf.1752719

* Corresponding author

ABSTRACT

This study comparatively investigated the dynamic properties of a fixed-supported T-frame using narrowband and broadband excitation in experimental modal analysis. The aim was to identify vibration modes and assess consistency in modal parameter extraction. Three significant modes (0-500 Hz) were precisely determined for natural frequencies, damping ratios, and mode shapes. Findings showed excellent agreement in natural frequency identification across both methods (differences < 0.15 Hz) and high mode shape correlation via the Modal Assurance Criterion. However, damping ratio estimations revealed notable discrepancies, especially for the first mode, where broadband excitation yielded significantly higher values. This highlights that the excitation method critically influences damping estimations, particularly for lower-frequency modes. In conclusion, while both methods effectively identify natural frequencies and mode shapes, this analysis underscores the sensitivity of damping ratio estimations to the selected excitation approach.

Introduction

Frame structures are among the most widely used structural forms in engineering due to their ability to provide rigidity, strength, and deformation capacity. They are commonly employed in buildings, bridges, industrial facilities, and mechanical frameworks, primarily because of their effectiveness in carrying both vertical and lateral loads. Frame systems are particularly advantageous in resisting bending moments and shear forces, thus maintaining structural integrity and minimizing deformations under external influences. Moreover, their modular nature offers significant flexibility in design, fabrication, and assembly processes. Understanding the behavior of frame structures under dynamic loading is critically important in fields such as structural dynamic, vibration control, and structural health monitoring. As a result, both theoretical modeling and experimental investigation of frame systems remain essential topics in modern structural engineering research.

Due to their structural configuration, frame systems can effectively resist bending moments and shear forces, maintaining global stability even under dynamic loading conditions such as seismic activity or machine-induced vibrations. As a result, understanding the dynamic behavior of such systems through modal analysis is essential for safe and efficient design [1]. Moreover, fixed (clamped) boundary conditions, often used to idealize real-world constraints, allow for the realistic modeling of structural components anchored to rigid foundations.

The determination of dynamic properties in structural systems is of paramount importance in numerous engineering applications, ranging from civil infrastructure to aerospace components [2]. These properties, which encompass natural frequencies, damping ratios, and mode shapes, dictate a structure's response to dynamic loads and are crucial for ensuring its stability, reliability, and safety [3]. Accurate identification of these modal parameters allows engineers to predict structural behavior under various operating conditions, optimize designs to mitigate unwanted vibrations, and implement effective structural health monitoring strategies [4]. Experimental Modal Analysis (EMA) stands as a widely accepted and powerful technique for extracting these dynamic characteristics from physical structures [5]. EMA involves exciting the structure with a known input force, measuring the resulting vibratory response at various points, and then using signal processing techniques to estimate the modal parameters [6]. The study of structural dynamics is essential for ensuring the safety and reliability of engineering structures [7]. This field

focuses on understanding how structures respond to dynamic loads, such as vibrations, impacts, and seismic activity [8]. Understanding a structure's dynamic properties, including its natural frequencies, damping ratios, and mode shapes, is crucial for predicting its behavior under various operating conditions and preventing potential failures. Among the various methods available for determining these properties, EMA stands out as a versatile and widely used technique [9].

In the realm of structural dynamics, boundary conditions play a pivotal role in defining the behavior of a structure. Fixed or clamped boundary conditions, where a structural element is rigidly constrained against translation and rotation, are commonly encountered in real-world applications [10]. These conditions significantly influence the structure's stiffness and mass distribution, consequently affecting its modal parameters [11]. Therefore, accurate modeling and simulation of fixed boundary conditions are crucial for obtaining reliable predictions of structural behavior. Simulating real-world structural constraints through fixed boundary conditions is essential for accurately predicting structural behavior [12]. The constraints imposed by fixed supports significantly influence a structure's stiffness and mass distribution, thereby affecting its modal parameters [13]. Accurately modeling these boundary conditions is crucial for obtaining reliable predictions of structural behavior under various loading scenarios. Experimental Modal Analysis is a powerful technique used to determine the dynamic characteristics of a structure by analyzing its response to controlled excitation [14]. The process involves exciting the structure with a known input force, measuring the resulting vibrations at various points, and then using signal processing techniques to extract modal parameters such as natural frequencies, damping ratios, and mode shapes [15].

Many large-span structures are highly susceptible to dynamic loads because they are light and flexible [16]. Structures with complex geometries, such as T-shaped frames, present unique challenges in dynamic analysis due to their intricate stress distributions and varying stiffness properties. The T-shaped frame configuration is frequently encountered in diverse engineering applications, including bridge piers, building frames, and machine components [17]. Analyzing the dynamic properties of these structures is essential to prevent failures caused by resonance or excessive vibrations. Modal analysis, both numerical and experimental, is extensively employed to investigate the dynamic characteristics of these structures. The T-shaped frame configuration is commonly found in bridge piers, building frames, and machine components, and understanding their dynamic properties is crucial for preventing failures caused by resonance or excessive vibrations.

The study of dynamic properties in structural systems has a rich history, with early investigations focusing on simple structures and analytical methods. Over time, advancements in computational power and sensor technology have led to the development of sophisticated numerical techniques and experimental methods for analyzing complex structures [18]. Finite element analysis has emerged as a powerful tool for simulating the dynamic behavior of structures, but its accuracy depends heavily on the fidelity of the model and the proper representation of boundary conditions [19]. Experimental modal analysis is essential for validating numerical models and identifying discrepancies between predicted and actual behavior. Numerous studies have investigated the dynamic properties of various structural configurations using EMA [20-26].

Frequency Response Functions (FRFs), which are used to identify dynamic properties via EMA, can be obtained by applying controlled excitation to the structure and measuring the resulting vibrations at multiple points. In EMA, the selection of the excitation method and excitation points is of critical importance for accurately and reliably obtaining FRFs. In cases where multiple excitation points are required, or when precise and repeatable excitations must be applied to the same location, electrodynamic shakers are often preferred. This is because impact hammer excitation depends heavily on the operator’s skill, consistency, and experience, making it more susceptible to variability. Shakers are widely used in modal testing since they can be rigidly connected to the test structure and allow for controlled force inputs over desired frequency ranges. This capability enables consistent excitation and enhances the accuracy of modal parameter estimation. However, for lightweight or small-scale structures, the interaction between the shaker and the test object may alter the boundary conditions due to the added mass or stiffness. In such situations, an instrumented impact hammer is typically preferred, as it minimizes disturbance to the system’s dynamic characteristics while still providing sufficient excitation energy. The FRFs obtained either experimentally from the physical structure or numerically via Finite Element (FE) models are widely used in the literature for identifying the dynamic characteristics of structures, forward or inverse structural dynamic modifications, validating modal parameters and model updating [27-35].

Despite extensive research in structural dynamics and modal analysis, there remains a need for comprehensive investigations into the dynamic behavior of T-shaped frame structures with fixed boundary conditions, especially concerning the comparative performance of different excitation methods. The interaction between the frame's unique geometry and the fixed supports introduces complexities that significantly influence its modal parameters, and the impact of connection rigidity on dynamic properties remains an active area of research. Filling this gap, this study specifically conducts the experimental modal analysis of a T-frame structure with one end fixed (clamped), focusing on a comparative analysis of narrowband and broadband excitation techniques. The dynamic characteristics of the structure, including natural frequencies, damping ratios, and mode shapes, were identified using these distinct modal parameter estimation band types and are presented in a comparative manner. The subsequent sections of this study provide detailed information on the experimental setup, measurement procedures, and the obtained results, followed

by a comprehensive discussion of our findings and concluding remarks.

Experimental procedure

In EMA, the structure is excited using an impulse hammer or shaker, and accelerometers are strategically placed to capture the vibrational response at various points. Signal processing techniques, such as Fourier analysis, are then applied to the measured data to extract modal parameters like natural frequencies, damping ratios, and mode shapes. The acquired data undergoes meticulous processing and analysis to extract accurate modal parameters. The subsequent steps involve the application of signal processing techniques to extract modal parameters, including natural frequencies, damping ratios, and mode shapes. Furthermore, by comparing the experimentally obtained modal parameters with those predicted by numerical models, the accuracy and reliability of the numerical models can be assessed and improved. In this study, a measurement technique was employed in which both the excitation force applied to the structure and the structural response were measured simultaneously. This approach allows for the direct experimental acquisition of FRFs, enabling the identification of the system's dynamic characteristics such as natural frequencies, damping ratios, and mode shapes. In the literature on vibration testing, different implementation strategies related to this method have been described [1]. One common approach involves exciting the structure from a single point, whereas the alternative method involves simultaneous excitation at multiple points on the structure.

The position and direction of the applied force and the corresponding measured response on the structure are critical in determining the type of FRF being calculated. If the force and response are measured at the same location and in the same direction, the resulting FRF is referred to as a point FRF. Point FRFs are typically used to reveal the local dynamic characteristics at a specific point on the structure (Fig. 1-a).

If the directions of the force and response are the same but their positions are different, the computed FRF is classified as a transfer FRF. Transfer FRFs are used to observe how a force applied at one point affects the response at another, providing insights into the propagation characteristics of the structure (Fig. 1-b).

Alternatively, if the force and response are measured at different positions and in different directions, the resulting FRF is termed a cross FRF. Cross FRFs play a crucial role in understanding the directional dynamic interactions within the structure (Fig. 1-c).

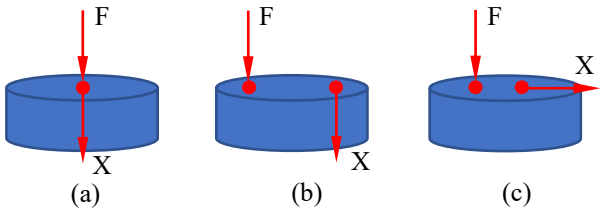


Figure 1. FRFs according to force and response positions

These different types of FRFs are essential in experimental modal analysis for capturing the directional dependencies and spatial variations in the vibrational behavior of the structure, thereby contributing to the accurate and reliable identification of modal parameters.

Experimental setup

In this study, the structure was excited using an instrumented impact hammer (Fig. 2-b) manufactured by KISTLER (Model: 9722A500, Serial No: 2078644). This hammer features a built-in piezoelectric force sensor that allows accurate measurement of the input force applied during impact. The hammer supports interchangeable impact tips made of materials such as plastic, rubber, and steel, which were selected based on the desired frequency range and energy content of the excitation signal. The vibration responses of the structure were measured using a piezoelectric accelerometer (Fig. 2-a) produced by KISTLER (Model: 8702B500 series, Serial No: 2078315), which employs ICP (Integrated Circuit Piezoelectric) technology. The sensor was mounted firmly onto the structure using a threaded stud, ensuring rigid contact and high-fidelity signal transmission. The accelerometer was positioned at various measurement points in accordance with the predefined test grid.



(a) (b)

Figure 2. Accelerometer and impact hammer

The technical specifications of the impact hammer and accelerometer are presented in Table 1 and Table 2, respectively.

Table 1. Technical specifications of the impact hammer

Technical Data Type	Force Range [N]	Maximum Force [N]	Sensitivity nom. [mV/N]	Resonant Frequency [kHz]
Units	0-500	2500	10	27

Table 2. Technical specifications of the accelerometer

Technical Data Type	Frequency Range [Hz]	Maximum Range [g]	Sensitivity nom. [mV/g]	Resonant Frequency [kHz]
Units	1-10000	500	10	54

The OROS OR 35 vibration analyzer was used to collect and analyze vibration data. Some technical specifications of the OROS OR35 vibration analyzer are given in Table 3.

Table 3. Technical specifications of the analyzer

Technical Data Type	Number of Chanel	Connection Type	Sampling Rate [kS/s]	Accuracy [dB]
Units	10	BNC	2-100	±0.02

The T frame, whose dimensions (mm) and support conditions are shown in Fig. 3, was used as the test structure. The T frame was divided into 14 elements with 15 nodes

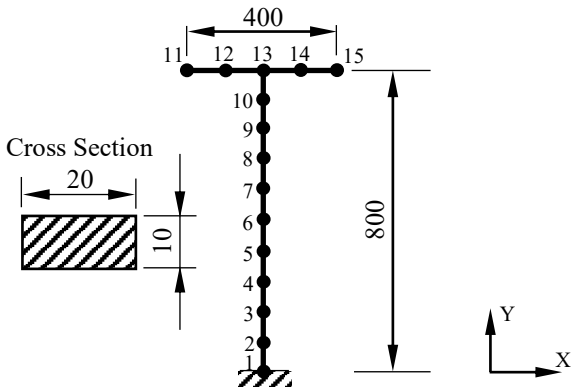


Figure 3. T frame performing EMA.

NvGate software was used for data acquisition and Oros Modal software was used for modal analysis. The data acquisition parameters used during the EMA, which reflect the measurement conditions and testing equipment in detail, are presented in Table 4.

Table 4. Data acquisition parameters.

Parameter	Frequency Range [Hz]	Frequency Resolution [Hz]	Sampling Frequency [Hz]	Measurement Time [sn]	Windowing [response/ impact]
Value	0-500	0.312	1601	3.2	uniform / uniform

As can be seen in Fig. 4, an accelerometer was placed at the 3rd node of the T-frame structure and impacts were applied with a modal hammer from each node in the direction shown in the figure.

Fig. 5 provides a detailed illustration of a measurement setup implemented during the EMA, which aims to capture the structural response under controlled excitation conditions as part of the overall dynamic characterization process.

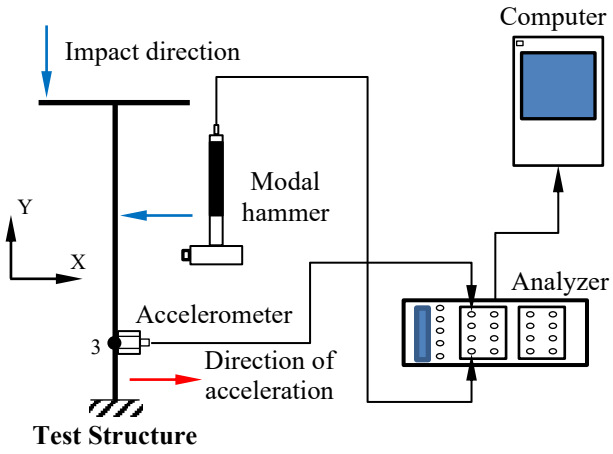


Figure 4. Experimental setup.



Figure 5. A measurement process and data analysis performed within the scope of EMA.

Evaluation of experimental results

Measurements were made from each node in 3 repetitions. In this way, the necessary measurements were made from all nodes and all elements belonging to the 3 rows of the FRF matrix were obtained.

Phase and amplitude graphs of $H_{3,4}$, $H_{3,5}$, $H_{3,6}$ and $H_{3,9}$ transfer FRFs are shown in Fig. 6.

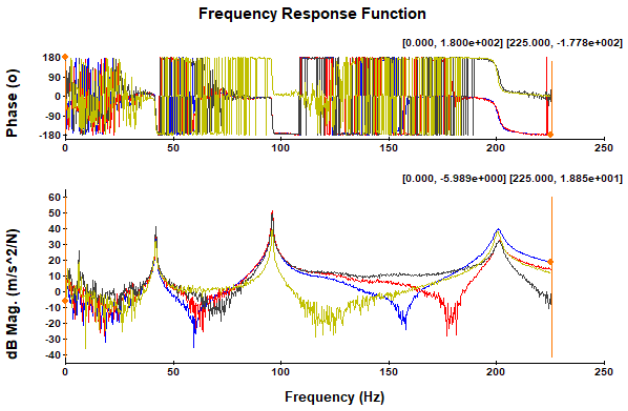


Figure 6. Transfer FRFs of T frame.

Coherence and amplitude graphs of $H_{3,11}$, $H_{3,12}$, $H_{3,14}$ and $H_{3,15}$ cross FRFs are shown in Fig. 7.

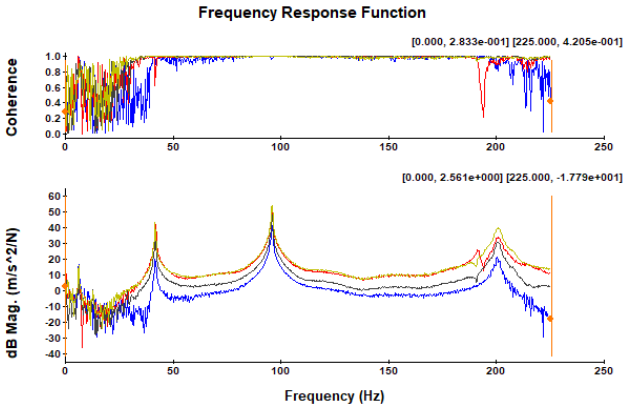


Figure 7. Cross FRFs of T frame.

The FRF graphs presented above illustrate both the magnitude and phase behavior of the structure under dynamic excitation. Despite being acquired using the same excitation method, the presence of measurement noise and coherence variability can be observed, particularly in the phase and low-magnitude regions. In the phase response plot, irregular and abrupt shifts suggest potential noise interference or phase instability in certain frequency bands, especially below 100 Hz. Additionally, the magnitude plots show well-defined resonance peaks near 42 Hz, 96 Hz, and 201 Hz, corresponding to the dominant modes of the system; however, the slight fluctuations in amplitude around these peaks imply the presence of environmental or electronic noise during acquisition. Although coherence plots are not provided for direct validation, the consistency across multiple measurement channels (indicated by different color curves) supports the reliability of the data, albeit with minor local deviations. Overall, the FRFs reveal a satisfactory signal-to-noise ratio and are suitable for modal parameter extraction.

In EMA, the selection of excitation methodology significantly influences the accuracy and efficiency of modal parameter identification. Two commonly employed excitation strategies are broadband and narrowband methods, each offering distinct advantages depending on the test objectives and structural complexity. Broadband excitation methods, such as white noise, random signals, swept sine waves, and impact hammer tests, apply energy across a wide frequency range, allowing multiple modes of the structure to be excited simultaneously. These methods are particularly useful for rapid testing, global system identification, and field applications, as they enable efficient data acquisition and provide a comprehensive overview of the structure's dynamic behavior. However, broadband techniques may suffer from limited resolution when closely spaced modes are present, and the signal-to-noise ratio may vary across the frequency spectrum, which can affect the accuracy of damping estimates.

In contrast, narrowband excitation methods, including single-frequency sine excitation and stepped sine sweeps, focus energy within a limited frequency band, typically around a specific mode. These methods are highly effective for precise identification of modal parameters, especially damping ratios, and for resolving closely spaced or interacting modes. Despite offering superior resolution, narrowband testing typically requires longer measurement times and is more suited to controlled laboratory environments where detailed dynamic characterization is required.

In this study, modal parameters were identified using both broadband and narrowband excitation techniques, and the results were presented and compared in order to evaluate the accuracy and sensitivity of each method. This comparative approach not only provides insight into the advantages and limitations of each technique but also contributes to a more robust understanding of the dynamic behavior of the tested structure. The damping ratios of the structure were determined using the half-power bandwidth method from the frequency response functions. This method is a simple and effective approach widely used for extracting modal parameters. However, it should be noted that factors such as measurement noise and frequency resolution can affect damping ratio estimates, particularly in underdamped systems and in the presence of adjacent modes. In the experimental study, three prominent vibration modes were identified within the 0–500 Hz frequency range, and their corresponding modal parameters were extracted using both narrowband and broadband excitation methods. The comparative results are presented in Table 5.

Table 5. Natural frequencies and damping ratios identified using narrowband and broadband excitation methods.

Modal Parameter	Natural Frequencies [Hz]			Damping Ratio [%]		
Mode Number	1	2	3	1	2	3
Narrowband	41,77	95,78	200,77	0,25	0,12	0,54
Broadband	41,72	95,79	200,62	0,40	0,11	0,49

Table 5 presents a comparison of the natural frequencies and damping ratios identified using narrowband and broadband excitation techniques for the first three vibration modes. The results indicate that the natural frequencies obtained from both methods are in excellent agreement, with differences less than 0.15 Hz across all modes, demonstrating consistency in frequency identification.

However, notable discrepancies can be observed in the damping ratios. For the first mode, the damping ratio identified using broadband excitation (0.40%) is significantly higher than that obtained using the narrowband method (0.25%). For the second and third

modes, the differences in damping ratios are relatively smaller but still present. These variations suggest that the choice of excitation method can influence damping estimation, particularly in the lower modes. Such differences may arise due to noise sensitivity, excitation bandwidth, or energy content in the input signal, especially in the case of broadband excitation.

Overall, while both methods provide reliable frequency estimations, care should be taken when interpreting damping values, particularly for low-frequency modes.

The Modal Assurance Criterion (MAC) is a widely used metric to quantify the correlation between two mode shapes, typically ranging from 0 (no correlation) to 1 (perfect correlation). In this study, the MAC was employed to assess the similarity between mode shapes identified through narrowband and broadband excitation methods. The MAC plot is presented in Fig. 8.

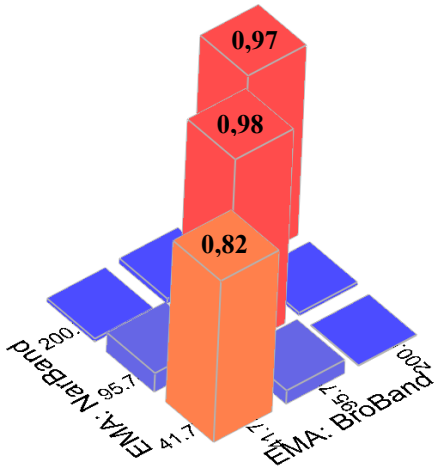


Figure 8. The MAC plot between narrowband and broadband

The 3D MAC plot presented in Fig. 8 illustrates the correlation between the mode shapes identified via narrowband and broadband excitation methods for the first three modes. The second and third modes exhibit MAC values close to 1, indicating excellent agreement between the two methods. Although the first mode shows a relatively lower MAC value compared to the others, it still falls within an acceptable range commonly cited in structural dynamics literature (typically above 0.8), suggesting that the correlation between the corresponding mode shapes is satisfactory. Furthermore, the off-diagonal elements remain close to zero, confirming the orthogonality of the extracted mode shapes and the reliability of the modal identification.

Conclusions

This study successfully investigated the dynamic properties of a fixed-supported T-frame, specifically focusing on the comparative analysis of experimental modal analysis using both narrowband and broadband excitation techniques. Three prominent vibration modes were identified within the 0-500 Hz frequency range, and their corresponding modal parameters, including natural frequencies and damping ratios, were extracted.

The results demonstrated excellent agreement in natural frequency identification between the two excitation methods, with differences consistently below 0.15 Hz across all modes. This consistency underscores the reliability of both techniques in determining a structure's inherent vibrational characteristics. However, notable discrepancies were observed in the damping ratio estimations, particularly for the first mode, where broadband excitation yielded a significantly higher damping value compared to narrowband excitation. The observed discrepancies in damping ratios, particularly the higher values obtained with broadband excitation, warrant further discussion. These differences can be attributed to several factors inherent in the experimental setup and data processing. One significant factor is the signal-to-noise ratio (SNR); broadband excitation often introduces lower SNR across specific frequency bands compared to narrowband excitation, which can lead to less precise damping estimates. Additionally, frequency resolution plays a crucial role; while narrowband excitation allows for very high frequency resolution around specific modes, broadband excitation, by covering a wider spectrum, may inherently offer a different resolution characteristic that impacts damping calculation accuracy. The method of damping estimation itself (half-power bandwidth, least squares complex exponential) can also interact differently with the characteristics of narrowband versus broadband FRFs, contributing to these observed variations. Understanding these nuances is vital for practitioners, as it underscores that the choice of excitation method is not merely a procedural preference but a critical decision with direct implications for the accuracy and interpretation of damping values in experimental modal analysis.

Furthermore, the Modal Assurance Criterion confirmed the high correlation between the mode shapes identified by both methods. The MAC values indicated excellent agreement, and the off-diagonal elements remained close to zero, confirming the orthogonality of the extracted mode shapes and reinforcing the reliability of the modal identification process. While both methods prove effective for reliable frequency estimations, the findings highlight the critical importance of exercising caution when interpreting damping values, particularly for low-frequency modes, as these can be sensitive to the excitation approach employed. This comparative analysis provides valuable insights into the advantages and limitations of each technique, contributing to a more robust understanding of the dynamic behavior of T-frame structures under different excitation conditions.

Ethics committee approval and conflict of interest statement

There is no need to obtain permission from the ethics committee for the article prepared

There is no conflict of interest with any person / institution in the article prepared

Authors' Contributions

Yasa AO: Production of the test sample, experimental setup, experimental modal analysis, drafting of manuscript

Huseyinoglu M: Data curation, writing original draft, review and editing

Acknowledgement

The analyzer used in this study was provided within the scope of TÜBİTAK 1001 Project (Project No: 223M423). The authors would like to thank TÜBİTAK for its support.

References

[1] D. J. Ewins, "Modal Testing: Theory, Practice and Application", 2nd ed., Baldock, Hertfordshire, England, Philadelphia, PA : Research Studies Press, 2000.

[2] A. Shmerling, R. Levy, and A. M. Reinhorn, "Seismic retrofit of frame structures using passive systems based on optimal control," *Structural Control and Health Monitoring*, vol. 25, no. 1, May 2017, doi: 10.1002/stc.2038.

[3] J. Jang and A. W. Smyth, "Data-driven models for temperature distribution effects on natural frequencies and thermal prestress modeling," *Structural Control and Health Monitoring*, vol. 27, no. 2, Nov. 2019, doi: 10.1002/stc.2489.

[4] P. Kulhavý, M. Petrů, and M. Syrovátková, "Possibilities of the Additional Damping of Unidirectional Fiber Composites by Implementation of Viscoelastic Neoprene and Rubber Layers," *Shock and Vibration*, vol. 2017, p. 1, Jan. 2017, doi: 10.1155/2017/4163485.

[5] M. S. M. Sani, N. A. Nazri, S. N. Zahari, N. A. Abdullah, and G. Priyandoko, "Dynamic Study of Bicycle Frame Structure," *IOP Conference Series Materials Science and Engineering*, vol. 160, p. 12009, Nov. 2016, doi: 10.1088/1757-899x/160/1/012009.

[6] V. Kastala, "Methods to measure implant stability," *Journal of Dental Implants*, vol. 8, no. 1, p. 3, Jan. 2018, doi: 10.4103/jdi.jdi_7_18.

[7] C. L. Bacquet and M. I. Hussein, "Dissipation engineering in metamaterials by localized structural dynamics," arXiv (Cornell University), Jan. 2018, doi: 10.48550/arxiv.1809.04509.

[8] M. N. Norwood and R. S. Dow, "Dynamic analysis of ship structures," *Ships and Offshore Structures*, vol. 8, p. 270, Mar. 2013, doi: 10.1080/17445302.2012.755285.

[9] V. V. Swami, V. Vijayaraghavan, and V. Swami, "Current trends to measure implant stability," *The Journal of Indian Prosthodontic Society*, vol. 16, no. 2. p. 124, Jan. 01, 2016. doi: 10.4103/0972-4052.176539.

[10] J. Xu, B. Diao, Q. Guo, Y. Ye, Y. L. Mo, and T. Zhou, "Parametric Study on Mixed Torsional Behavior of U-Shaped Thin-Walled RC Girders," *Advances in Civil Engineering*, vol. 2018, p. 1, Jan. 2018, doi: 10.1155/2018/3497390.

[11] Y. E. Yang and Q. M. Wang, "Study on Dynamics Analysis and Application of Vibration Modal Testing of Suspension Cable Structure Based on MEMS Sensor," *Applied Mechanics and Materials*, p. 2149, Oct. 2013, doi: 10.4028/www.scientific.net/amm.448-453.2149.

[12] J. Brownjohn et al., "Bayesian operational modal analysis of offshore rock lighthouses: Close modes, alignment, symmetry and uncertainty," *Mechanical Systems and Signal Processing*, vol. 133, p. 106306, Aug. 2019, doi: 10.1016/j.ymssp.2019.106306.

[13] M. F. Mitroi and A. Chiru, "Determinations regarding the influence on movement and comfort of different elastic suspension structures in N2 type vehicles," *in IOP Conference Series Materials Science and Engineering*, IOP Publishing, Dec. 2020, p. 12049. doi: 10.1088/1757-899x/997/1/012049.

[14] C. Gavriloaia, C. Corduban, D. N. Isopescu, N. Ţăranu, and M. Budescu, "Calibration of a Wooden Floor Calculation Model Based on the Experimentally Determined Dynamic Characteristics," *Key engineering materials*, vol. 601, p. 211, Mar. 2014, doi: 10.4028/www.scientific.net/kem.601.211.

[15] Z. C. Ong, E. T. Yap, Z. Ismail, and S. Y. Khoo, "Assessment on Structural Integrity of In-service Machine Using De-noised Vibrational Modal Data and Artificial Neural Network," *MATEC Web of Conferences*, vol. 237, p. 3002, Jan. 2018, doi: 10.1051/matecconf/201823703002.

[16] P. Liu, B. Tang, and S. Kaewunruen, "Vibration-Induced Pressures on a Cylindrical Structure Surface in Compressible Fluid," *Applied Sciences*, vol. 9, no. 7, p. 1403, Apr. 2019, doi: 10.3390/app9071403.

[17] E. El-Dardiry and T. Ji, "Modelling of the dynamic behaviour of profiled composite floors," *Engineering Structures*, vol. 28, no. 4, p. 567, Oct. 2005, doi: 10.1016/j.engstruct.2005.09.012.

[18] E. Stanciu, C.-N. Nitescu, Z.-I. Praisach, and G.-R. Gillich, "Integrity evaluation concerning vibrations of a welded structure," *MATEC Web of Conferences*, vol. 112, p. 3015, Jan. 2017, doi: 10.1051/matecconf/201711203015.

[19] A. Kovaļovs, S. Ručevskis, P. Akishin, and J. Kolupajevs, "Numerical Investigation on Detection of Prestress Losses in a Prestressed Concrete Slab by Modal Analysis," *in IOP Conference Series Materials Science and Engineering*, IOP Publishing, Oct. 2017, p. 12090. doi: 10.1088/1757-899x/251/1/012090.

[20] H. Liu, Y. Liu, and Y. Wu, "Numerical analysis and experimental investigation of modal properties for the

gearbox in wind turbine," *Frontiers of Mechanical Engineering*, vol. 11, no. 1, pp. 72–80, 2016.

[21] M. Şen and M. Hüseyinoğlu, "Investigation of the Effects of Polyurethane Foam Reinforcement Thickness on Modal Properties of Sandwich Beams," *Mus Alparslan University Journal of Science*, vol. 6, no. 1, pp. 511-517, 2018.

[22] G. Pasharavesh, M. T. Ahmadian, and H. Zohoor, "Complex modal analysis and coupled electromechanical simulation of energy harvesting piezoelectric laminated beams," *Proc. Inst. Mech. Eng., Part C: J. Mech. Eng. Sci.*, vol. 233, no. 7, 2019.

[23] J. Semm, M. Sellemond, C. Rebelein, and M. F. Zaeh, "Efficient dynamic parameter identification framework for machine tools," *J. Manuf. Sci. Eng.*, vol. 142, no. 8, art. no. 081003, 2020.

[24] B. Scheel, "Nonlinear modal testing of damped structures: Velocity feedback vs. phase resonance," arXiv:2108.06189, Aug. 2021.

[25] G. Sarı, A. F. Ak, A. A. Akış, and E. Aydınoğlu, "Experimental and numerical modal analysis of a bladed rotor," *Dicle Univ. J. Eng. Eng. Sci.*, vol. 13, no. 1, pp. 57–63, Mar. 2022.

[26] T. Qaumi and S. M. Hashemi, "Experimental and numerical modal analysis of a composite rocket structure," *Aerospace*, vol. 10, no. 10, p. 867, 2023.

[27] R. M. Lin and D. J. Ewins, "Modal updating using FRF data," in Proc. 15th Int. Sem. Modal Analysis, Leuven, Sep. 1990, pp. 141–162.

[28] S. Pradhan and S. V. Modak, "Normal response function method for mass and stiffness matrix updating using complex FRFs," *Mechanical Systems and Signal Processing*, vol. 32, pp. 232–250, 2012.

[29] J. D. Sipple and M. Sanayei, "Finite element model updating using frequency response functions and numerical sensitivities," *Structural Control and Health Monitoring*, vol. 21, pp. 784–802, 2014.

[30] H. N. Özgüven, "Structural modifications using frequency response functions," *Mechanical Systems and Signal Processing*, vol. 4, pp. 53–63, 1990.

[31] M. Huseyinoglu and O. Çakar, "Determination of stiffness modifications to keep certain natural frequencies of a system unchanged after mass modifications," *Archive of Applied Mechanics*, vol. 87, no. 10, pp. 1629-1640, 2017.

[32] M. Hüseyinoğlu, "A Method for the Assignment of Zeros Using Frequency Response Functions," *Journal of Vibration Engineering & Technologies*, vol. 12, no. 4, pp. 6043-6052, 2024.

[33] M. Hüseyinoğlu, "A method for substructure decoupling of mechanical systems by using frequency response functions," *Journal of the Brazilian Society of Mechanical Sciences and Engineering*, vol. 46, no. 4, p. 248, 2024.

[34] M. Şen and O. Çakar, "A new method for reducing the number of resonance frequencies of mechanical systems within a specified frequency range with inverse structural modification and pole-zero cancellation," *Journal of Vibration and Control*, vol. 30, no. 17-18, pp. 3985-3996, 2024.

[35] M. Şen and O. Çakar, "An efficient method for structural coupling of mechanical systems by using frequency response functions," *Journal of Vibration and Control*, vol. 30, no. 3-4, pp. 850–859, 2024.

Dicle University
Journal of Engineering
https://dergipark.org.tr/tr/pub/dumf
duje.dicle.edu.tr

Research Article

Tensile and Wear Behaviour of Hybrid SiC-C Reinforced Epoxy Composites

Mehmet Emin DEMİR[1*], Raşit Koray ERGÜN[2]

[1] Batman University, Textile Technology Department, memin.demir@batman.edu.tr, Orcid No 0000-0001-9630-6378
[2] Batman University, Mechanical Engineering Department, rasitkoray.ergun@batman.edu.tr, Orcid No 0000-0002-5440-0646

ARTICLE INFO

Article history:

Received 29 July 2025
Received in revised form 8 September 2025
Accepted 10 September 2025
Available online 30 September 2025

Keywords:

SiC, carbon, hybrid composite, epoxy, tensile load, wear behavior

Doi: 10.24012/dumf.1753416

* Corresponding author

ABSTRACT

In this study, the wear and tensile behaviours of epoxy composites reinforced with SiC (silicon carbide) and C (carbon) were investigated. The influence of SiC and C reinforcement ratios and load parameters on the wear performance were systematically evaluated. The ultimate tensile load and deformation values were observed in neat epoxy samples. The incorporation of SiC and C particles adversely affected the tensile load of hybrid composite due to agglomeration of particles and weak bonding between filler and epoxy. When the SiC content was kept constant and the C content was increased, a noticeable improvement in the tensile load of the composite was observed. Conversely, when the C content was constant and SiC content was increased from 3% to 6%, the tensile load increased from 2053 N to 2409 N. Wear tests were conducted under two different loads (3N and 7N). The lowest coefficient of friction (COF) values were observed in epoxy composites reinforced with 6% SiC and 2% C due to protective layer formation on matrix surface by hard SiC particles and C particles. The addition of hard particles into the epoxy enhanced the wear performance of hybrid composites. SEM analysis of worn samples revealed that, surface deformations and material loss were more pronounced in the neat epoxy samples.

Introduction

Polymer epoxy resins are highly effective materials for use in different industrial applications due to low weight, low cost, and excellent mechanical characteristics [1-3]. Some of these industrial applications include coatings, sports equipment, aerospace and military components, electronics, automotive, and marine engineering. However, epoxy resins exhibit low wear resistance and possess a brittle nature. It is worth noting that reinforcing epoxy resin composites can significantly improve their mechanical characteristics such as hardness, fracture toughness, and wear performance [4,5]. Certain micro and nano particles can decrease the brittleness of epoxy resins and enhance their wear performance. Additionally, the size and shape (e.g., spherical or irregular) of the added particles can effect the overall behaviour of the polymer matrix [6,7]. Shen et al. investigated wear characteristics of PTFE reinforced SiO_2 epoxy composite. As a result, they observed the highest wear performance in epoxy composites containing optimum PTFE at the sliding distance of 1000m and 60N load [8]. Siddhartha et al. researched dry slide wear and mechanical properties of functionally graded epoxy composite reinforced with TiO_2 by taguchi design experimental approach. The lowest wear rates were obtained functionally graded epoxy composites reinforced with 20%-TiO_2. In addition, reinforcement of TiO_2 into obtained functionally graded epoxy composites established an increment at tensile modulus, flexural strength and impact strength [9]. Guermazi et al. described the production process and properties of glass, carbon and glass-carbon hybrid composites. The highest tensile strength, elastic modulus values were found at carbon laminated composites [10]. Babu et al. investigated wear performance of epoxy composite reinforced with debris powder. Epoxy composites reinforced with debris powder demonstrated low wear rates compared to neat composites [11]. Kanchanomai et al. investigated wear performance of epoxy composite reinforced with crushed silica particles. As a result, it was observed that when volume losses of composite increased the contact load increased too. Moreover at high sliding velocities abrasive wear and at high temperature epoxy–matrix deformations were determined [12]. Abenojar et al. studied wear and mechanical characteristics of silica reinforced composite. Mechanical and wear characteristics were effected with nano-SiO_2 reinforcement. As a result it was observed that silica reinforced epoxy nanocomposites showed reduced strength, hardness and Young's modulus values [13]. Nhuapeng et al. conducted mechanical performance of

epoxy resin composites reinforced SiC nanowires. As a result, it was revealed that SiC nanowires enhanced mechanical performance of composite. The highest wear resistance values were obtained at epoxy resin composites reinforced 15% SiC nanowire. In addition tensile strength values of epoxy resin composites enhanced 341% approximately compared to neat epoxy resin composites [14]. Reinforcement of potassium titanate whisker was enhanced wear performance of resin composites and the lowest wear rate values, highest COF were observed in epoxy resin composites reinforced 15% potassium titanate whisker. Although strength and ductility values were exhibited increment by reinforcing [15]. Jagadeesh et al. examined hardness and tribological performance of thermoset and basalt-reinforced polymers. It was observed that hardness values of thermoset polymers were increased with basalt reinforcement and the optimum COF were found at basalt-reinforced polymers with 30% reinfircement ratio [16]. Mucha et al. searched effect of multiwall carbon nanotube on mechanical and wear performance of composites. It was observed that highest wear performance and tensile strength values with percentages between 0.25%-0.5% filled multiwall carbon nanotube between in epoxy resin composites [17]. Veena et al. investigated tribological performance of silica reinforced nanocomposites. Wear loss weights of unfilled and reinforced epoxy composites increased with increment of slide distance and load values. Silica reinforced epoxy nanocomposites revealed proof of mild abrasive wear because of hard ceramic reinforced particles [18]. Bobby and Samad investigated the wear performance of composites reinforced with nanoparticles. It was observed a considerable enhancement in wear behaviour of composites reinforced with particles to use many of tribological applications [19]. Abenojar et al. investigated wear characteristics of composite coated and reinforced with nano and micro ceramic particles. According to the wear test results the highest coefficient of friction values were found in coated epoxy resin composites [20]. Rong Lu et al. explored tribological and mechanical performance of composites reinforced with nano SiO_2 and TiO_2. As a result, it was proved that nano SiO_2 and TiO_2 can improve wear and mechanical features of composites [21]. Medina et al. analyzed tensile and toughness characteristics of epoxy resin reinforced with ZrO_2. It was determined that enhancement of tensile modulus, toughness by increment of ZrO_2 addition without lineal tendency [22]. Sakka et al. studied wear characteristics of epoxy resin reinforced with carbon nanotube and graphite. It was explored that optimum wear resistant results were found in epoxy resin reinforced with treated carbon nanotube [23]. Awwad et al. examined the impact of graphene platelets on wear and mechanical characteristics of composites. As a result, the increment impact of graphene platelets on stiffness, hardness and tribological performance and decrement influance of graphene platelets on tensile strength, strain and friction were observed [24]. Suresha et al. investigated mechanical and wear characteristics of carbon reinforced composite filled with graphite. It was observed that silane treated composites reinforced with graphite established enhanced wear, tensile strength and modulus, hardness values [25]. Suresha et al. investigated wear characteristics of composites. The lowest wear volume loss and ultimate tensile load and modulus were detected for nanocomposites at reinfoced higher than 5% organo-modified montmorillonite [26]. In a study conducted by Rout et al., the effect of SiC reinforcement on the sliding and erosive wear behavior of fiber-reinforced composites was investigated. It was found that the addition of SiC improved the wear resistance of the composites, while an increase in sliding velocity led to greater wear and material loss. Furthermore, it was reported that an increase in applied load resulted in a higher specific wear loss [27]. In another study, the wear resistance of composites obtained by placing SiC-reinforced epoxy plates between thin kraft papers was investigated. It was reported that composites with a high SiC content exhibited greater resistance to frictional forces, resulting in reduced wear loss. Furthermore, an increase in sliding velocity was noted to decrease the mass loss [28]. Li et al. investigated the mechanical and wear behaviors of carbon fiber-reinforced epoxy resin composites filled with SiC nanowires. They reported that the addition of SiC nanowires onto the carbon fibers enhanced the tensile and flexural strength of the hybrid composites. Furthermore, the SiC nanowires adhering to the surface of the carbon fibers provided mechanical interlocking, establishing a strong bond between the epoxy matrix and the fibers, which contributed to the improvement of wear resistance [29]. Apriliani et al. investigated the mechanical and wear characteristics of iron sand/epoxy composites reinforced with carbon powder. They found that the addition of carbon powder reduced the wear rate while increasing the flexural strength and hardness values of the composites [30].

A review of the existing literature reveals that studies investigating the combined use of SiC and C powder to enhance mechanical and wear properties are very limited. C powder possessing high chemical stability, good frictional performance, and favorable thermal properties [31,32] and SiC particles characterized by high hardness, high strength, and excellent impact and wear resistance, were used together to produce hybrid composite materials [33] to develop composites suitable for a wide range of applications in fields such as aerospace and energy.

The main purpose of the study is to reveal the influence of various reinforcements (SiC and C) and their contents (3% and 6%) on wear and tensile performance of epoxy resin. Tensile strength of neat samples and SiC and C particles reinforced composites at varying contents were determined, followed by an examination of their wear performance under different applied loads. Additionally, worn samples were evaluated utilizing Scanning Electron Microscopy (SEM) analysis.

Material and Method

The epoxy (ARC-152) and hardener (W-152) that had self curing property at room temperature for 24h were supplied by ARC Marin Ltd. Epoxy (ARC-152) was used, with tensile strength of 43.35 MPa, elastic modulus of 950 MPa, elongation of 6.5% [34]. SiC and C microparticles, with particle size of 75 and 150 μm respectively, were supplied by Ege Nanotek and KompozitShop. The weight ratio of

epoxy (ARC-152) and hardener (W-152) was 4:1. The epoxy, hardener and particles was stirred by an ultrasonic bath device to disperse homogeneously the reinforcement particles (SiC and C) into the matrix. To prevent agglomeration of reinforcement particles, the mixing process with an ultrasonic bath device continued at a constant temperature for 1 hour. The manufacture process of epoxy composites performed by a contacting open mold without pressure, at room temperature. The mixtures prepared in the proportions (given in Table 1) were poured into the silicon mold. The epoxy composite samples were removed from the mold after 24h curing process at room temperature. Five various types of epoxy composites were produced as given in Table 1.

Table 1. Codes and content of epoxy composites.

Codes	Content of epoxy composite
Neat	Epoxy resin
2SiC-3C	Epoxy resin + 2% SiC + 3% C
2SiC-6C	Epoxy resin + 2% SiC + 6% C
3SiC-2C	Epoxy resin + 3% SiC + 2% C
6SiC-2C	Epoxy resin + 6% SiC + 2% C

The silicon mold prepared for the production of epoxy composites and the produced bone-shaped epoxy composite samples were shown in Figure 1.

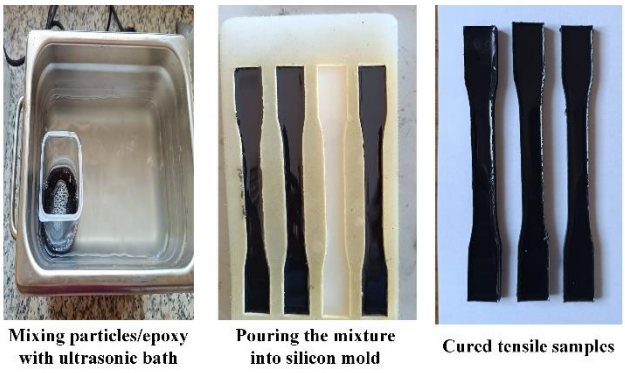


Figure 1. Silicon mold and bone-shaped epoxy composites.

Tensile tests were performed according to ASTM D638 test standard with crosshead speed of 1 mm/min by SHIMADZU AG-IC device. Wear tests were conducted under dry slide condition at room temperature utilizing the Turkyus brand pin on disk apparatus operating at constant 200 rpm rotational speed. Two different loads, 3N, 7N were performed during wear test. The effects of filler addition, filler content, and applied load on COF and wear rate were investigated. The wear testing apparatus used in the experiments is shown in Figure 2. For the tensile and wear tests, three samples were tested for each parameter, and the average of the obtained results was calculated.

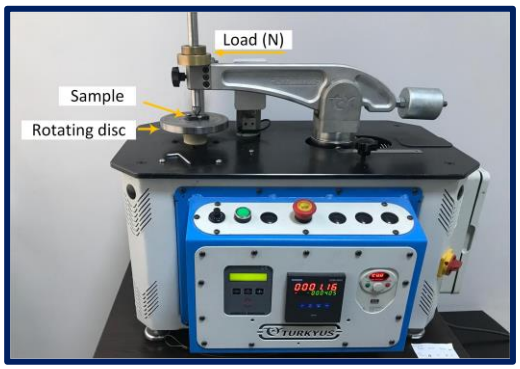


Figure 2. Wear device.

Results and Discussion

Tensile Test Results

Failure load (N) - displacement (mm) graphs of epoxy composites were given in Figure 3. Failure load values, displacements of epoxy composites and decrement ratios were given in Table 2.

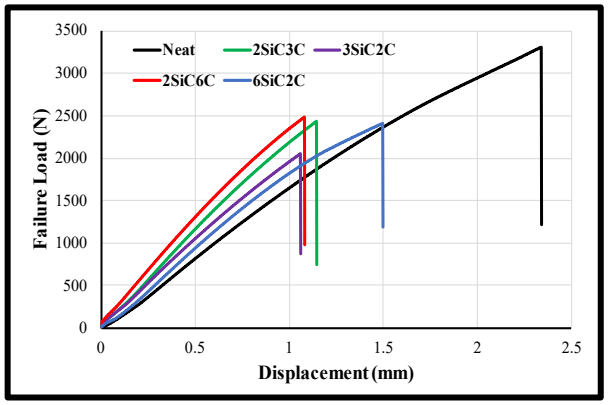


Figure 3. Failure load-displacement graphs of epoxy composites.

Table 2. Mechanical properties of epoxy composites.

Samples	Failure Load (N)	Tensile Strength (MPa)	Tensile Modulus (MPa)	Displacement (mm)
Neat	3307	42.39	1273	2.344
2SiC-3C	2438	31.25	1918	1.146
2SiC-6C	2491	31.94	2070	1.080
3SiC-2C	2053	26.32	1754	1.059
6SiC-2C	2409	30.88	1450	1.497

The characteristic of failure load (N) - displacement (mm) curve of neat and hybrid SiC and C reinforced epoxy composites was approximately identical. As seen in Table 2 maximum tensile load was obtained at neat epoxy samples as 3307 N and minimum tensile load was found in 3SiC2C reinforced epoxy composites as 2053 N. Tensile load values and displacements of epoxy composites with SiC and C microparticles tend to decrease with different percentages of hybrid SiC and C reinforcement compared to neat epoxy samples. The decrease in tensile strength of the epoxy matrix composite with the addition of particles is attributed

to the agglomeration of the added filler particles within the matrix and the weak bonding formed between the matrix and the particles. This phenomenon has been corroborated in similar studies [35,36]. In 3SiC2C and 6SiC2C hybrid reinforced epoxy composites, increasing the SiC microparticle reinforcement ratio also increased the tensile load values. Alaneme et al. observed increments in tensile strength with increasing SiC ratio in bamboo leaf ash particle reinforced aluminum matrix composites [37]. Suresha et al. produced hybrid carbon fiber and SiC reinforced epoxy composites and investigated the mechanical characteristics. Tensile load increment with the increasing of SiC reinforcement ratio in the composite matrix were discovered [38]. Tensile load values in 2SiC3C and 2SiC6C hybrid reinforced epoxy composites exhibited a slight increase tendency with increasing C particle reinforcement ratio. Zhou et al. increased tensile strength by increasing carbon nanotube reinforcement ratio in hybrid carbon nanotube and SiC filled composites [39]. In another study, Zhou et al. produced hybrid carbon nanotube and micro SiC filled AZ61 composites and observed increases in tensile strength with increasing carbon nanotube reinforcement ratio [40]. As seen in Table 2 maximum displacement was obtained in neat epoxy samples as 2.344 mm and minimum displacement was found in 3SiC2C hybrid reinforced epoxy composites as 1.059 mm. In 2SiC3C and 2SiC6C hybrid reinforced epoxy composites, as seen in Table 2, the increment of C particle reinforcement ratio from 3% to 6% increased the displacement values of epoxy composites. In 3SiC2C and 6SiC2C hybrid reinforced epoxy composite, as seen in Table 2, increment of SiC particle reinforcement ratio from 3% to 6% increased the displacement values of epoxy composites 41.4%. Alaneme et al. observed increments in displacement with increasing SiC ratio in bamboo leaf ash particle reinforced aluminum matrix composites [37]. Lv et al. observed decreases in displacements with increasing short carbon fiber reinforcement ratio in hybrid SiC and short carbon fiber-filled aluminum composites [41].

Wear Test Results

Figure 4 shows the variation of COF with applied load for neat epoxy samples, 3SiC2C and 6SiC2C samples over 200 m slide distance. It is detected that COF tends to decrease with increasing load for both neat and hybrid composites. For the neat epoxy samples, the COF decreased from 0.39 μ at a 3 N load to 0.33 μ when load was increased to 7 N, with addition of 3% SiC and 2% C particles to the epoxy matrix, the COF value at 3 N was found to decrease to 0.27 μ. When viscoelastic polymers come into contact with another material, heat is generated in the contact area, and this heat increases with higher contact loads. This results in softening of polymer, and transfer layer formation on counterface leads to a reduction in the COF [42]. These findings are consistent with those reported in similar studies [4,34].

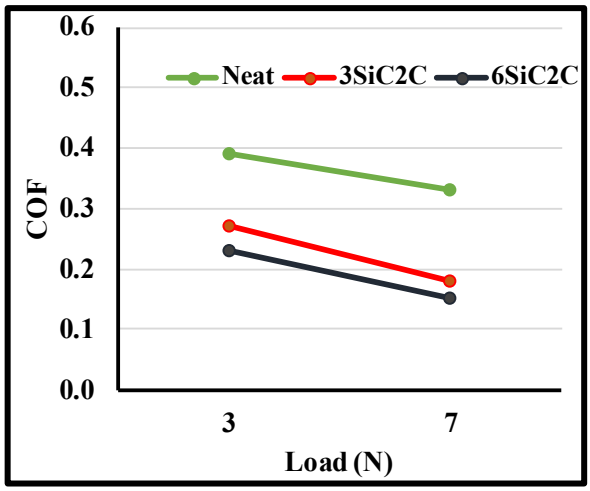


Figure 4. COF values of neat and hybrid composites depending on load.

Figure 5 illustrates variation in wear rates according to applied load and reinforcement content over 200 m sliding distance. For neat epoxy samples, wear rate increased from 2.40 mm^3/m at a 3 N load to 3.75 mm^3/m at 7 N. It was recognized that wear rate increased with the increment of load for all samples. The increment of wear loss with increment of load is a result of enhanced frictional heat, shear forces, and frictional thrust [44,45]. As the surface temperature rises and the matrix begins to soften, matrix degradation occurs under the influence of shear forces, leading to increased wear rates [45,46]. Adding of 3% SiC and 2% C particles decreased wear rate of hybrid composites from 2.40 mm^3/m to 1.06 mm^3/m at a 3 N load. This reduction in wear rate for hybrid composites is a result of protective layer formation on matrix surface by hard SiC particles and C particles, which limits the penetration of the counterface pin into the matrix [47]. Similarly, Suresha et al. stated that the inclusion of SiC particles to glass fiber reinforced composite improved wear resistance by enhancing interface adhesion between matrix and fiber [48]. Findings of Ji et al. are also consistent with these results [49]. When SiC reinforcement content in epoxy matrix was increased from 3% to 6%, the wear rate decreased from 1.60 mm^3/m to 0.93 mm^3/m under a 7 N load. Subbaya et al. examined effect of SiC filler content on wear performance of fiber reinforced composite and found that both presence and increased content of SiC improved the wear resistance. They concluded that existence of hard SiC particles within a ductile matrix enhances the overall matrix hardness, reducing the penetration of the counterface pin and thereby minimizing wear loss [50].

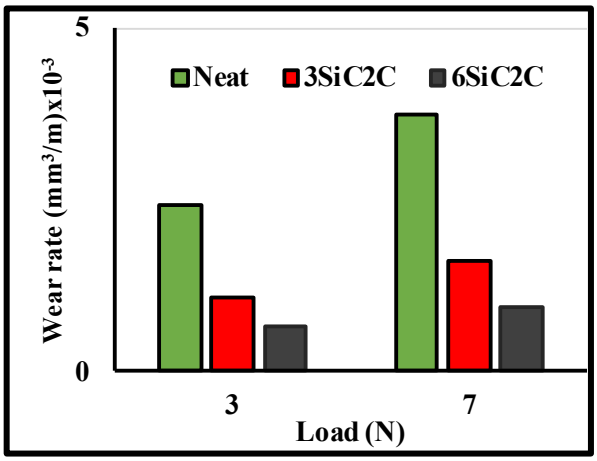


Figure 5. Wear rate values of neat and hybrid composites depending on load.

Wear Surface Morphology

Figure 6a presents worn surface morphology of the neat, 3SiC2C and 6SiC2C filled composites under a 3 N load. It was observed that the neat epoxy samples exhibited deep wear scars on their surface after wear test. In absence of hard filler particles, epoxy matrix could not withstand the applied load, resulting in more pronounced matrix detachments compared to the filled composites. As seen in Figure 6b, addition of 3% SiC and 2% C particles into the epoxy matrix significantly reduced plastic deformation. Matrix debris and surface pits became shallower, indicating improved surface integrity. The incorporation of SiC and C enhanced load-bearing capacity of matrix and acted as a protective barrier between abrasive pin and matrix, thereby enhancing wear resistance. Consequently, severely worn surface transformed into a relatively smoother morphology. In Figure 6c, increasing the SiC content from 3% to 6% further reduced matrix damage on the surface. The observed scratches and pit depths remained more superficial, indicating a decrease in wear loss with increasing SiC content. Moreover, microcrack formation was found to be less frequent at higher reinforcement levels. The enhanced interface adhesion between matrix and filler particles contributed to enhanced wear performance [51].

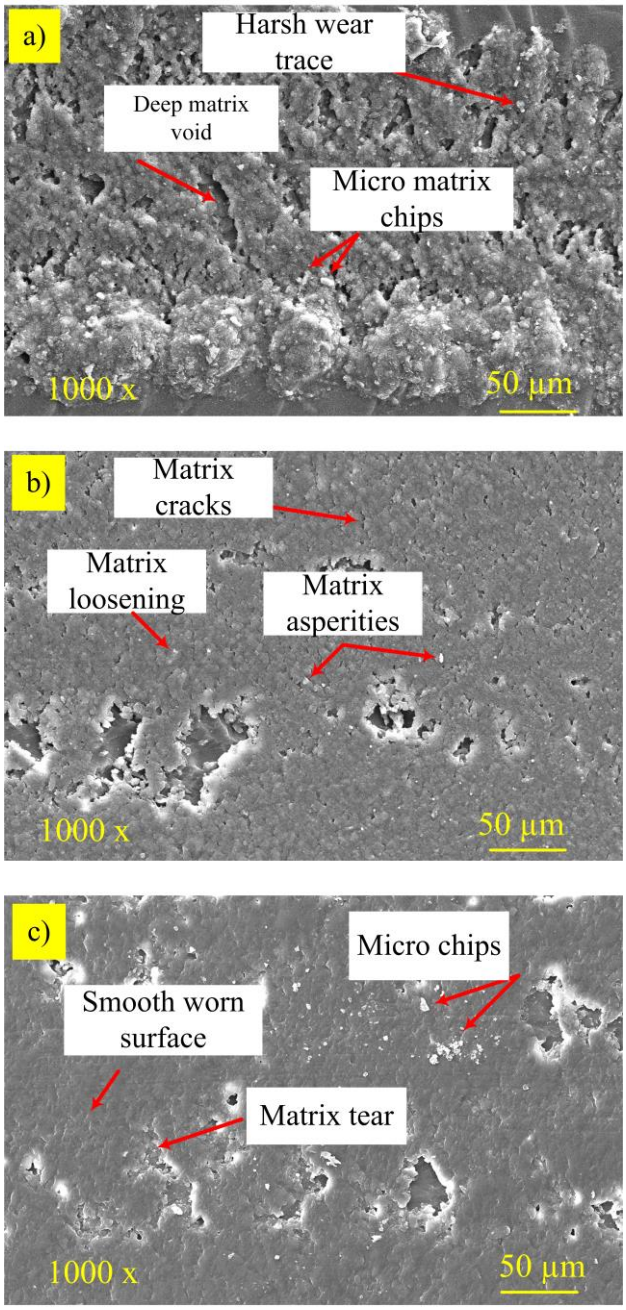


Figure 6. Morphology of worn surfaces a) Neat, b) 3SiC2C, c) 6SiC2C.

Conclusions

The primary objective of the study is to investigate tensile and tribological characteristics of composite produced by incorporating different types and proportions of fillers into epoxy resin. The neat epoxy samples indicated the highest tensile strength, reaching a maximum load of 3307 N, whereas the lowest tensile strength was obtained in the hybrid composites reinforced with 3SiC2C, with a value of 2053 N. Overall, the adding of SiC and C microparticles led to a noticeable reduction in both tensile load and displacement compared to the neat epoxy samples, with the extent of reduction dependent on the filler content. Tribological tests demonstrated that the neat epoxy samples exhibited the COF of 0.39 under a 3 N load, which decreased to 0.33 as the load increased to 7 N. The addition

of 3% SiC and 2% C microparticles resulted in a pronounced reduction in COF, reaching 0.27 under a 3 N load, indicating the significant role of hard fillers in improving frictional performance. For the neat epoxy samples, the wear rate increased from 2.40 mm^3/m under a 3 N load to 3.75 mm^3/m at 7 N. It was noted that the neat epoxy samples showed deep wear trace on its surface following the wear test. Due to lack of hard filler microparticles, epoxy matrix was unable to resist the applied load, leading to more significant matrix detachments in comparison to the reinforced composites.

Ethics committee approval and conflict of interest statement

There is no need to obtain permission from the ethics committee for the article prepared.

There is no conflict of interest with any person / institution in the article prepared.

Author contributions

The authors declare that they have contributed equally to the article.

References

[1] Q. Wang and D. S. Su, "Reinforcing epoxy resin with activated carbon: A way of high rate of quality and price," *Compos. Commun.*, vol. 9, pp. 54–57, 2018, doi: https://doi.org/10.1016/j.coco.2018.03.008.

[2] M. E. Demir, Y. H. Çelik, and E. Kilickap, "Effect of matrix material and orientation angle on tensile and tribological behavior of jute reinforced composites," vol. 61, no. 8, pp. 806–812, 2019, doi: doi:10.3139/120.111388.

[3] A. Khan *et al.*, "Low-Cost Carbon Fillers to Improve Mechanical Properties and Conductivity of Epoxy Composites," 2017. doi: 10.3390/polym9120642.

[4] M. E. Demir and R. K. Ergün, "Mechanical and wear performance of Al-, mica-, SiO2-filled glass fiber-reinforced composites and prediction of wear properties with artificial neural networks," *Proc. Inst. Mech. Eng. Part E J. Process Mech. Eng.*, p. 09544089241307840, Jan. 2025, doi: 10.1177/09544089241307840.

[5] B. Weidenfeller, M. Höfer, and F. R. Schilling, "Thermal conductivity, thermal diffusivity, and specific heat capacity of particle filled polypropylene," *Compos. Part A Appl. Sci. Manuf.*, vol. 35, no. 4, pp. 423–429, 2004, doi: https://doi.org/10.1016/j.compositesa.2003.11.005.

[6] M. E. Demir, H. Topkaya, T. Bağatır, and Y. H. Çelik, "Impact of Reinforcement Ratio on Mechanical Properties and Wear Behaviour of Graphene Nanoplatelet Reinforced Epoxy Composites TT - Grafen nanoplatelet takviyeli epoksi kompozitlerin mekanik özellikleri ve aşınma davranışı üzerinde takviye oranının etkisi," *Politek. Derg.*, vol. 27, no. 6, pp. 2181–2192, 2024, doi: 10.2339/politeknik.1307849.

[7] M. Kalin, M. Zalaznik, and S. Novak, "Wear and friction behaviour of poly-ether-ether-ketone (PEEK) filled with graphene, WS2 and CNT nanoparticles," *Wear*, vol. 332–333, pp. 855–862, 2015, doi: 10.1016/j.wear.2014.12.036.

[8] J. T. Shen, M. Top, Y. T. Pei, and J. T. M. De Hosson, "Wear and friction performance of PTFE filled epoxy composites with a high concentration of SiO2 particles," *Wear*, vol. 322–323, pp. 171–180, 2015, doi: https://doi.org/10.1016/j.wear.2014.11.015.

[9] Siddhartha, A. Patnaik, and A. D. Bhatt, "Mechanical and dry sliding wear characterization of epoxy–TiO2 particulate filled functionally graded composites materials using Taguchi design of experiment," *Mater. Des.*, vol. 32, no. 2, pp. 615–627, 2011, doi: https://doi.org/10.1016/j.matdes.2010.08.011.

[10] N. Guermazi, N. Haddar, K. Elleuch, and H. F. Ayedi, "Investigations on the fabrication and the characterization of glass/epoxy, carbon/epoxy and hybrid composites used in the reinforcement and the repair of aeronautic structures," *Mater. Des.*, vol. 56, pp. 714–724, 2014, doi: https://doi.org/10.1016/j.matdes.2013.11.043.

[11] N. B. Karthik Babu, T. Ramesh, and S. Muthukumaran, "Physical, tribological and viscoelastic behavior of machining wear debris powder reinforced epoxy composites," *J. Clean. Prod.*, vol. 272, p. 122786, 2020, doi: https://doi.org/10.1016/j.jclepro.2020.122786.

[12] C. Kanchanomai, N. Noraphaiphipaksa, and Y. Mutoh, "Wear characteristic of epoxy resin filled with crushed-silica particles," *Compos. Part B Eng.*, vol. 42, no. 6, pp. 1446–1452, 2011, doi: https://doi.org/10.1016/j.compositesb.2011.04.046.

[13] J. Abenojar, J. Tutor, Y. Ballesteros, J. C. del Real, and M. A. Martínez, "Erosion-wear, mechanical and thermal properties of silica filled epoxy nanocomposites," *Compos. Part B Eng.*, vol. 120, pp. 42–53, 2017, doi: https://doi.org/10.1016/j.compositesb.2017.03.047.

[14] W. Nhuapeng, W. Thamjaree, S. Kumfu, P. Singjai, and T. Tunkasiri, "Fabrication and mechanical properties of silicon carbide nanowires/epoxy resin composites," *Curr. Appl. Phys.*, vol. 8, no. 3, pp. 295–299, 2008, doi: https://doi.org/10.1016/j.cap.2007.10.074.

[15] M. Sudheer, R. Prabhu, K. Raju, and T. Bhat, "Effect of Filler Content on the Performance of Epoxy/PTW Composites," *Adv. Mater. Sci. Eng.*, vol. 2014, no. 1, p. 970468, Jan. 2014, doi: https://doi.org/10.1155/2014/970468.

[16] P. Jagadeesh, S. M. Rangappa, and S. Siengchin,

"Friction and wear analysis of basalt micro-filler loaded various epoxies and esters based thermoset polymer composites," *J. Build. Eng.*, vol. 86, p. 108927, 2024, doi: https://doi.org/10.1016/j.jobe.2024.108927.

[17] M. Mucha *et al.*, "Effect of MWCNTs on Wear Behavior of Epoxy Resin for Aircraft Applications," 2020. doi: 10.3390/ma13122696.

[18] M. G. Veena, N. M. Renukappa, B. Suresha, and K. N. Shivakumar, "Tribological and electrical properties of silica-filled epoxy nanocomposites," *Polym. Compos.*, vol. 32, no. 12, pp. 2038–2050, Dec. 2011, doi: https://doi.org/10.1002/pc.21221.

[19] S. Bobby and M. A. Samad, "Enhancement of tribological performance of epoxy bulk composites and composite coatings using micro/nano fillers: a review," *Polym. Adv. Technol.*, vol. 28, no. 6, pp. 633–644, Jun. 2017, doi: https://doi.org/10.1002/pat.3961.

[20] J. Abenojar, Y. Ballesteros, M. Bahrami, M. A. Martínez, and J. C. del Real, "Wear Behavior of Epoxy Resin Reinforced with Ceramic Nano- and Microparticles," 2024. doi: 10.3390/polym16070878.

[21] S. Lu, J.- Hongyu, H. Zhang, and X. Wang, "Wear and mechanical properties of epoxy/SiO2-TiO2 composites," *J. Mater. Sci.*, vol. 40, no. 11, pp. 2815–2821, 2005, doi: 10.1007/s10853-005-2437-2.

[22] R. Medina, F. Haupert, and A. K. Schlarb, "Improvement of tensile properties and toughness of an epoxy resin by nanozirconium-dioxide reinforcement," *J. Mater. Sci.*, vol. 43, no. 9, pp. 3245–3252, 2008, doi: 10.1007/s10853-008-2547-8.

[23] M. M. Sakka, Z. Antar, K. Elleuch, and J. F. Feller, "Tribological response of an epoxy matrix filled with graphite and/or carbon nanotubes," *Friction*, vol. 5, no. 2, pp. 171–182, 2017, doi: 10.1007/s40544-017-0144-z.

[24] K. Y. Eayal Awwad, B. F. Yousif, K. Fallahnezhad, K. Saleh, and X. Zeng, "Influence of graphene nanoplatelets on mechanical properties and adhesive wear performance of epoxy-based composites," *Friction*, vol. 9, no. 4, pp. 856–875, 2021, doi: 10.1007/s40544-020-0453-5.

[25] B. Suresha, B.N. Ramesh, K.M. Subbaya, and G. Chandramohan, "Mechanical and Three-body Abrasive Wear Behavior of Carbon-Epoxy Composite With and Without Graphite Filler," *J. Compos. Mater.*, vol. 44, no. 21, pp. 2509–2519, May 2010, doi: 10.1177/0021998310369589.

[26] B Suresha, BL Ravishankar, and L Sukanya, "Dynamic mechanical analysis and three-body abrasive wear behavior of epoxy nanocomposites," *J. Reinf. Plast. Compos.*, vol. 32, no. 1, pp. 61–71, Oct. 2012, doi: 10.1177/0731684412464914.

[27] L. N. Rout, D. Mishra, and P. T. R. Swain, "Influence of Silicon Carbide (SiC) Reinforcement on Sliding and Erosive Wear Characteristics of Glass Fiber/Epoxy Hybrid Composites," *Trans. Indian Inst. Met.*, vol. 76, no. 4, pp. 1113–1121, 2023, doi: 10.1007/s12666-022-02828-7.

[28] A. Nassar, M. Younis, M. Ismail, and E. Nassar, "Improved Wear-Resistant Performance of Epoxy Resin Composites Using Ceramic Particles," 2022. doi: 10.3390/polym14020333.

[29] B. Li, S. Qian, C. Sun, M. Wang, and X. Zhan, "Mechanical properties and wear resistance of Cf / epoxy resin composites with in-situ grown SiC nanowires on carbon fibers," *Compos. Interfaces*, vol. 30, no. 9, pp. 923–939, Sep. 2023, doi: 10.1080/09276440.2023.2179250.

[30] N. F. Apriliani, W. A. Wirawan, M. Muslimin, R. A. Ilyas, M. A. Rahma, and A. T. Agus Salim, "Improving wear performance, physical, and mechanical properties of iron sand/epoxy composite modified with carbon powder," *Results Mater.*, vol. 21, p. 100532, 2024, doi: https://doi.org/10.1016/j.rinma.2024.100532.

[31] Y. Li, D. Li, H. Cheng, C. Han, and L. Xiao, "Morphology and physical properties of composites based on high-density polyethylene/propylene-ethylene random copolymers blends and carbon black," *Polym. Test.*, vol. 123, p. 108050, 2023, doi: https://doi.org/10.1016/j.polymertesting.2023.108050.

[32] S. Wu, Y. Liu, Y. Ge, L. Ran, K. Peng, and M. Yi, "Structural transformation of carbon/carbon composites for aircraft brake pairs in the braking process," *Tribol. Int.*, vol. 102, pp. 497–506, 2016, doi: https://doi.org/10.1016/j.triboint.2016.06.018.

[33] Haixia Hu and Sinian Zhang, "Mechanical and tribological properties of silicon carbide /carbon fiber/epoxy resin based composites," *J. Eng. Fiber. Fabr.*, vol. 19, p. 15589250231214228, Jan. 2024, doi: 10.1177/15589250231214229.

[34] E. Çetkin, M. E. Demir, and R. K. Ergün, "The effect of different fillers, loads, and sliding distance on adhesive wear in woven e-glass fabric composites," *Proc. Inst. Mech. Eng. Part E J. Process Mech. Eng.*, p. 095440892211368, 2022, doi: 10.1177/09544089221136808.

[35] W. S. Kharat and J. S. Sidhu, "Development of epoxy based composites filled with boron carbide (B4C), tungsten disulphide (WS2) and evaluation of its mechanical properties," *Int J Mech Eng Res*, vol. 6, pp. 19–30, 2016.

[36] H. Gürbüz, İ. H. Akcan, Ş. Baday, and M. E. Demir, "Investigation of Drilling Performances, Tribological and Mechanical Behaviors of GFRC Filled with B4C and Gr," *Arab. J. Sci. Eng.*, 2024, doi: 10.1007/s13369-024-09392-w.

[37] K. Alaneme, B. O. Ademilua, and M. Bodunrin, "Mechanical Properties and Corrosion Behaviour of Aluminium Hybrid Composites Reinforced with Silicon Carbide and Bamboo Leaf Ash," *Tribol. Ind.*, vol. 35, pp. 25–35, Mar. 2013.

[38] B. Suresha, K. Adappa, and N. K. Subramani, "Mechanical and tribological behaviours of epoxy hybrid composites reinforced by carbon fibers and silicon carbide whiskers," *Mater. Today Proc.*, vol. 5, no. 8, Part 3, pp. 16658–16668, 2018, doi: https://doi.org/10.1016/j.matpr.2018.06.027.

[39] X. Zhou, D. Su, C. Wu, and L. Liu, "Tensile Mechanical Properties and Strengthening Mechanism of Hybrid Carbon Nanotube and Silicon Carbide Nanoparticle-Reinforced Magnesium Alloy Composites," *J. Nanomater.*, vol. 2012, no. 1, p. 851862, Jan. 2012, doi: https://doi.org/10.1155/2012/851862.

[40] M. Y. Zhou *et al.*, "Achieving ultra-high strength and good ductility in AZ61 alloy composites containing hybrid micron SiC and carbon nanotubes reinforcements," *Mater. Sci. Eng. A*, vol. 768, p. 138447, 2019, doi: https://doi.org/10.1016/j.msea.2019.138447.

[41] Z. Lv, J. Sha, G. Lin, J. Wang, Y. Guo, and S. Dong, "Mechanical and thermal expansion behavior of hybrid aluminum matrix composites reinforced with SiC particles and short carbon fibers," *J. Alloys Compd.*, vol. 947, p. 169550, 2023, doi: https://doi.org/10.1016/j.jallcom.2023.169550.

[42] Y. Yamaguchi, *Tribology of plastic materials: their characteristics and applications to sliding components*, vol. 16. Elsevier, 1990.

[43] H. Unal, A. Mimaroglu, U. Kadıoglu, and H. Ekiz, "Sliding friction and wear behaviour of polytetrafluoroethylene and its composites under dry conditions," *Mater. Des.*, vol. 25, no. 3, pp. 239–245, 2004, doi: https://doi.org/10.1016/j.matdes.2003.10.009.

[44] A. Erdoğan, M. S. Gök, V. Koç, and A. Günen, "Friction and wear behavior of epoxy composite filled with industrial wastes," *J. Clean. Prod.*, vol. 237, p. 117588, 2019, doi: https://doi.org/10.1016/j.jclepro.2019.07.063.

[45] M. E. Demir, "The effect of filler type (tungsten carbide, zinc oxide) and content on the mechanical and wear behavior of jute/flax reinforced epoxy hybrid composites: Experimental and artificial neural network analysis," *Polym. Compos.*, vol. n/a, no. n/a, Apr. 2025, doi: https://doi.org/10.1002/pc.29879.

[46] A. A. El-Hameed El-Ebissy, M. N. Michael, and S. K. Eldin Abdelhameed, "Effect of nano zinc oxide on the structural characteristic, tensile thermal properties of textile fabrics," *J. Ind. Text.*, vol. 46, no. 1, pp. 130–142, Mar. 2015, doi: 10.1177/1528083715576321.

[47] Amal Nassar, Mostafa Salem, Ismail El-Batanony, and Eman Nassar, "Improving wear resistance of epoxy/SiC composite using a modified apparatus," *Polym. Polym. Compos.*, vol. 29, no. 9_suppl, pp. S389–S399, Mar. 2021, doi: 10.1177/09673911211002731.

[48] B. Suresha, G. Chandramohan, Kishore, P. Sampathkumaran, and S. Seetharamu, "Mechanical and three-body abrasive wear behaviour of SiC filled glass-epoxy composites," *Polym. Compos.*, vol. 29, no. 9, pp. 1020–1025, Sep. 2008, doi: https://doi.org/10.1002/pc.20576.

[49] Q. L. Ji, M. Q. Zhang, M. Z. Rong, B. Wetzel, and K. Friedrich, "Friction and Wear of Epoxy Composites Containing Surface Modified SiC Nanoparticles," *Tribol. Lett.*, vol. 20, no. 2, pp. 115–123, 2005, doi: 10.1007/s11249-005-8301-3.

[50] K. M. Subbaya, B. Suresha, N. Rajendra, and Y. S. Varadarajan, "Taguchi approach for characterization of three-body abrasive wear of carbon-epoxy composite with and without SiC filler," *Compos. Interfaces*, vol. 19, no. 5, pp. 297–311, Jul. 2012, doi: 10.1080/15685543.2012.720903.

[51] K. Kumaresan, G. Chandramohan, M. Senthilkumar, B. Suresha, and S. Indran, "Dry Sliding Wear Behaviour of Carbon Fabric-Reinforced Epoxy Composite with and without Silicon Carbide," *Compos. Interfaces*, vol. 18, no. 6, pp. 509–526, Jan. 2011, doi: 10.1163/156855411X610241.

Dicle University
Journal of Engineering
https://dergipark.org.tr/tr/pub/dumf
duje.dicle.edu.tr

Araştırma Makalesi/Research Article

Değişken piyasalar için memetik algoritma ile sınır tenörleri eniyilemesi

Optimization of cut-off grades with memetic algorithms for volatile markets

Erhan Çetin[1*]

[1]Dicle Üniversitesi, Maden Mühendisliği Bölümü, erhan@dicle.edu.tr

ORCID: https://orcid.org/0000-0003-0053-6932

MAKALE BİLGİLERİ

Makale Geçmişi:

Geliş 8 Mayıs 2025
Revizyon 17 Haziran 2025
Kabul 25 Haziran 2025
Online 30 Eylül 2025

Anahtar Kelimeler:

Değişken piyasa, memetik algoritma sınır tenörü, eniyileme

ÖZ

Sınır tenörleri, maden ile yan kayacı ayırmada kullanılan, madenciliğin ve maden yataklarının değerlendirilmesinin en temel konularındandır. Paranın zaman değerini göz ardı eden ve maden yataklarının alt optimum düzeyde değerlenmesine neden olan, statik veya sabit bir sınır tenörünün, bir maden işletmesinde, madenin ömrü boyunca kullanılması şeklindeki geleneksel yöntem, maden yataklarının en ekonomik şekilde değerlendirilmesi önlemektedir. Maksimum net bugünkü değeri elde etmek için, dönemsel azalan bir sınır tenörleri silsilesi elde edilmelidir. Bir madenin ömrü boyunca statik bir sınır tenörü uygulaması yerine, optimum sınır tenörleri silsilesinin belirlenmesi, net bugünkü değeri en üst düzeye çıkaracaktır. Memetik algoritma, evrimsel algoritmalar ile yerel arama yöntemlerini birlikte kullanan ve büyük çaplı problemler için çok sağlam sonuçlar veren bir eniyileme yöntemidir. Madencilik ürünlerinin satış fiyatları dalgalıdır ve gelecekteki değerler bilinemez. Küresel pazarda bir madencilik ürününün satış fiyatındaki dalgalanma, öngörülmüş her ekonomik değerlemeyi geçersiz kılabilir. Ancak, satış fiyatlarının gelecekteki değerleri tahmin edilebilir. Bu makalede, sınır tenörleri eniyilemesi ile ilgili sorunlar açıklanmış, değişken piyasa koşullarında sınır tenörleri eniyilemesinde memetik algoritmanın kullanımı gösterilmiştir. Bu konuda geliştirilen yazılım, değişken piyasa koşulları altında maden yatakları için optimum sınır tenörleri silsilesini bulmaktadır.

ARTICLE INFO

Article history:

Received 8 May 2025
Received in revised form 17 June 2025
Accepted 25 June 2025
Available online 30 September 2025

Keywords:

Volatile market, memetic algorithms, cut-off grades, optimization

Doi: 10.24012/dumf.1695275

* Sorumlu Yazar

ABSTRACT

Cut-off grades are one of the most fundamental issues in mining and mineral deposits appraisal, used to separate ore from host rock. The traditional method of using a static or fixed cut-off grade throughout the life of a mine, which ignores the time value of money and causes sub-optimal valuation of mineral deposits, prevents the most economical valuation of mineral deposits. In order to obtain the maximum net present value, a gradually decreasing cut-off grades sequence should be obtained. Instead of applying a static cut-off grade throughout the life of a mine, determining the optimum cut-off grades sequence will maximize the net present value. Memetic algorithms is an optimization method that uses evolutionary algorithms and local search methods together and provides very robust results for large-scale problems. Sales prices of mining products are volatile and future values are unknown. Fluctuations in the sales price of a mining product in the global market can invalidate every predicted economic valuation. However, future values of sales prices can be estimated. In this article, the problems related to the optimization of cut-off grades are explained and the use of memetic algorithms in the optimization of cut-off grades under volatile market conditions is shown. The software developed in this regard finds the optimum cut-off grades sequence for mineral deposits under volatile market conditions.

Giriş

Sınır tenörü, cevher ve yan kayaç arasındaki sınırları belirlediği için, optimum sınır tenörlerinin belirlenmesi madenciliğin temel bir konusudur.

Sınır tenörlerine yönelik geleneksel yaklaşım, gelirin maliyete eşit olduğu kesim tenörünü, dolayısıyla sabit bir tenörü, kullanmaktır. Bu yaklaşım, paranın zaman değerini tamamen göz ardı eder ve genellikle maden kaynağının optimum olmayan bir şekilde değerlendirilmesine yol açar. Paranın zaman değeri, daha yüksek tenörlü bloklar hala mevcutken düşük tenörlü blokları çıkarmanın fırsat maliyetiyle birlikte, maden ömrünün ilk yıllarında daha yüksek sınır tenörlerinde madencilik yapmak ile maden ömrünün sonraki yıllarında daha düşük sınır tenörlerinde madencilik yapmak arasında avantajlı bir takas olmasını sağlar. Bir madencilik operasyonundan elde edilen kâr, uygulanan sınır tenörleri silsilesi ve sonucunda elde edilen cevher tonajlarının doğrudan bir fonksiyonudur. Kâr bu duruma göre değiştiğinden, en yüksek kârı veren bir eniyi sınır tenörleri silsilesi olacaktır. En yaygın kullanılan sınır tenörleri eniyileme kriteri, kârların maksimum net bugünkü değeridir. Net bugünkü değer, bir maden işletmesinde, işletmenin farklı üretim dönemlerinde elde edilen karların, belirlenen bir indirgeme oranı ile indirgenerek, işletmenin başlangıcında toplanması sonucu bulunan parasal ifadedir. Burada uygulanan indirgeme oranı yine paranın zaman değeri kaynaklıdır. Bir maden işletmesinin karlılığının değerlendirildiği yöntemler arasında en sık kullanılan yöntem net bugünkü değer yöntemidir. Net bugünkü değeri maksimize etme hedefi, birim zaman başına kârın maksimize edilmesiyle elde edilir. Bu süreç, operasyonun ilk yıllarında, cevher işleme tesisinin gereksinimlerini karşılamak için yeterli cevher sağlayabilen en yüksek sınır tenörlerinin uygulanmasını gerektirir. Zaman geçtikçe sınır tenörleri düşürülmeli ve böylece fırsat maliyeti düşürülmelidir. Dolayısıyla, en yüksek net bugünkü değer elde edilir. Fırsat maliyeti, paranın zaman değerinden kaynaklanmaktadır. Aynı ederdeki bir miktar para, enflasyonsuz bir ortamda, insanlar tarafından, farklı zamanlarda farklı değerde algılanmakta ve uygulanmaktadır. Önceki bir miktar para, sonraki aynı miktardaki paradan daha değerlidir. Bunun temel sebebi de insan ömrünün sonlu olmasıdır. Reel faizin sebebi de paranın bu zaman değeridir. Fırsat maliyeti ise, işletmenin ilk yıllarında, yüksek bir gelir, sonraki yıllarda daha düşük gelirle çalışmayı gerektirir. Bu da işletmenin işl yıllarında yüksek, sonraki yıllarında ise düşük sınır tenörleri uygulamasını, yani optimum sınır tenörlerini gerektirir. Sınır tenörleri eniyilemesinde, işletmenin ömrü boyunca hep aynı sınır tenörü ile çalışmak, işletmenin ilk yıllarında daha yüksek sınır tenörleri ile sonraki yıllarda ise azalarak değişen sınır tenörleri ile çalışmaya nazaran bir fırsat maliyeti oluşturmaktadır.

Ancak, işletme ömrü boyunca sabit bir sınır tenörü ile çalışmak yerine, optimum sınır tenörleri ile çalışmak, daha yüksek indirgenmiş kar elde edilmesini sağlar iken, işletme ömrünü kısaltmaktadır. Bunun sebebi, işletmenin ilk yıllarında yüksek sınır tenörlerinin uygulanması sonucunda, bir miktar orta seviyede ortalama tenöre sahip blokların, o yıllara has olarak, cevher olarak kabul edilmemesidir.

Bir sınır tenörü eniyilemesi işlemi için girdiler arasında, bir maden ürününün satış fiyatı en değişken olanıdır. Küresel pazarda bir madencilik ürününün satış fiyatındaki güçlü bir değişiklik, her türlü ekonomik değerlemeyi uygulanamaz hale getirebilir. Optimum sınır tenörleri silsilesini bulmadan en fazla geliri elde etmek mümkün olmadığından, kullanılacak sınır tenörlerini bulmak için algoritmaya bir madencilik ürününün değişken satış fiyatları eklenmelidir.

Bu makalenin amacı, memetik algoritmalar aracılığıyla maden yatakları için sınır tenörlerinin optimal silsilelerini belirlemek için genel yöntemler geliştirmek ve bu yöntemi bilgisayar programlarında uygulamaktır. Bu amaçla geliştirilen bilgisayar programı, maden yatakları için optimum sınır tenörleri silsilesini belirleme yeteneğine sahiptir. Bu çalışmanın özgünlüğü, cevher satış fiyatlarının değişkenliği dikkate alınarak satış fiyatının algoritmaya stokastik olarak eklendiği ve memetik algoritma yönteminin uygulandığı ilk çalışma olmasıdır.

Sınır Tenörleri Eniyilemesi

Sınır tenörleri madencilikte, iki eylemi ayırmada kullanılır. Çıkarılacak madenin mineral içeriği belirlenen sınır tenörünün üzerindeyse, cevher olarak sınıflandırılır ve belli bir kârla çıkarılabilir. Aksi takdirde, yan kayaç olarak sınıflandırılır ve kullanılan madencilik yöntemine bağlı olarak atık sahalarına gönderilir veya yerinde bırakılır.

Lane [1],[2], optimum sınır tenörleri teorisinin öncüsü olarak kabul edilmelidir. Kapsamlı bir ekonomik teori ve optimum sınır tenörlerini belirlemek için bir algoritma sağlamıştır. Çalışma, bir madencilik operasyonunu üç ana aşamaya ayırmaya dayanmaktadır: madencilik, mineral işleme ve rafinasyon ve/veya pazarlama. Sınır tenörleri, bu aşamaların her bir çifti arasındaki çeşitli sınırlamalara bağlıdır.

Lane'in birim başına net bugünkü değer için temel ifadesi aşağıdadır:

$$v = (p - k) * x * y * a - x * h - m - (f + F) * t \quad (1)$$

burada;
v: net bugünkü değer,
p: pazarlanan ürün birimi başına fiyat,
k: pazarlama değişken maliyeti,
x: cevher/malzeme oranı,
y: cevher işleme verimi,
a: ortalama tenör,
h: cevher işleme değişken maliyeti,
m: madencilik değişken maliyeti,
f: sabit maliyet,
F: fırsat maliyeti,
t: birim başına zaman.

Formüle fırsat maliyetinin dahil edilmesi, azalarak değişen sınır tenörleri silsilesini garanti eder.

Cetin and Dowd [3], polimetalik yataklarda sınır tenörleri eniyilemesinde genetic algoritma yöntemini uygulamışlardır. Asad [4] ve Asad and Topal [5] maliyetler ve metal fiyatlarında olası artışlar ve döküm sahasındaki bir

kısım malzemenin sonraki yıllarda düşen sınır tenörleri çerçevesinde yeniden değerlendirilmesi doğrultusunda sınır tenörleri eniyilemesi çalışmışlar, Gholamnejad [6, 7] sınır tenörleri eniyilemesi teorisine rehabilitasyon maliyetini eklemiştir. Azmi et al. [8] sınır tenörleri eniyilemesinde kullanılan indirgenmiş karın yanında gerçek opsiyonlar yöntemini de kullanmışlardır. Çetin [9] satış fiyatını algoritmaya stokastik olarak ekleyerek genetik algoritma ile optimum sonuca varmıştır.

Memetik Algoritma ile Eniyileme

Memetik algoritmalar evrimsel algoritmalar sınıfında değerlendirilir. Evrimsel algoritmalar 1970'lerden bu yana uzun bir yol kat etmiştir. Kökenleri Holland'a [10] kadar uzanır. Memetik algoritmalar, biyolojik ve kültürel evrimleri birleştiren bir kombinasyonel arama motorudur. Memetik Algoritmaların temel felsefesi Richard Dawkins'in [11] kavramına dayanmaktadır. Dawkins'ten alıntı: "Mem örnekleri melodiler, fikirler, sloganlar, giyim modaları, çanak çömlek veya kemer inşa etme yollarıdır. Genler, spermler veya yumurtalar aracılığıyla vücuttan vücuda sıçrayarak gen havuzunda kendilerini yaydıkları gibi, memler de geniş anlamda taklit olarak adlandırılabilecek bir süreçle beyinden beyne sıçrayarak kendilerini mem havuzunda yayarlar." Ayrıca, 'memetik' sıfatı Richard Dawkins tarafından türetilen 'mem' teriminden gelir.

Memetik algoritmalar, popülasyona dayalı genel bir yöntem ile her bir birey tarafından yapılan yerel bir arama arasındaki bir evlilik olarak görülebilir (Garg [12]).

Bu araştırmada kullanılan yerel arama, optimumun mevcut durum ile komşu yılların sınır tenörleri arasında yattığı varsayımına dayanan yerel bir iyileştirme amaçlı sezgisel yöntemdir. Genetik algoritmalar tarafından üretilen en iyi çözümleri ince ayarlamak (veya odaklamak) için kullanılır. Memetik algoritmanın genetik algoritmadan temel farkı olan yerel arama ile, genetik algoritmadan elde edilen optimum sonuçlar, değişikliklere uğratılarak, yeniden değerlendirilir. Genetik algoritma sonuçlarından daha iyi değerlere ulaşılır ise, yeni sınır tenörleri silsilesi kabul edilir. Ulaşılmaz ise, genetik algoritma sonucu elde edilen optimum yapı kabul edilir. Bu yüzden, memetik algoritmadan elde edilen sonucun genetik algoritmadan elde edilen sonuçtan kötü olması mümkün değildir. Ancak, tersi mümkündür.

Memetik algoritmalar, özellikle büyük ölçekli optimizasyon problemlerinin çözümüne uygun evrimsel algoritmalardır. Olasılıksal algoritmalar sınıfına aittirler ancak yönlendirilmiş ve stokastik aramaları birleştirdikleri için rastgele algoritmalardan çok farklıdırlar. Evrimsel arama yöntemlerinin bir diğer önemli özelliği, olası çözümlerden oluşan bir popülasyonu sürdürmeleridir. Memetik algoritmalar ayrıca genetik operatörleri kullanarak yerel optimumlardan kolayca kaçabilirler.

Memetik algoritmada her bir kromozom (ya da birey) bir sınır tenörleri silsilesini içeren genlerden oluşur, Her bir gen ise bitlerden oluşur. Her bir bit ise, kromozomdaki genlerin bir hanesini temsil eder. Bir memetik algoritma uygulamasında, her bir jenerasyon (ya da nesil) için araştırılan çözüm kümesine ya da kromozom sayısına popülasyon (ya da nüfus) denir. Her bir yeni jenerasyon için, popülasyon içerisinden rastgele seçilen her bir çift kromozom, ebeveynler olarak çaprazlamaya (eşleşme) tabi tutulur. Ayrıca, rastgele seçilen bazı kromozomlar mutasyona tabi tutulurlar.

Memetik algoritmada seçilen popülasyon ve jenerasyon sayısı parametreleri ne kadar yüksek seçilir ise, sonucu iyileştirme olasılığı artabilir, ancak programın çalışma süresini çok uzatabileceğinden, optimum bir düzeyde tutulmalıdır. Çaprazlama oranı ve mutasyon oranı parametrelerinin çok yüksek alınması arama alanını genişletip yerel optimumlardan kaçılmasını sağlayabilir ancak, mevcut iyi bölgelerden uzaklaşma riskini de barındırdığı için optimum bir düzeyde tutulmalıdır.

Memetik algoritmalar için geliştirilen bilgisayar programının akış şeması ve algoritma adımları aşağıdaki gibidir:

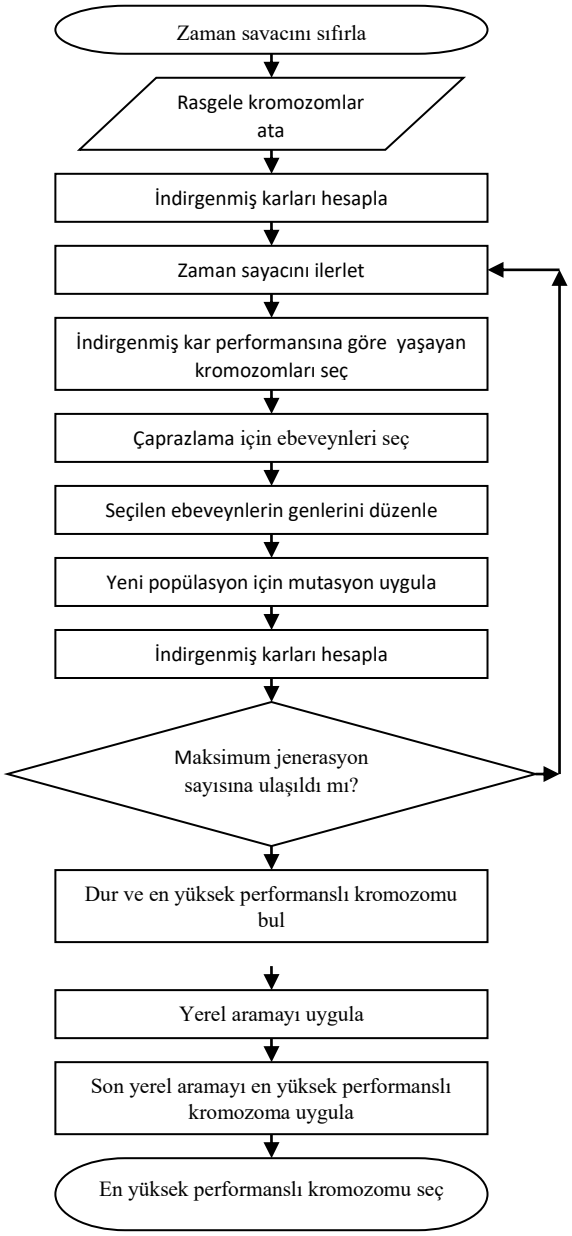


Figure 1. Memetik algoritma akış şeması

1. Çözüm alanını kodlama. İkili bitler kullanarak çözümleri aramak için kromozomları kodlama.
2. Popülasyon sayısını (kromozomlar) ve jenerasyon boyutunu ayarlama. Çaprazlama ve mutasyon oranlarını ayarlama.
3. Popülasyonu başlatma.
4. Genetik Algoritmaları uygulama.
5. Yerel aramayı uygulama.
6. Son yerel aramayı en uygun kişiye (kromozom) uygulama.

Değişken Piyasalar

Bir sınır tenörleri eniyilemesi işlemi için kullanılan girdiler arasında, bir maden ürününün satış fiyatı en değişken olanıdır. Küresel pazarda bir madencilik ürününün satış fiyatındaki herhangi bir değişiklik, tüm ekonomik değerlendirmeleri geçersiz kılabilir. Temel olarak, kimse fiyatların gelecekte nasıl değişeceğini bilemez, ancak tahmin edilebilir. Tüm hassasiyet ve risk analizleri, girişimcileri tahmini riskler konusunda bilgilendirmek için yapılır. Ancak, risk faktörü girişimcilere bir madencilik kuruluşunun riskleri hakkında bir fikir vermesine rağmen, optimumluk hesaplamalarını etkilemez.

Duyarlılık ve risk analizleri girişimcilikte karar alma için iyi araçlar olsa da, stokastik olarak tahmin edilen değişken piyasa koşulları için optimum sınır tenörü politikasına dair hiçbir ipucu vermezler. Daha iyi bir madencilik planı yapmak için, yıllık dinamik sınır tenörü problemini optimum şekilde çözmek gerekir ve bu da değişken piyasa koşullarını dikkate almayı gerektirir. Bu, bir projeyi kabul etme veya reddetme kararını vermekle ilgili değildir. Ancak mümkün olduğunca doğru bir şekilde optimum sınır tenörlerini bulmakla ilgilidir. Bu nedenle, bu çalışmada, bir madencilik ürününün değişken satış fiyatlarının, kullanılacak sınır tenörlerini bulma algoritmasına eklenmesi gerektiği kabul edilmektedir. Optimum sınır tenörleri silsilesi bulunmadan, en fazla geliri bulmak mümkün değildir. Bir emtianın bugünkü satış fiyatını, bunun tahmini gelecekteki değerleri yerine kullanmak, en iyi net bugünkü değerden fedakarlık yapmak anlamına gelebilir.

Geleceği tahmin etmek için geçmişi uygulamak gerekir. Geçmiş piyasa fiyatları, gelecekteki fiyat tahminleri için kimlik sağlar. Tahminler, doğası gereği, deterministik veya stokastik olabilir. Ayrıca, geleceği tahminde bulunurken, önceki yıllardan ziyade yakın yıllara daha fazla ağırlık verilmesi gerekmektedir.

Değişken Piyasalar İçin Sınır Tenörleri Eniyilemesine Memetik Algoritmanın Uygulanması

Bir sınır tenörleri eniyilemesi probleminin çözüm kümesi içerisinde, global optimum noktadan ve birbirlerinden oldukça uzakta olan çok sayıda yerel optimum nokta vardır. Stokastik arama yöntemleri, bu tür problemler için küresel optimum noktayı bulmada kolayca başarısız olabilir. Bu tür problemlerdeki gerçek zorluk, sınırlı bir süre içinde küresel optimum noktaya yakın çözümler bulmaktır. Memetik algoritmalar, bu bağlamda mevcut diğer birçok arama yönteminden daha güçlüdür.

Sınır tenörleri eniyilemesine memetik algoritmaların uygulanması için bu çalışmada kullanılan kodlama ve değerlendirme süreçleri aşağıda açıklanmıştır:

Kodlama

Bir cevher yatağında bir sınır tenörü değeri için bir bireyin kodlanması basit bir işlemdir. İkilik sistem kullanılırsa, bir dizenin uzunluğu fazla olacaktır. 5 bitlik bir dize, $2^5 = 32$ sınır tenörünü temsil edebilir. İkilik koddan gerçek değerleri türetmek (yani, dizeyi onluk sisteme çevirmek) için formül şudur:

$$X = X_{\min} + \frac{X_{\max} - X_{\min}}{2^L - 1} * Y \qquad (2)$$

burada;

X: Eşleme değeri,
X_{min}: Aranacak minimum sınır tenörü,
X_{max}: Aranacak maksimum sınır tenörü,
L: İkili dizenin uzunluğu,
Y: İkili gösterimin değeri.

5 bitlik bir dize için ikili gösterimin değeri, 00000 dizesi için 0 ile 11111 dizesi için 31 arasında bir tam sayı olacaktır.

Optimum sınır tenörleri probleminin çözümüne memetik algoritmaların uygulanması, dizenin uzunluğunda önemli bir artış gerektirir. Maden ömründeki her yılda farklı bir optimum sınır tenörü olabileceğinden, aynı dizede farklı genler olmalıdır. Maden ömrü 20 yıl ise, dizi her biri 5 bit uzunluğunda olan 20 genden oluşacaktır ve kromozomun toplam uzunluğu 100 bit olacaktır.

Değerlendirme

Memetik algoritmalarda, her bireye, performansına bağlı olarak, bir uygunluk değeri atanır. Sınır tenörleri eniyilemesinde amaç fonksiyonu, maksimum net bugünkü değerdir. İndirgenmiş kâr ne kadar yüksekse, birey o kadar iyidir.

Bu çalışmadan ve başkaları tarafından yapılan çalışmalardan (Lane [1], [2], Asad [4], Dowd[13], Cetin and Dowd [3], Cetin [14], Cetin and Dalgic [15]), maksimum net bugünkü değerin yalnızca azalan bir sınır tenörleri politikasıyla elde edilebileceği çok açıktır. Yani, madencilik operasyonu madenin ömrü boyunca kademeli olarak azalan nispeten yüksek bir sınır tenörüyle başlamalıdır. Bu nedenle ve hesaplamaların hızını artırmak için, azalarak değişenler dışındaki tüm sınır tenörleri silsilelerine sahip olan bireylersistemde ortadan kaldırılır.

Bu çalışmada kullanılan yerel arama, doğası gereği deterministiktir. Yani, program tüm olası değerleri tek tek arar. Hayatta kalan tüm kromozomların (popülasyon) ve en iyi kromozomun dizelerindeki tüm sınır tenörleri değiştirilir.

Satış fiyatı algoritmaya stokastik olarak eklenir. Algoritmaya satış fiyatlarını eklemek için üstel artımlar kullanılır. Her artışın algoritmada eşit ağırlığı vardır. Daha sonra, tahmini değeri seçmek için Monte Carlo Simülasyonu gerçekleştirilir. Algoritmaya eklenecek toplam artımlı yıl sayısı aşağıdaki gibi formüle edilebilir:

$$Y = \sum_{k=0}^{n} 2^{k} \quad (3)$$

burada;
Y : dahil edilecek geçmiş yılların sayısı.
n : artım sayısı.
2^0: bu yılın fiyatı.

Satış fiyatlarını sürece eklerken alınacak bir güvenlik önlemi, nominal fiyatlar yerine gerçek fiyatların kullanılmasıdır. Kullanılan paranın enflasyonunun etkisi açıkça ortadan kaldırılmalıdır.

Son olarak, simüle edilmiş satış fiyatlarının ortalama değeri algoritmaya eklenir. Algoritmaya stokastik fiyatların eklenmesinden sonra, Lane(1964)'in sınır tenörleri için denklemi şu hale gelir:

$$v = (\mu_\delta - k) * x * y * a - x * h - m - (f + F) * t \quad (4)$$

burada;
v : net bugünkü değer,
δ: pazarlanan ürün birimi başına stokastik satış fiyatı,
μ_δ: pazarlanan ürün birimi başına stokastik satış fiyatlarının ortalaması,
p: pazarlanan ürün birimi başına fiyat,
k: pazarlama değişken maliyeti,
x: cevher/malzeme oranı,
y: cevher işleme verimi,
a: ortalama tenör,
h: cevher işleme değişken maliyeti,
m: maden işletme değişken maliyeti,
f: sabit maliyet,
F: fırsat maliyeti,
t: birim başına zaman.

Örnek Çalışma

Memetik algoritmalar aracılığıyla optimum sınır tenörlerini belirlemek için geliştirilen yazılımın uygulamasını göstermek amacıyla buraya bir örnek uygulama eklenmiştir. Söz konusu olan bir bakır yatağıdır. Teknik ve ekonomik veriler Tablo1 ve Tablo2'de gösterilmiştir.

Bu konu için geliştirilen bilgisayar programı C++ kodlarıyla yazılmıştır. Program 13 CPU saniyesinde sonlanmaktadır. Sonuçlar Tablo3'de verilmiştir.

Tablo 1. Bakır yatağı için tenör-tonaj tablosu.

Grade (%)	Tonnage
0.0-0.3	1.2
0.3-0.4	6.3
0.4-0.5	13.1
0.5-0.6	20.4
0.6-0.7	22.2
0.7-0.8	24.9
0.7-0.8	23.1
0.8-0.9	21.5
0.9-1.0	20.4
1.0-1.1	19.6
1.1-1.2	17.1
1.2-1.3	13.7
1.3-1.4	10.2
1.4-1.5	9.3
1.5-1.6	7.2
1.6-1.7	5.1
1.7-1.8	3.0
1.8-1.9	2.4
1.9-2.0	1.1
2.1-2.2	0.5
2.2-2.3	0.2

Tablo 2. Memetik algoritma için ekonomik ve teknik veri.

Tanım	Değer
Sınır tenörleri alt limiti	0.3
Sınır tenörleri üst limiti	1.23
İşletme kapasitesi (ton/yıl)	13,000,000
İşleme kapasitesi (ton/yıl)	10,000,000

Rafineri kapasitesi (ton/yıl)	100,000
Satış fiyatı ($/ton)	8,193
Önceki yıl satış fiyatı($/ton)	10,139
Önceki yıl satış fiyatı($/ton)	8,217
Önceki yıl satış fiyatı($/ton)	9,377
Önceki yıl satış fiyatı($/ton)	10,162
Önceki yıl satış fiyatı($/ton)	5,240
Önceki yıl satış fiyatı($/ton)	6,018
Önceki yıl satış fiyatı($/ton)	6,825
Önceki yıl satış fiyatı($/ton)	5,600
Önceki yıl satış fiyatı($/ton)	4,695
Önceki yıl satış fiyatı($/ton)	6,295
Önceki yıl satış fiyatı($/ton)	6,891
Önceki yıl satış fiyatı($/ton)	7,249
Önceki yıl satış fiyatı($/ton)	7,956
Önceki yıl satış fiyatı($/ton)	8,960
Önceki yıl satış fiyatı($/ton)	6,838
Önceki yıl satış fiyatı($/ton)	4,569
Önceki yıl satış fiyatı($/ton)	8,383
Önceki yıl satış fiyatı($/ton)	7,681
Önceki yıl satış fiyatı($/ton)	8,046
Önceki yıl satış fiyatı($/ton)	3,249
Önceki yıl satış fiyatı($/ton)	2,734
Önceki yıl satış fiyatı($/ton)	1,648
Önceki yıl satış fiyatı($/ton)	1,596
Önceki yıl satış fiyatı($/ton)	1,682
Önceki yıl satış fiyatı($/ton)	1,786
Önceki yıl satış fiyatı($/ton)	1,511
Önceki yıl satış fiyatı($/ton)	1,733
Önceki yıl satış fiyatı($/ton)	2,514
Önceki yıl satış fiyatı($/ton)	2,658
Önceki yıl satış fiyatı($/ton)	2,773
Rafineri gideri ($/ton)	2200
Cevher kazanım oranı (%)	92
Birim işletme gideri($/ton)	3.5
Birim işleme gideri($/ton)	13.3
Sabit maliyet ($/yıl)	3,500,000
İndirgeme oranı (%)	10
Popülasyon sayısı	1000
Jenerasyon sayısı	1000
Çaprazlama oranı	50
Mutasyon oranı	60

Tablo 3. Sonuçlar. (Toplam indirgenmiş kar 3,019.76M$)

Yıl	Sınır Tenörü (%)	Ortalama tenör (%)	Tükenme hızı (Mt)	Üretim hızı (Mt)	Rafineri hızı (1000 ton)	Yıllık Kar (M$)
1	0.66	1.13	14.88	11.54	120.00	378.80
2	0.63	1.11	14.58	11.72	120.00	377.55
3	0.63	1.11	14.58	11.72	120.00	377.55
4	0.60	1.10	14.31	11.89	120.00	376.15
5	0.60	1.10	14.31	11.89	120.00	376.15
6	0.60	1.10	14.31	11.89	120.00	376.15
7	0.60	1.10	14.31	11.89	120.00	376.15
8	0.60	1.10	14.31	11.89	120.00	376.15
9	0.60	1.10	14.31	11.89	120.00	376.15
10	0.57	1.08	14.02	12.00	119.43	372.94
11	0.54	1.07	13.61	12.00	117.76	366.18
12	0.48	1.04	13.00	12.00	114.83	354.09
13	0.48	1.04	13.00	12.00	114.83	354.09
14	0.45	1.03	12.74	12.00	113.73	349.52
15	0.42	1.02	12.52	12.00	112.62	344.83
16	0.39	1.01	12.35	12.00	111.69	340.86
17	0.36	1.01	12.25	12.00	111.13	338.46
18	0.30	1.00	9.18	9.13	83.68	253.71

Tablo 3'de görüldüğü gibi, sınır tenörleri ve tükenme hızları azalarak değişmektedir. Sınır tenörleri %0,66'dan başlamakta ve kademeli olarak %0,30'a düşmektedir. Memetik algoritma, çaprazlama ve mutasyon araçları vasıtasıyla yerel bir optimum noktadan kolayca kaçabildiği, doğal seçilim ortamı ve algoritmanın stokastik kısmından gelen optimum verilerin yerel bir arama vasıtasıyla yeniden değerlendirildiği için çok güçlü bir eniyileme aracıdır.

Sonuçlar

Bu araştırmadan da anlaşılacağı gibi, maksimum net bugünkü değerin ancak azalarak değişen bir sınır tenörleri politikasıyla elde edilebileceği çok açıktır. Yani, madencilik operasyonu, madenin ömrü boyunca kademeli olarak azalan nispeten yüksek bir sınır tenörü değeriyle başlamalıdır.

Sınır tenörleri eniyilemesinde evrimsel algoritmaların kullanımı son yıllarda popülerlik kazanmaktadır. Memetik algoritmalar yöntemi çok güçlü bir arama motorudur. Yöntemin çaprazlama, mutasyon ve doğal seçilim davranışı, yerel bir optimum noktadan kaçmasını sağlar. Ve takip eden yerel arama, stokastik işlemler sonucu elde edilen optimumu daha da iyileştirir.

Örnek çalışmadan elde edilen sonuç, evrimsel algoritmaların optimum sınır tenörlerini aramada çok yararlı olduğunu göstermektedir.

Piyasa fiyatları belirsiz olduğundan, tahmin edilmeleri gerekir. Bunu yapmamak ve madencilik ürünlerinin güncel satış fiyatlarını kullanmak maden yataklarının verimsiz değerlendirilmelerine yol açabilir. Bu nedenle, maden değerlendirmesi yapılmadan önce satış fiyatları geleceğe yönelik olarak tahmin edilmelidir.

Etik kurul onayı ve çıkar çatışması beyanı

Hazırlanan makalede etik kurul izni alınmasına gerek yoktur.

Hazırlanan makalede herhangi bir kişi/kurum ile çıkar çatışması bulunmamaktadır.

Kaynaklar

[1] K. F. Lane, "Choosing the optimum cutoff grade," *Colorado School of Mines quarterly*, vol. 59, no. 4, pp. 811-829, 1964.

[2] K. F. Lane, *The Economic Definition of Ore*, Mining Journals Books Ltd., London, UK, 1988.

[3] E. Cetin and P. A. Dowd, "The use of genetic algorithms for multiple cut-off grade optimization," in *Proc. 30th Int. Symp. APCOM,* Littleton, Colorado, USA, Apr. 11-13, 2002.

[4] M. W. A. Asad, "Optimum cut-off grade policy for open pit mining operations through net present value algorithm considering metal price and cost escalation. *Engineering Computations*, vol. 24, no. 7, pp. 723-736, 2007.

[5] M. W. A. Asad and E. Topal, "Net present value maximization model for optimum cut-off grade policy of open pit mining operations," *Journal of the SAIMM*, vol. 111, no. 11, pp. 741–750, 2011.

[6] J. Gholamnejad, "Determination of the optimum cutoff grade considering environmental cost," J. Int. Environmental Application & Science, vol. 3, no. 3, pp. 186-194, 2008.

[7] J. Gholamnejad, "Incorporation of rehabilitation cost into the optimum cut-off grade determination," *Journal of the SAIMM*, vol. 109, no. 2, pp. 89-94, 2009.

[8] Y. Azimi, M. Osanloo, and A. Esfahanipour, "Selection of the open pit mining cut-off grade strategy under price uncertainty using a risk based multi-criteria ranking system," *Archives of Mining Sciences*, vol. 57, no. 3, pp. 741-768, 2012.

[9] E. Çetin, Kararsız market koşullarında genetik algoritma ile sınır tenörleri optimizasyonu. *Dicle Üniversitesi Mühendislik Fakültesi Mühendislik Dergisi*, vol. 7, no. 1, pp. 103-112, 2016.

[10] J. H. Holland, *Adaptation in Natural and Artificial Systems*, University of Michigan Press, 1975.

[11] R. Dawkins, *The Selfish Gene.* Oxford University Press, 1976.

[12] P. Garg, "A Comparison between Memetic algorithm and Genetic algorithm for the Cryptanalysis of Simplified Data Encryption Standard Algorithm," *IJNSA*, vol. 1, no. 1, pp. 34-42, Apr. 2009.

[13] P. A. Dowd, "Application of dynamic and stochastic programming to optimise cut-off grades and production rates," *Transactions of the Institution of Mining and Metallurgy Section A: Mining Industry*, Vol. 81 pp. 160-179, 1976.

[14] E. Cetin, "Assessment of costs in cut-off grades optimization by using grid search method," *Gospodarka Surowcami Mineralnymi*, vol.34, no. 2, pp. 67-80, Jan. 2018.

[15] E. Cetin, and A. Dalgic, "The optimization of cut-off grades by means of memetic algorithms," *Gospodarka Surowcami Mineralnymi-Mineral Resources Management*, vol.38, no. 1, pp.107-122, 2022.

Dicle University
Journal of Engineering
https://dergipark.org.tr/tr/pub/dumf
duje.dicle.edu.tr

Araştırma Makalesi / Research Article

Yerel zemin koşullarının ve deprem ivmelerinin betonarme yüksek katlı binaların performansına etkisi

The Effect of Local Soil Conditions and Earthquake Zones on the Performance of High-Rise RC Buildings

Jülide Yüzbaşı[1], Fatih Avcil[2*], Aydın Büyüksaraç[3], Mehmet Salih Keskin[4], Ercan Işık[5], Enes Arkan[6]

[1] Çukurova Üniversitesi, İnşaat Mühendisliği Bölümü, jyuzbasi@cu.edu.tr,
ORCID: https://orcid.org/0000-0002-4034-5666
[2] Bitlis Eren Üniversitesi, İnşaat Mühendisliği Bölümü, favcil@beu.edu.tr,
ORCID: https://orcid.org/0000-0001-6550-550X
[3] Çanakkale Onsekiz Mart Üniversitesi, Çan Meslek Yüksekokulu, absarac@comu.edu.tr
ORCID: https://orcid.org/0000-0002-4279-4158
[4] Dicle Üniversitesi, İnşaat Mühendisliği Bölümü, mskeskin@dicle.edu.tr
ORCID: https://orcid.org/0000-0003-1973-4437
[5] Bitlis Eren Üniversitesi, İnşaat Mühendisliği Bölümü, eisik@beu.edu.tr
ORCID: https://orcid.org/0000-0001-8057-065X
[6] Bitlis Eren Üniversitesi, Mimarlık Bölümü, earkan@beu.edu.tr
ORCID: https://orcid.org/0000-0002-6588-7234

MAKALE BİLGİLERİ

Makale Geçmişi:

Geliş 4 Mart 2025
Revizyon 3 Eylül 2025
Kabul 5 Eylül 2025
Online 30 Eylül 2025

Anahtar Kelimeler:

Deprem, çok katlı, betonarme, hasar, yerel zemin, deprem bölgesi, hedef yer değiştirme

ÖZ

Artan nüfus yoğunluğu kentleşmeyi hızlandırmış ve dünya genelinde çok katlı betonarme binaların yaygın olarak tercih edilen bir seçenek haline gelmesine neden olmuştur. Bu yapıların dinamik yükleri taşıyabilme kapasitesine sahip olmaları hem yapısal karakteristiklerine hem de yerel zemin koşulları ile deprem düzeyleri gibi yapısal olmayan faktörlere bağlıdır. Bu makale, betonarme çok katlı yapıların performansını, farklı yerel zemin koşulları ve deprem bölgelerinin etkileri açısından incelemektedir. Yapıların deprem performanslarının belirlenmesinde kullanılan hedef yer değiştirmeler bağlamında bu etkiler incelenmiştir. Bu amaç doğrultusunda seçilen 12 katlı betonarme yapı modeli üzerinden dört farklı yerel zemin sınıfı ve dört farklı deprem düzeyi dikkate alınarak yapısal analizler ayrı ayrı gerçekleştirilmiştir. Çalışmada, zemin kaynaklı hasarların yanı sıra çok katlı betonarme yapılarda oluşan hasarlar 2023 Kahramanmaraş depremleri ışığında incelenmiştir. Çalışma ile farklı yerel zemin koşulları ve farklı deprem düzeylerinin yanı sıra farklı deprem aşılma olasılıkları için elde edilen hedef yer değiştirmeler karşılaştırılarak öneriler yapılmıştır. Maksimum yer ivmesi arttıkça ve yerel zemin koşulları zayıfladıkça yapılardan beklenen hedef yer değiştirmeler artmaktadır. Hatay ili için en büyük hedef yer değiştirme değerleri elde edilirken, Adıyaman ilinde ise en küçük hedef yer değiştirme değerleri elde edilmiştir.

ARTICLE INFO

Article history:

Received 4 March 2025
Received in revised form 3 September 2025
Accepted 5 September 2025
Available online 30 September 2025

Keywords:

Earthquake, multi-storey, rc, damage, local soil, earthquake zone, target displacement

Doi: 10.24012/dumf.1651028

* Sorumlu Yazar

ABSTRACT

The rise in population density has accelerated urbanization, making reinforced concrete multi-story buildings a widely preferred choice for construction globally. The capacity of these structures to withstand dynamic loads depends on both their structural characteristics and non-structural factors, such as local soil conditions and earthquake levels. This article examines the performance of reinforced concrete multi-storey structures concerning the effects of different local soil conditions and earthquake zones. These effects are analyzed in the context of target displacements used to determine the earthquake performance of structures. For this purpose, structural analyses were conducted separately, considering four local soil classes and four earthquake levels on a selected 12-storey reinforced concrete structure model. In addition to ground-related damages, the study examines damages to multi-storey reinforced concrete structures in light of the 2023 Kahramanmaraş earthquakes. The study compares the target displacements obtained for various local soil conditions, earthquake levels, and earthquake exceedance probabilities and offers recommendations based on the findings. As the maximum ground acceleration increases and local ground conditions weaken, the target displacements expected from the structures increase. While the largest target displacements were obtained for Hatay province, the lowest target displacement values were obtained for Adıyaman province.

Giriş

Betonarme çok katlı yapılar, modern inşaat dünyasında, büyük şehirlerdeki konut ve ticaret alanlarının gereksinimlerini karşılamak amacıyla yaygın olarak inşa edilmektedir. Bu tür yapılar, zemin ile etkileşimleri, deprem riski ve yapı güvenliği açısından büyük önem taşımaktadır. Özellikle Türkiye gibi deprem tehlikesi yüksek ülkelerde, yerel zemin koşullarının ve farklı deprem düzeylerinin etkileri, yapıların güvenliğini doğrudan etkilemektedir. Yapıların tasarımı ve performansı, yalnızca tasarım ve malzeme seçiminden değil, aynı zamanda zeminin ve çevresel koşulların etkilerinden de büyük ölçüde etkilenmektedir.

Yerel zemin koşulları; temel taşıma kapasitesi, zemin sıvılaşma riski, zemin deformasyonu ve yer hareketi gibi faktörleri içermektedir. Yerel zemin koşulları, yapıların temel taşıma kapasitesinden sismik davranışına kadar pek çok özelliğini etkilemektedir. Zemin koşulları yapıların stabilitesini, hareketlerini ve genel olarak güvenliğini belirlemede kritik bir rol oynamaktadır. Bu bağlamda yapıların deprem etkileri altındaki davranışlarında zemin-deprem-yapı etkileşiminin doğru olarak ortaya konulması kritik bir öneme sahiptir. Zemin sınıfları, genellikle zeminin taşıma kapasitesine, esneklik ve rijitlik özelliklerine göre sınıflandırılmaktadır. Zemin koşullarının doğru bir şekilde belirlenmesi, yapı tasarım ve değerlendirilmesinde yapı-zemin etkileşiminin gerçekçi olarak elde edilmesine imkan tanıyacaktır. Zemin ve yapı arasındaki etkileşim, deprem anındaki yapısal davranışı büyük ölçüde etkileyebilmektedir. Bu etkileşim, çok katlı yapıların tasarımında dikkate alınması gereken önemli parametrelerden biridir [1]-[9].

Bunların yanı sıra, yapıların tasarımında dikkate alınacak parametrelerden biri de yapının bulunduğu veya inşa edileceği bölgenin deprem tehlikesidir. Aktif deprem kuşağında yer alan diğer bölgelerde olduğu gibi, Türkiye'de de yapıların tasarımında deprem tehlikesi dikkate alınmaktadır. 2007 yılında yürürlüğe giren Deprem yönetmeliğinde deprem bölgeleri olarak dikkate alınan bu parametre güncel yönetmelikte ise deprem tehlikesi olarak dikkate alınmaktadır. 2007 yılında yürürlüğe giren Deprem bölgeleri haritasında Türkiye, 1. dereceden 4. dereceye kadar farklı deprem bölgelerine ayrılmıştır. 1. derecede yer alan bölgelerde yapılar daha büyük sismik yükler altına gireceğinden daha yüksek tasarım kriterlerine sahip olmalıdır. Bunların yanı sıra, performansa dayalı deprem mühendisliği kapsamında diğer yapılarda olduğu gibi, çok katlı yapıların olası bir depremde performanslarının belirlenmesinde hedef yer değiştirmeler kullanılmaktadır. Bu noktada, betonarme yüksek yapıların tasarımında ve inşasında hedef yer değiştirmelerin belirlenmesi ve bu hedeflere ulaşılmasının sağlanması kritik bir öneme sahiptir. Çok katlı yapılar, yer değiştirme limitlerini aşmamalı ve yapısal elemanlar, istenmeyen deformasyonları engellemek amacıyla doğru bir şekilde tasarlanmalıdır. Bu makale kapsamında betonarme çok katlı yapılarda hedef yer değiştirmelerin önemi, yerel zemin koşulları ve deprem tehlikesi bağlamında değerlendirilmiştir.

Betonarme yapılarda yerel zemin koşulları ve deprem düzeylerinin incelendiği çalışmaların yanı sıra yerel zemin koşullarının deprem üzerindeki etkilerinin incelendiği çalışmalar da bulunmaktadır. Bu çalışmalarda yapıların sismik davranışı üzerindeki etkileri farklı sonuç değerleri üzerinden değerlendirilmiştir. Dorum vd. [10], deprem bölgesi ve yerel zemin koşullarının yapı maliyetine etkisini karşılaştırmalı olarak değerlendirmişlerdir. Galal ve Naimi [11], 20 ve 6 katlı betonarme bina modelleri için zemin sınıflarının etkisini yakın alan depremlerini dikkate alarak belirlemeye çalışmışlardır. Tabatabaiefar vd. [12] çerçeveli yapı sistemlerinin sismik performanslarını zeminlerin dinamik özelliklerini kullanarak belirlemeye çalışmışlardır. Yön vd. [13] farklı deprem bölge ve yerel zemin koşullarının etkisini beş katlı betonarme yapı özelinde incelemişlerdir. Yön ve Calayır [14] farklı zemin sınıflarının betonarme yapıların deprem davranışına etkisini ortaya koymaya çalışmışlardır. Karapetrou vd. [15] sünek olmayan yüksek betonarme binaların deprem performanslarını zemin-yapı etkileşimi kapsamında değerlendirmişlerdir, binalarda deprem performansını önemli ölçüde etkilediğini ortaya koymuştur. Yeşil ve Ateş [16] yaptıkları çalışmada, Düzce ili özelinde farklı yerel zemin sınıflarının yapısal hasar ve performansa etkilerini incelemişlerdir. Özşahin ve Eroğlu [17] yerel zemin koşullarının deprem duyarlılığına etkisini Erzincan ili özelinde incelemişlerdir. Akyıldız vd. [18] TBDY-2018'de verilen beş farklı yerel zemin sınıfını kullanarak betonarme yapı için kesit tesirlerini karşılaştırmışlardır. Aykaç vd. [19] zeminlerin dinamik davranışlarını belirlemede kullanılan kayma dalgası hızı (V_s) değerlerini kullanarak, deprem–hasar ilişkini 2011 Van depremi (Mw=7.1) özelinde değerlendirmişlerdir. Pitilakis ve Petridis [20] mevcut yapılar için hasar görebilirlik eğrilerini zemin-yapı etkileşimini dikkate alarak elde etmişlerdir ve zemin büyütme etkisinin yapısal hasar olasılıklarını artırdığını göstermiştir. Özgür ve Bozdoğan [21] on katlı üç farklı betonarme yapı modeli için farklı yerel zemin sınıflarını kullanarak yapısal analizler gerçekleştirmiş ve yapı-zemin etkileşiminin sismik tasarım parametrelerine etkisini ortaya koymaya çalışmışlardır. Requena-Garcia-Cruz vd. [22] orta yükseklikteki betonarme binalarda zemin-yapı etkileşimini Lizbon özelinde incelemişlerdir ve sismik kırılganlık üzerinde belirleyici olduğunu vurgulamıştır. Fiamingo vd. [23] depremde hasar almış bir yapı için zemin etkisini analitik olarak incelemişlerdir. Eroğlu ve İpek [24] beş katlı betonarme yapıda farklı temel tipleri kullanılarak zemin-yapı etkileşimini incelemişlerdir. Büyüksaraç vd. [25] çok katlı yapı planlanan bir alanda zemin özelliklerini incelemişler ve (sert kaya tabakasına ulaşılan derinlik çok fazla olduğu koşullarda sismik temel derinliği bilgisinin V_s hız değerine bağlı olarak elde edilebileceğine dair örnek bir çalışma gerçekleştirmişlerdir. Ekmen ve Avcı [26] Kahramanmaraş depremlerinin sismik kayıtlarını kullanarak farklı zemin sınıfları deprem etkilerini yapay zeka uygulamaları ile ortaya koymaya çalışmışlardır. Işık vd. [27] yerel zemin koşullarından kaynaklı hasarları ve bu koşullarının yapı performansına etkisini detaylı olarak incelemişlerdir. Algın vd. [28] kapsamlı olarak elde edilen zemin verilerini kullanarak yüksek katlı betonarme bir yapının sismik performansını değerlendirmişlerdir. Trifunac [29] yerel zemin koşulları ve deprem yer hareketi ile birçok çalışmayı derleyerek, yerel zemin koşullarının etkilerini ortaya koymaya çalışmıştır. Bu çalışmaların yanı sıra, deprem karakteristiklerinin, farklı türde zemin ve temellerin etkilerini inceleyen ve bunların farklı taşıyıcı sistemlerin deprem performansına etkisi üzerine çalışmalar da literatürde kendine yer bulmuştur [30]-[43].

Bu çalışmalara ek olarak, yapılarda hedef yer değiştirmelerin yapı performansları üzerindeki etkilerinin incelendiği

çalışmalar da literatürde bulunmaktadır. Uçar vd. [44] betonarme çerçeve tür yapılarda hedef yer değiştirme değerlerini, PSV (pseudo spectral velocity) spektrumu ve enerji dengesi etkileşimini dikkate alarak belirlemişlerdir. Monavari vd. [45] betonarme yapılar için elde ettikleri hedef yer değiştirme değerlerini FEMA-356'da verilen sınır değerler ile karşılaştırmışlardır. Fardis ve Panagiotakos [46] betonarme yapılarda deplasmana dayalı tasarım için önerilen ve yapılan uygulamaları değerlendirmişlerdir. Işık vd. [47] farklı ülkeler için deprem verilerini kullanarak orta yükseklikteki betonarme binalar için hedef yer değiştirme değerlerini elde etmişlerdir. Işık vd. [48] Doğu Anadolu Fay Zonu üzerinde yer alan yirmi farklı yerleşim birimi için öngörülen ve ölçülen ivme değerlerini kullanarak, betonarme yapı modeli için hedef yer değiştirme değerlerini karşılaştırmışlardır.

Bu çalışma kapsamında, yerel zemin kaynaklı hasarlar ve çok katlı betonarme binalarda meydana gelen hasarlar 2023 yılında meydana gelen Kahramanmaraş depremleri ışığında değerlendirilmiştir. 06 Şubat 2023 Kahramanmaraş depremleri (Mw=7.7 ve Mw=7.6), betonarme yapıların performans düzeylerinin yeterli düzeyde olmadığını gözler önüne sermiştir. Bu depremlerin ardından yapılan çalışmalar, yapılarda bulunan düzensizlik ve olumsuzlukların hasarların ana nedeni olduğunu göstermektedir. Gözleme dayalı olarak yapılan hasar değerlendirmeleri ile sayısal analizler uygulanarak yapılan çalışmalar bu durumu açıkça ortaya koymaktadır. Akar vd. [49] Adıyaman iline bağlı Gölbaşı ilçesinde betonarme yapılarda meydana gelen hasarların yanı sıra zemin kaynaklı hasarları gözleme dayalı olarak değerlendirmişlerdir. İnce [50] ve Işık vd. [51] Adıyaman ilindeki betonarme yapı hasarlarını değerlendirirken, Avğın vd. [52] Kahramanmaraş ilindeki betonarme yapı hasarlarını değerlendirmişlerdir. Deprem bölgesinde özellikle betonarme yapı hasarlarının incelendiği çalışmaların büyük bir bölümü gözleme dayalı hasar değerlendirilmesini içermektedir. Bu çalışmaların bir kısmında, farklı parametreler dikkate alınarak sayısal analizler de gerçekleştirilmiştir [53]-[63].

Depremler sırasında, yapıların davranışı büyük ölçüde yerel zemin özellikleri ve deprem bölgesine bağlı olarak değişmektedir. Zemin koşulları, yapıların titreşim frekansını ve yer değiştirmelerini etkileyebilir. Çok katlı yapılar, deprem sırasında daha fazla dinamik kuvvetlere ve yer değiştirmelere maruz kalabilmektedir. Bu faktörler yapıların sismik davranışlarını doğrudan etkilemektedir. Bu çalışmada bu iki faktörün, yapıların deprem performanslarının belirlenmesinde kullanılan hedef yer değiştirmeler üzerindeki etkileri ortaya konulmaya çalışılmıştır. Bu amaçla 12 katlı betonarme yapı modeli oluşturulmuştur. Bu model için öncelikle farklı yerel zemin grupları dikkate alınarak sayısal analizler gerçekleştirilmiştir. Yerel zemin sınıfları olarak dünya genelinde daha yaygın bir şekilde kullanılan Eurocode-8'de verilen dört farklı zemin sınıfı dikkate alınmıştır. Bir diğer değişken olarak, deprem bölgesi etkisini ortaya koymak için 0.1g, 0.2g, 0.3g ve 0.4g olmak üzere dört farklı en büyük yer ivmesi (PGA) seçilmiş; seçilen betonarme yapı modeli için sayısal analizler gerçekleştirilmiştir. Çalışmada ayrıca çok katlı yapılarda oluşan hasarlar 06 Şubat 2023 Kahramanmaraş depremleri ışığında incelenmiştir. Bu depremlerden en çok etkilenen Hatay, Kahramanmaraş ve Adıyaman il merkezlerinde farklı aşılma olasılıkları için elde edilen PGA değerleri kullanılarak sayısal analizler gerçekleştirilmiştir. Çalışma, yerel zemin sınıfı, deprem bölgesi ve deprem düzeyi olmak üzere üç farklı değişkenin, yapıların hedef yer değiştirmeleri üzerindeki etkilerini ortaya koymaktadır. Çalışmanın temel amacı, özellikle son 30 yılda yaygın olarak inşa edilmeye başlanan çok katlı betonarme yapılarda, yapısal olmayan parametrelerin etkilerinin ortaya konmasıdır.

06 Şubat 2023 Kahramanmaraş Depremlerinde Zemin Kaynaklı Hasarlar

Zayıf zeminler, daha fazla yer değiştirme ve sıvılaşma riski taşıyabilirken, sert zeminler daha az deformasyon gösterir ve dolayısı ile üzerindeki yapılar daha stabil olabilir. Deprem sırasında sıvılaşan zeminler, temelin taşıma kapasitesini ciddi şekilde düşürebilir. Özellikle suya doygun gevşek kohezyonsuz zeminlerin deprem sırasında oluşan tekrarlı gerilmeler nedeniyle zeminin boşluk suyu basıncındaki aşırı artışına paralel olarak kayma mukavemetindeki ve rijitliğindeki ciddi düşüş, sıvılaşmaya neden olur. Bu durum, özellikle çok katlı yapıların stabilitesini tehlikeye atabilir. Zemin sıvılaşması, yapının temelinde yer değiştirmelere yol açarak, yapıların performansını doğrudan etkileyebilir. Sert zeminlerde yapılar genellikle daha rijit bir davranış sergilerken, yumuşak zeminlerde yapı, daha esnek hareketler gösterir. Adıyaman iline bağlı Gölbaşı ilçesinde zemin kaynaklı gözlemlenen hasar örnekleri Şekil 1'de gösterilmiştir.



Şekil 1. Adıyaman ili Gölbaşı ilçesinde zemin kaynaklı hasar örnekleri

06 Şubat 2023 Kahramanmaraş Depremlerinde Çok Katlı Yapılarda Oluşan Hasarlar

2023 Kahramanmaraş depremleri, Türkiye'nin güneydoğusunda büyük yıkıma yol açan, özellikle Kahramanmaraş, Gaziantep, Adıyaman, Hatay, Osmaniye, Adana, Malatya ve Diyarbakır illerinde ciddi etkiler bırakan, dokuz saat arayla aynı günde M_w=7.7 ve M_w=7.6 büyüklüğünde iki ana depremle gerçekleşmiştir. Bu depremlerin özellikle çok katlı betonarme yapılarda büyük hasarlara yol açmasıyla inşaat sektörü ve afet yönetimi açısından önemli dersler çıkarılmıştır. Herhangi bir yapısal hasar almayan çok katlı betonarme yapı örnekleri Şekil 2'de gösterilmiştir. Çok katlı yapılarda oluşan büyük deprem kuvvetlerini karşılamak üzere kullanılan betonarme perdeler bu tür yapılardaki hasar seviyelerini büyük ölçüde sınırlandırmıştır.



Şekil 2. Hasarsız çok katlı bina örnekleri

Taşıyıcı elemanlarında herhangi bir hasar gözlemlenmeyen ancak yapısal olmayan elemanlarda hafif düzeyde hasar almış çok katlı betonarme yapı örnekleri Şekil 3'te gösterilmiştir.



Şekil 3. Hafif hasarlı çok katlı betonarme yapı örnekleri

Aynı gün içerisinde birbirine yakın lokasyonlarda yaşanan iki büyük depremden dolayı binlerce yapı toptan göçmeye maruz kalmıştır. Çok katlı betonarme yapılarda da toptan göçmeler gerçekleşmiştir. Toptan göçmeye maruz kalmış çok katlı betonarme bir yapı örneği Şekil 4'te gösterilmiştir.



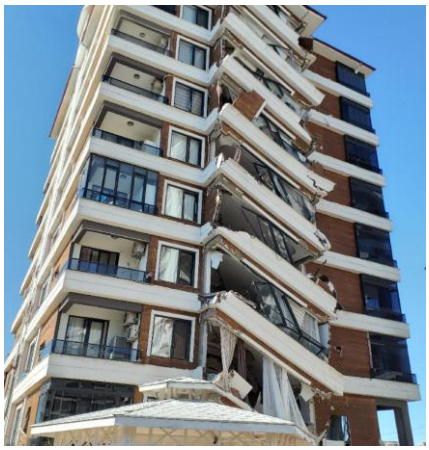
Şekil 4. Toptan göçmeye maruz kalmış betonarme yapının deprem öncesi ve sonrası durumu

Betonarme yapılarda, kolon yüksekliklerinin yapı içerisinde değişiminden dolayı oluşan kısa kolon düzensizliği çok katlı betonarme yapılarda da etkisini göstermiştir. Bunun yanı sıra betonarme yapılarda katlar arası rijitlik/dayanım değişiminin göreceli olarak sebep olduğu yumuşak/zayıf kat düzensizliği de çok katlı betonarme yapılarda hasarlara neden olmuştur. Kısa kolon ve yumuşak/zayıf kat düzensizliği kaynaklı gözlemlenen hasar örnekleri Şekil 5'te gösterilmiştir.



Şekil 5. Kısa kolon ile yumuşak/zayıf kat hasar örnekleri

Betonarme çerçeveleri meydana getiren taşıyıcı elemanlarda yetersiz kenetlenme, yük altında taşıyıcı elemanların birlikte çalışmasına engel olmuştur. Bu durumda bu elemanlar arasındaki süreklilik ortadan kalkmış ve hasara neden olmuştur. Yetersiz betonarme çerçeve sonucu oluşan hasar örneği Şekil 6'da gösterilmiştir.



Şekil 6. Yetersiz betonarme çerçeve kenetlenmesi sonucu oluşan hasar örneği

Çok katlı betonarme yapılarda çerçeve dışına çıkılarak oluşturulan kapalı ağır çıkmalar da hasarların nedenlerinden biridir. Aynı zamanda yapıda bulunan pencere ve kapı boşlukları, deprem esnasında boşluk momentine maruz kalarak hafif çaplı hasarlara neden olabilmektedir. Bu iki nedene bağlı olarak oluşan hasar örnekleri Şekil 7'de gösterilmiştir.



Şekil 7. Ağır çıkma ve pencere boşluklarından dolayı gözlemlenen hasar örneği

Betonarme yapıları meydana getiren iki ana yapı malzemesi olan beton ve donatının özellikleri hasarların ana nedenleri arasındadır. Yetersiz beton örtü kalınlığından (pas payı) dolayı donatılarda meydana gelen korozyon, betonda uygun olmayan agrega kullanımı, kötü donatı işçiliği, düşük dayanımlı beton, donatı-beton arası yetersiz kenetlenme,

düşük dayanımlı beton özellikle kolonlarda farklı düzeylerde yapısal hasarlara neden olmuştur (Şekil 8). Şekil 8'de ayrıca boyuna donatıda kopma örneği bulunmaktadır.



Şekil 8. Beton ve donatı kusurlarından dolayı oluşan farklı düzeylerdeki hasar örnekleri

Betonarme yapılarda mekânları ayırmak ve dış etkilerden korumak amacı ile kullanılan dolgu duvarların düşük malzeme özellikleri ve kötü duvar işçiliğinden dolayı çok büyük hasarlara maruz kalmıştır. Bu tür duvarlarda eskiden olduğu gibi kaba sıvanın uygulanmaması, onun yerine doğrudan alçı sıva uygulanması bu tür taşıyıcı olmayan elemanlarda hasarları olumsuz olarak etkilemiştir. İç ve dış dolgu duvarlarda gözlemlenen hasar örnekleri Şekil 9'da gösterilmiştir.



Şekil 9. Betonarme yapılarda dolgu duvarlarda meydana gelen hasarlar

Özelikle 2000 yılı öncesi inşa edilen çok katlı binalarda derelerden elde edilen agregaların kullanıldığı betonlarda hasarların daha fazla olduğu gözlemlenmiştir.

Yapısal Analizler

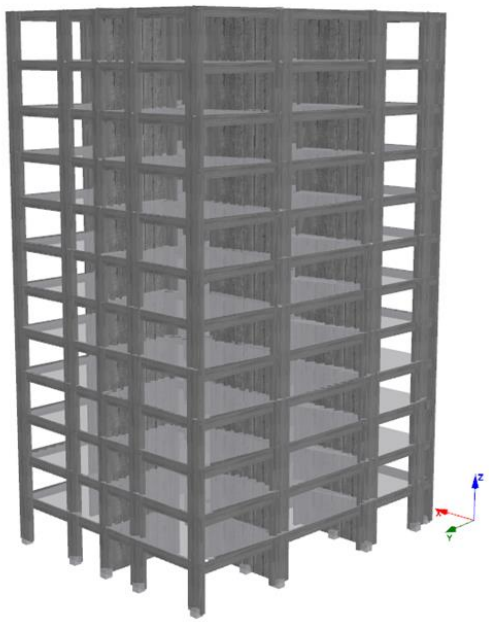
Çalışmanın bu kısmında, çok katlı betonarme yapıları temsil etmesi için örnek olarak seçilen betonarme yapı için sayısal analizler gerçekleştirilmiştir. Farklı zemin sınıfları ve farklı deprem bölgelerinin etkilerini ortaya koymak amacıyla yapılan analizlerde, statik itme analizi kullanılmıştır. Her bir yapısal model, Seismostruct [64] yazılımı kullanılarak modellenmiş ve bu programda analizlere tabi tutulmuştur. Zemin sınıflarının etkisini ortaya koymak amacıyla, dünyada daha yaygın olarak kullanılan Eurocode-8'de verilen dört farklı zemin sınıfı dikkate alınmıştır. Bu zemin sınıflarına ait karakteristik özellikler Tablo 1'de gösterilmiştir.

Tablo 1. Zemin sınıfları ve özellikleri (Eurocode-8) [65]

Zemin Sınıfı	Stratigrafik profilin tanımı	V_{s30} (m/s)	N_{SPT} (blows/30cm)	C_u (kPa)
A	Yüzeyde en fazla 5 m'lik zayıf malzeme içeren kaya veya diğer kaya benzeri jeolojik formasyonlar	>800	---	---
B	En az birkaç on metre kalınlığında, mekanik özelliklerin derinlikle birlikte kademeli olarak arttığı, çok yoğun kum, çakıl veya çok sert kil sedimanları	360-800	>50	>250
C	Kalınlığı birkaç on metreden birkaç yüz metreye kadar değişen yoğun veya orta yoğunlukta kum, çakıl veya sert kilden oluşan derin sedimanter birimler	180-360	15-50	70-250
D	Gevşek ila orta kohezyonlu az toprak (bazı yumuşak kohezyonlu tabakalarla veya tabakalar olmaksızın) veya baskın olarak yumuşak ila sıkı kohezyonlu toprak sedimanları.	<180	<15	<70

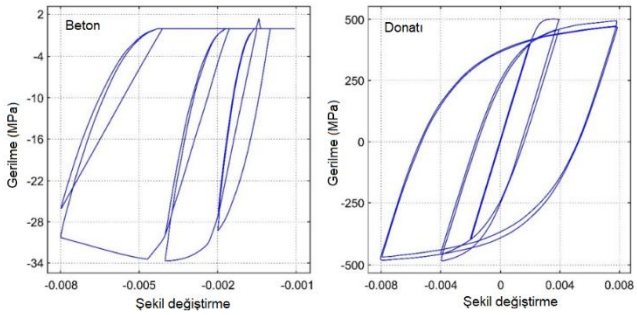
Betonarme çerçevenin yanı sıra betonarme perdeler içeren yapıda her bir kat 3m olup toplam yapı yüksekliği 36m'dir. Herhangi bir düzensizlik içermeyen yapı modelinde, malzeme C35-B420C olarak seçilmiştir. Bina, X doğrultusunda 21.50m iken Y doğrultusunda 26.60m uzunluğunda olup, toplam kat alanı 571.90 m^2'dir. Yapısal analizlerde değişken olarak zemin sınıfı ve en büyük yer ivmesi (PGA) değerleri değişken olarak seçilmiştir.

Modellemesi yapılan binaya ait 3 boyutlu model Şekil 10'da gösterilmiştir.



Şekil 10. Örnek yapı için oluşturulan 3 boyutlu yapısal model

Tüm yapısal modellerde kolonlar ve kirişler için kuvvete dayalı plastik mafsal çerçeve elemanları (infrmFBPH) dikkate alınmıştır. Bu elemanlar, yayılı inelastisiteyi kuvvete dayalı formulasyonla modeller, yalnız plastisiteyi sonlu bir uzunlukla sınırlandırmaktadır. Kesit içindeki gerilme-şekil değiştirme dağılımını doğru bir şekilde temsil etmek için yeterli sayıda fiber eleman kullanılmalıdır. Seçilen kesitler için toplam 150 fiber eleman tanımlanmıştır. Seçilen plastik mafsal uzunluğu (L_p/L), %16.67 olarak dikkate alınmıştır. Taşıyıcı elemanlarda malzeme modelleri seçimi yapılırken donatı için Menegotto-Pinto (stl_mp) malzeme modeli dikkate alınırken, beton için ise Mander vd. (con_ma) malzeme modeli analizlerde kullanılmıştır. Kullanılan bu malzeme modelleri için gerilme-şekil değiştirme ilişkileri Şekil 11'de gösterilmiştir.



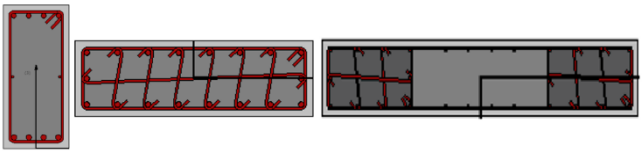
Şekil 11. Beton ve donatı için kullanılan malzeme modelleri

Bu çalışma kapsamında oluşturulan betonarme yapı modeli için dikkate alınan taşıyıcı eleman boyutları ve diğer yapısal parametreler Tablo 2'de verilmiştir.

Tablo 2. Betonarme yapı modeli için dikkate alınan parametreler

Parametre	Değer
Kirişler	300 x 600 mm
Döşeme kalınlığı (mm)	140 mm
Kat yüksekliği (m)	3 m
Beton pas payı (mm)	25 mm
Kolonlar	300x950mm; 300x700mm
Betonarme perdeler	300x1900mm
Sönüm oranı	5%
Yapı önem derecesi	II
Hedef yer değiştirme	0.34m

Çalışmada dikkate alınan örnek betonarme yapıda kullanılan kiriş, kolon ve betonarme perde için örnek en kesitler Şekil 12'de gösterilmiştir.



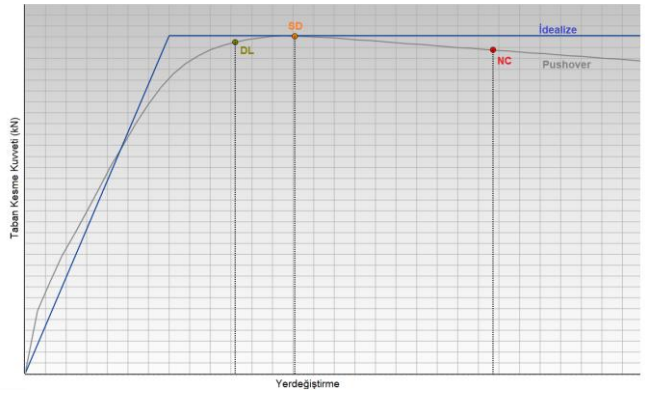
Şekil 12. Taşıyıcı elemanlara ait örnek en kesitler

Çalışmada dikkate alınan her yapı modeli için ayrıca statik itme analizi yapılmıştır. Bu tür bir analiz, yapıların deprem etkisinde nasıl davranacağını hesaplamak için yaygın şekilde kullanılmaktadır. Statik itme analizi, yapıların deprem gibi dinamik yükler altında nasıl davranacağını anlamak amacıyla yapılan, nonlineer statik bir analiz yöntemidir. Analiz yardımı ile taşıyıcı sistem elemanlarında meydana gelebilecek hasar seviyeleri belirlenebilir. Statik itme analizi, "tepe yer değiştirmesi – taban kesme kuvveti" koordinatları ile itme eğrisinin elde edilmesini sağlamaktadır. Bu eğri, yapının başlangıç durumundan kararsız hale gelene kadar artan yük etkisi altında taban kesme kuvvetlerine karşılık gelen çatı deplasman değerlerini gösteren bir etkileşim diyagramıdır. Statik itme analizinin temel amacı, yapının hangi katlarında ve hangi elemanlarında hasar oluşacağını, yapının ne zaman çökmeye başlayacağını veya kapasitesinin tükeneceğini tahmin etmektir [66]-[70]. Çalışma kapsamında dikkate alınan her bir yapısal model için yapılan statik itme analizlerinde hedef yer değiştirmeler elde edilmiştir. Performansa dayalı deprem mühendisliğinde, yapı elemanlarının belirli performans sınırlarına ulaşıldığında hasar tahmini için hedef yer değiştirmelerin belirlenmesi büyük önem taşımaktadır [71], [72]. Dünya çapında çok daha yaygın olarak kullanılan Eurocode-8'de (Bölüm 3) hedef yer değiştirmeler sınır durumlar dikkate alınarak elde edilmektedir [65], [73], [74]. Çalışmada dikkate alınan sınır durum değerlerinin detaylı açıklamaları Tablo 3'te gösterilmektedir.

Tablo 3. Sınır durumlar (Eurocode 8-Part 3) [65], [74]

Sınır Durumu	Tanımlama	Dönüş Periyodu (Yıl)	Aşılma Olasılığı (50 Yılda)
Sınırlı Hasar Durumu (DL)	Sadece hafif hasar, yapısal olmayan bileşenlerdeki hasar ekonomik olarak onarılabilir	225	0.20
Önemli Hasar Sınır Durumu (SD)	Taşıyıcı ve yapısal olmayan bileşenler önemli ölçüde hasar görmüş, onarımı ekonomik değil	475	0.10
Göçmenin Önlenmesi (NC)	Ağır hasarlı, düşük dayanım ve rijitlik, büyük yer değiştirmelere rağmen göçmenin gerçekleşmemesi	2475	0.02

Eurocode-8'e göre dikkate alınan bu sınır durumlar, idealize edilmiş ve statik itme eğrileri Şekil 13'te gösterilmiştir.



Şekil 13. Tipik itme ve idealize edilmiş kapasite eğrileri

Bu çalışma kapsamında öncelikle iki farklı değişken dikkate alınarak 7 farklı model için yapısal analizler gerçekleştirilmiştir. Deprem bölgesi ve yerel zemin sınıfının değişken olarak seçildiği sayısal analizlerde dikkate alınan yapısal modellerdeki değişkenler Tablo 4'te verilmiştir. Tüm yapısal modellerde sönüm oranı %5 olarak seçilmiştir. Deprem bölge değişiminin incelemesi yapılırken, Türkiye'de 2007 yılında yürürlüğe giren Deprem yönetmeliğinde belirtilen dört farklı deprem bölgesi dikkate alınmıştır.

Tablo 4. Oluşturulan yapısal modellerdeki değişkenler

Model	PGA (g)	Yerel Zemin Sınıfı
Model I	0.100	ZA
Model II	0.200	ZA
Model III	0.300	ZA
Model IV	0.400	ZA
Model V	0.400	ZB
Model VI	0.400	ZC
Model VII	0.400	ZD

Birbirine dik iki deprem doğrultusunun herhangi biri için, herhangi bir katta en büyük göreli kat ötelemesinin (Δ_{imax}), o katta aynı doğrultudaki ortalama göreli ötelemeye oranını (Δ_{iort}) ifade eden burulma düzensizliği katsayısı her bir katta 1.2'den daha küçük olarak elde edilmiştir. Bu analiz sonucunda ilk 10 mod için elde edilen kütlesel katılım oranlarının toplamı, yapının toplam kütlesinin %80' inden fazlasını kapsamaktadır.

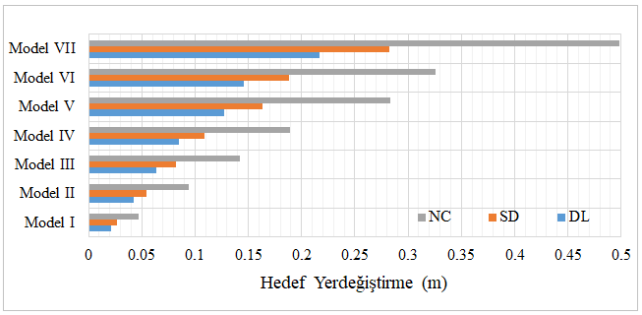
Oluşturulan toplam yedi farklı yapısal model için yapılan analizler sonucunda yapının periyodu, taban kesme, etkin ve efektif rijitlik değerlerinde herhangi bir değişiklik olmamıştır. Zemin sınıfı ve PGA değişimlerinin periyodu etkilemediği, tüm modeller için yapı periyodu 0.497s, taban kesme kuvveti 33755.26kN, etkin rijitlik 1009678.70kN/m ve efektif rijitlik değeri ise 300407.61 kN/m olarak elde edilmiştir.

Seçilen bu iki değişken özellikle yapıların sismik performanslarının belirlenmesinde kullanılan hedef yer değiştirmeleri büyük ölçüde etkilemiştir. Dikkate alınan bu yedi farklı yapısal model için elde edilen hedef yer değiştirmelerin karşılaştırılması Tablo 5'te verilmiştir.

Tablo 5. Farklı yapısal modeller için elde edilen hedef yer değiştirmelerin karşılaştırılması

Model	Hedef yer değiştirmeler (m)		
	DL	SD	NC
Model I	0.021	0.027	0.047
Model II	0.042	0.054	0.094
Model III	0.064	0.082	0.142
Model IV	0.085	0.109	0.189
Model V	0.127	0.163	0.283
Model VI	0.146	0.188	0.326
Model VII	0.217	0.282	0.498

Deprem tehlikesinin artması ile birlikte yapıdan beklenen hedef yer değiştirmeler artmıştır. Benzer şekilde, yerel zemin koşullarının zayıflaması ile birlikte de hedef yer değiştirmelerde artış meydana gelmiştir. Bu da yapılarda daha büyük depremlerde zayıf zemin koşullarının önemini bir kez daha ortaya koymakladır. Elde edilen sonuçların grafik üzerinde gösterimi Şekil 14'te yapılmıştır.



Şekil 14. Hedef yer değiştirmelerin karşılaştırılması

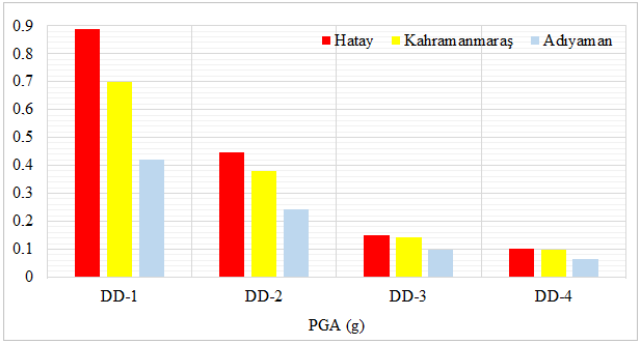
Bu çalışma kapsamında ayrıca, yapısal modellerin yanı sıra 06 Şubat 2023 Kahramanmaraş depremlerinden en fazla etkilenen Hatay, Kahramanmaraş ve Adıyaman il merkezlerinde seçilen herhangi bir konum için yapısal analizler gerçekleştirilmiştir. Dört farklı aşılma olasılığı dikkate alınarak bu üç il için yapılan analizlerde yerel zemin sınıfı, ortalama yerel zemin sınıfı olan ZC seçimi ile gerçekleştirilmiştir. Bu üç il için farklı aşılma olasılıkları için İnteraktif Web Deprem Uygulaması üzerinden elde edilen PGA değerleri ve model isimleri Tablo 6'da gösterilmiştir.

Tablo 6. Kahramanmaraş depremlerinin en çok etkilediği üç il için farklı aşılma olasılıkları için elde edilen PGA değerleri

İl	PGA (g)			
	DD-1	DD-2	DD-3	DD-4

Hatay	0.890	0.446	0.148	0.100
Kahramanmaraş	0.699	0.380	0.142	0.097
Adıyaman	0.419	0.241	0.098	0.065

Çalışmada dikkate alınan bu üç il için farklı aşılma olasılıkları için PGA değerlerinin karşılaştırılması Şekil 15'te yapılmıştır.



Şekil 15. Farklı aşılma olasılıkları PGA değerlerinin karşılaştırılması

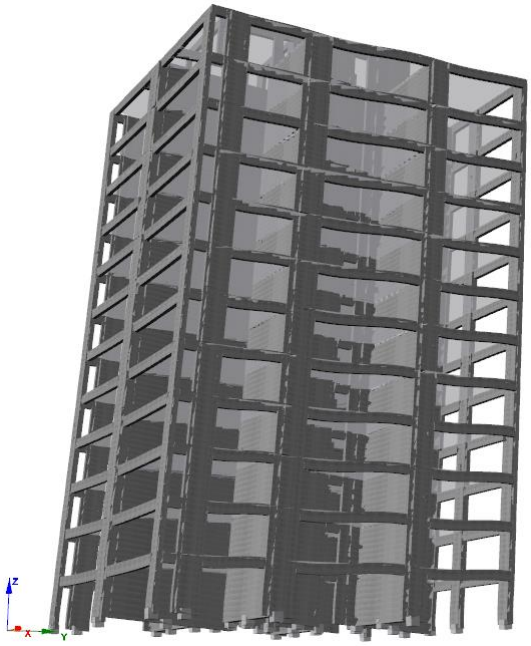
En büyük PGA değerleri Hatay ili için elde edilirken, en düşük değerler Adıyaman için elde edilmiştir. Farklı aşılma olasılıkları dikkate alınarak üç il için gerçekleştirilen yapısal analizler sonucu elde edilen hedef yer değiştirmelerin karşılaştırılması Tablo 7'de yapılmıştır.

Tablo 7. Farklı aşılma olasılıkları için elde edilen hedef yer değiştirmelerin karşılaştırılması

İl		Hedef Yerdeğiştirmeler (m)		
		DL	SD	NC
Hatay	DD-1	0.326	0.418	0.724
	DD-2	0.163	0.209	0.363
	DD-3	0.054	0.070	0.204
	DD-4	0.037	0.047	0.081
Kahramanmaraş	DD-1	0.256	0.328	0.569
	DD-2	0.139	0.178	0.309
	DD-3	0.052	0.067	0.116
	DD-4	0.035	0.046	0.079
Adıyaman	DD-1	0.153	0.197	0.341
	DD-2	0.088	0.113	0.196
	DD-3	0.036	0.046	0.080
	DD-4	0.023	0.031	0.053

En büyük hedef yer değiştirme değerleri, deprem tehlikesinin en büyük olduğu Hatay ili için elde edilirken, en düşük hedef yer değiştirmeler ise en düşük deprem tehlikesine sahip Adıyaman için elde edilmiştir.

Çalışma kapsamında örnek olarak seçilen betonarme bina için gerçekleştirilen statik itme analizinden elde edilen sonuç deformasyon durumu, 3 boyutlu model üzerinden örnek olarak Şekil 16'da gösterilmiştir. Bu deformasyon durum örneği, yerel zemin sınıfının ZA ve PGA değerinin 0.3g olması için oluşturulan yapısal modelden elde edilmiştir.



Şekil 16. Örnek olarak seçilen betonarme yapının deformasyon durumu

Sonuçlar ve Tartışma

Zemin ve yapı etkileşimi, yapının deprem anındaki davranışını etkileyen kritik bir parametredir. Bu makalede, betonarme yüksek yapıların farklı yerel zemin koşulları ve farklı deprem bölgeleri üzerindeki etkileri incelenmiş, çeşitli analizler ve örnekler ile bu etkilerin yapı güvenliği üzerine olan sonuçları tartışılmıştır. Çalışmada üç farklı değişken düşünülmüştür. İlk parametre yerel zemin sınıfı, ikinci parametre deprem bölgesi ve üçüncü parametre olarak da farklı deprem yer hareket düzeyleri dikkate alınmıştır. Zemin sınıfı değişkeni için dünyada daha yaygın olarak kullanılan Eurocode-8'de verilen dört farklı zemin sınıfı dikkate alınmıştır. Deprem bölgesi için de 2007 yılında yürürlüğe giren Deprem yönetmeliğinde yer alan dört farklı deprem bölgesi dikkate alınmıştır. Farklı aşılma olasılıkları için ise üç farklı il için dört farklı yer hareket düzeyi seçilerek, yerel zemin koşullarının etkisi ortaya konmaya çalışılmıştır.

Bu çalışma, çok katlı betonarme yapılar için yerel zemin sınıfı, deprem bölgesi ve deprem düzeyi etkilerini bir arada değerlendirerek, yapıların hedef yer değiştirmeleri üzerindeki birleşik etkilerini sayısal olarak ortaya koymaktadır. Depremlerde en fazla yapısal hasarın oluştuğu üç farklı ilin farklı deprem aşılma olasılıkları ve farklı yerel zemin koşullarının hedef yer değiştimelere etkisi detaylı bir şekilde incelenmiştir. Bunun yanı sıra, ülkemizde son 30 yılda yaygınlaşan çok katlı betonarme yapı stokunun yapısal olmayan parametreler ışığında performansını incelemesi ise çalışmanın yenilikçi yönünü oluşturmaktadır. Özellikle 2023 Kahramanmaraş depremleri sonrasında oluşan hasarların ışığında, hedef yer değiştirme analizlerinin gerçekleştirilmiş olması, çalışmayı hem güncel hem de uygulamaya yönelik hale getirmektedir. Farklı iller bazında yapılan karşılaştırmalar sayesinde, yerel zemin koşullarının ve maksimum yer ivmesinin yapısal taleplere etkisi detaylı

biçimde ortaya konulmuştur. Bu bütüncül yaklaşım, hem mevcut yapı stokunun performans temelli değerlendirilmesinde hem de yeni yapıların tasarımında dikkate alınması gereken önemli parametreleri ortaya koyarak çalışma alanına özgün bir bakış açısı kazandırmaktadır.

Yerel zemin koşullarının zayıflaması, özellikle yumuşak ve gevşek zemin sınıflarına geçilmesi durumunda, deprem sırasında yapıya iletilen yer hareketlerinin genliği ve süresinde belirgin artışlara olabilmektedir. Bu durum, PGA değerlerinde artışa yol açarak yapıların maruz kaldığı sismik talepleri önemli ölçüde yükseltmektedir. Artan yer ivmesi ve uzayan titreşim süreleri, yapıların deplasman taleplerini artırmakta ve dolayısıyla hedef yer değiştirme değerleri daha büyük seviyelere ulaşmaktadır. Bu etki, özellikle doğrusal olmayan davranışın baskın olduğu statik itme analizi ve zaman tanım alanında yapılan analizlerde daha belirgin hale gelmekte; yapı performans düzeylerinin değerlendirilmesinde daha hassas parametrik analizlerin gerekliliğini ortaya koymaktadır. Bu nedenle, zemin özelliklerindeki değişimlerin doğru şekilde modellenmesi, hedef yer değiştirme değerlerinin gerçekçi bir biçimde tahmin edilebilmesi açısından kritik öneme sahiptir. Yerel zemin koşullarının zayıflaması ve PGA değerinin artması ile birlikte yapıların deprem performansları için öngörülen hedef yer değiştirmeler daha büyük değerler almaktadır. Bu nedenle hem yerel zemin sınıfı hem de PGA, hedef yer değiştirme değerlerinin belirlenmesinde kritik rol oynamaktadır. Bu bağlamda en büyük PGA değeri elde edilen Hatay ili için en büyük hedef yer değiştirmeler elde edilirken, en düşük PGA değerine sahip Adıyaman için en düşük hedef yer değiştirmeler elde edilmiştir.

Diğer yapısal analiz yöntemlerin de olduğu gibi çalışmada kullanılan statik itme analizinin de birtakım kısıtlamaları bulunmaktadır. Öncelikle, analizde yapıya uygulanan yatay yüklerin dağılımı sabit kabul edilmekte ve bu durum, özellikle mod şekli değişkenlik gösteren sistemler için gerçekçi sonuçlar vermeyebilir. Ayrıca, statik itme analizinde çoğunlukla tek mod etkisi göz önünde bulundurulduğundan, çok modlu davranışın baskın olduğu sistemlerde yetersiz kalabilmektedir. Bu nedenlerle, statik itme analizi özellikle karmaşık geometrilere, düzensizliklere veya kuvvetli ikinci mertebe etkilerine sahip betonarme yapılar için dikkatle değerlendirilmelidir.

Etik kurul onayı ve çıkar çatışması beyanı

Hazırlanan makalede etik kurul izni alınmasına gerek yoktur.

Hazırlanan makalede herhangi bir kişi/kurum ile çıkar çatışması bulunmamaktadır.

Yazar Katkıları

Tüm yazarlar eşit oranda katkıda bulunmuşlardır.

Kaynaklar

[1] R. Borcherdt, G. Glassmoyer, M. Andrews, and E. Cranswick, "Effect of Site Conditions on Ground Motion and Damage," *Earthquake Spectra*, vol.5, no.1_suppl, pp.23-42, 1989.

[2] S. L. Kramer and C. H. Wang, "Empirical model for estimation of the residual strength of liquefied soil," *Journal of Geotechnical and Geoenvironmental Engineering*, vol.141, no.9, pp.04015038, 2015.

[3] M. D. Trifunac, "How to model amplification of strong earthquake motions by local soil and geologic site conditions," *Earthquake Engineering & Structural Dynamics*, vol.19, no.6, pp.833–846, 1990.

[4] B. Siyahi, K. Ö. Çetin, and H. T. Bilge, "Geoteknik deprem mühendisliği açısından zemin-temel-yapı etkileşimine kritik bakış," *Türkiye Mühendislik Haberleri*, no.484, pp.41-50, 2013.

[5] İ. B. Karaşin and E. Işık, "Farklı yapı davranış katsayıları için zemin koşullarının yapı performansına etkisi," *Dicle Üniversitesi Mühendislik Fakültesi Mühendislik Dergisi*, vol.8, no.4, pp.661–673, 2017.

[6] R. İyisan and M. E. Haşal, "Zemin büyütmesi ve yerel koşulların spektral ivmeye etkisi," *İTÜDERGİSİ/d*, vol.10, no.4, pp.47-56, 2012.

[7] E. Yalçınkaya, "Bytnet (Bursa-Yalova-Türkiye ivme ölçer ağı) istasyonlarında yerel zemin etkilerinin incelenmesi," *Dokuz Eylül Üniversitesi Mühendislik Fakültesi Fen ve Mühendislik Dergisi*, vol.7, no.2, pp.75–85, 2005.

[8] F. Ü. Peker and E. Işık, "TBDY-2018'deki yerel zemin koşullarının çelik yapı deprem davranışına etkisi üzerine bir çalışma," *Bitlis Eren Üniversitesi Fen Bilimleri Dergisi*, vol.10, no.3, pp.1125–1139, 2021.

[9] F. Avcil, E. Işık, and A. Büyüksaraç, "The effect of local soil conditions on structure target displacements in different seismic zones," *Gümüşhane Üniversitesi Fen Bilimleri Dergisi*, vol. 12, no.4, pp.1000–1011, 2022.

[10] A. Dorum, Ö. Özkan, and M. Erdal, "Farklı deprem bölgeleri ve farklı zemin sınıflarının kaba yapı maliyetine etkisi," *Selcuk University Journal of Engineering Sciences*, vol.5, no.1, pp.1–9, 2006.

[11] K. Galal and M. Naimi, "Effect of soil conditions on the response of reinforced concrete tall structures to near-fault earthquakes," *The Structural Design of Tall and Special Buildings*, vol.17, no.3, pp.541–562, 2008.

[12] R. Tabatabaiefar, B. Fatahi, and B. Samali, "Seismic behavior of building frames considering dynamic soil-structure interaction," *International Journal of Geomechanics*, vol.13, no.4, pp.409–420, 2013.

[13] B. Yön, M. E. Öncü, and Y. Calayır, "Effects of seismic zones and local soil conditions on response of RC buildings," *Građevinar*, vol.67, no.6, pp.585–596, 2015.

[14] B. Yön and Y. Calayır, "The soil effect on the seismic behaviour of reinforced concrete buildings," *Earthquakes and Structures*, vol.8, no. 1, pp.133–152, 2015.

[15] S. T. Karapetrou, S. D. Fotopoulou, and K. D. Pitilakis, "Seismic vulnerability assessment of high-rise non-ductile RC buildings considering soil–structure interaction effects," *Soil Dynamics and Earthquake Engineering*, vol.73, pp.42–57, 2015.

[16] B. Yeşil and A. Ateş, "Düzce ilindeki farklı zemin sınıfları dikkate alınarak zemin sınıfının yapı hasarı ve deprem performansına etkisi," *İleri Teknoloji Bilimleri Dergisi*, vol.7, no.3, pp.48–56, 2018.

[17] E. Özşahin and İ. Eroğlu, "Erzincan kentinde yerel zemin özelliklerinin deprem duyarlılığına etkisi," *Doğal Afetler ve Çevre Dergisi*, vol.5, no.1, pp.41-57, 2019.

[18] M. H. Akyıldız, A. E. Ulu, and K. Adar, "TBDY-2018'deki yerel zemin koşullarının deprem kesit tesirlerine etkisi," *Dicle Üniversitesi Mühendislik Fakültesi Mühendislik Dergisi*, vol.12, no.4, pp.679–687, 2021.

[19] Z. Aykaç, M. Akın, and A. F. Çabalar, "V_S(30) tabanlı yerel zemin koşulları ve deprem hasar ilişkisi: Van-Abdurrahmangazi örneği," *Jeoloji Mühendisliği Dergisi*, vol.45, no.2, pp.181–198, 2021.

[20] D. Pitilakis and C. Petridis, "Fragility curves for existing reinforced concrete buildings, including soil–structure interaction and site amplification effects," *Engineering Structures*, vol.269, p.114733, 2022.

[21] M. Özgür and K.B. Bozdoğan, "Betonarme binalarda zemin-yapı etkileşiminin sismik tasarım parametrelerine etkileri," *El-Cezeri*, vol.9, no.2, pp.507–521, 2022.

[22] M. V. Requena-Garcia-Cruz, R. Bento, P. Durand-Neyra, and A. Morales-Esteban, "Analysis of the soil structure-interaction effects on the seismic vulnerability of mid-rise RC buildings in Lisbon," *Structures*, vol.38, pp.599–617, 2022.

[23] A. Fiamingo, M. Bosco, and M. R. Massimino, "The role of soil in structure response of a building damaged by the 26 December 2018 earthquake in Italy," *Journal of Rock Mechanics and Geotechnical Engineering*, vol.15, no.4, pp.937–953, 2023.

[24] İ. Eroğlu and C. İpek, "Deprem Yükleri Altında Yapı ve Zemin Etkileşimi," *International Journal of New Horizons in the Sciences*, pp.18–27, 2023.

[25] A. Büyüksaraç, B. Ateş, Ö. Bektaş, E. Pamuk, and E. Işık, "Bedrock investigation based on shear wave velocity (Vs) on the sites of high-rise buildings," *OTO-2024*, 2025.

[26] A.B. Ekmen, and Y. Avci, "Development of novel artificial intelligence functions based on 3D finite element method using February 6 Kahramanmaraş Seismic Records for earthquake effects prediction in various soils," *Engineering Geology*, vol.336, pp.107570, 2024.

[27] E. Işık, F. Avcil, A. Büyüksaraç, E. Arkan, and E. Harirchian, "Impact of local soil conditions on the seismic performance of reinforced concrete structures: in the context of the 2023 Kahramanmaraş earthquakes," *Applied Sciences*, vol.15, no.5, pp.2389, 2025.

[28] H. M. Algin, A. B. Ekmen, and E. Kaya, "3D seismic response assessment of barrette piled high-rise building with comprehensive subsurface modelling," *Soil Dynamics and Earthquake Engineering*, vol. 163, pp.107488, 2022.

[29] M.D. Trifunac, "Site conditions and earthquake ground motion–A review," *Soil Dynamics and Earthquake Engineering*, vol.90, pp.88-100, 2016.

[30] Y. Avcı and A. B. Ekmen, "Artificial intelligence assisted optimization of rammed aggregate pier supported raft foundation systems based on parametric three-dimensional finite element analysis," *Structures*, vol. 56, pp.105031, 2023.

[31] K.Ö. Cetin, S. Altun, A. Askan, M. Akgün, A. Sezer, C. Kıncal, C., ... and Karaali, E. (2022). The site effects in Izmir Bay of October 30 2020, M7. 0 Samos earthquake. *Soil Dynamics and Earthquake Engineering*, vol.152, pp.107051, 2022.

[32] E. Bol, A. Özocak, S. Sert, K.Ö. Çetin, E. Arslan, K. Kocaman, and B.U. Ayhan, "Evaluation of soil liquefaction in the city of Hatay triggered after the February 6, 2023 Kahramanmaraş-Türkiye earthquake sequence," *Engineering Geology*, vol.339, pp.107648, 2024.

[33] O. Sivrikaya, E. Türker, E. Cüre, E.E. Atmaca, Z. Angin, H.B. Başağa, and A.C. Altunişik, "Impact of soil conditions and seismic codes on collapsed structures during the 2023 Kahramanmaraş earthquakes: An in-depth study of 400 reinforced concrete buildings," *Soil Dynamics and Earthquake Engineering*, vol.190, pp.109119, 2025.

[34] M. Senkaya, E.F. Erkan, A. Silahtar, and H. Karaaslan, "Implementation of clustering algorithms for damage prediction through seismic local-site parameters: 2023 Kahramanmaraş earthquake sequence," *Bulletin of Earthquake Engineering,* vol.22, no.13, pp.6545-6566, 2024

[35] B. Đ. Bulajić, G. Pavić, and M. Hadzima-Nyarko, "PGA vertical estimates for deep soils and deep geological sediments–A case study of Osijek (Croatia)," *Computers & Geosciences*, vol.158, pp.104985, 2022

[36] S. Lozančić, B. Đ.Bulajić, G. Pavić, I. Bulajić, and M. Hadzima-Nyarko, "Spectral characteristics of strong ground motion time series for low to medium seismicity regions with deep soil atop deep geological sediments," *Engineering Proceedings*, vol.68, no.1, pp.32, 2024.

[37] Ö.F. Nemutlu, and B. Balun, "Evaluation of November 23, 2022, Duzce earthquake data with ground motion prediction equations," *Bitlis Eren Üniversitesi Fen Bilimleri Dergisi,* vol.12, no.4, pp.1248-1260, 2023.

[38] Ö. Yıldız, and C. Kına, "Geotechnical and structural investigations in Malatya province after Kahramanmaraş Earthquake on February 6, 2023," *Bitlis Eren Üniversitesi Fen Bilimleri Dergisi*, 12(3), 686-703, 2023.

[39] M. Çavuşlu, "Assessing seismic crack performance of Diyarbakır Çüngüş Masonry stone bridge

considering 2023 Kahramanmaraş, Hatay, Malatya, Gaziantep earthquakes," *Bitlis Eren Üniversitesi Fen Bilimleri Dergisi*, vol.12, no.2, pp.544-556, 2023.

[40] O. Akyürek, "Analysis of different cross-frame placements to enhance torsional irregular buildings against structural failure under earthquake bidirectional loadings: A case study," *Bitlis Eren Üniversitesi Fen Bilimleri Dergisi*, vol.10, no.2, pp.480-491, 2021.

[41] K. Beyen, and M. Erdik, "Two-dimensional nonlinear site response analysis of Adapazarı plain and predictions inferred from aftershocks of the Kocaeli earthquake of 17 August 1999," *Soil Dynamics and Earthquake Engineering*, vol.24, no.3, pp.261-279, 2004.

[42] M. Batı, and K. Beyen, "8 katlı yapının dinamik yükler altında titreşim kontrolü," *Kocaeli Üniversitesi Fen Bilimleri Dergisi*, vol.3, no.1, pp.65-76, 2020.

[43] G. Eren, and K. Beyen, "Zemin davranışı ve mesnet koşullarının tarihi yapıların dinamik davranışına etkisi," *Eskişehir Teknik Üniversitesi Bilim ve Teknoloji Dergisi B-Teorik Bilimler*, vol.6, pp.244-252, 2018.

[44] T. Ucar, O. Merter, and M. Duzgun, "A study on determination of target displacement of RC frames using PSV spectrum and energy-balance concept," *Structural Engineering and Mechanics*, vol.41, no.6, pp.759–773, 2012.

[45] B. Monavari, A. Massumi, and A. Kazem, "Estimation of displacement demand in RC Frames and comparing with target displacement provided by FEMA-356," in *15th World Conference on Earthquake Engineering*, 2012.

[46] M. N. Fardis and T. B. Panagiotakos, "Displacement-based design of RC buildings: Proposed approach and application," in *Seismic Design Methodologies for the Next Generation of Codes*, Routledge, pp.195–206, 2019.

[47] E. Işık et al., "A comparative study of the effects of earthquakes in different countries on target displacement in mid-rise regular RC structures," *Applied Sciences*, vol.12, no.23, pp.12495, 2022.

[48] E. Işık et al., "Comparison of seismic and structural parameters of settlements in the East Anatolian Fault Zone in light of the 6 February Kahramanmaraş Earthquakes," *Infrastructures*, vol.9, no.12, pp.219, 2024.

[49] F. Akar et al., "Geotechnical and structural damages caused by the 2023 Kahramanmaraş Earthquakes in Gölbaşı (Adıyaman)," *Applied Sciences*, vol.14, no.5, pp.2165, 2024.

[50] O. İnce, "Structural damage assessment of reinforced concrete buildings in Adıyaman after Kahramanmaraş (Türkiye) Earthquakes on 6 February 2023," *Engineering Failure Analysis*, vol.156, pp.107799, 2024.

[51] E. Işık et al., "Field reconnaissance and earthquake vulnerability of the RC buildings in Adıyaman during 2023 Türkiye earthquakes," *Applied Sciences*, vol.14, no.7, pp. 2860, 2024.

[52] S. Avgın, M. M. Köse, and A. Özbek, "Damage assessment of structural and geotechnical damages in Kahramanmaraş during the February 6, 2023 earthquakes," *Engineering Science and Technology, an International Journal*, vol.57, pp.101811, 2024.

[53] M. Öztürk, M. H. Arslan, and H. H. Korkmaz, "Effect on RC buildings of 6 February 2023 Turkey earthquake doublets and new doctrines for seismic design," *Engineering Failure Analysis*, vol.153, pp.107521, 2023.

[54] B. Binici et al., "Performance of RC buildings after Kahramanmaraş earthquakes: lessons toward performance-based design," *Earthquake Engineering and Engineering Vibration*, vol.22, no. 4, pp. 883–894, 2023.

[55] J. Yuzbasi, "Post-earthquake damage assessment: field observations and recent developments with recommendations from the Kahramanmaraş earthquakes in Türkiye on February 6th, 2023 (Pazarcık M7.8 and Elbistan M7.6)," *Journal of Earthquake Engineering*, pp.1–26, 2024.

[56] E. Işık et al., "Seismic performance and failure mechanisms of reinforced concrete structures subject to the earthquakes in Türkiye," *Sustainability*, vol.16, no.15, pp.6473, 2024.

[57] M. Tan, Ö. Avşar, F. Yıldızhan, and N. Atmaca, "Effect of infill walls on the seismic performance of a severely damaged substandard RC building during the February 6, 2023, Kahramanmaras earthquake sequence," *Engineering Failure Analysis*, pp.109117, 2024.

[58] C. Öser et al., "Geotechnical aspects and site investigations on Kahramanmaraş earthquakes, February 06, 2023," *Natural Hazards*, pp.1–32, 2024.

[59] B. Yön et al., "Evaluation of the seismic response of reinforced concrete buildings in the light of lessons learned from the February 6, 2023, Kahramanmaraş, Türkiye earthquake sequences," *Natural Hazards*, pp.1–37, 2024.

[60] H. Ulutaş, "Investigation of the causes of soft-storey and weak-storey formations in low-and mid-rise rc buildings in Türkiye," *Buildings*, vol.14, no.5, pp.1308, 2024.

[61] I. B. Karasin, "Comparative analysis of the 2023 Pazarcık and Elbistan Earthquakes in Diyarbakır," *Buildings*, vol.13, no.10, p.2474, 2023.

[62] E. Işık et al., "Study on effectiveness of regional risk prioritisation in reinforced concrete structures after earthquakes," *Applied Sciences*, vol.14, no.16, pp.6992, 2024.

[63] M. H. Arslan et al., "Code-based damage assessment of existing precast industrial buildings following the February 6th, 2023 Kahramanmaraş earthquakes (Pazarcık Mw 7.7 and Elbistan Mw 7.6)," *Journal of Building Engineering*, vol.86, p.108811, 2024.

[64] Seismostruct, "Seismic Analysis Software for Structures," [Online]. Available: https://www.seismosoft.com.

[65] Eurocode 3, "Design of steel structures – Part 1-1: General rules and rules for buildings," *European Standard EN 1993-1-1*, 2005.

[66] S. Antoniou, R. Pinho . "Seismostruct – Seismic Analysis program by Seismosoft. Technical manual and user manual", 2003.

[67] N. Ademovic, M. Hrasnica, D.V. Oliveira. "Pushover analysis and failure pattern of a typical masonry residential building in Bosnia and Herzegovina, " *Engineering Structures*, vol.50, pp.13- 29, 2013.

[68] J.M. Estêvão, C.S. Oliveira, "A new analysis method for structural failure evaluation," *Engineering Failure Analysis*, vol.56, pp.573-584, 2015.

[69] A.K. Chopra, R.K. Goel. "A modal pushover analysis procedure for estimating seismic demands for buildings," *Earthquake Engineering & Structural Dynamics*, vol.31, no.3, pp.561-582, 2002.

[70] H. Krawinkler, G.D.P.K. Seneviratna, "Pros and cons of a pushover analysis of seismic performance evaluation," *Engineering Structures*, vol.20, no.4-6, pp.452-464, 1998.

[71] E. Işık et al., "Time-dependent model for earthquake occurrence and effects of design spectra on structural performance: a case study from the North Anatolian Fault Zone, Turkey," *Turkish Journal of Earth Sciences*, vol.30, no.2, pp.215–234, 2021.

[72] E. Işık and E. Harirchian, "A comparative probabilistic seismic hazard analysis for Eastern Turkey (Bitlis) based on updated hazard map and its effect on regular RC structures," *Buildings*, vol.12, no.10, pp. 1573, 2022.

[73] A. Antoniou and R. Pinho, "Displacement-based seismic design of structures," *Journal of Earthquake Engineering*, vol.7, no.S1, pp.1–25, 2003.

[74] P. Pinto and E. Franchin, "Performance-based seismic design: Concepts and implementation," in *Seismic Design Methodologies for the Next Generation of Codes*, Routledge, pp.259–280, 2011.

Dicle University
Journal of Engineering
https://dergipark.org.tr/tr/pub/dumf
duje.dicle.edu.tr

Research Article

Effects of Alternative Binder and Aggregate Use on the Compressive Strength of Concrete

Mustafa PALA[1], Nihan GÜLMEZ[2*]

[1] Munzur University, Civil Engineering Department, mstfpalaa23@gmail.com, Orcid No: 0000-0002-1623-9978
[2] Munzur University, Civil Engineering Department, nihangulmez@munzur.edu.tr, Orcid No: 0000-0002-8650-9670

ARTICLE INFO

Article history:

Received 31 March 2025
Received in revised form 13 June 2025
Accepted 29 June 2025
Available online 30 September 2025

Keywords:

Cement, ferrochromium slag, chromium powder, olivine, strength

Doi: 10.24012/dumf.1668362

* Corresponding author

ABSTRACT

The use of industrial wastes in concrete production is of significant importance in reducing environmental impacts and lowering costs. In this study, concrete mixtures were designed by using olivine minerals as a substitute for Portland cement (PC), chromite powder as fine aggregate, and ferrochromium slag as coarse aggregate. The effects of different binder and aggregate ratios on the compressive strength of the concrete were examined after a 7-day curing period. Experimental results showed that mixtures with 5% olivine substitution achieved the highest compressive strength of 22.30 MPa, particularly in mixtures with a cement dosage of 500 kg/m³. This result indicates that the low water/cement ratio and the addition of olivine contribute to increased early-age strength. Furthermore, increasing the chromite powder content to 20% in mixtures with a water/cement ratio of 0.61 led to an 11.7% increase in compressive strength, demonstrating the positive impact of chromite powder on the mechanical performance of the concrete. These findings highlight that cement replacements and aggregate types can significantly affect the mechanical properties of concrete, emphasizing the need for careful selection of both material compositions.

1. Introduction

Since the early 20th century, rapid industrialization has contributed to the progress of civilization while also bringing about environmental issues [1]. This situation has increased the importance of recycling in order to reduce the negative environmental impacts of waste materials and ensure more efficient use of resources [2]. The sustainable utilization of waste materials provides both environmental and economic benefits, particularly in the construction industry [3]. In Turkey and worldwide, the disposal or storage of waste is considered one of the major environmental challenges to be faced in the future [4].

The environmental impacts and high costs of Portland cement have encouraged the investigation of alternative binder materials in concrete production [5]. In this context, the use of industrial waste contributes to objectives such as reducing CO_2 emissions, limiting harmful chemical additives, and decreasing the consumption of natural resources [6], [7], [8]. The utilization of waste materials in concrete production is a crucial step to reduce environmental pollution and lower production costs [9]. Numerous studies have been conducted in the literature on the use of industrial by-products, such as silica fume, blast furnace slag, and fly ash, in concrete production [10], [11].

Chromite ore is a material widely used in the metallurgy and mining industries, and various waste materials are produced during its processing [12], [13]. The use of chromite ore and its processing by-products, such as chromite powder and chromite slag [14], in concrete production enhances environmental sustainability and has the potential to improve the physical and mechanical properties of concrete. In the literature, there are studies indicating that chromium compounds enhance the engineering properties of concrete. For example, Aygün et al. [15] reported that the addition of chromite ore and other metal oxides (Fe_2O_3, TiO_2, $FeO(OH)nH_2O$, $FeCO_3$, PbS, Cr_2O_3, MnO_2) to concrete increases the neutron and gamma radiation absorption capacity and achieves strength up to 30 MPa.

The use of olivine in refractory materials has also become another notable topic in the construction industry. Acar [16] stated that olivine samples obtained from the chromite processing plant were used directly without any pre-treatment and exhibited acceptable shrinkage properties at high temperatures, indicating their potential for use in the production of refractory materials. With these characteristics, olivine is becoming a valuable material that can be utilized in concrete production.

However, there are limited studies in the literature on the combined use of olivine and chromite powder in concrete production. In response to this gap, this study investigates the use of olivine, chromite powder, and ferrochromium slag as replacements in specific proportions to enhance the compressive strength of concrete. This research aims to contribute to the effective use of waste materials in concrete production and improve the strength properties of concrete.

The study seeks to provide significant findings in terms of both environmental sustainability through the utilization of waste and the enhancement of mechanical properties in the construction industry's concrete.

2. Material and Method

2.1. Materials

In this study, CEM I/42.5R Portland cement with a specific gravity of 3.06 was used as the binder material. The specific gravity of the olivine mineral, which was substituted for cement in various proportions, was found to be 3.30. The XRF analysis results of both the cement and olivine are presented in Table 1.

For the preparation of concrete samples, ferrochromium slag was used as the coarse aggregate and chromite powder as the fine aggregate. The specific gravity and water absorption of the aggregates were determined according to ASTM C128 [17], while the loose and compacted bulk densities were measured in accordance with ASTM C29 [18]. The specific gravity of the ferrochromium slag was found to be 2.86, with a water absorption rate of 3.63% and a moisture content of 0.36%. Its loose and compacted bulk densities were 1590 kg/m³ and 1800 kg/m³, respectively. The specific gravity of the chromite powder was determined as 4.94, and its loose and compacted bulk densities were 2520 kg/m³ and 2930 kg/m³, respectively. The granulometric curves of the fine and coarse aggregates are presented in Figure 1. Images of the materials used in the study are shown in Figure 2.

Table 1. XRF analysis results of cement and olivine samples: Oxide composition distribution

Oxide (%)	Cement	Olivine
CaO	63.0	1.6
SiO_2	18.7	34.8
MgO	1.5	48.0
Fe_2O_3	3.7	12.7
Al_2O_3	4.8	1.0
Cr_2O_3	-	0.5
Na_2O	0.3	< 0.11
K_2O	0.6	-
SO_3	2.9	-
MnO	-	0.2
P_2O_5	-	0.4
LOI	3.7	-

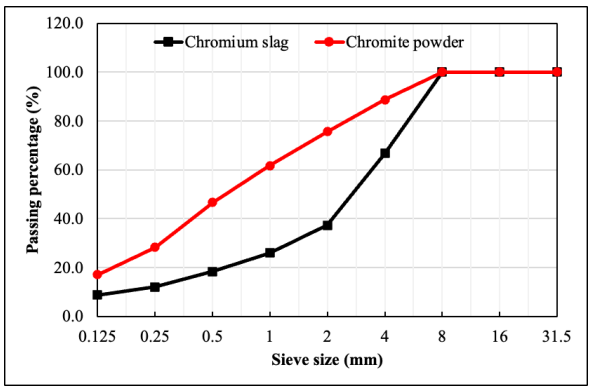


Figure 1. Granulometric curves of the aggregates used in the mixtures

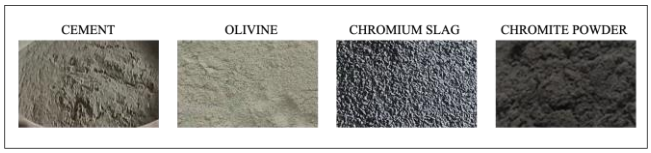


Figure 2. Images of the materials used in the experimental mixtures

2.2. Method

In the experimental study, concrete mixtures were prepared using Portland cement, olivine, chromite powder, and chromium slag. Olivine was used as a partial replacement for Portland cement at a volume ratio of 5%. In addition, chromite powder was incorporated into the mixtures by replacing chromium slag at volume-based replacement ratios of 0%, 10%, and 20%, respectively.

The C20 concrete class, which is commonly used in the construction industry and compliant with the TS EN 206-1 [19] standard, has been determined as the target compressive strength. In this study, the mix proportions were calculated according to the TS 802 [20] standard, and the relevant values are presented in Table 1. Fresh concrete samples were removed from molds with dimensions of 10×10×10 cm one day after casting and placed in a water curing pool. After a 7-day curing period, the samples were subjected to compressive strength testing. The compressive strength tests were conducted in accordance with TS EN 12390-3 [21] standard, with the testing machine applying a uniform load to the samples in the axial direction at a rate of 3 kN/s.

Table 2. Mix proportions of the components used in the experimental design

Mix No.	Olivine (%)	PC (%)	Chromium slag (%)	Chromite powder (%)	Water-Binder	Cement content (kg/m³)
Mix 1	0	100	100	0	0.61	377
Mix 2	5	95	90	10	0.61	377
Mix 3	5	95	80	20	0.61	377
Mix 4	5	95	80	20	0.46	504
Mix 5	5	95	80	20	0.41	561
Mix 6	5	95	80	20	0.41	500

3. Results and Discussion

3.1. Effect of mix components on compressive strength

3.1.1. Binder content and ratio

The binder contents and ratios are among the key factors determining the compressive strength of concrete [22]. Cement is widely used as the primary binder material in concrete [23]. The cement content typically contributes directly to the strength of the concrete [24], [25]. However, excessive increases in cement content can negatively affect the performance of concrete [25]. On the other hand, partial replacement of cement can be beneficial both economically and environmentally [27]. In this context, the experiments conducted with 5% olivine replacement have revealed significant results affecting the strength of concrete, depending on the cement dosage. This observed effect of olivine on compressive strength can be better understood by considering the physical and chemical characteristics of olivine-derived nano silica reported in recent studies. For instance, research by Oesman and Haryadi [28]

demonstrated that amorphous silica extracted from ground olivine via sulfuric acid dissolution forms particles ranging from 1 to 10 μm, influenced by acid concentration and temperature during synthesis. Although these particles were larger than the optimal nano scale (<0.1 μm) for high-performance concrete, the presence of reactive siloxane (Si–O–Si) bonds suggests a notable binding potential. This supports the idea that olivine replacement, even at low proportions, can contribute positively to the binder matrix through its reactive silica content, impacting early strength development and hydration kinetics.

Figure 3 shows the 7-day compressive strengths of the mixtures. In the mixtures with cement dosages of 377, 504, and 500 kg/m³, the replacement of 5% of cement with olivine resulted in higher compressive strengths compared to the mixtures containing 100% cement. In each of these mixtures, it was observed that the replacement of cement with olivine improved the performance of the concrete. This finding suggests that replacing cement with olivine in specific proportions can enhance the strength of concrete. Particularly, at low and medium cement dosages, it was found that olivine replacement could optimize the compressive strength of the concrete, which aligns with previous findings emphasizing the beneficial behavior of olivine in cementitious systems under varying conditions [29]. Additionally, even outside of Portland-based systems, Mg-rich olivine has shown significant reactivity and binding potential — for instance, in phosphate cement systems, olivine dissolution up to 57% was achieved under acidic conditions, highlighting its capacity as a viable reactive mineral [30].

However, when the cement dosage was increased to 561 kg/m³ and 5% olivine was used, it was experimentally observed that the resulting compressive strength decreased by 34.3% compared to the mixtures containing 100% cement. This result suggests that as the cement content increases, the potential for replacement materials, such as olivine, to improve the strength of concrete may be limited. High cement dosages can affect the hydration process of concrete, potentially restricting the capacity of replacement materials to contribute effectively. This highlights the critical role of binder ratios in optimizing the strength of concrete and indicates that replacement materials may only be effective at specific cement dosages.

In conclusion, binder contents and ratios are factors that directly affect the compressive strength of concrete. Proper selection of cement dosage and replacement materials is essential to optimize the early strength and long-term performance of concrete. These experimental findings serve as an important guide for determining the optimal proportions of cement and replacement materials.

3.1.2. Aggregate type, content, and size

The type of aggregate [31], particle size [32], and specific gravity [33] are important parameters that directly affect the microstructure and mechanical strength of concrete [34]. In the experiments, the specific gravity of the ferrochromium slag used as aggregate was 2.86, while the specific gravity of the chromite powder was determined to be 4.94. These values indicate that chromite powder has the potential to form a denser and more compact structure.

When the experimental results were examined, the compressive strength of the samples containing only ferrochromium slag was measured at 9.16 MPa. However, significant improvements in the mechanical performance of the concrete were observed when chromite powder was added as fine aggregate. In the mix containing 10% chromite powder, the strength increased by 6.98%, reaching 9.80 MPa, while in the mix containing 20% chromite powder, the strength increased by 11.7%, reaching 10.23 MPa. This indicates that chromite powder better integrates with the binder matrix, forming a denser internal structure and providing a strengthening effect.

In mixtures where the proportions of ferrochromium slag and chromite powder were kept constant, but the cement content was increased and the water/cement ratio was reduced, the effect of aggregate type and size became more pronounced. In the mixture with 504 kg/m³ of cement, the compressive strength was measured at 13.00 MPa, indicating that the aggregates worked harmoniously with the cement to optimize the strength. However, when the cement dosage was increased to 561 kg/m³ and the water/cement ratio was reduced to 0.41, the strength of the mixture containing 80% ferrochromium slag and 20% chromite powder decreased dramatically by 53.7%, dropping to 6.02 MPa. This dramatic decrease suggests that exceeding a certain limit in the interaction of aggregates with the binder system can adversely affect mechanical strength.

On the other hand, when the cement dosage was optimized to 500 kg/m³, the strength of the mixture with the same aggregates was measured at 22.30 MPa, showing a significant increase of 270.5%. This suggests that a balanced use of coarse and fine aggregates ensures more effective functioning of the binder phase and that appropriate ratios of ferrochromium slag and chromite powder can significantly enhance the strength. Similarly, Panda et al. [35] reported that ferrochrome slag possesses excellent physico-mechanical properties, and its use as both coarse and fine aggregate resulted in concrete with satisfactory compressive strength for general-purpose applications. In a more recent study, Panda et al. [36] demonstrated that the inclusion of ferrochromium slag as coarse aggregate led to more than 20% improvement in compressive strength compared to conventional concrete. Moreover, they emphasized that chromium leaching remained minimal, even under acidic conditions, confirming both technical viability and environmental safety of ferrochrome slag in concrete production.

In conclusion, the combined use of ferrochromium slag and chromite powder positively contributes to the mechanical strength of concrete, provided that the aggregate distribution is properly optimized. The coarse structure of ferrochromium slag plays a crucial role in load-bearing by forming a skeleton, while the high specific gravity of fine chromite powder strengthens the binder matrix, enhancing strength. However, excessive binder content or improper aggregate-binder ratios can reduce the effectiveness of the aggregates, negatively impacting mechanical performance. Therefore, the use of ferrochromium slag and chromite powder in concrete

production should be carefully considered to achieve an optimal aggregate-binder balance.

3.2. Effect of water/cement ratio on compressive strength

The water/cement (w/c) ratio is one of the most critical parameters of concrete in terms of cement hydration, microstructure development, and ultimate mechanical performance [37]. A high W/C ratio enhances the workability of the concrete mix [38] but can reduce strength by increasing the porosity of the matrix [39, 40]. On the other hand, a low w/c ratio can limit the efficiency of hydration [41], increasing the risk of shrinkage [42]. Experimental results clearly demonstrate the decisive influence of the water/cement ratio on concrete compressive strength.

In the experiments, the cement dosage was set at 377 kg/m³ for mixtures with a 0.61 W/C ratio, and the compressive strengths of specimens incorporating specific proportions of ferrochromium slag and chromite powder were measured as 9.16 MPa (Mix 1), 9.80 MPa (Mix 2), and 10.23 MPa (Mix 3), respectively. When the W/C ratio was kept constant, a gradual increase in strength was observed with the increasing amount of chromite powder. However, when the W/C ratio was reduced to 0.46 and the cement content was increased to 504 kg/m³, the compressive strength increased by 27.1%, reaching 13.00 MPa. This improvement can be attributed to the enhanced interaction between the increased binder phase and water, resulting in a denser internal structure.

In mixtures where the W/C ratio was reduced to 0.41, different strength trends were observed depending on the increase in cement dosage. When the cement dosage was 561 kg/m³, the compressive strength of specimens containing 80% ferrochromium slag and 20% chromite powder decreased by 53.7%, reaching 6.02 MPa. This decline can be attributed to the limitation of complete hydration of cement particles at very low W/C ratios, leading to internal stresses. Additionally, the high binder content may have restricted the mechanical contribution of aggregates, accelerating the formation of microcracks and further contributing to the strength reduction.

However, in the mixture where the W/C ratio remained at 0.41 but the cement dosage was optimized to 500 kg/m³, the compressive strength exhibited a significant increase of 270.5%, reaching 22.30 MPa. This finding suggests that while very low W/C ratios can have a positive effect at specific cement dosages, excessive cement content may negatively impact early-age strength.

In conclusion, low W/C ratios can enhance strength in certain binder and aggregate combinations; however, when combined with excessive cement dosage, they may lead to adverse effects. Determining the optimal W/C ratio is a critical design parameter to ensure the completion of the hydration process and maximize mechanical strength.

3.3. Effect of mix design on application areas

In this study, only 7-day compressive strength tests were conducted. This parameter is a crucial indicator for evaluating the early-age performance of concrete. However, examining other properties, such as the long-term durability of concrete and its resistance to environmental conditions, could provide a more comprehensive assessment of its potential applications.

The strength of concrete is critical for the stability and safety of a structure, and its intended use is determined by various parameters, primarily mechanical performance [43]. In this study, different binder and aggregate combinations exhibited significant variations in early-age (7-day) compressive strength. Mix design not only ensures that concrete reaches its target strength level but also directly influences key factors such as workability, durability, and resistance to environmental conditions [44], [45].

According to the experimental results, the highest compressive strength was achieved in Mix 6. This mixture, containing 500 kg/m³ of cement and a 0.41 water/cement ratio, reached a compressive strength of 22.30 MPa at 7 days, outperforming all other mixes. The low water/cement ratio and balanced binder content supported the formation of a denser matrix, thereby enhancing early-age strength. Similar to findings by Dehghanpour et al. [46], where olivine filler promoted the formation of a robust calcium silicate hydrate (C-S-H) structure in cementitious mixtures, the denser matrix in Mix 6 likely benefited from such binding phases. This result suggests that Mix 6 could be a suitable candidate for prefabricated concrete elements requiring early strength, floor coverings, and structural elements that demand high load-bearing capacity.

On the other hand, the lowest strength value was observed in Mix 5. In this mixture, where the cement dosage was increased to 561 kg/m³ and the water/cement ratio was 0.41, the 7-day compressive strength dropped to 6.02 MPa. This suggests that excessive cement content may negatively affect the hydration process, leading to the formation of microcracks. Due to its low early-age strength, this mixture is not suitable for use in structural elements subjected to heavy loads. However, it could be considered for non-load-bearing applications, such as void filling or temporary site fillers, under specific conditions.

Mixtures with lower cement dosages, such as Mix 1, Mix 2, and Mix 3, exhibited limited mechanical performance in terms of their 7-day compressive strength. For example, Mix 1, containing 100% ferrochromium slag (9.16 MPa), Mix 2 with partial chromite powder (9.80 MPa), and Mix 3 (10.23 MPa) may be more suitable for applications such as filler concretes, walkable surfaces, or elements with low load-bearing capacity, where high early strength is not required.

These results highlight that in concrete design, not only the type of binder and aggregate but also the water/cement ratio, cement dosage, and the targeted early-age strength must be considered. Choosing an appropriate mix for the application area is crucial for producing sustainable and durable concrete, both in terms of mechanical and environmental performance.

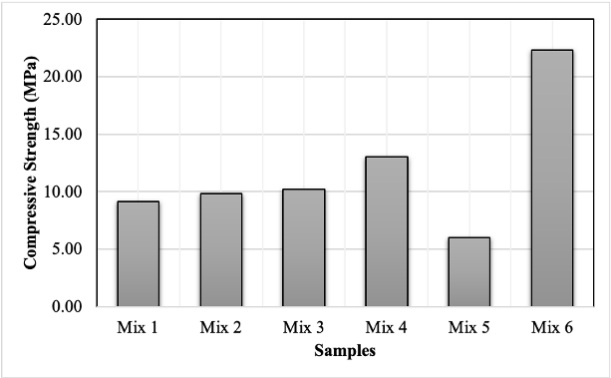


Figure 3. 7-day compressive strength values of the test samples

4. Conclusion

The use of industrial wastes in cement and concrete production is an important approach for reducing environmental pollution and lowering production costs. In this study, the effects of the partial replacement of cement with olivine mineral, along with the use of chromite powder as fine aggregate and ferrochromium slag as coarse aggregate in specific proportions, on concrete compressive strength were investigated. The following findings were obtained from the experiments, which reveal the effects of different binder and aggregate compositions on concrete strength:

- Mixtures with 5% olivine replacement for cement exhibited higher compressive strengths than the mixtures containing 100% cement. Specifically, Mix 3, which included 80% ferrochromium slag and 20% chromite powder, achieved a compressive strength of 10.23 MPa, indicating that olivine can enhance the strength of concrete.
- Increasing the cement dosage generally improves the compressive strength of concrete. Mix 6 (500 kg/m³ cement) achieved a compressive strength of 22.30 MPa. This result suggests that high cement dosages, up to a certain level, can significantly enhance the early-age strength of concrete.
- While reducing the water/cement ratio is generally a factor that increases strength, when the ratio falls below a certain threshold, hydration reactions may become limited, leading to potential strength losses.
- Among the mixtures with a 0.41 water/cement ratio, the mixture containing 500 kg/m³ of cement showed a compressive strength of 22.30 MPa, while the mixture with 561 kg/m³ of cement dropped to 6.02 MPa. This suggests that high cement dosages do not always result in higher strength and that the optimal water/cement ratio should be determined in balance with the binder content.

Conflict of Interest

The prepared article does not have any conflict of interest with any individual/institution.

Acknowledgment

This study was supported by the Scientific Research Coordination Unit of Munzur University under project number YLMUB021-17.

References

[1] S. Mehmood, K. Zamani, S. Khan, Z. Ali, and H. U. Rashid Khan, “The role of green industrial transformation in mitigating carbon emissions: Exploring the channels of technological innovation and environmental regulation,” Energy and Built Environment, vol. 5, pp. 464–479, 2024. https://doi.org/10.1016/j.enbenv.2023.03.001.

[2] Y. A. Hajam, R. Kumar, and A. Kumar, “Environmental waste management strategies and vermi transformation for sustainable development,” Environmental Challenges, vol. 13, 100747, 2023. https://doi.org/10.1016/j.envc.2023.100747.

[3] A. I. Almohana, M. Y. Abdulwahid, I. Galobardes, J. Mushtaq, and S. F. Almojil, "Producing sustainable concrete with plastic waste: A review," Environ. Challenges, vol. 9, p. 100626, 2022. https://doi.org/10.1016/j.envc.2022.100626.

[4] T. Esin and N. Cosgun, “A study conducted to reduce construction waste generation in Turkey,” Building and Environment, vol. 42, pp. 1667–1674, 2007. https://doi.org/10.1016/j.buildenv.2006.02.008.

[5] İ. Şanal, “Beton üretiminin karbondioksit emisyonları açısından önemi: Toplumsal ve çevresel etkiler,” Politeknik Dergisi, vol. 21, no. 2, pp. 369–378, 2018.

[6] J. M. Etcheverry, Y. A. Villagran-Zaccardi, P. Van den Heede, V. Hallet, and N. De Belie, “Effect of sodium sulfate activation on the early age behaviour and microstructure development of hybrid cementitious systems containing Portland cement, and blast furnace slag,” Cement and Concrete Composites, vol. 141, 105101, 2023. https://doi.org/10.1016/j.cemconcomp.2023.105101.

[7] M.A.G.P. Perera and P.G. Ranjith, “Eco-friendly cementitious composites for enhanced strength: Emerging trends and innovations,” Journal of Cleaner Production, vol. 468, 142962, 2024. https://doi.org/10.1016/j.jclepro.2024.142962.

[8] M. Şahin Yön, B. Yön, M. Karataş, and A. Benli, “Sustainable use of boron waste and volcanic scoria in slag-based self-compacting alkali-activated mortars: Fresh, mechanical and durability properties,” Sustain. Chem. Pharm., vol. 41, 101664, 2024. https://doi.org/10.1016/j.scp.2024.101664.

[9] S. Cemalgil, O. Onat, M. K. Tanaydın, and S. Etli, “Effect of waste textile dye adsorbed almond shell on self-compacting mortar,” Construction and Building Materials, vol. 300, 123978, 2021. https://doi.org/10.1016/j.conbuildmat.2021.123978.

[10] M. Şahin Yön, “Mechanical, durability and microstructure properties of eco-friendly self-compacting mortars with addition of volcanic scoria, silica fume and boron waste as cement replacement,” Construction and Building Materials, vol. 462, 139894, 2025. https://doi.org/10.1016/j.conbuildmat.2025.139894.

[11] A. Benli, O. Y. Bayraktar, M. Karataş, B. Bodur, M. U. Yılmazoğlu, and G. Kaplan, “Dunite powder as a green precursor in one-part alkali-activated composites: Effects on

mechanical and durability properties," Sustainable Chemistry and Pharmacy, vol. 44, 101964, 2025. https://doi.org/10.1016/j.scp.2025.101964.

[12] Y. Lan, L. Zhang, X. Li, W. Liu, X. Su, and Z. Lin, "Efficient immobilization and utilization of chromite ore processing residue via hydrothermally constructing spinel phase Fe2+(Cr3+X, Fe3+2-x)O4 and its magnetic separation," Science of the Total Environment, vol. 813, 152637, 2022. http://dx.doi.org/10.1016/j.scitotenv.2021.152637.

[13] Z. Bayer Öztürk, S. Dal, Characterization of industrial ceramic glazes containing chromite processing waste: Experimental factorial design effects on color parameters, Mater. Chem. Phys. 282 125928, 2022. https://doi.org/10.1016/j.matchemphys.2022.125928.

[14] S.K. Das, A. K. Tripathi, S. K. Kandi, S. M. Mustakim, B. Bhoi, and P. Rajput, "Ferrochrome slag: A critical review of its properties, environmental issues and sustainable utilization," Journal of Environmental Management, vol. 326, 116674, 2023. https://doi.org/10.1016/j.jenvman.2022.116674.

[15] B. Aygün, E. Şakar, O. Agar, M. I. Sayyed, A. Karabulut, and V. P. Singh, "Development of new heavy concretes containing chrome-ore for nuclear radiation shielding applications," Prog. Nucl. Energy, vol. 133, 103645, 2021. https://doi.org/10.1016/j.pnucene.2021.103645.

[16] İ. Acar, "Sintering properties of olivine and its utilization potential as a refractory raw material: Mineralogical and microstructural investigations," Ceram. Int., vol. 46, pp. 28025–28034, 2020. https://doi.org/10.1016/j.ceramint.2020.07.297.

[17] ASTM C128, Standard Test Method for Density, Relative Density (Specific Gravity), and Absorption of Fine Aggregate, ASTM International, West Conshohocken, PA, 2015.

[18] ASTM C29, Standard Test Method for Bulk Density ("Unit Weight") and Voids in Aggregate, ASTM International, West Conshohocken, PA, 2017.

[19] TS EN 206-1, Concrete – Part 1: Specification, performance, production and conformity, Turkish Standards Institution, Ankara, 2002.

[20] TS 802, Design of concrete mixes, Turkish Standards Institution, Ankara, 2016.

[21] TS EN 12390-3, Testing hardened concrete – Part 3: Compressive strength of test specimens, Turkish Standards Institution, Ankara, 2009.

[22] K. Kaewmanee and S. Tangtermsirikul, "Properties of binder systems containing cement, fly ash, and limestone powder," Songklanakarin J. Sci. Technol., vol. 36, no. 5, pp. 569–576, Sep.–Oct. 2014.

[23] G.C. Wang, "Slag use in cement manufacture and cementitious applications," The Utilization of Slag in Civil Infrastructure Construction, pp. 305-337, 2016. https://doi.org/10.1016/B978-0-08-100381-7.00013-6.

[24] H. Polat and C. Özel, "The effects of water/cement ratio and cement dosage variables on the performance of shotcrete: Compressive strength and drying shrinkage perspective," Turkish Journal of Engineering and Environmental Sciences, vol. 12, no. 2, pp. 82-87, 2023. https://doi.org/10.46810/tdfd.1291146.

[25] S. Khalid, K. Rashid, K. Mawra, Z. Tariq, H. Kim, and M. Ju, "Multimodal optimization of concrete mix design for sustainable load bearing wall panels: Mean-mix − Artificial Intelligence − experimentation fusion," Case Stud. Constr. Mater., vol. 21, e03868, 2024. https://doi.org/10.1016/j.cscm.2024.e03868.

[26] W. Piasta and B. Zarzycki, "The effect of cement paste volume and w/c ratio on shrinkage strain, water absorption and compressive strength of high performance concrete," Construction and Building Materials, vol. 140, pp. 395-402, 2017. https://doi.org/10.1016/j.conbuildmat.2017.02.033.

[27] B. Song, J. Huang, M. Yang, M. Zheng, L. Yang, and F. Wang, "Study on high supplementary cementitious materials content cement: Design and analysis based on response surface method," Construction and Building Materials, vol. 467, 140398, 2025. https://doi.org/10.1016/j.conbuildmat.2025.140398.

[28] M. Oesman and Haryadi, "Production and application of olivine nano-silica in concrete," IOP Conf. Ser.: Mater. Sci. Eng., vol. 204, 012008, 2017. https://doi.org/10.1088/1757-899X/204/1/012008.

[29] M. Achang and M. Radonjic, "Adding olivine micro particles to Portland cement based wellbore cement slurry as a sacrificial material: A quest for the solution in mitigating corrosion of wellbore cement," Cem. Concr. Compos., 121, 104078, 2021. https://doi.org/10.1016/j.cemconcomp.2021.104078.

[30] D. Bernasconi, A. Viani, L. Zárybnická, S. Bordignon, J. R. A. Godinho, A. Maximenko, C. Celikutku, S. F. Jafri, E. Borfecchia, Q. Wehrung, R. Gobetto, and A. Pavese, "Setting reaction of a olivine-based Mg-phosphate cement," Cem. Concr. Res., 186, 107694, 2024. https://doi.org/10.1016/j.cemconres.2024.107694.

[31] D. Alfonso, M. Dugarte, J. Carrillo, and C. A. Arteta, "Effect of aggregate type on the elastic modulus and compressive behavior of concrete: A case study in Colombia," Constr. Build. Mater., vol. 411, 134131, 2024. https://doi.org/10.1016/j.conbuildmat.2023.134131.

[32] A.-I. Ndon and A. E. Ikpe, "Experimental study on the effect of different coarse aggregate sizes on the strength of concrete," Int. J. Eng. Innov. Res., vol. 3, no. 1, pp. 29–38, 2021. https://doi.org/10.47933/ijeir.779307.

[33] R. Vandhiyan, T. J. Vijay, and M. K. M., "Effect of fine aggregate properties on cement mortar strength," Mater. Today Proc., vol. 37, pp. 2019–2026, 2021. https://doi.org/10.1016/j.matpr.2020.07.498.

[34] G. A. Rao, "Role of water–binder ratio on the strength development in mortars incorporated with silica fume," Cem. Concr. Res., vol. 31, pp. 443–447, 2001. https://doi.org/10.1016/S0008-8846(00)00500-7.

[35] C.R. Panda, K.K. Mishra, K.C. Panda, B.D. Nayak, and B.B. Nayak, “Environmental and technical assessment of ferrochrome slag as concrete aggregate material,” Constr. Build. Mater., 49, pp. 611–621, 2013. https://doi.org/10.1016/j.conbuildmat.2013.08.002.

[36] C. Panda, A. Pujari, S.S. Biswal, T. Jena, N. Pradhan, and S.K. Mallick, “Environmental appraisal of ferrochromium slag as concrete pavement material,” Mater. Today Proc., 67, pp. 1064–1068, 2022. https://doi.org/10.1016/j.matpr.2022.07.011.

[37] P. Wang, L.-Y.-W. Ke, H.-L. Wu, and C. K. Y. Leung, "Effects of water-to-cement ratio on the performance of concrete and embedded GFRP reinforcement," Constr. Build. Mater., vol. 351, p. 128833, 2022. https://doi.org/10.1016/j.conbuildmat.2022.128833.

[38] S. A. Ayanlere, S. O. Ajamu, S. O. Odeyemi, O. E. Ajayi, and M. A. Kareem, “Effects of water-cement ratio on bond strength of concrete,” Mater. Today: Proc., vol. 86, pp. 134–139, 2023. https://doi.org/10.1016/j.matpr.2023.04.686.

[39] Y.Y. Kim, K.-M. Lee, J.-W. Bang, and S.-J. Kwon, "Effect of W/C ratio on durability and porosity in cement mortar with constant cement amount," Adv. Mater. Sci. Eng., vol. 2014, 273460, 2014. https://doi.org/10.1155/2014/273460.

[40] C. Wang and M. Song, "Influence of water-cement ratio and type of mixing water on the early hydration performance of calcium sulphoaluminate (CSA) cement," Adv. Mater. Sci. Eng., vol. 2021, 5557763, 10 pages, 2021. https://doi.org/10.1155/2021/5557763.

[41] D.P. Bentz, “Influence of water-to-cement ratio on hydration kinetics: Simple models based on spatial considerations,” Cement Concr. Res., vol. 36, pp. 238–244, 2006. https://doi.org/10.1016/j.cemconres.2005.04.014.

[42] R. Cortas, E. Rozière, S. Staquet, A. Hamami, A. Loukili, and M.-P. Delplancke-Ogletree, “Effect of the water saturation of aggregates on the shrinkage induced cracking risk of concrete at early age,” Cement Concr. Compos., vol. 50, pp. 1–9, 2014. https://doi.org/10.1016/j.cemconcomp.2014.02.006.

[43] A. Ashokan, S. Rajendran, and R. Dhairiyasamy, "A comprehensive study on enhancing the mechanical properties of steel fiber reinforced concrete through nano silica integration," Sci. Rep., vol. 13, p. 20092, 2023, https://doi.org/10.1038/s41598-023-47475-0.

[44] H. Mostafaei, B. Badarloo, N.F. Chamasemani, M.A. Rostampour, and P. Lehner, "Investigating the effects of concrete mix design on the environmental impacts of reinforced concrete structures," Buildings, vol. 13, no. 5, 1313, 2023, https://doi.org/10.3390/buildings13051313.

[45] B.K. Mussey, L.N.W. Damoah, R.N.A. Akoto, and Y.D. Bensah, "Optimization of concrete mix design for enhanced performance and durability: integrating chemical and physical properties of aggregates," Cogent Eng., vol. 11, no. 1, p. 2347370, 2024, https://doi.org/10.1080/23311916.2024.2347370.

[46] H. Dehghanpour, F. Doğan, S. Subaşı, and M. Maraşlı, “Experimental study on engineering properties of recycled olivine aggregate filled CF reinforced electrically conductive mortars,” Sakarya Univ. J. Sci., vol. 28, no. 3, pp. 452–465, 2024. https://doi.org/10.16984/saufenbilder.1156414

Dicle University
Journal of Engineering
https://dergipark.org.tr/tr/pub/dumf
duje.dicle.edu.tr

Derleme Makale / Review Article

Tarihi yapılarda tespit edilen sorunların yapı malzemeleri üzerinden iyileştirilmesi

Improving the deteriorations of historic buildings through building materials

Ebru Kılıç Bakırhan[1*]

[1] Karabük Üniversitesi, Mimarlık Bölümü, ebrukilic@karabuk.edu.tr
ORCID: https://orcid.org/0000-0003-0650-8297

MAKALE BİLGİLERİ

Makale Geçmişi:

Geliş 7 Nisan 2025
Revizyon 11 Temmuz 2025
Kabul 29 Temmuz 2025
Online 30 Eylül 2025

Anahtar Kelimeler:

Tarihi çevre, doğal çevre, koruma, mimari sürdürülebilirlik, malzeme iyileştirmeleri

ÖZ

Tarihi yapılar günümüz şartlarına uyum sağlayabilmeleri ve varlıklarını sürdürebilmeleri adına çeşitli müdahalelere ihtiyaç duyabilmektedir. Bu süreçte yapılarda tespit edilen sorunların yenilikçi bir çerçevede ele alınarak tarihi dokuya ve çevreye zarar vermeden giderilmesi gerekir. Bu çalışmada yıllar içerisinde tarihi yapılarda görülen aksaklıklar ve ihtiyaçlar ele alınarak bunların yapı malzemesi ölçeğinde giderilmesine yönelik çözüm önerileri sunulmuştur. Çalışmanın metodolojisine göre, nem sorunu, enerji performansı, termal konfor, çevresel etkiler ve iç mekân hava kalitesi olarak belirlenen beş farklı kategoride son on yılda literatüre kazandırılmış olan çalışmalar incelenmiştir. Bu çalışma, yeni malzeme ve teknoloji kullanımının tarihi çevre kadar doğal çevreye olan etkilerinin de incelenmesi açısından bilinçlendirici bir yaklaşıma sahiptir.

ARTICLE INFO

Article history:

Received 7 April 2025
Received in revised form 11 July 2025
Accepted 29 July 2025
Available online 30 September 2025

Keywords:

Historic environment, natural environment, conservation, architectural sustainability, material improvements

Doi: 10.24012/dumf.1671361

ABSTRACT

Historic buildings may need various interventions to adapt to changing conditions and maintain their existence. The problems identified in the buildings should be addressed in an innovative framework and should be eliminated without harming the historical texture and the environment. In this study, the problems and needs of historical buildings over the years are discussed and solutions are proposed to eliminate them on the scale of building materials. Recent studies in five different categories, namely humidity and dampness, energy performance, thermal comfort, environmental impacts, and indoor air quality, were examined. This study has an awareness-raising approach in terms of examining the effects of the use of new materials on the natural environment as well as the historical environment.

* Sorumlu Yazar

Giriş

İnşa edildiği döneme ait fiziksel özelliklerini bütüncül bir şekilde barındıran ve toplumsal, görsel veya tarihi açıdan bir değere sahip yapılar, tarihi bina kategorisinde değerlendirilmektedir [1]. Ayrıca kültürel mirasa ait olan bir yapının 100 yıl boyunca yıkılmadan ayakta kalması ona 'tarihi yapı' unvanı kazandırır [2]. Ancak bu kadar uzun süre tarihe tanıklık eden yapılarda yıllar içerisinde değişen çevresel koşullar, kullanıcı hataları veya yapı malzemelerinin ömrünü tüketmesi nedeniyle çeşitli deformasyonlar görülmeye başlar. Bu tür sorunların üstesinden gelinmesinde yeni malzeme ve tekniklerden faydalanılması, yapıların ömrünü uzatarak tarihi yapıların sürdürülebilirliğe katkı sunabilmektedir [3].

Tarihi yapıların koruma işlerinin yapının bütünlüğünü bozmayacak şekilde gerçekleştirilmesi gerekir. Ancak koruma işlemleri doğal kaynakların kullanıldığı, atık malzemelerin ortaya çıktığı, maliyetli ve özen gerektiren bir süreçtir. Bu sürecin doğal ve yapılı çevreye en az etki edecek şekilde yürütülmesi elzemdir. Tarihi binaların restorasyonunda kullanılan malzemeler, yapı ile uyumu, rengi, dokusu, işlevi ve özellikleri açısından dikkatle seçilmelidir [4].

Yöntem

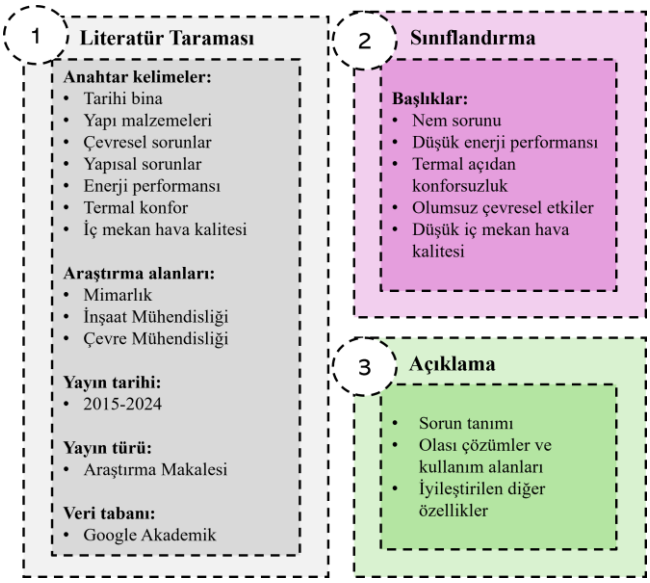
Kültürel mirasın korunmasına yönelik alınması gereken önlemlerin gözler önüne serilmesi, güncel malzeme teknolojilerinin tartışılması ve tarihi yapıların korunması ile ilgilenen yetkililerin bilinçlendirilmesi çalışmanın temel amaçlarındandır.

Bu çalışmada tarihi yapılarda sıkça görülen çeşitli sorunları ele alan ve son on yılda yayınlanmış olan çalışmalar incelenmiştir. Seçilen çalışmaların yapı malzemesi ölçeğinde bir yenilik sunmasına da ayrıca özen gösterilmiştir. Tarihi yapılardaki problemler nem sorunu, düşük enerji performansı, termal açıdan konforsuzluk, olumsuz çevresel etkiler ve düşük iç mekan hava kalitesi olmak üzere beş ana başlık altında toplanmıştır.

Her bir başlık altında açıklanan tarihi yapı sorunu; (1) ilgili sorunun tanımlanması, (2) olası çözümlerin ve yapıda kullanım alanlarının verildiği bir görsel ve (3) yapıda iyileştirilen diğer özelliklerin açıklamasını içeren bir tablo ile desteklenmiştir (Şekil 1).

Bulgular

Beş ana başlık altında incelenen çalışmalarda, nem sorunu için odun külü katkısı ve kil bariyeri; düşük enerji performansının artırılmasına yönelik olarak soğuk renk malzeme ve membran kullanımı; termal konforsuzluğun giderilebilmesi için termal kütle, faz değiştiren malzeme (FDM) ve çeşitli gölgelendirme elemanları; çevresel etkilerin düşürülmesinde atık malzemeden yararlanılması ve atık yönetimi; iç mekan hava kalitesinin iyileştirilmesinde ise yeşil yapı malzemelerinin kullanımına değinilmiştir.



Şekil 1. Çalışmanın metodolojisi.

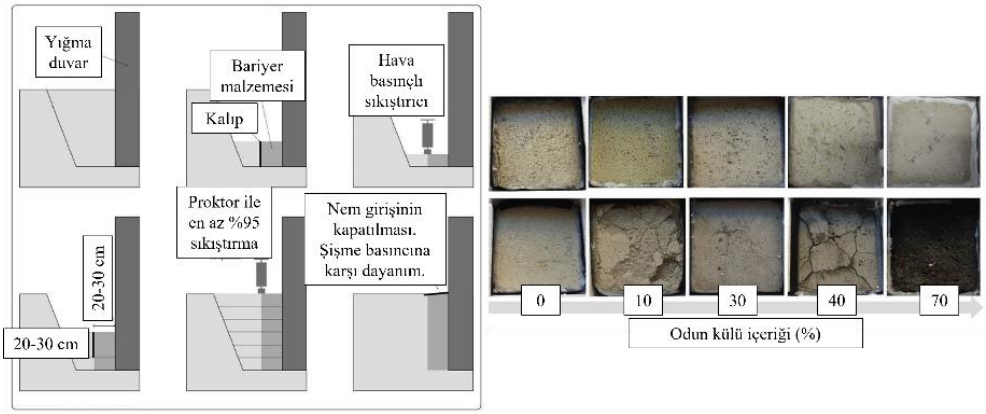
Nem sorunu

Yapı malzemelerinde yıllar içerisinde meydana gelen hasar, topraktan gelen neme karşı yapıyı savunmasız hale getirebilir. Nem, yapı strüktürüne ve kaplamalara zarar vererek bina kabuğunda gerçekleşen ısı alışverişini artırır ve bu durum binanın enerji tüketiminin de artmasına neden olur. Ayrıca kullanıcılarda konforsuzluk hissine de yol açan iç mekanlardaki yüksek nem artışı, küf oluşumuna ve bina kullanıcılarında çeşitli sağlık problemlerinin gelişmesine neden olabilmektedir [5].

Tarihi yapılardaki nem artışı, yapının taşıyıcı sisteminin zarar görmemesi adına üstesinden gelinmesi gereken ciddi bir sorundur. Bu aşamada düşük maliyetli, tarihi dokuda en az etkiye neden olacak nem bariyerlerinden faydalanılabilir. Piyasada düşük hidrolik iletkenliğe sahip olarak satılan bentonit kil-kum karışımı ve buzul tortusu içeren farklı bariyerler tarihi bir bina kapsamında değerlendirilmiş ve test edilen toprak numunelerinin zeminden nem girişi ve buna bağlı gerçekleşen hasarı önlemede etkili olabileceği görülmüştür. Bahsi geçen kil karışımları birçok koruma projesinde uygulanmış ve laboratuvarda test edilmiştir [6].

Neme maruz kalmış tarihi binalardan nemin uzaklaştırılmasında kireç harcının içine katılan odun külü de etkili olabilmektedir [7]. Yapılan deneysel bir çalışmada kireç harcına %20 ila %40 oranında katılan odun külünün harç üzerinde puzolanik aktivite göstererek kılcal doygunlukta odun külü içermeyen harçlara göre daha fazla suyu emdikleri ortaya çıkmıştır (Tablo 1). Bunun nedeninin harç içeriğindeki gözenek sayısının artması olduğu bilinmektedir. Kullanılan biyokütle özelliğindeki odun külü, nemli ortamlarda bulunan yığma duvarların derzlerinin onarılmasında, belirtilen ideal oranlarda olmak kaydıyla, kullanılabilir. Bu oranların üzerine çıkılması durumunda ise kuruma aşamasında harçta büzülmeler gözlemlenmiştir [7].

Tablo 1. Nem sorunu ve olası çözümler

Sorunlar	Nemin bina strüktürüne zarar vermesi, dayanımı düşürmesi, kullanıcı konforsuzluğuna neden olması ve yalıtımı zedelemesi sonucunda binanın enerji tüketiminde artışa neden olması.
Olası çözümler ve yapıda kullanım alanları	Yığma duvarların toprakla temas eden yüzeyinde kil bariyerlerinin [6] ve kireç harcında odun külünün kullanımı [7].  Yukarıdaki görsellerde yığma duvara uygulanan kil bariyerin inşa edilme aşamaları (solda) ve farklı oranlarda odun külü içeren kireç harcındaki bozunmalar (sağda) gösterilmektedir.
İyileştirilen özellikler	Tarihi dokuya minimum müdahale, malzeme gözeneklerinin kapatılarak nem girişinin ve hasarın önüne geçilmesi.

Düşük Enerji Performansı

Tarihi yapıların enerji tüketimlerinin azaltılmasında genellikle içten uygulanan yalıtım katmanı ve bunun yeterli gelmemesi durumunda aktif olarak enerji tüketen cihazlarla iyileştirmelere gidilir. Yakın zamanda bu yöntemlere ek olarak etkin şekilde enerji verimliliği sağlayacak yenilikçi çözüm ve malzemelerin arayışına girişilmiştir.

Bu çalışmalardan biri İtalya'da gerçekleştirilen soğuk renkli cephe malzemelerinin kullanımıdır. Ilık veya sıcak iklimlere sahip bölgelerde termal konforun sağlanması ve soğutma yükünün düşürülmesi adına genellikle açık renkli elemanlar tercih edilmektedir. Ancak tarihi çevrelere hâkim olan renkler gri veya kırmızı tonlarındadır. Bu durum dikkate alınarak seçilen tarihi bir yapı üzerinden yürütülen çalışmada, enerji performansının iyileştirilmesi adına tarihi binaların dış görünüşüne etki etmeden yenilikçi, soğuk renkli, çimento bazlı malzeme kullanımı önerilmiştir. Laboratuvarda elde edilen çıktılar, dinamik simulasyonlarda vaka çalışması ölçeğinde kullanılmıştır. Harçlara renk pigmentleri eklenerek oluşturulan bu yeni cephelerin yüzey sıcaklıkları geleneksel cephelerle kıyaslandığında 8°C düşüş ve soğutmadan kaynaklı enerji tüketiminde %3 oranında azalma sağlandığı görülmüştür [8].

Gerilebilir membranlar, maliyet etkin ve sürdürülebilir bir şekilde binaların strüktürel performanslarını iyileştirmek için yaygın olarak tarihi binalarda uygulanmaktadır. Ancak bu tür membranların iç mekân konforuna ve enerji tüketimine olan etkilerini ortaya koymak önemlidir. Bu amaçla İtalya'da yer alan ve orta avluya sahip tarihi bir yapının orta avlusunun plastik bir polimer türü olan ETFE ile kaplanmasının binanın enerji performansına olan etkisi araştırılmıştır (Tablo 2). Enerji simülasyonlarının sonucunda, uygulanan membran sayesinde özellikle kış aylarında en yüksek enerji kazanımının sağlandığı görülmüştür. Yıllık karbon salımlarında sıcak aylarda %6, soğuk aylarda %10 düşüş gözlemlenmiştir [9].

Tablo 2. Enerji performansının iyileştirilmesine yönelik olası çözümler

Sorunlar	Enerji performansında düşüş, iklim değişikliği, geleneksel iyileştirme hamlelerinin yetersiz olması.
Olası çözümler ve yapıda kullanım alanları	Yapı kabuğunda soğuk renkli malzemeler [8] ve avlu üzerinde ETFE membran kullanımı [9].  Yukarıdaki görsellerde soğuk renk pigmenti eklenen harç karışımı (solda) ve tarihi bina avlusuna gerilen üst örtünün detayları (sağda) gösterilmektedir.

İyileştirilen özellikler	Termal konfor, enerji performansı, maliyet etkinliği, strüktürel performans, çevresel etkiler.

Termal Konfor Eksikliği

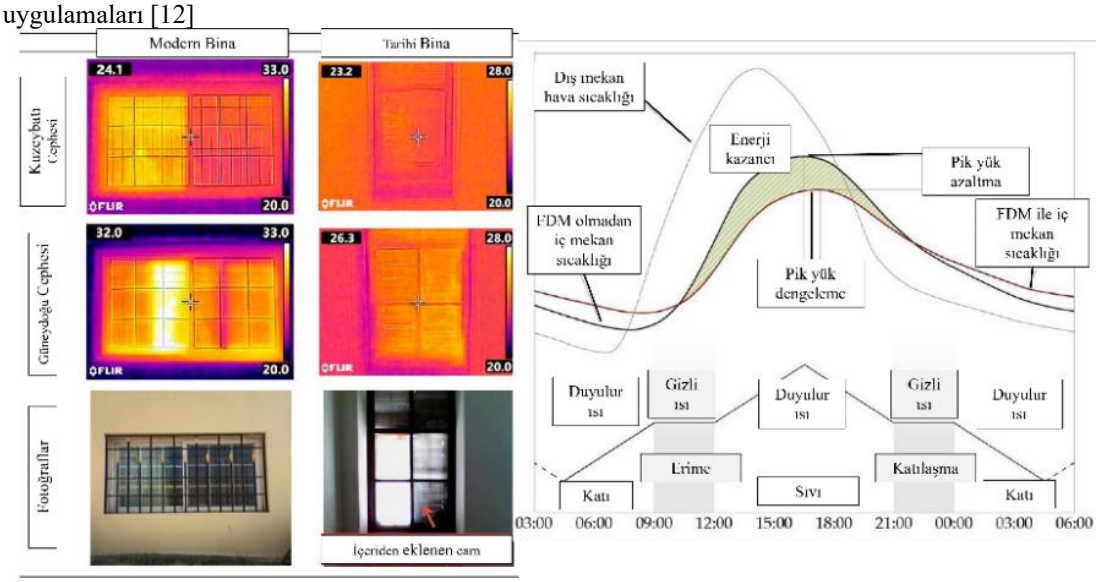
Küresel çapta gerçekleşen iklim değişikliği tarihi yapıların iç mekân sıcaklıkları ve dolayısıyla kullanıcıların termal konforu üzerinde olumsuz etkilere neden olabilmektedir. Bu nedenle mevcut binalar daha fazla aktif sistemlere bağlı kalmakta ve yeni binalara göre bu tür yapıların enerji tüketimleri artış göstermektedir. Neticede daha fazla karbon salımı gerçekleşmekte ve küresel ısınma artış göstererek iklim değişiklikleri de bundan payına düşeni almaktadır. Bu kısır döngüden çıkabilmek adına termal konforun sağlanması, konunun kilit noktasını teşkil etmektedir [10].

Termal konforun sağlanmasında aktif sistemlerin büyük rol üstlendikleri ve kullanımları süresince harcanan enerjinin tarihi binaların mevcut enerji tüketiminden daha az olduğu bilinse de [10], aktif sistemlerden önce pasif tasarım ilkeleri bağlamında malzemelerin sağladıkları avantajların irdelenmesi mimari sürdürülebilirliğin sağlanması açısından esastır.

Bu pasif ilkelerden biri olan termal kütlelerin kullanımının ısıl konforun sağlanmasında etkili olduğu bilinmektedir. Saha araştırmasına dayalı bir çalışmada doğru yönelim, cam seçimi, gölgelendirme elemanları ve havalandırma ile bu etkinin daha da güçlendirilebildiği görülmüştür. Özellikle sıcak iklimlerde konfor şartlarının sağlanmasında cam türü seçiminin termal kütleden daha etkili olduğu bilinmektedir. Tüm bu bahsi geçen yapı malzemelerinin ekstrem hava koşullarında ve gerekli görüldüğü durumda aktif sistemlerle desteklenmesi, ısıl konfor ve enerji performansı açısından etkili olacaktır [11].

Diğer yandan tarihi binaların çoğunluğunda halihazırda termal kütle kullanıldığı bilinmektedir. Ancak termal kütlenin yeterli olmadığı durumlarda restorasyon aşamasında faz değiştiren malzeme (FDM) içeren harçların kullanımı, binaların termal ataletini iyileştirebilir ve bu müdahale aynı zamanda tarihi binanın dış görünüşüne etki etmez (Tablo 3). Kireç harcına granül parafin FDM'nin eklendiği deneysel ve sayısal simülasyonlara dayalı bir çalışmada, ağırlıkça %10 FDM harcı içeren numunenin referans numuneye göre enerji kullanımında %9-18 düşüş ve malzemenin termal iletkenliğinde %22,5 azalma sağladığı gözlemlenmiştir [12].

Tablo 3. Termal konforun iyileştirilmesine yönelik olası çözümler

Sorunlar	Termal konforsuzluk ve buna dayalı enerji tüketiminde gerçekleşen artış, küresel ısınma, karbon salımlarındaki artış.
Olası çözümler ve yapıda kullanım alanları	Yapı kabuğunda termal kütle kullanımı, uygun cam seçimi, gölgelendirme elemanları [11] ve FDM uygulamaları [12]  Yukarıdaki görsellerde 2020 yılı ilkbahar sezonunda saat 10:00-14:00 aralığında elde edilen tarihi ve modern binalara ait termal kamera görüntüleri (solda) ve FDM kullanımından kaynaklanan enerji kazanımı (sağda) gösterilmektedir.
İyileştirilen özellikler	Termal konfor, enerji performansı, maliyet etkinliği, aktif sistemlere olan bağımlılığın azaltılması, çevresel etkiler.

Olumsuz Çevresel Etkiler

Tarihi yapıların korunmasında kullanılan her yeni malzeme yeni ham madde ihtiyacını da beraberinde getirerek çevre

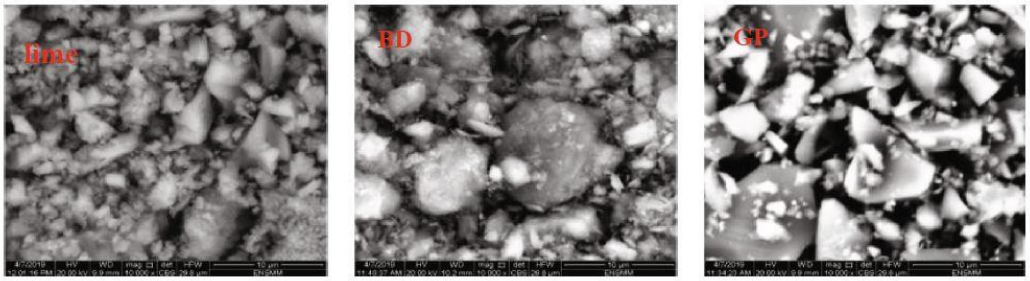
üzerinde bir yük oluşturur. Bunun çözümlerinden biri de atık malzeme kullanımına yönelmektir. Bu sayede yapı malzemelerinin mekanik ve fiziksel özelliklerinin geliştirilebilmesinin yanı sıra çevresel etkilerinin düşürülebilmesi de mümkün olabilmektedir.

Kuzey Cezayir'de gerçekleştirilen ve vaka çalışmasına dayalı olarak laboratuvarda gerçekleştirilen deneysel bir çalışmada kireç harçlarına eklenen %30 oranındaki seramik atığı ve cam şişelerden elde edilen cam tozu sayesinde puzolanik aktivitenin görüldüğü ve özellikle basınç dayanımında artış sağlandığı tespit edilmiştir. Sınanan numuneler arasında %30 oranında cam tozu içeren harçta, en düşük açık gözenekliliğe sahip olması nedeniyle suya karşı en yüksek direncin sağlandığı görülmüştür (Tablo 4). İyileştirilen özelliklerin yanı sıra ham madde ihtiyacının kullanılan atık oranınca düşürülmesi çevresel açıdan kayda değerdir [13].

Meksika'da saha araştırması ve sayısal hesaplamalara dayalı bir çalışmada atık yönetiminin önemine değinilmiştir. Koruma projelerinde inşaat atıklarının geri dönüştürülecek, yeniden kullanılacak ve atık sahasına gönderilecek yapı malzemeleri şeklinde tasniflenmesinin Toolkit gibi araçlarla basitleştirilebildiği ortaya çıktı. Bu yaklaşım kaynak verimliliğinin sağlanması yoluyla çevresel etkileri düşürebildiği gibi restorasyon maliyetlerinin azaltılmasında da önemli katkılar sağlanmıştır [14].

Ayrıca tarihi binaların kullanım aşamasında gösterdiği çevresel etkilerin yüksek olduğu düşünüldüğünde, uyarlanabilir yeniden kullanım süresinde yenilikçi ve enerji performansı yüksek yapı malzemelerinin kullanımı çevresel etkilerin düşürülmesinde etkili olabilmektedir [15]. Ancak yapı malzemelerinin üretim aşamalarında harcanan gömülü etki ile kullanım aşamasındaki operasyonel etkilerin birlikte ele alınması bütüncül bir yaklaşım için daha uygundur [16].

Tablo 4. Çevresel etkilerin azaltılmasına yönelik olası çözümler

Sorunlar	Artan karbon salımı ve ham madde ihtiyacı.
Olası çözümler ve yapıda kullanım alanları	Harçlarda atık taş, cam ve tuğla tozu kullanımı [13] ve yapı malzemelerinin tasniflenmesi yöntemiyle atık yönetimi [14]  Yukarıdaki görselde harçlara ait SEM (Taramalı Elektron Mikroskobu) görüntüleri yer almaktadır.
İyileştirilen özellikler	Malzemelerin fiziksel ve mekanik özelliklerinin iyileştirilmesi, çevresel etkilerin düşürülmesi.

Düşük İç Mekan Hava Kalitesi

Tarihi binalarda kullanılan yeni malzemeler, açığa çıkardıkları uçucu organik bileşikler nedeniyle iç mekanlarda çeşitli sağlık sorunlarını da beraberinde getirebilir. Bu nedenle tercih edilen yeni malzemelerin formaldehit gibi kansere yol açan madde içeriklerinin önceden tespit edilmesi, kullanıcı sağlığı açısından son derece önemlidir. İç mekân hava kalitesinin düşük olduğu ortamlarda hasta bina sendromu görülebilmektedir. Bu sendrom, alerji, astım, öksürük, yorgunluk, baş ağrısı, göz ve burunda tahriş gibi rahatsızlarla kendini belli etmektedir [17, 18].

Yeşil yapı malzemelerinin kullanımı ile iç mekanlarda istenen hava kalitesinin sağlanabilmesi mümkündür. Bu malzemeler, ekolojik, sağlıklı, geri dönüştürülebilen veya yüksek performansa sahip özellikte olup yaşam döngüleri boyunca çevreye ve insan sağlığına etkileri en aza indirgenmiş olan yapı malzemeleridir [19].

Tayvan'da yapılan ve yasal düzenlemeleri inceleyen bir araştırmada yasalarla güvence altına alınan iç mekan hava kalitesinin standartlarına ve yeşil malzeme özelliklerine değinilmiştir. 2000'li yılların başından beri sağlanan farkındalık ve denetimde sağlanan etkinlik nedeniyle piyasadaki ürünlerin %75'inin yeşil yapı malzemelerinden oluştuğu bildirilmiştir. Binanın iç yüzey alanının en az %45'i ve dış mekana bakan yüzey alanının en az %10'unun yeşil yapı malzemelerinden oluşmasının gerekliliği standartlarla belirtilmiştir. Bina Teknik Yasası'nda yer alan geri dönüştürülmüş plastik, kauçuk, tuğla ve ahşabın yanı sıra EPA tarafından belirlenen zehirli malzemeleri içermeyen ve Montreal Protokolü'ne uygun yalıtım ürünleri, su bazlı boya ve kaplamalar ve diğer sertifikalı malzemeler yeşil yapı malzemelerini oluşturur (Tablo 5). Bu tür malzemelerin çevreye ve insan sağlığına karşı zararsız olması ve ulusal standartlara uygun olması zorunludur [20].

Diğer yandan Steinemann vd. [21], yeşil binaların iç mekan hava kalitesi ile doğrudan bir ilişki kurabilmeleri için yapı malzemelerin emisyonlarının araştırılmasının yanı sıra kullanıcı beklenti ve görüşlerinin alınmasının gerekliliğine değinmişlerdir.

Tablo 5. İç mekân hava kalitesinin iyileştirilmesine yönelik olası çözümler

<table>
<tr><td>Sorunlar</td><td>Düşük iç mekân hava kalitesi, hasta bina sendromu, kanserojen madde içerikleri.</td></tr>
<tr><td>Olası çözümler ve yapıda kullanım alanları</td><td>Yeşil yapı malzemelerinin kullanımı [20]
<table>
<tr><th rowspan="2">İç ortamdaki hava kirleticileri</th><th colspan="2">Standard</th></tr>
<tr><th>Konsantrasyon</th><th>Test süresi</th></tr>
<tr><td>Karbondioksit (CO_2)</td><td>1000 ppm</td><td>8 sa</td></tr>
<tr><td>Karbonmonoksit (CO)</td><td>9 ppm</td><td>8 sa</td></tr>
<tr><td>Formaldehit (HCHO)</td><td>0,06 ppm</td><td>1 sa</td></tr>
<tr><td>T. uçucu organik bileşikler</td><td>0,56 ppm</td><td>1 sa</td></tr>
<tr><td>Bakteri</td><td>1500 CFU/m³</td><td>Tavan değer</td></tr>
<tr><td>Mantar</td><td>1000 CFU/m³</td><td>Tavan değer</td></tr>
<tr><td>Kaba partiküller (PM10)</td><td>75 µg/m³</td><td>24 sa</td></tr>
<tr><td>İnce partiküller (PM2.5)</td><td>35 µg/m³</td><td>24 sa</td></tr>
<tr><td>Ozon (O_3)</td><td>0,06 ppm</td><td>8 sa</td></tr>
</table>
CFU: Koloni oluşturabilen birim, ppm: milyondaki partikül miktarı
Yukarıdaki grafikte çeşitli iç mekan hava kirleticilerine ait sınır değerler verilmiştir.</td></tr>
<tr><td>İyileştirilen özellikler</td><td>Döngüsel ekonomiye katkı, insan sağlığının ve doğal çevrenin korunması, malzemelerde standardizasyon.</td></tr>
</table>

Sonuç ve Değerlendirme

Tarihi yapılar kültürel ve evrensel mirası oluşturdukları için geleceğe aktarılmaları son derece mühimdir. Bu hususta bu tür yapıların zaman içerisinde maruz kaldıkları sorunların giderilmesine yönelik çağdaş önlem ve metotlara ihtiyaç duyulmaktadır. Bu çalışma tarihi dokuya, bina kullanıcılarına ve doğal çevreye olumsuz etkileri olan beş farklı sorunun yapı malzemeleri üzerinden çözümlenmesine ve/veya etkilerinin azaltılmasına odaklanmaktadır. Sorunun öncelikle malzeme ölçeğinde ele alınması, tarihi binaların aktif sistemlere olan bağımlılığını azaltmak ve küresel iklim değişikliğine katkı sunacak yeni sorunların önüne geçilebilmesi adına önemlidir. Çalışma kapsamında okuyuculara sunulan öneriler şu şekilde özetlenebilir:

- Nem sorununa karşın doğal bir malzeme olan kil bariyerlerinin yığma duvarların önünde toprak seti olarak kullanımı önerilmiştir. Böylelikle suyun yapı kabuğu ile olan teması en aza indirilmiş; yapısal unsurlara ve kullanıcı konforuna zarar verebilecek nemin binadan uzaklaştırılması sağlanmıştır. Ayrıca odun külünün kireç harcına %20-40 oranında eklenmesi ile harçların su emme özellikleri iyileştirilebilir.
- Tarihi yapıların kabuğunda soğuk renkli malzeme kullanımı ile yüzey sıcaklıklarında 8ºC düşüş ve yazın soğutma için harcanan enerjide %3 azalma sağlanabilmektedir. Ayrıca avluların membran ile kapatılması, yıllık karbon salımını soğutmadan kaynaklı harcanan enerji üzerinden %6; ısıtmadan kaynaklanan enerji üzerinden ise %10 düşürebilmektedir.
- Kullanıcı konforunun sağlanması kaynak tüketimi ve çevresel etkilerin düşürülmesinde bir diğer kilit noktadır. FDM gibi yenilikçi teknolojilerin tarihi binalarda %10 oranında uygulanması enerji tüketimini %18'e kadar düşürebilmekte ve malzemenin termal iletkenliğini %22,5 oranında düşürebilmektedir.
- Yapılarda yeni malzeme kullanımı daha fazla ham madde ihtiyacı anlamına geldiğinden bunun yerine daha önceden kullanılmış malzemelere başvurulması, çevresel sürdürülebilirliğin sağlanmasında etkilidir. Yapılan çalışmalarda %30 oranında seramik ve cam atıkları içeren kireç harcının su direncinin artırıldığı ve basınç dayanımında artış sağlandığı görülmüştür.
- Yapılarda yeşil yapı malzemelerinin kullanımı, atık kullanımına teşvik etmesi, insan sağlığına olan etkileri ve malzeme onarımları açısından doğal ve tarihi çevre üzerinde olumlu etkilere sahiptir. Tayvan'da binanın iç yüzeylerinde %45 ve dış yüzeylerinde ise %10 oranında yeşil malzeme kullanım zorunluluğu bulunmaktadır.

Özetlenen çalışmaların önerdiği çözümler ve uygulama yöntemleri Tablo 6'da verilmiştir. Tüm bu önerilerin değerlendirilmesinde tarihi dokuya zarar verilmemesi, kullanıcı konfor ve sağlığının gözetilmesi ve doğal çevreye yönelik tahribatın öne geçilmesi elzemdir. Sonraki çalışmalarda yapılı çevrede karşılaşılan çeşitli sorunlara dair yenilikçi teknoloji ve sistemler sürdürülebilir mimari çerçevesinde kapsamlı olarak ele alınabilir.

Tablo 6. Tarihi bina sorunlarına yapı malzemesi ölçeğinde öneride bulunan çalışmalar

Yapı sorunu	Malzeme ölçeğindeki olası çözümler	Araştırma metodu	Kaynak
Rutubet	Kil bariyeri	Saha uygulamaları Laboratuvar testleri	[6]
	Odun külü	Laboratuvar testleri	[7]
Enerji performansı	Soğuk renkli malzeme	Laboratuvar testleri Dinamik simülasyon	[8]
	Membran örtü	Dinamik simülasyon	[9]
Termal konfor	Termal kütle	Saha araştırmaları	[11]
	FDM uygulamaları	Laboratuvar testleri Dinamik simülasyon	[12]
Çevresel etki	Atık malzeme	Laboratuvar testleri	[13]
	Malzemelerin sınıflandırılması	Saha araştırması Sayısal hesaplamalar	[14]
İç mekân hava kalitesi	Yeşil yapı malzemesi	Yasal düzenlemelerin incelenmesi	[20]

Kaynakça

[1] A.L., Webb, "Energy retrofits in historic and traditional buildings: A review of problems and methods", Renewable and Sustainable Energy Reviews, vol.77, pp. 748-759, 2017.

[2] B.M. Feilden, "Conservation of Historic Buildings", 3rd ed., Londra, Architectural Press, 2003. [Online]. Available: https://www.academia.edu/

[3] A. Buda, E.J.P. Hansen, A. Rieser, E. Giancola, V.N. Pracchi, S. Mauri, V. Marincioni, V. Gori, K. Fouseli, C.S.P. Lopez, A. Lo Faro, A. Egusquiza, F. Haas, E. Leonardi and D. Herrera-Avellanosa, "Conservation-Compatible Retrofit Solutions in Historic Buildings: An Integrated Approach", *Sustainability*, vol.13, no.5, 2021. DOI: 10.3390/su13052927

[4] B. Sayın, "Tarihi yığma yapıların malzeme özelliklerinin belirlenmesi ve uygulama önerileri", *Dicle Üniversitesi Mühendislik Fakültesi,* vol. 7, no. 3, pp. 387-398, 2016.

[5] P.B. Lourenço, E. Luso, and M.G. Almeida, "Defects and moisture problems in buildings from historical city centres: a case study in Portugal", *Building and Environment*, vol.41, no.2, pp.223-234, 2006.

[6] M. Michette, R. Lorenz, and C. Ziegert, "Clay barriers for protecting historic buildings from ground moisture intrusion", *Heritage Science*, vol.5, no.31, 2017.

[7] L. Fusade, H. Viles, C. Wood, and C. Burns, "The effect of wood ash on the properties and durability of lime mortar for repointing damp historic buildings", *Construction and Building Materials,* vol.212, pp. 500-513, 2019.

[8] F. Rosso, A.L. Pisello, V.L. Castaldo, M. Ferrero and F. Cotana, "On Innovative Cool-Colored Materials for Building Envelopes: Balancing the Architectural Appearance and the Thermal-Energy Performance in Historical Districts", *Sustainability*, vol. 9, 2017.

[9] M. De Vita, P. D'Antonio, Beccarelli and P. Berardinis, "Energy performance of film membranes in the retrofitting of Architectural Heritage: an Italian case study," in *Proc. of the TensiNet Symposium*, Politecnico di Milano, Milan, Italy, 2019, pp. 624-633.

[10] C.M.M. Gonzalez, A.L.L. Rodriguez, R.S. Medina and J.R. Jaramillo, "Effects of future climate change on the preservation of artworks, thermal comfort and energy consumption in historic buildings", *Applied Energy*, vol. 276, 2020.

[11] M. Alwetaishi, A. Balabel, A. Abdelhafiz, U. Issa, I. Sharaky, A. Shamseldin, M. Al-Surf, M., Al-Harthi and M. Gadi, "User Thermal Comfort in Historic Buildings: Evaluation of the Potential of Thermal Mass, Orientation, Evaporative Cooling and Ventilation", *Sustainability*, vol. 12, 2020.

[12] E. Baccega and M. Bottarelli, "Granular PCM-Enhanced Plaster for Historical Buildings: Experimental Tests and Numerical Studies", *Energies*, vol. 15, 2022.

[13] A. Ayat, H. Bouzerd, T. Ali-Boucetta, A. Navarro and M.L. Benmalek, "Valorisation of waste glass powder and brick dust in air-lime mortars for restoration of historical buildings: Case study theatre of Skikda (Northern Algeria)", *Construction and Building Materials*, vol. 315, 2022.

[14] F. Colmenero-Fonseca, A. Salas-Montoya, A. Preciado, J. Palomino-Bernal and J. Carcel-Carrasco, "Case Study on the Application of New Technologies forConstruction Waste Management in a Historic Building inJalisco, Mexico", *Advances in Civil Engineering,* Wiley, vol. 2024.

[15] Y. Takva, Ç. Takva ve Z.Y. İlerisoy, "Sustainable Adaptive Reuse Strategy Evaluation for Cultural Heritage Buildings", International Journal of Built Environment and Sustainability, vol.10, no.2, pp.25-37, 2023.

[16] K. Kertsmik, E. Arumagi, J. Hallik ve T. Kalamees, "Low carbon emission renovation of historical residential buildings", *Energy Reports,* vol. 11, pp. 3836-3847, 2024.

[17] M.J. Jafari, A.A. Khajevandi, S.A.M. Najarkola, M.S. Yekaninejad, M.A. Pourhoseingholi, L. Omidi and S. Kalantary, "Association of Sick Building Syndrome with Indoor Air Parameters", *Tanaffos*, vol. 14, no. 1, pp. 55-62, 2015.

[18] Y. Zhang, P. K. Hopke and C. Mandin, "History and Perspective on Indoor Air Quality Research", *Handbook of Indoor Air Quality*, Springer, Singapore, 2022.

[19] S. M. Khoshnava, R. Rostami, R. M. Zin, D. Streimikiene, A. Mardani and M. Ismail, "The Role of Green Building Materials in Reducing Environmental and Human Health Impacts", *International Journal of Environmental Research and Public Health*, vol. 17, 2020.

[20] W. Tsai, "Overview of Green Building Material (GBM) Policies and Guidelines with Relevance to Indoor Air Quality Management in Taiwan", *Environments*, vol. 5, no. 4, 2018.

[21] A. Steinemann, P. Wargocki and B. Rismanchi, "Ten questions concerning green buildings and indoor air quality", *Building and Environment*, vol. 112., pp. 351-358., 2017.

Dicle University
Journal of Engineering
https://dergipark.org.tr/tr/pub/dumf
duje.dicle.edu.tr

Research Article

Damage and Interventions to Historical Masonry Buildings: Good and Ill Practices

Elizabeth VINTZILEOU[1*]

[1] National Technical University of Athens, Greece, elvintz@central.ntua.gr, Orcid No: 0000-0002-4891-7091

ARTICLE INFO

Article history:

Received 29 April 2025
Received in revised form 27 June 2025
Accepted June 30, 2025
Available online 30 September 2025

Keywords: *unreinforced masonry, interventions, seismic behaviour, stiffening of floors, grouting, RC slabs*

Doi: 10.24012/dumf.1685914

* Corresponding author

ABSTRACT

This paper presents typical damage observed during recent earthquakes in Türkiye and elsewhere, along with their qualitative interpretation revealing the main weaknesses of existing stone masonry buildings. Historical structural systems, having a stone masonry ground storey and upper storeys made of timber framed masonry are also included. Strengthening techniques, frequently applied to alleviate the inherent inadequacies of stone masonry buildings are commented on, while their rationale, their efficiency and the effect of their misuse are presented, based on field observations after recent earthquakes and/or experimental results. The paper focuses on good and ill practices with the purpose of opening the discussion on the selection of adequate intervention techniques that may ensure an improved seismic behaviour, thus protecting human lives and property and contributing to the preservation of the built cultural heritage.

Introduction

Earthquakes in several countries throughout the globe have repeatedly demonstrated the inherent weaknesses of old unreinforced stone masonry buildings. On the contrary, there is evidence about the satisfactory behaviour of some historical structural systems, e.g., buildings made of timber-laced or timber-framed masonry. In countries around the Mediterranean and elsewhere, heritage buildings present similarities in their structural system and, hence, they undergo similar damage due to seismic events. Consequently, similar interventions are adequate for their pre- or post-earthquake strengthening and improvement of their overall behaviour. The international engineering community is being quite active in this field in the recent decades, while several national and regional regulatory documents were or are being produced, providing guidance related to the selection of adequate intervention techniques, to the investigation of their efficiency, as well as to their design and application. A survey of the internationally available relevant research data and guidelines is obviously beyond the scope of this paper. The purpose of this work is to briefly identify the main weaknesses or strong points of historical structural systems, as revealed by in situ observations after several earthquakes. On this ground, and based on the effect of recent earthquakes, including the 2023 Türkiye-Syria earthquakes, this paper focuses on some frequently applied intervention techniques and offers evidence on their positive or negative effects on the seismic behaviour of stone masonry buildings.

The main weaknesses of stone masonry buildings

Unreinforced stone masonry is known to be a heavy, composite, anisotropic and brittle material, with mechanical properties of low value. The old Constructors, building using this material were frequently taking measures to ensure the survival of their constructions, especially in earthquake prone areas. Some of those measures are: Thick walls of significant lateral stiffness, limited length of openings (doors and windows) compared to the total length of the building, strengthening of the perimeter of the openings (e.g., arched lintels, elaborate construction using larger stones embedded to masonry piers, etc.), proper connection of perimeter walls at the corners of the building, etc. There are, however, some typical weaknesses of old masonry buildings, repeatedly revealed because of many earthquakes in the last decades. Those weaknesses, aggravated by non-repaired slight to moderate damage due to previous earthquakes, by ageing and decay, by the lack of maintenance, by the abandonment of rural areas, etc., can serve as a basis for the selection of adequate remedial measures to protect the lives and the

property of the inhabitants and, indeed, the built cultural heritage. It is noted that the weaknesses mentioned herein have been repeatedly identified, and described in several publications (e.g., [1]), including those referring to damage due to the 2023 earthquake sequence in Türkiye-Syria (e.g., [2], [3] and [4]. The related typical damage is presented and interpreted.

Vulnerable Construction Typology of Masonry

There is a vast variety of construction typologies of masonry, both on the faces of bearing elements and within their thickness. Quite frequently, the exterior face of masonry is of more elaborate construction than the interior one and it remains unplastered. Therefore, within the thickness, there are two leaves of different construction typology either in contact between them (two-leaf masonry) or with a space between them (three-leaf masonry). That space may be of more or less solid structure, made of small stones and large mortar quantity. As a rule, the exterior leaves of masonry are not transversely connected, using header stones (Fig. 1).



Figure 1. Typical construction typologies of stone masonries in Greece, Italy and Türkiye

The seismic vulnerability of those construction typologies is two-fold: (a) The material filling the space between the two exterior leaves of masonry being of poor mechanical properties, the actual resisting thickness of the masonry elements is substantially smaller than their nominal thickness. Thus, the bearing capacity in compression, shear and out-of-plane bending is significantly reduced as compared to a solid wall of the same thickness. More importantly, (b) the weak bond between the exterior leaves and the filling material can be broken, either due to decay or due to previous even small to moderate earthquakes. Thus, with the masonry transversely delaminated, the bearing elements become more slender, the exterior leaves resist the seismic action separately from one another, both in- and out-of-their plane. The consequence of this behaviour was repeatedly observed after strong earthquakes (Fig. 1 and Fig. 2).



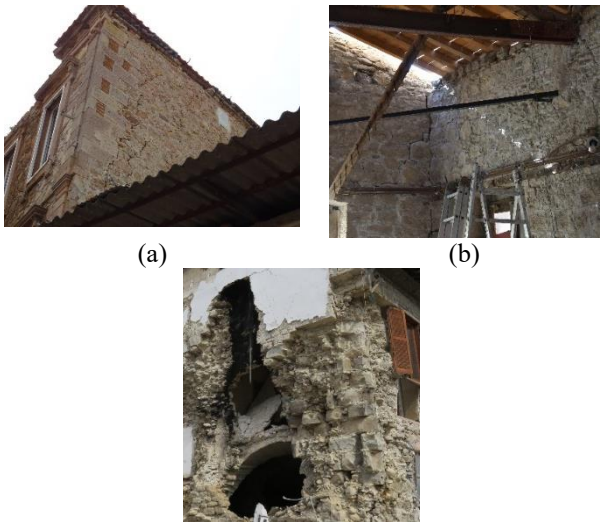
Figure 2. Delamination of three-leaf masonry and damage due to seismic actions in Amatrice and in Samos

Inadequate connection between cross walls

Although special attention was often given by the Constructors in the connection of walls at the corners of buildings (Fig. 3a), there are cases where this rule was not applied. Indeed, especially in case of three-leaf masonry, the transverse connection of the exterior leaves of masonry (by interlocking of the corner stones) was not always ensured. Furthermore, quite frequently, the perimeter bearing walls were constructed first, and the interior bearing walls were following, unconnected with the perimeter ones. The ensuing damages (Fig. 3b, c) are quite eloquent. The almost linear vertical crack in Figure 3b proves the lack of connection of the two walls, while in Fig. 3c, one may observe the large stones at the corner of the building, connecting the interior leaves of the two walls. The lack of connection between the interior and the exterior leaf is proven by the collapse of the latter, at the corner of the building as well.

Flexible diaphragms loosely connected to walls

Typically, floors and roof in unreinforced stone masonry buildings are made of timber (e.g., joists or trusses, and timber planking). The diaphragms, flexible in their plane, are connected only to the supporting them vertical elements, this connection being of limited fixity. Thus, the walls are subjected to largely different deformations during a seismic event. Furthermore, the overall lateral stiffness of the building is decreased (compared to a box-like building composed of well connected among them walls and diaphragms) and, thus, the deformations imposed to the walls are larger. This behaviour affects mainly the out-of-plane behaviour of walls, increasing the probability of damage and out-of-plane partial or total collapse. The situation is aggravated by the vulnerable construction typologies of masonry, typical for those buildings. The related damage is very frequent and illustrated also in the photographs of Figs 1 to 3.



(a) (b) (c)

Figure 3. (a) Solid connection of cross walls, (b) Almost vertical crack suggesting a deficient connection between walls, (c) Lack of connection between the exterior and the interior leaves of the three-leaf masonry walls.

Interventions to alleviate the weaknesses of unreinforced stone masonry buildings

The aforementioned typical construction characteristics of stone masonry buildings, leading to the repeatedly observed problematic seismic behaviour thereof, may guide the engineer to adopt the most adequate measures towards the improvement of this behaviour. Indeed, providing a monolithic behaviour to two- and three-leaf masonries, enhancing the in-plane stiffness of floors and roof and ensuring proper connection among all bearing elements (horizontal and vertical) would allot box-like behaviour to the building, reducing the deformations imposed to the bearing elements for the same input action, imposing practically equal deformations to all vertical elements, etc. Therefore, the following paragraphs focus on systemic schemes of interventions that may alleviate the seismic vulnerability of historical buildings and, hence, contribute to their preservation. It has to be admitted that there are cases where the difference between the targeted behaviour and that ensured by the aforementioned techniques is such that further measures (e.g., masonry or steel buttresses, new bearing system at the interior of the building, etc.) are to be taken. Those buildings are to be examined on a case by case basis. General solutions, applicable to the vast majority of buildings to be preserved, may not be sufficient.

Transversely connecting the leaves of masonry

This is an intervention of major importance, and it constitutes a precondition for the application and the efficiency of several other intervention techniques, as explained herein. The transverse connection of the leaves of masonry and, hence, the monolithic behaviour of masonry can be achieved through grouting and by using transverse (metallic or non-metallic) connectors. The development of grouts able to be injected (at low pressure) to historical masonries and to fill internal cracks and voids is a long process. So is the development of adequate equipment and sequence of mixing the grout constituent materials, as well as the application methodology.

While the first attempts were directed to grouts with high cement content, the current state-of-the-art [5], based on numerous experimental campaigns and applications, shows the preponderance of hydraulic lime-based or ternary grouts. Indeed, those grouts constitute a durable intervention, they ensure the homogenization of masonry (Fig. 4), while they provide significant enhancement of the mechanical properties of masonry [6], [7], [8].

Thanks to the improved bond of masonry materials within the thickness of the bearing elements, delamination of masonry is significantly delayed or avoided and the severe damages shown in Figs 1 and 2 are prevented.



(a) (b)

Figure 4. A three-leaf masonry (a) before and (b) after the application of a hydraulic grout

Some documents (e.g., [9]) focus on the transverse connection of masonry leaves, using connectors. Those connectors may be steel bars, arranged at intervals, and bonded to masonry elements using a strong cementitious mortar. Alternatively, the steel connectors are positioned in drilled-through holes, they are bonded to masonry and anchored on the faces of masonry elements using steel anchorage plates. The recently approved Greek Code for

the assessment and structural interventions of masonry structures [10] does not allow the transverse connectors to be the only technique applied to transversely connect the masonry leaves. Indeed, the positioning of such connectors at distances to a non-grouted masonry (like that in Fig. 4a) provides only local connection of masonry leaves and it does not prevent delamination and damage in regions between the anchors locations. The results of tests on three-leaf masonry walls (e.g., [11]) have proven that the application of transverse connectors does not increase neither their bearing capacity in compression nor their stiffness. The most efficient technique is grouting, while the combination of grouting and transverse connectors yields the best results in terms of transverse deformations of masonry walls. It is noted that the same techniques are adequate for the re-instatement or the improvement of the connection between bearing walls.

Enhancement of the in-plane stiffness of floors and roof

As aforementioned, the in-plane flexibility of timber floors and roofs of historical stone masonry buildings, and their loose connection to the vertical bearing elements are responsible for severe damage, especially, due to out-of-plane actions. This is more so, when flexible diaphragms are resting on vulnerable masonries liable to delamination. It has to be noted that any technique to enhance the in-plane stiffness of diaphragms should be applied to homogenized masonry elements and it should include the adequate connection of the diaphragms to the walls [10]. The examples presented and commented on herein prove the necessity of those measures.

Until few decades ago, the replacement of timber roofs by reinforced concrete slabs was a rather frequent intervention to existing masonry buildings. RC slabs were combined with the construction of an RC tie beam. The latter was usually cast on top of the walls, its width being smaller than or equal to the thickness of the masonry walls. At intermediate floors, casting a continuous RC tie-beam over a significant portion of the wall thickness is not feasible and, thus, the slabs replacing the timber floors did not extend to the outer face of the walls. It should also be noted that there are many cases, where the timber roof was preserved (or replaced by a new timber one, of the same geometry). In those cases, typically, a RC tie-beam was cast on top of the walls and underneath the roof, presumably ensuring diaphragm action at roof level. Nonetheless, simple mechanics may prove and, unfortunately, several earthquakes have evidenced that this assumption is far from being accurate. Another ill practice related to interventions at roof level is that no connection (using dowels) was provided between the RC tie beam and the walls. It was assumed that the friction between the concrete and the top face of the wall was sufficient for the transfer of actions from the roof to the walls. However, the vertical loads at the top of the building being of small value, the frictional force at that level may not be adequate. Modena [11] refers also to damage observed in strengthened buildings, following earthquakes in Italy. For example, a RC slab was cast monolithically with a tie beam at the level of an intermediate floor. The tie beam was cast on the interior leaf of masonry walls only, while the three-leaf masonry walls were not strengthened. The eccentric application of actions (due to the eccentricity of the tie beam), combined with the horizontal movement of the added mass of the RC slab with respect to the vulnerable three-leaf walls have led to the out-of-plane expulsion and collapse of the latter.

In another building, the stiff RC roof, seated on top of unstrengthened three-leaf masonry, has moved as a solid body by almost one meter out of the facade of the building. The inadequacy of replacing timber roofs by RC slabs and tie beams simply seated on masonry walls was observed also by Munari et al. [12], after the 2009 L'Aquila earthquake. Similar are the observations that can be made on the photographs of Fig. 5. The significant mass of the RC slab added at the top of unstrengthened masonry walls of vulnerable construction typology, without any connection to them, cannot prevent the out-of-plane failure of the walls and, thus, it does not offer any improvement to the seismic behaviour of the building. On the contrary, in cases where the slab loses support due to the collapse of the walls (e.g., Fig. 5 c, e and f), casualties or injuries of the inhabitants are imminent.

Although this work does not consider the case of mosques or churches, where typical damage is observed in arches and domes, as well as in minarets and belfries (e.g., [13], [14]), it is interesting to observe that, as reported in [15], based on observation and numerical work, interventions using RC, prior to the 2023 earthquakes, did not prove to be beneficial to the monuments, while in some cases their effect may be characterized as negative for the seismic behavior.

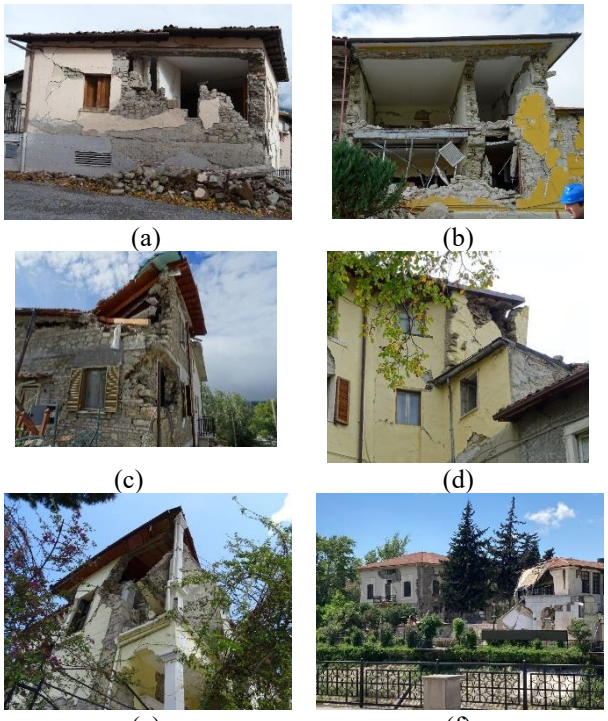
The purpose to enhance the in-plane stiffness of floors and roofs can be served by means other than the construction of RC slabs. Several techniques are studied (e.g., by Piazza [16], Valluzzi et al., [17] and [18]) and applied in historical buildings and monuments, namely, the addition of a second planking in floors and roofs (at an angle with respect to the original ones), the use of a system of steel ties (parallel, perpendicular, and diagonal with respect to the walls), etc. A non-negligible advantage of the alternative techniques is their application in-dry and the minimal increase of the mass of the building.

The application of those alternative techniques as well, is paired with the consolidation of masonry and the provision of adequate connection among the vertical and the horizontal bearing elements. Shake table tests on a two-story building model (scale 1:2), made of three-leaf stone masonry (Vintzileou et al., [19]), strengthened through grouting and enhancement of the diaphragm action of the floors (by double timber planking) have proven the adequacy of the interventions, as the box-action of the

model was achieved, while the model was able to sustain significantly higher base accelerations than at its as-built state.

Enhancing the bearing capacity of stone masonry buildings

In addition to the systemic interventions applied to improve the overall behaviour of stone masonry buildings, interventions aiming at enhancing the mechanical properties of masonry (and, by way of consequence, of the masonry structural members) are often needed for the building to meet the requirements dictated by its new use, as well as by current seismic codes. In addition to grouting of masonry, deep rejointing of masonry is considered as an adequate and efficient intervention. This may be the case, provided that many conditions are fulfilled, namely, (a) the masonry is grouted (Modena, [11]), (b) the thickness of the masonry elements is limited (say, to 0.50m approx.), (c) the workmanship (meticulous removal of mortar from all joints, cleaning, application of the stronger mortar to completely fill all the joints) is of high quality, etc. Thus, deep rejointing is, in the majority of cases, an intervention of high cost and of limited efficiency. Last but not least, the new mortar cannot be of excessively higher mechanical properties than the replaced one. Otherwise, the concentration of stresses close to the outer faces of masonry -where the strong and stiff mortar is located- may lead to spalling of the masonry units and, finally, even to reduction of the pre-intervention mechanical properties of masonry, as observed by Vintzileou [20] for the compressive strength.



(a) (b) (c) (d) (e) (f)

Figure 5. The effect of RC slabs on top of unstrengthened masonry walls. (a) to (d) Italy, 2016, (e) and (f) Antakya, Türkiye, 2023.

Another technique, frequently applied in the past and currently prohibited by the competent authorities in several countries, is RC jacketing of stone masonry walls. In addition to the obvious reason of the harm caused by jacketing to the aesthetic and architectural values of historical buildings (Fig. 6), there are further reasons that justify the exclusion of this intervention, namely, the increase of the mass of the building, the radical change of the movement of moisture and vapour within walls enclosed in concrete (leading with time to the disintegration of masonry), the limited efficiency of one-sided RC jackets, usually applied in the interior of the building, etc. The need of bridging the gap between the targeted and the available bearing capacity can be served by alternative techniques (e.g., transforming partition walls to bearing ones, providing a new internal bearing system, constructing external buttresses, etc.) to be selected on a case-by-case basis. Last but not least, the new use of a historical building should be compatible with the potential of the structural system to safely host it, after due rehabilitation, respecting the values to be preserved.



Figure 6. RC jacket applications in listed stone masonry buildings in Greece

Mixed -stone masonry and timber-framed masonry- structural systems

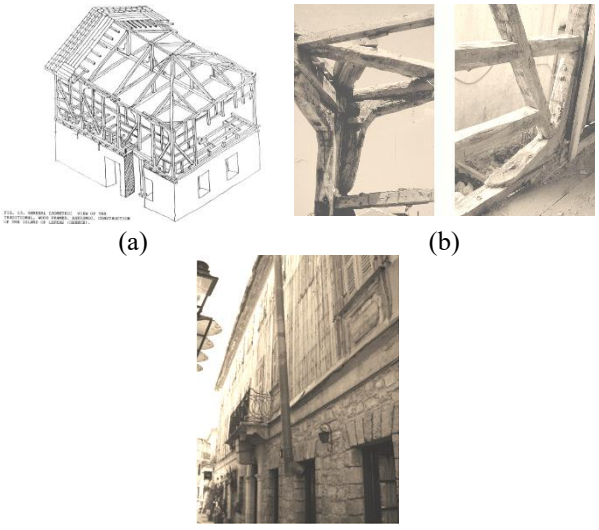
In several earthquake prone areas, structural systems were developed to ensure improved seismic behavior and, hence, protection of human lives and property. A frequently met structural system is that of timber-framed masonry, presenting several alternatives in terms of materials, arrangement of timber elements, etc. In many locations, timber-framed masonry (in the upper story(ies)) is combined with unreinforced stone masonry in the ground story (e.g., Fig. 7a, and [21]).

A historical overview of this structural system is found in Vasconcelos et al. [22]. Timber-framed masonry is more or less elaborate. Indeed, there are cases where only vertical and horizontal timber elements are used, while in others,

diagonal elements are also used (Fig. 7a). The connections among timber elements are simple (nails are used throughout the timber-framed masonry walls), while in other cases, special care is taken in the area of connection between walls and roof or floor, as well as in the corners of the building (Figure 7b).

Typically, the timber frames are filled with small size stones or bricks (fired or unfired), while the thickness of the walls is equal to the respective dimension of the timber elements. The main enemy of timber-framed masonry being the changes in moisture, the walls are typically protected either by the plaster (Figure 8) or by timber planking (Figure 7c).

The historical system combining stone masonry at the lower story and timber-framed masonry at the upper story is found in a number of buildings in Antakya (Figure 8). This structural system is reported to behave reasonably well after several earthquakes. For example, Bal and Vatan [23] report on the survival of buildings made according to the historical structural system, in contrast to modern buildings in the same area. This is confirmed by Gülhan and Güney [24], who have report on their study in Kocaeli and Sakarya, after the 1999 Marmara earthquake.



(a) (b)

(c)

Figure 7. Island of Lefkada, Greece (a) Typical historical building, (b) Connections of timber elements, (c) Protection of timber-framed walls using timber planks (Vintzileou and Touliatos, [25]).

Similar are the observations after the recent strong earthquakes in Türkiye-Syria, 2023. Although statistical data on the percentage of buildings belonging to the historical structural system that has suffered significant damage or collapse are not available to the author of this paper, the in situ observations prove that many of those buildings have survived, thus offering to the inhabitants better chance to save their lives.

However, in several cases, the damage typical to this building typology were observed, namely, severe cracking or partial collapse of the stone masonry at the ground storey (Fig. 8b), loosening of connections between timber elements, damage to masonry filling the timber frames, etc. (see also [3]). It is admitted that the severity of damage depends on several parameters, such as the quality of stone masonry (quality of materials and construction typology), the level of elaboration of the timber-framed walls (in terms of arrangement of timber elements and their connections), as well as on the state of preservation (maintenance included).



(a) (b)

Figure 8. The historical structural system of Antakya

Regarding the pre- or post-earthquake interventions to preserve the historical structural systems, one can distinguish between techniques to be applied to the ground story and those adequate for the rehabilitation of the upper stories.

Indeed, the aforementioned interventions aiming at transversely connecting the leaves of stone masonry, enhancing the bearing capacity of masonry walls, stiffening the floor on top of the ground storey, and providing a proper connection between vertical elements, as well as between walls and floor, are to be applied.

As for the upper storeys, adequate interventions are to be chosen, depending on the state of timber-masonry. Thus, extensive biological attack of timber elements or large residual deformations may lead to the need of partial or complete reconstruction. If the state of preservation is, in general, good, local damages of filling masonry may be repaired, loose connections are to be improved (e.g., using metal plates nailed on joints), etc. In other cases, e.g., in buildings like the one shown in Figure 8b, interventions may need to be limited to the lower storey.

Concluding remarks

The work of numerous researchers throughout the globe, and many seismic events that occurred in the last decades, have provided evidence on typical characteristics of masonry buildings that make those structures vulnerable to earthquakes. At the same time, the interpretation, in terms of Mechanics, of the observed damage shows the path to follow with the purpose of improving the seismic performance of masonry buildings.

In this paper, several systemic interventions are mentioned, aiming at alleviating the inherent weaknesses of stone masonry buildings. Those systemic interventions, aiming to improve the box-like behaviour of buildings, include consolidation of two- and three-leaf masonry elements

through grouting (to avoid their delamination and to increase their mechanical properties), improvement of connection between walls (through stitching and/or using connectors), enhancement of diaphragm action of floors and roofs (to ensure almost equal displacements of all vertical elements) and adequate connection between horizontal and vertical bearing elements (to ensure the efficiency of the aforementioned interventions and the joint action of all structural elements).

Of course, there are further intervention techniques contributing to improved seismic behaviour. Those comprise repair and/or strengthening techniques.

It is noted that even when strengthening of the building is required, repair of damage should precede. Repointing, plastering, grouting or stitching of cracks, local reconstruction of heavily damaged regions, etc., aim at reinstating the pre-earthquake capacity of the structure.

Among the most commonly applied strengthening techniques are the reinforced plaster (preferably, double-sided and made of materials allowing masonry to breathe), the confinement of stone masonry piers and columns (using metallic or non metallic external reinforcement), filling of openings or the installation of (timber or steel) frames in the perimeter of openings, provision of struts and ties to reduce the detachment of walls from their transverse ones or -when installed to arches and domes- to resist the horizontal component of the thrust, constructing buttresses (adequately connected to masonry) to alleviate the out-of-plane vulnerability of long and high walls, etc.

Those and other techniques the Designer may apply are distinguished from the systemic ones. Indeed, the systemic interventions aim at improving the overall behaviour of the building, whereas the aforementioned techniques may be applied to a more or less limited number of bearing elements, when the systemic interventions prove not to be sufficient to bridge the gap between the available and the target margins of safety at the level of each distinct structural member.

It is noted that, if the state of the building or the required performance level are such that the combined application of several techniques cannot provide the necessary safety, the construction of a new internal bearing system may be sought. For such a new bearing system to efficiently protect the existing one against seismic actions, it has to be adequately connected to it, while the compatibility of deformations of the two systems (old and new) has to be ensured.

Some final remarks are needed here:

(a) In the common case of application of more than one intervention techniques, the final overall improvement in stiffness, resistance or ductility should not be taken as the sum of the contributions of all the applied techniques, as -up to now- there is no evidence (experimental or observed in situ after a seismic event) supporting this assumption.

(b) There are techniques applied to the existing masonry elements themselves (e.g., grouting, rejointing, etc.) and others applied to the exterior of them (e.g., reinforced plaster, buttresses, etc.). It is advisable to first consider those techniques that are applicable to the body of the existing construction and, only if those are not sufficient, to prescribe further external interventions.

(c) The in-time efficiency of the interventions constitutes a fundamental requirement, set in Codes and Guidelines. The selection of adequate materials, techniques, and application procedures satisfying the durability requirement is, therefore, of major significance.

References

[1] Yön, B., Onat, O., Öncü, M.E., and Karaşın, A. Failures of masonry dwelling triggered by East Anatolian Fault earthquakes in Turkey, *Soil Dynamics & Earthquake Engineering,*133/2020 https://doi.org/10.1016/j.soildyn.2020.106126.

[2] Izol, R., Işık, E., Avcil, F., Arslan, M.H., Arkan, E., Büyüksaraç, A. Seismic performance of masonry structures after 06 February 2023 earthquakes; site survey and FE modelling approach, *Soil Dynamics and Earthquake Engineering,* Volume 186/2024 108904, https://doi.org/10.1016/j.soildyn.2024.108904.

[3] Damcı, E., Temür, R., Kanbir, Z., Şerkeci, Ç., Öztorun Köröğlu, E., Comprehensive investigation of damage due to 2023 Kahraman maraş earthquakes in Türkiye: Causes, consequences and mitigation, *Journal of Building Engineering,* 99 (2025) 114420, https://doi.org/10.1016/j.jobe.2024.114420.

[4] Avcil, F., Işık, E., Izol, R., Büyüksaraç, A., Arkan, E., Arslan, M.H., Aksoylu, C., Eyisüren, O., Harirchian, E., Effects of the February 6, 2023, Kahramanmaraş earthquake on structures in Kahramanmaraş city, *Natural Hazards, (*2024) 120-2953-2991, https://doi.org/10.1007/s11069-023-06314-1.

[5] Miltiadou-Fezans, A., and Tassios, Th.P. *Mix-design and Application of Hydraulic Grouts for Masonry Strengthening*, 1st Edition, Springer Tracks in Civil Engineering, Springer Nature Switzerland AG 2022, 283 pp.

[6] Valluzzi, M.R. *Comportamento meccanico di murature storiche consolidate con materiali e tecniche a base di calce*, Doctor Thesis, University of Trieste, Italy, 2000 (in Italian).

[7] Vintzileou E., Miltiadou-Fezans A. Mechanical properties of three-leaf stone masonry grouted with ternary or hydraulic lime-based grouts, *Engineering Structures*, Volume 30, Issue 8, August 2008, Pages 2265-2276, https://doi.org,10.1016/j.engstruct.2007.11.003.

[8] Vintzileou E. Three-leaf masonry in compression, before and after grouting: A review of literature, *International Journal of Architectural Heritage*, Vol. 5 (4-5), pp. 513-538. DOI: 10.1080/15583058.2011.557137.

[9] Bothara, J., and Brzev, S. A. EERI *Tutorial: Improving the Seismic Performance of Stone Masonry Buildings*, First Edition 2011.

[10] EPPO (Earthquake Planning and Protection Organization) (2023) *Code for assessment and structural interventions to masonry structures*, Athens, Greece.
(https://oasp.gr/kanonismoi/kanonismos-gia-apotimisi-kai-domitikes-epembaseis-toihopoiias).

[11] Modena C. (2012) Analisi e interventi strutturali su edifici in muratura secondo le Norme Tecniche per le Costruzioni 2008, Ordine degli Ingegneri della Provincia di Pistoia (https://www.ordineingegneri.pistoia.it/wp-content/uploads/Lezione-2012-11-05_Prof-Modena.pdf, last accessed online, April 28th, 2025)

[12] Munari, M., da Porto, F., Bartolozzi, A., Mocellini M., Valdesolo, A., Modena, C. Analisi di vulnerabilità sismica e interventi di miglioramento strutturale di un aggregato nel centro storico di L'Aquila. *Conference ANIDIS*, Bari, Italy.

[13] Kocaman, I., Kazaz, I., Collapse mechanism of historical masonry mosques under strong ground motions, *Engineering Failure Analysis,* 144(2023) 106983. https://doi.org/10.1016/j.engfailanal.2022.106983

[14] Onat, O., Özmen, A., Özdemir, E., Sayın, E., Damage propagation and failure mechanism of single dome historical masonry mosque after February 6, 2023, Kahramanmaraş earthquake doublets (M_w=7.7 and M_w=7.6), *Structures* 69 (2024)107288 https://doi.org/10.1016/j.istruc.2024.107288.

[15] Kocaman, I., Eroğlu, E., Yıldız, M.E., Yıldız, M.A., Mercimek, Ö., Çetin, S., Reinforced concrete interventions on the collapse mechanism of historical masonry structures with detailed finite element analyses: Kabasakal Mosque, *Engineering Failure Analysis,* 174 (2025) 109504. https://doi.org/10.1016/j.engfailanal.2025.109504.

[16] Piazza, M. The Role of In-Plane Floor Stiffness in the Seismic Behaviour of Traditional Buildings, in *Proceedings of the 14th World Conference on Earthquake Engineering*, 12-17 October 2018, Beijing, China.

[17] Valluzzi, M. R., Garbin, E., Dalla Benetta, M., and Modena, C. In-plane strengthening of timber floors for the seismic improvement of masonry buildings, in *Proceedings of the World Conference on Timber Engineering*, 20-24 June 2010, Riva del Garda, Italy.

[18] Valluzzi, M.R., di Bella, A., and Garbin, E. Optimization of mechanical and acoustic performance of timber floors, *Advanced Materials Research*, 690–697, doi:10.4028/www.scientific.net/AMR.778.690.

[19] Vintzileou, E., Mouzakis, C., Adami, C.-E., and Karapitta, L. Seismic behavior of three-leaf stone masonry buildings before and after interventions: Shaking table tests on a two-storey masonry model, *Bulletin of Earthquake Engineering* 13(10), 3107-3133, DOI: 10.1007/s10518-015-9746-x.

[20] Vintzileou E. The effect of deep rejointing on the compressive strength of brick masonry, *Masonry International*, Vol. 15, No 1, 2001, pp. 8-12.

[21] Dikmen, N. (with contributions by Randolph Langenbach) An investigation on traditional timber-framed buildings in Çankırı Province of Turkey, http://fbe.trakya.edu.tr/tujs, *Trakya Univ J Sci.* 11(1):15-27, ISSN 1305-6468 DIC: 282NDIT3041006100610.

[22] Vasconcelos, G., Lourenço P.B., Poletti, E. An overview on the seismic behaviour of timber frame structures, Chapter 10 in *Historical Earthquake-Resistant Timber Frames in the Mediterranean Area*, Ruggieri, N., Tampone, G., Zinno, R., Eds, Springer, ISBN 978-3-319-16186-0 ISBN 978-3-319-16187-7 (eBook) DOI 10.1007/978-3-319-16187-7.

[23] Bal, I. E., Vatan, M. Earthquake resistance of traditional houses in Turkey: Timber-frame infilled structures, in *Timber Structures: From Antiquity to the Present,* Publisher: T.C. HALİÇ ÜNİVERSİTESİ, Istanbul, Turkey, Eds. Chilton, J., Mungan, I., ISBN: 978-975-8574-25-4.

[24] Gülhan, D., Güney, I.Ö. The behavior of traditional building systems against earthquake and its comparison to reinforced concrete frame systems: experiences of Marmara earthquake damage assessment studies in Kocaeli and Sakarya. *Proceedings of Earthquake-safe: Lessons to be Learned from Traditional Construction*, Istanbul, Turkey. http://www.icomos.org/iiwc/seismic/Gulhan.pdf

[25] Vintzileou, E., and Touliatos, P. Seismic behaviour of the historical structural system of the island of Lefkada, Greece, in *Proceedings of the Conference STREMAH 2005*, 22-24 June, 2005, Malta, pp. 291-300.

Dicle University
Journal of Engineering
https://dergipark.org.tr/tr/pub/dumf
duje.dicle.edu.tr

Araştırma Makalesi / Research Article

Nanofiber Selüloz Katkılı Kireç Esaslı Enjeksiyon Malzemelerinin Tasarımı ve İncelenmesi

Design and Investigation of the Lime Based Grouts Incorporated with Nanofiber Cellulose

Ali Sayar[1], Didem Oktay[2*]

[1] Yıldız Teknik Üniversitesi, İnşaat Mühendisliği Bölümü, sayar_ali97@hotmail.com
ORCID: https://orcid.org/ 0009-0008-6133-5871

[2] Yıldız Teknik Üniversitesi, İnşaat Mühendisliği Bölümü, dyasar@yildiz.edu.tr
ORCID: https://orcid.org/0000-0002-0093-1994

MAKALE BİLGİLERİ

Makale Geçmişi:

Geliş 30 Nisan 2025
Revizyon 19 Haziran 2025
Kabul 21 Haziran 2025
Online 30 Eylül 2025

Anahtar Kelimeler:

Tarihi yapılar
Kireç esaslı enjeksiyon malzemesi
Nanofiber selüloz
Lif katkısı
Mekanik özellikler

ÖZ

Tarihi yapılardaki özgün harçlarda çeşitli liflerin ilave malzeme olarak kullanıldığı ve bu liflerin harçların fiziksel ve mekanik özelliklerini geliştirdiği bilinmektedir. Günümüzde yapı malzemelerinde sürdürülebilir nano malzemelere duyulan ihtiyaç araştırmacıları nanoselülozlara yönlendirmiştir. Bu çalışmada kireç esaslı ve nanofiber selüloz (NFS) katkılı enjeksiyon malzemeleri üretilerek malzemelerin taze ve sertleşmiş hal özellikleri incelenmiştir. Çalışmanın amacı; tarihi yapıların onarımında ve güçlendirilmesinde kullanılabilecek yeni bir kireç esaslı enjeksiyon malzemesi geliştirmektir. Deney sonuçlarına göre NFS ilavesi akışkanlık ve penetrasyon özelliklerini olumsuz etkilese de mekanik özellikleri ve rötre direncini ciddi oranda artırmaktadır. Ayrıca NFS'nin, doğal viskozite düzenleyici olarak çalıştığı ve sentetik katkı maddeleri yerine tercih edilebileceği görülmüştür.

ARTICLE INFO

Article history:

Received 30 April 2025
Received in revised form 19 June 2025
Accepted 21 June 2025
Available online 30 September 2025

Keywords:

Historical structures
Lime-based grout
Nanofiber cellulose
Fiber additive
Mechanical properties

Doi: 10.24012/dumf.1687825

ABSTRACT

It is known that various fibers were used as additives in the original mortars of historical buildings and these fibers improved the physical and mechanical properties of the mortars. Today, the need for sustainable nanomaterials in building materials has led researchers to investigate nanocelluloses. In this study, nanofiber cellulose (NFS) incorporated lime-based grouts were produced and the fresh and hardened state properties of the materials were examined. The main purpose of the study is to develop a new lime-based grout that can be used for consolidation of historical buildings. According to the test results, although the addition of NFS negatively affects the fresh state properties, it significantly increases the mechanical properties and shrinkage resistance. It has also been observed that NFS works as a natural viscosity modifier and can be preferred over synthetic additives.

* Sorumlu Yazar

Giriş

İnsanlar, temel fizyolojik ihtiyaçlardan biri olan barınma ihtiyacını karşılamak için çeşitli yapılar inşa etmiş ve bu yapıları geliştirmeye çalışmışlardır. Bu gelişim sırasında harçlarda kullanılan agregalar pek değişim göstermemiş genellikle bağlayıcı malzemenin özellikleri geliştirilmeye çalışılmıştır. Harçlara çeşitli katkı maddeleri ilave ederek zayıf olan mekanik özellikler güçlendirilmiştir. Literatürde, harçlarda saman, kıtık, hayvan kılları, gübre, bitki özleri, yonga ve talaş parçaları, kan, süt, yumurta vb. pek çok organik veya inorganik katkı maddesi kullanıldığını kanıtlayan çalışmalar mevcuttur [1],[2].

Tarihi yapılar, geçmişten günümüze kadar uzanan, inşa edildiği dönemin tarihi, kültürü, sosyolojisi, mimarisi, malzeme bilgisi, mühendislik anlayışı gibi pek çok alanda bilgi edinmemizi sağlayan kültürel değerlerdir. Her yapı gibi tarihi yapılar da çevre koşulları, doğal afetler, savaşlar, yapının kullanımına bağlı etkenler, tasarım ve yapım hataları, malzeme bozulması gibi çeşitli nedenlerle hasar görebilir [3]. Sahip oldukları kültürel önem düşünüldüğünde tarihi yapıların onarımı ve güçlendirilmesi hassas bir konudur ve disiplinler arası ciddi bir çalıştırma gerektirir. Tarihi yapıların onarımı ve güçlendirilmesi için kullanılan farklı teknikler vardır, bu tekniklerden biri de enjeksiyon yöntemi (grouting)'dir.

Enjeksiyon yöntemi (grouting), bağlayıcı malzemenin su ve çeşitli katkılarla karıştırılması sonucu elde edilen akıcı kıvamdaki enjeksiyon malzemesinin (grout), basınçla yığma duvardaki çatlakları ve boşlukları doldurması prensibine dayanan bir güçlendirme yöntemidir [4]. Enjeksiyon yönteminin genel amacı; yapıdaki özgün malzemeye uygun olarak üretilen enjeksiyon malzemesinin duvara açılan uygun deliklerden enjekte edilerek yapıdaki süreksizliklerin giderilmesi, çatlakların doldurulması ve mekanik dayanım özelliklerinin iyileştirilmesidir [5]. Enjeksiyon yönteminde dikkat edilmesi gereken en önemli husus yapıya enjekte edilecek malzemenin özgün harçla fiziksel, kimyasal ve minerolojik açıdan uyumlu olmasıdır. Tarihi harçlarda bağlayıcı malzeme olarak kireç, katkı malzemesi olarak da doğal lif kaynaklarının kullanıldığı düşünüldüğünde enjeksiyon malzemelerinin de kireç esaslı ve doğal lif katkılı olarak üretilmesinin bu uyumu artıracağı düşünülmektedir.

Kireç esaslı harçlar, mekanik özelliklerinin çimento esaslı harçlara göre daha zayıf olması, hızlı su buharlaşmasına bağlı oluşan rötre çatlakları, moleküler arası zayıf kohezyon, kırılgan yapı, uzun priz süresi gibi bazı olumsuz özellikler göstermektedir. Kireç harçlarının ve kireç esaslı enjeksiyon malzemelerinin zayıf özellikleri, bünyesinde lif içeren katkı maddeleri kullanılarak güçlendirilebilir [6]. Lifler, özellikle malzemenin maksimum direncine ulaşıldığı yumuşama aşamasında dikiş etkisi yoluyla gerilme kuvvetlerini aktararak çatlakların başlamasını ve ilerlemesini önler [7],[8]. Bu durum yapının yük altındaki basınç mukavemetini ve deprem, rüzgar gibi yanal etkiler altındaki eğilme mukavemetini artırarak yapının mekanik özelliklerinin güçlenmesini sağlar. Lif katkılı kireç esaslı enjeksiyon malzemeleri tarihi yapıların onarımında kullanıldığında hem yapıdaki boşluklar ve çatlaklar doldurularak monolitik bir yapı elde edilmekte hem de liflerin varlığı sayesinde yapının mekanik özellikleri güçlendirilmektedir. Lif takviyeli bir malzemenin performansı, kullanılan lifin elastik özellikleri, lifin geometrisi ve dağılımı, matris yapışması gibi pek çok faktöre bağlı olmakla birlikte literatürde liflerin yapıya olumlu özelliklerini gösteren çalışmalar mevcuttur [9],[10].

Nanofiber selüloz (NFS), çeşitli bitki hücrelerinin çeperlerinden elde edilen selülozun, mekanik ve/veya kimyasal yollarla nano boyuta getirilmesi ile elde edilen, fizik, kimya, biyoloji, malzeme bilimi, elektronik, endüstri vb. pek çok alanda kullanılan bir lif türüdür. Literatürde NFS'nin tek başına veya farklı katkı maddeleri ile bir arada kullanımına dair çalışmalar mevcuttur. Örneğin; Ardanuy vd. [11] yaptıkları çalışmada çimento esaslı harçları güçlendirmek ve yüksek performanslı beton elde edebilmek amacı ile ürettikleri harçlarda NFS katkısı kullanmışlardır. Çalışmada, NFS'nin özgül yüzey alanı sayesinde fiber-matris etkileşiminin artmasını sağladığı, NFS bünyesindeki güçlü liflerin de gerilme kuvvetlerini köprüleme yolu ile aktararak beton harcının eğilme mukavemetini artırdığı belirtilmiştir. Goncalves vd. [12] NFS'nin çimento harçlarının taze haldeki özelliklerine etkilerini araştırmışlardır. NFS'nin hidrofilik yapısı sebebi ile yüksek miktarda suyu bünyesine hapsederek akışkanlık özelliğini ciddi oranda düşürdüğünün vurgulandığı çalışmada %1.2 NFS ilavesinin terleme miktarını da %75 düşürdüğü belirlenmiştir. Kolour vd. [13] yaptıkları çalışmada NFS katkısının plastik rötre üzerine etkilerini incelemişlerdir. Az miktarda NFS kullanımının plastik rötreyi azalttığını yüksek dozda NFS kullanımının ise plastik rötreyi artıracağını belirtmişlerdir. Bu durum diğer özellikler için de geçerli olup NFS miktarı uygun dozajın üstünde kullanıldığında olumsuz etki yaratmaktadır [11],[13].

Literatürdeki çalışmalar incelendiğinde NFS'nin çimento esaslı harçlarda ve enjeksiyon malzemelerinde kullanımına dair pek çok çalışma olmasına rağmen kireç esaslı enjeksiyon malzemelerinde NFS kullanımına dair herhangi bir çalışmaya rastlanmamıştır. NFS katkısının kireç esaslı enjeksiyon malzemelerinde de mekanik özelliklerin gelişmesine katkı sağlayacağı düşünülmektedir.

Bu çalışmanın temel amacı; NFS ilavesinin kireç esaslı enjeksiyon malzemelerine etkilerini araştırarak tarihi yapıların onarımında ve güçlendirilmesinde kullanılabilecek yeni bir enjeksiyon malzemesi geliştirmektir. Bu kapsamda ilk olarak enjeksiyon malzemelerinin taze halde sağlaması gereken akışkanlık, penetrasyon ve hacim sabitliği özellikleri deneysel çalışmalarla incelenerek serilerin karışım oranlarına karar verilmiştir. Tasarımı yapılan seriler tekrar üretilerek taze ve sertleşmiş hal özelliklerine ek olarak reolojik özellikleri ve içyapısı da incelenmiştir. Son olarak, elde edilen tüm veriler yorumlanarak NFS ilavesinin kireç esaslı enjeksiyon malzemelerine etkileri yorumlanmıştır.

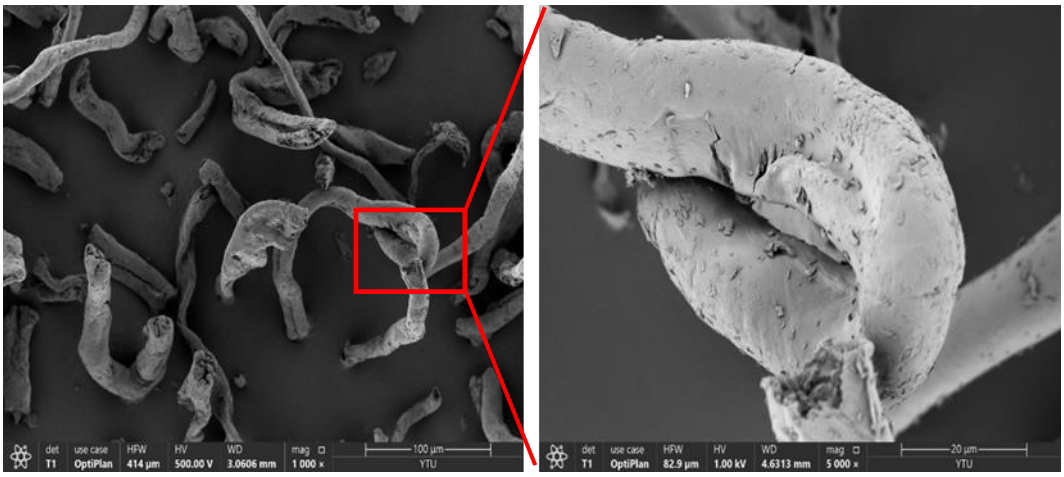
Materyal ve Metot

Materyal

Çalışmada, Nanografi firmasından temin edilen, 10-20 nm çapında, 2-3 µm uzunluğunda, yoğunluğu 1,50 gr/cm^3, selüloz kristalinitesi (XRD) %92 olan nanofiber selüloz (NFS), lif katkısı olarak kullanılmıştır. Liflerin, Şekil 1'de verilen geçirimli elektron mikroskobu (TEM) görüntüsünde lif formunda olduğu görülmektedir. Tarihi yapılarda bulunan özgün malzemelerle olan fiziksel ve kimyasal uyumu, yeterli mekanik dayanımı, biyo-esaslı yapısı, geri dönüştürülebilir

olması nedenleri ile NHL 5 sınıfı doğal hidrolik kireç bağlayıcı malzeme olarak tercih edilmiştir. Doğal hidrolik kirece ait kimyasal özellikler Tablo 1'de verilmiştir. Kimyasal bileşimde yüksek oranda CaO içeri ön plana çıkmaktadır. SiO_2i Al_2O_3 ve MgO miktarları ikici ana bileşenlerdir. Kireç TS EN 459-1'de verilen sınıfı sağlamaktadır.

Karışımlara kireç miktarının %0.1, %0.2 ve %0.3'ü oranında NFS ilave edilmiştir. Üretilen enjeksiyon malzemelerinin taze hal özelliklerinin sağlanması amacı ile karışımlarda kimyasal katkı maddeleri kullanılmıştır. Enjeksiyon malzemelerinin akışkanlık ve penetrasyon özelliklerini sağlamak amacı ile Chryso Yapı Kimyasalları'ndan temin edilen Lab Bet 10291 polikarboksilik eter esaslı süper akışkanlaştırıcı, yüksek oranda suyun neden olduğu terleme oranının dengelenebilmesi amacı ile de Quad 20 sentetik kopolimer çözeltisi viskozite düzenleyici katkı maddesi kullanılmıştır.



Şekil 1. NFS liflerinin TEM görüntüsü

Tablo 1. NHL 5'in kimyasal bileşenleri

Bileşenler (%)	NHL 5
CaO	54.9
SiO_2	9.3
Al_2O_3	2.6
MgO	2.4
Fe_2O_3	1.6
K_2O	0.8
TiO_2	0.2
Na_2O	0.1
P_2O_5	<0.1
MnO	<0.1
Cl	-
Kızdırma Kaybı	1.5

Metot

Enjeksiyon Malzemelerinin Üretimi

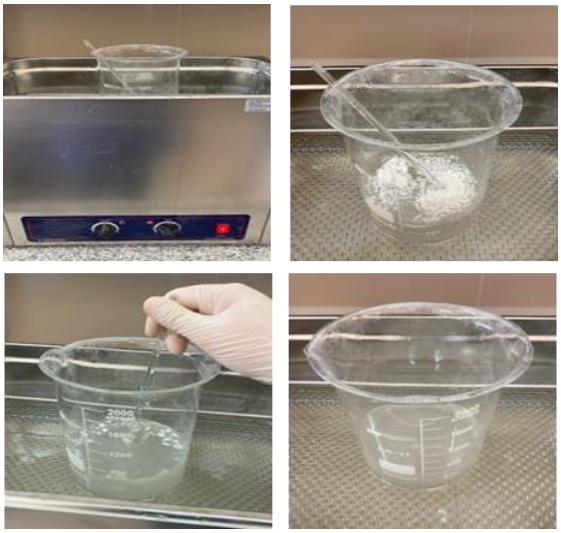
Çalışma kapsamında NFS ilavesinin kireç esaslı enjeksiyon malzemelerine etkilerini araştırmak amacı ile dört farklı numune üretilmiştir. Üretilen ilk numunede NFS ilavesi yapılmamış ve referans olarak kabul edilmiştir. Diğer numunelerde NFS oranı sırasıyla %0.1, %0.2 ve %0.3'tür. Üretilen numunelerin karışım oranları Tablo 2'de verilmiştir. Kireç esaslı enjeksiyon malzemelerinin üretim ve karıştırma yöntemleri için herhangi bir standart olmaması sebebiyle literatürde bulunan daha önceki çalışmalar dikkate alınarak üretim ve karışım yöntemi belirlenmiştir [14],[15]. Üretim ve karışım aşamaları aşağıda sıralanmıştır.

- Tüm numuneler laboratuvar ortamında 23±2 °C ve %50 bağıl nem koşullarında üretilmiştir.
- Enjeksiyon malzemesinin üretiminde kullanılacak tüm malzemeler Tablo 2'de belirtilen oranlarda tartılarak hazırlanmıştır.
- Karışım suyunun %10'u kimyasal katkıların seyreltilmesi için ayrılmıştır.
- NFS'nin matris içinde homojen dağılmasını sağlamak için üretim öncesinde nano malzeme karışım suyu ile birlikte 1 saat boyunca 40 kHz frekansta ultrasonik banyoda karıştırılmış ve jel formuna getirilmiştir (Şekil 2). Dağıtma süresi görsel değerlendirme yapılarak belirlenmiştir.
- Karıştırma işlemi için spiral uçlu mekanik mikser kullanılmıştır.
- Spiral uçlu mekanik mikserin hızı karıştırma süreci boyunca sabit ve 800 rpm'dir.
- Topaklanmayı engellemek amacı ile 1 dakika kuru karıştırma yapılmıştır.
- Jel formdaki NFS karışım suyu içerisinde karışıma ilave edilmiştir.
- Karıştırma süresi toplam 13 dakika 30 saniyedir.
- Kimyasal katkılar 3. dakikadan itibaren 30 saniye içerisinde ilave edilerek 10 dakika daha karıştırılmış ve enjeksiyon malzemeleri elde edilmiştir.

Tablo 2. Enjeksiyon malzemelerinin üretiminde kullanılan malzemelerin ağırlıkça oranları (gr)

SERİ	Kireç	Su/Kireç	NFS	SA*	VD**
REF	1000	0.8	-	-	10
NFS 1	1000	0.8	1	18	-
NFS 2	1000	0.8	2	18	-
NFS 3	1000	0.8	3	18	-

*Süper Akışkanlaştırıcı
** Viskozite Düzenleyici



Şekil 2. NFS'nin ultrasonik banyoda su içerisinde dağıtılması

Deneysel Çalışmalar

Taze Hal Özelliklerinin İncelenmesi

Enjeksiyon yönteminin telafisi mümkün olmadığından, konsolidasyon hatalarına sebep olarak yapıya zarar vermemek için tasarım aşamasında enjeksiyon malzemesinin taze halde akışkanlık, penetrasyon, hacim sabitliği gibi performans yeterliliklerini sağlaması gerekmektedir. Enjeksiyon malzemesinin kıvamı hakkında bilgi veren akışkanlık özelliği ASTM D6910'da [16] belirtilen "Marsh Hunisi" ve TS EN445'te [17] belirtilen "Akış Konisi" deneyleri ile ölçülmüştür. Penetrasyon özelliği EN 1771'de [18] belirtilen "Kum Kolonu" deneyi ile terleme özelliği ise ASTM C940 [19] referans alınarak ölçülmüştür. Tüm taze hal deneyleri 23±2 °C ve %50 bağıl nem koşullarında yapılmıştır.

Reolojik Özelliklerin Belirlenmesi

Doğru bir enjeksiyon uygulaması için malzemenin reolojik özelliklerinin de incelenmesi gerektiği bilinmektedir. Reolojik özellikler rotasyonal bir reometre (Anton Paar Reolab QC) ve tek eksenli silindirik uç kullanılarak incelenmiştir. Ölçüm prosedüründe ilk olarak enjeksiyon malzemesinin içerisinde bulunan hava kabarcıklarını yok etmek amacıyla 300 s^{-1} kayma hızında 20 sn ön karışım uygulanmıştır. Ardından malzeme 20 sn dinlendirilip asıl ölçüme geçilmiştir. Ölçümde malzemeye uygulanan kayma hızı kademeli olarak önce 0,1 s-¹'den 300 s-¹'ye artarak, sonrasında ise 300 s-¹'den 0,1 s-¹'ye azalarak uygulanmıştır. Cihaza ait Rheoplus yazılımı kullanılarak serilere ait reolojik davranışlar elde edilmiştir. Enjeksiyon malzemesine ait eşik kayma gerilmeleri ve plastik viskozite değerleri Herschel-Bulkley modeli kullanılarak hesaplanmıştır.

Sertleşmiş Hal Özelliklerinin İncelenmesi

Taze hal özellikleri incelenen ve performans yeterliliğini sağlayan numunelerin ilk olarak fiziksel özellikleri incelenmiştir. Üretilen serilerin kılcal su emme katsayısı, ağırlıkça ve hacimce su emme oranları, özgül ağırlık, birim hacim ağırlık, porozite, kompasite gibi fiziksel özellikleri deneysel çalışmalarla belirlenmiştir. Toplam prorozite oranı hesap yöntemi ile belirlenmiştir. Deneyler numuneler üretildikten sonraki 28. günde yapılmıştır. Fiziksel özelliklerin ardından numunelerin mekanik özellikleri de incelenmiştir. Serilerin eğilme ve basınç dayanımları TS EN 1015-11'e [20] göre yapılan eğilme ve basınç dayanım deneyleri ile (Şekil 3) ölçülmüştür. Deney için üretilen numunelerin boyutları 40×40×160 mm'dir. Deneyler, numuneler üretildikten sonraki 28. ve 56. günde yapılmış, numuneler deney gününe kadar kür koşullarına tabi tutulmuştur. Deneyler, deformasyon kontrollü 60 ton kapasiteli yükleme cihazında gerçekleştirilmiştir. Yükleme hızı tüm testlerde 1.0 mm/dk olarak sabit tutulmuştur. Eğilme deneyi sonucunda ortadan ikiye bölünen numuneler, 40 mm×40 mm ölçülerindeki çelik plakaların arasına yerleştirilerek basınç deneyine tabi tutulmuştur. Eğilme deneyinde mesnet açıklığı standarda uygun olarak 100 mm olarak ayarlanmıştır.

Enjeksiyon malzemelerinin kür koşulları ile ilgili herhangi bir standart bulunmadığından TS EN 1015-11 [20] referans alınarak kür yapılmıştır. Üretilen numuneler 7 gün boyunca %95±5 bağıl nemde ve kalıp içerisinde kür edilmiştir. Numuneler 7. günde kalıptan çıkarılarak deney gününe kadar %65±5 bağıl nemde küre devam edilmiştir. Kür sırasında sıcaklık (20±2) °C sabit tutulmuştur.



Şekil 3. Eğilme ve basınç dayanım deneyi

Kuruma Rötresinin Ölçülmesi

Kireç esaslı enjeksiyon malzemelerinin en büyük dezavantajlarından biri hızlı su buharlaşmasından kaynaklı oluşan kuruma rötresidir. Malzemenin büzülerek hacminin küçülmesi olarak tanımlanan rötre, yüksek oranlarda oluştuğunda enjeksiyon malzemesinin fiziksel yapısının bozulmasına neden olarak enjeksiyon uygulamasının kalitesini düşürebilir. Literatürde kireç esaslı enjeksiyon malzemelerinin rötre ölçümleri için özel

bir standart bulunmadığından numunelerin boy değişim ölçümleri ASTM C-940'a [19] göre yapılmıştır. Numuneler 4×4×16 cm boyutlarında pimli kalıplarda üretilerek kalıptan çıkarıldıkları ilk gün 0. gün kabul edilmiş, standartta belirtilen günlerde boy değişimleri ölçülerek kaydedilmiştir (Şekil 4). Üretilen numuneler 7 gün boyunca %95±5 bağıl nemde ve kalıp içerisinde kür edilmiştir. Numuneler 7. günde kalıptan çıkarılarak deney gününe kadar %65±5 ve 20±2 °C sıcaklıktaki nem kabininde bekletilmiştir.



Şekil 4. Rötre ölçümü

Taramalı Elektron Mikroskobu (SEM-EDS) ile İçyapının İncelenmesi

Üretilen enjeksiyon malzemelerinin içyapısını görüntülemek amacı ile uygun ebatlarda numuneler çıkarılarak şeffaf epoksi reçineden tabanlık yapılmış daha sonra altın kaplama yapılarak Zeıss marka EVO LS10 model taramalı elektron mikroskobu kullanılarak kesitler incelenmiştir. Ölçüm öncesi numuneler ilk olarak 24 saat etüvde kurutulmuş sonrasında ise vakumda bekletilmiştir. Serilerin kimyasal yapılarını incelemek amacı ile uygun noktalardan enerji dağılımlı spektroskopi (EDS) yapılmıştır.

Bulgular

Taze Haldeki Enjeksiyon Malzemesi Deney Sonuçları

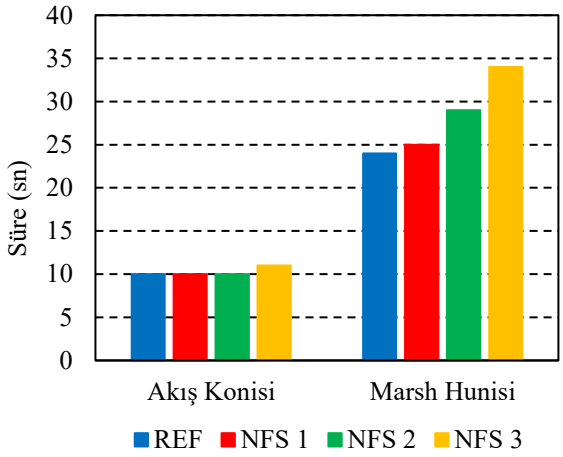
Üretilen enjeksiyon malzemelerinin taze haldeki özelliklerini belirlemek amacı ile akışkanlık, penetrasyon ve hacim sabitliği deneyleri yapılmıştır. Deneylere ait sonuçlar ve değerlendirmeler aşağıda verilmiştir.

Akışkanlık Özelliği Deney Sonuçları

Serilerin akışkanlık özelliği ASTM D6910'da [16] belirtilen "Marsh Hunisi" ve TS EN445'te [17] belirtilen "Akış Konisi" deneyleri ile ölçülmüştür. Üretilen tüm seriler her iki deney için de limit değerleri sağlamaktadır. Akış konisinde numunelerin akış süresi 10 - 11 sn, Marsh hunisinde ise 24 - 34 sn aralığında ölçülmüştür. Her iki deney sonucunda da nanofiber selüloz (NFS) katkısının akış süresini artırdığı gözlemlenmiştir. Akışkanlık özelliğine dair sonuçlar Tablo 3'te ve Şekil 5'te verilmiştir. Sonuçlar üretilen tüm serilerin aritmetik ortalaması alınarak hesaplanmıştır.

Tablo 3. Enjeksiyon malzemelerinin akışkanlık deney sonuçları

SERİ	Akış Konisi (sn)	Marsh Hunisi (sn)
REF	10	24
NFS 1	10	25
NFS 2	10	29
NFS 3	11	34
Limit	*≤ 25 sn [21]*	*≤ 45 sn [22],[23]*



Şekil 5. Serilere ait akış süresi değerleri

Penetrasyon Özelliği Deney Sonuçları

Serilerin enjekte edilebilirliği EN 1771 [18]' de belirtilen "Kum Kolonu" deneyi ile ölçülmüştür. Üretilen tüm seriler penetrasyon özelliği için gereken performans yeterliklerini sağlamıştır. EN 1771 [18]'e göre REF, NFS 1 ve NFS 2 numuneleri için enjekte edilebilirlik sınıfı "kolay", NFS 3 için "uygulanabilir"dir. NFS katkısının enjekte edilebilirliği düşürdüğü gözlemlenmiştir. Deney sonuçları Tablo 4'te verilmiştir. Sonuçlar üretilen tüm serilerin aritmetik ortalaması alınarak hesaplanmıştır.

Tablo 4. Enjeksiyon malzemelerinin penetrasyon deney sonuçları

SERİ	T_{36} süresi (sn)	20 ml toplanma süresi (sn)	Enjekte Edilebilirlik
REF	4	12	Kolay
NFS 1	5	14	Kolay
NFS 2	6	28	Kolay
NFS 3	7	-	Uygulanabilir
Limit	*≤ 50 sn [22],[23]*		

Hacim Sabitliği Özelliği Deney Sonuçları

Serilerin hacim sabitliği TS EN 445 [17] ve ASTM C940 [19] referans alınarak ölçülmüştür. Yapılan ön üretim çalışmalarında referans numunenin terleme oranı ortalama %12.5 ölçülmüştür. Limit değeri sağlamak amacı ile referans numunede % 1 oranında viskozite düzenleyici katkı maddesi kullanılmıştır. NFS katkılı

numunelerin ön üretiminde limit değer aşılmadığı için viskozite düzenleyici katkı maddesi kullanılmamıştır. NFS'nin %0.1 ilave edilmesi ile terleme değeri referans seriye kıyasla yaklaşık %20 artmış, ancak üretilen tüm serilerde terleme oranı limit değer olan %5'in altındadır. NFS'nin %0.2 ve %0.3 oranında ilavesi ile de enjeksiyon malzemelerinin terleme değerleri referans seriye benzer sonuçlar vermiştir. Elde edilen bu sonuçlara göre, NFS'nin doğal viskozite düzenleyici olarak çalıştığı söylenebilir [12]. Ortalama deney sonuçları Tablo 5'te verilmiştir.

Tablo 5. Enjeksiyon malzemelerinin hacim sabitliği deney sonuçları

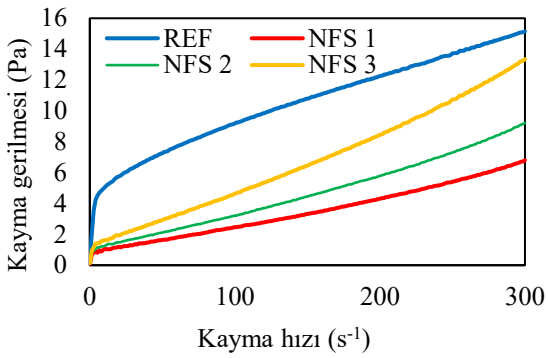
SERİ	Terleme Oranı (%)
REF	3.8
NFS 1	4.5
NFS 2	3.7
NFS 3	3.6
Limit	*5 [22],[24],[25]*

Reolojik Özelliklerin İncelenmesi

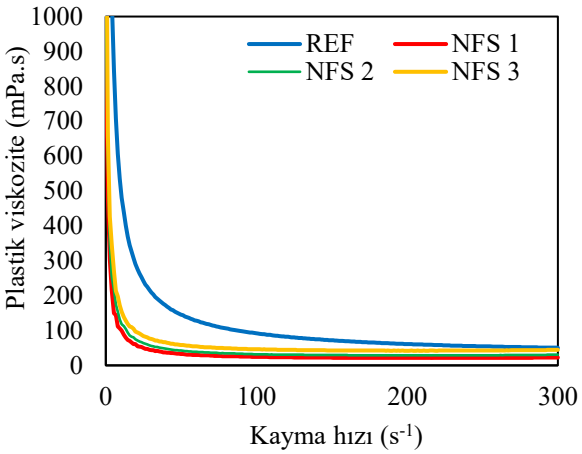
Malzemelerin reolojik davranışı dikkate alınarak seçilen Herschel-Buckley modeline göre hesaplanan reolojik parametreler Tablo 6'da verilmiştir. Enjeksiyon malzemelerinin reolojik ölçümlerinden elde edilen akış ve viskozite eğrileri Şekil 6 ve Şekil 7'de verilmiştir. Tüm serilerde R değeri 0.98'in üzerinde sağlanmıştır. Deney sonuçları incelendiğinde, tüm parametrelerin aynı olduğu NFS katkılı serilerde NFS ilavesinin artması ile birlikte enjeksiyon malzemelerinin eşik kayma gerilmelerinin de arttığı görülmüştür. REF serisinin eşik kayma gerilmesinin NFS katkılı serilerden daha yüksek olmasına enjeksiyon malzemelerinin tasarımı sırasında hacim sabitliği özelliğinin limit değerini sağlamak amacı ile REF serisinde kullanılan yüksek miktarda viskozite düzenleyici katkı maddesinin neden olduğu düşünülmektedir. Reolojik parametrelerin kullanılan katkı maddeleri, sıcaklık, bekleme süresi gibi pek çok değişkenden etkilendiği bilinmektedir [26]. Çimento esaslı harçlar üzerinde yapılan çalışmalarda da NFS ilavesi ile doğru orantılı şekilde akma gerilmesinin ve plastik viskozitenin arttığı ve malzemelerin kayma incelmesi davranışı gösterdiği belirtilmiştir [13]. Bu çalışma kapsamında üretilen NFS katkılı kireç esaslı enjeksiyon malzemelerinin de kayma incelmesi davranışı gösterdiği Şekil 7'de görülmektedir. Bu duruma lifler arası oluşan bağların akış hareketini yavaşlatmasının neden olduğu düşünülmektedir.

Tablo 6. Herschel-Buckly modeline göre hesaplanan reolojik parametreler

SERİ	Eşik Kayma Gerilmesi (τ_0) (Pa)	Kararlılık İndeksi (K)	Akış İndeksi (n)
REF	2.99	0.430	0.58
NFS 1	0.96	0.005	1.24
NFS 2	1.21	0.006	1.25
NFS 3	1.49	0.012	1.21



Şekil 6. Enjeksiyon malzemelerine ait akış eğrileri



Şekil 7. Enjeksiyon malzemelerine ait viskozite eğrileri

Sertleşmiş Hal Özelliklerinin İncelenmesi

Kılcallıkla Su Emiliminin Belirlenmesi

Serilerin kılcal su emme katsayıları TS EN 15801 [27] uyarınca 28. günde gerçekleştirilen kılcal su emme deneyi ile belirlenmiş, sonuçlar Tablo 7'de verilmiştir.

Tablo 7. Serilerin kılcal su emme katsayıları

SERİ	Kılcal Su Emme Katsayısı (kg/(m^2.√sn))
REF	1.08 ± 0.19
NFS 1	0.46 ± 0.02
NFS 2	0.47 ± 0.03
NFS 3	0.68 ± 0.03

Deney sonuçları incelendiğinde NFS katkısının kılcallıkla su emilimini NFS 1 ve NFS 2 serilerinde %56 - %57, NFS 3 serisinde ise %37 düşürdüğü görülmektedir. Bu duruma NFS'nin hidrofilik yapısının neden olduğu söylenebilir. NFS 3 serisinde kılcal su emme miktarının diğer NFS katkılı serilere oranla yüksek olma nedeninin uniform olmayan dağılım olduğu düşünülmektedir [9],[10].

Temel Fiziksel Özelliklerin Belirlenmesi

Enjeksiyon malzemelerinin temel fiziksel özellikleri deneysel çalışmalara ait bağıntılar kullanılarak

hesaplanmıştır. Deneyler üretimden sonraki 28. günde yapılmıştır. Deney sonuçları sırasıyla Tablo 8'de verilmiştir.

Tablo 8. Serilerin temel fiziksel özellikleri

SERİ	Birim Hacim Ağırlık Özgül Ağırlık (g/cm^3)		Ağırlıkça Su Emme (%)	Hacimce Su Emme (%)	Porozite (%)
REF	0.96	2.55	63.5 ±0.7	60.9 ±0.5	62.4 ± 0.1
NFS1	0.97	2.64	61.6 ±0.4	60.0 ±0.4	63.0 ±0.0
NFS 2	0.96	2.60	61.9 ±0.4	59.5 ±0.4	63.1 ±0.0
NFS 3	0.95	2.59	60.8 ±0.1	58.0 ±0.4	63.2 ±0.2

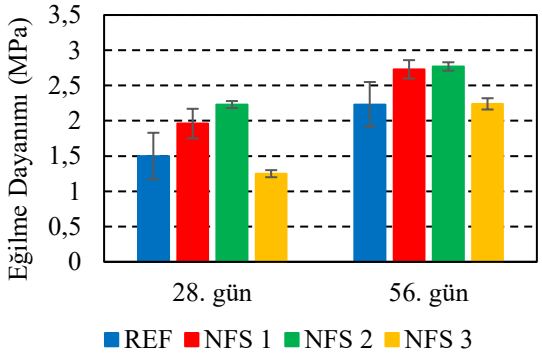
Enjeksiyon malzemelerinin temel fiziksel özellikleri incelendiğinde tüm serilerde toplam boşluk oranının oldukça fazla olduğu, boşlukların tamamına yakınının dışa açık olduğu ve NFS katkısının toplam boşluk oranını az miktarda da olsa artırdığı söylenebilir. Toplam boşluk oranının malzemenin su muhtevası ile doğru orantılı olduğu düşünüldüğünde enjeksiyon malzemelerinin bünyesindeki yüksek su oranı ve NFS'nin yüksek su talebi bu durumu açıklamaktadır. Toplam boşluk oranı daha fazla olmasına rağmen NFS katkılı enjeksiyon malzemelerinin %1.5 - %4 arasında daha yoğun olduğu, en yoğun malzemenin ise %0,1 NFS katkısı içeren seri olduğu görülmektedir. Ağırlıkça ve hacimce su emme oranları incelendiğinde NFS katkısının su emme miktarını %1 - %3 azalttığı gözlemlenmiştir. NFS liflerinin karışım suyunun bir kısmını hapsederek bünyesinde tutması enjeksiyon malzemesinin kılcallıkla emdiği su miktarının azalmasına yol açmıştır. Serilerin kılcal su emme katsayıları da bu durumla örtüşmektedir.

Eğilme Dayanımı Deney Sonuçları

Enjeksiyon malzemelerinin eğilme dayanımı TS EN 1015-11 [20]'e göre yapılan eğilme deneyi ile ölçülmüştür. 40×40×160 mm boyutlarında üretilen numuneler, 28. ve 56. günde deformasyon kontrollü 60 ton kapasiteli yükleme cihazında eğilmeye tabi tutularak kırılmıştır. Deneyde kullanılan numune sayısı her seri için 6'dır. Yükleme hızı tüm testlerde 1,0 mm/dk'dır. Eğilme dayanımı deney sonuçları Tablo 9 ve Şekil 8'de verilmiştir. Sonuçlar üretilen tüm serilerin aritmetik ortalaması alınarak hesaplanmıştır.

Tablo 9. Eğilme dayanımı deney sonuçları

SERİ	f_e (28.gün) (MPa)	f_e (56.gün) (MPa)
REF	1.50 ± 0.33	2.23 ± 0.32
NFS 1	1.96 ± 0.21	2.73 ± 0.13
NFS 2	2.23 ± 0.05	2.77 ± 0.06
NFS 3	1.25 ± 0.05	2.24 ± 0.08



Şekil 8. Enjeksiyon malzemelerinin eğilme dayanımları

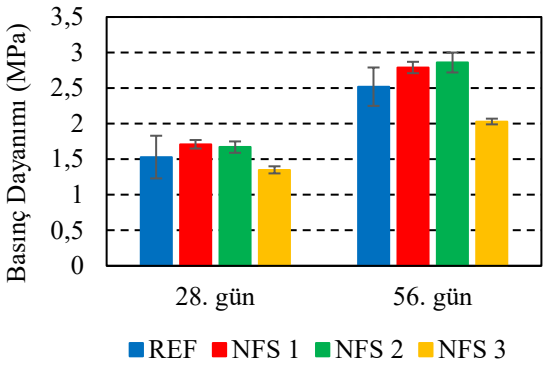
Deney sonuçları incelendiğinde, NFS katkısının hem 28. günde hem de 56. günde eğilme dayanımında artış sağladığı görülmektedir. Her iki deney gününde de en yüksek eğilme dayanımı NFS 2 serisinde elde edilmiştir. NFS 2 serisi referans numuneye kıyasla 28. günde %49, 56. günde ise %24 daha fazla mukavemet göstermiştir. NFS 1 ve NFS 2 serilerinde kademeli bir artış söz konusuyken NFS 3 serisinde 28. günde %17 düşüş gözlemlenmiş, 56. günde ise referans numuneye yakın sonuçlar elde edilmiştir. Bu duruma liflerin topaklanması sonucu homojen olmayan dağılımın neden olduğu düşünülmektedir [9],[10]. NFS ilavesi optimum miktarda kullanıldığında enjeksiyon malzemelerinin eğilme dayanımına olumlu yönde etki etmiştir.

Basınç Dayanımı Deney Sonuçları

Serilerin basınç dayanımı TS EN 1015-11 [20] referans alınarak yapılan basınç dayanım deneyi ile ölçülmüştür. Eğilme deneyi sonucunda ortadan ikiye bölünen numuneler, 40×40 mm ölçülerindeki çelik plakaların arasına yerleştirilerek deformasyon kontrollü 60 ton kapasiteli yükleme cihazında basınca tabi tutularak kırılmıştır. Deneyde kullanılan numune sayısı her seri için 12'dir. Yükleme hızı tüm testlerde 1,0 mm/dk'dır. Ortalama basınç dayanımı sonuçları Tablo 10 ve Şekil 9'da verilmiştir.

Tablo 10. Basınç dayanımı deney sonuçları

SERİ	f_b (28.gün) (MPa)	f_b(56.gün) (MPa)
REF	1.53 ± 0.30	2.52 ± 0.27
NFS 1	1.71 ± 0.06	2.79 ± 0.08
NFS 2	1.67 ± 0.08	2.86 ± 0.14
NFS 3	1.35 ± 0.05	2.03 ± 0.04

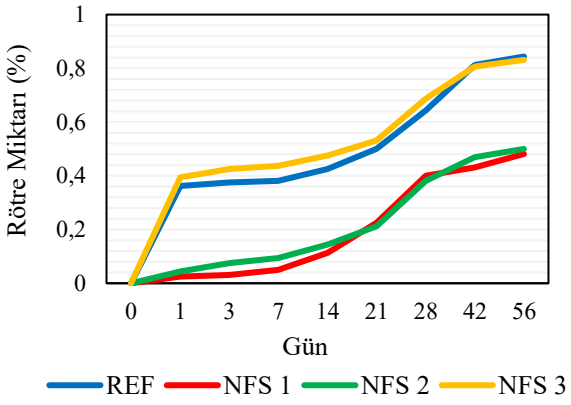


Şekil 9. Enjeksiyon malzemelerinin basınç dayanımları

Deney sonuçları incelendiğinde, NFS ilavesinin 28. gün basınç dayanımında %9 - %12, 56. gün dayanımında ise %11 - %14 arasında dayanım artışı sağladığı görülmüştür. NFS 1 ve NFS 2 serilerinin dayanımları birbirine çok yakın olmakla birlikte en yüksek dayanım 28. günde NFS 1 serisinde, 56. Günde ise NFS 2 serisinde elde edilmiştir. NFS 3 serisinde hem 28. hem de 56. gün dayanımında liflerin topaklanması sonucu homojen olmayan dağılımdan kaynaklanan dayanım kaybı gözlemlenmiştir [9],[10]. Elde edilen sonuçlar, kireç esaslı enjeksiyon malzemelerinde NFS kullanımına dair herhangi bir çalışma bulunmaması nedeniyle literatürdeki diğer çalışmalarla kıyaslanmıştır. Çimento esaslı harçlarda ve yonga levhalarında yapılan çalışmalarda da optimum miktardaki NFS ilavesinin basınç dayanımını olumlu yönde etkilediği söylenebilir [12]. Basınç dayanımı açısından değerlendirildiğinde, bu çalışma kapsamında üretilen kireç esaslı enjeksiyon malzemeleri için optimum NFS miktarı %0,2 olarak kabul edilmiştir. Mekanik özellikler incelendiğinde NFS ilavesinin eğilme dayanımını daha fazla artırdığı görülmektedir. Nano yapısı sayesinde mekanik özelliklerde iyileştirme sağlarken, lifli yapısı sayesinde de eğilme dayanımını da artırmıştır.

Kuruma Rötresi Ölçüm Sonuçları

Serilerin rötre ölçümleri, ASTM C-940'a [19] göre ölçülmüştür. Serilerin kalıptan çıkarıldıkları ilk gün 0. gün kabul edilerek ilk kez ölçüm yapılmış daha sonra 1. 7. 14. 21. 28. 42. ve 56. günlerde de ölçüm yapılarak boy farkları hesaplanmıştır. Sonuçlar Şekil 10'da verilmiştir. Sonuçlar tüm serilerin boy değişimlerinin aritmetik ortalaması alınarak hesaplanmıştır.

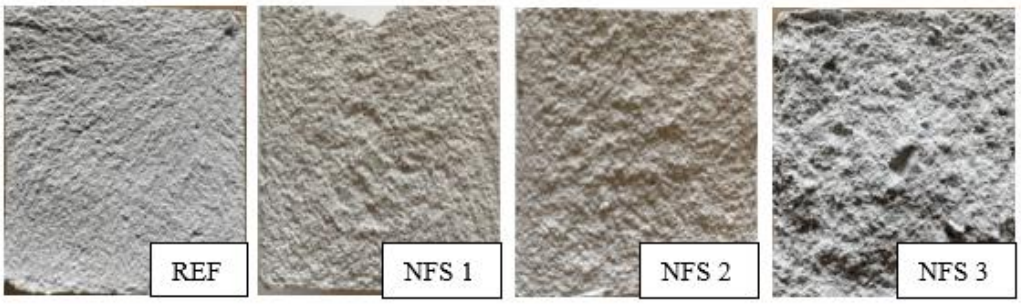


Şekil 10. Enjeksiyon malzemelerinin rötre ölçümleri

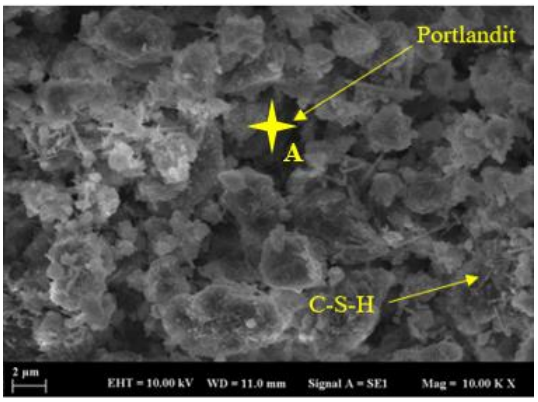
Serilerin rötre ölçümleri incelendiğinde NFS 1 ve NFS 2 serilerinde rötre oranının sırasıyla %43 ve %41 azaldığı görülmektedir. Buna karşın liflerin topaklanmasına bağlı homojen dağılımın elde edilemediği NFS 3 serisi REF serisi ile benzer rötre miktarlarında seyretmiştir. Sonuç olarak, NFS katkısı kireç esaslı enjeksiyon malzemelerinde rötreyi azaltıcı bir etkiye sahiptir. Rötre miktarının fazla olduğu enjeksiyon malzemelerinde katkı maddesi olarak tercih edilebilir [13].

Taramalı Elektron Mikroskobu (SEM-EDS) ile İçyapının İncelenmesi

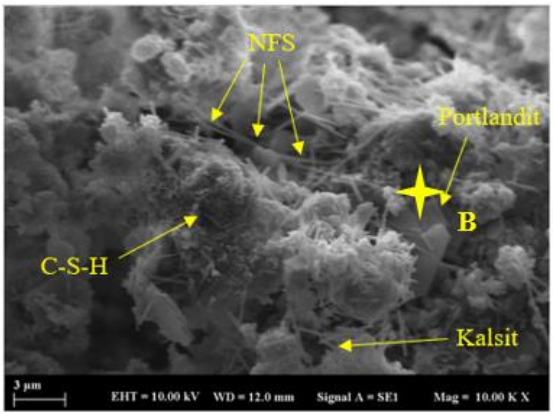
Enjeksiyon malzemelerinin 28. günde yapılan eğilme testi sonrasında numunelerin kırılma yüzeylerine ait fotoğraflar Şekil 11'de verilmiştir. Enjeksiyon malzemelerinin kesit görüntülerinde NFS liflerinin topaklanması net bir şekilde görülmektedir. REF numune pürüzsüz bir yapıya sahipken NFS katkısı ile doğru orantılı olarak topaklanmaya bağlı pürüzlülük artmaktadır. Taramalı elektron mikroskobu ile 28 günlük numunelerde yapılan SEM-EDS analizine ait görüntülerden referans numunenin iç yapı özellikleri Şekil 12'de, NFS 1'in iç yapı özellikleri Şekil 13'te, NFS 2'nin iç yapı özellikleri Şekil 14'te, NFS 3'ün iç yapı özellikleri Şekil 15'te verilmiştir.



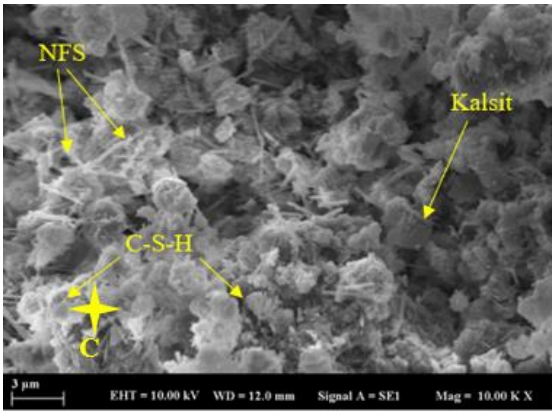
Şekil 11. Enjeksiyon malzemelerinin kesit görüntüleri



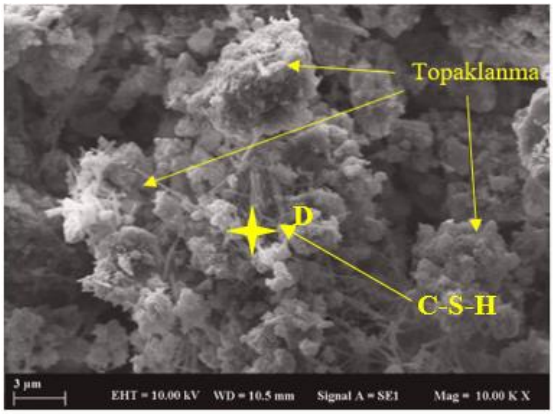
Şekil 12. REF serisinin iç yapı analizi



Şekil 13. NFS 1 serisinin iç yapı analizi



Şekil 14. NFS 2 serisinin iç yapı analizi



Şekil 15. NFS 3 serisinin iç yapı analizi

Tablo 11. SEM-EDS analizi sonuçları

Elementler	Serilere Ait Nokta/Atomik Oran (%)			
	REF (A)	NFS1 (B)	NFS2 (C)	NFS3 (D)
Ca	54.48	42.43	39.59	34.23
O	34.82	40.97	39.58	43.30
C	0.78	2.36	2.18	3.06
Si	3.41	3.54	3.51	5.80
Al	1.20	1.89	3.74	3.67

Serilerin SEM-EDS sonuçları incelendiğinde, hidratasyon tepkimeleri sonucu oluşması beklenen portlandit ($Ca(OH)_2$), kalsit ($CaCO_3$) ve C-S-H jellerinin oluştuğu gözlemlenmiştir. EDS analizleri genel olarak portlandit, kalsit ve C-S-H jellerinin bulunduğu noktalarda yapılmıştır. Görüntülere ait EDS sonuçları Tablo 11'de verilmiştir. NFS 1 serisinde liflerin homojen şekilde dağıldığı ve dikiş etkisi yoluyla yükü aktaracak köprüler kurduğu, NFS 2 serisinde liflerin oldukça yoğunlaştığı ancak homojen dağılımın devam ettiği görülmektedir. NFS 3 serisinde ise liflerin topaklanarak kümeler oluşturduğu ve homojen dağılmadığı görülmektedir. Bu durum liflerin istenildiği gibi çalışmamasına ve mekanik özelliklere etki etmemesine veya negatif etki etmesine yol açmaktadır [9],[10]. Tablo 11'de verilen EDS sonuçları incelendiğinde sonuçlar arasında tipik bir farklılık olmamakla birlikte A ve B noktalarındaki yüksek Ca miktar portlandit oluşumunu işaret etmektedir. C-S-H oluşumlarının görüldüğü noktalarda (C ve D) Ca ve O ek olarak Si ve Al elementlerinin daha yüksek olduğu görülmektedir. Artan C-S-H bileşimi miktarı mekanik özelliklerin artmasına katkı sağlamış, ancak NFS3 serisinde meydana gelen topaklanmalar nedeniyle dayanımda değerler daha düşük olarak ölçülmüştür.

4. Sonuçlar ve Tartışma

Bu çalışma kapsamında, tarihi yapıların onarımında ve güçlendirilmesinde kullanılan kireç esaslı enjeksiyon malzemelerine nanofiber selüloz katkısının etkilerini araştırmak amacı ile dört farklı enjeksiyon malzemesi geliştirilmiştir. Yapılan deneysel çalışmalarla, üretilen enjeksiyon malzemelerinin fiziksel, reolojik, mekanik özellikleri ve rötre davranışı incelenerek NFS katkısının kireç esaslı enjeksiyon malzemelerinin taze ve sertleşmiş haldeki özelliklerine etkileri belirlenmiştir. Çalışma sonunda elde edilen tüm bilgiler ışığında ulaşılan sonuçlar ve sunulan öneriler aşağıda sıralanmıştır.

- Enjeksiyon malzemelerinin taze halde sağlaması gereken üç temel özellik olan akışkanlık, penetrasyon ve hacim sabitliği limit değerleri sağlamıştır.
- NFS katkısı kullanılan hiçbir seride viskozite düzenleyici katkı maddesine ihtiyaç duyulmamıştır. Bu bakımdan NFS, hacim sabitliği özelliğini dengelemede viskozite düzenleyici kimyasal katkı maddeleri yerine tercih edilebilecek doğal bir alternatiftir. Terleme deneyi sonuçlarına bakıldığında REF serisinde %1 viskozite

düzenleyici ilavesi ile elde edilen %3,8 terleme değeri, NFS ilave serilerde viskozite düzenleyici katkı ilave edilmeden %4,5 ila %3,6 arasında ölçülmüştür. Artan NFS oranı ile REF seriden daha düşük terleme değeri elde edilmiştir. Reolojik özellikler incelendiğinde, NFS ilavesi plastik viskozite ve eşik kayma gerilmesi değerlerini düşürmektedir.

- NFS katkısının temel fiziksel özelliklere etkileri incelendiğinde kılcallıkla su emilimini düşürdüğü görülmüştür. Diğer fiziksel özelliklere belirgin bir etkisi görülmemiştir. Boşlukların büyük çoğunluğu dışa açıktır. NFS katkısının toplam boşluk miktarına belirgin bir etkisi görülmemiştir.

- Serilerin 28. ve 56. günlerinde yapılan eğilme dayanım deneyleri sonucunda NFS ilavesinin kireç esaslı enjeksiyon malzemelerinin eğilme ve basınç dayanımını artırdığı görülmüştür.

- Mekanik deney sonuçlarında dikkat edilmesi gereken bir diğer husus optimum karışım oranlarının belirlenmesidir. %0,3 oranında NFS katkısı içeren seri hem eğilme dayanımında hem de basınç dayanımında tüm serilerden daha düşük bir performans göstermiştir. Bu durum liflerin topaklanması sonucu dağılımın uniform olmamasından kaynaklanmaktadır. Bu nedenle enjeksiyon malzemesi tasarlanırken bu durum göz önünde bulundurularak optimum katkı oranına karar verilmelidir. Bu çalışma için optimum NFS katkısı %0,2 olarak belirlenmiştir.

- Kuruma rötresi ölçümleri sonucunda NFS katkılı enjeksiyon malzemelerinin katkısız olana göre daha az rötre yaptığı ortaya çıkmıştır. Topaklanma gözlenen NFS 3 serisinde ise referans seriye benzer şekilde yüksek rötre değerleri ölçülmüştür. Rötre davranışı açısından da optimum katkı oranı önem taşımaktadır.

Bütün deneysel çalışmalar sonucunda, optimum miktarda kullanılan NFS katkısının kireç esaslı enjeksiyon malzemelerinin mekanik performansını düşük oranda da olsa artırması, rötre büzülmelerinden kaynaklanan çatlaklara karşı dayanım sağlaması ve hacim sabitliği özelliğini dengelemesi gibi olumlu katkılar sunduğu görülmüştür. Küresel ısınma, iklim değişikliği ve çevre kirliliğinin büyük sorunlar oluşturduğu günümüzde biyo-esaslı, yenilenebilir ve sürdürülebilir yapı malzemeleri büyük önem taşımaktadır. Bu nedenle NFS ve diğer lifli katkı maddelerinin araştırılması, geliştirilmesi ve yapı malzemelerinde kullanımı inşaat sektörü için umut verici bir alternatif olarak değerlendirilmektedir.

NFS ilavesi ile üretilen bu kireç esaslı enjeksiyon malzemeleri, onarımı yapılacak tarihi yapının özgün malzeme özellikleri ile uyumlu olduğu sürece yapıdaki çatlakların doldurulması ve süreklilik sağlanması için kullanılabilir. Uygulamada nano malzeme kullanımına ve bu malzemenin matris içerisinde homojen olarak dağıtılmasına özen gösterilmelidir. Nano malzemelerin saha uygulamalarında pratik bir şekilde dağıtılmasının zor olması nedeni ile uygulama öncesinde gerekli konsantrasyonda su içinde dağıtılması ve stabilitesini koruyan bu karışımın yerinde kireç ile karıştırılması önerilmektedir.

Etik kurul onayı ve çıkar çatışması beyanı

"Hazırlanan makalede herhangi bir kişi/kurum ile çıkar çatışması bulunmamaktadır"

Yazar Katkıları

Makale tüm yazarlar tarafından okunarak ve onaylanarak yüklenmeli, her yazara ait katkı makalede açıkça belirtilmelidir. Yazarlar makale hazırlamada tasarım, veri toplama, verilerin analizi, revizyon gibi aşamalarda kapsamlı katkı sağlayıp makaleye son şeklini verirler. Tüm yazarlar makaleye yeterli derecede katkıda bulunmak zorundadır. Her yazarın 'Soyadını' ardına aşağıda verilen en uygun kategorilerden birini veya birkaçını ekleyerek belirtebilirsiniz:

-Çalışma konsepti ve tasarım

-Veri toplama

-Verilerin analizi ve yorumlanması

-Taslağın oluşturulması

-Revizyon

-Diğer katkılar (Yukarıda listelenen faktörlerin dışında yazar katkıları için yapılan katkı 1 cümle ile özet olarak bu başlık altında belirtilebilir.)

Teşekkür

Bu çalışmayı, FYL-2023-5642 numaralı projesi ile destekleyen Yıldız Teknik Üniversitesi Bilimsel Araştırma Projeleri Koordinatörlüğü'ne teşekkür ederiz.

Kaynaklar

[1] N. Davey, A History of Building Materials. London: Phoenix House, 1961.

[2] L. B. Sickels, "Organic Additives in Mortars," Edinburgh Architecture Research, vol. 8, pp. 7–20, 1981.

[3] Z. Ahunbay, Tarihi Çevre Koruma ve Restorasyon. İstanbul: YEM Yayın, 1999.

[4] G. Penelis, M. Karaveziroglou and J. Papayanni, "Grouts for Repairing and Strengthening Old Masonry Structures," in Structural Repair and Maintenance of Historical Buildings, C. A. Brebbia, Ed., Basel, Switzerland: Computational Mechanics Publications, 1989, pp. 79–188.

[5] L. Binda, A. Saisi and C. Tedeschi, "Compatibility of Materials Used for Repair of Masonry Buildings: Research and Applications," in Fracture and Failure of Natural Building Stones – Applications in the Restoration of Ancient Monuments. Netherlands: Springer, 2006.

[6] D. A. Lange, C. Ouyang and S. P. Shah, "Behavior of Cement Based Matrices Reinforced by Randomly Dispersed Microfibers," Advanced Cement Based Materials, vol. 3, no. 1, pp. 20–30, 1996.

[7] W. Yao, J. Li and K. Wu, "Mechanical Properties of Hybrid Fiber-Reinforced Concrete at Low Fiber Volume Fraction," Cement and Concrete Research, vol. 33, no. 1, pp. 27–30, 2003.

[8] S. Pascal, A. Alliche and P. Pilvin, "Mechanical Behaviour of Polymer Modified Mortars," Materials Science and Engineering: A, vol. 380, no. 1–2, pp. 1–8, 2004.

[9] M. L. Santarelli, F. Sbardella, M. Zuena, J. Tirillo and F. Sarsini, "Basalt Fiber Reinforced Natural Hydraulic Lime Mortars: A Potential Bio-Based Material for Restoration," Materials & Design, vol. 63, pp. 398–406, 2014.

[10] M. M. Barbero-Barrera and N. F. Medina, "The Effect of Polypropylene Fibers on Graphite-Natural Hydraulic Lime Pastes," Construction and Building Materials, vol. 184, pp. 591–601, 2018.

[11] M. Ardanuy, J. Claramunt, R. Arévalo, F. Parés, E. Aracri and T. Vidal, "Nanofibrated Cellulose (NFS) as a Potential Reinforcement for High Performance Cement Mortar Composites," BioResources, vol. 7, pp. 3883–3894, 2012.

[12] J. Goncalves, Y. Boluk and V. Bindiganavile, "Turbidity-Based Measurement of Bleeding in Fresh Cement Paste as Affected by Cellulose Nanofibres," Cement and Concrete Composites, vol. 123, Art. no. 104197, 2021.

[13] H. H. Kolour, M. Ahmed, E. Alyaseen and E. N. Landis, "An Investigation on the Effects of Cellulose Nanofibrils on the Performance of Cement Paste and Concrete," Advances in Civil Engineering Materials, vol. 7, pp. 463–478, 2018.

[14] L. G. Baltazar, F. M. A. Henriques, F. Jorne and M. T. Cidade, "The Use of Rheology in the Study of the Composition Effects on the Fresh Behaviour of Hydraulic Lime Grouts for Injection of Masonry Walls," Rheologica Acta, vol. 52, no. 2, pp. 127–138, 2013.

[15] F. Jorne, F. M. A. Henriques and L. G. Baltazar, "Evaluation of Consolidation of Grout Injection with Ultrasonic Tomography," Construction and Building Materials, vol. 66, pp. 494–506, 2014.

[16] ASTM D6910, Standard Test Method for Marsh Funnel Viscosity of Clay Construction Slurries. ASTM International, 2009.

[17] TS EN 445, Şerbet-Öngerilmeli Tendonlar İçin Deney Yöntemleri. Türk Standartları Enstitüsü, 2012.

[18] BS EN 1771, Products and Systems for the Protection and Repair of Concrete Structures – Test Methods – Determination of Injectability and Splitting Tests. British Standards Institution, 2004.

[19] ASTM C940, Standard Test Method for Expansion and Bleeding of Freshly Mixed Grouts for Preplaced-Aggregate Concrete in the Laboratory. ASTM International, 2010.

[20] TS EN 1015-11, Kâgir Harcı – Deney Metotları – Bölüm 11: Sertleşmiş Harcın Basınç ve Eğilme Dayanımının Tayini. Türk Standartları Enstitüsü, 2000.

[21] TS EN 447, Şerbet-Öngerilmeli Tendonlar İçin Temel Gerekler, Türk Standartları Enstitüsü, 2012.

[22] A. Kalagri, A. Miltiadou-Fezans, and E. Vintzileou, "Design and evaluation of hydraulic lime grouts for the strengthening of stone masonry historic structures," Materials and Structures, vol. 43, pp. 1135–1146, 2010.

[23] A. Miltiadou-Fezans, "Fluidity of hydraulic grouts for masonry strengthening," Materials and Structures, vol. 45, pp. 1817–1828, 2012.

[24] A. Bras and F. M. A. Henriques, "Natural hydraulic lime based grouts–The selection of grout injection parameters for masonry consolidation," Construction and Building Materials, vol. 26, no. 1, pp. 135–144, 2012.

[25] A. Miltiadou-Fezans and T. P. Tassios, "Stability of hydraulic grouts for masonry strengthening," Materials and Structures, vol. 46, no. 10, pp. 1633–1652, 2013.

[26] B. Dinç-Sengönül, D. Oktay and N. Yüzer, "Effect of Temperature, Resting Time and Brick Dust (Horasan) on the Rheological Properties of Hydraulic Lime-Based Grouts," Construction and Building Materials, vol. 265, Art. no. 120644, 2020.

[27] TS EN 15801, Kültürel Varlıkların Korunması – Deney Metotları – Suyun Kılcal Emiliminin Tayini. Türk Standartları Enstitüsü, 2010

Dicle University
Journal of Engineering
https://dergipark.org.tr/tr/pub/dumf
duje.dicle.edu.tr

Araştırma Makalesi / Research Article

Zayıf bir zeminin ıslahı için oluşturulan geçirimli kazıklarda farklı agrega ve bağlayıcı kullanımının etkisinin araştırılması

Investigation the effect of using different aggregates and binders in pervious piles for the soil stabilization of a weak soil

Talha Sarıcı[1*], Mustafa Özcan[2], Rüçhan Enes Korkmaz[3]

[1] İnönü Üniversitesi, İnşaat Mühendisliği Bölümü, talha.sarici@inonu.edu.tr
ORCID: https://orcid.org/0000-0001-8488-5851

[2] İnönü Üniversitesi, İnşaat Mühendisliği Bölümü, mustafa.ozcan@inonu.edu.tr
ORCID: https://orcid.org/0000-0001-5745-8694

[3] İnönü Üniversitesi, İnşaat Mühendisliği Bölümü, korkmazruchanenes@gmail.com
ORCID: https://orcid.org/0009-0008-7504-774X

MAKALE BİLGİLERİ

Makale Geçmişi:

Geliş 21 Mayıs 2025
Revizyon 17 Haziran 2025
Kabul 29 Haziran 2025
Online 30 Eylül 2025

Anahtar Kelimeler:

Zemin Islahı, Geçirimli beton kazık, Geçirimli geopolimer kazık, İnşaat ve Yıkıntı Atığı, Uçucu kül, Yüksek fırın cürufu.

ÖZ

Bu çalışma kapsamında doğal ve inşaat yıkıntı atığından elde edilen agrega kullanılarak oluşturulan geçirimli kazıkların davranışını araştırmak üzere deneysel çalışmalar gerçekleştirilmiştir. Bu çalışma kapsamında geçirimli beton kazık için geleneksel çimento kullanılırken geçirimli geopolimer kazık oluşturmak için alkali aktivatör ile uçucu kül ve yüksek fırın cürufu kullanılarak geopolimer hamuru elde edilmiştir. Deneysel çalışmaların ilk aşamasında, oluşturulan geçirimli kazıkların basınç dayanımları belirlenmiş, su emme kapasiteleri ve ultrasonik darbe hızları ölçülmüştür. Daha sonrasında, kazıklar, zayıf bir zemine yerleştirilerek yük-deformasyon davranışları araştırılmıştır. Çalışma kapsamında elde edilen sonuçlar değerlendirildiğinde, geçirimli beton ve geopolimer kazıkların güçlendirilmemiş zeminin taşıma gücünü önemli ölçüde arttırdığı bulunmuştur. Güçlendirilmemiş zemin ile kıyaslandığında, doğal agrega kullanımında geçirimli geopolimer kazık ile 3 kat; inşaat yıkıntı atığı agrega kullanımında ise geçirimli beton kazık ile 2 kat daha fazla taşıma kapasitesi elde edilmiştir. İnşaat yıkıntı atığı agregaları su emme kapasitesini arttırırken, doğal agrega kullanımı ultrasonik darbe hızını arttırmıştır. Taşıma kapasitesi ihtiyacı daha düşük projelerde, inşaat yıkıntı atığı agregaları ile geçirimli geopolimer kazıkların kullanılması, molozların ve üretim atığı olan öncülerin değerlendirilmesini sağlayabilecektir. Özellikle afet sonrası ortaya çıkan atıkların dönüştürülmesi/değerlendirilmesi bölgenin dönüşümü ve insanların sağlığı için hayati önem taşımaktadır.

ARTICLE INFO

Article history:

Received 21 May 2025
Received in revised form 17 June 2025
Accepted 29 June 2025
Available online 30 September 2025

Keywords:

Soil stabilization, Pervious concrete piles, Pervious geopolymer piles, Construction and demolition waste, Fly ash, Blast furnace slag

Doi: 10.24012/dumf.1702843

* Sorumlu Yazar

ABSTRACT

Within the scope of this study, experimental studies were carried out to investigate the behavior of pervious piles using natural aggregate and construction demolition waste aggregate. In this study, geopolymer paste was obtained by using fly ash and blast furnace slag with alkali activator to form pervious geopolymer piles while using traditional cement for pervious concrete piles. In the first stage of the experimental studies, the compressive strengths of the pervious piles were determined, water absorption capacities and ultrasonic impact velocities were measured. Then, the piles were placed in a weak soil and their load-deformation behavior was investigated. When the results obtained within the scope of the study were evaluated, it was found that pervious concrete and geopolymer piles significantly increased the bearing capacity of the unreinforced soil. Compared to the unreinforced soil, 3 times more bearing capacity was obtained with pervious geopolymer piles when using natural aggregates and 2 times more bearing capacity was obtained with pervious concrete piles when using construction demolition waste aggregates. Construction demolition waste aggregates increased the water absorption capacity, while the use of natural aggregates increased the ultrasonic pulse velocity. In projects with lower bearing capacity requirements, the usage of pervious geopolymer piles with construction demolition waste aggregates may provide the utilization of rubble and production waste precursors. The transformation/recycling of post-disaster wastes is vital for the regeneration of the region and the public health.

Giriş

Yapılaşma süreçlerinde inşaat çalışmalarına başlamadan önce yapının oturacağı zemin ile ilgili gerekli araştırmaları yapmak yapı sağlığı ve sürdürülebilirliği için oldukça önemlidir [1]. Temel zemininin yapılaşma için yeterli mühendislik özelliklerine sahip olmaması durumunda (farklı oturmalar, yetersiz taşıma gücü, sıvılaşma potansiyelleri vb.) farklı uygulamalar ile temel zeminin özelliklerinin iyileştirilmesi gerekmektedir [2]. Bu iyileştirme uygulamaları arasında son zamanlarda popülerliği artan geçirimli kazık kullanımı ile kazık elemanların suya maruz kaldığı ortamlarda suyun farklı noktalara tahliyesi sağlanarak, su etkisinin, konsolidasyon miktarının ve sıvılaşma potansiyellerinin engellenmesi mümkün olmaktadır [3]. Geçirimli kazıklar geleneksel granüler kolonlara oranla 4.4 kat daha fazla taşıma kapasitesine ulaşabilmektedir [4]. Geçirimli kazıkların davranışının esnek kazıklar gibi olduğu ve bu sebeple geçirgenlik artarken stabilitenin korunabildiği belirtilmiştir [5]. Öyle ki, yüksek taşıma kapasitesiyle beraber geçirimlilik özelliğinin korunmasının özellikle konsolidasyon zamanını azalttığını ve bununla beraber kumlu zeminlerde siltli zeminlere nazaran daha yüksek taşıma kapasitesinin elde edilebildiği bulunmuştur [6]. Uygulamalarda yaygın olarak beton içerikli kazıklar kullanılıyor olsa dahi, sanayi üretim atığı olan uçucu kül (UK) ve yüksek fırın cürufu (YFC) gibi bağlayıcılar ile alkali aktivatörlü karışımlar kullanılarak geopolimer yapılar oluşturulabilmektedir [7-10]. Oluşturulan geopolimer yapıların çimento kullanımına oranla daha ekonomik ve çevre dostu olduğu yapılan çalışmalar ile ortaya konulmuştur [11-12]. Ayrıca, doğal agrega yerine inşaat yıkıntı atığı (İYA) kullanılarak elde edilen agregalar ile oluşturulacak geopolimerler sayesinde özellikle afetler sonrasında ortaya çıkan moloz atığının dönüştürülmesi ve zemin iyileştirme uygulamalarında kullanılabilmesi mümkün olmaktadır [13-15]. Öyle ki, geri dönüştürülmüş agregalardan elde edilen geçirimli kazıkların sıvılaşmaya karşı oldukça başarılı olduğu yapılan çalışmalar ile ortaya konulmuştur [16]. Ayrıca, uzun vadeli olarak İYA depolanması, afetlerin büyüklüğüne göre çok güç olmakta ve depolama süresi boyunca hem hava kalitesini hem de yer altı su kaynaklarının kalitesini doğrudan tehdit edebilmektedir. 6 Şubat 2023 tarihinde gerçekleşen Kahramanmaraş deprem sekansı nedeniyle 580 milyon ton inşaat yıkıntı atığı (İYA) oluşacağının öngörüldüğü göz önünde bulundurulduğunda [17], inşaat yıkıntı atığının farklı alanlarda değerlendirilmesi hayati önem taşımaktadır. İYA içeriklerinin ve türlerinin çeşitli olması farklı alanlarda iyileştirmelerin önünü açmaktadır. Öyle ki, tuğla duvar İYA ile kohezyonlu zeminin karıştırılması ile Kaliforniya taşıma gücü oranı (CBR) değerinde %260'a varan artış elde edilebilmektedir [18]. Bununla beraber, alkali aktivatör, yüksek fırın cürufu ve İYA kullanımı ile güçlendirilmemiş dolgu zeminin taşıma gücü değeri 4.72 kata kadar arttırılabilmektedir [19]. İYA dönüşümleri büyük inşaat yapılarında kullanılabildiği gibi, yaya yolları gibi spesifik ve küçük projelerde de kullanılabilmektedir [20]. Dolayısıyla, küçük ve/veya büyük ölçekli projelerde İYA kullanımı ile geri dönüşümün önemli ölçüde gerçekleştirilebileceği düşünülmektedir.

Bu çalışma kapsamında zayıf bir zeminin ıslahında farklı bağlayıcı (uçucu kül, yüksek fırın cürufu ve çimento) ve agrega (doğal ve inşaat yıkıntı atığından elde edilen agrega) içeriğine sahip geçirimli kazıkların kullanılabilirliğini araştırmak üzere deneysel çalışmalar gerçekleştirilmiştir. Üretilen farklı geçirimli kazıklar üzerinde serbest basınç deneyleri gerçekleştirilmiş ve basınç dayanımları araştırılmıştır. Ayrıca ultrasonik darbe hızı testi ve su emme deneyleri ile kazıkların su emme kapasiteleri ve ultrasonik darbe hızları ölçülmüştür. Sonraki aşamada kohezyonsuz zayıf zemin içerisine yerleştirilen kazıklar ile model yükleme deneyleri gerçekleştirilmiştir. Böylelikle geçirimli kazıkların düşey yükler altında güçlendirilmemiş zeminin taşıma kapasitesine nasıl etki ettiği araştırılmıştır. Daha önceki çalışmalar değerlendirildiğinde geçirimli kazıklar İYA agregalarının ve geopolimer kullanımının yeteri kadar irdelenmediği görülmüştür. Özellikle afetler sonrasında oluşan molozların tekrar değerlendirilmesinin hayati önem taşıması ve çimento endüstrisinin faaliyetlerinin çevresel zararının yüksek olması nedeniyle çevreci çözümlerin bulunması gerekmektedir. Bu bağlamda çalışma kapsamında farklı bağlayıcı ve agregaların kullanılması ile elde edilen sonuçların, geopolimer ve İYA agregalı kazıkların kullanılabilirliği için fikir verici olacağı ve tercih edilebilirliğini arttırabileceği düşünülmektedir.

Materyal ve metot

Deneysel çalışmalarda kazık üretiminde kullanılmak üzere temin edilen ve molozlardan geri dönüştürülen agregaların tane boyutu 2.36 mm ve 4.75 mm aralığına seçilmiştir. Doğal agregalar Malatya'da faaliyet gösteren bir taş ocağından, inşaat yıkıntı atığı ise Osmaniye ili Düziçi ilçesinde daha önceden faaliyet gösteren İl Özel İdaresi Binasının yıkılması sonrası oluşan molozdan temin edilmiştir [21]. Doğal agrega ve İYA'ya ait özellikler Tablo 1'de verilmiştir.

Tablo 1. Doğal agrega (DA), İYA agrega [21] ve kohezyonsuz zemine [9] ait özellikler

Özellikler	Birimler	İYA	DA	Zemin (SP)	Standard
Uniformluk Katsayısı (C_u)	-	20.00	19.8	2.375	[22]
Eğrilik Katsayısı (C_c)	-	1.12	1.26	0.926	[22]
Yassılık İndeksi	%	11.14	13.99	-	[23]
Los Angeles Aşınma Kaybı	%	32.38	25.25	-	[24]
Özgül Ağırlık (G_s)	-	2.62^{f}-2.62^{c}	2.71^{f}-2.72^{c}	2.74	[25]
Su Emmesi	%	6.91^{f}-3.94^{c}	0.89^{f}-0.68^{c}	-	[26]
Maksimum Kuru Birim Ağırlık (γ_{kmaks})	kN/m^3	19.79	22.00	16.5	[27]
Optimum Su Muhtevası (ω_{opt})	%	11.25	6.10	-	[28]

f: İnce Kısım, c: İri Kısım

Çalışma kapsamında bağlayıcı olarak çimento bazlı karışımlarda CEM II tip çimento ve geopolimer karışımlarında F sınıfı UK, YFC ve kütlece yarı yarıya YFC ile UK karıştırılarak dört farklı bağlayıcı kullanılmıştır. Çimento hamuru TS EN 197-5 standartlarında üretilen CEM II tip çimento ile oluşturulmuştur ve kütlece su/çimento oranı 0.55 olarak belirlenmiştir. Özellikleri Tablo 2'de gösterilen UK ve YFC ile oluşturulan geopolimer hamur için alkali aktivatörlü çözelti olarak 8 M NaOH çözeltisi (320 gram katı NaOH ile 1 litrelik su çözeltisi) kullanılmıştır.

Tablo 2. Geopolimer hamur için kullanılan bağlayıcıların özellikleri [21]

Bileşen	Birim	Uçucu Küle ait Değer	Yüksek Fırın Cürufuna ait Değer
SiO_2	%	63.09	32.47
Al_2O_3	%	3.74	9.94
Fe_2O_3	%	6.11	1.25
CaO	%	6.75	32.45
SrO	%	0.2	-
MgO	%	10.53	9.31
SO_3	%	0.63	0.82
K_2O	%	5.63	0.85
P_2O_5	%	1.43	-
TiO_2	%	1.62	1.16
S^{-2}	%	-	0.33
Na_2O	%	-	0.31
Mn_2O_3	%	-	3.51
CL^-	%	-	0.015
Kızdırma kaybı	%	2.6	-

Alkali aktivatörlü çözelti/bağlayıcı oranı 0.65 olarak belirlenmiştir. Deneylerde kullanılan sodyum hidroksitin özellikleri ise Tablo 3'te görülmektedir. Çalışma kapsamında kullanılacak bütün kazıklar eşit boy (10 cm) ve çapta (4.5 cm), Tablo 4'te verilen karışım oranları ile üretilmiştir. Çalışma kapsamında %20 boşluk oranına sahip 8 farklı geçirimli kazık (Tablo 4) verilen karışım oranları ile (Tablo 5) üretilmiştir. Örnek hamur ve kazık görseli Şekil 1'de görülmektedir.

Tablo 3. Sodyum hidroksite ait özellikler [29]

Fiziksel ve Kimyasal Özellikler	Değer
Molekül formülü	*NaOH*
Molekül kütlesi (g/mol)	40
Renk	Beyaz
pH	13-14
Bağıl yoğunluk (g/cm^3)	2.13

Tablo 4. Çalışma kapsamında kullanılan farklı türdeki kazıklar

Kazık Adı	Bağlayıcı	Agrega
NPCC	Çimento	Doğal Agraga
NPCF	UK	Doğal Agraga
NPCB	YFC	Doğal Agrega
NPCBF	YFC+UK	Doğal Agrega
WPCC	Çimento	İnşaat Yıkıntı Atığı
WPCF	UK	İnşaat Yıkıntı Atığı
WPCB	YFC	İnşaat Yıkıntı Atığı
WPCBF	YFC+UK	İnşaat Yıkıntı Atığı

Tablo 5. Kazıklar için kullanılan karışım oranları

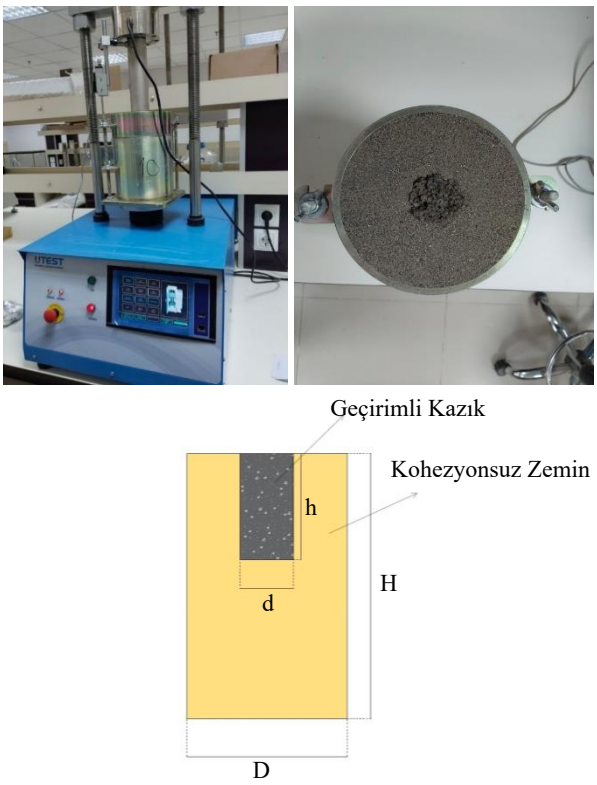
Kazık Adı	a	b	c	d	e	f
NPCC	20%	0.55	39.76	231.70	21.86	-
NPCF	20%	0.55	39.76	231.70	-	21.86
NPCB	20%	0.55	39.76	231.70	-	21.86
NPCBF	20%	0.55	39.76	231.70	-	21.86
WPCC	20%	0.65	39.76	134.36	25.84	-
WPCF	20%	0.65	39.76	134.36	-	25.84
WPCB	20%	0.65	39.76	134.36	-	25.84
WPCBF	20%	0.65	39.76	134.36	-	25.84

Burada; a boşluk oranı, b su-alkali sıvı/bağlayıcı oranı, c bağlayıcı kütlesi (g), d agrega kütlesi (g), e su kütlesi, f alkali çözelti (g)

Kazıklar için oluşturulan hamur derin kapta karıştırılarak oluşturulmuş ve belirlenen oranlarda kalıplara yerleştirilerek priz almaya bırakılmıştır. İYA ile oluşturulan karışımlar yapısı itibariyle doğal agregaya oranla kendi üzerine daha fazla su emdiği için işlenebilirliğin önemli ölçüde düştüğü gözlemlenmiştir. Ayrıca İYA içeriğine ve karışım maruz kaldığı İYA kompozisyonuna bağlı olarak oluşturulan hamurun kendi içinde de farklı yapılarda olduğu gözlemlenmiştir. Ayrıca İYA'yı doygun yüzey kuru duruma getirmek içerdiği çeşitli maddeler nedeniyle de oldukça zordur. Bu da karışım suyunun hamur içinde tutulmasını zorlaştırmaktadır. Bu yüzden deneme-yanılma yolu ile en işlenebilir su-alkali sıvı/bağlayıcı oranı belirlenmiştir. 24 saat geçtikten sonra kazıklar kalıplardan çıkarılmıştır. Öncelikle üretilen kazıklar ile serbest basınç deneyleri gerçekleştirilmiş ve farklı tip kazıkların dayanımları yorumlanmıştır. Daha sonrasında imal edilen kazıklar yapılaşma bulunmayan bir bölgeden temin edilen kohezyonsuz zemin ile oluşturulan zayıf zemin ortamına yerleştirilmiştir. Kohezyonsuz zemin Birleşik Zemin Sınıflandırma Sistemi'ne [31] göre SP olarak sınıflandırılmış ve zayıf zemin ortamı oluşturmak için rölatif sıkılık (D_r) 10% olacak şekilde yerleşimi yağmurlama yöntemi ile yapılmıştır. Sonrasında kazıklar üzerine 5 cm çapında dairesel rijit temel yerleştirilmiş ve temel üzerine yük uygulanarak model yükleme deneyleri gerçekleştirilmiştir (Şekil 2). Burada; H zemin derinliği, h kazık boyu, d kazık çapı, D zemin ortamının çapını ifade etmektedir. Model yükleme deneylerinde yükleme hızı 1.27 mm/dk olarak belirlenmiş ve yükleme pistonu kazık merkezine gelecek şekilde yükleme yapılmıştır. Her kazık türü için 4 adet numune oluşturulmuş, kuru kür seçilmiş ve oluşturulan kazıklardan yüke maruz kalmamış numuneler ile ultrasonik darbe hızı testi (UPV) ve su emme deneyleri gerçekleştirilmiştir. UPV deney cihazı numunenin vericiden çıkan ses dalgasının numuneden geçerek alıcıya ulaşma süresini, numune boyunu da değerlendirerek hesaplamaktadır. Böylelikle malzemenin bütünlüğü/boşluk durumuna bağlı olarak ses hızlarındaki değişimler kaydedilebilmektedir ve ilgi standarda göre gerçekleştirilmiştir [30]. Su emme deneylerinde ise etüvde kurutulmuş, kuru hali tartılmış numunelerin yanal yüzeyleri kaplanmış ve numunelerin yalnızca alt yüzeyi su yüzeyine temas edecek şekilde yerleştirilmiştir. 24 saat geçtikten sonra kazıklar tekrar tartılarak su içeriği nedeniyle oluşan kütle artışı ile emilen su miktarı hesaplanabilmektedir.



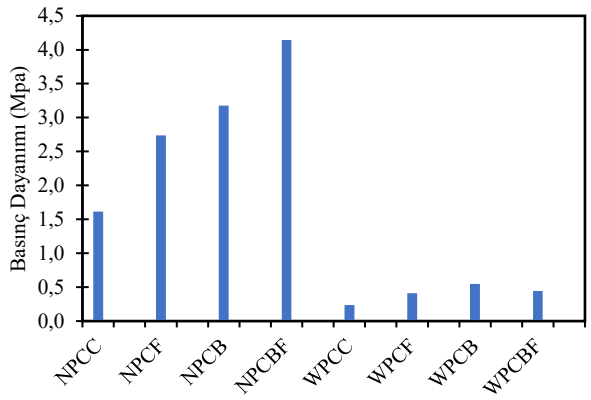
Şekil 1. Karışım hamuru ve geçirimli kazık görselleri



Şekil 2. Model yükleme deney seti, sırasıyla, kazık yerleştirilmiş zayıf zemin ortamı, model yükleme deney cihazı, şematik gösterim

Bulgular ve tartışma

İlk aşamada farklı kazıkların basınç dayanımı değerlerini elde etmek üzere 7 günlük kür süresi sonunda geçirimli kazık numuneleri üzerinde basınç dayanım testleri gerçekleştirilmiştir ve elde edilen sonuçlar Şekil 3'te verilmiştir.



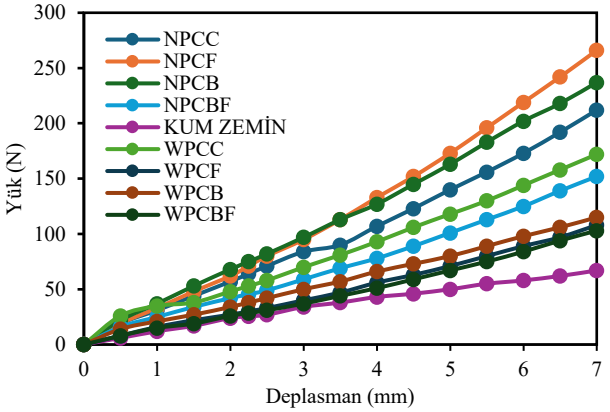
Şekil 3. 7 günlük kür süresinin sonunda geçirimli kazık numunelerin basınç dayanımı sonuçları

Şekil 3 incelendiğinde, NPCBF'nin (doğal agrega ve %50 YFC ve %50 UK kullanılarak hazırlanan bağlayıcı ile imal edilen kazık) en yüksek 7 günlük basınç dayanımına (4.143 MPa) ulaştığı görülmüştür. Her iki agrega tipinde de UK ve YFC'nin bağlayıcı olarak kullanıldığı geopolimer kazıklarda, çimentoya oranla, daha yüksek basınç dayanım değerlerine ulaşılmıştır. Bunun nedeninin, uçucu kül daha geç reaksiyona girerken, yüksek fırın cürufunun hızlı reaksiyona girmesi ve dolaysısıyla hem erken hem de geç dönemde reaksiyonların devam etmesine neden olması ve iki farklı bağlayıcının CSH jel oluşumunu arttırması vasıtasıyla daha yoğun bir matris elde edilebilmesi olduğu düşünülmektedir. Bununla birlikte en düşük basınç dayanımı sonucu ise 0.234 MPa ile WPCC'ye (atık malzeme ve çimento bağlayıcılı kazık) aittir. İYA ile oluşturulan beton kazık numunelerinin basınç dayanımının daha düşük olduğu görülmektedir. İYA karışımlarında agreganın yapısı itibariyle daha fazla su emmesi nedeniyle, geopolimer yapının oluşmasında rol alacak sıvı miktarını eksilmesine ve daha az sıvının bağlayıcı ile etkileşime girmesine sebep olduğu düşünülmektedir. Ayrıca İYA'nın dane dayanımının doğal agregalardan daha düşük olmasının da [21] bu davranışının nedenlerinden biri olduğu düşünülmektedir.

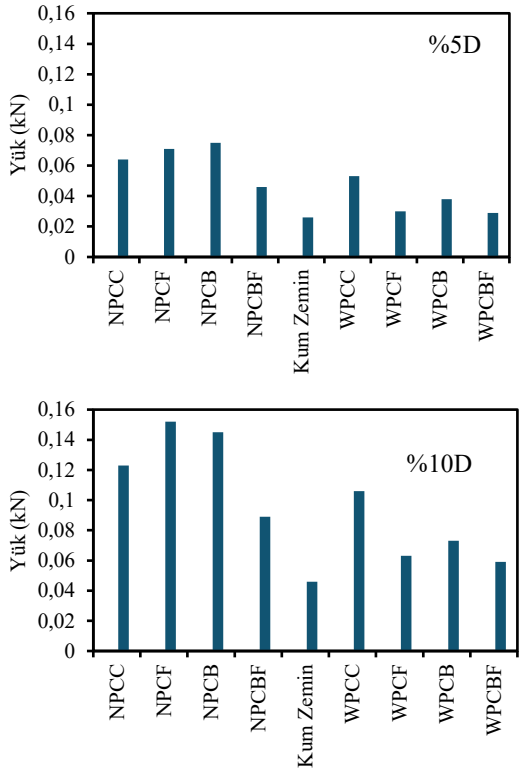
Sonraki aşamada kohezyonsuz zayıf zemine yerleştirilen geçirimli kazıkların yük altındaki davranışını araştırmak üzere model yükleme deney seti ile deneysel analizler gerçekleştirilmiştir. Her deneyde kazıkların üzerinde dairesel model rijit temel yerleştirilmiş ve yük temel üzerine uygulanmıştır. Kazıklar ve model temel, deney tankının merkezine konumlandırılmıştır. Model yükleme deneylerine ait yük deplasman eğrileri Şekil 4'te verilmiştir. Kazıkların yük-deplasman davranışının değerlendirilmesi için göçme yükü değerleri yük-deplasman eğrisinde kazık çapının (D) %5 ve %10'una denk gelen deplasmana karşılık gelen yük değeri olarak seçilmiştir [2,9,32] ve Şekil 5'te görülmektedir.

Şekil 4-5 değerlendirildiğinde, geçirimli kazıkların güçlendirilmemiş kohezyonsuz zeminin yük altındaki davranışını önemli ölçüde iyileştirdiği görülmektedir. NPCF kullanımında 0.1D deplasmana karşılık gelen yük değerleri değerlendirildiğinde, güçlendirilmemiş zeminin 3.30 katı yük değerleri ölçülmüştür. Aynı bağlayıcıya sahip kazıklardan doğal agrega ile oluşturulan kazıkların İYA ile oluşturulan kazıklara oranla daha yüksek sonuçlar verdiği görülmektedir.

Bunun nedeninin yük altında yanal sınırlamanın kohezyonsuz zeminin gevşek olması nedeniyle düşük olması, İYA agregaların doğal agregalara oranla daha zayıf yapıda olması olduğu düşünülmektedir. Öyle ki, doğal agregalar yapısı daha fazla yük karşılayabilirken, İYA agregalar daha düşük yüklerde bile deforme olabilmektedir.



Şekil 4. Model yükleme deneylerine ait yük-deplasman eğrileri



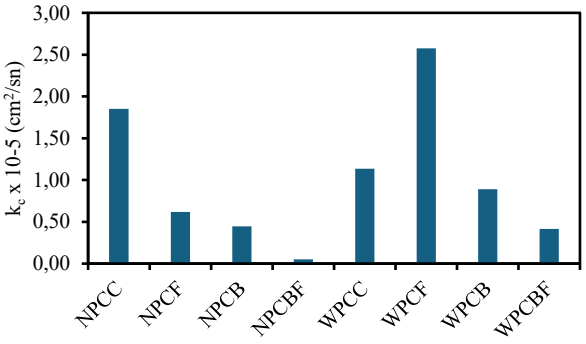
Şekil 5. %5D ve %10D deplasmana karşılık gelen göçme yükü değerleri

Şekil 5 değerlendirildiğinde, normal agrega kullanımı ile güçlendirilmemiş zemine oranla NPCC, NPCF, NPCB ve NPCBF için sırasıyla 2.67, 3.30, 3.17 ve 1.93 katı kadar göçme yükü elde edilmiştir. İYA kullanımında ise, güçlendirilmemiş zemine oranla, WPCC, WPCF, WPCB ve WPCBF için sırasıyla, 2.30, 1.37, 1.58 ve 1.28 katı kadar göçme yükü elde edilebilmiştir. Doğal agrega yapısı itibariyle İYA'ya kıyasla daha homojen ve rijit yapıdadır. Dolayısıyla doğal agrega ile hazırlanan numunelerde daha yüksek göçme yükleri elde edilmiştir. Öyle ki %5 D deplasman değeri için en yüksek değeri NPCB verirken %10 D için NPCF ile en yüksek göçme yükü elde edilmiştir. Her iki deplasman değeri için de NPCB ve NPCF değeri birbirine oldukça yakındır. Ayrıca, geçirimli geopolimer kazıkların geçirimli beton kazıklardan daha yüksek taşıma güçlerine ulaşmasının, geopolimerizasyon sürecinde bağlayıcıların daha yoğun matrisler oluşturmasından kaynaklandığı düşünülmektedir. Ancak, doğal agrega kullanımında İYA kullanımına oranla daha yüksek değerler elde edilse dahi, İYA kullanımı da güçlendirilmemiş zeminin göçme kapasitesini önemli ölçüde arttırmaktadır.

Daha sonra, geçirimli kazıkların geçirimlilik katsayısını belirlemek üzere su emme deneyleri gerçekleştirilmiştir. Su emme katsayısı (k_c) Bağıntı 1 ile hesaplanmıştır. Hesaplanan değerler Şekil 6'da görülmektedir.

$$k_c = \left(\frac{Q}{A}\right)^2 \times \frac{1}{t} \quad (1)$$

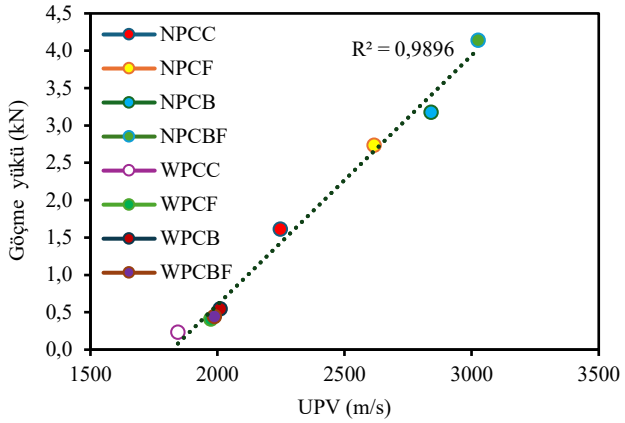
Burada; k_c: Kapiler su emme katsayısı (cm^2/s), Q: t süresi boyunca emilen su miktarı (cm^3), A: Su ile temas eden yüzey alanı (cm^2), t: Geçen süre (s).



Şekil 6. Farklı geçirimli kazıklara ait k_c değerleri

Şekil 6 incelendiğinde, İYA ile imal edilen kazıkların DA ile imal edilen kazıklara nispeten daha fazla su emdikleri görülmüş olup en yüksek kılcal su emme katsayısına sahip kazığın WPCF olduğu görülmektedir. İYA agregalarının homojen yapıda olmaması, İYA danelerinin daha fazla su emme potansiyelinin olması (Tablo 1) ve daha boşluklu olması nedeniyle daha fazla su emdiği düşünülmektedir.

Farklı içeriklerde oluşturulmuş kazıkların sürekliliklerini değerlendirmek üzere UPV deneyleri gerçekleştirilmiştir. Elde edilen darbe hızı deneyleri ve kazıkların göçme yükleri birlikte değerlendirilmiş ve Şekil 7'de verilmiştir. UPV deneylerinde en yüksek hız değeri NPCBF ile elde edilmiş ve basınç dayanımı değerleri de göz önünde bulundurulduğunda yüksek dalga hızına sahip elemanların yüklere karşı da daha dayanıklı olabileceği düşünülmektedir. Bu bağlamda, elde edilen sonuçlar değerlendirildiğinde boşluk miktarı arttıkça UPV değerlerinin azalmakta olduğu ve boşluk miktarı nedeniyle basınç dayanımlarının da aynı şekilde düşüş yaşadığı görülebilmektedir. Noktalar arasında çizilen eğilim çizgisinin R^2 değeri (0.9896) 1'e çok yakın olup, UPV değerleri ve basınç dayanımlarındaki değişimin tutarlı olduğunu göstermektedir.

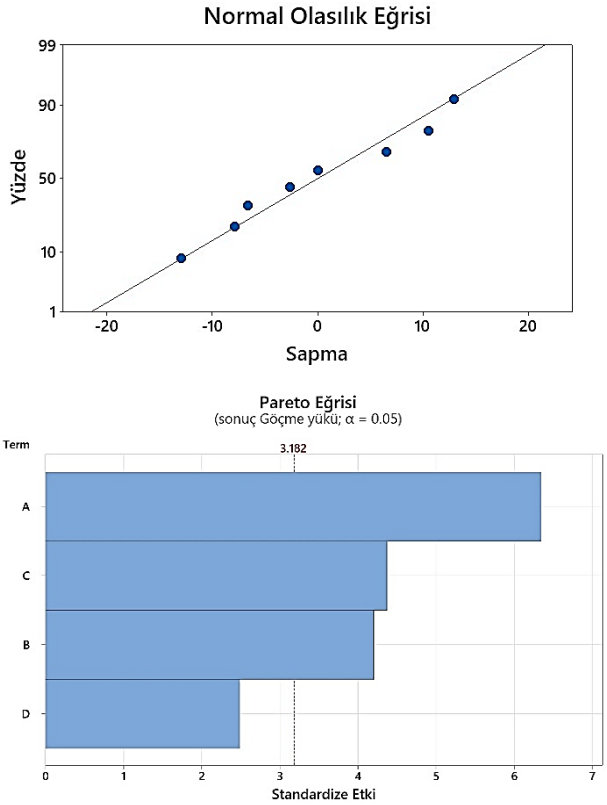


Şekil 7. Farklı geçirimli kazıkların göçme yükü ve ultrasonik darbe hızı değerleri

Farklı parametrelerin göçme yükü üzerindeki etkisini daha detaylı incelemek üzere multi-lineer regresyon gerçekleştirilmiştir. Regresyona ait normal olasılık eğrisi ve Pareto grafiği Şekil 7'de görülmektedir. Gerçekleştirilen regresyona ait R^2 değeri 0.9347 bulunmuş ve regresyon denklemi Denklem 2'de verilmiştir.

$$Göçme\ yükü = 145.2 + 30.84\ A - 88.2\ B - 95.7\ C + 59.2D \quad (2)$$

Burada; A: Basınç dayanımı; B: Uçucu kül varlığı; C:Yüksek fırın cürufu varlığı; D: Çimento varlığını ifade etmektedir.



Şekil 7. Regresyona ait normal olasılık eğrisi ve Pareto grafiği

Regresyon denklemi değerlendirildiğinde, göçme yükü üzerinde en fazla etki katsayısının basınç dayanıma ait olduğu görülmektedir. Bu etkiyi uçucu kül ve yüksek fırın cürufu varlığı takip etmektedir.

Sonuçlar

Bu çalışma kapsamında kohezyonsuz zayıf zemin içerisine yerleştirilen farklı özelliklerdeki geçirimli kazıkların basınç dayanımları, zayıf zemin içerisindeki yük-deformasyon davranışları, su emme katsayıları ve ultrasonik darbe hızlarını belirlemek üzere deneysel çalışmalar gerçekleştirilmiştir. Oluşturulan kazıklarda doğal agrega ve inşaat yıkıntı atıklarından elde edilen agregalar kullanılarak farklı karışımlar oluşturulmuştur. Bununla beraber, bağlayıcı olarak çimento, uçucu kül, yüksek fırın cürufu kullanılmıştır. Uçucu kül ve yüksek fırın cürufu uygulamalarında alkali aktivatör çözeltisi ile geopolimer bir yapı oluşturulmuştur. Farklı özelliklerdeki geçirimli kazıklar üzerinde gerçekleştirilen deneylerin sonuçları değerlendirildiğinde şu sonuçlar elde edilmiştir:

1. Geçirimli kazık uygulaması ile kohezyonsuz zeminin taşıma kapasitesi önemli ölçüde arttırılabilmiştir. Bu bağlamda geçirimli kazıkların oturma miktarlarını azaltabilmesi, sıvılaşma potansiyellerini engelleyebilmesi ve taşıma kapasitesini arttırabilmesi gibi avantajları sayesinde, derin temel çözümlerinde kullanılabileceği düşünülmektedir.

2. Doğal agrega ile oluşturulan geçirimli kazıkların yük altındaki davranışının İYA agregalarına oranla daha yüksek olduğu görülmüştür. Doğal agrega homojen bir yapıdayken, İYA agregalar heterojen ve daha zayıf bir dane yapısını sahiptir. Bununla beraber, farklı agregaların farklı su tutma kapasitelerine sahip olması ve karışım su oranları etkilemesi nedeniyle etkileşime giren bağlayıcı miktarlarının önemli ölçüde değiştiği düşünülmektedir. Yine su emme deneylerinden de görüleceği üzere, İYA agrega içerikli karışımların su emme miktarları doğal agrega kullanımına göre daha yüksektir. Ancak, UK ve YFC'nin yarı yarıya kullanımı ile oluşturulan kazıkların ise en düşük emilimi sağladığı görülmüştür. Bunun nedeninin UK+YFC kullanımın daha yoğun bir matris oluşturması olduğu düşünülmektedir.

3. Göçme yükleri karşılaştırıldığında, normal agrega kullanımı ile güçlendirilmemiş zemine kıyasla 3.30 kata ve İYA kullanımında ise 2.30 kata varan göçme yükü elde edilmiştir. Bu bağlamda geçirimli kazık uygulamalarında hem İYA kullanımı hem de doğal agrega kullanımı için önemli derece iyileştirme elde edilebileceği görülmektedir. Elde edilen iyileşme miktarının da bağlayıcı ve agrega türü ile doğrudan ilişkili olduğu da çalışma kapsamında elde edilen sonuçlardan görülmektedir.

4. Geopolimer hamur ile oluşturulan geçirimli kazıkların performansının çimento hamuru ile oluşturulan kazıklara oldukça yakın ve yer yer daha iyi olduğu görülmüştür. Bu bağlamda çimento kullanımının azaltılması ile hem geopolimer içeriğinde kullanılan atıklar ile hem de çimento endüstrisinin çevresel zararının azaltılması ile daha sürdürülebilir sistemler oluşturulabileceği düşünülmektedir. Daha düşük dayanım gereksinimli projelerde İYA tercih edilerek, afetler sonrasında oluşan molozların değerlendirilmesi sağlanabilecektir.

Sınırlamalar

Bu çalışma kapsamında elde edilen sonuçlar özellikleri çalışmada verilen doğal agrega, inşaat yıkıntı atığı, kohezyonsuz zemine has olup tasarımda tek başına kullanılamaz. Çalışmada kazıklar basınç yüküne maruz bırakılmıştır ve deney tankı tarafından zemin çevresi sınırlandırılmıştır. Alkali aktivatörlü karışımın içeriğindeki bileşenlerin özellikleri yine önceki bölümlerde açıklanmış olup elde edilen sonuçlar bu karışım yöntem ve bileşenleri için geçerlidir. Her inşaat mühendisliği projesi için projeye has analizler ilgili yönetmelik ve yönergeler uyarınca gerçekleştirilmelidir.

Etik kurul onayı ve çıkar çatışması beyanı

Hazırlanan makalede etik kurul izni alınmasına gerek yoktur. Hazırlanan makalede herhangi bir kişi/kurum ile çıkar çatışması bulunmamaktadır.

Yazar Katkıları

Sarıcı: Yazım- gözden geçirme ve düzenleme, Yazım-orijinal taslak, Doğrulama, Denetim, Yazılım, Kaynaklar, Proje yönetimi, Metodoloji, Araştırma.

Özcan: Yazım- gözden geçirme ve düzenleme, Metodoloji, Biçimsel analiz.

Korkmaz: Doğrulama, Metodoloji, Araştırma

Kaynaklar

[1] T. Sarici and R. T. Ozcan, “Interpretation of geotechnical risk maps for Malatya province in terms of earthquake sequence on February 6, 2023,” *Environ. Earth Sci.*, vol. 84, no. 3, p. 91, 2025.

[2] A. Demir and B. Ok, “Uplift response of multi-plate helical anchors in cohesive soil,” *Geomech. Eng.*, vol. 8, no. 4, 2015.

[3] R. S. V. Rashma, B. R. Jayalekshmi, and R. Shivashankar, “Liquefaction mitigation potential of improved ground using pervious concrete columns,” *Indian Geotech. J.*, vol. 52, no. 1, pp. 205–226, 2022.

[4] M. T. Suleiman, L. Ni, and A. Raich, “Development of pervious concrete pile ground-improvement alternative and behavior under vertical loading,” *J. Geotech. Geoenviron. Eng.*, vol. 140, no. 7, p. 04014035, 2014.

[5] T. Munaga, M. M. Khan, and K. K. Gonavaram, “Axial and lateral loading behaviour of pervious concrete pile,” *Indian Geotech. J.*, vol. 50, no. 3, pp. 505–513, 2020.

[6] H. Xia, G. Du, J. Cai, and C. Sun, “Model tests on the bearing capacity of pervious concrete piles in silt and sand,” *Geomech. Eng.*, vol. 38, no. 1, pp. 79–91, 2024.

[7] F. Xu et al., “Influence of aggregate reinforcement treatment on the performance of geopolymer recycled aggregate permeable concrete: From experimental studies to PFC 3D simulations,” *Constr. Build. Mater.*, vol. 354, p. 129222, 2022.

[8] M. Muthu and Ł. Sadowski, “Performance of permeable concrete mixes based on cement and geopolymer in aggressive aqueous environments,” *J. Build. Eng.*, vol. 76, p. 107143, 2023.

[9] T. Sarici and M. Ozcan, “Using geopolymer coated and uncoated geotextile as a hybrid method to improve uplift capacity of screw piles in cohesionless soil,” *Alexandria Eng. J.*, vol. 105, pp. 666–681, 2024.

[10] A. Yolcu, M. B. Karakoç, E. Ekinci, A. Özcan, and M. A. Sağır, “Effect of binder dosage and the use of waste rubber fiber on the mechanical and durability performance of geopolymer concrete,” *J. Build. Eng.*, vol. 61, p. 105162, 2022.

[11] S. Gupta, A. GuhaRay, A. Kar, and V. P. Komaravolu, “Performance of alkali-activated binder-treated jute geotextile as reinforcement for subgrade stabilization,” *Int. J. Geotech. Eng.*, 2021.

[12] S. Parathi, P. Nagarajan, and S. A. Pallikkara, “Ecofriendly geopolymer concrete: A comprehensive review,” *Clean Technol. Environ. Policy*, vol. 23, pp. 1701–1713, 2021.

[13] A. Vásquez, V. Cárdenas, R. A. Robayo, and R. M. De Gutiérrez, “Geopolymer based on concrete demolition waste,” *Adv. Powder Technol.*, vol. 27, no. 4, pp. 1173–1179, 2016.

[14] S. Dadsetan, H. Siad, M. Lachemi, and M. Sahmaran, “Construction and demolition waste in geopolymer concrete technology: a review,” *Mag. Concr. Res.*, vol. 71, no. 23, pp. 1232–1252, 2019.

[15] O. Youssf, D. Safaa Eldin, and A. M. Tahwia, “Eco-Friendly High-Strength Geopolymer Mortar from Construction and Demolition Wastes,” *Infrastructures*, vol. 10, no. 4, p. 76, 2025.

[16] Y. R. V., S. Ganesh Kumar, and G. Santha Kumar, “Sustainable pervious concrete pile for liquefaction and reliquefaction mitigation,” *Géotech. Lett.*, vol. 15, no. 1, pp. 32–37, 2025.

[17] G. Doğdu ve S. N. Alkan, “Deprem Sonrası Oluşan İnşaat ve Yıkıntı Atıklarının Değerlendirilmesi: 6 Şubat 2023 Kahramanmaraş Depremleri.” *Artvin Çoruh Üniversitesi Mühendislik ve Fen Bilimleri Dergisi,* 1(1), 38-50, 2023.

[18] A. Ahmad, U. Khalid, Z. U. Rehman, and M. J. Iqbal, “Reclaimed brick masonry waste recycling in macro–micro amelioration of cemented clayey soil: an eco-friendly construction waste solution,” *J. Mater. Cycles Waste Manag.*, vol. 27, pp. 1–22, 2025.

[19] T. Sarici, T. Geckil, B. Ok, and H. S. Aksoy, “An investigation of the usability of alkali-activated blast furnace slag-additive construction demolition waste as filling material,” *Materials*, vol. 18, no. 2, p. 398, 2025.

[20] M. Hussain, H. Zmamou, A. Provost, P. A. H. Romero, A. Mahieu, N. Leblanc, and A. Kane et. al., “Stabilization and recycling of sand in pedestrian walkways,” *Buildings*, vol. 14, no. 1, p. 205, 2024.

[21] T. Sarici, "Puzolan ile güçlendirilmiş inşaat ve yıkıntı atıklarının granüler dolgu olarak kullanılabilirliğinin değerlendirilmesi," Ph.D. dissertation, Dept. of Civil Eng., İnönü Univ., Malatya, Turkey, 2019.

[22] *Standard Test Method for Particle-Size Analysis of Soils*, ASTM D422–63, ASTM Int'l., 2007.

[23] *Standard Test Method for Flat Particles, Elongated Particles, or Flat and Elongated Particles in Coarse Aggregate*, ASTM D4791-10, ASTM Int'l., 2010.

[24] *Standard Test Method for Resistance to Degradation of Small-Size Coarse Aggregate by Abrasion and Impact in the Los Angeles Machine*, ASTM C131-06, ASTM Int'l., 2010.

[25] *Standard Test Methods for Specific Gravity of Soil Solids by Water Pycnometer*, ASTM D854-02, ASTM Int'l., 2002.

[26] *Standard Test Method for Relative Density (Specific Gravity) and Absorption of Coarse Aggregate*, ASTM C127-24, ASTM Int'l., 2024.

[27] *Standard Test Methods for Minimum Index Density and Unit Weight of Soils and Calculation of Relative Density*, ASTM D4254, ASTM Int'l., 2017.

[28] *Standard Test Methods for Laboratory Compaction Characteristics of Soil Using Standard Effort*, ASTM D698-12, ASTM Int'l., 2021.

[29] Ö. Çetkin, "Zemin stabilizasyonunun karayolu üstyapı kalınlığına ve maliyetine etkisi," M.S. thesis, Dept. of Civil Eng., İnönü Univ., Malatya, Turkey, 2022.

[30] *Standard Test Method for Pulse Velocity Through Concrete,* ASTM C597–16, ASTM International, 2016.

[31] *Standard Practice for Classification of Soils for Engineering Purposes (Unified Soil Classification System,* ASTM-D2487, ASTM Int'l., 2017.

[32] K. Terzaghi and R. B. Peck, "Soil Mechanics in Engineering Practice", 2nd edition, *Wiley Publications*, New York, 1967.

Dicle University
Journal of Engineering
https://dergipark.org.tr/tr/pub/dumf
duje.dicle.edu.tr

Araştırma Makalesi / Research Article

Endüstri Tipi Çelik Yapıların Farklı Rüzgâr Yönetmeliklerine Göre Yapısal Analizlerinin Karşılaştırılması

Comparative Analysis of Structural Performance of Industrial Steel Buildings According to Different Wind Codes

Hakan Küni[1], İbrahim Behram Uğur[2*]

[1] Şırnak Üniversitesi, Fen Bilimleri Enstitüsü, İnşaat Mühendisliği Anabilim Dalı, hakankuni@hotmail.com
ORCID: https://orcid.org/0009-0008-7642-4543

[2] Şırnak Üniversitesi, Mühendislik Fakültesi, İnşaat Mühendisliği Bölümü, behramugur@sirnak.edu.tr
ORCID: https://orcid.org/0000-0002-0950-4876

MAKALE BİLGİLERİ

Makale Geçmişi:

Geliş: 29 Mayıs 2025
Revizyon: 5 Eylül 2025
Kabul: 11 Eylül 2025
Online: 30 Eylül 2025

Anahtar Kelimeler:

Rüzgar yükleri, TS 498, ASCE 7-10, Eurocode 1-4, Endüstriyel Çelik Yapılar.

ÖZ

Rüzgâr yükleri, çelik yapıların taşıyıcı sistem davranışını doğrudan etkileyen en önemli dış yüklerden biridir. Bu çalışmada, üç farklı endüstriyel çelik yapı modeli (çift eğimli düzlem kafes sistem, dolu gövdeli kiriş sistemi ve düzlem yüzeyli uzay kafes sistem) üzerinde TS 498, Eurocode 1-4 ve ASCE 7-10 standartlarına göre hesaplanan rüzgâr yükleri uygulanarak karşılaştırmalı analizler yapılmıştır. Statik analizler SAP2000 yazılımı ile gerçekleştirilmiş, tasarımlar Çelik Yapıların Tasarım, Hesap ve Yapım Esasları (ÇYTHYE 2018) esas alınarak yapılmış, deprem etkileri ise Türk Bina Deprem Yönetmeliği (TBDY 2018) kapsamında modele dâhil edilmiştir. Analiz sonuçları, yapı ağırlıkları açısından TS498 standardı ile Eurocode1-4'e göre yaklaşık %10, ASCE 7-10 ile ise yaklaşık %14 daha hafif tasarımlar elde edildiğini göstermiştir. Buna göre, Eurocode 1-4'ün ayrıntılı yaklaşımı nedeniyle en yüksek yapı ağırlıklarını ve taban kesme kuvvetlerini verdiğini; ASCE 7-10'un yüksekliği nispeten daha az olan yapılar için maruziyet katsayısının düşük kalması sonucu daha düşük rüzgâr yükleri ve dolayısıyla en hafif çözümleri ürettiğini; TS 498'in ise pratik ancak detay açısından sınırlı hesap yöntemiyle iki standart arasında sonuçlar sunduğunu göstermektedir. Elde edilen bulgular, yönetmelik seçimlerinin endüstriyel çelik yapıların kesit boyutları, ağırlıkları ve güvenlik düzeyi üzerinde belirleyici rol oynadığını ortaya koymaktadır.

ARTICLE INFO

Article history:
Received 29 May 2025
Received in revised form: 5 September 2025
Accepted 11 September 2025
Available online: 30 September 2025

Keywords:

Wind Loads, TS 498, ASCE 7-10, Eurocode 1-4, Industrial Steel Structures

ABSTRACT

Wind loads are one of the key external effects influencing the structural behavior of steel buildings. This study examines three typical industrial steel structures; a pitched roof truss, a solid-web girder, and a flat space truss by applying wind loads determined according to TS 498, Eurocode 1-4, and ASCE 7-10. The analyses were performed in SAP2000, with designs carried out in line with the Turkish Steel Structures Code (ÇYTHYE 2018), while seismic effects were incorporated following the Turkish Seismic Code (TBDY 2018).The results show that, in terms of structural weight, TS 498 produced designs roughly 10% lighter than Eurocode 1-4, and ASCE 7-10 about 14% lighter. Eurocode 1-4, with its detailed treatment of wind pressures, consistently gave the highest structural weights and base shear forces. By contrast, ASCE 7-10, where exposure coefficients remain relatively low for shorter buildings (8 m in this case), led to lower wind effects and lighter structural solutions. TS 498 fell between the two, offering a simpler but less detailed approach.Overall, the findings underline that the selected wind load standard has a direct impact on cross-sectional dimensions, total weight, and the safety level of industrial steel structures.

Doi: 10.24012/dumf.1709003

* Sorumlu Yazar

Giriş

Çelik, birim ağırlık başına yüksek mukavemeti nedeniyle, betonarme gibi geleneksel yapı malzemelerine kıyasla daha hafif ve dayanıklı bir seçenek sunmakta olup, bu özelliği sayesinde mimari açıdan daha esnek ve karmaşık tasarımların hızlı ve verimli bir şekilde gerçekleştirilmesine olanak tanımaktadır. Fabrikalar, spor tesisleri ve depolar gibi çeşitli yapı türlerinde çelik yapılar, hızlı inşa edilebilmeleri ve yüksek taşıma kapasitesi sunmaları nedeniyle yaygın olarak tercih edilmektedir.

Endüstriyel çelik yapılar, dünya genelinde nüfus artışıyla birlikte artan insan gücü ve üretim ihtiyacını karşılamak amacıyla giderek daha fazla önem kazanmaktadır. Bu yapılar, teknolojik makinelerle insan emeğinin bir arada uyum içinde çalışabileceği, doğal afetlere karşı güvenli ve büyük yapılar olarak öne çıkmaktadır [1]. Çoğunlukla şehir dışındaki geniş arazilerde inşa edilen endüstriyel çelik yapılar, sağlamlıkları ve dayanıklılıklarıyla tanınmakta ve farklı sektörlerde çeşitli işlevlerle kullanılmaktadır. Modern inşaat teknolojileriyle entegre edilen bu yapılar, hem insan yaşam kalitesini artırmak hem de ekonomik kalkınmaya katkıda bulunmak amacıyla tasarlanmaktadır.

Çelik endüstri yapılarının açık alanlarda yaygın olarak tercih edilmeleri nedeniyle rüzgar yüklerine maruziyeti artmakta, bu da yapısal tasarım sürecinde rüzgar etkisinin detaylı bir şekilde değerlendirilmesini zorunlu kılmaktadır. Endüstriyel çelik yapılar, özellikle rüzgarın hızına bağlı olarak yatay yüzeylere doğrudan etki eden rüzgar yüklerinden etkilenir. Bu etkiler, yapının rüzgar yüklerine karşı gösterdiği tepkilerle doğrudan ilişkilidir. Rüzgarın şiddetinin arttığı durumlarda, yapının stabilitesi büyük bir tehdit altına girebilir. Yüksek rüzgar hızları, yapının devrilmesine, çökmesine veya önemli ölçüde hasar görmesine yol açabilecek potansiyele sahiptir. Rüzgârın etkisi, özellikle büyük açıklıklara sahip çelik yapılar gibi yapı türlerinde daha belirgin hale gelir. Bu tür yapılarda, rüzgar yüklerinin oluşturduğu kuvvetler, yapı elemanları üzerinde yüksek gerilmeler meydana getirebilir ve bu gerilmeler, yapı elemanlarının deformasyonuna veya yapısal zayıflıklara yol açabilir. Bu nedenle, rüzgar yüklerinin doğru bir şekilde hesaplanması ve yapıların bu yükler karşısında tasarlanması, yapıların güvenliğini sağlamak için kritik bir öneme sahiptir.

Son yıllarda çelik yapılarda farklı geometrik, yapısal ve deprem parametreleri dikkate alınarak yapılan analizler literatürde önemli bir yer edinmiştir. Örneğin, Dikiciaşık ve ark. [2] endüstriyel hangar tipi çelik yapıların farklı makas ve çapraz düzenleri için gerçekleştirdikleri çalışmada, dışmerkez çaprazlı sistemlerin yapısal ağırlık açısından, merkezi çaprazlı sistemlerin ise ötelenme bakımından avantajlı olduğunu ortaya koymuşlardır. Sancıoğlu ve ark. [3] ise beş katlı simetrik çelik bina üzerinde farklı çapraz sistemleri dikkate alarak deprem etkisi altındaki performansları değerlendirmiş ve çapraz kullanımının ötelemeleri önemli ölçüde azalttığını göstermiştir. Bunun yanında, Peker ve Işık [4], TBDY 2018 kapsamında tanımlanan farklı yerel zemin koşullarını dikkate alarak sekiz katlı çelik yapı üzerinde sahaya özgü tasarım spektrumları ile analizler gerçekleştirmiş ve zemin koşullarının yapısal tepkiler üzerindeki belirleyici etkisini vurgulamıştır. Karaşin ve ark. [5] tarafından yapılan bir diğer çalışmada ise Türkiye'nin yedi farklı coğrafi bölgesinden seçilen örnek iller dikkate alınmış ve sekiz katlı bir çelik yapı üzerinde, bölgesel deprem tehlikesi değişken alınarak özel tasarım spektrumlarıyla statik adaptif itme analizleri yapılmıştır.

Rüzgar yüklerinin çelik yapı tasarımına etkisi ilgili literatürde bulunan bazı çalışmalar şu şekilde sıralanabilir:

Polat [6] 2010'da yaptığı tez çalışmasında rüzgarın meteorojik özelliklerini, rüzgar türbülansını, rüzgar yük hesaplamalarını ve hareketlerini incelemiştir. ASCE 7-05 [7] , Eurocode 1-4 [8] ve TS 498 [9] standartlarını kullanarak rüzgar basınçlarının bulunması hakkında yöntemleri örnekler üzerinde açıklamıştır. Çalışma kapsamında yapılan hesaplamalar sonucunda Eurocode 1-4'ün genel olarak ASCE 7-05'e göre daha etkin olduğu öne sürülmüştür.

Özlek [10], ASCE 7-10 [11] , Eurocode 1-4 ve TS 498 standartlarını, iki farklı yapı türü üzerinde incelenmiştir. Araştırmada, 100 metre yüksekliğinde bir yüksek katlı yapı ile 20 metre mahya yüksekliğine sahip bir sanayi yapısı seçilmiş olup, bu yapılara ilgili yönetmeliklerin rüzgar yükü hesaplamaları yapılmış ve sonuçlarını karşılaştırmıştır. Yapılan örnekler üzerinde bulunan değerler karşılaştırıldığında Eurocode 1-4'ün daha yüksek sonuçlar verdiği gözlemlenmiştir.

Zeyrek ve Bekiroğlu [12], farklı çatı eğimlerine sahip dikdörtgen planlı binalar için Eurocode 1, TS 498 ve Hesaplamalı Akışkanlar Dinamiği (CFD) analizleri kullanarak dış duvar rüzgar basınçlarını hesaplamış ve karşılaştırmışlardır. Çalışma, TS 498'in, özellikle türbülans etkilerini dikkate almaması nedeniyle, diğer yöntemlere göre daha düşük basınç değerleri verdiğini göstermiştir.

Bashir [13], Zonguldak'ta bulunan bir endüstriyel betonarme baca için TS 498, Eurocode 1 ve ASCE 7 standartlarına göre rüzgar ve deprem yüklerini hesaplamış ve elde edilen eleman moment ve gerilme değerlerini karşılaştırmıştır. Çalışma, Eurocode 1'in daha yüksek rüzgar yükleri öngördüğünü ve bu durumun yapı tasarımı üzerinde önemli etkileri olabileceğini belirtmiştir.

Aghaei [14], 2022 yılında yaptığı tez çalışmasında , SAP2000 [15] bilgisayar programını kullanarak Çelik Yapıların Tasarım, Hesap ve Yapım Esasları- 2018 (ÇYTHYE 2018) ve TS-1991-1-4 "Yapılar üzerindeki etkiler Rüzgar Etkileri" standartlarını dikkate alarak çelik yapı modelleri oluşturmuştur. Kırk sekiz adet çelik sisteminin analizini gerçekleştiren bu çalışmada çelik yapı tiplerinin yapısal davranışları ve yapı ağırlıkları karşılaştırılarak detaylı bir analiz yapılmıştır.

Sever ve Yüksel [16], Yüksekliği 80 metre olan ve parapetli örnek bir bina modeli üzerinde rüzgârın meteorolojik oluşumu, sınıflandırılması ve Türkiye'de rüzgâr yükü hesaplamalarına yönelik kullanılan standartlar açıklanmıştır. ASCE 7-16 ve TS 498 standartlarının hesaplama yöntemlerini ve sonuçlarını karşılaştırmıştır. Yapılan karşılaştırmalar sonucunda, ortaya çıkan farklılıkların tek bir nedene bağlı olmadığını, aksine birden fazla parametrenin etkili olduğu görülmüştür.

Bu çalışmada, üç farklı endüstriyel çelik yapı tasarlanarak bu modellere üç ayrı rüzgar standardı (TS 498, Eurocode 1-4 ve ASCE 7-10) uygulanmıştır. Çalışma kapsamında, SAP2000

gibi tüm dünyada kabul görmüş bir yapısal analiz programı kullanılarak modellenen endüstriyel çelik yapılara rüzgar yüklerinin yanı sıra deprem yükleri, kar yükleri, ölü yükler ve sıcaklık yüklemeleri tasarım yönetmeliklerine [8], [16–18] uygun olarak etki ettirilmiştir. Deprem yükleri, yapının bulunduğu lokasyonu göz önüne alınarak Türkiye Deprem Tehlike Haritası'ndaki [20] deprem verileri kullanılarak hesaplanmıştır. Taşıyıcı sistem olarak; çift eğimli düzlem (trapez) kafes sistem, dolu gövdeli/profil kiriş sistemi ve düzlem yüzeyli uzay kafes sistem olmak üzere üç farklı endüstriyel yapı modeli seçilmiş, farklı taşıyıcı sisteme sahip bu yapıların farklı rüzgar yüklemeleri etkisindeki yapısal performansları sistematik bir şekilde karşılaştırılmıştır.

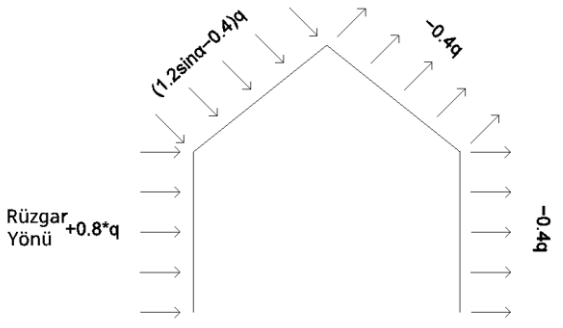
Bu çalışma, mevcut yönetmeliklerdeki farkların mühendislik pratiklerine etkisini değerlendirerek, endüstri tipi çelik yapı tasarımında hangi yönetmeliğin daha avantajlı olduğu konusunda mühendislik literatürüne katkı sağlamayı hedeflemektedir.

Materyal ve Metot

Bu bölümde, Türkiye, Avrupa ve Amerika'da rüzgar yüklerinin hesabı için kullanılan sırasıyla TS 498, Eurocode 1-4 ve ASCE 7-10 standartlarında rüzgar yüklerinin hesabı ile ilgili adımlar detaylı bir şekilde sunulmuştur.

TS 498 Rüzgar Yük Hesaplamaları

Türk Standardı TS 498, yapıların rüzgar yüklerine karşı dayanıklı olmalarını sağlamak amacıyla hesap yöntemleri sunmaktadır. TS 498, rüzgar yüklerinin belirlenmesinde, yapının yükseklik faktörleri göz önünde bulundurur. Yapının yüksekliği, rüzgarın yapıya etkisini doğrudan belirleyen önemli bir parametre olup, rüzgar yükü hesapları bu yüksekliğe bağlı olarak yapılır. TS 498'e göre rüzgar yükü hesabı, aşağıda belirtilen hesaplamalarla yapılmaktadır. Şekil 1'de, TS 498'e göre ana taşıyıcı sistemde rüzgar yükünün dağılımı gösterilmiştir. Bu dağılım TS 498 standardına göre rüzgar yüklerinin yapı yüzeylerine nasıl etki ettiğini göstermektedir. Rüzgarın estiği yönde 0.8 q değerinde bir basınç uygular. Çatı yüzeyinde rüzgar yükü eğime bağlı olarak değişmektedir ve rüzgarın estiği yöndeki çatı yüzeyinde çatı eğimi (α) artıkça, rüzgar yükü artmaktadır. Küçük açılarda yük emme olurken, büyük açılarda basınca dönüşebilmektedir.



Şekil 1. TS498 Rüzgar yükünün ana taşıyıcı sistemde dağılımı [9]

Rüzgar basıncı

TS 498 standardı için rüzgar basıncı aşağıdaki eşitlik ile hesaplanır:

$$w = C_p \cdot q \quad kN/m^2 \tag{1}$$

Burada, C_p emme katsayısını, q ise rüzgar basıncını ifade etmektedir.

Emme basıncı

TS 498 standardına göre rüzgar yükü, rüzgar hızına bağlıdır ve aynı zamanda yapının bulunduğu yükseklikle de doğrudan ilişkilidir. Bu bağlamda, rüzgar basıncı yüksekliğe bağlı olarak değişkenlik gösterir ve yükseklik etkisini rüzgar yükü hesaplamalarında kritik bir parametre olarak değerlendirir. Emme basıncı Denklem (2) 'de gösterildiği gibi hesaplanır.

$$q = \frac{\rho V^2}{2g} \quad kN/m^2 \tag{2}$$

Havanın birim hacim kütlesi ρ = 1.25 kg/m^3 alınıp rüzgar hızı (V) m/s cinsinden yerine konulduğunda Denklem (3)'te görüldüğü gibi denklem daha sade bir yapıya geçer.

$$q = \frac{V^2}{1600} \quad kN/m^2 \tag{3}$$

TS 498 standardına göre, zeminden yüksekliğin ve rüzgar hızının emme basıncı üzerindeki etkisi Tablo 1'de gösterilmiştir.

Tablo 1. Yüksekliğe bağlı rüzgar hızı ve emme basıncı [9]

Zeminden Yükseklik (m)	Rüzgar Hızı 'V' (m/s)	Emme Basıncı 'q' kN/m^2
0-8	28	0.5
9-20	36	0.8
21-100	42	1.1
>100	46	1.3

Eurocode 1-4 Rüzgar Yük Hesaplamaları

Eurocode 1-4'e göre, yapı üzerindeki rüzgar etkisi, yapının boyutuna, şekline ve dinamik özelliklerine bağlı olduğunu belirtir. Eurocode 1-4, yapı üzerindeki rüzgar etkileri sırasıyla şu şekilde açıklanır, rüzgar basıncının yapının yüksekliği ile doğrudan ilişkili olduğunu vurgular. Yüksekliğin artması durumunda rüzgar hızının da artış gösterdiğini ve bunun sonucunda rüzgar basıncının yükseklikle birlikte arttığını ifade eder. Ayrıca, Eurocode 1-4 için yapının genişliği de önemli bir parametredir. Genişlik arttıkça, yapı daha büyük bir yüzey alanıyla rüzgara maruz kalır ve bu durum rüzgar yükünün büyüklüğünü etkiler. Yapının rüzgar basınç hesapları, rüzgarın temel özellikleri (temel rüzgar hızı ve türbülans), arazinin engebeliliği, orografik etkiler ve referans yüksekliği gibi faktörlere bağlı olarak belirlenmektedir. Aşağıda, Eurocode 1-4 standardına göre rüzgar hesabı gösterilmiştir.

Rüzgar Basıncı Hesabı

Eurocode 1-4 standardına göre rüzgar hesabı, rüzgar hızı, arazi engebeliliği, rüzgar türbilansı gibi parametreler göz önünde bulundurularak yapılır. Bu bölümde, rüzgar yüklerinin hesaplanmasına yönelik yöntemler ve ilgili formüller sunulmuş ve her bir adım detaylı bir şekilde açıklanmıştır.

Esas Temel Rüzgar Hızı Değeri

Burada esas rüzgar hızını yılın herhangi bir döneminde ve rüzgar yönünden bağımsız olarak, çayır gibi az bitki örtüsüne sahip ve aralarındaki mesafe en az engel yüksekliğinin 20 katı olan engellerin bulunduğu açık kırsal alanda, yer seviyesinden 10 metre yükseklikteki karakteristik 10 dakikalık ortalama rüzgar hızıdır. Esas rüzgar hızı Denklem (4) 'te ifade edildiği şekilde hesaplanır.

$$v_b = C_{dir} \cdot C_{season} \cdot v_{b,0} \quad (4)$$

v_b: Arazi kategorisi II'de, yer seviyesinden 10 metre yükseklikte, yılın herhangi bir döneminin ve rüzgar yönünün bir fonksiyonu olarak tanımlanan temel rüzgar hızıdır,

$v_{b,0}$: Esas rüzgâr hızının temel değeri,

C_{dir} : Doğrultu katsayısı,

C_{season} : Mevsim katsayısı

Ortalama Rüzgar Hızı

Ortalama rüzgar hızı $v_m\ (Z)$, yapının zemin seviyesinden Z metre yüksekliğindeki ortalama ortalama rüzgar hızıdır. Denklem (5) 'teki gibi hesaplanır.

$$v_m(Z) = c_r(Z) \cdot c_o(Z) \cdot v_b \quad (5)$$

$c_r(Z)$: Engebelilik katsayısı,

$c_o(Z)$: Orografi katsayısı

Arazi Engebelilik Katsayısı

Yapının zeminden yüksekliği ve arazi parçasının engebeliliği durumlarına bağlı olarak engebelilik katsayısı $c_r(Z)$, ortalama rüzgar hızı değişkenliği hesabı yapılır. Denklem (6) 'da detayları gösterilmiştir.

$$c_r(Z) = k_r(Z) \cdot ln\ (\frac{Z}{Z_0}) \quad (6)$$

Arazi katsayısı k_r, Denklem (7) ile hesaplanır.

$$k_r = 0.19\ .\ (\frac{Z_0}{Z_{0.ıı}})^{0.07} \quad (7)$$

Z_0 : 0.05 (TS EN 1991-1-4 Çizelge 4.1),

Z_{min} : en düşük yükseklik (TS EN 1991-1-4 Çizelge 4.1),

Z_{max} : 200 m alınır.

Rüzgar Türbülansı

Rüzgar türbülans şiddeti $I_v(Z)$, türbülansın standart sapmasının ortalama rüzgar hızına oranıdır. Rüzgâr hızının türbülans bileşeninin ortalama değeri 0, standart sapması ise σv'dir. Standart sapma Denklem (8) ile hesaplanır.

$$\sigma_v = k_r \cdot v_b \cdot k_ı \quad (8)$$

k_r : Arazi katsayısı,

v_b : Esas rüzgar hızı,

$k_ı$: Türbülans katsayısı

$I_v(Z)$ 'nin hesaplanması için yönetmeliğin tavsiye ettiği işlem Denklem (9)'da gösterilmiştir.

$$I_v(Z) = \frac{\sigma_v}{V_m(Z)} = \frac{kı}{co(Z) \cdot\ In\ \left(\frac{Z}{Z_0}\right)} \quad (9)$$

$$Z_{min} \leq Z \leq Z_{max}$$

Tepe Hız Kaynaklı Rüzgar Basıncı

Yapı yüksekliğine bağlı olan tepe hız kaynaklı rüzgar basıncı q_pz 'nin belirlenmesi gereklidir. Rüzgar basıncı için tavsiye edilen hesap yöntemi Denklem (10) 'da gösterilmiştir.

$$q_p(z) = [1 + 7\ .\ l_v(z)].\frac{1}{2}\ \rho.\mathrm{v}^{\,2}_m(z) \quad (10)$$

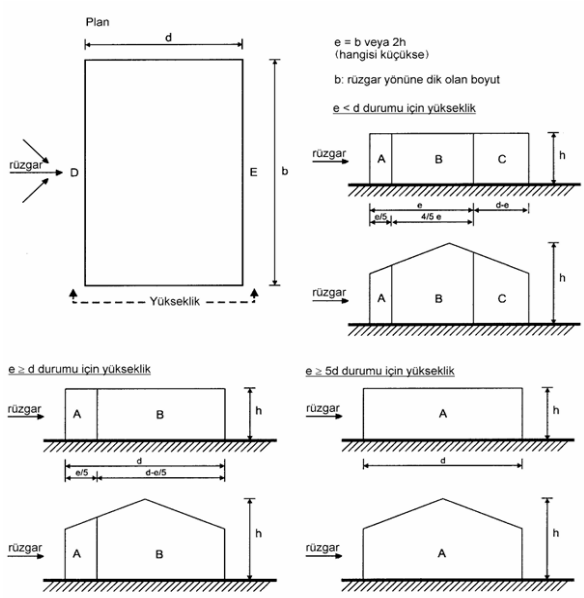
ρ : Rakıma bağlı hava yoğunluğu 1.25 kg/m^3 alınabilir,

$c_e(z)$: Maruz kalma katsayısı, aşağıdaki Denklem (11) ile hesaplanır.

$$c_e(z) = \frac{q_p(z)}{q_p} \quad (11)$$

A,B,C,D ve E bölgeleri için dış basınç katsayıları $c_{pe,10}$ ve $c_{pe,1}$ aşağıdaki şekilde tanımlanmışır. Şekil 2'de gösterildiği üzere, rüzgârın estiği yönde hesaplamalarda e değeri, b (rüzgar yönüne dik olan boyut) veya 2h (yapının iki kat yüksekliği) değerlerinden küçük olan esas alınarak kullanılmaktadır. Bölgelere göre tanımlanan dış basınç katsayıları, her bir bölge için uygun interpolasyon yöntemleri kullanılarak hesaplanır ve bu doğrultuda bölgelerin dış basınç katsayıları elde edilir.

$c_{pe,10}$ ve $c_{pe,1}$ değerleri h/d oranına bağlıdır. Ara değerlerde interpolasyon işlemi uygulanarak uygun katsayı değeri bulunur. Tablo 2'de tavsiye edilen değerler gösterilmiştir.



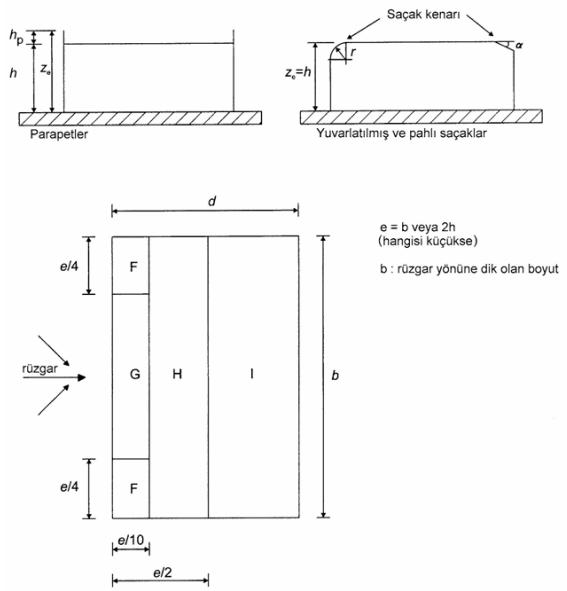
Şekil 2. Düşey duvarlar için açıklamalar [8]

Tablo 2. Dikdörtgen planlı binaların düşey duvarları için önerilen dış basınç katsayısı değerleri [8]

Bölge	**A**		**B**		**C**		**D**		**E**	
h/d	$c_{pe,10}$	$c_{pe,1}$	$c_{pe,10}$	$c_{pe,1}$	$c_{pe,10}$	$c_{pe,1}$	$c_{pe,10}$	$c_{pe,1}$	$c_{pe,10}$	$c_{pe,1}$
5	-1,2	-1,4	-0,8	-1,1	-0,5		+0,8	+1,0	-0,7	
1	-1,2	-1,4	-0,8	-1,1	-0,5		+0,8	+1,0	-0,5	
≤ 0,25	-1,2	-1,4	-0,8	-1,1	-0,5		+0,7	+1,0	-0,3	

Düz Çatılarda Rüzgâr

Eğimi -5° ile 5° arasında olan çatılar için geçerlidir. Keskin kenarlı saçaklar, parapetli, kenarları yuvartılmış saçaklı ve kenarları pahlı saçaklı olmak üzere çatı tipleri mevcuttur. Düz çatılarda çatı dört farklı bölgeye ayrılır bu bölgeler Şekil 3'te gösterilmiştir.

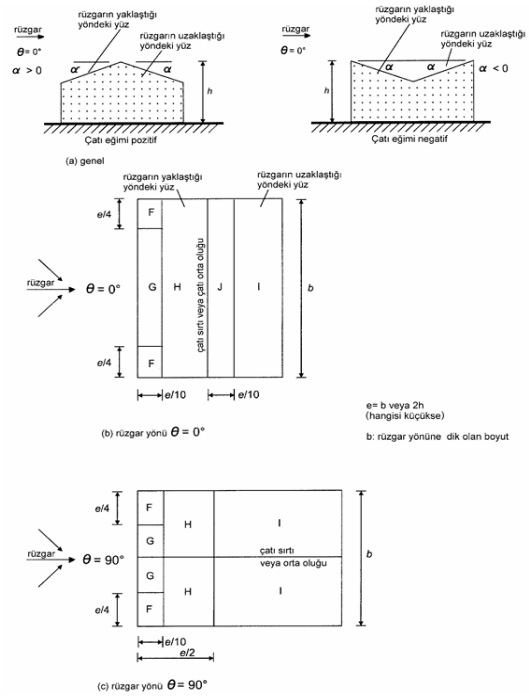


Şekil 3. Düz çatılar için açıklamalar [8]

Düz çatılarda farklı çatı tipleri için dış basınç katsayıları mevcuttur. TS EN 1991-1-4 bölüm 7.2.3'te her tip çatı modeli için dış basınç katsayıları detaylıca gösterilmiştir.

Çift Eğimli Çatılarda Rüzgâr

Çift eğimli çatılarda rüzgârın geliş yönüne bağlı olarak çatı farklı bölgelere ayrılır. Şekil 4'te çift eğimli çatılar için gerekli açıklamalar mevcuttur.



Şekil 4. Çift eğimli çatılar için açıklamalar [8]

Çift eğimli çatılarda rüzgâr yönüne bağlı olarak dış basınç katsayıları değişmektedir. TS EN 1991-1-4 bölüm 7.2.5'te rüzgâr yönüne bağlı olarak çift eğimli çatılar için dış basınç katsayıları gösterilmiştir.

Eurocode 1-4 kapsamında rüzgâr yüklemelerinde yapıyı farklı bölgelere ayırdığı incelenmiştir. Bu süreçte, yapı türüne bağlı olarak dış basınç katsayıları belirlenmektedir. Bu standartta yer alan dış basınç katsayılarına ilişkin tablolar, belirli çatı eğimlerine karşılık gelen değerleri içermektedir. Çatı eğiminin tabloda yer alan değerler arasında kalması durumunda, ilgili dış basınç katsayısının belirlenebilmesi için interpolasyon yöntemi uygulanarak ara değerler hesaplanır. Elde edilen dış basınç katsayıları, tepe hız kaynaklı rüzgâr basıncı değeri ile çarpılarak hesaplamalar gerçekleştirilir ve yapı için uygun rüzgar yükleri belirlenir.

ASCE 7-10 Rüzgâr Yük Hesaplamaları

ASCE 7-10 standardı, farklı yapı kategorileri için temel rüzgar hızlarını belirlemeye yönelik ayrıntılı rüzgar hızı haritaları sunmaktadır. Bu haritalar, yapının kullanım kategorisine bağlı olarak temel rüzgar hızının belirlenmesini sağlar. Örnek modellerde yapının konumu Şırnak Üniversitesi Mehmet Emin Acar Kampüsü olarak belirlenmiştir ve yapının Türkiye'de yapılacağı varsayıldığından ASCE 7-10 standardında Türkiye için rüzgar hız haritası belirtilmemiştir. ASCE 7-10 standardı, rüzgar yükü hesaplamalarını sistematik bir şekilde ele alarak

adım adım ve her bir adımın düzenli bir sırayla takip edilmesini sağlayarak hesaplama yöntemi sunar. Hesaplama süreci yapının risk kategorisinin belirlenmesi ile başlar. Risk kategorisinin belirlenmesine yönelik gerekli haritalar ve kategoriler, ASCE 7-10 standardında Bölüm 26.5.1 altında detaylı olarak sunulmaktadır. Daha sonraki adımda, yüzey engebelilik kategorisi belirlenir. Üç yüzey engebelilik kategorisi bulunmaktadır ve bu kategoriler sırasıyla aşağıdaki gibidir:

Yüzey engebelilik kategorisi B: Kent ve banliyö alanları, yoğun ağaçlık alanlar, sık engebeli arazi veya büyük boyutlu konutlara sahip araziler.

Yüzey engebelilik kategorisi C: Yükseklikleri genellikle 9,1 m altında olan sık engellerin bulunduğu açık araziler.

Yüzey engebelilik kategorisi D: Düz engelsiz araziler ve su yüzeyleri, yumuşak çayırlı ovalar ve kırılmamış buz bölgeleri.

Yüzey engebelilik kategorisi belirlendikten sonra maruz kalma kategorisi belirlenir. Üç maruz kalma kategorisi vardır ve bunlar aşağıdaki gibidir:

Maruz kalma kategorisi B: Ortalama çatı yüksekliği 9,1 metre veya daha düşük olan yapılar için kullanılır. Rüzgâr yönünde en az 457 metre mesafede Yüzey Engebeliği B koşullarının hâkim olduğu durumlarda, Maruz Kalma B uygulanır. Çatı yüksekliği 9,1 metreden büyük olan yapılarda ise, Maruz Kalma B'nin geçerli olması için Yüzey Engebeliği B'nin rüzgâr yönünde en az 792 metre veya binanın yüksekliğinin 20 katı kadar bir mesafede bulunması gerekir; bu iki değerden büyük olanı esas alınır.

Maruz kalma kategorisi C: Maruz Kalma B veya D'nin uygulanmadığı tüm durumlarda, Maruz Kalma C uygulanır.

Maruz kalma kategorisi D: Maruz Kalma D yüzey engebeliğinin, rüzgar yönünde 1.524 metre veya binanın yüksekliğinin 20 katı kadar bir mesafede hâkim olduğu durumlarda, bu iki değerden büyük olan değer esas alınır.

Rüzgar hız basıncı

Rüzgar hız basıncı q_z, aşağıdaki Denklem (12) ile hesaplanır:

$$q_z = 0.613\, K_z\, K_{zt}\, K_d\, V^2 \ (\mathrm{N/m^2}) \qquad (12)$$

K_d : Rüzgar doğrultu faktörü,

K_z : Hız basıncı maruz kalma katsayısı,

K_{zt} : Topoğrafik faktör,

V : Temel rüzgar hızı

Topografik faktör K_{zt} 1.0 olarak alınmıştır.

Rüzgar doğrultu faktörü K_d

Rüzgar doğrultu faktörü K_d, yapının geometrisini dikkate alarak gerçekçi bir yük tahmini yapılmasını sağlar. Tablo 3 ile belirlenir ve burada yapı tipine uygun olan katsayı seçilir.

Tablo 3. Rüzgar doğrultu faktörü [11]

Yapı Türü	**Rüzgar doğrultu faktörü (K_d)**
Binalar	0.85
Kemerli Çatılar	0.85
Duman Bacaları, Depolar ve Benzer Yapılar	
Kare	0.90
Altıgen	0.95
Yuvarlak	0.95
Serbest duvar, serbest ve bağlı levhalar	0.85
Açık Levhalar ve Kafes Çerçevesi	0.85
Çelik Kafes Kuleler	
Üçgen, kare, dikdörtgen	0.85
Tüm diğer kesitler	0.95

Maruz kalma katsayısı K_z

Yapıyla ilgili bilgiler ışığında belirlenen maruz kalma kategorisine göre, yapının yüksekliği ile ilişkilendirilen maruz kalma katsayısı Tablo 4'te ayrıntılı bir şekilde sunulmuştur.

Tablo 4. Maruz kalma katsayıları [11]

Zemin seviyesinden yükseklik (m)	**Maruz kalma kategorisi**		
	B	C	D
0-4.6	0.57	0.85	1.03
6.1	0.62	0.90	1.08
7.6	0.66	0.94	1.12
9.1	0.70	0.98	1.16
12.2	0.76	1.04	1.22
15.2	0.81	1.09	1.27
18.0	0.85	1.13	1.31
21.3	0.89	1.17	1.34
24.4	0.93	1.21	1.38
27.4	0.96	1.24	1.40
30.5	0.99	1.26	1.43
36.6	1.04	1.31	1.48
42.7	1.09	1.36	1.52
48.8	1.13	1.39	1.55
54.9	1.17	1.43	1.58
61.0	1.20	1.46	1.61
76.2	1.28	1.53	1.68
91.4	1.35	1.59	1.73
106.7	1.41	1.64	1.78
121.9	1.47	1.69	1.82
137.2	1.52	1.73	1.86
152.4	1.56	1.77	1.89

Tüm yükseklikteki binalar için rüzgar basıncı Denklem (13) ile hesaplanır.

$$p = qGC_p - q_i(GC_{pi}) \ \left(\frac{N}{m^2}\right) \qquad (13)$$

Burada;

G : Fırtına etki faktörü,

C_p : Dış basınç katsayısı,

q_i : Ortalama çatı yüksekliğinde hesaplanan rüzgar hız basıncı,

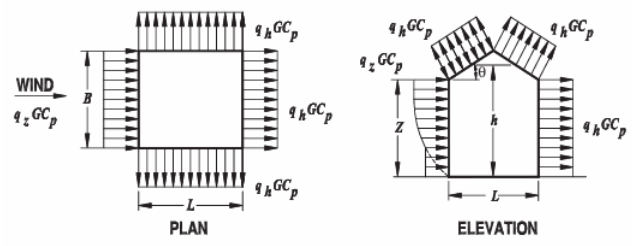
GC_{Pi} : İç basınç katsayısı

Fırtına etki faktörü (G), Yapının rüzgâr yüküne verdiği dinamik tepkiyi ve rüzgârın ani değişimlerinin etkisini dikkate almak için kullanılır. İç basınç katsayısı, yapının içindeki hava basıncının dış basınca etkisini ifade eder. ASCE 7-10 yönetmeliğine göre, açık binalar, kısmen kapalı binalar ve kapalı binalar için iç basınç katsayıları Tablo 5'te gösterilmiştir.

Tablo 5. İç basınç katsayıları [11]

Kaplama Sınıflandırılması	(GC_{Pi})
Açık binalar	0.00
Kısmen kapalı binalar	+0.55 -0.55
Kapalı binalar	+0.18 -0.18

ASCE 7-10 standardına göre dış basınç katsayısı, rüzgar yükü hesaplamalarında önemli bir parametredir. Hesaplamalar, duvarlar ve çatılar için farklı basınç katsayıları kullanılarak yapılır. Duvarlar için katsayı, rüzgar yönüne bağlı olarak yapının x ve y boyutlarının oranı (L/B) üzerinden belirlenir. Çatılar için ise katsayı, yapının ortalama yüksekliğinin ve rüzgar yönüne bağlı olarak duvar uzunluğuna oranı (h/L) ile ilişkilidir. Bu ilişki aşağıda Şekil 5 'te gösterilmiştir.



Şekil 5. Rüzgar yük dağılım [11]

Duvarlar için dış basınç katsayılarına ilişkin değerler, Tablo 6'da detaylı bir şekilde sunulmuştur. Bu değerler uygun dış basınç katsayılarının belirlenmesini ve doğru bir net basınç değerinin hesaplanması için önemlidir. Çatı için dış basınç katsayılarına ilişkin değerler, ASCE 7-10 standardının 27.4 numaralı bölümünde detaylı olarak sunulmuştur.

Tablo 6. Duvar dış basınç katsayıları [11]

Yüzey	L/B	C_p	Basınç
Rüzgara dik duvar	Tüm değerler	0.8	q_z
Rüzgar arkası duvar	0-1	-0.5	q_h
	2	-0.3	
	≥ 4	-0.2	
Çapraz duvarlar	Tüm değerler	-0.7	q_h

Endüstri Yapı Modelleri

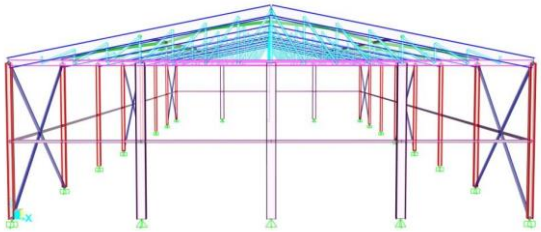
Bu çalışmada 20 metre uzunluğa, 42 metre genişliğe ve 8 metre yüksekliğe sahip Endüstri tipi çelik yapı modelleri ele alınmıştır. Bu çalışmada ele alınan örnekler, Siamak AGHAEI'nin tez çalışmasında [14] kullandığı yapı modellerinden yararlanılarak oluşturulmuştur. Oluşturulan çift eğimli düzlem (trapez) kafes sistem, dolu gövdeli/profil kiriş sistemi ve düzlem yüzeyli uzay kafes sistem, endüstriyel yapılar arasında en yaygın kullanılan taşıyıcı sistemleri temsil etmektedir. Söz konusu sistemler, gerek ülkemizde gerekse dünyada hangar, depo ve fabrika binaları gibi endüstriyel yapılarda sıklıkla tercih edilmektedir. Ayrıca, kafes, dolu gövdeli ve uzay kafes sistemlerin farklı yük aktarım mekanizmalarına sahip olması, rüzgâr yüklerinin taşıyıcı sistemler üzerindeki etkilerinin karşılaştırmalı olarak incelenmesine olanak sağlamaktadır. Benzer boyutlara sahip olmalarına karşın farklı konstrüktif düzenlemeler göstermeleri ise yönetmelikler arasındaki sonuç farklarının daha açık ve sistematik biçimde ortaya konmasına katkı sağlamıştır. Türkiye Bina Deprem Yönetmeliği-2018 yönetmeliğinin belirlediği esaslara uygun olarak gerekli yükler uygulanmış ve kontroller sağlanmıştır. Modellerin tasarımları, Çelik Yapıların Tasarım, Hesap ve Yapım Esasları – 2018 (ÇYTHYE 2018) standardına uygun olarak gerçekleştirilmiştir. Modellerde baz alınan yapının lokasyonu 37.50° enleminde ve 42.42° boylamında bulunan Şırnak Üniversitesi Mehmet Emin Acar Kampüsü olarak göz önüne alınmıştır. Zemin sınıfı ZB (az ayrışmış, orta sağlam kayalar) olduğu kabul edilerek analiz ve tasarım süreçleri bu varsayım doğrultusunda gerçekleştirilmiştir.

İlgili rüzgar yönetmeliklerinin ve diğer yönetmeliklerin belirlediği esaslara uygun olarak endüstri tipi çelik yapı modelleri tasarlanmış olup Tablo 7'de modellere ilişkin genel bilgiler verilmiştir.

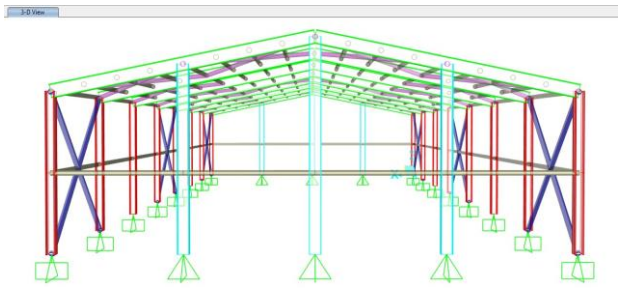
Tablo 7. Modellere ilişkin genel bilgiler

	Model A	**Model B**	**Model C**
Yapı Bölgesi	Şırnak Üniversitesi Mehmet Emin Acar Kampüsü	Şırnak Üniversitesi Mehmet Emin Acar Kampüsü	Şırnak Üniversitesi Mehmet Emin Acar Kampüsü
Enlem	37.505107°	37.505107°	37.505107°
Boylam	42.427409°	42.427409°	42.427409°
Yerel Zemin Sınıfı	ZB	ZB	ZB
S_{DS}	$0.50 \leq S_{DS}<0.75$	$0.50 \leq S_{DS}<0.75$	$0.50 \leq S_{DS}<0.75$
Yapı Uzunluğu	42 m	42 m	42 m
Yapı Genişliği	20 m	20 m	20 m
Yapı Yüksekliği	8 m	8 m	8 m
Kolon Yüksekliği	6 m	6,7,8 m	6 m
Çatı Eğimi (α)	11.31°	11.31°	0.0°

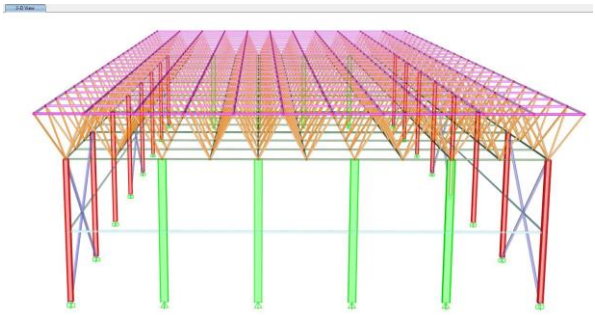
Ele alınan üç farklı endüstri tipi çelik yapı modelleri Şekil 6, Şekil 7 ve Şekil 8'de gösterilmiştir.



Şekil 6. Çift Eğimli Düzlem (Trapez) Kafes Sitemi (Model A)



Şekil 7. Dolu gövdeli/profil kiriş sistemi (Model B)



Şekil 8. Düzlem Yüzeyli Uzay Kafes Sistem (Model C)

Ölü yükler zaman içerisinde değişmeyen yapı üzerine her zaman etki eden yüklerdir. Yapı sistemlerinin eleman ağırlıklıları SAP2000 programı kullanılarak hesaplanmıştır. Aşıklar yapıda modellenmediği için aşık yükü ayrı olarak hesaplanıp modele etki ettirilmiştir. Aşık yükü 0.10 kN/m^2, Kaplama yükü 0.15 kN/m^2 ve Kuşak yükü 0.30 kN/m^2 olarak hesaba katılmıştır.

Hareketli yükler yapının kullanım türüne ve insan hareketliliğine göre değişebilen yüklerdir. Tasarlanan modellerde hareketli yükün (Q) alınmasına gerek duyulmamıştır.

Sıcaklık yüklemesi yapının dayanıklılığı ve güvenliği için önemlidir. Yapıya +20°C ve −20°C sıcaklık yüklemesi yapılmıştır.

Modellenen endüstri yapıları, Şırnak bölgesinde yer aldığından dolayı kar yükleri önemli bir etkiye sahiptir. Kar yükleri, tüm modellerde Yapılar Üzerindeki Etkiler – Bölüm 1-3: Genel Etkiler – Kar Yükleri [17] yönetmeliğine uygun olarak hesaplanmıştır. Kar yükü hesabı, Denklem (14) 'te sunulmuştur.

$$S = \mu_i C_e C_t S_k \qquad (14)$$

μ_i: Kar yükü şekil katsayısı,

S_k: Karakteristik zemin kar yükü değeri,

C_e: Maruz kalma katsayısı,

C_t: Isı katsayısı.

Modellerdeki çatı eğimi (α) 0° ve 11.31° olduğundan dolayı, aşağıda Tablo 8'de gösterildiği üzere μ_i 0.8 olarak alınmıştır.

Tablo 8. Kar yükü şekil katsayıları [17]

Çatı eğim açısı, α	0°≤ α ≤ 30º	30º< α < 60º	α ≥60º
μ_1	0.8	0.8 (60-α)/30	0.0
μ_2	0.8+0.8 α/30	1.6	--

Şırnak, Türkiye kar haritasında IV. Bölgede 1400 metre rakımda yer aldığından, S_k değeri, Tablo 9'da gösterildiği gibi %10 artırılarak 1,76 olarak alınmıştır.

Tablo 9. Karakteristik zemin kar yükü (Sk) değerleri kN/m^2 [9]

	1	2	3	4	5
1	Yapı yerinin denizden yüksekliği	BÖLGELER			
	m	I	II	III	IV
	≤ 200	0.75	0.75	0.75	0.75
2	300	0.75	0.75	0.75	0.80
	400	0.75	0.75	0.75	0.80
	500	0.75	0.75	0.75	0.85
3	600	0.75	0.75	0.80	0.90
	700	0.75	0.75	0.85	0.95
	800	0.80	0.85	1.25	1.40
4	900	0.80	0.95	1.30	1.50
	1000	0.80	1.05	1.35	1.60
5	>1000	1000 m'ye tekabül eden değerler, 1500 m'ye kadar % 10, 1500 m'den yukarı yüksekliklerde % 15 artırılır.			
Kar yağmayan yerlerde kar yükü hesap değeri sıfır alınır.					

Genel olarak ısı katsayısı C_t 1.0 olarak alınır. Maruz kalma katsayısı C_e çatı kar yükünün belirlenmesinde kullanılır. Özel değerler ifade edilmedikçe C_e değeri 1.0 olarak alınır. Tablo 10'da tavsiye edilen C_e değerleri verilmiştir.

Tablo 10. Farklı topografik alanlar için tavsiye edilen C_e değerleri [17]

Topografik bölge	**C_e**
Rüzgara açık	0.8
Normal	1
Korunmuş	1.2

$S = \mu_i C_e C_t S_k$

$= 0.8 \cdot 1 \cdot 1 \cdot 1.76$

$= 1.408\ kN/m^2$

Yapılar, deprem anında yatay ve düşey kuvvetlere maruz kalırlar. Sismik yüklemeler, yapının deprem anında maruz kaldığı kuvveti ifade eder. Yapıların bulunduğu konuma ait sismik parametreler, AFAD'ın web sitesinde sunulan Türkiye Deprem Tehlike Haritası [20] kullanılarak elde edilmiştir . Bu sismik parametreler ile birlikte yapı zemin sınıf ve tasarım depremi bilgileriyle TBDY 2018'de verilen bağıntılar ile yapılara etki eden deprem kuvvetleri belirlenmiştir. Bu sayede yapıya deprem kuvveti uygulanmış ve yapının güvenliği bu doğrultuda sağlanmıştır. DD-2: 50 yıl içerisinde aşılma olasılığı %10 olan deprem yer hareketi düzeyi (tekrarlanma periyodu 475 yıl) seçilmiştir. Bina kullanım amacına bağlı olarak, Endüstri yapıları BKS-3 kategorisinde yer aldığından, Bina Önem Katsayısı (I) 1.0 olarak alınmıştır. Deprem tasarım sınıfı (DTS), Bina kullanım sınıfına (BKS) ile ve Kısa Periyot Tasarım Spektral İvme Katsayısı S_{DS} değerine bağlı olarak belirlenmektedir. Bu çalışmada S_{DS} değeri 0.719 olarak hesaplanmış ve yapının BKS 3 kategorisinde olduğundan $0.50 \leq S_{DS} < 0.75$ aralığına karşılık gelen DTS 2 olarak elde edilmiştir. Bina yüksekliği (H_N) 8 metre olup, DTS değeri 2 olarak belirlendiğinden, bu bina için $7.0 \leq H_N < 10.5$ aralığında yer almaktadır. Bu durumda, Bina yükseklik sınıfı (BYS) 7 olarak kabul edilmiştir. Çelik bina taşıyıcı sistemleri, taşıyıcı sistemlere ve Bina Yükseklik Sınıfı (BYS) koşullarını sağlamasına göre belirlenir. Taşıyıcı Sistem Davranış Katsayısı (R) ve Dayanım Fazlalığı Katsayısı (D), taşıyıcı sistemin süneklik düzeyine bağlı olarak tanımlanmaktadır. X yönünde çelik bina taşıyıcı sistemleri Deprem etkilerinin tamamının moment aktaran süneklik düzeyi yüksek çelik çerçevelerle karşılandığı binalar sınıfına girdiği için C11 ve Y yönündeki çelik bina taşıyıcı sistemleri, Deprem etkilerinin tamamının süneklik düzeyi yüksek merkezi çaprazlı çelik çerçeveler tarafından karşılandığı binalar sınıfına girdiği için C13 olarak seçilmiştir. Söz konusu ilgili parametreler, Türkiye Bina Deprem Yönetmeliği (TBDY, 2018)'nde belirtilen esaslar doğrultusunda belirlenmiştir.

Türkiye'de yapıların güvenli ve ekonomik tasarımı için kullanılan ÇYTHYE [18], yük birleşimlerinin modellenmesi ve analizi konusunda kapsamlı bir rehber sunmaktadır. ÇYTHYE 2018 yönetmeliğine göre yük birleşimleri modellere etki edilmiştir. Deprem etkisi, E için yürürlükteki TBDY 2018 [19] koşulları esas alınmıştır. Bu çalışmadaki yük kombinasyonları, Siamak AGHAEI 'nin çalışmasında [14] yer alan kombinasyonlardan faydalanılarak uygulanmıştır.

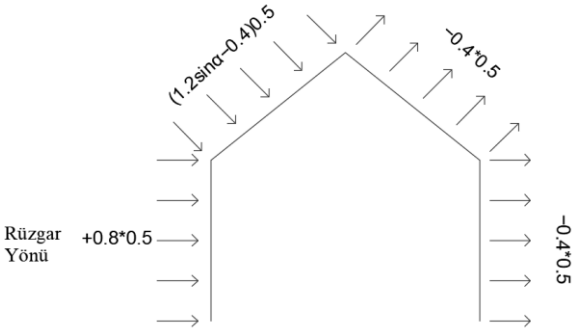
Rüzgar Yükü Hesaplamaları

Bu bölümde, tasarlanan modeller için rüzgar yük hesaplamaları, ilgili standartlara uygun olarak yapılmıştır ve bu hesaplamalar detaylı bir şekilde gösterilmiş olup şekiller ve tablolar aracılığıyla sunulmuştur.

TS 498 Standardına Göre Çözüm

Yapı yüksekliği 8 metre olduğundan yüksekliğe bağlı rüzgâr hızı ve emme basıncı tablosu dikkate alınarak, 0-8 metre

aralığı için rüzgâr hızı 28 m/s olarak ve emme basıncı q = 0.5 kN/m^2 alınmıştır. Şekil 9'da, TS 498'e göre ana taşıyıcı sistemde rüzgar yükünün dağılımı gösterilmiştir.



Şekil 9. TS498 Rüzgar yükünün ana taşıyıcı sistemde dağılımı

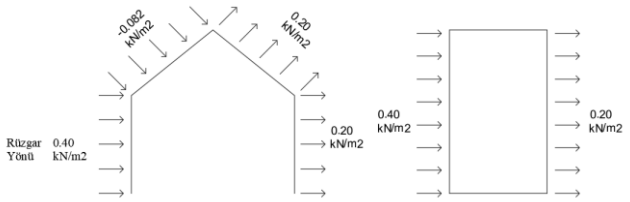
Rüzgarın 0° açıyla esmesi durumunda rüzgar yük hesabı aşağıda yapılmıştır. Şematik gösterim Şekil 10'da sunulmuştur.

F1= 0.5 · 0.8 = 0.4 kN/m^2

F2= (1.2sinα – 0.4) · 0.5 = -0.082 kN/m^2 kN/m^2

F3= 0.5 · 0.4 = 0.2 kN/m^2

F4= 0.5 · 0.4 = 0.2 kN/m^2



Şekil 10. W$_x$ yönünde (0° açıyla) etkiyen rüzgar yükü

Rüzgarın 90° açıyla esmesi durumunda rüzgar yük hesabı aşağıda yapılmıştır.

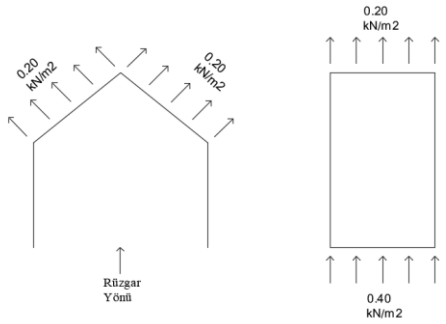
F1= 0.5 · 0.8 = 0.4 kN/m^2

F2= 0.5 · 0.4 = 0.2 kN/m^2

F3= 0.5 · 0.4 = 0.2 kN/m^2

F4= 0.5 · 0.4 = 0.2 kN/m^2

Şekil 11'de, W$_y$ yönünde hesaplanan rüzgar yükünün yapı üzerinde yüklerin dağılımı görsel olarak sunulmuştur.



Şekil 11. W$_y$ yönünde (90° açıyla) etkiyen rüzgar yükü

Düz çatılar için rüzgar yük hesabı Sin0 = 0 olduğundan, çatı için elde edilen sonuç 0.4 q olarak hesaplanmıştır. Bu değer, $q = 0.5\ kN/m^2$ alınarak $0.4 \cdot 0.5 = 0.2\ kN/m^2$ olarak bulunmuştur

Eurocode 1-4 Standardına Göre Çözüm

Arazi kategorisi olarak, çayır gibi az seviyede bitki örtüsü olan ve aralarından en az engel yüksekliğinin 20 katı kadar mesafe bulunan engellere sahip olan Arazi kategorisi II seçilmiştir. Temel rüzgar hızı değeri aşağıda belirtilen şekilde hesaplanmıştır.

$v_b = C_{dir} \cdot C_{season} \cdot v_{b,0}$

$v_{b,0}$: Esas rüzgâr hızının temel değeri 27.78 m/s,

C_{dir} : Doğrultu katsayısı 1.0

C_{season} : Mevsim katsayısı 1.0

olarak alınmıştır.

$= 1 \cdot 1 \cdot (27.78) = 27.78\ m/s$

Esas hız kaynaklı rüzgar basıncı aşağıda belirtildiği şekilde hesaplanmıştır.

$q_b = \frac{1}{2} \cdot \rho \cdot \mathrm{v}_b^2$

ρ : Rakıma bağlı hava yoğunluğu 1.25 kg/m^3 alınmıştır.

$= \frac{1}{2} \cdot (1.25) \cdot (27.78)^2 = 482.3\ N/m^2$

$= 0.48\ kN/m^2$

Arazi katsayısı k_r, aşağıda hesaplanmıştır.

$k_r = 0.19 \cdot (\frac{Z_0}{Z_{0,II}})^{0,07}$

$= 0.19 \cdot (0.05/0.05)^{0,07} = 0.19$

Arazi engebelilik katsayısı aşağıda hesaplanmıştır. Yapı yüksekliği 8 m olduğundan Z 8 alınmıştır.

$c_r(Z) = k_r(Z) \cdot \ln(\frac{Z}{Z_0})$

$= 0.19 \cdot ln(\frac{8.00}{0.05}) = 0.96$

$c_r(Z) = k_r(Z).\ln(\frac{Z}{Z_0})$

$= 0.19 \cdot ln(\frac{8.00}{0.05}) = 0.96$

Ortalama rüzgar hızı $v_m(Z)$ aşağıdaki şekilde hesaplanmıştır. Orografi katsayısı $c_o(Z)$, 1 olarak alınmıştır.

$v_m(Z) = c_r(Z) \cdot c_o(Z) \cdot v_b$

$=0.96 \cdot 1 \cdot 27.78 = 26.67\ m/s$

Türbülans şiddeti $I_v(Z)$'nin hesaplaması aşağıda sunulmuştur. Türbülans katsayısı $k_ı$ için tavsiye edilen değer 1,0 dir.

$I_v(Z) = \frac{\sigma_v}{V_m(Z)} = \frac{kı}{co(Z)\ In(\frac{z}{z_0})}$

$= \frac{1}{1 \cdot \ln\left(\frac{8.00}{0.05}\right)} = 0.20$

Tepe hız kaynaklı rüzgar basıncı $q_p(z)$, aşağıda hesaplanmıştır.

$$q_p(z) = [1 + 7\,.\,l_v(z)] \cdot \frac{1}{2}\ \rho.\mathrm{v}^2_m(z)$$

$$= [1 + 7\,(0.20)]\left(\frac{1}{2}\right) \cdot (1.25).26.67^2$$

$$= 1.07\ kN/m^2$$

Rüzgarın 0° açıyla esmesi ve düşey duvarlara etkimesi durumunda yapılan hesaplamalar aşağıda sunulmuştur.

e = b veya 2h (hangisi küçükse) $e < d$

b = 42 m, e = 16 m, d = 20 m, h = 8 m

Tablo 11'de Rüzgarın 0° açıyla esmesi durumunda interpolasyon işlemi uygulanıp dış basınç katsayı değerleri hesaplanmıştır.

Tablo 11. Rüzgarın 0° açıyla esmesi durumunda dış basınç katsayı değerleri

h/d=0.4	Rüzgarın W_x 0° açıyla esmesi durumunda				
Bölge	A	B	C	D	E
$c_{pe,10}$	-1.2	-0.8	-0.5	0.7	-0.3
$c_{pe,net}$	-1.2	-0.8	-0.5	0.72	-0.3
$q_p(z)$			1.07		
$q_p(z).c_{pe,net}$	-1.28	-0.86	-0.54	0.77	-0.34

W_x için gerçekleştirilen işlemler, W_y için de uygulanmış olup, elde edilen değerler Tablo 12'de verilmiştir.

Tablo 12**.** Rüzgarın 90° açıyla esmesi durumunda dış basınç katsayı değerleri

h/d=0.19	Rüzgarın W_y 90 açıyla esmesi durumunda				
Bölge	A	B	C	D	E
$c_{pe,10}$	-1.2	-0.8	-0.5	0.7	-0.3
$c_{pe,net}$	-1.2	-0.8	-0.5	0.7	-0.3
$q_p(z)$			1.07		
$q_p(z)\cdot c_{pe,net}$	-1.28	-0.86	-0.54	0.75	-0.32

Eurocode 1-4 çatı için farklı bir etkime yöntemi belirlemiştir. Çatıyı farklı bölümlere ayırarak her bir bölüme farklı rüzgar basınç katsayılarını etki ettirerek değerlendirir ve bölgelere bu yöntem sayesinde farklı rüzgar yükleri etkimiş olur. Bu projede, 11.31° eğime sahip çift eğimli çatı tasarımı yapılmış ve bu doğrultuda örnek modeller oluşturulmuştur. Tablo 13 ve Tablo 14'te, çift eğimli çatılar için dış basınç katsayıları interpolasyon yöntemi kullanılarak hesaplanmış ve sunulmuştur.

Tablo 13. Rüzgarın W_x 0° açıyla esmesi durumunda dış basınç katsayıları

	Rüzgarın W_x 0° açıyla esmesi durumunda				
Bölge	F	G	H	I	J
5°	-1.7	-1.2	-0.6	-0.6	0.2
11.31°	-1.2	-0.95	-0.41	-0.47	-0.56
15°	-0.9	-0.8	-0.3	-0.4	-1
$q_p(z).c_{pe,net}$	-1.28	-1.01	-0.44	-0.51	-0.6

Tablo 14. Rüzgarın W_y 90° açıyla esmesi durumunda dış basınç katsayıları

	Rüzgarın W_y 90° açıyla esmesi durumunda			
Bölge	F	G	H	I
5°	-1.6	-1.3	-0.7	-0.6
11.31°	-1.41	-1.3	-0.64	-0.54
15°	-1.3	-1.3	-0.6	-0.5
$q_p(z).c_{pe,net}$	-1.51	-1.39	-0.68	-0.58

Bu projede, düz çatı tipi tasarımı kapsamında keskin kenarlı saçaklar için örnek bir model oluşturulmuştur. Düz çatılar için dış basınç katsayıları Tablo 15'de verilmiştir.

Tablo 15. Düz çatılar için dış basınç katsayıları

Bölge	F	G	H	I
Keskin kenarlı saçaklar	-1.8	-1.2	-0.7	-0.2
$q_p(z)$		1.07		
$q_p(z).c_{pe,net}$	-1.93	-1.28	-0.75	-0.21

ASCE 7-10 Standardına Göre Çözüm

ASCE 7-10 standardına göre rüzgar hesabı bu bölümde yapılmıştır. Yüzey engebelilik kategorisi, yükseklikleri genellikle 9.1 m altında olan seyrek engellerin bulunduğu açık araziler olarak C kategorisi seçilmiştir. Maruz kalma kategorisi, yapı yüksekliğinin 8 m olması dikkate alınarak, ortalama çatı yüksekliği 9.1 m veya daha az olan binalar için Kategori B olarak belirlenmiştir. Rüzgar doğrultu faktörü K_d 0.85 olarak belirlenmiştir. Yapıların yüksekliği 8 m olduğundan Maruz kalma katsayısı K_z 0.674 olarak hesaplanmış ve Topografik faktör K_{zt} 1.0 olarak alınmıştır. ASCE 7-10 standardında Türkiye için bir rüzgâr hız haritası bulunmadığından, Çelik Yapılar Yönetmeliği'nde rüzgar hızı için alt sınır olarak belirtilen 28 m/s olarak göz önüne alınmıştır. Bu değer ile diğer yönetmeliklerle aynı hız esas alınarak karşılaştırmaların tutarlılığı sağlanmıştır

Örnek yapı modellerinin yüksekliği 8 metre olduğundan, rijit bir bina veya diğer yapı türleri için rüzgâr etkisi faktörü (G) 0,85 olarak alınabilir. Düşük yükseklikteki binaların rijit olarak kabul edilmesine izin verilmektedir. Örnek yapı modelleri kapalı binalar olduğundan dolayı iç basınç katsayıları pozitif ve negatif olarak +0.18 ve -0.18 olarak alınmıştır. Rüzgar basıncı, tüm modeller için ayrı ayrı

hesaplanmış olup, hesaplama sonuçları örnek model A için detaylı olarak Tablo 16 ve 17'de verilmiştir.

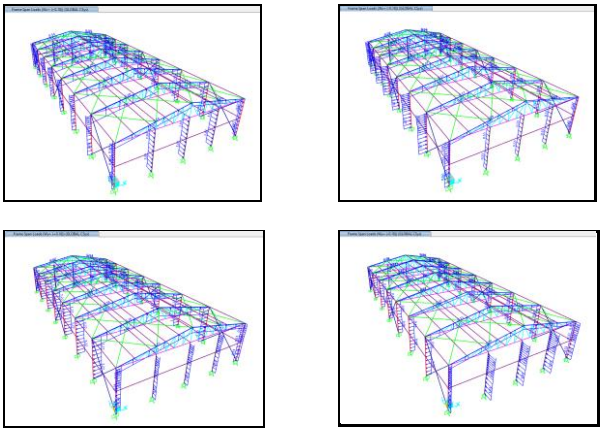
Tablo 16. Model-A W_x (0°) yönünde rüzgar basınç değerleri

MODEL-A W_x Yönü (0°)	h (m)	B K_z	q_z (N/m²)	G	C_p	Net Basınç N/m²	
						GC_{pi}=+ 0.18	GC_{pi}=- 0.18
Rüzgara Dik Duvar	0-4.6	0.57	232.85	0.85	0.8	110.98	205.689
	6	0.62	253.27	0.85	0.8	124.871	219.578
Rüzgar Arkası Duvar	hepsi	0.644	263.08	0.85	-0.5	-159.161	-64.453
Çapraz Duvarlar	hepsi	0.644	263.08	0.85	-0.7	-203.883	-109.176
Rüzgar Yönündeki Çatı	hepsi	0.644	263.08	0.85	-0.85	-237.426	-142.71
					-0.18	-87.604	7.103
Rüzgar Arkası Çatı	hepsi	0.644	263.08	0.85	-0.5	-159.161	-64.453

Tablo 17. Model-A W_y (90°) yönünde rüzgar basınç değerleri

MODEL A Wy Yönü (90°)	h (m)	B (k_z)	q_z (N/m²)	G	c_p	Net Basınç	
						GC_{pi}=+ 0.18	GC_{pi}=- 0.18
Rüzgara Dik Duvar	0-4.6	0.57	232.85	0.85	0.8	110.98	205.68
	6	0.62	253.27	0.85	0.8	124.87	219.57
Rüzgar Arkası Duvar	hepsi	0.64	263.08	0.85	-0.3	-114.43	-19.73
Çapraz Duvarlar	hepsi	0.64	263.08	0.85	-0.7	-203.88	-109.17
Çatı	0-7 m	0.64	263.08	0.85	-0.9	-248.60	-153.89
					-0.18	-87.60	7.10
	7-14 m	0.64	263.08	0.85	-0.5	-159.16	-64.45
					-0.18	-87.60	7.10
	14-42 m	0.64	263.08	0.85	-0.3	-114.43	-19.73

Örnek olarak Model A için duvarlarda ve çatıda oluşan rüzgar yüklemeleri aşağıda Şekil 12'de gösterilmiştir.

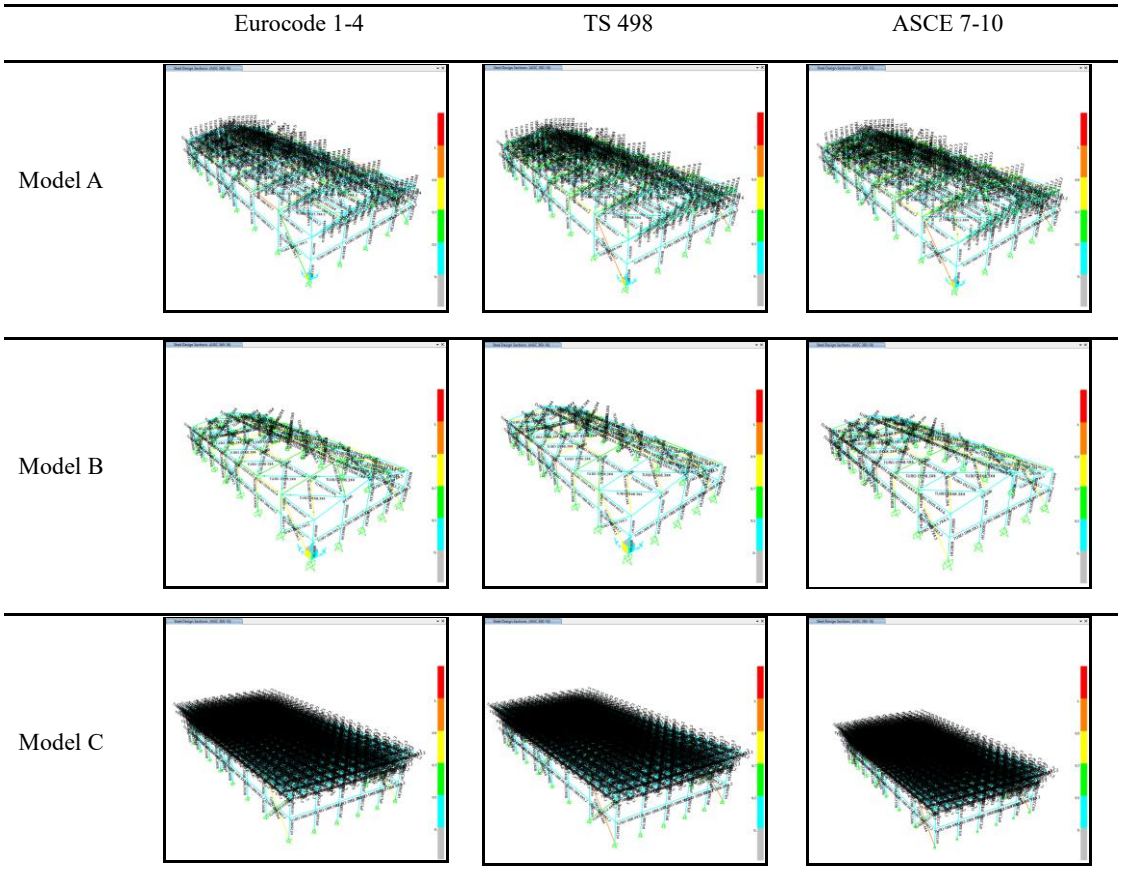


Şekil 12. ASCE 7-10 standardına göre Model A yapısı üzerinde etki eden rüzgar yüklemeleri

Bulgular ve Tartışma

Bu bölümde, SAP 2000 programı kullanılarak yapıların modelleri oluşturulmuş ve analizleri yapılmıştır. Yönetmeliklere uygun olarak değerler hesaplanıp kontrol edilmiş ve elde edilen hesaplar sonucunda da yapının dayanıklılığı ve ekonomik yönü incelenmiştir.

Yapı elemanlarının kapasite kullanım oranlarına ilişkin üç boyutlu görseller, gerçekleştirilen analizler sonucunda elde edilen değerler doğrultusunda hazırlanmıştır. Bu görseller Şekil 13'te detaylı bir şekilde sunulmuştur.



Şekil 13. ASCE 7-10 standardına göre Model A yapısı üzerinde etki eden rüzgar yüklemeleri

Kesit zorlanmaları, yalnızca rüzgar yükleri içeren kombinasyonlar göz önünde bulundurularak analiz edildiğinde; Model A için yapılan kesit incelemelerinde Eurocode 1-4 standardında, en fazla zorlanma gözlemlenen kesitlerin A 2-3, A 6-7 ve E 2-3, E 6-7 aksları arasında yer alan stabilite kirişlerinde meydana geldiği belirlenmiştir. Bu kesitler için dayanım oranı (D/C) 0.91 olarak tespit edilmiştir. Ayrıca, 1. ve 8. aks üzerindeki çatı makaslarının birleşim noktasında bulunan alın dikmelerinde de zorlanmalar meydana gelmiş olup, bu noktalardaki dayanım oranı 0.9 olarak hesaplanmıştır. TS 498 standardına göre yapılan kesit incelemelerinde, aynı akslarda bulunan stabilite kirişlerinde zorlanmalar oluşmuş ve bu kesitler için dayanım oranı 0.8 olarak tespit edilmiştir. Benzer şekilde, 1. ve 8. akslar üzerindeki çatı makaslarının birleşim noktasında bulunan alın dikmelerinde de gerilmeler gözlemlenmiş olup, bu noktadaki dayanım oranı 0.78 olarak hesaplanmıştır. ASCE 7-10 standardında yapılan incelemelerde ise, aynı akslarda bulunan stabilite kirişlerinde gerilmeler meydana gelmiş ve bu kesitler için dayanım oranı 0.81 olarak belirlenmiştir. A 1-2, A 7-8 ve E 1-2, E 7-8 aksları arasında bulunan cephe çaplarında da zorlanmalar oluşmuş olup ve bu kesitler için dayanım oranı 0.74 olarak tespit edilmiştir.

Model B'nin kesit yapısı üzerinde gerçekleştirilen analizler sonucunda, en fazla zorlanmanın gözlemlendiği kesitlerin A 6-7 ve, E 6-7 aksları arasında yer alan stabilite kirişlerinde meydana gelmiştir.

Model C'nin yapısal analiz sonuçları incelendiğinde ise, en fazla zorlanmanın A 7-8 ve F 7-8 aksları arasında yer alan cephe çaprazlarında meydana geldiği tespit edilmiştir.

Modellerin analizleri sonucunda seçilen kesitler detaylı bir şekilde aşağıdaki Tablo 18-20'de listelenmiştir. Eurocode 1-4 için genel olarak daha büyük kesitler kullanılmıştır. Model C'nin yapı ağırlığının Model A ve Model B'ye kıyasla daha düşük olduğu görülmüştür.

Tablo 18. Model A için kullanılan yönetmelikler ve uygun kesitler

Model A	**Kullanılan Yönetmelikler ve Seçilen Kesitler**		
Yapı Elemanları	Eurocode 1	TS 498	ASCE 7-10
Kolon	HE 220B	HE 200B	HE 180B
Rüzgar Kolonları	HE 340B	HE 240B	HE 200B
Stabilite Kirişler	TUBO- D88.9X3.2 TUBO-D133X4	TUBO-D88.9X3.2 TUBO-D133X4	TUBO-D88.9X3.2 TUBO-D133X4
Çatı üst başlık	IPE 400	IPE 400	IPE 400
Çatı alt başlık	IPE 330	IPE 240	IPE 220
Makas	TUBO-D133X4	TUBO-D108X3.6	TUBO-D76.1X3.2
Çatı Çapraz	TUBO-D193.7X4.5	TUBO-D168.3X4	TUBO-D152.4X4
Cephe Çapraz	TUBO-D193.7X4.5	TUBO-D168.3X4	TUBO-D168.3X4
Alın Dikmesi	HE 160A	HE 100A	HE 100A
Çatı Aşık	UPN 120	UPN 120	UPN 120
Toplam Ağırlık	**59.87 ton**	**50.80 ton**	**46.74 ton**

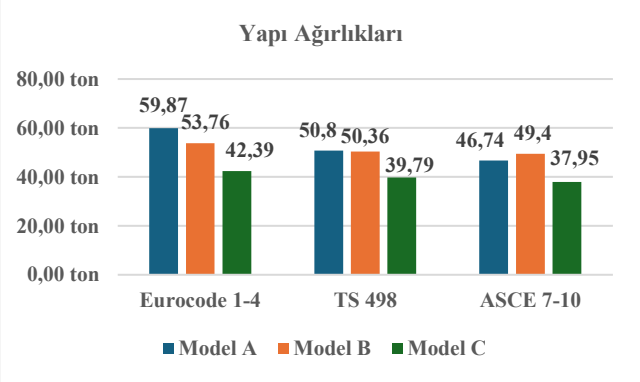
Tablo 19. Model B için kullanılan yönetmelikler ve uygun kesitler

Model B	**Kullanılan Yönetmelikler ve Seçilen Kesitler**		
Yapı Elemanları	Eurocode 1	TS 498	ASCE 7-10
Kolon	HE 300B	HE 280B	HE 280B
Rüzgar Kolonları	HE 340B	HE 240B	HE 200B
Stabilite Kirişler	TUBO-D88.9X3.2 TUBO-D101.6X3.6 TUBO-D127X4 TUBO-D168.3X4	TUBO-D88.9X3.2 TUBO-D101.6X3.6 TUBO-D127X4 TUBO-D193.7X4.5	TUBO-D88.9X3.2 TUBO-D101.6X3.6 TUBO-D127X4 TUBO-D193.7X4.5
Çatı üst başlık	IPE 500	IPE 500	IPE 500
Çatı Çapraz	TUBO-D168.3X4	TUBO-D168.3X4	TUBO-D168.3X4
Cephe Çapraz	TUBO-D193.7X4.5	TUBO-D193.7X4.5	TUBO-D193.7X4.5
ÇatıAşık	UPN 120	UPN 120	UPN 120
Toplam Ağırlık	**53.76 ton**	**50.36 ton**	**49.40 ton**

Tablo 20. Model C için kullanılan yönetmelikler ve uygun kesitler

Model C	Kullanılan Yönetmelikler ve Seçilen Kesitler		
Yapı Elemanları	Eurocode 1	TS 498	ASCE 7-10
Kolon	HE 260B	HE 240B	HE 220B
Rüzgar Kolonları	IPE 500	IPE 360	IPE 300
Stabilite Kirişler	TUBO-D88.9X3.2	TUBO-D88.9X3.2	TUBO-D88.9X3.2
Çatı üst başlık	TUBO-D88.9X3.2	TUBO-D88.9X3.2	TUBO-D88.9X3.2
Çatı alt başlık	TUBO-D88.9X3.2	TUBO-D88.9X3.2	TUBO-D88.9X3.2
Diyagonel	TUBO-D76.1X3.2	TUBO-D76.1X3.2	TUBO-D76.1X3.2
Cephe Çapraz	TUBO-D159X4	TUBO-D152.4X4	TUBO-D152.4X4
Toplam Ağırlık	**42.39 ton**	**39.79 ton**	**37.95 ton**

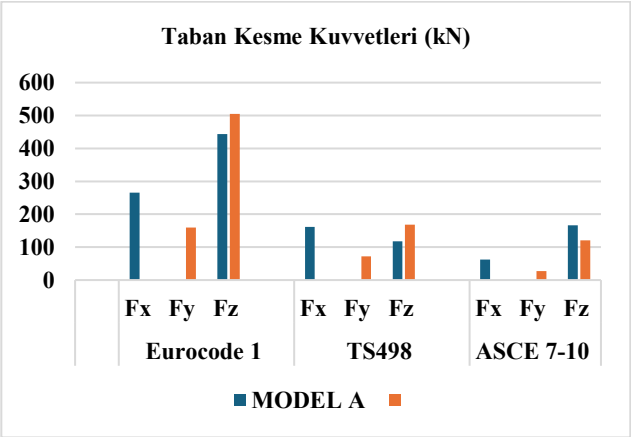
Aşağıda, Şekil 13'te yapıların ağırlıkları karşılaştırmalı bir şekilde grafiksel olarak verilmiştir. Burada, en düşük yapı ağırlığı 37.95 ton ile C yapı sistemi için hesaplanırken, en yüksek yapı ağırlığı 59.87 ton ile A yapı sistemi için belirlenmiştir.



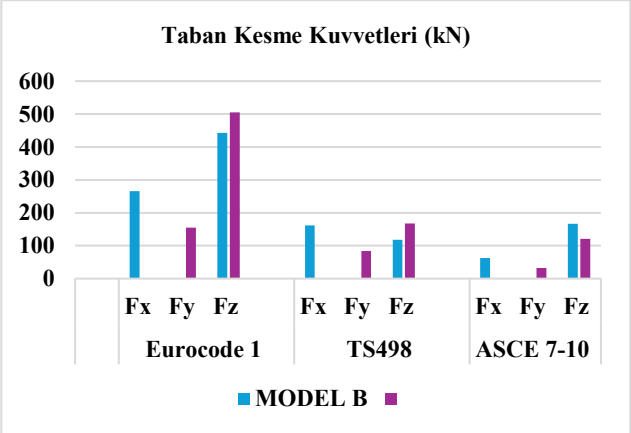
Şekil 14. Yapı ağırlıkları

Taban Kesme Kuvvetleri

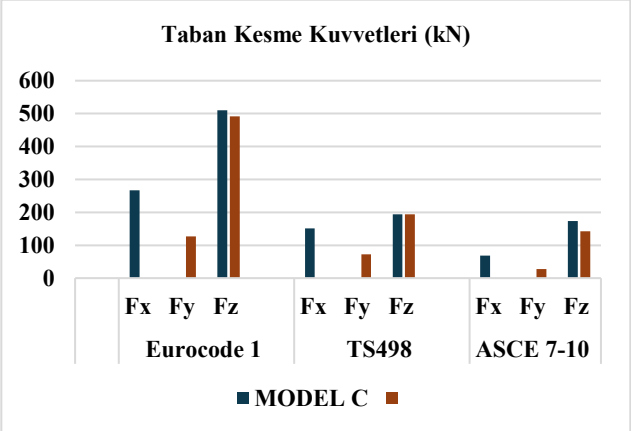
Şekil 14, Şekil 15 ve Şekil 16'da, Eurocode 1-4, TS 498 ve ASCE 7-10 standartlarına göre rüzgar yüklemeleri sonucunda oluşan taban kesme kuvvet değerleri, Model A, Model B ve Model C için karşılaştırmalı bir şekilde grafiksel olarak sunulmuştur. F_x, W_x yönünde esen rüzgarın yapı üzerinde oluşturduğu taban kesme kuvvetini ifade ederken, F_y, W_y yönünde esen rüzgarın oluşturduğu taban kesme kuvvetini ifade etmektedir. F_z ise, W_x ve W_y yönlerinde esen rüzgarların oluşturduğu düşey tepki kuvvetini ifade etmektedir. Üç modelin taban kesme kuvvetleri karşılaştırıldığında, Eurocode 1-4 standardı ile hesaplanan değerlerin diğer standartlara göre daha yüksek olduğu görülmüştür. ASCE 7-10 standardı ise daha düşük taban kesme kuvveti değerleri ortaya koyarken, TS 498 standardı her iki yaklaşım arasında orta değerlerde kaldığı gözlemlenmiştir.



Şekil 15. Model A için ilgili standartlara göre hesaplanan taban kesme kuvvetleri (kN)



Şekil 16. Model B için ilgili standartlara göre hesaplanan taban kesme kuvvetleri (kN)



Şekil 17. Model C için ilgili standartlara göre hesaplanan taban kesme kuvvetleri (kN)

ASCE 7-10 sonuçlarının daha düşük çıkmasının bir nedeni de yapının görece alçak (8 m) olmasıdır. Bu yükseklikte ASCE'nin maruziyet katsayısı (K_z) düşük kalmakta, Eurocode'un ise türbülans ve basınç bölgelerini ayrıntılı şekilde dikkate alması daha yüksek rüzgâr yüklerinin hesaplanmasına yol açmaktadır.

Sonuç

Üç farklı endüstri tipi çelik yapı modeli üzerinde yapılan analizlerde, TS 498, Eurocode 1-4 ve ASCE 7-10 standartlarına göre hesaplanan rüzgâr yüklerinin yapı davranışları üzerinde belirgin farklar oluşturduğu görülmüştür. Yapı ağırlıkları bakımından Eurocode 1-4 en yüksek değerleri vermiş, TS 498 ortalama %6–15, ASCE 7-10 ise %8–22 oranında daha hafif çözümler ortaya koymuştur. Taban kesme kuvvetleri açısından ise Eurocode 1-4 tüm modellerde en büyük değerleri üretmiş; TS 498 sonuçları Eurocode'a kıyasla ortalama %40–65 daha düşük taban kesme kuvvetleri, ASCE 7-10 sonuçları ise %70–80 oranında daha düşük taban kesme kuvvetleri oluşturmuştur.

Bu farklılıkların temel nedenleri yönetmeliklerin hesaplama yaklaşımlarından kaynaklanmaktadır. Eurocode 1-4, cephe ve çatı yüzeylerini farklı basınç bölgelerine ayırarak her bölgeye özgü basınç katsayıları tanımlamakta, ayrıca türbülans ve pürüzlülük etkilerini ayrıntılı şekilde dikkate almaktadır. Bu yaklaşım, rüzgâr yüklerinin daha yüksek hesaplanmasına ve dolayısıyla daha büyük kesitlerin seçilmesine yol açmaktadır. ASCE 7-10 ise yapı yüksekliği, topoğrafya, maruziyet kategorileri ve rüzgâr doğrultu faktörü gibi parametreleri dikkate almakla birlikte, 3 saniyelik ani rüzgâr hızını esas alması ve maruziyet katsayısının 8 m gibi görece düşük yapılarda küçük kalması nedeniyle daha düşük taban kesme kuvvetleri ve daha hafif çözümler üretmektedir. TS 498'de ise çatı yüzeyleri farklı bölgelere ayrılmamakta, yüklemeler homojen olarak etki ettirilmektedir. Rüzgâr yüküne etki eden faktörler ise sabit katsayılarla hesaba katılmaktadır; bu durum hesaplama açısından pratiklik sağlarken, detaylı değerlendirme açısından bu yönetmeliğin zayıf kalmasına yol açmaktadır.

Sonuç olarak, rüzgâr yüklerinin hesaplanmasında kullanılan standart seçiminin, çelik yapıların kesit boyutları, ağırlıkları ve güvenlik düzeyleri üzerinde doğrudan belirleyici olduğu görülmektedir.

Kaynakça

[1] S. M. Azıtepe and B. Sözen, "Çelik Yapıların İnsanlardaki Görsel Algısı Üzerine Bir Araştırma," *Akdeniz Univ. J. Fac. Archit.*, vol. 1, no. 2, pp. 135–150, 2022.

[2] Y. Dikiciaşık, İ. T. Sen, and S. Çarbaş, "Endüstriyel Hangar Tipi Çelik Yapıda Farklı Makas ve Çapraz Türlerinin Yapısal Sistem Üzerindeki Etkilerinin İncelenmesi TT - Investigation The Effects Of Various Truss And Brace Kinds On The Structural System In Industrial Hangar Type Steel Structure," *Int. J. Eng. Res. Dev.*, vol. 15, no. 3, pp. 209–233, 2023, doi: 10.29137/umagd.1362366.

[3] S. Sancıoğlu, S. Arıbaş, B. Bayram, M. Şimşek, and S. Çarbaş, "Çelik Bir Binada Kullanılan Çapraz Tiplerinin Deprem Etkisi Altında Analizi," 2019.

[4] F. Ü. Peker and E. Işık, "TBDY-2018'deki yerel zemin koşullarının çelik yapı deprem davranışına etkisi üzerine bir çalışma," *Bitlis Eren Üniversitesi Fen Bilim. Derg.*, vol. 10, no. 3, pp. 1125–1139, 2021.

[5] İ. B. Karaşin, E. Işık, A. Büyüksaraç, and A. Karaşin, "The Comparison of Seismic and Structural Parameters in Steel Structures for Different Spectra," in *International Symposium on Innovative and Interdisciplinary Applications of Advanced Technologies*, 2022, pp. 65–76.

[6] Ö. O. Polat, "Asce 7-05, Eurocode 1-4 Ve Ts 498 Yönetmelikleri Kullanılarak Yapılara Gelen Rüzgar Yüklerinin Karşılaştırılması," 2010.

[7] Anon, *Minimum design loads for buildings and other structures*, no. 7 98. Reston, Virginia: American Society of Civil Engineers (ASCE), 2000. doi: 10.1061/9780872629042.

[8] TS EN 1991-1-4, "Yapılar Üzerindeki Etkiler - Bölüm 1-4: Genel Etkiler-Rüzgar Etkileri (Eurocode 1)," 2007.

[9] T. S. E. (TSE), "Yapı elemanlarının boyutlandırılmasında alınacak yüklerin hesap değerleri," *Ankara, Türkiye*, vol. 498.

[10] C. Özlek, "ASCE 7-10, Eurocode 1-4 Ve Ts 498 Yönetmelikleri Kullanılarak Yapılara Etki Eden Rüzgar Yüklerinin Karşılaştırılması," 2015.

[11] A. Engineers, "Minimum design loads for buildings and other structures," *ASCE 7*, vol. 10, 2010.

[12] H. Zeyrek and S. Bekiroğlu, "Assessment of wind pressure by eurocode-1, ts 498 and cfd analyses for double-sloped roof building," *Sigma J. Eng. Nat. Sci.*, vol. 37, no. 1, pp. 251–272, 2019.

[13] I. Bashir, "Comparative study of an rc chimney as per different codes." Middle East Technical University (Turkey), 2019.

[14] S. Aghaei, "Tek Katlı Endüstryel Yapıların Çatı Sistemlerinin Ekonomik Tasarımı." Konya Teknik Üniversitesi, 2022.

[15] Computers & Structures Inc, "Sap 2000," *Sap 2000*. 2019.

[16] A. E. Sever and İ. Yüksel, "Bir Yüksek Bina Özelinde Asce-7-16 Ve Ts-498 Standartlarına Göre Hesaplanan Rüzgar Yüklerinin Karşılaştırılmasi," *Uluslararası Sürdürülebilir Mühendislik ve Teknol. Derg.*, vol. 6, no. 2, pp. 66–79, 2022.

[17] T. S. EN, "1-3 (Yapılar Üzerindeki Etkiler Bölüm 1-3: Genel Etkiler-Kar Yükleri). 2007," *Ankara Türk Stand. Enstitüsü*, 1991.

[18] *Çelik Yapıların Tasarım, Hesap ve Yapım Esaslarına Dair Yönetmelik*. Ankara: Çevre ve Şehircilik Bakanlığı, 2018.

[19] TBDY, *Türkiye Bina Deprem Yönetmeliği*. Ankara: Afet ve Acil Durum Yönetimi Başkanlığı, 2018.

[20] AFAD, "Türkiye Deprem Tehlike Haritası," 2024. https://tdth.afad.gov.tr/)

Dicle University
Journal of Engineering
https://dergipark.org.tr/tr/pub/dumf
duje.dicle.edu.tr

Research Article

Seismic Risk Assessment of Existing RC Buildings in Muğla

Vesile Hatun AKANSEL[1*], Mehmet Artun BAKİ[2]

[1] Ankara Yıldırım Beyazıt University, Civil Engineering Department, vhakansel@aybu.edu.tr, Orcid No: 0000-0003-3152-1215
[2] Ministry of Interior, Disaster and Emergency Management Presidency, m.artunbaki@gmail.com, Orcid No 0000-0002-6549-8386

ARTICLE INFO

Article history:

Received 26 July 2025
Received in revised form 17 August 2025
Accepted 18 August 2025
Available online 30 September 2025

Keywords:

Seismic Vulnerability, Walk-Down Survey, Preliminary Assessment, Reinforced Concrete Building

Doi: 10.24012/dumf.1751630

* Corresponding author

ABSTRACT

Turkey is located in a highly seismic region and has experienced major earthquakes with substantial casualties and economic losses in the past two decades. The February 6, 2023, Mw 7.7 and 7.6 sequential earthquakes were catastrophic ones that affected eleven cities with many casualties and high economic losses. The increased financial burden would not be necessary if our building stock were in decent shape. Therefore, it is critical to assess the seismic vulnerability of existing buildings to be able to take precautions. Muğla is one of the high-seismic cities located in the western part of Türkiye. In this study, a walk-down survey method proposed by the code The Principles of Identifying Risky Buildings (RYTEIE, 2019), a simple and rapid method, is used to assess the risk levels of RC buildings in the Emirbeyazıt neighborhood of Menteşe, Muğla. 469 RC buildings are examined considering parameters such as age, number of stories, and technical deficiencies, including soft or weak stories. The performance score is calculated for each building and ranked in ascending order to decide the risk prioritization. 26 RC buildings were selected from a different range of performance scores to be able to evaluate the preliminary assessment method using the concrete compressive strength and confinement rebar searched by non-destructive testing methods. The blueprints were used to calculate the base shear capacities and assessed by a preliminary assessment method to observe the performance levels and relationship with performance score.

Introduction

Turkey is situated in a highly seismic region, where the active tectonic plates can cause major earthquakes. The February 6, 2023 Kahramanmaraş earthquake sequence was catastrophic and resulted in many casualties and high economic losses. It affected eleven cities and the building stock showed poor performance with heavy and collapse damage. The increased financial burden would not be necessary if our building stock were in decent shape. This situation initiates the urgent necessity for the risk assessment of the existing building stock [1]. Principles for Identifying Risky Structures (RYTEİE, [2]) introduce a walk-down survey and ranking system for the regional risk assessment for existing reinforced concrete and masonry buildings.

The risk assessment can be classified into three groups. The walk-down method is the simplest, requiring few queries to identify deficiencies and calculate a performance score, which is similar to the approach used by RYTEİE (2019) [2], [3] and Coskun et al. (2020) [4]. The second group includes more parameters and calculations to check the capacity or capacity-related parameters. Hassan and Sozen (1997) [5] studied seismic vulnerability assessment of low-rise buildings. They adapted the risk assessment method proposed by Shiga, Schibata, and Takahashi in Erzincan [6], which was developed after the 1968 Tokachi-Oki earthquake. Sucuoğlu et al. (2007) [7] developed a risk assessment method for reinforced concrete buildings in urban building stocks, and 16,523 reinforced concrete buildings in the Fatih district were examined using the walk-down survey procedure. Yakut (2004) [8] and Yakut et al.(2012) [9] used workmanship or capacity concepts to develop risk ranking methodologies. Coskun et al. (2020) [4] developed a preliminary assessment method using statistical methods for the walk-down assessment parameters for the 2020 Elazığ earthquake. The third group of the risk assessment is the detailed analysis, such proposed in RYTEİE (2019) [2] for risk assessment and Turkish Building Earthquake Code (TBEC 2018) [10] performance assessment.

This study aims to predict the vulnerability of existing RC buildings in Mugla, Emirbeyazıt Neighborhood, which is given in Fig.1, using the walkdown survey method according to RYTEİE (2019) and preliminary assessment technique (Yakut 2004) [8] to make a risk ranking and performance check to create a database for the existing buildings of Muğla Emirbeyazıt Neighborhood, since no similar research exists in this location. This study is

focused on the parameters such as age of the buildings, the occupancy type, the number of stories, vertical and plan irregularities, seismic intensity, strength of the concrete, soil type, the apparent quality, and the construction quality. Approximately 469 buildings have been evaluated with a walk-down survey according to RYTEİE (2019) [2], and performance scores are evaluated, and 26 buildings have been examined from these rankings to investigate the performance according to the Yakut (2004) [8] procedure. The results are expressed separately for each building by calculating a performance score.



Figure 1 Muğla, Emirbeyazıt Neighborhood (The Survey Area)

The Methodology

Walk-Down Survey

Many risk assessment methods have been developed by researchers for reinforced concrete buildings in urban settlements as described above. A walk-down survey, which is the simplest method, is used to identify the risky RC buildings for regional risk assessment purposes. The analysis, data collection, and decision-making process are carried out in the field, and the average time spent per building is approximately 15 to 30 minutes. The main purpose is to create a ranking according to the evaluated performance score for each building and allow the decision makers to take precautions for potentially risky buildings via a more detailed performance assessment and retrofitting options.

The age of building, the occupancy type, the number of stories, the vertical and plan irregularities, seismic hazard, apparent quality, heavy overhangs, and structural system type are some of these parameters required for RYTEİE (2019) [2] walk-down survey method, which is given in Fig. 2. The stated parameters can be determined quite easily in site-investigation. The year of construction, or namely the age of the building, gives an idea about the seismic code in force during construction and can be observed on site if the structural member sizes are not suitable to the recent code in force. More details about the parameters used in the survey are given in Fig. 2.

Technical deficiencies such as soft story, overhang and apparent quality are described in detail with photos from the site investigation to clarify how the database is constructed.

Soft Story

Soft stories usually exist in buildings when the ground story has less stiffness and strength compared to upper stories [7], . Generally, it can be observed in buildings where the infill walls are removed or discontinuous vertically. Fig. 3 gives structure examples with the soft stories in the site investigation.

BUILDING ID FORM					Date:	
					No:	
Builidng ID						
City						
Sub-premises						
District						
Street						
Builidng No					PHOTO	
Block						
Lot						
Parcel						
UAVT Code						
Estimated Age of Building						
Coordinates	LATITUDE :			LONGITUDE :		
Occupancy Type	☐ Residential	☐ Commercial	☐ Industrial	☐ Government	☐ Disused	
Building Technical Details						
Structural System	☐ RC Frame		☐ RC Frame with Shear Wall			
Number of Stories						
Apparent Quality	☐ Good	☐ Modarate	☐ Bad			
Soft / Weak Story	☐ Yes	☐ No				
Vertical Irregularity	☐ Yes	☐ No				
Overhang	☐ Yes	☐ No				
Plan Irregularity	☐ Yes	☐ No				
Short Ccolumn	☐ Yes	☐ No				
Adjacency	☐ Seperate	☐ Adjacent	☐ Adjacent at corner			
Floor Level in Adjacent Buildings	☐ Same	☐ Different				
Elevation	☐ Straigth	☐ Slope (Slope > 30)				
Site Class	☐ ZA	☐ ZB	☐ ZC	☐ ZD	☐ ZE	
NOTE :						

Figure 2 Data Collection Form for RC Buildings (RYTEİE 2019 *[2]*)



Figure 3 Soft Story Examples

Overhangs

This effect is related to the area changes in the plan between the ground story and the upper stories. According to the Construction Zoning Regulation, open and closed cantilevers can be made on each facade of the building, provided that it does not exceed the boundaries of their garden, except for the floor area. However, heavy overhangs cause mass and stiffness irregularity in the building. Fig. 4 gives examples of heavy overhangs.



Figure 4 Heavy Overhang Examples

Apparent Quality

The apparent quality is examined by observing the overall appearance of the structure in terms of maintenance and evaluations are classified into three levels: good, average, and poor as seen in Fig. 5.

Short Column

A short column is identified when change in floor levels or adjacent partial infill walls may result in a short column effect which makes the column stiffer than surrounding structural members and take more shear forces. Compared to long columns, the short columns are indeed stiffer therefore they take most of the earthquake forces acting on the building. One of the identified short column effect is given in Fig. 5 (c).

which varies with the number of stories for the buildings with shear wall. For frame system, YSP is equal to 0. TP and YSP values are given in Table 1.

$$PP = TP + \sum_{i=1}^{N}(0_i + 0P_i) + YSP \quad (1)$$

O_i is the penalty parameter coefficient and OP_i is the penalty parameter value. The penalty parameters are related to the existence of the situation. In example, if there exist soft story in the building, it is checked as "Yes" and O_i is "1", else it is "0". Similarly, for apparent quality, if it is in

Table 1 Base Score and Structural System Score (RBTEİE 2019 Table A.1)

	Base Score (TP)				Structural System Score (YSP)	
	Hazard Zone				Structural System	
	I	II	III	IV	RC Frame	RC Frame w/Shear Walls
1 and 2	90	120	160	195	0	100
3	80	100	140	170	0	85
4	70	90	130	160	0	75
5	60	80	110	135	0	65
6 and 7	50	65	90	110	0	55

Table 2 Technical Deficiencies and The Penalty Parameter Coefficients, O_i (RBTEİE 2019 Table A.3)

Parameter Number	Technical Deficiency	Situation 1		Situation 2	
		Parameter Existence	Parameter Coefficient	Parameter Existence	Parameter Coefficient
1	Apparent Quality	Good	0	Moderate (Bad)	1 (2)
2	Soft Story	No		Yes	1
3	Heavy Overhang	No		Yes	
4	Vertical Irregularity	No		Yes	
5	Plan Irregularity	No		Yes	
6	Short Column	No		Yes	
7	Adjacency	Separate		Adj. / Corner	
8	Slope	No		Yes	



Figure 5 Apparent Quality Evaluation (a, b, c) and Short Column Effect (c) Examples

Performance Score Calculation According to RYTEİE (2019) [2] *Walk-Down Survey Method*

In RYTEİE (2019) [2], Annex A is related a ranking method using the walk-down survey parameters. The performance score is calculated for each building according to Eq. 1. TP is the base score which varies depending on the number of stories and seismic zone. YSP is the structural system score

"Good" condition that is "0", else if it is "Moderate", that is "1" and else it is "2". (Table 2)

According to the identified existence of the technical deficiency parameters, the penalty parameter score is chosen from Table 3 to multiply with the penalty parameter coefficients. Calculated performance scores (Eq.1) are ranked in ascending order. By using the ranked scores, the risk priority can be determined for the region and the decision makers such as municipalities can take precautions for probable casualty and economic loss.

Preliminary Assessment Method, Yakut (2004)

The preliminary assessment methods are varies depending on the purpose and the richness of the data availability. In this study Yakut (2004) [8] will be used to perform a second step detailed analysis to compare the capacity check of the buildings according to the regulations in force year built.

Table 3 The Penalty Parameter Score, OP_i (RBTEİE, 2019 Table A.4)

Number of Stories	Soft Story	Apparent Qualtiy	Heavy Overhang	Adjacency / Level of Floors				Vertical ırregularity	Plan Irregularity	Short Column	Slope
				Same		Different					
				Middle	Edge	Middle	Edge				
1,2	-10	-10	-10	0	-10	-5	-15	-5	-5	-5	-3
3	-20	-10	-20	0	-10	-5	-15	-10	-10	-5	-3
4	-30	-15	-30	0	-10	-5	-15	-15	-10	-5	-3
5	-30	-25	-30	0	-10	-5	-15	-15	-10	-5	-3
6,7	-30	-30	-30	0	-10	-5	-15	-15	-10	-5	-3

The preliminary assessment methods need more variable most of the time. Yakut (2004) [8] needs extra variables such as sizes and dimensions of the structural components, material mechanical properties and blueprints for the plan layouts in addition to the walk-down survey parameters. In this method, comprehensive field studies are performed to collect the data relevant to building characteristics. The base shear capacity for each building is calculated by using the Eq. 2. "V_{ci}" represents the shear capacity of the rectangular reinforced concrete column in dimensions of b_w and h. "f_{ctk}" is the reinforced concrete tensile strength. "c" is taken as 2/3 in the considered direction and 1/3 for for the other one. The value of "a" is chosen as 0.65 which is as given by TS500 for RC buildings.

$$V_{ci} = caf_{ctk}b_w h \quad (2)$$

The recommended compressive strength of reinforced concrete values for the apparent quality technical deficiency parameters from site investigation are given in Table 4. The compressive strength of the concrete can also be determined using the non-destructive testing method such as Schmidt hammer test. The tensile strength of reinforced concrete is related to compressive strength directly.

Table 4 Recommended f_{ck} values by Yakut (2004), [8]

Apparent quality (from visual inspection)	Recommended compressive strength (f_{ck}) (MPa)
Poor	<10
Average	10-16
Good	>16

V_y, which represents yield base shear capacity without infill walls, is calculated by Eq. 3. In this equation, it is assumed that no infill walls contributing to the lateral load resistance [11]. If the infill walls included in the lateral resistance, then taken into account using the ratio of the total infill wall cross-sectional areas, A_w, to the total floor area, A_{tf}. V_{yw} which represents yield base shear capacity with infill wall can be determine by Eq. 4 as given.

$$V_y = \frac{V_c}{0.95^{0.125n}} \quad (3)$$

$$V_{yw} = V_y\left(46\frac{A_w}{A_{tf}} + 1\right) \quad (4)$$

Basic Capacity Index (BCPI) is computed from Eq. 5 by dividing V_{yw} to the code specified design base shear V_{code}.

$$BCPI = \frac{V_{yw}}{V_{CODE}} \quad (5)$$

In Eq. 6, Capacity Index (CPI) has been developed using the Basic Capacity Index (BCPI) in order to take into account the effects such as soft story, heavy overhangs, torsional irregularity. Two coefficients derived from visual inspection are used. C_A and C_M are coefficients that reflect the architectural features and construction quality, respectively.

$$CPI = C_A C_M BCPI \quad (6)$$

In Eq. 7, C_{AS} reflects the soft story and C_{ASC} takes into account the presence of short column effect. C_{AP} and C_{AF} stand for plan irregularity and frame discontinuity, respectively. In order to prevent relative values for the parameters used during the calculation of the C_A value, the Table 5 has been given.

$$C_A = 1.0 - (C_{AS} + C_{ASC} + C_{AP} + C_{AF}) \quad (7)$$

Table 5 Adapted from Yakut, 2004, *[8]*

	FEMA 154	GULKAN and Yakut	Sucuoğlu and Yazgan
C_{AS}	0.36	0.5	0.32
C_{ASC}	0.18	0.25	0.11
C_{AP}	0.19	0.125	0.19
C_{AF}	0.27	0.125	0.38

In Table 6, the suggested C_M, where it is defined for the material and workmanship quality, formulas are given [8]. In this study, Q_r value is considered as 0.55 for Turkey which is suggested by Yakut, 2004, [8]. The CPI is calculated for each building and it is decided whether the buildings are safe or not.

Table 6 Suggested C_M values (Yakut, 2004, *[8]*)

Poor	$1.0 - Q_r (1 - C_A)$
Average	$1.0 - Q_r (1 - C_A)/3$
Good	1

Results

The results are evaluated in two parts as the walk-down survey and preliminary analysis results.

The Walk-Down Survey Results

A total of 469 RC buildings were examined and walk-down survey parameters are collected. In buildings that do not have an earthquake design, the horizontal loads create a great risk with incomplete capacity design. The number of stories in a building is an essential parameter for earthquake design and Fig 6. displays the number of buildings for varying story numbers for the investigated database.

In Fig. 7, different classifications are displaced to observe the data. The buildings are classified according to their occupancy type as 93% residential, 5% government and 2% commercial buildings. 77% of the buildings are reinforced concrete frame system and the rest have a structural system type as reinforced concrete frame with shear walls. It has been determined that the apparent quality of 35% of the buildings is "Bad", 44% is "Medium" and 21% is "Good".

The majority of the buildings suffer from the heavy overhang effects. Heavy overhangs were observed in 82% of the buildings examined. Among all buildings, 27% of the buildings have a plan irregularity.

Another problem mostly observed in buildings was the irregularities in the vertical. The vertical irregularity caused by the discontinuity of the vertical elements of the structural system was found in 68% of the buildings examined. Among these buildings, the soft story was the most common problem encountered. Furthermore, gusset-supported cantilever beams or columns were also determined. Soft story irregularity was encountered in 65% of the total buildings. Short column effect, which is one of the other weaknesses that negatively affects the behavior of the buildings during earthquakes, is not common and the ratio is at the level of 22% in database.

Another important parameter is the floor level difference between adjacent buildings. Leveling differences of adjacent buildings can increase the failure during earthquake. Since 62% of the buildings are separate, the probability of collapse is less than the adjacent ones. The floor level of 25% of the adjacent buildings is at same level or critical and at different levels in 12% of adjacent buildings.

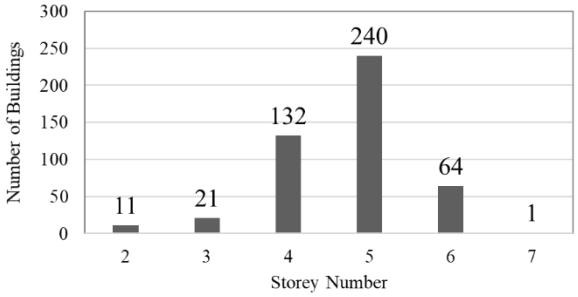


Figure 6 Distribution of the number of stories in the database

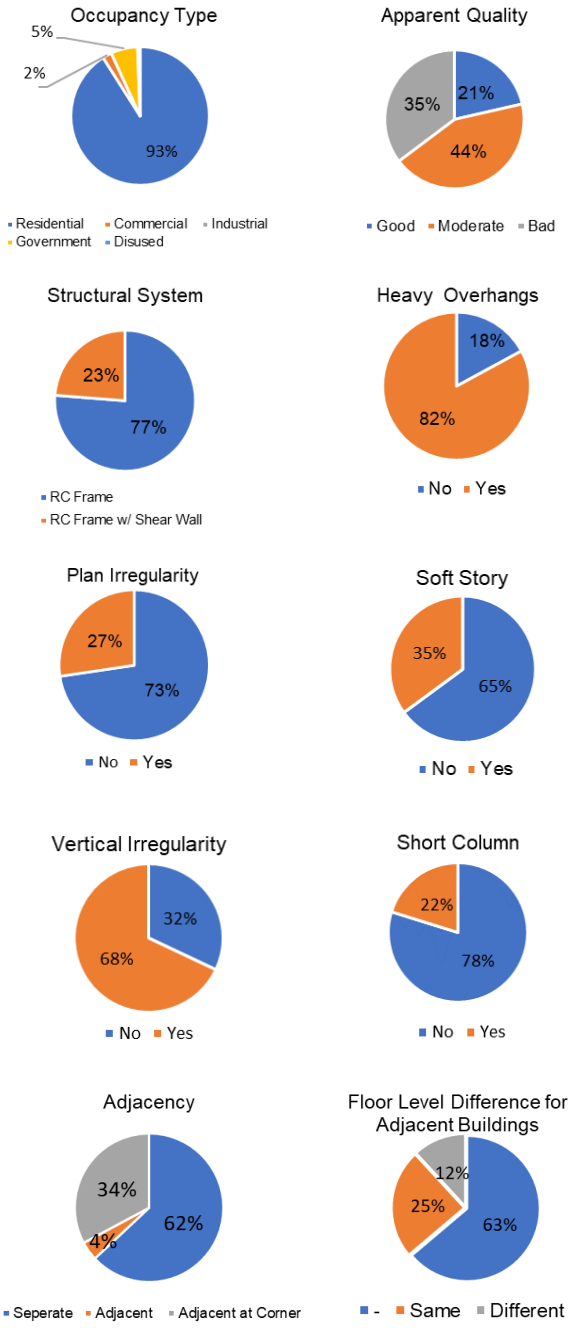


Figure 7 Classified Data for RYTEİE (2019) survey parameters

The performance score results of walk-down method according to RYTEİE (2019) [2] are given for all reinforced concrete buildings in Fig. 8. 249 buildings received less than zero performance score. The lowest performance score is -118. The performance score of 8 buildings is calculated as zero. The remaining reinforced concrete buildings score is higher than zero, but the highest performance score is 145. The walk-down survey method proposed by [2] is a ranking system there for the result given in Fig. 8 is ranked in an ascending order. There is no limit or threshold value for risk prioritization. The decision makers can use this data to create their risk mitigation plan.

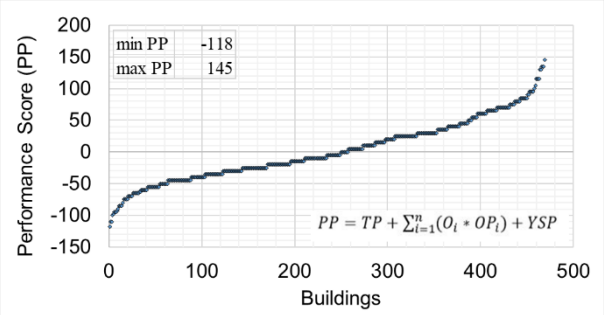


Figure 8 Performance Points calculated according to RYTEİE (2019) *[2]* of the buildings examined

Preliminary Assessment Results

In this study, Yakut (2004) [8] one of the preliminary methods which is derived using Türkiye database. There is no threshold limit for the performance scores obtained by the walk-down method [2] and it is a ranking system. Preliminary assessment methods are simpler than detailed performance analysis, but require more data than screening procedure. In this study, the geometrical properties of the structural elements, mechanical properties of the materials, and plan layouts were taken into account. The earthquake regulations in-force the year built for each building was considered to calculate base shear capacities [12] [13] [14] [15] [16] [17]. The earthquake regulations in-force for the selected buildings and corresponding base shear capacities were given in Table 7.

A building set consisting of 52 buildings was selected in order to make a preliminary assessment study among the dataset from the site investigation. A second field study was performed for this selected building set, to determine the concrete strength with the Schmidth hammer test and confinement rebar detection. The f_{ck} values in Fig. 9 were calculated from R values of Schmidth hammer test conversion curve. The existence of confinement rebar in the columns and shear walls also investigated.

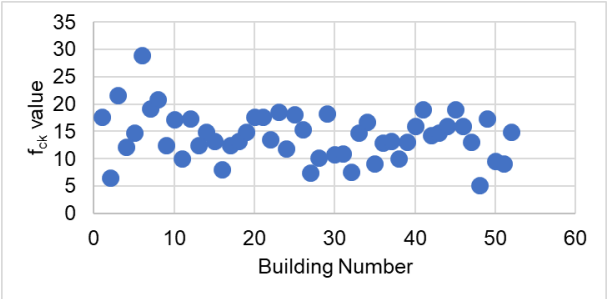


Figure 9 Schmidth test f_{ck} values of each building

The blueprints of the buildings were taken from the Menteşe Municipality. However, only 26 building blueprints could be used for being relevant with the existence ones. By using the blueprints and walk-down survey parameters, the selected building were investigated for the risk according to (Yakut 2004) [8]. BCPI refers to basic capacity index and CPI refers to the capacity index. The limit for CPI value is taken as 1.0 [8].

Table 7 The set created with the static projects and the calculations made according to *[8]*

Bldg. No	Design Code	RYTEİE (2019)	$V_{yw,X}$	$V_{yw,Y}$	V_{CODE}	BCPI	CPI
		PP	(kN)	(kN)	(kN)		
1	1975	-5	1985.0	3349.8	2414.6	0.82	0.64
2	1975	-25	2437.8	2353.7	2203.2	1.07	0.83
3	2007	95	952.7	1295.9	914.4	1.04	0.89
4	**2007**	75	1572.1	3095.5	1132.0	1.39	**1.08**
5	1975	55	1655.9	1698.1	2283.6	0.73	0.57
6	**1968**	-30	2328.7	1689.4	1153.0	1.47	**1.14**
7	1998	5	1149.8	1221.6	1374.9	0.84	0.65
8	**1998**	55	2576.3	2458.3	1341.2	1.83	**1.43**
9	**1975**	-20	3785.5	5435.2	1650.9	2.29	**1.79**
10	**1975**	-45	3216.5	4618.1	1650.9	1.95	**1.52**
11	**1975**	10	3216.5	4618.1	1650.9	1.95	**1.52**
12	1975	25	3016.5	2366.3	2869.1	0.82	0.64
13	1975	-25	3110.3	2440.0	2758.2	0.88	0.69
14	1975	25	3547.7	2783.1	2758.2	1.01	0.79
15	2007	75	924.2	1257.2	850.0	1.09	0.92
16	1975	-30	2738.8	2981.9	2740.0	1.00	0.78
17	1975	-25	3248.9	3537.3	2740.0	1.19	0.92
18	1975	45	3723.8	4382.5	4934.9	0.75	0.59
19	**2007**	65	6302.9	6133.2	4916.8	1.25	**1.06**
20	**2007**	65	7181.4	6988.0	4916.8	1.42	**1.21**
21	**2007**	65	6207.8	6040.7	4916.8	1.23	**1.04**
22	**2007**	65	6578.0	6400.8	4916.8	1.30	**1.11**

23	1998	95	4319.0	3164.0	3670.5	0.86	0.67
24	1975	15	2919.0	1759.6	2058.1	0.85	0.67
25	2007	-40	5321.4	2919.7	3348.0	0.87	0.74
26	2007	-45	1170.0	1295.3	1096.9	1.07	0.83

In Table 7 and Fig. 10-11, it can be observed that 9 of the buildings have a value less than one. 15 buildings are expected to be risky via CPI value. While calculating the CPI values, it is assumed that the ratio of the infilled wall area to the total construction area is 0.02. The soil class was assumed as ZC, reflecting Muğla in general. The buildings which were built according to the 1975 Earthquake Code [13] with large column sizes and good concrete quality are evaluated as non-risky.

In Fig. 12, the performance scores [2] and CPI [8] values are plotted. The number of buildings compared with preliminary analysis is for sure not enough to make a certain conclusion, however, even with good performance score the CPI values are below 1.0 even the proposed value for CPI is 1.2 [8].

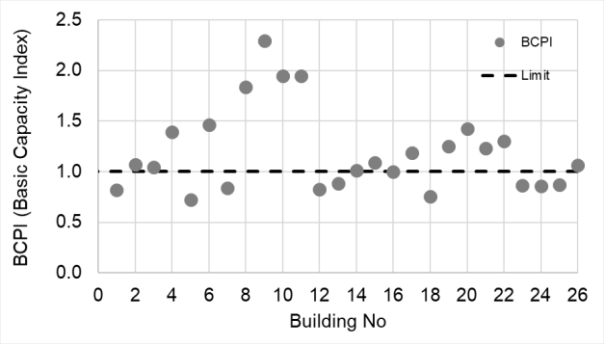


Figure 10 Basic Capacity Index Values (BCPI)

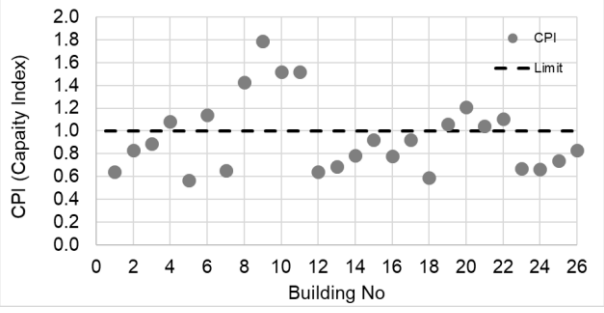


Figure 11 Capacity Index Values (CPI)

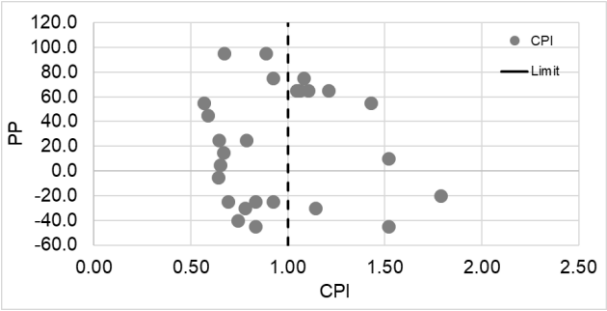


Figure 12 Capacity Index Values (CPI) [8] vs Performance Score [2]

Conclusion and Discussion

In this study, seismic risk assessment of existing RC building stock in Emirbeyazıt Neighborhood of Muğla investigated by using the walk-down survey method [2] and preliminary assessment method [8]. 461 RC buildings investigated and 26 RC buildings of them examined in detail. Based on the results of this research, the following key conclusions are derived and discussions come out:

- The main reason for using two methods for research is the determine the risk level of buildings that should be prioritized for a comprehensive risk mitigation plan.
- The majority of the buildings suffer from the heavy overhang and vertical irregularity deficiencies. The lowest performance score was calculated as -118 and the maximum as 145 according to [2].
- The ranking system [2] needs a threshold to differ the risky and non-risky buildings to make a risk mitigation plan in short budget, otherwise the decision makers such as municipalities cannot lose the focus on their risk mitigation plans.
- In preliminary assessment analysis 15 of 26 buildings are not passing the CPI threshold value and therefore they can be labeled as Risky.
- The buildings built according to the 1975 Earthquake Code [13] with large column sizes and good concrete quality are classified as non-Risky according to the preliminary risk assessment analysis [8].
- The results of the preliminary analysis showed that if the existing building is designed according to the specification [2], it may have bad performance score, however, the CPI value may become higher such as building 6 in Table7.
- The results of this study will provide a data source for future seismic risk mitigation plan for Muğla. The current study can be extended to a larger area also including masonry structures.

Ethics committee approval and conflict of interest statement

"There is no conflict of interest with any person / institution in the article prepared"

Authors' Contributions

-Study conception and design: Akansel, Baki
-Acquisition of data: Akansel and Baki
-Analysis and interpretation of data: Akansel and Baki
-Drafting of manuscript: Akansel and Baki
-Critical revision: Akansel
-Site Investigation: Baki

Acknowledgement

This work presented here is supported in part by Scientific and Technological Research Council of Turkey (TUBITAK) and the authors very much appreciate the support by the Muğla, Menteşe Municipality.

References

[1] H. A. Alcik, G. Tanircan and A. Korkmaz, "Bodrum Strong Motion Network, Mugla, Turkey.," in *In AGU Fall Meeting Abstracts*, 2015.

[2] RYTEİE, "Riskli yapıların tespit edilmesine ilişkin esaslar," T.C. Çevre, Şehircilik ve İklim Değişikliği Bakanlığı (Altyapı ve Kentsel Dönüşüm Hizmetleri Genel Müdürlüğü). , Ankara, 2019.

[3] ATC-21, "Rapid Visual Screening of Buildings for Potential Seismic Hazards: A Handbook, FEMA-154," Applied Technology Council, Redwood City, California., 2002.

[4] O. Coskun, A. Aldemir and M. Sahmaran, "Rapid screening method for the determination of seismic vulnerability assessment of RC building stocks," *Bulletin of Earthquake Engineering,* vol. 18, no. 4, pp. 1401-1416, 2020.

[5] A. F. Hassan and M. A. Sozen, "Seismic vulnerability assessment of low-rise buildings in regions with infrequent earthquakes," *ACI Structural Journal,* vol. 94, no. 1, pp. 31-39, 1997.

[6] T. Shiga, A. Shibata and T. Takahashi, "Earthquake Damage and Wall Index of Reinforced Concrete Buildings," in *Tohuku District Symposium, Architectural Institute of Japan*, Tohuku, 1968.

[7] H. Sucuoğlu, U. Yazgan and A. Yakut, "A screening procedure for seismic risk assessment in urban building stocks," *Earthquake Spectra,* vol. 23, no. 2, pp. 441-458, 2007.

[8] A. Yakut, "Preliminary seismic performance assessment procedure for existing RC buildingss," *Engineering Structures,* vol. 26, no. 10, pp. 1447-1461, 2004.

[9] A. Yakut, H. Sucuoğlu, B. Binici, E. Canbay, C. Donmez, A. İlki, ... and B. Ö. Ay, "Performance of structures in İzmir after the Samos island earthquake," *Bulletin of Earthquake Engineering,* pp. 1-26, 2012.

[10] TBEC, "Turkish Building Seismic Code," Prime Ministry, Disaster and Emergency Management Presideny (AFAD), Ankara, 2018.

s[11] P. Gulkan and M. A. Sozen, "Procedure for determining seismic vulnerability of building structures," *Structural Journal,* vol. 96, no. 3, p. 336, 1999.

[12] ABYBHY, "Afet bölgelerinde yapılacak yapılar hakkında yönetmelik," T.C. Bayındırlık ve İskan Bakanlığı, Afet İşleri Genel Müdürlüğü, Deprem Daire Başkanlığı, Ankara, 1968.

[13] ABYBHY, "Afet bölgelerinde yapılacak yapılar hakkında yönetmelik," T.C. Bayındırlık ve İskan Bakanlığı, Ankara, 1975.

[14] ABYBHY, "Afet bölgelerinde yapılacak yapılar hakkında yönetmelik," T.C. Bayındırlık ve İskan Bakanlığı, Afet İşleri Genel Müdürlüğü, Deprem Araştırma Dairesi, Ankara, 1999.

[15] DBYBHY, "Deprem Bölgelerinde Yapılacak Binalar Hakkında Yönetmelik," T.C. Bayındırlık ve iskan Bakanlığı, Afet İşleri Genel Müdürlüğü, Deprem Araştırma Dairesi , Ankara, 2007.

[16] H. Özkaynak and A. E. Ö. Özbay, "Seismic Vulnarability Assessment of Reinforced Concrete Buildings Located in Esenler District of İstanbul," *Afyon Kocatepe Üniversitesi Fen Ve Mühendislik Bilimleri Dergisi,* vol. 18, no. 1, pp. 285-294, 2018.

[17] M. Ş. Balaban, "Marmara depremlerinin 20. yılında kentlerimiz doğal ve çevresel tehlikelere hazır mı?," vol. 56, no. 409, pp. 22-24, 1997.